CRANFIELD UNIVERSITY

PABLO BELLOCQ

MULTI-DISCIPLINARY PRELIMINARY DESIGN ASSESSMENTS OF PUSHER COUNTER-ROTATING OPEN ROTORS FOR CIVIL AVIATION

SCHOOL OF ENGINEERING
POWER AND PROPULSION

PhD THESIS

Supervisor: Dr. V. Sethi
December 2012

CRANFIELD UNIVERSITY

SCHOOL OF ENGINEERING
POWER AND PROPULSION

PhD

PABLO BELLOCQ

MULTI-DISCIPLINARY PRELIMINARY DESIGN ASSESSMENTS OF PUSHER COUNTER-ROTATING OPEN ROTORS FOR CIVIL AVIATION

Supervisor: Dr. V. Sethi
December 2012

ABSTRACT

As a consequence of fuel cost escalation and increased stringent engine emission regulations, interest in counter-rotating open rotor engines (CRORs) has been renewed. R&D efforts are currently ongoing to develop the technologies required to ensure the appropriate levels of structural integrity, noise, vibrations and reliability.

The assessment of the impact of the main low pressure preliminary design and control parameters of CRORs on mission fuel burn, certification noise and emissions is necessary to identify optimum design regions. These assessments aid the development process when compromises need to be performed as a consequence of design, operational or regulatory constraints. These assessments are not possible with the state-of-the-art aero-engine preliminary design simulation tools.

Novel 0-D performance models for counter-rotating propellers (CRPs) and differential planetary gearboxes, as well as 1-D and 0-D performance models for counter-rotating turbines (CRTs) were developed and verified using available data. These models were used to create 0-D pusher geared (GOR) and direct drive (DDOR) open rotor engine performance simulation modules allowing the independent definition of the design and operation of each of the two counter-rotating parts of the CRP and CRT.

A multi-disciplinary preliminary design simulation framework was built using the novel engine performance modules together with dedicated CROR aircraft performance, engine geometry and weight, gaseous emissions and certification noise simulation modules. Design space exploration and trade-off studies were performed and minimum fuel burn design regions were identified for both the pusher GOR and DDOR. A 160 PAX aircraft flying a business mission of 500 NM was chosen for these studies.

Based on the assumptions made, the main conclusions of these studies are as follows.

- Fuel burn reductions of ~1-2% are possible through optimised propeller control
- The propeller diameter for minimum mission fuel burn lies between 4.26 and 4.7 m
- The design nozzle pressure ratio for minimum mission fuel burn lies between 1.55 and 1.6
- CRPs with 13 or 14 blades per propeller provide minimum mission fuel burn
- Increasing spacing between the propellers reduces noise significantly (~6 EPNdB for each certification point) with a relatively small fuel burn penalty (~0.3-0.5%)
- Relative to unclipped designs, 20% clipped CRPs reduce flyover noise by at least 2.5 EPNdB and approach noise by at least 4.5 EPNdB. The corresponding fuel burn penalty is ~2 % for a GOR and ~3.5% for a DDOR.
- Sideline and flyover noise can be reduced by increasing the diameter of the CRP and appropriately controlling CRP rotational speeds. Approach noise can be reduced by either reducing the diameters or the rotational speeds of the propellers.
- The rotational speed of the forward propeller for minimum noise is higher than that for minimum mission fuel burn for all the studied CROR designs.
- Regardless of clipping, reducing the rotational speed of the rear propeller relative to the forward propeller reduces noise and, to a certain limit, also mission fuel burn. (further reductions in rotational speed would have an adverse effect on fuel burn)
- An increase in the number of blades results in an increase in certification noise.

The main recommendations for further work are as follows.

- Integrating the 1-D CRT model with the 0-D DDOR performance model in order to assess the impact of different CRT design criteria at engine and mission levels
- Developing preliminary design methods to account for changes in aircraft weight and aerodynamics due to changes in engine design and required cabin noise treatment.

To my wife and sons

ACKNOWLEDGEMENTS

I would like to gratefully thank:

- Professor Pericles Pilidis for giving me the opportunity of doing this PhD and Dr Vishal Sethi for his supervision and continuous support.
- Nicolas Tantot for his technical guidance and continuous support during this project.
- Emidio Giordano, Kosmas Kritikos, Gunter Kapler, Bernard Lehnmayer, Olivia Argos, Holger Lipowsky, Heidemarie Jäger, Tomas Gronstedt, Luca Cerasi, Jaime Martinez, Sebastian Ahlefelder, Jordane Legrand, Alexis Patin and Stefano Capodanno for their direct contribution to the development of the OR-TERA2020 simulation platform.
- Dr. Ken Ramsden, Dr. Anthony Jackson, Dr. David Mac Manus, Dr. John Baurradaile, Professor Herbert Saravanamuttoo, Manuel Morales, Dr. Joachim Kurzke, Almudena Rueda, Pedro Covas, Fernando Martinez and Dr. Alex Alexiou for their technical advice and support.
- Gill, Nicola, Clare, Mandy and Josh for their constant help
- My friends Rajeve ,Cesar, Raja, Andy, Badar, Martin, Yan, Giusepina, Panagiotis, Alice, Thierry, Erminio, Luis, Pericles, Ioannis, Rukshan, Wei Chung, Tom, Esmail, Emad, Atma, Bupendra, Domenico, Julian, Therese, Nachin, Mary, Barbara, Shirley, Alaistair, Marc, Alline, Elodie, Thomas, Manuel, Jesus Maria, Jacinto, Jorge, Joseba, Ignacio, Yann, Fernando, Fabian, Martin, Pedro, Veronica, Iñaki, Fr. Joe, Pablo, Javier, Peter, Alvaro, Miguel, Rafi, George, Vera, Mikel, Iker, Angel, Pierre, Tekena, Paulas, Ela, Agustina, Carlos, Ikena, Eni, Paco, Thibaut, Bernat, Elena, Cannon Seamus, Ramon, Peter, Aaron, Ryan, Clair, Giacomo, Susan, Rita, Giuseppe, David, Patrick, Romain, Fabien, Bernard, Laurent, Mathieu, Maxime and Jean-Christophe for the support they gave me during the PhD and the good moments we spent together.
- Fr Kenn for his quintessential friendship and the pastoral care he gives to Cranfield students.

Finally, I would like to thank my family, specially my wife and sons, for their continuous support and endless patience.

The research leading to these results has received funding from the European Union Seventh Framework Programme (FP7/2007-2013) under grant agreement n° 211861.

TABLE OF CONTENTS

NOMENCLATURE

Abbreviations

0-D	dimensionless (zero dimensions)
1-D, 2-D, 3-D	one, two and three dimensions
AEA	Association of European Airlines
ATF	Advanced Turbofan
BETA	Parameter used to define the position of a point in a constant speed line of a compressor map
BPR	Bypass Ratio
Clipping	Reduction of rear propeller diameter with respect to the forward propeller diameter (defined as a roman symbol).
CFM	CFM International (consortium between GE and SNECMA)
CR	Counter Rotating
CROR	Counter Rotating Open Rotor
CRP	Counter Rotating Propeller
CRPe	CRP PROOSIS components used for engine calculations
CRPv	CRP PROOSIS components used for verification calculations
CRT	Counter Rotating Turbine
CRT-DPe	1-D mean line code used to size a CRT
CRT-DPv	1-D mean line code used to verify the 1-D performance methodology developed for CRTs
CRT-OD	1-D mean line code used to predict OD performance of a CRT
CRT-k	Known CRT design used for verification purposes
CU	Cranfield University
DDOR	Direct Drive counter rotating Open Rotor
DP	Design Point
DPGB	Differential Planetary GearBox
DREAM	valiDation of Radical Engine Architecture systeMs
EAS	Equivalent Air Speed
EI	Emissions Index
EPNL	Effective Perceived Noise Level
EU	European Union
EU ETS	European Emissions Trading Scheme

FF	Form Factor of the velocity triangles of a CRT
FOB	Free On Board or Freight on Board
Foo	Maximum engine take-off thrust at ISA SL as approved by the certificating authority
FPR	Fan Pressure Ratio
GE	General Electric
GOR	Geared counter rotating Open Rotor
GTF	Geared Turbofan
Hermes	Aircraft performance simulation code developed by Cranfield University
HP	High Pressure
HPC	High Pressure Compressor
HPT	High Pressure Turbine
ICAO	International Civil Aviation Organisation
IGV	Inlet Guide Vane
IP	Intermediate Pressure
IPC	Intermediate Pressure Compressor
IPT	Intermediate Pressure Turbine
ISA	International Standard Atmosphere
LP	Low Pressure
LPC	Low Pressure Compressor
LPT	Low Pressure Turbine
LTO	Landing and Take-Off
M	Mach number (also defined as Roman symbol)
MF	Mid Frame (frame between the IPT and LPT or CRT)
MTOW	Maximum take-off weight (also defined as Roman symbol)
NASA	National Aeronautics and Space Administration
NOx	Nitrogen Oxide
NPR	Nozzle Pressure Ratio (also defined as Roman symbol)
NUMECA	CFD software
OD	Off Design
OEM	Original Equipment Manufacturer
OR	Open Rotor
P&W	Pratt & Whitney
PAX	Passengers

PC	Personal Computer
PCM	Pitch Change Mechanism
PROOSIS	PRopulsion Object Oriented SImulation Software
SFC	Specific Fuel Consumption (also defined as a Roman symbol)
SLS	Sea Level Static
SME	Small and Medium Enterprise
SNECMA	Société Nationale d'Etude et de Construction de Moteurs d'Aviation
SPL	Sound Pressure Level
SR	Single Rotating
Stage-DP	Calculation brick used in the 1-D mean line CRT DP calculations
Stage-OD	Calculation brick used in the 1-D mean line CRT OD calculations
TENOR	TEra Noise module for Open Rotor
TET	Turbine Entry Temperature (K)
TOC	Top Of Climb
TR	Torque Ratio (also defined as Roman symbol)
UHC	Unburned HydroCarbons
USA	United States of America
WeiCo	Preliminary mechanical design code developed by Chalmers University
ZETA	Parameter used to define the position of a point in a constant speed line of a turbine map

Roman Symbols

A	Area (m^2)
Aeff	Effective flow area (m^2)
Aeff rel	Effective flow area with respect to relative velocity (m^2)
Alt	Altitude (m)
A_{disk}	Propeller disk area (πr^2 - hub area) (m^2)
AxialChord	Axial blade chord
AR	A function of aspect ratio of the blade (-)
BETA	Parameter used to define the position of a point in a constant speed line of a compressor map
$blade_h$	Blade height (m)
c	Speed of sound (m/s)
C_L	Lift coefficient

Clipping	Reduction of D_1 with respect to D_2 (-). $\text{Clipping} = 100\frac{D_1 - D_2}{D_1 - D_h}$
Chord	Blade chord
C_P	Power coefficient (-)
$C_{P\,TOT}$	Overall CRP power coefficient (calculated using Pw_1+Pw_2) (-)
Cp	Specific heat capacity at constant pressure (J/(kg K))
C_{RE}	Reynolds correction for Y_P (-)
C_T	Thrust coefficient (-)
Cv	Specific heat capacity at constant volume (J/(kg K))
D	Diameter (m)
dISA	Deviation from ISA temperature (K)
Drag	Aircraft Drag (N or kN)
EI	Emissions index (-)
EINOx	NOx emissions index (-)
FAR	Fuel to air ratio (-)
FF	Form factor of the velocity triangles of a CRT
Fn	Net thrust (N or kN)
Fg	Gross thrust (N or kN)
Foo	Maximum engine take-off thrust at ISA SL as approved by the certificating authority (kN)
h	Specific enthalpy (J/kg)
Heat	Heat rejected by an engine component (W or kW)
ht	Total specific enthalpy (J/kg)
hum	Specific humidity (kg water / kg dry air) (-)
i	Incidence (º)
J	Advance Ratio (-)
LHV	Low heating value (kJ)
K	Constant (-)
k	Shroud seal clearance (-)
KE	Kinetic energy (J or KJ)
$KE_{increase}$	Increase in kinetic energy (J or KJ)
K_{LP}	Propeller efficiency technology factor (-)
L_P	Propeller power loading (Pw_{mech}/A_{disk}) (kW/m^2)
M	Mach number (-)
m	mass (kg)
$\dot{m}$	mass flow rate (kg/s)
M^*rel_{out}	Guessed relative outlet Mach number in 1-D mean line CRT code
$M^*_{h0.75}$	Critical Mach number for propeller compressibility corrections
M_0	Flight M (-)
Mabs	Absolute Mach number (-)
MTOW	Maximum take-off weight (kg)
Mrel	Relative Mach number (-)
N	Rotational peed (rpm)
n	Rotational peed (revolutions/s = N/60)
N_b	Number of blades of a propeller(-)

Nb	Number of blades of a turbine (-)
NbStages	Number of stages (-)
NbSeals	Number of seals in a turbine shroud (-)
NPR	Nozzle Pressure Ratio ($Pt_{nozzle\ in}$ / P_{amb}) (-)
nR	Speed ratio of the CRT or CRP (n_1 / n_2 = N_1 / N_2) (-)
o	Turbine throat opening (m)
P	Pressure (Pa)
P3	Total pressure at combustor inlet (Pa)
Ps	Static pressure (Pa)
Pt	Absolute total pressure (Pa)
Pt rel	Relative total pressure (Pa)
PQA	Modified propeller power coefficient (-)
PR	Pressure ratio (-) (Compressors = Pt_{out}/Pt_{in}. Turbines = Pt_{in}/Pt_{out})
Pw	Power (W or kW)
PwR	CRT Power Ratio (Pw_{drum1} / Pw_{drum1}) (-)
Pw_{stage}	Power extracted in a turbine stage (W or kW)
Q	Torque (Nm)
R	Gas constant (Cp – Cv) (J/(kg K))
RAM	Ram drag (N)
r	Radius (m)
rR	Radius ratio of the gears of a DPGB (r_{Planet}/r_{Sun}) (-)
SE	(Space) / (mean radius of curvature of the blade suction surface between the throat and the trailing edge) (-)
SF	Scaling factor used to scale a component map (-)
SFC	Specific Fuel Consumption (g/(kN s)) (fuel flow rate/Thrust)
$Slope_{Mcor}$	Mach number effects correction slope (-)
Stagger	Blade stagger angle (^{o})
T	Temperature (K)
t	Time (s)
T3	Total temperature at combustor inlet (K)
t_{MAX}	Maximum turbine blade thickness (m)
t_{TE}	Trailing edge blade thickness (m)
Ts	Static temperature (K)
Tt	Absolute total temperature (K)
Tt rel	Relative total temperature (K)
TQA	Modified propeller thrust coefficient (-)
TR	Torque Ratio (-) Q_1/Q_2 for the CRP Q_{drum1}/Q_{drum2} for the CRT $Q_{Carrier}$ / Q_{Ring} for the DPGB
U	Mid span blade tangential velocity (m/s)
V	Velocity (m/s)
V_0	Flight velocity (m/s)
Vabs	Absolute velocity (m/s)
Vind	Propeller induced velocity (m/s)
Vrel	Relative velocity (m/s)
V_j	Jet velocity (m/s)

Weight	Weight of the aircraft (kg)
Y_P	Pressure loss coefficient of profile losses (-)
Y_{P1}	Pressure loss coefficient of profile losses of an axial inlet turbine stage (-)
Y_{P2}	Pressure loss coefficient of profile losses of an impulse turbine stage (-)
Y_{PA}	Low subsonic speed pressure loss coefficient of profile losses (-)
Y_S	Pressure loss coefficient of secondary losses (-)
Y_{SA}	Low subsonic speed pressure loss coefficient of secondary losses (-)
Yt	Total pressure loss coefficient (-)
Y_{TC}	Pressure loss coefficient of tip clearance losses (-)
Y_{TE}	Pressure loss coefficient of trailing edge losses (-)
z_{12}	Axial distance between roots of the forward and rear propellers (m)
ZETA	Parameter used to define the position of a point in a constant speed line of a turbine map

Greek Symbols

α	Absolute flow angle (º) used in 1-D CRT calculations
β	Relative flow angle (º) used in 1-D CRT calculations
β'	Relative flow angle (º) sign adapted to loss calculations conventions
$\beta_{0.75}$	Blade angle at 0.75 radius (º) used in CRP calculations
β_{metal}	Blade metal angle (º) used in 1-D CRT calculations
β'_{metal}	Blade metal angle (º) sign adapted to loss calculations conventions
Δ	Variation (out-in)
γ	Heat capacity ratio (Cp/Cv) (-)
η	Efficiency (-)
η^*	Guessed value of efficiency (-)
η_{NET}	Propeller net efficiency (-)
ρ	Density (kg/m^3)
μ	Dynamic viscosity kg/(m s)
ψ	Stage loading coefficient ($\Delta h/U^2$) (-)
Φ	Flow coefficient (V_A/U) (-)
ϕ_P	Kinetic energy loss coefficient of the profile losses (-)
ϕ_{TE}	Kinetic energy loss coefficient of the trailing edge losses (-)
ϕ_{Ax}	Kinetic energy loss coefficient of the trailing edge losses of an axial inlet turbine stage (-)
ϕ_{Imp}	Kinetic energy loss coefficient of the trailing edge losses of an impulse turbine stage (-)
ζ	Enthalpy loss coefficient (-)
Ωind_{12}	Angular velocity induced by Propeller 1 on Propeller 2 (rad/s)

Subscripts

1	Forward propeller, first stage of the CRT or external drum of the CRT (connected to the forward propeller)
2	Rear propeller, second stage of the CRT or internal drum of the CRT (connected to the rear propeller)
11	Propeller 1 on propeller 1 (auto induced)
12	Propeller 1 on propeller 2
21	Propeller 2 on propeller 1
22	Propeller 2 on propeller 2 (auto induced)
A	Axial
amb	Ambient
blade	Blade
COR	Corrected
CRT	Counter-rotating turbine
Des	At design point
DPGB	Differential planetary gearbox
drum1	Exterior drum of the CRT linked to the first stage of the CRT and the forward propeller
drum2	Interior drum of the CRT linked to the last stage of the CRT and the rear propeller
even	Corresponding to even CRT stages
h	Hub
i	i^{th} stage
im	Imaginary
in	Inlet
int	corresponding to CRT stages between and including 2 and (NbStages-1)
is	Isentropic
ISA	International standard atmosphere conditions
LE	Leading edge
LPT	Low power turbine
odd	Corresponding to odd CRT stages
out	Outlet
Ov	Overall
map	Used to read or obtained from a map of a component
mean	mean ($r_{mean} = (r_{tip} + r_{hub}) /2$)
mech	Mechanical
NbStages	Total number of CRT stages
partial	Not considering the last stage of the CRT
Path	Corresponding to the gas path
Prop	Propulsive
rd	Representative drum
Rdes	Relative to the design value
Ref	Reference
req	Required
SLS	Sea Level Static

Scoop	Corresponding to the inlet of the air cooling system of the DPGB
T	Tangential
Th	Thermal
tip	blade tip

1 INTRODUCTION

1.1 Context

This section presents the counter rotating open rotor engines (CROR) in the present civil aviation context. It also provides a historical view of the use and developments of CRORs as well as the technological challenges they face. The need for a multi-disciplinary preliminary design assessment of this engine architecture at mission level is identified. A literature review of the existing open rotor preliminary design assessments, simulation tools and modelling methodologies is also included. These elements conduce to the definition of the project objectives and methodology and put the contribution to knowledge of this PhD thesis into perspective.

1.1.1 Civil aviation

There are four main factors that currently influence the civil aviation industry:

- Market demand: Over the past 20 years, the air transport industry has experienced a constant average growth of 5% per year [Ref. 1]. The same rate of growth is forecasted for the next 20 years [Ref. 1]. The short range market is the largest contributor to this growth. In USA, Europe and the emergent economies such as China and India more than half of the passengers fly for less than two hours. In the USA in 2007 there were two connecting passengers for every local passenger [Ref. 2] suggesting that long range flights are normally fed from other short range flights.

- Fuel price: Although the price of Jet-A is highly unstable, an average increase tendency has been observed since 1999 (Figure 1). From January 2000 to July 2011, the average of the USA airlines global operating cost increased by 163% [Ref. 4]. In this same period, the fuel price increased by 267% being one of the main drivers of the global operating cost (insurance increased by 56% and airport fees by 62%) [Ref. 4]. In 2007, fuel cost represented 37% of the direct operating cost, and 23% of the global operating cost of the average European airline [Ref. 5][1].

[1] This was the last “Operating Economy of AEA Airlines” report published by the Association of European airlines. More recent European airlines cost statistics were not found.

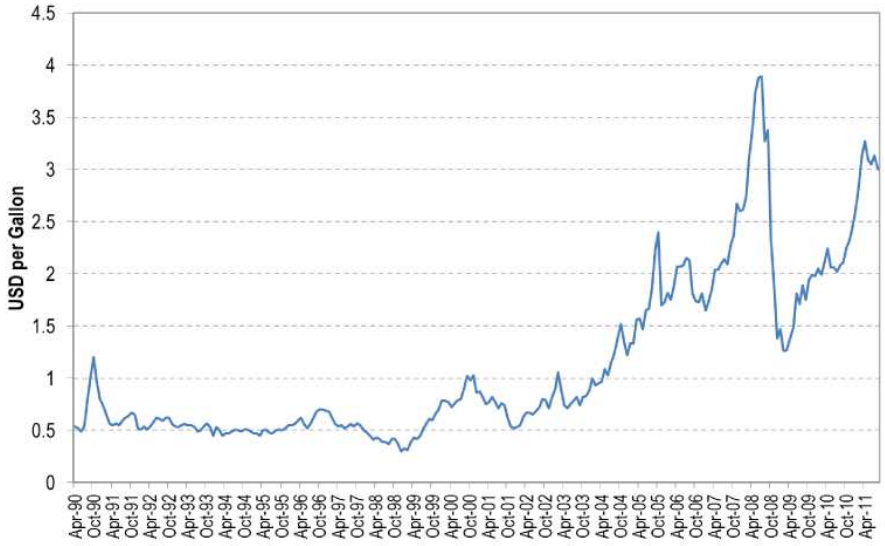

Figure 1: U.S. Gulf Coast Kerosene Jet-A Spot Price FOB Apr 90 - Apr 11[2]

- Certification:
  - Gaseous emissions: In 1998 air transport deemed was responsible for 7.2% of global transportation emission, in terms of greenhouse gases and other pollutants, and it was estimated to be 10.9% in 2010 [Ref. 3]. Engine gaseous emissions regulations have became more stringent since December 2007, in particular with respect to landing and take-off (LTO) NOx emissions. Engines applying for certification after December 2007 are required to comply with the requirements stated in the ICAO Annex 16 Volume II [Ref. 6].
  - Noise: Aircraft noise regulations have become more stringent since 2006. Aircraft applying for certificate of airworthiness after January 2006 have to comply with the requirements defined in Chapter 4 of the ICAO Annex 16 Volume I [Ref. 7].
- European Emissions Trading Scheme (EU ETS): The EU ETS is a regulatory framework that obliges the main EU CO_2 emitters to monitor their CO_2 emissions, report them, and pay a proportional allowance. According to article 16 in Ref. 8, the emissions from all flights arriving at and departing from European airports, should have been included in the EU ETS from 2012.

To ensure economic and environmental sustainability of the civil aviation sector in the present context, significant improvements in terms of fuel burn, gaseous

[2] Plotted using data published by the US Energy Information Administration on its website http://www.eia.gov.

emissions and noise must be achieved by aircraft and engine manufacturers as well as operators, without diminishing the present comfort, safety and security standards. Bodies like the Advisory Council for Aeronautics Research in Europe (ACARE) have set ambitious intermediate and long term targets for civil aviation including improvements in fuel burn, gaseous and noise emissions, and safety amongst others. The ACARE goals for 2020 are reductions of 50% in perceived noise, 50% in fuel burn and CO_2 and 80% in NOx emissions relative to year 2000 in-service technologies [Ref. 47]. For 2050 the goals are reductions of 65% in perceived noise, 75% in fuel and CO_2, and 90% in NOx emissions relative to year 2000 technologies [Ref. 48]. These improvements can be achieved by implementing technologies for novel aircraft and powerplant systems as well as optimising operational rules [Ref. 9]. With respect to the 2020 goals, ACARE further suggests that improvements in propulsion technologies alone could contribute to reductions of 6dB per operating point, 60 to 80% NOx emissions and 15 to 20% fuel consumption relative to year 2000 engines.

“In the present situation, the key for the airlines economic success is the introduction of right sized new aircraft. For this reason there are very high expectations on the 100 to 200 airliners replacements” [Ref. 2]. This statement describes the market needs at the start of this research project (2008). Consequently this work focuses on 100 - 200 passenger aircraft which correspond to the payload of Airbus A320 and Boeing 737 families.

During the first year of this PhD project, the main aircraft manufacturers were about to launch their 100-200 passengers (PAX) replacement programmes and were evaluating the following engine technologies:

- Advanced high bypass ratio turbofan (ATF) proposed by IAE and CFM: The high bypass ratio turbofan is the engine technology currently used in the Airbus and Boeing aircraft families (Figure 2). They were developed during the 60s and they are nowadays approximately 20% more efficient than their initial versions, thanks to the gradual introduction of technological improvements. The extensive introduction of the latest advances in aerodynamics, materials, cooling and burner technologies can still yield further efficiency improvements. In July 2008, the CFM consortium started developing their next generation turbofan engine, named LEAP, promising to be 16% more efficient than today’s best engines [Ref. 10]

Figure 2: High bypass ratio turbofan engine [Ref. 116]

- Geared Turbo Fan (GTF) proposed by Pratt & Whitney (P&W): The GTF consists of a turbofan engine in which the fan is linked to the low pressure turbine (LPT) through a gearbox. This gearbox allows the LPT and the fan to rotate at their optimum speeds, increasing the engine overall efficiency. P&W announced that the first GTFs to be certified on a 150 passenger aircraft will be 15% more fuel efficient than a year 2000 turbofan [Ref. 11]. This technology also offers lower noise levels and higher resistance to foreign objects ingestion than conventional turbofans, due to the relatively lower fan rotational speeds.

- Counter Rotating Open Rotors proposed by Rolls Royce and CFM: The CROR is an advanced turboprop with counter rotating propellers (see Figure 3). The first CROR preliminary designs and demonstrators date from the 80s (after the two severe oil crises of the 70s). They were designed to fly faster than turboprops (cruising at M0.75 - 0.85, very close to turbofan powered aircraft) while significantly reducing the fuel consumption with respect to turbofans due to their relatively higher propulsive efficiency [Ref. 12]. Three successful technology demonstrators were flown at the end of the 80s but significant development efforts were still required to ensure the appropriate levels of structural integrity, noise, vibrations and reliability [Ref. 13]. At the end of the 80s as the oil price reduced significantly and since environmental impact was not considered to be as important as today, the required development efforts were not economically justified. Consequently, none of the demonstrated concepts were selected to power commercial aircraft and the CROR development activities were abandoned. A description of the CROR benefits, the different possible engine architectures and the technological challenges associated to them is provided in section 1.1.2.

Figure 3: CROR engine [Ref. 117]

Still today, the introduction of the CROR technology into the commercial aviation represents a major challenge for engine and aircraft manufacturers, as well as for certification authorities due to the differences with respect to conventional turbofan technology.

During the course of the present research project, the ATF and the GTF were selected to power the new generation 100 to 200 PAX aircraft, as shown in Table 1.

Engine	ATF		GTF		Both
	LEAP-1B	LEAP-1C	PW1500G	PW1400G	LEAP-1A/PW1100G
Air-framer	Boeing	Comac	Bombardier	Irkut	Airbus
Country	USA	China	Canada	Russia	France - Europe
Programme	737 Max	C919	CS series	MS-21	A320 neo
PAX	108 - 215	168 - 190	100 - 145	150 - 230	124 - 220
Launched in	Aug 2011	Dec 2009	July 2008	Dec 2009	Dec 2010
First delivery	2017	2016	2013	2017	2015

Table 1: 100 – 200 PAX aircraft programmes launched since January 2008

The CROR engines were not selected for the aircraft programmes listed in Table 1 since they were not mature enough to be certified in the required timescale. At the same time, open rotors appear to have a higher technology readiness level than thermal efficiency enhancing disruptive technologies like wave rotors, pulse detonators and constant volume combustors. Consequently, the CROR is a strong candidate to power the next generation civil aircraft and its multi-disciplinary preliminary design assessment is the focus of the present research work.

1.1.2 Open rotor engines

Open rotor (OR) engines, also called prop-fans, are advanced turboprop engines capable of flying at relatively high subsonic speeds (Mach 0.7 to 0.85) and altitude (35000ft to 39000ft) while maintaining high propulsive efficiency [Ref. 14].

Conventional turboprop engines can be efficiently used up to a flight Mach number (M_0) of 0.6, but further increase in flight speed results in drastic efficiency losses due to compressibility effects [Ref. 15]. The OR high efficiency operation at high speeds is possible thanks to the use of advanced propeller designs incorporating highly loaded, swept back and transonic profiled propellers [Ref. 14]. The previously mentioned propeller features were investigated in wind tunnels during the 40s and 50s [Ref. 16 to Ref. 18], but were not brought into flight demonstrators until the late 70s [Ref. 14] due to the success that turbojets and turbofans were having at that time. The term prop-fan was introduced by Hamilton Standard in 1975 [Ref. 19] which presented this concept as an unducted turbofan offering the fuel benefits of the turboprop engine.

OR engines can be classified as either single rotating open rotors (SROR) (equipped with a single propeller) or counter rotating open rotors (CROR) (equipped with two counter rotating propellers) (Figure 4). These engines are also called single rotating propfan and counter rotating propfan respectively.

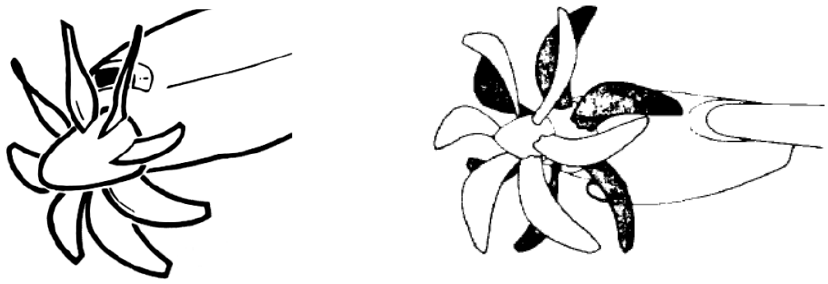

Figure 4: Single rotating OR [Ref. 20] and Counter rotating OR [Ref. 14]

The propeller or propellers can either be mounted in front or at the rear of the OR engine. When the propeller is located in front of the engine it “pulls” the aircraft and it is called a puller or tractor OR. On the contrary, when the propeller is located at the rear of the engine, it “pushes” the aircraft and it is called pusher OR. Figure 5 shows the four possible OR configurations with respect to the type and location of the propeller.

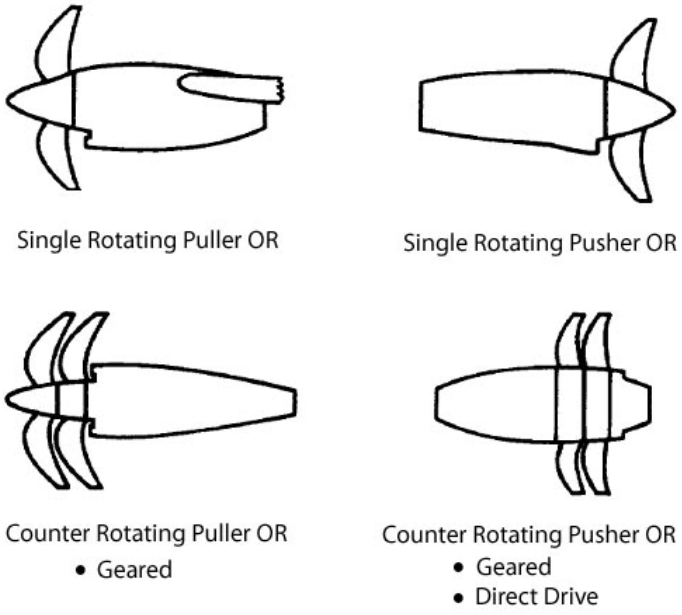

Figure 5: Possible open rotor engine configurations [Ref. 14]

The pusher CROR can be geared or direct drive. The geared architecture features a conventional LPT and its power is transmitted to the counter rotating propeller (CRP) through a gearbox. The direct drive engine has a stator-less counter rotating turbine (CRT) and each propeller is directly linked to one of the two drums composing the CRT. The direct drive puller CROR is not realistic from a mechanical point of view because it requires four concentric shafts. The SRORs are both geared, since a conventional LPT is not feasible at the required propeller rotational speeds. The specific features, advantages and challenges of the different OR configurations are described in the following sections.

1.1.2.1 Improving engine efficiency: benefits of the OR technology

The aim of an aircraft engine is to produce a propelling power. For achieving this, the engine accelerates a certain amount of air, and a certain amount of fuel is burned. Consequently engine overall efficiency can be expressed as:

$$\eta_{Ov} = \frac{Pw_{Aircraft}}{Pw_{Fuel}} = \frac{Pw_{Airflow}}{Pw_{Fuel}} \times \frac{Pw_{Aircraft}}{Pw_{Airflow}} \quad \text{[Eq. 1]}$$

where:

$$\frac{Pw_{Airflow}}{Pw_{Fuel}} = \eta_{Th} \quad \text{[Eq. 2]}$$

$$\frac{Pw_{Aircraft}}{Pw_{Airflow}} = \eta_{Prop} \quad \text{[Eq. 3]}$$

This implies that the overall efficiency of an aero-engine can be improved by either:

A) Improving thermal efficiency

Theoretically, the thermal efficiency of a simple gas turbine cycle (simple Brayton cycle) can be improved by increasing the pressure ratio of the compressors and the combustion temperature. In practice, the maximum thermal efficiency is dictated by the maximum temperature that the high pressure turbine blades can withstand and other technological factors such as the effectiveness of blade cooling technologies and coating technologies [Ref. 21]. An additional limiting factor is the capability to manufacture very small compressor blades (with acceptable performance), which are necessary for the final stages of very high pressure ratio compressors. Figure 6 shows an estimation of the theoretical thermal efficiency of a simple gas turbine cycle using year 2000 technologies (component efficiencies, materials and blade cooling)[3]. According to this study, the highest thermal efficiency is achieved at pressure ratio 50 and turbine entry temperature 2200K. It can also be seen that a realistic year 2000 engine operating at pressure ratio 35 and turbine entry temperature 1700K is only 2% less efficient. This suggests that the technological challenges associated with high pressures and temperatures may not be justified unless new materials and cooling technologies are developed.

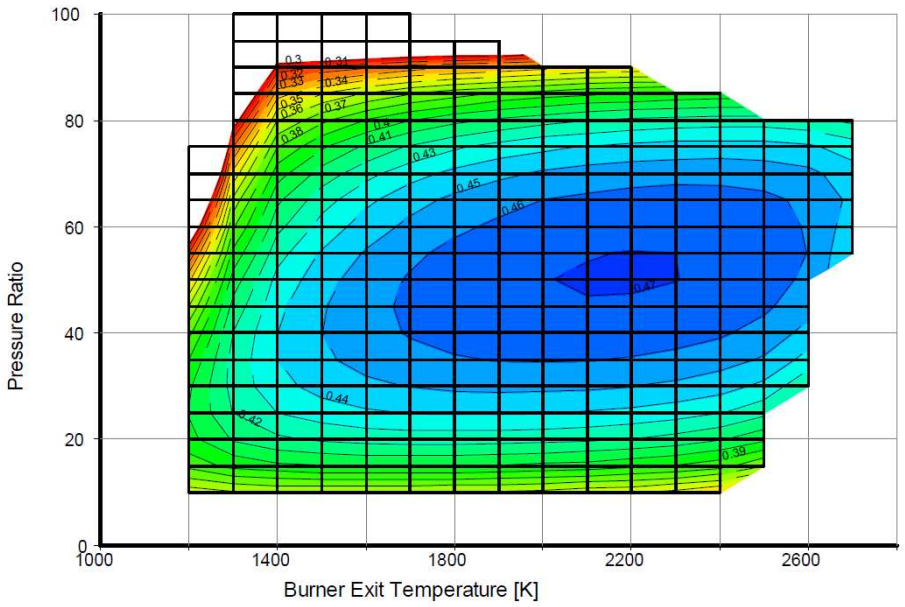

Figure 6: Estimation of a simple gas turbine cycle thermal efficiency using present technology [Ref. 21]

More complex gas turbine cycles, such as the intercooled recuperative cycle, could offer improvements in terms of thermal efficiency [Ref. 22]. At the present, they

[3] Further details of the assumptions used to produce this figure are provided in Ref. 21.

appear to be justified for long range aircraft only, due to the voluminous required heat exchangers and the associated installation penalties [Ref. 22 to Ref. 24]. Alternative combustion technologies such as wave rotors, pulse detonation and constant volume combustion may also offer improvements in terms of thermal efficiency, but they appear to have relatively low technology readiness levels [Ref. 25].

B) Improving propulsive efficiency

The engine net thrust, produced by the acceleration of the air going through it, can be expressed as suggested in Eq. 4. Consequently, the propulsive efficiency can be expressed in terms of the flight and jet velocities[4].

$$Fn = \dot{m}\left(V_j - V_0\right) \qquad \text{[Eq. 4]}$$

$$\eta_{Prop} = \frac{Pw_{Aircraft}}{Pw_{Airflow}} = \frac{Fn.V_0}{\frac{1}{2}\dot{m}V_j^{\,2} - \frac{1}{2}\dot{m}V_0^{\,2}} = \frac{2}{1+\frac{V_j}{V_0}} \qquad \text{[Eq. 5]}$$

It can be seen that propulsive efficiency can be increased by reducing the jet velocity, provided that the jet mass flow is increased in order to maintain a required level of thrust. In a conventional turbofan, the jet mass flow and its acceleration can be directly related to the bypass ratio (BPR) and the fan pressure ratio (FPR) respectively. For a given core technology and selected BPR, an optimum FPR can be found. Details of this optimisation process can be found in Ref. 26. These optimisations were also reported in Ref. 27 and Ref. 28 and optimum FPR vs. BPR charts were provided. A simplified[5] version of this chart (for a bare engine) is presented in Figure 7 for a wide range of BPRs [Ref 244].

Two zones can be distinguished with respect to the evolution of the propulsive efficiency:

- Low and moderate BPRs (1-30) for which the BPR has a significant influence on propulsive efficiency.
- High to very high BPRs (>30) for which the BPR has a relatively low impact on propulsive efficiency.

---

[4] The presented expressions are simplified assuming that the inlet and outlet mass flow rates are the same, considering average velocities, not considering rotating components of velocities, pressure thrust, and that the thrust is produced in the same direction as the flight. These simplifications are done in order to simplify the equations since they are introduced to build the argument and are not to be used for fully rigorous calculations.

[5] The efficiencies of the components are kept constant. The rotating components of the velocities of the inlet and outlet airflows are not considered. A detailed calculation would need to adjust the efficiencies of the components and introduce discontinuities when different technological solutions are used. This figure is presented for illustrative purposes only. The values corresponding to rigorous calculations (for BPR from 1 to 25) can be found in Ref. 27 and Ref. 28.

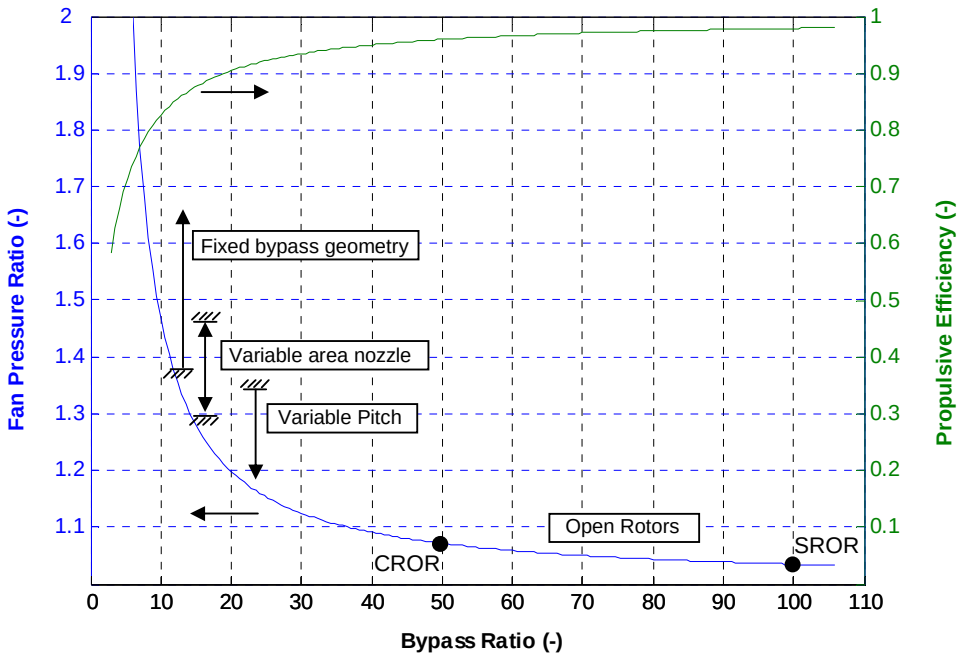

Figure 7: Optimum FPR and propulsive efficiency vs. BPR at a typical cruise condition

Modern TFs used in the 150 PAX class aircraft have BPRs between 5 and 6. At cruise conditions, their FPR are approximately between 1.6 and 1.8. It can be seen (Figure 7) that the increase in BPR could yield significant improvements in propulsive efficiency. As BPR is increased, FPR and the rotational speed of the fan have to be reduced. The reduced fan rotational speed results in an increase in the number of stages of the LPT as well as larger LP shafts (due to the high torques). At a certain value of BPR, the use of a gearbox (that decouples the rotational speed of the fan and the LPT) is required to obtain optimum engie weight and fuel consumption. An alternative to avoid the use of a gearbox could be a counter rotating turbine which gives place to the contra-fan concepts (Figure 8) such as the RB529 [Ref. 28]. The propulsive efficiency of a 12-14 BPR GTF or a contra-fan appears to be around 10% higher than that of a modern TF [Ref. 28].

Further increases in BPR would impose the need of a variable area bypass nozzle or a variable pitch fan in order to maintain a stable fan operation at low flight speeds [Ref. 26 and Ref. 28]. This operational limit is close to 1.4 FPR [Ref. 27]. The NK-93 (not yet certified) is an example of this technology, featuring a geared variable pitch counter rotating fan that enables a BPR around 17 [Ref. 29]. Figure 9 shows a section view of the NK-93 engine as well as a real prototype mounted on an aircraft next to a conventional turbofan. The relatively large nacelle diameter of this engine concept compared to a TF can be appreciated in the picture. The bigger nacelle results in higher weight and drag as well as strong limitations in terms of aircraft integration that reduce the final benefits of these concepts.

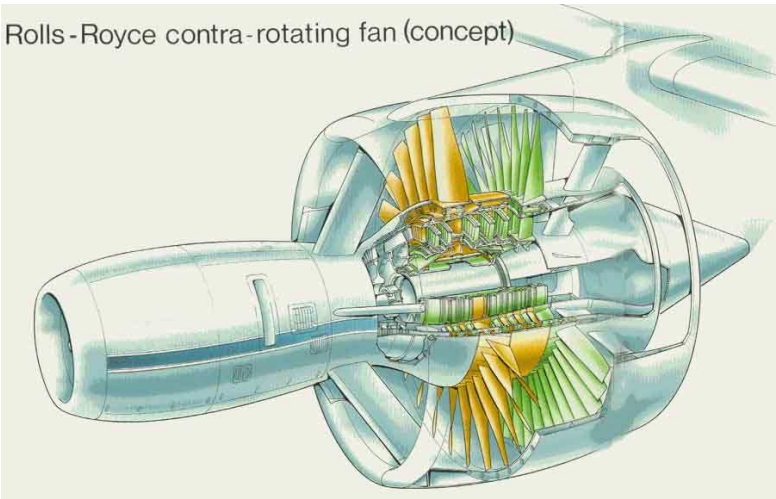

Figure 8: Rolls-Royce Contra-fan RB529 concept [Ref. 118]

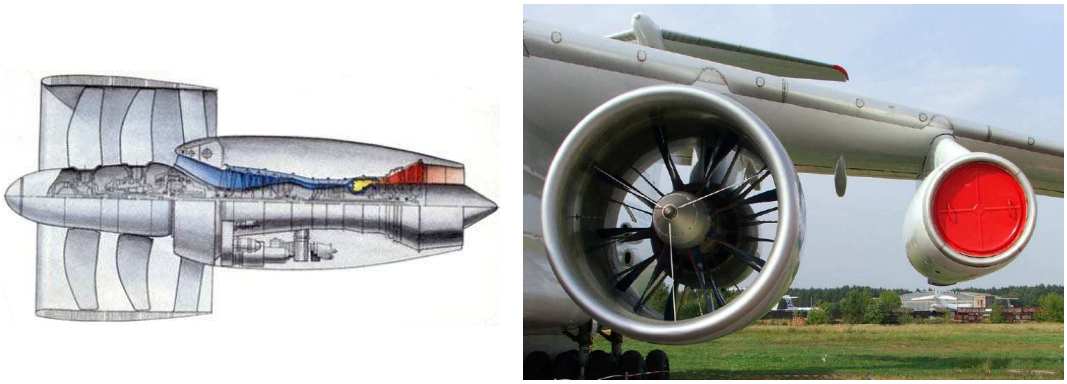

Figure 9: NK-93 prototype engine [Ref. 119, Ref. 120]

A further increase in BPR would require the elimination of the nacelle, resulting in OR engines. At typical cruise conditions, the FPRs of SRORs and CRORs are approximately 1.03 [Ref. 14] and 1.08 [Ref. 14 and Ref. 30] respectively. These values of FPR correspond to a BPR close to 50 for CRORs and 100 for SRORs. It can be seen from Figure 7 that the improvement in propulsive efficiency of a SROR over a CROR would be marginal. More over, the CR configuration is capable of delivering the same thrust at a reduced propeller diameter (enabling reduced propeller tip speeds) and offers the advantage of recovering the swirl on the propellers exit flow (not considered in Figure 7). For these reasons, a CROR can offer a higher propulsive efficiency than a SROR at high subsonic flight speeds (9% more efficient at 8000 ft (~2438 m) and 140kts climb [Ref. 15], and 5 to 6% more efficient at a 35000 ft (10668 m) and M 0.8 cruise [Ref. 31]). This could be beneficial at a mission level, since time is a first order variable affecting mission fuel consumption. Figure 10 presents installed[6] propulsive efficiency trends for different engine concepts at different cruise M_0.

[6] Installed efficiency includes engine installation drag such as the nacelle and the pylon drag.

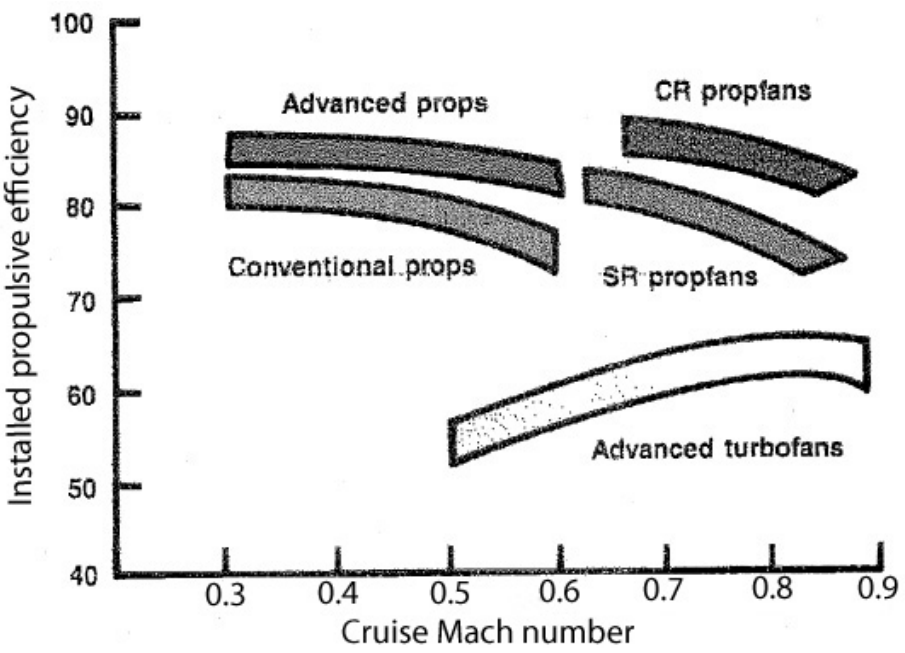

Figure 10: Installed propulsive efficiency trends [Ref. 14]

To summarise, it has been shown that there is a higher potential to improve the propulsive efficiency than the thermal efficiency of a single engine at the present technological level. The CROR offers a significantly higher propulsive efficiency than other high BPR shrouded concepts while presenting a similar degree of complexity (gearbox, variable pitch and challenging installations) making it a promising candidate to power future aircraft.

1.1.2.2 Geared CROR

Pusher configuration

Figure 11 shows an artists impression and section view of a pusher geared CROR (GOR). It comprises a two spool gas generator and a power turbine that drives a counter rotating propeller through a differential planetary gearbox. The turbine gas flow is discharged to the atmosphere through a fixed area convergent nozzle.

Note that the propellers are driven by the LPT and the front compressor (intermediate pressure compressor (IPC)) is driven by the intermediate pressure turbine (IPT). This applies to the OR concepts presented in the following sections.

In the particular design of Figure 11, the shafts which drive the CRP pass through the hot gas exhaust. The pitch angle of the propellers can be adjusted through a pitch change mechanism (PCM) in order to control the rotational speeds of the propellers.

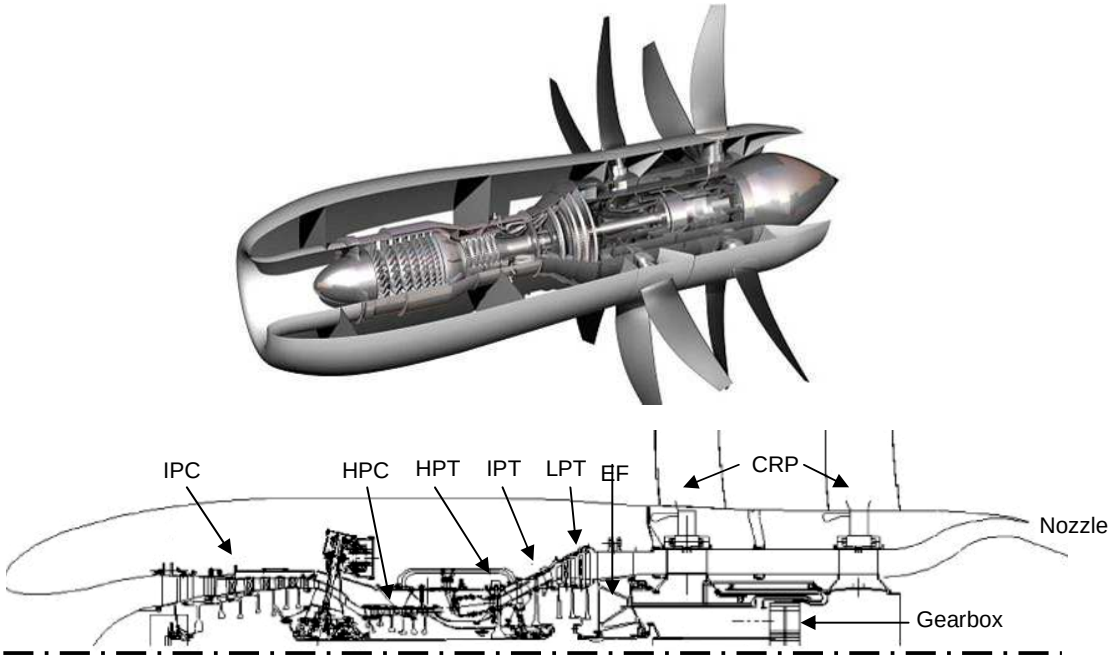

Figure 11: Artists impression and section view of a pusher GOR [Ref. 32]

Between the LPT and the CRP modules there is a relatively big frame called exit frame (EF). This frame is a key structural component of the engine since it supports the gearbox and CRT (two heavy modules).

The gearbox oil is cooled by cold fuel coming from the aircraft tanks and external air. The cooling air flow enters through a specific air intake installed in the nacelle (not seen in Figure 11), passes through a heat exchanger and is finally discharged to the atmosphere. At low flight speeds, the unforced airflow through the cooling system is not enough to reject the produced heat. For this reason, a dedicated blower is installed and used at low flight speeds (powered by the high pressure (HP) shaft).

Figure 12: Pusher OR engine rear fuselage installation [Ref. 121]

Pusher OR engines are typically installed at the rear of the aircraft as suggested in Figure 12. Note that the CRP is behind the engine pylon.

Puller configuration

Figure 13 shows an artists impression and section view of a puller geared CROR (GOR). It has the same core engine definition as the pusher GOR. The LP shaft goes through the engine core and drives the CRP through a gearbox located at the front of the engine. This configuration has a longer air intake (behind the CRP blades) and a shorter exit nozzle than the pusher GOR. The PCM is visible in Figure 13.

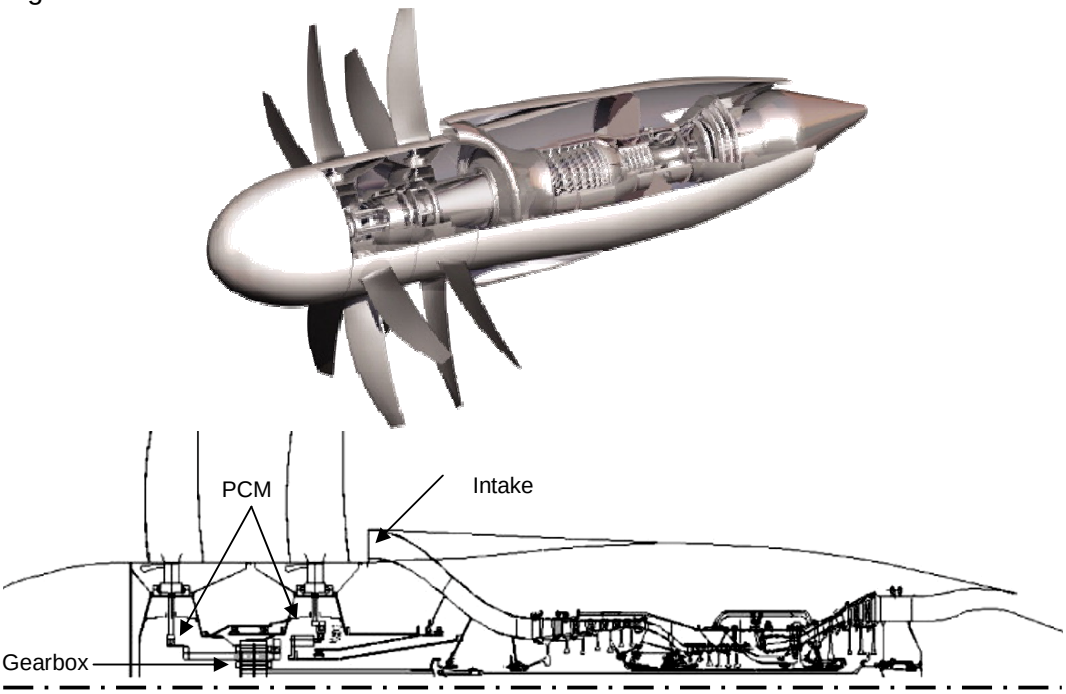

Figure 13: Artists impression and section view of a puller GOR [Ref. 32]

Puller OR engines are typically installed on the wings as suggested in Figure 14 and the CRP is directly exposed to the free stream air.

Figure 14: Wing mounted puller OR engine (Antonov An-70) [Ref. 122]

1.1.2.3 Direct drive CROR

The direct drive CROR (DDOR) can only be realistically produced as a pusher configuration and would be typically rear fuselage installed (Figure 12). A puller configuration with the CRP on the front of the engine would require two extra shafts going through its core.

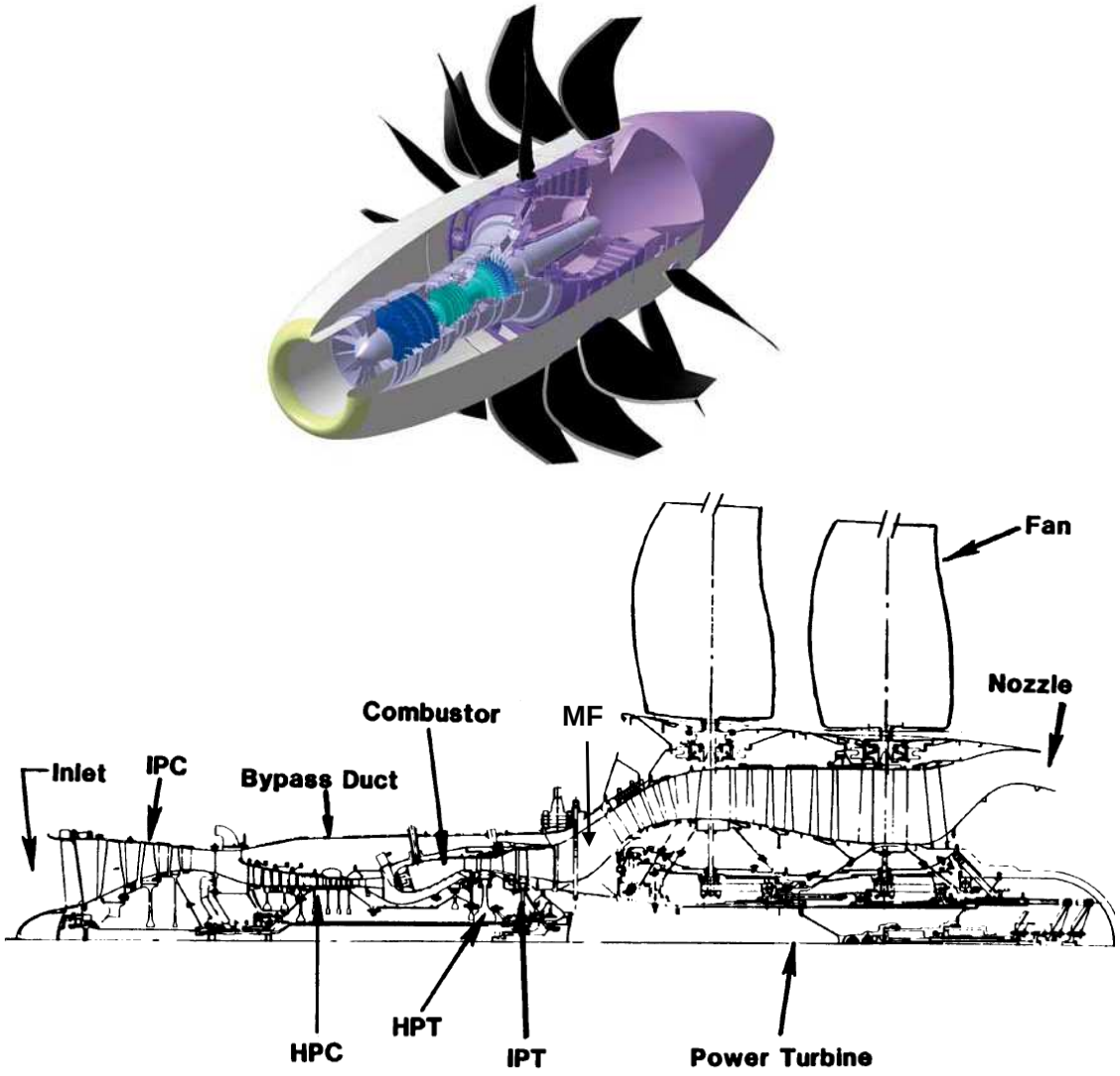

Figure 15: Artists impression and section view of a pusher DDOR [Ref. 33]

Figure 15 shows an artists impression and section view of a pusher DDOR. It is formed by a two spool gas generator (same nomenclature as for the GOR), a CRT that drives a CRP and discharges to a fixed area convergent nozzle. Figure 16 shows a cross sectional drawing of a CRT. It is formed by an internal and an external drum (mounted on a central beam) to which the turbine blades are attached. These drums rotate in opposite directions generating opposite torques which are directly transferred to the CRP. The forward propeller is directly linked to

the first CRT stage and the rear propeller to the last stage. It can be seen in Figure 16 that the first and last stages have longer chords than the rest of the turbine stages. This is due to the structural functions they perform. Note that there are no turbine outlet guide vanes in this engine configuration.

Similarly to the GOR, the DDOR features a PCM enabling the control the CRPs rotational speeds. The PCM can go through the CRT structural blade rows (the fifth and last blade rows in Figure 15, or the first and last in a design such as the one shown in Figure 16) or can be integrated outside the CRT as suggested in Ref. 35.

An important characteristic of this engine configuration is that the CRT, CRP, the exhaust nozzle and even the after body are rotating parts. Consequently, the last fixed component of the engine is the mid frame (frame connecting the IPT with the CRT, marked as MF in Figure 15) and all the LP modules are supported by it. This makes it a key structural engine component. At the same time, the MF is exposed to the hot gas stream exiting the IPT and therefore it requires a relatively high cooling airflow to ensure its structural integrity. This cooling flow is mainly taken from the back of the IPC and in the example of Figure 15 it is conduced through a bypass duct and injected back to the main gas stream through cooling holes in the MF.

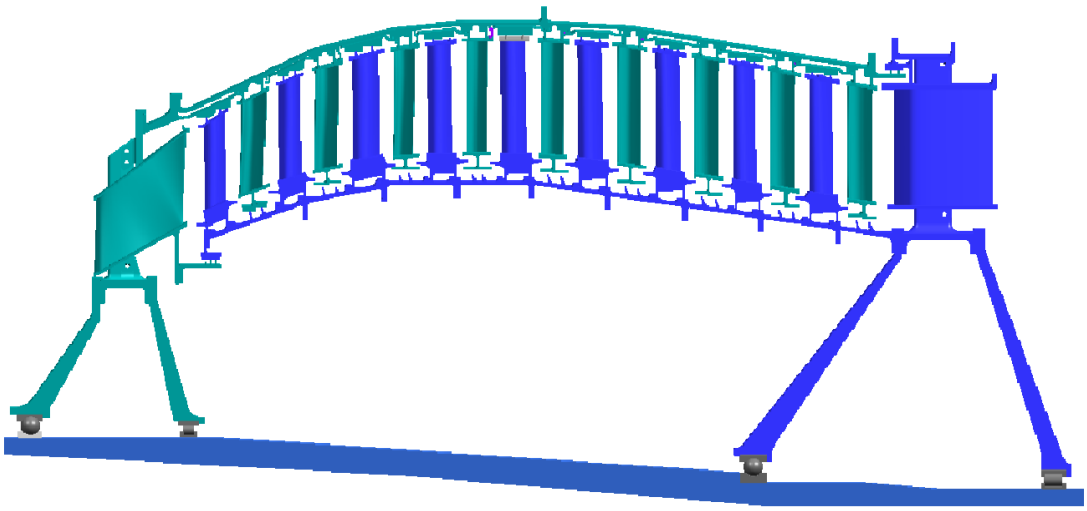

Figure 16: CRT cross sectional drawing [Ref. 34]

1.1.2.4 Existing OR engines and demonstrators

Several CRP aircraft were built during the 40s and 50s. Some of them used gas turbines (such as the Armstrong Siddeley Python engine) and others used piston engines (such as the Rolls-Royce Griffton engine). Some of them were powered by a single engine while others, such as the Fairey Gannet, used the Double Mamba which combined the power of two engines to drive both propellers. Figure 17 shows two of the first CRP aircraft that flew in 1946 [Ref. 36].

Figure 17 a: Westland Wyvern [Ref. 123] b: FX-11 prototype aircraft [Ref. 36]

During this period, CRPs were mainly used for military aircraft as they had smaller diameters than conventional propellers thereby allowing simpler installations and shorter landing gears. However, they were not designed to operate at the flight speeds for which CRPs may offer significant advantages with respect to SRPs (see Figure 10). The early CRP designs had lower reliability and required higher maintenance than SRPs and were consequently not economically justified for civil aviation [Ref. 37]. The only CRP engine to be introduced to the civil market was the Russian NK-12 powering the Tupolev Tu-114 (Figure 18) which was designed for a cruise speed of $M_0 = 0.7$ and remained in service for about 15 years in Russia.

Figure 18: Tupolev Tu-114[7] [Ref. 124]

During the 60s, the progress of propeller engines radically reduced as engine manufacturers focused their efforts on the development of turbofans [Ref. 14]. After the oil crisis of the 70s, in order to maintain the economic viability of civil aviation, there was a need for significant fuel burn reductions. This, once again, raised the

[7] From Figure 18 it can be seen that the length of the forward landing gear is relatively large. A similar aircraft with SRPs would require even longer landing gear or a low wing aircraft configuration.

interest for propellers. The NASA Advanced Turboprop (ATP) project was launched in 1973 and led the main efforts of the USA to develop high speed propeller engine technologies. The project aimed to develop design calculation methods, gearbox designs, propeller designs, engine installation technologies and cabin noise treatments [Ref. 20]. Initially, a series of high speed and high efficiency propeller blades (SR-1 to SR-7 and CR-1 to CR-5) were designed manufactured and tested. The SR series and CR-1 to CR-3 used existing NACA airfoils, while only CR-4 and CR-5 used specifically designed advanced high speed airfoils (PF-1 airfoil series) [Ref. 31]. It can be seen that these blade series are different from the conventional blades used for the NK-12 civil engine (Figure 19).

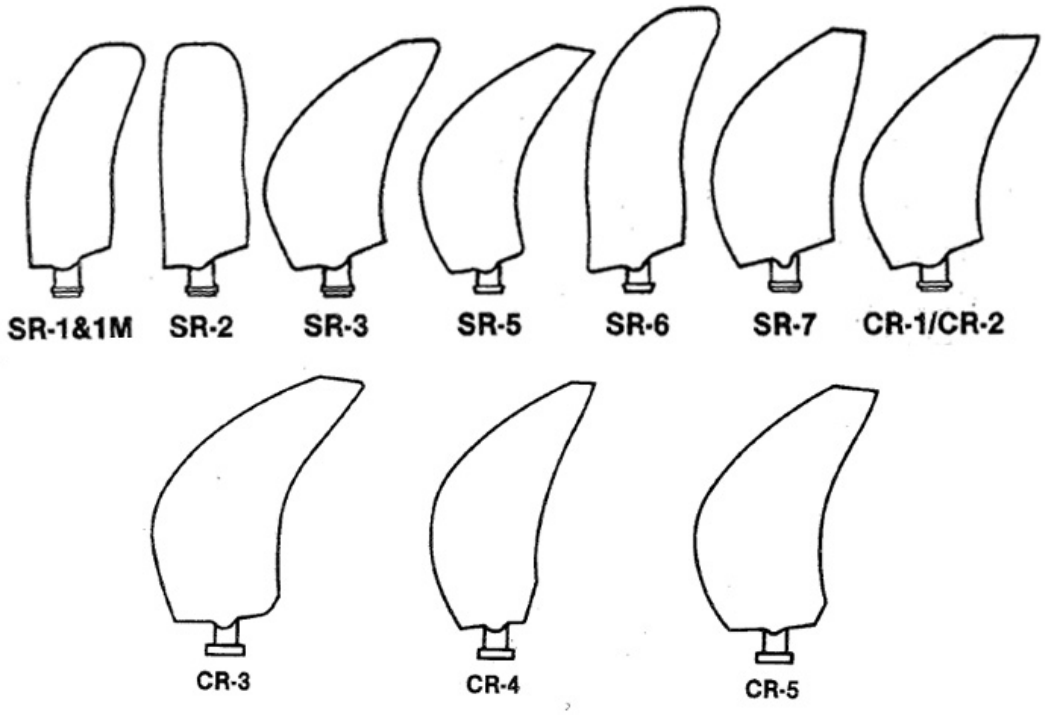

Figure 19: Example of ATP project SR and CR lade series [Ref. 31]

The Large-Scale Advanced Propeller (LAP) sub-project was subsequently established, to provide a deeper understanding of the real scale SR propellers mechanical characteristics, to ensure that they could operate with the infinite-fatigue life necessary for commercial aircraft propellers. Specific engine installation aspects were then studied and wind tunnel tested. Cabin acoustic liners were also designed as part of this project. Finally, SR and CR gearboxes and pitch change mechanisms were designed built and tested under the APET and AGBT sub-programmes. Ultimately, several flight demonstrators were launched:

- The Propfan Test Assessment (PTA) was set to improve knowledge on noise characteristics of SRORs to determine if: (a) the cabin noise treatment weight penalties were acceptable, and (b) propfan-powered aircraft could meet community noise standards [Ref. 38]. A 9 ft (~2.7 m) diameter

propeller comprising 8 SR-7 blades was tested on a Gulfstream II business jet (Figure 20). This SR propeller was designed to cruise at M_0 = 0.8 and 35000 ft (10668 m) and it was tested up to M_0 = 0.85 at 40000ft (12192 m). Cabin, en route and community noise as well as structural vibrations were recorded and used to validate the SR-7 blades as well as its design tools and process.

Figure 20: NASA PTA SR-7 SROR Gulfstream II demonstrator [Ref. 20]

- The Unducted Fan Engine (UDF, also known as the GE-36 or GE-UDF) was a DDOR developed collaboratively, led by NASA, SNECMA and General Electric. It featured a modified F404 gas generator and a 12 stage CRT driving an 11.7 ft (~3.6 m) diameter CRP. It was designed to cruise at 35000 ft (10668 m), M_0 = 0.78 and to deliver 25000 lbf (~111.2 kN) of thrust at take-off. It was first flown on a Boeing 727 in an 8x8 blade configuration [Ref. 39] and later flown on an MD-80 in 8x8 and 10x8 blade configuration [Ref. 40]. The objectives of these two flight demonstrators were to obtain operability, performance, acoustics and vibration data for the complete flight envelope. The first test flight identified the need for blade modifications to reduce the blade stress levels produced by an unpredicted coupling with the fuselage flow field [Ref. 20]. After these modifications, the UDF-727 flight program was completed and demonstrated satisfactory operability and performance up to 35000ft (10668 m) and M_0 = 0.85 [Ref. 39]. A significant reliability demonstration was also achieved during the transatlantic flights to and from the 1988 Le Bourget airshow. Several cabin acoustic liners were also tested [Ref. 20]. Subsequently, the UDF-MD-80 demonstrator was launched to further investigate the installation effects, operability and noise

characteristics of this engine on board of an MD-80. 8x8 and 10x8 CRP configurations were tested in the same conditions and compared. It was expected that increasing the number of blades of the forward propeller would reduce 5dB in blade passing noise. The 10x8 design proved to be only 3dB quieter than the 8x8 [Ref. 40] but it was concluded that further work was required to meet the FAR-36 noise certification requirements applicable at the time [Ref. 20].

Figure 21: UDF flight demonstrators (top) Boeing 727, (bottom) MD-80 [Ref. 20]

- P&W-Allison built the 578-DX GOR engine in collaboration with NASA. This project used technologies developed in the ATP project, but was not part of it. The 578-DX was designed to fly at 30000ft (9144 m) and $M_0 = 0.77$, used the gearbox technology developed during the AGBT sub-project and flew on an MD-80 [Ref. 41]. A peculiarity of this design is that the core flow exited the engine through a series of pipes before the propeller module (Figure 22). It was predicted that these gases would produce high fluctuations on the pressure field ingested by the CRP and be a dominant source of noise. This could be avoided on a product engine by exiting the core flow downstream the propeller or by using an annular nozzle. However both solutions were not feasible in the demonstrator timescale. The 578-DX was a successful demonstrator which contributed to the better understanding of aircraft/engine interactions, near and far field acoustic characteristics and established the GOR as a competitive alternative to the UDF DDOR [Ref. 42].

Figure 22: P&W-Allison 578-DX GOR demonstrator on an MD-80 [Ref. 125]

During the 80s, two main research efforts were active in Western Europe. France launched a national funded collaborative project called “Concept d’Helice pour Avion Rapide en vue d’une Meilleure Economie” (CHARME). Part of the aims of this project were to improve the methods for the design of CRPs. ONERA was the main contributor to this work and very little information has been made public [Ref. 43 and Ref. 44]. In the United Kingdom, Rolls-Royce, Dowty Rotol, British Aerospace and the Aircraft Research Association (ARA) established a collaborative project to develop advanced CROR concepts. During 1985 and 1986, a 30 in CRP test rig (Rig-140) was designed by Rolls-Royce. It was then commissioned and used during 1988 and 1989 in the ARA transonic wind tunnel to acquire performance, and noise data and to perform detailed aerodynamic investigations [Ref. 45].

In the Soviet Union, Ivchenko Progress ZMKB started the developments of the D-236 in 1979. It was a puller three spool GOR demonstrator with a 4.2 m diameter 8x6 CRP designed to fly at 11000 m and M_0 = 0.7 and produce a take-off thrust of 16500 lbf (73.4 kN) [Ref. 46]. It flew on an Ilyushin Il-76 in 1987 and then on a YAK-42E-LL in 1991 (Figure 23). This demonstrator then evolved into the D-27 engine which has a 4.5 m diameter CRP and is designed to cruise at 11000 m and M_0 = 0.7 and produces 21200 lbf (94.3 kN)of thrust at take-off [Ref. 46]. This engine is still in operation on a prototype Antonov An-70 aircraft (Figure 23).

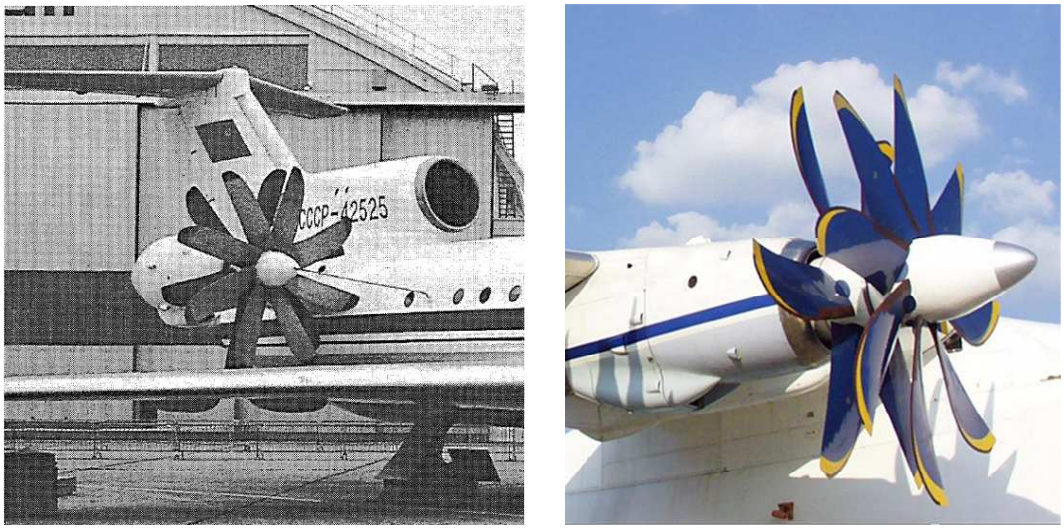

Figure 23: Russian puller OR demonstrators (L) D-236 [Ref. 46], (R) D-27 [Ref. 126]

All the previously described demonstrators proved to be at least 20% more fuel efficient (at any flight power setting and speed) than TF engines using the same level of technology [Ref. 39, Ref. 40, Ref. 42 and Ref. 46].

1.1.2.5 Challenges of CROR technology

Although CRORs demonstrated significant potential to reduce fuel consumption, many remaining challenges still required significant development efforts [Ref. 13]. At the end of the 80s as the oil price reduced significantly and since environmental issues were not a top priority, the required development efforts were not economically justified and the OR development activities were shelved. Some of these challenges were:

At aircraft level:

1. Cabin and community noise: Despite all the efforts done to reduce CROR noise, none of the demonstrators met the FAR-36 noise certification applicable at the time [Ref. 20]. One of the main challenges of CROR is meeting the current (Chapter 4) and anticipated future noise certification requirements which are more stringent than those of the 80s. High levels of cabin noise were also recorded [Ref. 53]. Figure 24 presents the main CROR noise generation mechanisms. Unlike TFs which produce broad band noise, CRORs produce high levels of tonal noise dominated by the blades operation and their interactions.

In the case of a pusher configuration the CRP noise is increased by the ingestion of the pylon wake and the interaction with the fuselage boundary layer. It was recently proved that blowing air through the pylon trailing edge is an effective way to mitigate these effects [Ref. 115]. In the case of a puller configuration the CRP noise is increased by the interaction with the engine intake [Ref. 55].

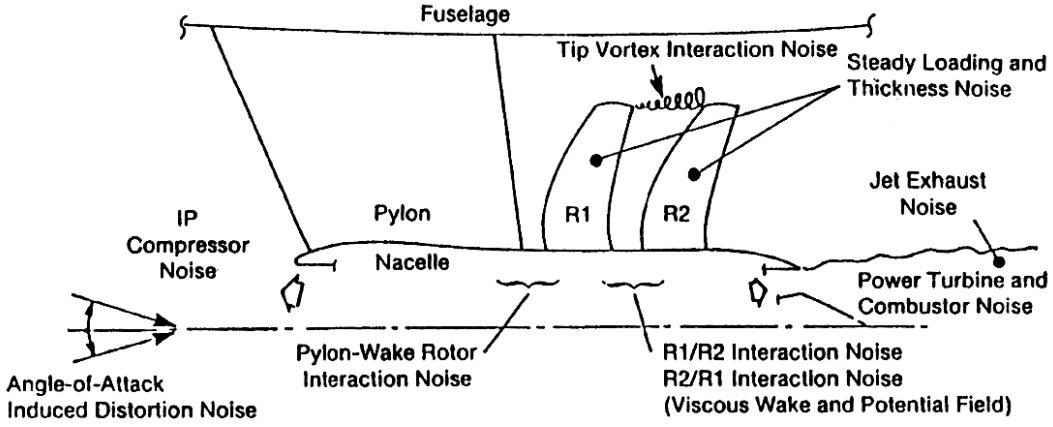

Figure 24: CROR noise generating mechanisms [Ref. 54]

At cruise speeds, the CRP tips operate in a transonic regime. The shock waves produced result in very high noise levels at a very short distance from the fuselage [Ref. 56]. The noise is transmitted through the fuselage structure and high noise levels are perceived at unexpected large distances [Ref. 53]. Figure 25 shows the sound pressure levels (SPL) measured at the SRP planes during the PTA flight tests.

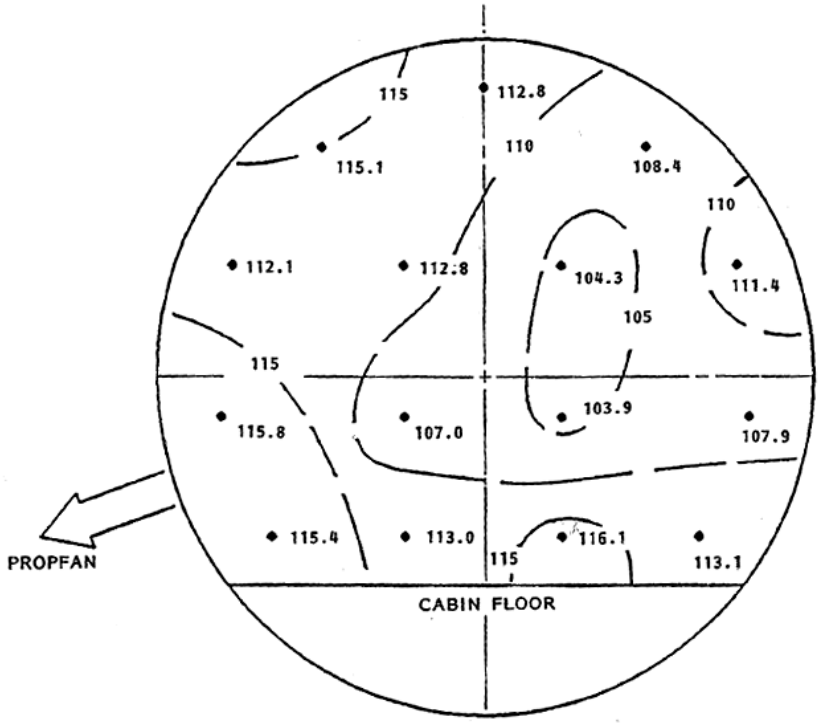

Figure 25: Cabin sound pressure level at the SRP plane (PTA demonstrator) [Ref. 53]

The tonal noise produces higher levels of annoyance to passengers than the same level of broad band noise. For this reason psychoacoustic tests are required to determine the necessary cabin treatment and damping mechanisms to ensure the

correct level of passengers comfort [Ref. 56]. The required acoustic liners and damping systems increase the aircraft weight increasing the mission fuel burn [Ref. 56 and Ref. 53].

The noise generated by rear mounted engines is expected to be easier to isolate than the noise produced by wing mounted engines which are located approximately at the centre of the cabin. The engines location with respect to the fuselage has also an influence on the certification noise as parts of the fuselage may shield or re-direct noise.

2. Fuselage and structural components fatigue: As it was mentioned before, the CRP blades operate at transonic regimes during cruise. The shock waves produced in the CRP create an unprecedented challenge associated with the design of fatigue resistant fuselage skins structures. Furthermore, these vibration effects can be amplified at high aircraft incidences, when the CRP receives the wing wake. Sonic fatigue tests of structural pieces are required to build a better understanding of this mechanism [Ref. 56]. The specific reinforcements adopted to overcome this problem would result in weight penalties that are directly translated into fuel burn penalties.

3. Engine installation: Figure 26 presents a hypothetical installation of a 14 ft (4.26 m) diameter puller CROR on a low wing aircraft compared to a TF. It can be seen that a low wing installation is not feasible and a high wing aircraft configuration as the An-70 would be required to install such engines. High wings result in aircraft structural weight penalties since specific reinforcements are required to re locate the landing gears. An alternative to avoid the high wing aircraft configuration is to mount the engines at the rear of the fuselage like the UDF and P&W-Allison demonstrators. This integration requires long pylons and significant structural reinforcements on the rear part of the fuselage which is also heavy, and impacts the aircraft longitudinal weight balance. It is interesting to note that long range or high capacity aircraft require four engines that can only be installed on a high wing aircraft configuration. A thorough description of the implications of the installation choices at aircraft level (weight, aerodynamics, noise, safety, etc) can be found in Ref. 58.

Figure 26: CROR and TF installation on a low wing aircraft [Ref. 57]

4. Aircraft aerodynamics: Rear mounted OR engines operate in a complex flow field resulting from the combined effects of the wing wake, the pylon wake and the fuselage boundary layer. Furthermore, at low flight speeds, the propeller produces a great stream contraction and during reverse thrust operations the flow is inversed. All these specific effects and interactions create unique aerodynamic problems [Ref. 56]. As an example, the UDF blades required two consecutive sets of design modifications after the first test flights since the stress levels resulting of the flow interactions were higher than predicted [Ref. 20]. The loss of the effectiveness of the rear control surfaces due to the unusual flows was also observed during the UDF flight tests [Ref. 56].

Wing mounted ORs also offer specific aerodynamic challenges since the propellers operate at a wide range of angle of attack (rear fuselage mounted ORs benefit from aircraft wing "downwash" which reduces the range of the angle of attack). Furthermore, as cruise speeds rise above M 0.75, the flow acceleration caused by the propeller creates shocks over the wings raising considerably their drag [Ref. 58].

5. Safety and airworthiness: To be accepted in civil air transport, the OR aircraft must meet the same safety standards achieved by modern turbofan aircraft [Ref. 60]. This means that the OR, despite the added complexity (variable pitch, gearbox or CRT, etc), must match the standards set by the turbofans which have fixed pitch fan blades and a nacelle capable of retaining a released fan blade. Amongst others, the following issues have to be adequately addressed:

- It has to be proven that the advanced blades can be produced with infinite fatigue life characteristics [Ref. 53]. This is specially challenging since the aerodynamic excitations over the CRP are highly unknown as previously highlighted. At the same time, the centre of gravity of the tip sections are outside of the blades root projection and generates out of balance induced vibrations [Ref. 61]. Moreover, an infinite fatigue life of the propeller hub has to be demonstrated. The engineering practices and tests are consolidated for compact propeller hubs located at the front of the engine, but are not developed for large diameter hubs which could be less stiff and operate in the hot back end of the engine [Ref. 60]. The placement of critical speeds and the flutter characterisation of advanced CRPs also required further investigation in order to ensure the correct levels of blade integrity [Ref. 31].

- It has to be proven that in the event of a blade loss the aircraft airworthiness is not compromised. Consequently, the blade debris should not affect the pressurised cabin zone and the control surfaces, and the vibrations produced by the unbalanced engine should not compromise the aircraft structural integrity [Ref. 58].

- The CRP has to be resistant to foreign objects ingestion. During the 578-DX ground test campaign, a 5/8 inch (~1.5 cm) bolt of the test facility failed and went through the CRP. Two forward blades and a rear blade were damaged and had to be repaired [Ref. 41]. In the case of rear mounted ORs, debris

coming out from the landing gears may impact the propellers [Ref. 58] and this issue requires special design efforts.

- The PCM has to ensure that it is very unlikely that a propeller can be blocked close to the 90º of incidence. This situation would be catastrophic since the aircraft controls will not be able to balance the amount of drag produced by a large diameter propeller in a blocked position [Ref. 60]. The auto-feather capability is therefore to be considered for the PCM design.

6. Public perception: The Rolls-Royce Clyde was the first turboprop engine to be certified under civil regulations but was never sold since it was perceived as an old technology engine compared to the recently developed turbojets. This example shows that a successful engine not only needs to be certified but also to be accepted and wanted by the market. A poll carried out by United Airlines during the 80s showed that only 50% of the passengers would accept flying on an OR aircraft [Ref. 59]. This could have been caused by previous experiences of travelling in old propeller aircraft built in the 40s and 50s which were considerably less reliable than the 80s turbofan aircraft. A more recent poll (not yet published) shows an improvement of the public perception of OR engines.

At engine level

1. **Small core size:** For a given level of thrust, an OR has a lower core mass flow rate than a TF (due to its higher overall efficiency). Consequently its performance and operation is very sensitive to bleeds and core power off-take [Ref. 56]. At the same time, CRORs require relatively high bleed mass flows to cool the hot LP components such as the CRP roots, CRT, gearbox, PCM and the MF of the pusher CRORs which support the heavy LP assembly. For example in the case of the UDF demonstrator, approximately 20% of the IPC inlet mass flow was bled to cool the MF only. This large amount of bleed was required because an existing core was used for the demonstrator which imposed mechanical and thermal constraints. A CROR product would require between 20 and 25% of the IPC inlet mass flow rate for all engine cooling purposes, whch is considerably higher than the cooling flows of year 2000 turbofans (10 - 15%). New materials, manufacturing processes, innovative designs and highly efficient cooling systems are required in order to produce lightweight and reliable LP components which do not compromise the engine performance.

2. **Thrust reverse:** Wind tunnel tests showed that very large amounts of reverse thrust (up to 60% of take-off thrust at $M_0 = 0.2$) can be generated by a CROR [Ref. 62 and Ref. 245]. These tests were done at static propeller pitch settings. A dynamic application of reverse thrust from a forward thrust position is more challenging since the blades have to pass through a fully stalled position and recover the attachment of the flow. As an example, for variable pitch TFs, despite extensive research carried out in the US and UK at the end of the 70s, adequate levels of reverse thrust following a dynamic selection of reverse pitch in a variable pitch TF were only demonstrated for forward speeds lower than 60 kts ($\sim M_0 = 0.09$ at sea level and ISA conditions). Both the UDF and 578-DX were only tested in

dynamic reverse thrust during 100kts (~M_0 = 0.15 at sea level and ISA conditions) ground rolls [Ref. 39, Ref. 40 and Ref. 42]. A further challenge for the reverse thrust dynamic transition is to ensure the correct loading on the propellers to avoid over speeds of the LP system. Another issue that requires careful design efforts is the aerodynamic operation of the core intake at reverse thrust setting and the ingestion of the hot exit gases which the propeller may re-circulate towards the intake [Ref. 65].

3. **PCM:** A detailed 3-D view of the 578-DX PCM can be found in Ref. 41. It is a highly complex system that has to ensure high reliability and precision while operating at high levels of mechanical stress. This is especially challenging for the pusher configurations because the PCM operates in a hot environment [Ref. 55]. A failure in the PCM could result in catastrophic events and therefore it has to demonstrate a high level of reliability [Ref. 66]. The two most dangerous mal functions are the blockage of the propellers close to 90º (previously described) and the failure to impose a minimum propeller loading which could result in propellers and LP system over speed Ref. 66.

4. **Mechanical design of the blades:** More experience is required to ensure infinite fatigue life of CRP blades with novel shapes [Ref. 53]. Mounting the blades on a hot rotating structure around the exhaust end of the engine (pusher configuration) makes it a more difficult challenge [Ref. 55]. The blade root design is a key element of its structural integrity as well as its aerodynamic performance. Large CRP hub diameters and thick blade roots resulted in high inter blade M and choke on both the suction and pressure side of the blades during high speed wind tunnel tests [Ref. 14]. This structure was propagated until blade mid radius being responsible for an efficiency loss of approximately 3% [Ref. 31]. An efficient aerodynamic design of the blade roots is more difficult for blades requiring large pitch variations to produce reverse thrust [Ref. 31].Improvements in materials and manufacturing processes are required to produce safe blades with thin transonic profile roots [Ref. 14].

5. **Gearbox reliability and oil cooling technologies:** During the first years of the ATP project, gearbox reliability was identified as one of the key challenges of geared CROR engines [Ref. 66]. Consequently, two ATP sub-projects were devoted to the development of advanced gearbox technologies targeting a mean time between unscheduled removals of 30000 hours [Ref. 20]. The designed counter rotating gearbox was tested on ground for 550 hours and in flight for 20 hours [Ref. 42], which is not enough to demonstrate the reliability objectives. No detailed information was found regarding the D-27 gearbox reliability. A further challenge is the design and integration of highly efficient and compact gearbox oil cooling technologies. An inefficient oil heat exchanger increases the engine weight and the drag produced by the required cooling airflow.

6. **Maintainability and acceptable maintenance cost:** CROR engines are mechanically more complex that fixed pitch TFs. For this reason they risk of having higher maintenance costs that may offset the economical benefit of the fuel

savings. Ref. 67 predicts that the maintenance cost of a CRORs propeller and gearbox would be 12% higher than a TFs fan and thrust reverse actuator. Ref. 68 predicts an equivalent maintenance cost for TFs and CRORs in 1990 taking into account the advances in health monitoring systems. Accurate maintenance costs can only be known after a product has accumulated a large amount of service hours. Another challenge is to maintain the same mean time between overhauls than TFs while being mechanically more complex and having a radically different architecture. As a comparison, the most popular modern turboprops have a mean time between overhaul close to 8000 hours while a CFM-56-7B is close to 23000 hours [Ref. 69]. Finally, a compact and modular design is required to facilitate maintenance operations of the LP modules.

7. **CRT seals and blade containment:** The high pressure ratio large diameter seal required at the front of the CRT is a potential source of leakage and in-service deterioration and considerable design efforts are required to ensure its satisfactory operation [Ref. 28]. Another challenge for the mechanical design of the CRT is to ensure blade retention capabilities of the stressed external rotating drum (instead of a static casing).

1.1.2.6 Recent efforts to develop CROR technologies

As a response to the fuel price escalation of 2007/2008, the interest in CROR engines was renewed. It was believed that the progress made during the previous 30 years in the fields of computational techniques, aerodynamics, control, materials, instrumentation and health monitoring, mechanical design and manufacturing processes could provide the basis to develop CROR engines able to meet present certification and market requirements. Consequently, several efforts were made to apply these advances to the design of CROR components and systems.

USA

In 2008 GE and NASA reconditioned some of the test facilities used during the 80s. Subsequently they developed and wind tunnel tested new blade designs targeting to meet present noise level requirements (Chapter 4 of the ICAO Annex 16 Volume I) [Ref. 50 and Ref. 51]. The results of these test campaigns are not available in the public domain.

Although it was not a publicly known effort, some university thesis sponsored by P&W show their present interest for CRORs [Ref. 52].

Europe

After the publication of the ACAREs vision for 2020 [Ref. 47], the EU has launched several projects in which industrial manufacturers, universities and research institutes collaborate to develop sustainable technologies. The following chart shows the continuous efforts done in the field of engines through the 5th and 6th

Framework Projects and their contributions to the DREAM project (valiDation of Radical Engine Architecture systeMs).

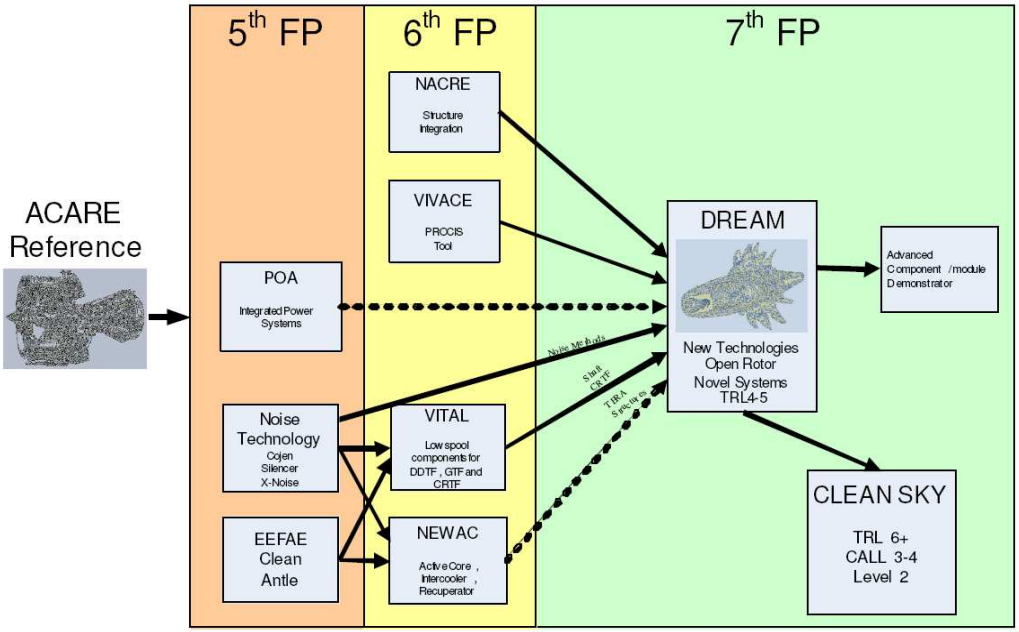

Figure 27: Aircraft engine European collaborative projects [Ref. 49]

The DREAM project was aiming to design, integrate and validate new engine concepts based on pusher CROR architectures to reduce:

- 27% fuel consumption and CO_2 emissions with respect to the year 2000 engines (this represents a 7% step beyond the ACARE 2020 objectives)
- noise emissions by 3dB per operation point compared to the year 2000 engines [Ref. 49].

DREAM started in 2008 and finished in 2012 and successfully matured the technologies offering the potential to go beyond the ACARE objectives for fuel consumption, achieving a TRL of 4-5 during the project. These technologies are now being further developed within the CLEAN SKY programme [Ref. 70].

The consortium, led by Rolls-Royce, was composed of 44 partners from 13 countries, including all the European leading engine manufacturers, key research institutes, universities and SMEs, providing the best expertise and capability from the EU aeronautical industry and Russia.

The efforts were divided in five sub-projects (SP) addressing the main DREAM issues:

SP1 Whole engine architecture (Led by SNECMA): Work Package 1.1 performed detailed specific designs of pusher CROR engines (using original equipment manufacturers (OEM) detailed tools) incorporating the technologies developed during the DREAM project, and compared them against the projects overall targets. Work Package 1.2 explored a broad design space to identify the trade-offs of fuel

burn, certification noise and emissions with respect to the main LP preliminary design parameters of both GOR and DDOR pusher configurations. These two sets of assessments, performed at different levels, contribute to a better understanding of the open rotor technology, its potential and its main design trade-offs. The Work Package 1.2 was led by CU and is the framework of this PhD project. Note that only pusher OR engines were studied within the DREAM project. This is the reason why the puller CROR configuration is not assessed in this thesis.

SP2 Geared open rotor (Led by Rolls Royce): Developed advanced propeller blades, installed noise reduction through pylon blowing, PCM technologies, as well as LPT and hot structures for a pusher GOR.

SP3 Direct drive open rotor (Led by SNECMA): Developed advanced propeller blades, LPC and CRT technologies for a DDOR.

SP4 Innovative systems (Led by MTU): Developed innovative active control and vibration damping systems applicable to both OR and TF engines.

SP5 Alternative fuels demo (Led by Turbomeca): Selected and performed combustion tests of alternative fuels. Synthetic fuels were tested and proved to be compatible with the aviation Jet-A for a limited temperature range. The compatibility temperature range does not fully cover the present civil aviation flight envelope.

Further CROR technologies are being developed within the CLEAN SKY EU collaborative project and a flight demonstration is scheduled for the end of 2016 [Ref. 70].

Apart from the press communications and some research publications, limited technical information about recent developments is available in the public domain due to their strategic importance. Appendix A presents the result of an extensive patents search conducted during the course of the PhD. The main patenting fields are: engine architecture, CRP mechanical design, PCM design, CRP blades design and control for noise reduction, propellers anti icing, cooling for structural components, gearbox oil cooling, CRT mechanical design, core flow exhaust, vibration monitoring, pylon design and engine installation on the aircraft. This gives an indication of the areas in which companies are currently working.

1.1.3 Multi-disciplinary preliminary design assessments

As presented in section 1.1.2.5, CRORs have significant potential to reduce aircraft fuel burn, however there are challenges that need to be addressed both at aircraft and at engine level. Currently, diverse efforts (refer to section 1.1.2.6) are being devoted to develop novel solutions in order to overcome the main challenges. Some of these solutions may impact different aspects of the engine and aircraft design, operation and performance.

For example, a noise reduction technique for a DDOR may require a slower operation of the CRP. This would result in slower CRT rotational speeds (they are

directly linked) which would reduce its design point efficiency (constant turbine diameter and number of stages) and therefore increase the engine specific fuel consumption (SFC). Furthermore, as the CRT is less efficient, a higher core mass flow rate would be required to maintain the same thrust level, and an additional pair of CRT stages may also be required (depending on the reduction in rotational speed). As a result, not only is the engine less efficient, but it is also heavier and both aspects consequently increase the mission fuel consumption. Another possible noise reduction technique is to blow air through holes in the trailing edge of the engine pylon. The required air flow would be bled from the core of the engine, affecting its performance, operation and weight. It is then clear that a multi-disciplinary assessment at mission level of the impact of the main preliminary design parameters of CRORs is required to assist the design process of these engines.

The A380 was the first aircraft for which a compromise between engine efficiency and noise had to be done in order to comply with the strict noise regulations at Heathrow airport [Ref. 240]. In the case of CRORs, it is likely that this compromise may need to be done and therefore it is necessary to quantify the impact of the various noise reduction techniques on fuel burn.

A design space exploration (or parametric study) is an effective way to carry out these assessments and establish the trade-offs between the desired design variables (CRPs diameters, rotational speeds, etc.) and the overall mission performance (mission fuel burn and time, LTO emissions, certification noise, etc.). A broad design space exploration is a useful tool to identify the optimum design regions to be explored in further detail with dedicated design tools. Additionally, it aids the development process when compromises need to be performed as a consequence of design, operational or regulatory constraints. This can be particularly interesting for assessing novel architectures, such as the CRORs, since all the specific technical solutions may not be known before hand and it would be very time consuming to evaluate each one independently.

The simulation tools used to perform design space explorations (or parametric studies) at preliminary design level are based on physics, simplified design methods, correlations built using previous experience. They also include non dimensional characteristics of components (0-D), and require relatively simple geometrical definitions (normally 1-D or 2-D). Due to their simplified nature, these tools are normally used to calculate design trends and tradeoffs, while absolute values and the technical feasibility of particular designs are obtained from detailed design efforts. The nature and complexity of the tools may vary according to the stage of the project, knowledge of the particular technology, required level of detail and available computational power.

The following paragraphs present a review of the existing OR preliminary design multi-disciplinary assessments and preliminary design aero engine simulation tools, available in the public domain.

1.1.3.1 Existing multi-disciplinary OR engine assessments

1.1.3.1.1 Recent assessments

Four recent (2006 - 2012) multi-disciplinary CROR engines assessments were found. The four of them analyse particular aircraft and engine designs and use different methods and simulation tools.

Assessment 1

Ref. 71 compares the performance of a conventional TF, a GOR and a DDOR for a 162 passenger, 3250 nm range aircraft cruising at M_0 = 0.72. The mission fuel burn, total and LTO cycle NOx, and certification noise levels were calculated for the reference mission using the three different engine alternatives. The results were subsequently compared showing the potential benefits of the OR technology. This assessment was carried out using the state of the art NASA preliminary design evaluation tools.

Firstly, the aircraft was sized using FLOPS [Ref. 74] and PDCYL [Ref. 75] aircraft preliminary design tools. Secondly, suitable GOR and DDOR engine performance simulation models were developed using NPSS [Ref. 76]. Ref. 72 describes the performance modelling methodology developed for both a DDOR and a GOR using NPSS. Thirdly, the engine dimensions and weight were estimated using WATE [Ref. 78 and Ref. 79], a mechanical preliminary design tool. Finally, a mission[8] calculation was performed using FLOPS, to assess the previously sized GOR and DDOR. The NOx emissions were calculated using the empirical correlations presented in Ref. 77. The CRPs noise emissions characteristics at different power settings were obtained from F31/A31 acoustic wind tunnel test results (conducted during the 80s). They were subsequently scaled from a model to real size and speed. The effective perceived noise levels (EPNL) at the three certification points produced by the CRP was calculated using ANOPP [Ref. 80]. The study concluded that CRORs may offer 40% reduction in mission fuel burn and 80% reduction in LTO NOx with respect to a year 1990 turbofan. These conclusions are highly dependent on the assumptions made at aircraft level (acoustic liners weight, rear mounted engines required structures, etc) which are not explicitly mentioned. Accurate values for these assumptions would typically come from a detailed design effort. More over a year 1990 TF is compared to OR engines and there is not a clear statement on the overall pressure ratio, turbine entry temperature (TET) and combustor technologies assumptions for each engine.

The tools and methodologies used for this study are analysed in the following paragraphs. Their potential for CROR design space explorations is assessed.

[8] Only the mission range is provided in this report (the detailed mission profile is not presented).

Aircraft performance: The aircraft performance calculation methodology implemented in FLOPS is the state of the art used at preliminary design level. It has been extensively used and validated for diverse aircraft applications allowing a flexible mission definition.

Engine performance: The engine gas generator is modelled using the state of the art performance modelling methodology. It allows different compressor, turbine, combustor and cooling definitions. The CRP is modelled as a single propeller and the CRT as a conventional turbine. The gearbox used for the GOR is modelled as a single input and output shaft with an associated speed reduction and constant efficiency.

The CRP operation is described by a global power coefficient (C_P), thrust coefficient (C_T) and efficiency (η_{NET}) which are a function of the forward propeller advance ratio (J_1) and blade angle ($\beta_{0.75\ 1}$)[9] ($_1$ denotes the forward propeller and $_2$ the rear propeller). The particular functions to obtain C_P and η_{NET} used in Ref. 72 were obtained from wind tunnel tests. These tests were performed at various pairs of fixed blade angles ($\beta_{0.75\ 1}/\beta_{0.75\ 2}$= 55.7/53.7, 56.5/54.4, 58.5/55.7 and 60.2/56.8) and various propeller rotational speeds (keeping $n_1 = -n_2$). Even though it is not presented in Ref. 72, the power absorbed by each propeller during these tests was measured independently, and a torque ratio was obtained for every operating point. In addition to C_T, C_P and η_{NET}, the CRP torque ratio (TR_{CRP}) can be expressed as a function of J_1 and $\beta_{0.75\ 1}$. Consequently, the power balance between this CRP characteristic and the output shafts of a differential planetary gearbox (DPGB) can only be satisfied for one operating point, since such a gearbox delivers a constant TR_{DPGB}. An analogous situation occurs with a CRT because it delivers almost a constant TR_{CRT}. Therefore, a single propeller representation of a CRP needs to be produced matching the particular DPGB or CRT torque ratio. In this case, the power balance between the CRP and DPGB or CRT will be satisfied, but a specific propeller characteristic is required for every different DPGB or CRT design to be evaluated. Furthermore, it is very time consuming to produce constant TR wind tunnel tests, since the blade angle setting is set manually for every blade. In fact, constant TR_{CRP} characteristics were not found in the public domain. Moreover, even if such a characteristic was available, the relative CRP diameters and relative rotational speeds are not explicit parameters. Consequently, this representation of the performance of a CRP would only valid for a specific diameter ratio and rotational speed control law, and only compatible with a particular DPGB or CRT design. These limitations make the single propeller representation not suitable for a design space exploration.

The use of a conventional turbine model to describe the operation of a CRT has several limitations. First of all, the CRT has two independent drums that can rotate

[9] These are the usual non dimensional parameters used to represent a single propellers performance. Their definition and use are described in most propeller performance books and a summary is presented in section 2.2.3.2.2.

at different speeds and deliver different amounts of power. The independent operation of both parts of the CRT can not be captured with a conventional turbine performance model. Even if a constant speed ratio is selected, the conventional turbine representation is not appropriate because it does not provide a means of calculating the power split between both CRT parts. Furthermore, the use of a conventional turbine map to represent a CRT is not appropriate. Conventional turbines generally choke on the inlet guide vanes and their maximum non dimensional mass flow rate is relatively independent from its rotational speed. In the case of CRTs, the choke is produced at the throat of rotating blades and therefore the maximum non dimensional mass flow rate is highly dependant on its rotational speed.

The DPGB used in a GOR engine has three shafts (one used as input and two as output). It delivers a constant torque ratio (instead of speed ratio) allowing the two propellers to rotate at different speeds. The use of a single input and output shaft with an associated speed reduction and constant efficiency is not suitable for a design space exploration because it does not allow the evaluation of the engine performance at $n_1 \neq n_2$. Moreover, the DPGBs efficiency is not constant, and is a function of the power transmitted and the rotational speeds of the shafts.

As a conclusion, the engine gas generator is modelled using the state of the art performance modelling methodology. It allows different compressor, turbine, combustor and cooling definitions. Consequently it is suitable for engine design space explorations. On the contrary, none of the specific CROR components performance models proposed by Ref. 72 are suitable for detailed performance modelling and design space exploration.

Engine mechanical preliminary design and weight estimation: The gas generator components are calculated using the state of the art mechanical preliminary design methodologies. It allows the flexible definition of compressors, turbines, combustors, nacelles, frames, shafts and accessories. The DPGB, propeller and CRT are not reported in the list of available WATE components[10]. The weight estimation methodologies for these components are probably late developments not yet made public. Figure 28 presents the graphical representations of a GOR and a DDOR produced by WATE.

[10] Ref. 79 is the latest reference found in the public domain describing WATE capabilities.

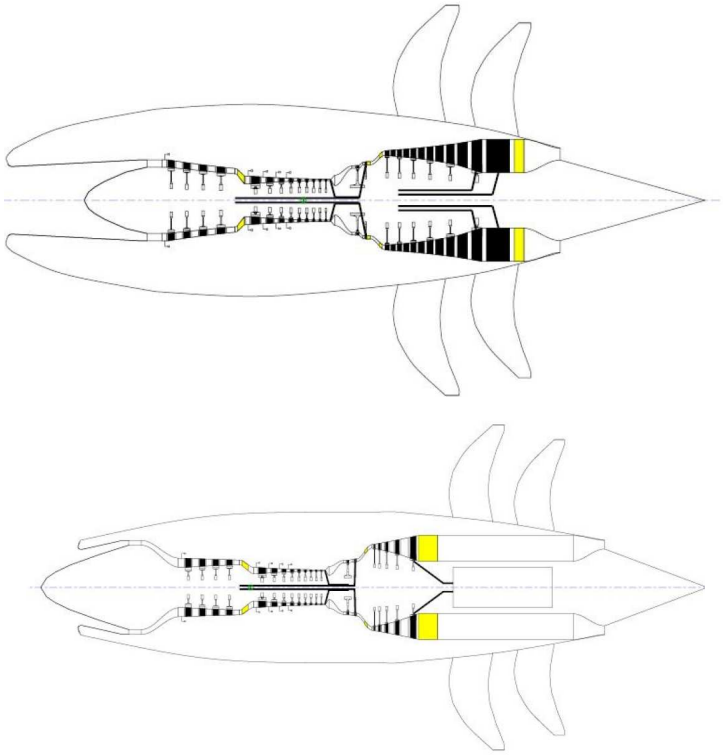

Figure 28: DDOR and GOR preliminary mechanical design from WATE [Ref. 71]

The DDOR CRT is illustrated as a conventional turbine featuring stators and rotors. Furthermore the CRT rotors are illustrated as having conventional turbine disks instead of drums. The GOR differential planetary gearbox is illustrated as a rectangle and its length is twice as long as those of real gearbox designs (for example the AGBT gearbox). The shafts linking the gearbox and the propellers are not shown and would be relatively heavy as they transmit high torques and have large diameters. These aspects suggest that it is likely that the mechanical preliminary design methods used for the CRT and DPGB do not have the same level of detail and fidelity as the conventional engine components.

Gaseous emissions: The NOx emissions at ISA (International Standard Atmosphere) sea level static (SLS) conditions are calculated from a combustor operation curve which is a function of its inlet pressure and temperature. This function is a characteristic of the combustor technology and therefore is applicable to different core designs. This is the sate of the art used for design space exploration at preliminary design level.

Certification noise: The methodology used in ANOPP to calculate the certification noise produced by a known source is the state of the art used at preliminary design level. It enables the calculation of the certification noise of any noise source taking into account its directivity and spectral composition. The characteristics of the CRP emitted noise used in Ref. 71 correspond to a particular design and no methodology is proposed to estimate the noise of different CRP designs.

Assessment 2

Ref. 133 presents a parametric study of the engine weight and mission fuel burn for a DDOR on a 737-800 type aircraft with respect to its core definition (NPR, IPC PR, HPC PR, maximum mission TET and core mass flow rate). This parametric study is performed using the same tools and methods as Ref. 71 (Assessment 1). The performance of the DDOR engine is modelled as a turboprop with a conventional turbine and a single propeller. Only a parametric study of the core components definition was performed due to the simplifications of the LP system modelling. It is difficult to interpret the results of this study because:

- the definition of the OR aircraft and the mission profile are not presented.
- a CRT delivers an almost constant torque ratio[11]. The CRP map used in Ref. 133 was not produced at a constant TR_{CRP}. Consequently, the power balance between the CRT and CRP is not satisfied along an operating line.
- the variation of the cooling flows with respect to the pressure ratios of the compressors and TET is not described. Cooling flows have a large impact on OR engine performance as outlined in section 1.1.2.5.
- it is mentioned that the design point (DP) efficiencies of the compressors and turbines are varied with their pressure ratios, but no details of these variations are provided.
- no information is provided regarding the variation of the CRP DP efficiency with respect to its definition and operation.

Assessment 3

Ref. 73 compares the performance of a GTF and a GOR for a 150 passenger, 3000 nm range aircraft cruising at $M_0 = 0.73$. The mission fuel burn, total and LTO cycle NOx, as well as direct operating costs were calculated and expressed as a difference compared to the GTF. Both engines were designed to minimise the mission fuel burn under certain constraints and design assumptions. The results of this assessment are highly dependent on the assumptions made at aircraft level (acoustic liners weight, differences in required structures for a wing mounted GTF and a rear mounted OR, acquisition and maintenance costs, etc) which are not explicitly mentioned. It is very likely that the difference between the rear fuselage OR and wing mounted GTF aircraft weight was not considered since both engines were designed to deliver the same take-off thrust. Moreover the engine design parameters varied during the optimisation exercise are not mentioned. The modelling methodologies used for this assessment are described in Ref. 81 and Ref. 82 being analogous to those used in Ref. 71. The CRP performance model is a late development not yet reported in the open literature. It uses a single propeller

[11] The TR variations for take-off, climb and cruise power settings are lower than 3% for the CRTs studied in this PhD research project. Refer to Figure 68 - Figure 70 in section 2.2.3.3.2.8.

characteristic to describe the CRT similarly to the NPSS model reported in Ref. 72. The limitations of this methodology were previously discussed in this section. The mechanical preliminary design model of the gearbox used to estimate the weight of the DPGB of the GOR considered a planetary gearbox with one input and one output. This simplification introduces an error in the weight estimation of approximately 15% [Ref. 97]. As a conclusion, the modelling methodologies used for the assessment in Ref. 73 and Ref. 71 are analogous. Consequently they have the same limitations to perform CROR preliminary design space explorations.

Assessment 4

Ref. 36 estimates the difference in fuel burn between a Boeing 737-800 with a CFM-56 and the same aircraft with a CROR for different mission ranges. The software Advanced Aircraft Analysis (AAA) [Ref. 83] was used to perform this assessment. It integrates correlations from existing aircraft and engines [Ref. 84] and simplified performance equations such as the Breguet range and endurance equations. The CROR weight and SFC were obtained by scaling the existing SRP engine correlations. The CROR engine weight was judged to be 17% higher than a turboprop. The CRP efficiency was considered 3% higher than the SRP and the fuel consumption correlation was scaled accordingly. The results of this assessment are difficult to interpret since the same aircraft is used for both engines without considering the implications of different engine installation requirements. Due to their nature, the methods used for this assessment (correlations from existing designs) are very useful to rapidly evaluate conventional designs, but are not appropriate for assessments of novel designs.

1.1.3.1.2 Assessments from the 1970s and 1980s

Five CROR assessments from the 1970s and 1980s were found in the public domain. The first three, Ref. 85, Ref. 86 and Ref. 87 report detailed design efforts of various military aircraft equipped with TFs, SR and CRORs. The fuel consumption of the various engine alternatives are compared for different missions. These studies were done by engine, aircraft and propeller manufacturers within the framework of the ATP project. The estimated fuel savings of the SR and CROR engine aircraft compared to the TF aircraft vary from 9% to 50% depending on the aircraft design and mission. These assessments were performed using design tools of aircraft manufacturers, performance decks of engine manufacturers and data packages of propeller manufacturers. The three studies used the same SR and CROR engine performance simulation tools. Both the SR and the CR GORs were simulated as turboprop engines with a single propeller. P&W provided the decks to simulate the engine cores while Hamilton Standard produced single propeller characteristics for the CRPs. The DDOR was simulated with a deck provided by GE and no details of the modelling methodologies were reported. All engine models were scaled to match the specific aircraft requirements following scaling rules provided by the corresponding engine and propeller manufacturers. Amongst these three assessments, only Ref. 86 presents the impact of engine preliminary design choices at a mission level. The variation in engine static thrust and mission fuel are

presented for different propeller diameters and tip speeds at constant engine power. These variations are only calculated for the geared SR and CROR. Figure 29 shows the variation of the mine warfare mission fuel with respect to the diameter and tip speed of the propeller for a CR GOR. Note that both propellers (forward and rear) have equal diameters and tip speeds.

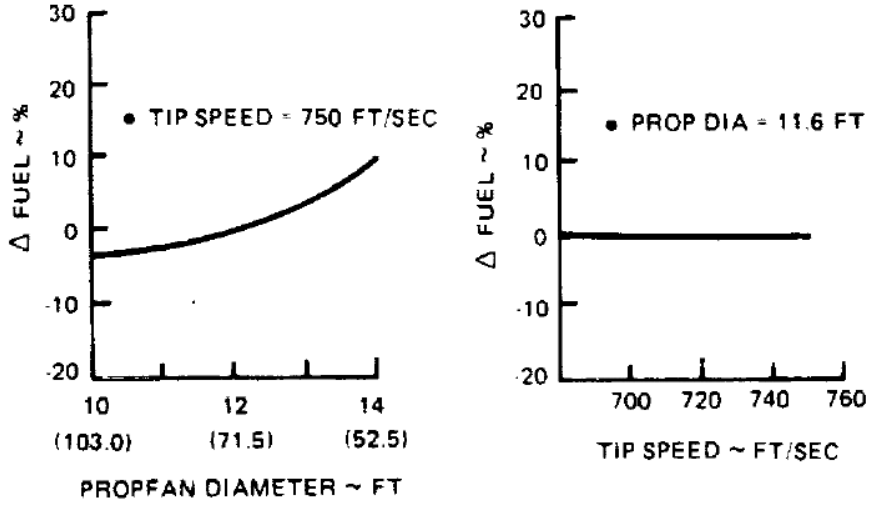

Figure 29: Fuel burn sensitivity analysis (CR GOR, mine warfare mission) [Ref. 86]

The fourth assessment [Ref. 88] is also the outcome of a detailed design effort by aircraft and engine manufacturers but for a civil application. It compares a geared puller SR and CROR in terms of mission fuel burn and noise. Both aircraft were designed for 100 passengers and 1300 nm, cruising at M_0 = 0.8 and 35000 ft (10668 m). It also provides a parametric study of the CRP cruise efficiency with respect to its geometrical definition. This study was done using the PANPER software [Ref. 89][12]. It is important to note that a single component and single operating point parametric study is different than an engine parametric study performed at mission level. Firstly, the single operating point study only captures the changes in one operating point while neglecting the rest of the mission. Secondly, the single component study does not reflect the impact of that single component on the rest of the engine. The mission level simulation tools used in this study are comparable to those used in the three previous assessments.

The fifth assessment [Ref. 114] was carried out by P&W, focusing on the design of the suitable core for a GOR, as well as a suitable SR and a CR gearbox. This reference contains a detailed parametric study of the engine weight, mission fuel, and direct operating costs of a GOR with respect to the main preliminary design

[12] Ref. 89, describing the PANPER software was made public 6 years after the studies in Ref. 88. Ref. 89 existed as an internal document at the United Technologies Research Center since 1979.

parameters of the gas generator (overall pressure ratio, pressure ratio split between spools and design point TET).

A literature review of parametric studies of CRP noise with respect to its main design parameters was conducted. Only one study was found [Ref. 31] and it estimates the variation of free-field perceived noise with respect to the diameter and tip speed of the CRP. It was performed for a 5x5 CRP producing 15000 lbs (66.7 kN) thrust and equal forward and rear propeller blade design, diameters and rotational speeds.

A literature review of SROR assessments was also conducted. Ref. 66 and Ref. 90 to Ref. 95 present various SROR aircraft designs and their performance at mission level. They were carried out by aircraft and engine manufacturers using simulation tools comparable to those used for the CROR assessments previously described. Diverse trade off studies of aircraft design parameters are reported in these studies. The only reported parametric studies with respect to engine design variables were found in Ref. 66 and Ref. 93. They both quantify the influence of the SR propeller diameter on the mission fuel burn. Ref. 96 presents the variation in efficiency of an advanced propeller design at cruise with respect to its tip speed (parametric study at component level).

1.1.3.2 Aero engine preliminary design simulation platforms and tools

The following sections describe the engine preliminary design simulation platforms and tools available at the beginning of this project. In particular, the limitations of these tools to model CRORs are presented.

1.1.3.2.1 Simulation platforms

Two multi-disciplinary aero-engine simulation platforms were found in the open literature.

1) VITAL and NEWAC TERA2020: Technoeconomic Environmental Risk Assessment

TERA2020 is a multi-modular assessment and optimisation platform for civil aero engines. It has been developed collaboratively by European universities under the leadership of CU during VITAL [Ref. 128] and NEWAC [Ref. 129] projects. It consists in a series of executable modules that simulate different aspects of the engine and its use such as the aircraft mission, noise, gaseous emissions and economics. These modules are integrated in a commercial optimizer (ISIGHT [Ref. 127]) that manages the data transfer between modules and provides a graphic interface for TERA2020. This environment enables the user to perform sensitivity analysis, design space exploration, multi objective optimisations among other analyses using all or some of the TERA2020 modules.

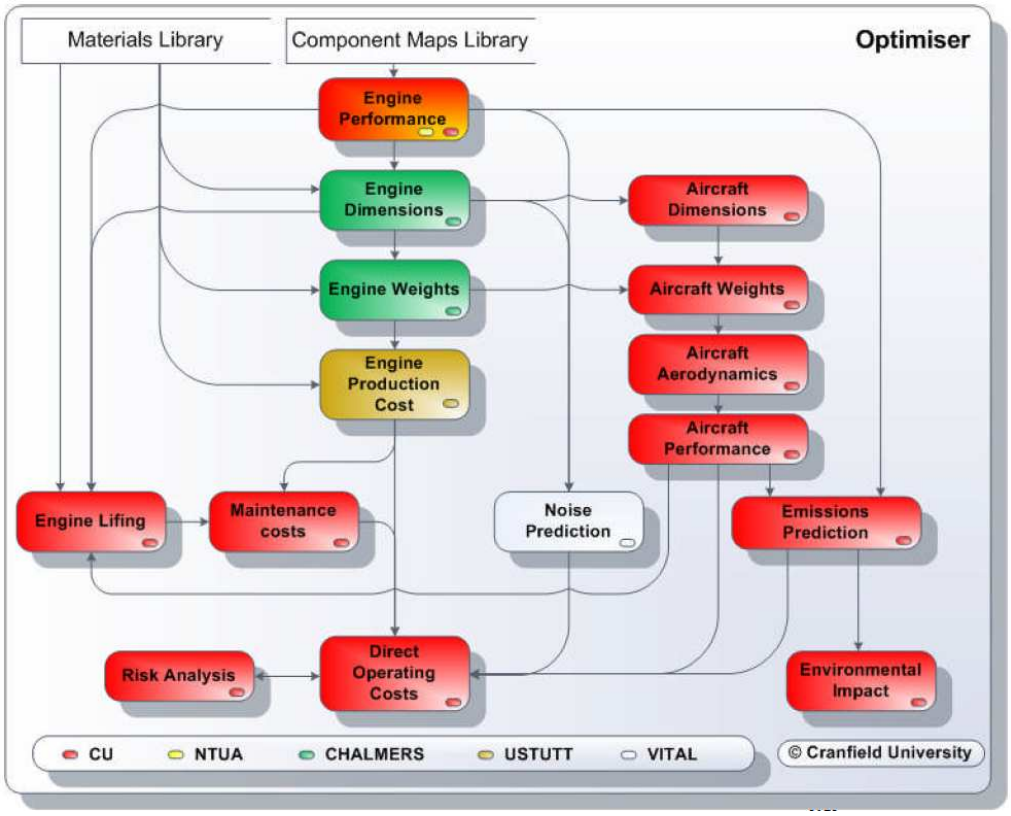

Figure 30: TERA2020 structure [Ref. 105]

Figure 30 shows the structure of the VITAL and NEWAC TERA2020. In the current TERA2020 implementation, the simulation modules are executed in sequence and no loops are required to evaluate a given engine design. The required set of inputs are: the engine preliminary design parameters (e.g.: design point BPR, FPR, etc), an aircraft definition and mission profile, and an economic scenario. The Engine Performance is the first module to be executed and simulates the operation of the defined engine along the specified mission and the noise and emissions certification points. The results enable the Engine Dimensions and Weight module to size the engine and subsequently the Aircraft Performance module to simulate the desired mission. Finally, the noise, gaseous emissions and operating costs are calculated.

The following paragraphs provide a description of each of the tools included in the TERA2020 platform.

***Engine performance*:** Turbomatch [Ref. 110 - Ref. 111], EVA [Ref. 81 - Ref. 82] and PROOSIS [Ref. 112 - Ref. 113] are the three engine performance codes used in the TERA2020. They calculate the engine performance operation at the defined certification and mission points. This data is then used by the other modules to do the mechanical preliminary design, mission performance, emissions, noise and economic calculations. The three of them are 0-D performance simulation codes. This means that the operation of the different components is modelled through thermodynamic equations (based on gas properties) and component operating

maps. The detailed geometrical definition of components is not considered[13] in this type of codes since the maps contain a complete description of the components operation[14]. This makes these tools suitable for performance studies at preliminary design stage and it is important to differentiate it from component design tools. None of them comprise specific CRP, CRT or DPGB components and therefore have the same limitations as NPSS (detailed in section 1.1.3.1.1) to perform CROR design space explorations.

Engine preliminary mechanical design: WeiCo, developed by Chalmers University, can perform a mechanical preliminary design of an aero engine using its performance operation and preliminary design criteria as inputs. It is based on the methodology reported in Ref. 78 and improved during the course of VITAL and NEWAC to reflect the state of the art technologies. It estimates the geometry and mass of each component independently, and the complete list of available components can be found in Ref. 82. It does not comprise DPGBs and propellers. WeiCo also features an engine cost calculation model, developed by Stuttgart University, but this aspect is outside the scope of this thesis.

Aircraft performance: Hermes, developed by CU, calculates an aircraft discrete mission and the exact engine operation at every mission point [Ref. 108]. It requires an aircraft (geometry and weight) and mission definition (flight speeds, altitudes and aircraft configurations) and uses engine performance tables generated by the engine performance module. It considers the aircraft as a punctual mass and solves the motion equations accounting for the aerodynamic forces, aircraft weight and engine thrust. The aerodynamic characteristics of the aircraft at the various configurations (flaps and landing gears settings) are calculated from its geometry. The existing aerodynamic model [Ref. 107] does not allow the accurate calculation of "T" tail aircraft with the engines mounted at the rear. This module can be used to assess novel CROR engines provided that the appropriate aircraft aerodynamic calculation methodology is implemented.

Gaseous emissions model and environmental impact: Hephaestus, developed by CU, calculates the gaseous emissions produced during the LTO cycle and along the entire mission. It also calculates the global warming potential and radiative forces of the different gaseous species for every mission segment. It uses the engine performance along the mission, the aircraft trajectory, combustor characteristics at SLS and the P3T3 method [Ref. 106]. This methodology is valid for CROR engines and it can be used for its assessments.

---

[13] Although the detailed 3-D geometrical definition of the components is not required, some geometrical parameters such as cross sectional area, diameter or overall length may be used.

[14] The non dimensional (0-D) component operating maps are scaled in their various axes in order to fit a particular design requirement. This technique is valid to a first order and its detailed explanation and limitations can be found in Ref. 109.

Noise model: SOPRANO, developed by ANOTEC within the FP6 project SILENCER, can calculate the certification noise produced by an aircraft and its engines. It uses semi-empirical correlations to predict the noise generated by the various sources (airframe, engine fan, combustor, turbine and jet). It then uses the landing and take-off trajectory and a propagation method to calculate the effective perceived noise in the three certification points. SOPRANO can not be used to assess CROR engines because it can not calculate propeller noise, and the CRP is the dominant source of the engine.

Economic model: The economic analysis of OR engines is outside the scope of this thesis. Details of the VITAL and NEWAC TERA2020 Economic module can be found in Ref. 82.

2) EDS: Environmental Design Space

EDS is a multi-disciplinary engine evaluation simulation platform developed collaboratively between the Georgia Institute of Technology, the Massachusetts Institute of Technology (MIT), NASA, and the Federal Aviation Administration (FAA). It is part of a larger simulation framework called Environmental Tool Suit, which includes further simulation tools to assess fleet operations and impacts of regulations [Ref. 104]. It integrates NPSS, WATE, FLOPS, ANOPP and other NASA simulation tools [Ref. 104]. Its structure, data flow and data exchange methods are similar to those of TERA2020. This simulation framework was used for the GOR and DDOR assessment reported in Ref. 71. Its limitations to perform CROR design space explorations are described in section 1.1.3.1.1. Older NASA engine evaluation platforms used NEPCOMP and QNEP [Ref. 103] instead of NPSS as engine performance simulation tool. The performance modelling methodologies used in these two codes are comparable to those used in NPSS. Consequently, they have the same limitations with respect to CROR modelling.

1.1.3.2.2 Simulation tools and methodologies

Two other established gas turbine performance simulation software available in the public domain are Gasturb [Ref. 100] and GSP [Ref. 101]. None of them include CRT, CRP or DPGB components.

No performance modelling methodology was found for CRTs at the beginning of this research project[15].

[15] Ref. 132 (published 9 months after the completion of the present research project but before the thesis submission) proposes a performance modelling methodology for a 1+1/2 HP-IP counter rotating turbine (see detailed description of such turbines in section 2.2.3.3). The only reported details of this model are that it is 1-D and that losses are estimated using the method proposed in Ref. 174. Performance maps for a 1+1/2 HP-IP turbine design are also presented in Ref. 132. However, the operation of a high speed 1+1/2 HP-IP turbine is not representative of the operation of a low speed LP CRT with a large number of stages (~20). For example, the maximum turbine corrected mass flow rate for the maps presented in Ref. 132 is the same for all the rotational speeds and speed ratios. This means that the choke condition occurs first at

Various 2-D and 3-D CRP aerodynamics and performance calculation methods exist which require a 2-D or 3-D detailed design of the CRP (a comprehensive bibliography is presented in Appendix B). These methods are not suitable for a preliminary design space exploration since a dedicated CRP has to be designed for every evaluated engine.

The necessary three shaft DPGB performance model can be implemented from a kinematic analysis of the gearbox and the efficiency characteristics presented in Ref. 102.

No mechanical preliminary design and weight estimation methodology of DPGBs was found. A method to estimate the weight of advanced propellers is available in Ref. 99. It is proposed by Hamilton Standard (propeller manufacturer) and further details are presented in section 2.3.

Several recent works present 3-D CFD unsteady calculations from which the CRP certification noise can be calculated. Due to the required computational resources, these methodologies are not suitable for a design space exploration. The only analytical CRP noise prediction code found in the public domain was CRPFAN [Ref. 98]. It predicts loading and thickness noise as well as the interactions between the two propellers. However, it is not capable of evaluating broadband noise and the noise of rotors having advanced low-noise blade designs [Ref. 71].

1.1.3.3 Summary

A multi-disciplinary engine design space exploration is required for the OR preliminary design studies. Various existing GOR and DDOR assessment studies were reviewed. They present the performance of specific aircraft and OR engine designs at mission level. The limitations of the used CRT, CRP and DPGB simulation models were identified. Only one of the reviewed studies [Ref. 86] present the influence of LP engine design parameters on the mission fuel burn. It shows the variation of mission fuel with respect to the CRP diameter and tip speed (for equal forward and rear diameter and tip speed). One study [Ref. 31] containing CRP noise trends with respect to its diameter and tip speed was found. No trade-off studies of the mission fuel burn, noise and emissions of GOR and DDOR designs were found. The modelling methodologies to predict aircraft performance, gaseous emissions, engines gas generator performance and mechanical preliminary design reported in Ref. 71 and Ref. 73 (available in the VITAL and NEWAC TERA2020 platform) can be used for a CROR design space exploration. Adequate preliminary design methods to calculate the CRP weight and the DPGB performance and

---

the inlet guide vane (IGV). This is not the case for a low speed CRT with large number of stages, where the choke occurs first at the last rotating stage (and therefore the maximum turbine corrected mass flow rate is a function of rotational speeds). Consequently even if the maps presented in Ref. 132 would have been available before, it would not have been appropriate to use them for the DDOR model.

operation were found. No methodology was found to perform a preliminary mechanical design and weight estimation of a DPGB. No methodology to model the performance of CRTs was found. The existing CRP performance and noise calculation tools are not suitable for design space exploration.

1.2 Research objectives and methodology

The main objective of the present research work is to assess the variation in mission fuel burn, noise and emissions of a pusher GOR and a DDOR with respect to the following preliminary design and control variables:

- IPC bleed mass flow rate (for cooling and noise reduction techniques)
- Nozzle pressure ratio (NPR) at DP[16]
- Spacing between propellers
- Hub diameters of the propellers
- Number of blades of the forward and rear propellers
- Diameters of the forward and rear propeller
- Forward and rear propeller rotational speeds at top of climb (TOC) and take-off (design variables)
- Forward and rear propeller rotational speeds as control variables
- Number of stages of LPT or CRT
- DPGB torque ratio (for the GOR)
- Efficiencies of core compressors, turbines and DPGB at DP

These assessments focus on the specific CROR LP components while the engine gas generator technology level (overall pressure ratio and design point TET) is fixed and is the same for the GOR and DDOR.

The present study is the main contribution of Work Package 1.2 to the DREAM project. It is the result of a collaborative effort between CU, Aristotle University of Thessaloniki, Stuttgart University and Chalmers University. It was performed using a customised OR-TERA2020 framework, based on the VITAL and NEWAC TERA2020 methodologies. While both EDS and TERA2020 were deemed to be equally capable for performing these assessments, the TERA2020 tool was selected as the DREAM university partners could have complete control of the source code and integration of the modules.

In order to overcome the limitations of the VITAL and NEWAC TERA2020 simulation tools and perform the assessments defined above, the following objectives and requirements were defined:

- Development of a 0-D performance modelling methodology for CRPs allowing the independent definition of the forward and rear propeller design and operation. For example, it should be capable of calculating the

[16] The DP NPR defines the pressure drop across the LPT and consequently the ratio between the core thrust and the power of the propellers.

performance of a CRP with a clipped rear propeller operating at a different rotational speed than the forward propeller.

- Development of a 1-D methodology and simulation tool to predict the performance operation of CRTs. This methodology should allow the study of different CRT designs at various operating conditions including, for example, different rotational speeds of the rotors (both at design point and off design).
- Development of a 0-D performance modelling methodology for CRTs resulting from studies carried out with the 1-D CRT simulation tool. This methodology should enable the flexible definition of the CRT design and operation in terms of its flow parameters, extracted power and the rotational speeds of both drums.
- Implementation of a DPGB performance simulation methodology capturing the independent operation of its three shafts.
- Development of advanced GOR and DDOR engine performance simulation models in PROOSIS using the previously developed component models. They should capture the effects of the variation of the previously listed LP design and control variables on the design and off design performance of the GOR and DDOR engines.
- Implementation of aerodynamic characteristics for pusher OR powered aircraft in Hermes.
- Implementation of the propeller weight estimation methodology of Ref. 99 in WeiCo.
- Development a mechanical preliminary design model of a DPGB as well as pusher GOR and DDOR (by Chalmers University and Stuttgart University). Development of a CROR certification noise prediction code (by Aristotle University of Thessaloniki)[17].
- Development of a CROR multi-disciplinary assessment platform, integrating the developed engine and aircraft performance, preliminary mechanical design and noise modules as well as the existing emissions module using ISIGHT [Ref. 127].

[17] Other than these tasks, all the other tasks were performed by the author or by MSc researchers under the direct technical leadership of the author.

1.3 Contribution to knowledge

The overall contribution to knowledge is the assessment of the impact of the main LP GOR and DDOR preliminary design and control parameters on mission fuel burn, certification noise and emissions. These assessments identify the optimum design regions to be explored in further detail with dedicated design tools. Additionally, they aid in the design process when compromises need to be performed as a consequence of design, operational or regulatory constraints.

Novel methodologies to model the performance of CRPs (0-D) and CRTs (1-D and 0-D) were developed. Additionally, a performance model of a DPGB was developed. Using these component models, novel CROR engine performance models were developed which allow the independent definition of the design and operation of the two parts of the CRP and CRT. This is not possible with other state of the art modelling tools.

1.4 Thesis outline

This thesis is divided into four chapters:

Chapter one presents the CROR engines in the present civil aviation context, a literature review of the main OR technological challenges and developments, as well as the existing OR assessments and preliminary design simulation tools. The project objectives and methodology of the present research work are defined and the main contributions to knowledge are presented.

Chapter two describes the development and verification of the specific CROR simulation tools as well as the integrated multi-disciplinary assessment framework.

Chapter three presents the assessment of the impact of the main LP GOR and DDOR preliminary design and control parameters on mission fuel burn, certification noise and emissions.

Chapter four contains the conclusions of the assessment studies and recommendations for further work.

2 SIMULATION PLATFORM

This chapter presents the requirements and developments of the preliminary design simulation tools and integrated platform required to assess the GOR and DDOR engines. This platform, named OR-TERA2020, is the result of a collaborative effort between universities during the DREAM project, under the technical leadership of SNECMA. It comprises the following modules: engine and aircraft performance, engine preliminary mechanical design and weight, gaseous emissions and noise. The main contributions of the present research work to the OR-TERA2020 platform are the CROR engine and aircraft performance modules. The modelling methodologies used in the engine and aircraft performance modules are presented in detail in this chapter. Descriptions of the modelling methodologies of the three other modules: engine preliminary mechanical design and weight (co-developed by Chalmers and Stuttgart Universities), CROR certification noise (developed by the Aristotle University of Thessaloniki) and engine gaseous emissions (developed by Cranfield University during NEWAC) are also provided. Another contribution of the present research work to the OR-TERA2020 is the design and integration of the framework using ISIGHT. An overview of its structure, the calculation sequence and flow of information between the different modules is provided in this chapter. The global understanding of the framework and its individual modules provides a basis to interpret the results of the assessments presented in this thesis.

2.1 Simulation platform requirements

To perform the CROR assessments, it was envisaged that the simulation platform would be required to have the following capabilities:

- the platform and individual modules would be able to capture the variation of mission fuel burn, certification noise and emissions with respect to the main preliminary design and control variables for a GOR and a DDOR engine (defined in section 1.2).
- the evaluation of an engine design would be performed in less than 30 seconds, using a standard PC, so that the execution of broad design space explorations are possible within a maximum of five hours. This computational limit set the types of methods used in the different modules. It also imposed that the various modules had to be run in sequence since iterations between modules require a significantly higher computational power or calculation time.

The performance of the different engine designs was assessed for a fixed aircraft definition. This is consistent with the current aircraft manufacturer and engine OEM approach. An alternative approach could have been to match the aircraft design (aerodynamic, structural and acoustic treatments) with respect to the engine definition and performance in an iterative process. This approach would have required iterations between the various OR-TERA2020 modules which is not

compatible with the computational time requirements of the platform. Furthermore, the development of a dedicated detailed aircraft conceptual design tool would have also been required.

The requirements of the specific modules are presented in their respective sections.

2.2 Engine performance

2.2.1 Requirements

Two engine performance decks, one for the GOR model and another for the DDOR model, were required for the OR-TERA2020 platform. It was envisaged that these decks would be able to size the thermodynamic cycle of the engine at a design point (DP) and then calculate its steady state performance at all the off-design (OD) conditions required by the different modules of the framework. The models included in these decks were required to capture the variation in DP performance with respect to the following engine design and DP cycle definition parameters:

- thrust requirement
- pressure ratios of the compressors
- power off-takes
- TET
- pressure losses of the burner, ducts and secondary air system (SAS)
- cooling flows
- NPR
- spacing between the propellers
- hub diameters of the propellers
- number of blades of the forward and rear propellers
- diameters of the forward and rear propellers
- rotational speeds of the forward and rear propellers
- number of stages of LPT or CRT
- TR_{DPGB} for the GOR.

The models were also required to capture the variation in OD performance with respect to the following operational parameters:

- control variables: forward and rear propeller rotational speeds and TET (see sections 2.2.4 and 2.2.5)
- flight conditions: Alt, M_0 and ambient temperature (dISA). The minimum flight speed to be simulated was M_0 = 0.1. This is because at static conditions and very low forward speeds, the flow field around a propeller is very dependent on its installation. For representative predictions of the operation of ORs at very low forward speeds, detailed engine-aircraft installation studies are required.
- thrust and power off-take requirements

The performance models had to be 0-D in order to comply with the computational time requirements. The DP component efficiencies had to reflect an estimated year 2020 technology level. Technology curves were required in order to predict the DP efficiency of the various components as a function of their preliminary design definition and performance operation. These technology curves had to be integrated into the DP iterative calculation process since they affect the engine cycle definition. The direct input of DP efficiencies of the components was also required in order to assess the impact of not achieving the efficiency targets predicted by the technology curves.

It was deemed necessary for the performance models to incorporate preliminary design feasibility criteria (such as maximum loadings, achievable stage turning angles, diffusion factors, de Haller numbers, etc) for the turbomachinery components. Mechanical feasibility criteria were also required for the mechanical preliminary design module. These two sets of criteria had to be consistent with the choices made for the technology curves and were used to determine the feasibility of an engine definition. It is important to highlight that these are simplified criteria that give an indication of the feasible design space. The detailed design and manufacturing feasibility of an engine, taking into account all certification requirements, can only be determined by OEMs using dedicated design tools.

2.2.2 Performance model description

The following sections describe the developed CROR engine performance models. Firstly, the engine component models as well as their technology curves and feasibility criteria are described. Secondly, the DDOR and GOR engine models are presented. Finally, a description of the OR-TERA2020 performance decks is provided.

PROOSIS was selected to develop the CROR performance models because of its flexibility to create and modify engine component models, access to the source code of the components, flexibility to define the mathematical methods to be used and its capability to generate stand alone executable decks.

2.2.3 Component models

This section describes the performance models of the components used in the DDOR and GOR engines. The CRP, CRT and DPGB component models were developed within the present research project and are described in detail. Some specific aspects of the conventional component models are also presented.

2.2.3.1 Conventional components

The conventional aero engine components of the CRORs were modelled using the PROOSIS TURBO V1.0 library components indicated in Table 2. A complete description of these models can be found in Ref. 130 and Ref. 131.

Component	TURBO V1.0 library component
Fluid model	General
Atmosphere	Atmosphere
Inlet	InletAtm
Compressors	Compressor4SasPMapBETA
Simple ducts	Duct0SasP
Shafts	Shaft, ShaftStart, ShaftEnd
SAS mixer and splitter	SasMixer2in1out, FS2FlowOutletSas
Burner	Burner
Turbines	turbineBasicMapZETA
SAS reintroduction	BldBack1SasP, BldBack2SasP
Nozzle	Nozzle

Table 2: Used PROOSIS TURBO V1.0 Components

Two sets of modifications were done to these components:

- manipulation of the equations to improve the numerical stability of the engine models.
- use of the industry standard definitions of corrected mass flow rate and corrected rotational speeds of compressors and turbines.

$$\dot{m}_{COR} = \frac{\dot{m}_{in}\sqrt{\frac{Tt_{in}}{288.15}}}{\frac{Pt_{in}}{101325}} \quad \text{instead of} \quad \dot{m}_{COR} = \frac{\dot{m}_{in}\sqrt{\frac{Tt_{in}}{T_{REF}}}}{\frac{Pt_{in}}{P_{REF}}} \quad \text{[Eq. 6]}$$

$$n_{COR} = \frac{n}{\sqrt{\frac{Tt_{in}}{288.15}}} \quad \text{instead of} \quad n_{COR} = \frac{n}{\sqrt{\frac{Tt_{in}}{T_{REF}}}} \quad \text{[Eq. 7]}$$

where P_{REF} and T_{REF} are the reference total pressure and total temperature of the design points of the component maps used for the gamma and Reynolds corrections. The adopted modifications do not have an influence on the results of engine performance calculations, but provide consistency between the different turbomachinery components and with industry standard.

2.2.3.1.1 Technology curves and feasibility criteria

The DP efficiencies of the conventional components were calculated as follows:

Compressors and HP and IP turbines

The polytropic efficiency of the compressors and HP and IP turbines were kept constant for all the designs. The selected values are judged to be representative of year 2020 technology level for each component. The compressors and turbines

were then consistently designed (in terms of flow path, rotational speeds and number of stages) in WeiCo to achieve the target polytropic efficiencies. This choice was possible because the flow path, rotational speeds, axial velocities and number of stages of the IP and HP turbines and compressors were neither constrained nor used as design variables for the assessments.

The feasibility of these components was ensured by the design criteria imposed in WeiCo.

Inlet, burner, ducts and SAS components

These components were considered to have a fixed DP pressure loss expressed as a percentage of the inlet total pressure. This was possible since no specific geometric parameters of these components were used as input to the simulations. Some of these values vary between the DDOR and the GOR since the architectures are different and therefore require different ducts and SAS components designs.

No specific feasibility criteria were used for these components.

Burner and shafts

These components were considered to have a constant DP efficiency. This was possible since no specific shaft or burner design parameters were used as inputs.

No specific feasibility criteria were used for these components.

LPT for GOR

The efficiency of the LPT was calculated in order to capture the effects of the desired preliminary design variables on the engine DP performance whilst respecting the specific GOR design constraints. The DP rotational speed of the GOR LPT is given by the DP rotational speeds of the propellers and TR_{DPGB}. Both the DP rotational speeds of the propellers and TR_{DPGB} are inputs to the performance model. The power extracted by the LPT at the DP mainly depends on the propeller DP efficiency and the NPR. The inlet conditions (mass flow rate, Pt and Tt) of the LPT depend on various engine design parameters. The number of stages of the LPT is also an input to the performance model (2 and 3 stages LPT concepts are studied). Both the internal and external diameters of the LPT are constrained[18].

DP Efficiency calculation: A set of preliminary design assumptions for the LPT were adopted in the performance and in the mechanical preliminary design and weight estimations modules. A DP efficiency calculation procedure was developed based on the following assumptions.

[18] The external diameter of the LPT has to be smaller than internal diameter of the CRP module. The internal diameter of the LPT has to be larger than the diameter of the DPGB module.

Preliminary design assumptions for the LPT:

- The mean radius ($r_{mean\ i}$) of each turbine stage is known (not equal for all the turbine stages).
- The axial inlet velocity to every turbine stage is the same for all the stages. Different values are used for the 2 and 3 stage turbines.
- The LPT power extraction is divided equally into the number of stages.
- The calculations are based on a constant Cp and γ. (implications presented in Ref. 109)

Both the mean radii and the axial inlet velocities for the 2 and 3 stages turbines are taken from the work by WP.2.5 during the DREAM project reviews [Ref. 134]. This WP performed a detailed design of a 2 and 3 stages LPT for the GOR using OEM design methods and tools. The specific details and values are included in sections 3.2.1.1 and 3.2.3.6.2.

Proposed DP efficiency calculation and verification

The isentropic efficiency of every stage ($\eta_{is\ i}$) is obtained from the Smith chart [Ref. 109] with:

$$Pw_{Stage} = \frac{Pw_{LPT}}{NbStages_{LPT}} \qquad \text{[Eq. 8]}^{19}$$

$$\Delta ht_{Stage} = \frac{Pw_{Stage}}{\dot{m}_{LPT\,in}} \qquad \text{[Eq. 9]}$$

$$U_i = r_{mean\ i}\, 2\pi n_{LPT} \qquad \text{[Eq. 10]}$$

where Pw_{LPT} and $\dot{m}_{LPTin}$ are calculated during the engine matching procedure, and n_{LPT} is calculated from n_1, n_2 and the DPGB definition (see Eq. 162). The mean axial flow velocity (V_A), required to read the Smith chart, is calculated by the performance model from the LPT inlet conditions and cross sectional area, and it is assumed constant along the stages.

After this, the outlet Tt and Pt is calculated for every the turbine stage:

$$\Delta Tt_{Stage} = \frac{\Delta ht_{Stage}}{Cp} \qquad \text{[Eq. 11]}$$

$$Tt_{out\,i} = Tt_{in\,i} + \Delta Tt_{Stage} \qquad \text{[Eq. 12]}$$

[19] Note that Pw_{LPT} is negative since it is extracted from the flow.

$$Pt_{out\,i} = Pt_{in_i}\left(1-\frac{\left(1-\frac{Tt_{out\,i}}{Tt_{in\,i}}\right)}{\eta_{is\,i}}\right)^{\frac{\gamma}{\gamma-1}} \quad \text{[Eq. 13]}$$

$$Tt_{in\,i+1} = Tt_{out\,i} \quad \text{[Eq. 14]}$$

$$Pt_{in\,i+1} = Pt_{out\,i} \quad \text{[Eq. 15]}$$

Finally, the isentropic LPT efficiency ($\eta_{is\,LPT}$) is calculated

$$\eta_{is\,LPT} = \frac{1-\frac{Tt_{LPTout}}{Tt_{LPTin}}}{1-\left(\frac{Pt_{LPTout}}{Pt_{LPTin}}\right)^{\frac{\gamma-1}{\gamma}}} \quad \text{[Eq. 16]}$$

For the baseline engine the average LPT Tt was close to 950K and the following gas properties were adopted for all the efficiency estimations:

$\gamma = 1.338$

$Cp = 1135\ (J/(kg\,K))$

Verification of the proposed DP efficiency calculation methodology

The proposed DP efficiency calculation methodology was included in the DP calculation process for the GOR engine (the CRP and DPGB not yet described were used in this model). The DP efficiencies of the two turbine designs presented in Ref. 134 were calculated for the baseline GOR engine. TR_{DPGB} was selected to match the DP LPT rotational speeds used in Ref. 134 (6056 for the 3 stage LPT and 7570 for the 2 stage LPT) and the mean radius of each turbine stage was obtained from the cross sectional drawings of the turbine flow paths. The total turbine power, inlet mass flow rate and mean axial velocity at the DP were calculated with the GOR performance model (described in section 2.2.4) during the DP iterative calculation procedure. The obtained DP efficiencies were 0.9003 for the 2 stages LPT and 0.9049 for the 3 stages LPT. According to Ref. 134, the DP efficiency of the 2 stages and 3 stages LPTs are 0.9 and 0.905 respectively. The difference between the estimations produced by the proposed methodology and the OEM design tools is smaller than 0.03%.

Year 2020 technology

The efficiency levels calculated by WP 2.5 during the DREAM project correspond to 2009 technology. It was decided to multiply the single stage efficiencies obtained

from the Smith chart by a factor of 1.02[20] to account for the progress in turbine technologies (sealing, materials, tip clearance control, etc) that could be achieved by 2020.

As it can be seen, the LPT efficiency obtained with this methodology would increase as the LPT rotational speed increases. This is true up to a certain limit in which the increase of "speed dependant" losses is higher than the reduction of "angle dependant" losses. In order to simulate this limit which is not considered in the Smith chart, a maximum limit of $\eta_{is\ LPT} = 0.93$ was set to this function. This value was judged to be representative of the maximum efficiency that could be achieved by 2020.

Feasibility: Feasibility criteria are required to asses in a simple way the aerodynamic and mechanical feasibility of the LPT designs generated with the simplified preliminary design assumptions. A complete feasibility study of a turbine design would require dedicated turbine design tools and methods.

Two criteria were used:

- Stage turning angle < 120º due to geometric limitations in the design of the turbine channels [Ref. 168].
- LPT rotational speed < 7650 rpm to ensure the mechanical integrity of the LPT and to limit the tip Mach numbers (based on discussions with OEM).

General statement for conventional components

The exact values of the DP efficiencies, pressure losses of the conventional engine components, as well as the LPT preliminary design assumptions are presented in sections 3.2.1 and 3.3.1 which describe the baseline GOR and DDOR engines respectively. The technology curves and feasibility criteria for of the CRP, CRT and DPGB are presented in sections 2.2.3.2.5, 2.2.3.2.6, 2.2.3.3.3.1, 2.2.3.4.4 and 2.2.3.4.5.

2.2.3.2 CRP

A description of the advanced CRP concept, its advantages and the challenges associated to its use were described in sections 1.1.2, 1.1.2.1 and 1.1.2.5 respectively. The following sections present the CRP performance model requirements, the proposed model, its implementation in PROOSIS and its verification against experimental data available in the public domain.

2.2.3.2.1 CRP performance model requirements

From a performance point of view, a CRP comprises two single propellers driven by two independent power sources. They are aerodynamically coupled (the operation

[20] Based on discussion with OEM experts.

of the rear propeller has an impact on the operation of the forward propeller and vice versa) because they operate in the same flow field and they are relatively closely spaced. Both propellers may differ in terms of number of blades, blade geometry and diameter.

The limitations of a single characteristic representation of a CRP for engine performance calculations and design space exploration were described in section 1.1.3.1.1 (Assessment 1). In order to simulate different OR engine designs and control strategies, it is necessary to model each propeller independently and account for their interactions. 2-D and 3-D modelling approaches (a comprehensive bibliography describing these methods is provided in Appendix B) are not compatible with the time requirements of the simulation platform since a dedicated CRP has to be designed for every evaluated engine and its performance has to be computed at all the mission points for different control strategies.

It was envisaged that the CRP model would calculate the performance of a CRP from the 0-D characteristics of both propellers operating in isolation, allowing a flexible and independent definition of the:

- diameters of the forward and rear propellers (with $D_2 < D_1$)
- hub diameters of the propellers (both hubs have the same diameter)
- spacing between propellers
- rotational speeds of the forward and rear propellers
- the power absorbed by the forward and the rear propellers
- flight conditions in terms of altitude, temperature and flight speed. A minimum $M_0 = 0.05$ was considered as a requirement. The static operation of a CRP is highly dependent on installation effects and its computation is beyond the scope of this PhD research project. Ref. 147 gives an insight to some specific aspects of the static thrust calculation of CRPs.

A technology curve was also required to calculate the DP efficiency of both propellers with respect to the aforementioned variables as well as the number of blades of the propellers. Designs with 8 to 16 blades were considered.

2.2.3.2.2 Proposed CRP performance model

First of all, a brief description of the isolated propeller operation and the non dimensional representation of its performance are presented (based on Ref. 135). Subsequently, a performance calculation methodology is proposed for the forward and rear propellers of a CRP based on the operation of the isolated propellers and their interactions.

2.2.3.2.2.1 Isolated propeller

Figure 31 shows that, by keeping the advance ratio (J defined in Eq. 17) constant while varying the flight speed and rotational speed, the air incidence angle remains constant over every section of the blade. A propeller can be considered as a series of adjoining airfoils. Applying non dimensional airfoil theory, it can be deduced that

for all the operating cases with the same advance ratio J, the resultant force vector (the sum of lift and drag forces for all blade sections) has a defined position and direction and its magnitude is proportional to:

- The square of the blade-air relative speed at a given section (typically 75% blade span)
- The blade area (which is proportional to the square of the propeller diameter)
- The air density

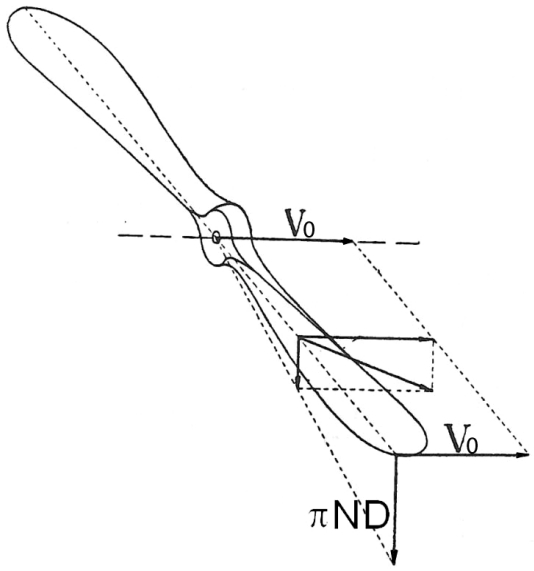

Figure 31: Air incidence distribution along a propeller blade [Ref. 136]

The thrust, power and efficiency for a given propeller are subsequently expressed as:

$$J = \frac{V_0}{nD} \qquad \text{[Eq. 17]}$$

$$Fn = \rho V_0{}^2 D^2 f\left(\frac{V_0}{nD}\right) = \rho J^2 n^2 D^4 f(J) = \rho n^2 D^4 C_T \qquad \text{[Eq. 18]}$$

$$Pw_{mech} = \rho n^3 D^5 C_P \qquad \text{[Eq. 19]}$$

$$\eta_{NET} = \frac{Pw_F}{Pw_{mech}} = \frac{Fn\ V_0}{Pw_{mech}} = J\frac{C_T}{C_P} \qquad \text{[Eq. 20]}$$

(where: C_P (power coefficient), C_T (thrust coefficient)and η_{net} (net efficiency) are all functions of J, the blades angle setting and the propeller design)

Figure 32 shows a typical propeller map where the power coefficient (C_P) and net efficiency (η_{NET}) are plotted as a function of advance ratio (J) for various blade angle settings (typically measured with respect to the propeller plane at 0.75 r and noted as $\beta_{0.75}$). This non dimensional representation allows the calculation of the

performance of propellers with a given design and different sizes at different operating conditions. For example, for a given propeller design of a given diameter operating at a given flight speed and rotational speed, and absorbing a given power, the required blade angle can be obtained from this characteristic map. The blade angle can then be used to obtain the propeller efficiency and subsequently the thrust produced by that propeller at those operating conditions.

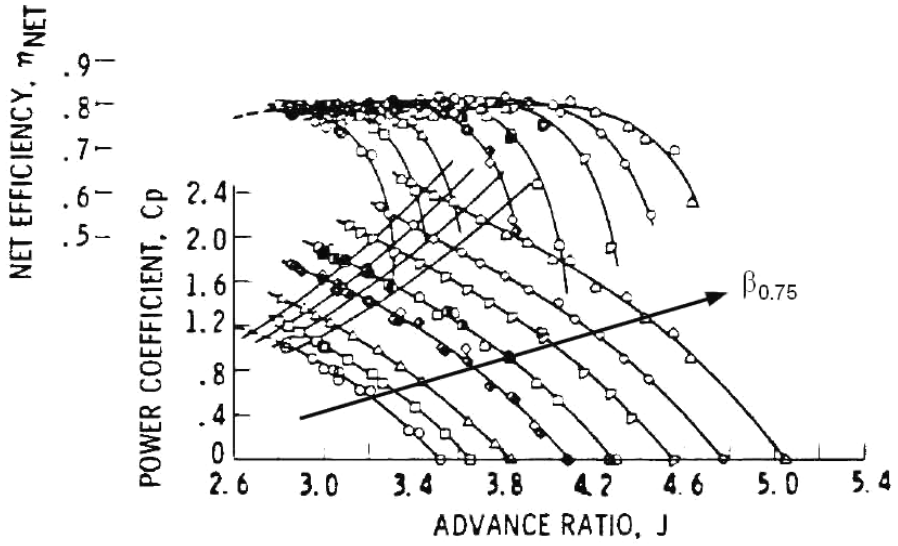

Figure 32: Typical propeller performance map [Ref. 137]

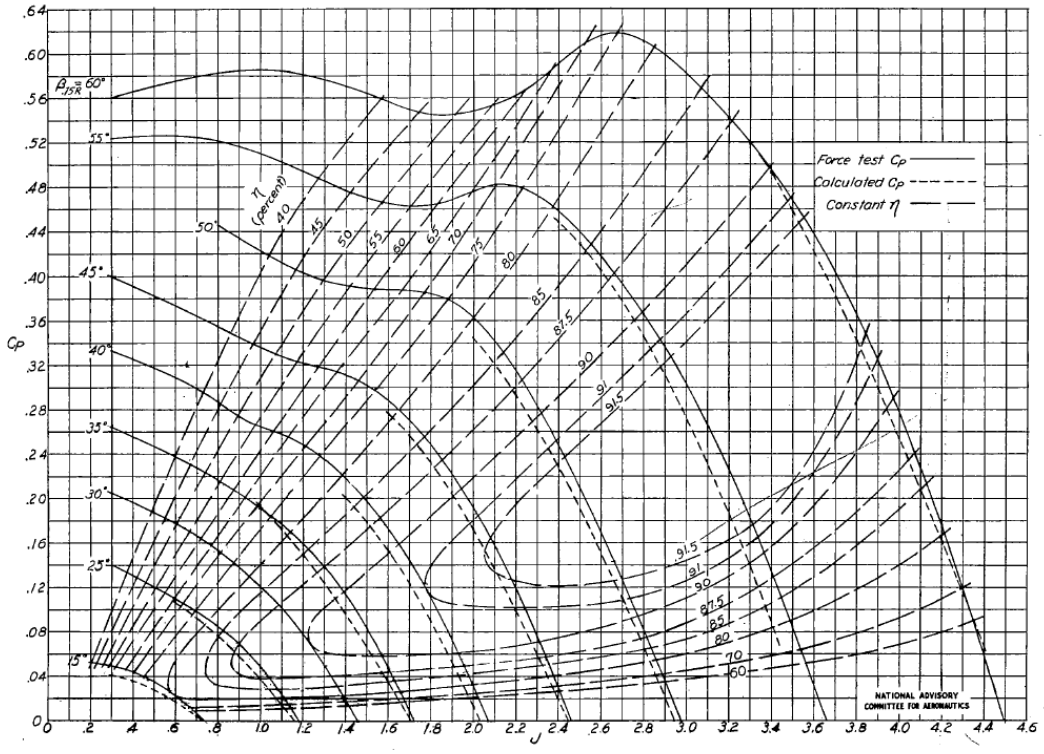

Figure 33: Alternative propeller performance map [Ref. 138]

Figure 33 presents an alternative propeller performance map, commonly used in literature, containing the efficiency values as contours on the C_P vs. J characteristic map.

A single propeller map is non-dimensional and is a valid representation of the operation of propellers of any diameter (with a given design) but is not valid for different:

Hub to tip ratios

For two propellers with different hub to tip ratios operating at the same J, the incidence angles to each blade airfoil (and consequently the distribution of forces) cannot be equal. This implies that for a given advance ratio and propeller pitch, the thrust produced and power required will also be different.

Hub or nacelle shapes

The shape of the hub (for puller configuration) and the engine nacelle (for the pusher configuration) have an influence on the flow field across the propeller. The evaluation of the variation in propeller performance with respect to the hub or nacelle shape is part of a detailed design effort and is outside of the scope of this work.

Flight Mach numbers

Compressibility effects have a significant influence on the performance of a propeller, particularly for $M_0 > 0.6$. The Reynolds effects are negligible compared to the compressibility effects for:

- thin airfoil blade designs
- $M_0 > 0.2$
- the dimensions typically used in aircraft engines and propeller wind tunnel tests [Ref. 140].

The chosen approaches to overcome these limitations were respectively:

Hub to tip ratios

A first order approximation to account for the effects of changing the hub to tip ratio can be achieved by rewriting Eq. 18 to Eq. 20. This time, since the hub to tip ratio may vary, the blade area is not proportional to the square of the propeller diameter any more, but proportional to the area of the propeller disk (A_{disk} defined in Eq. 21). A set of modified non dimensional power coefficient and thrust coefficients (denoted PQA and TQA respectively) are obtained:

$$A_{disk} = \frac{\pi}{4} D^2 \left(1 - \left(\frac{D_h}{D} \right)^2 \right) \qquad \text{[Eq. 21]}$$

$$Fn = \rho {V_0}^2 A_{disk} f\left(\frac{V_0}{nD} \right) = \rho J^2 n^2 D^2 A_{disk} f(J) = \rho n^2 D^2 A_{disk} TQA \qquad \text{[Eq. 22]}$$

$$Pw_{mech} = \rho n^3 D^3 A_{disk} PQA \qquad \text{[Eq. 23]}$$

$$\eta_{NET} = \frac{Pw_F}{Pw_{mech}} = \frac{Fn\ V_0}{Pw_{mech}} = J\frac{TQA}{PQA} \qquad \text{[Eq. 24]}$$

(where: TQA, PQA and η_{NET} are all functions of J, the blades angle setting and the propeller design)

The use of PQA and TQA to describe the performance of a propeller with different hub to tip ratios is only a first order approximation. It can be seen in Figure 31 that for a constant J, the angle of attack to every blade airfoil changes with the hub to tip ratio. The calculation of a propeller is correct for the specific hub to tip ratio used to produce its map (or PQA TQA η_{NET} functions). The error in the calculations increases as the difference between the hub to tip ratio of the calculated propeller and the hub to tip ratio used to produce its map increases. For this reason only very small changes in hub to tip ratio (±5%) are assessed within this thesis.

Flight Mach numbers

A fully rigorous performance calculation of a high speed propeller would require the use of a series of propeller maps corresponding to different flight Mach numbers. Based on this library of maps, the flight Mach number, advance ratio and power coefficient can be used to determine the blade angle, propeller efficiency and thrust. This methodology requires an extensive wind tunnel test database for a given propeller at different flight Mach numbers which is usually not available.

A simplified approach was adopted, based on the analysis reported in Ref. 139 for an advanced SR propeller. A 10 blade SR-6 SR propeller was tested in a wind tunnel at free stream velocities of M 0.6 to 0.85 (intervals of M 0.05) and 7 different blade angle settings. After having concluded that choke occurred at the hub region and knowing that the tips were operating at Mach numbers higher than the unity, the author of Ref. 139 tried to identify which was the section of the propeller that dominated the transonic drag rise effects. η_{NET} for different advance ratios and dimensionless power loadings[21] was plotted against the helical Mach number (M_h[22]) at different blade sections. Figure 34 shows one of these plots for

[21] The dimensionless power loading is defined as the propeller power loading divided by the density of the air and the free stream velocity to the power of three. A propeller flying on an aircraft would operate close to a constant dimensionless power loading for a given power setting. This is because the power required by an aircraft is proportional to the air density and its flight speed to the power of three.

[22] The helical Mach number at a blade section is defined as the addition of the blade tangential velocity and the free stream velocity divided by the speed of sound. Note that these two velocities are perpendicular.

100% of dimensionless power loading (100% corresponds to the design cruise condition) and M_h at 0.75r ($M_{h0.75}$). The arrows indicate the $M_{h0.75}$ for which η_{NET} decreases by 0.2% with respect to the maximum value of the curve. It can be observed that regardless the advance ratio, η_{NET} declines at nearly the same $M_{h0.75}$. After a complete analysis of all the wind tunnel data, Ref. 139 concluded that the transonic drag rise was not dominated by any particular blade section, but that it was distributed along the entire blade. It was also deduced that in such cases, in agreement with common practice, the conditions at 0.75 radius represent the blade operation as a whole including compressibility losses.

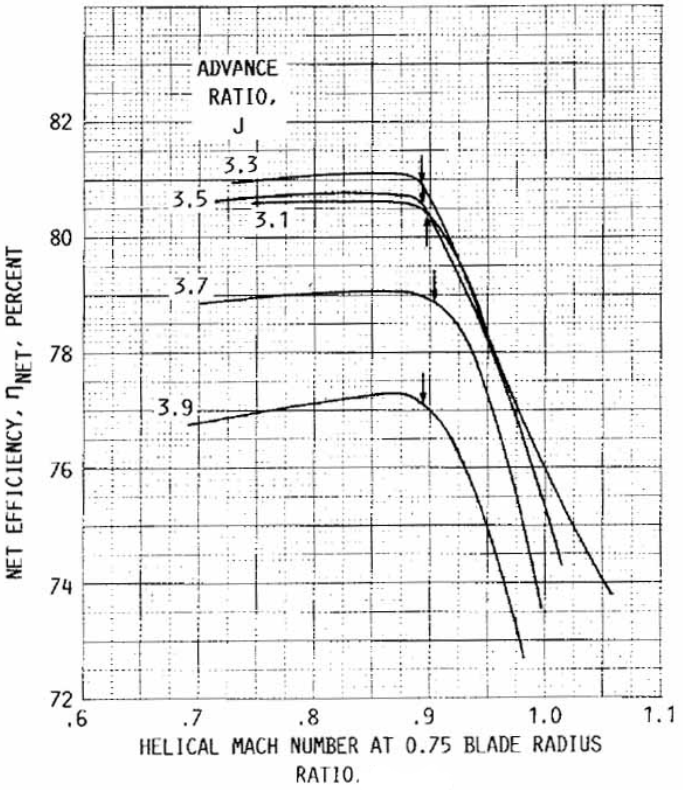

Figure 34: Effect of helical M at 0.75 blade radius on net efficiency for 100% dimensionless power loading (SR-6 10 blade propeller) [Ref. 139]

The following common features are observed between the curves of Figure 34:

- apart from the curve of J = 3.9 (which is at a very high power and speed), the efficiency is almost constant (variations smaller than 0.25%) until a critical value of $M_{h0.75}$ (indicated with arrows).
- the critical $M_{h0.75}$ ($M^*_{h0.75}$) is almost the same (variation smaller than 1%) for all the curves.
- the slope of the curves efficiency vs. $M_{h0.75}$ are similar after $M^*_{h0.75}$

These similarities can also be observed on the data presented for the other dimensionless power loadings covering a broad portion of the propeller map.

Based on the conclusions of Ref. 139 and the similarities existing between the presented set of data, the following simplified approach was adopted to model the effects of flight Mach number on the performance of a propeller:

- A propeller map produced at low speeds is used ($M_{h0.75} < M^*_{h0.75}$).
- The efficiency of the propeller is obtained from the low speed map from its Cp and J (or PQA and J).
- The low speed efficiency is corrected with the following function:

$$\eta_{NET} = \eta_{NET@low\ speed} \qquad \text{for } M_{h0.75} < M^*_{h0.75}$$

$$\eta_{NET} = \eta_{NET@low\ speed} - \left(M_{h0.75} - M^*_{h0.75}\right)Slope_{corrM} \qquad \text{for } M_{h0.75} > M^*_{h0.75}$$

[Eq. 25]

where the $M_{h0.75}$ is calculated as

$$M_{h0.75} = \sqrt{\left(\frac{V_0}{c}\right)^2 + \left(\frac{0.75D\pi n}{c}\right)^2} = \sqrt{\left(\frac{V_0}{c}\right)^2 + \left(\frac{V_0\,0.75D\pi n}{V_0 c}\right)^2}$$

$$= \sqrt{\left(\frac{V_0}{c}\right)^2 + \left(\frac{V_0}{c}\right)^2\left(\frac{0.75D\pi n}{V_0}\right)^2} = M_0\sqrt{1+\left(\frac{0.75D\pi n}{V_0}\right)^2}$$

$$= M_0\sqrt{1+\left(\frac{0.75\pi}{J}\right)^2} \qquad \text{[Eq. 26]}$$

and the values of $M^*_{h0.75}$ and $Slope_{corrM}$ (the slope of the decrease in efficiency with respect to $M_{h0.75}$) are inputs to the model.

2.2.3.2.2.2 Counter rotating propeller

Having introduced standard 0-D isolated propeller performance representation in the previous section, a methodology to calculate the CRP performance is presented in this section. The interactions between both propellers are estimated, and the operating point of each propeller on its isolated performance map is determined. Once the operating point of each propeller is known, total CRP values can be computed.

Assumptions

All the reviewed 2-D CRP calculation methodologies [Ref. 141 to Ref. 146] use the following assumptions to evaluate the flow velocities for each blade element of the propeller:

- blade element theory assumptions [Ref. 135].
- each propeller is assumed to work on the flow field generated by the flight speed and the effects of the other propeller. The influence of the rear

propeller (propeller 2) on the velocity field of the forward propeller (propeller 1) is called interference velocity of the rear propeller on the forward propeller and is denoted by $Vind_{21}$ (analogous definition for $Vind_{12}$). $Vind_{21}$ is decomposed in the axial and tangential directions as $Vind_{21A}$ and $Vind_{21T}$ (analogous definition for $Vind_{12A}$ and $Vind_{12T}$).

- each propeller produces its own induced velocity ($Vind_{11}$ and $Vind_{22}$). It corresponds to the change in velocity (both axial and tangential) produced by the operation of each propeller. $Vind_{ii}$ for a propeller operating in a CRP arrangement is assumed to be equal to $Vind_{ii}$ for a SRP operating in isolation but in the velocity field produced by the flight speed and the other propeller[23].
- the velocities induced by the other propeller have an oscillating nature. They are replaced by time constant magnitudes equal to the time average of the induced velocities.
- the tangential interference velocity of the rear propeller on the forward propeller ($Vind_{21T}$) is neglected for being an order of magnitude smaller than other interference velocities [Ref. 143].

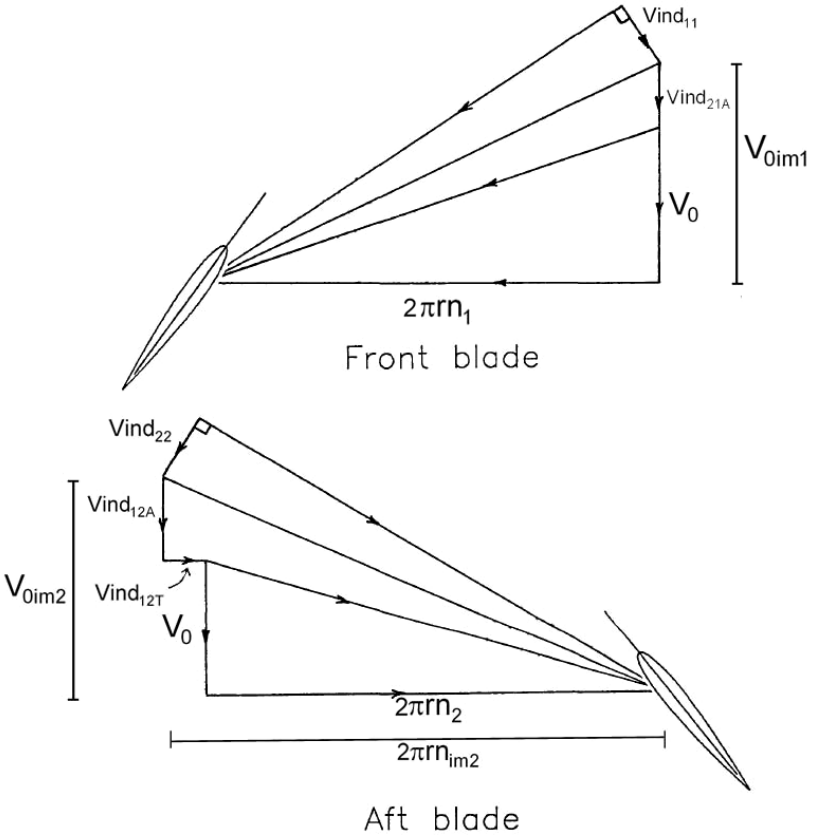

Figure 35: Interference velocity components of a CRP [Ref. 142]

[23] This implies that the forward propeller only influences the velocity field and not the pressure field of the rear propeller and vice versa.

Figure 35 shows the velocity diagram of a CRP at a given blade section according to the previously presented assumptions.

Based on these assumptions, Ref. 141 - Ref. 146 propose different ways to estimate the performance operation of a CRP by calculating the induced velocities iteratively using lifting line or vortex models, together with aerodynamic data of each blade element. A radial integration and the adequate projection of the forces acting on each blade element allow the calculation of the total propeller thrust and consumed power. Based on the requirements of the framework and the models, an alternative simplified methodology was used based on the following two assumptions:

- $Vind_{21A}$ and $Vind_{12A}$ are uniform for every blade element of the propeller
- $Vind_{12T} = \Omega ind_{12} r$ with constant Ωind_{12}

Forward propeller calculation

The calculation of the CRP performance is done iteratively. This is because both propellers influence each other and their equations have to be solved simultaneously. For argumentation sake, $Vind_{21A}$ is used as an iteration variable. It is guessed at the beginning of the CRP calculation process and is obtained at the end. According to the module requirements, the input power to each propeller, the diameters of the propellers, the flight speed, ambient conditions and rotational speeds of the propellers are known (input variables). A different set of known variables can be chosen. The selection of known variables and iteration variables is treated in more detail in section 2.2.3.2.3.

Since $Vind_{21A}$ is the same for every blade element, an imaginary flight velocity (V_{0im1}) can be calculated as

$$V_{0\,im1} = V_0 + Vind_{21A} \qquad \text{[Eq. 27]}$$

An imaginary advance ratio can be calculated for this imaginary flight condition as

$$J_{im1} = \frac{V_{0\,im1}}{n_1 D_1} \qquad \text{[Eq. 28]}$$

It can be seen that a propeller operating at a J_{im1} and a propeller at a J_1 plus an extra axial uniform component $Vind_{21A}$ have the same angle of attack to every blade section. Consequently these two operating conditions represent the same dimensionless point on the propeller map. The thrust produced by the forward propeller is calculated as follows.

The propeller efficiency is read from the map using J_{im1} and PQA_1, and corrected for compressibility losses as defined in Eq. 25 and Eq. 26 (M_0 is calculated as V_{0im1}/c and J_{im1} is used instead of J_1 in Eq. 26). The atmosphere and air fluid model indicated in Table 2 are used to calculate ρ and c at the specified flight conditions.

$$PQA_1 = \frac{Pw_{mech1}}{\rho n_1^{\ 3} D_1^{\ 3} A_{disk1}} \qquad \text{with} \qquad A_{disk1} = \frac{\pi}{4} D_1^{\ 2} \left(1 - \left(\frac{D_h}{D_1}\right)^2\right) \qquad \text{[Eq. 29]}$$

$$\eta_{NET1} = \frac{Pw_{F1}}{Pw_{mech1}} = \frac{Fn_1 \ V_{0im1}}{Pw_{mech1}} = J_{im1} \frac{TQA_1}{PQA_1} \qquad \text{[Eq. 30]}$$

$$Fn_1 = \rho n_1^{\ 2} D_1^{\ 2} A_{disk1} TQA_1 = \rho n_1^{\ 2} D_1^{\ 2} A_{disk1} \left(\frac{\eta_{NET1} PQA_1}{J_{im1}}\right) \qquad \text{[Eq. 31]}$$

Rear Propeller calculation

The calculation of Fn_2 can be broken into the following four main steps:

Step 1: Obtain the inlet flow conditions for the rear propeller.

According to the model assumptions, the inlet conditions to any section of the rear propeller are defined by V_0, $Vind_{A12}$ and Ωind_{12}. The magnitudes of these inlet conditions are calculated using momentum theory. More sophisticated methods for calculating these magnitudes exist (lifting line and vortex models), but they are not necessarily more precise [Ref. 148] and require a complete 2-D analysis of the propeller.

Axial induced velocity calculation

The momentum theory indicates that the axial auto induced velocity at the plane of the propeller is ([Ref. 135])

$$Vind_{A@prop} = \frac{\sqrt{V_0^{\ 2} + \frac{2Fn}{\rho A}} - V_0}{2} \qquad \text{[Eq. 32]}$$

This formula applied to the forward propeller results in

$$Vind_{11A@1} = \frac{\sqrt{V_{0im1}^{\ 2} + \frac{2Fn_1}{\rho A_{disk1}}} - V_{0im1}}{2} \qquad \text{[Eq. 33]}$$

with

$$A_{disk1} = \frac{\pi}{4} D_1^{\ 2} \left(1 - \left(\frac{D_h}{D_1}\right)^2\right) \qquad \text{[Eq. 34]}$$

The axial induced velocity at the plane of the rear propeller ($Vind_{12A} = Vind_{11A@2}$) is obtained from the axial induced velocity at the plane of the forward propeller

($\mathrm{Vind}_{12A@1}$) and the stream tube contraction. The stream tube contraction model proposed in Ref. 149 (based on vortex theory) is used:

$$\mathrm{Vind}_A(z) = \mathrm{Vind}_{A@prop}\left(1+\frac{z/r_{prop}}{\sqrt{1+\left(\frac{z}{r_{prop}}\right)^2}}\right) \quad \text{[Eq. 35]}$$

where z is the axial coordinate of a plane with respect to the plane of the propeller in the direction of the flow. This formula applied to the forward propeller results in

$$\mathrm{Vind}_{12A} = \mathrm{Vind}_{11A@1}\left(1+\frac{z_{12}/r_1}{\sqrt{1+\left(\frac{z_{12}}{r_1}\right)^2}}\right) \quad \text{[Eq. 36]}$$

The stream contraction model described in Appendix C of Ref. 165 (based on momentum theory and the Navier-Stokes equations for inviscid and incompressible flow) was also tested. Both models were used for the CRP model verification described in section 2.2.3.2.4. The difference in total CRP power and total CRP efficiency calculated using either of the two models was smaller than 0.2%. The observed global trends were identical for both models. The contraction model of Ref. 149 was selected because it is simpler than the one of Ref. 165.

Tangential induced velocity calculation

The momentum theory considers that the torque applied by the actuator disk is equal to the change in angular momentum of the flow crossing the actuator disk. At any radial position (r) of the actuator disk, the torque balance can be written as

$$dQ(r) = 2\pi\rho r\,(V_0 + \mathrm{Vind}_A(r))\,\mathrm{Vind}_T(r)\,r\,dr \quad \text{[Eq. 37]}$$

Considering $\mathrm{Vind}_T(r) = \Omega\mathrm{ind}\,r$ and a uniform axial induced velocity $\mathrm{Vind}_A(r) = \mathrm{Vind}_A$, the integral of Eq. 37 from the hub to the tip of the propeller results in

$$Q = \frac{2}{4}\pi\rho\,(V_0 + \mathrm{Vind}_A)\,\Omega\mathrm{ind}\left(r^4 - r_h^4\right) \quad \text{[Eq. 38]}$$

and

$$\Omega ind = \frac{Q}{\frac{2}{4}\pi\rho\left(V_0 + Vind_A\right)\left(r^4 - r_h{}^4\right)} \qquad \text{[Eq. 39]}$$

This formula applied to the forward propeller results in

$$\Omega ind_{11} = \frac{Q_1}{\frac{2}{4}\pi\rho\left(V_{0im1} + Vind_{A11@1}\right)\left(r_1{}^4 - r_h{}^4\right)} \qquad \text{[Eq. 40]}$$

Finally, Ωind_{12} is considered to be equal to Ωind_{11} and therefore considered not affected by the stream contraction. The justification for this choice is given in section 2.2.3.2.4.2.

Step 2: Establish a point on the map of the rear propeller which corresponds to the inlet flow conditions calculated in Step 1.

Since $Vind_{12A}$ is equal for every blade element, an imaginary flight velocity ($V_{0\ im\ 2}$) can be calculated as

$$V_{0\,im\,2} = V_0 + Vind_{12A} \qquad \text{[Eq. 41]}$$

Since $Vind_{12T} = \Omega ind_{12} r$ with constant Ωind_{12}, an imaginary rotational speed (n_{im2}) can be defined adding the tangential component of the velocity due to the rotation of the propeller and the tangential component of the induced velocity of the forward propeller.

$$2\pi r n_{im2} = 2\pi r n_2 + \Omega ind_{12} r \qquad \text{[Eq. 42]}$$

and

$$n_{im2} = n_2 + \frac{\Omega ind_{12}}{2\pi} \qquad \text{[Eq. 43]}$$

An imaginary advance ratio can be calculated for this imaginary operating condition as

$$J_{im2} = \frac{V_{0\,im\,2}}{n_{im2} D_2} \qquad \text{[Eq. 44]}$$

It can be seen that a propeller operating at a J_{im2} and a propeller at a J_2 plus an extra axial uniform component $Vind_{12A}$ and a tangential component of uniform angular velocity Ωind_{12} have the same angle of attack to every blade section. Consequently these two operating conditions represent the same point on the propeller map and the resultant force vectors as well as torques are equal for both operating conditions.

PQA_{im2} and J_{im2} define the operating point of the rear propeller on the isolated SRP performance map (refer to Figure 33). PQA_{im2} is calculated as follows.

$$Q_{im2} = Q_2 = \frac{Pw_{mech\ im2}}{n_{im2}} = \frac{Pw_{mech\ 2}}{n_2} \qquad \text{[Eq. 45]}$$

The imaginary power required to drive the propeller at n_{im} is then calculated as

$$Pw_{mech\ im2} = \frac{Pw_{mech\ 2} n_{im2}}{n_2} \qquad \text{[Eq. 46]}$$

$$PQA_{im2} = \frac{Pw_{mech\ im2}}{\rho {n_{im2}}^3 {D_2}^3 A_{disk2}} \quad \text{with} \quad A_{disk2} = \frac{\pi}{4} {D_2}^2 \left(1 - \left(\frac{D_h}{D_2}\right)^2\right) \qquad \text{[Eq. 47]}$$

Step 3: Obtain the thrust of the rear propeller.

As it was presented in Step 2, the resultant force vectors for real and imaginary cases are equal. This implies that the thrust for both cases is equal and it can be calculated as follows.

$$\eta_{NET\ im2} = \frac{Pw_{Fn2}}{Pw_{mech\ im2}} = \frac{Fn_2\ \ V_{0im2}}{Pw_{mech\ im2}} = J_{im2} \frac{TQA_{im2}}{PQA_{im2}} \qquad \text{[Eq. 48]}$$

$$Fn_2 = \rho {n_{im2}}^2 {D_2}^2 A_{disk2} TQA_{im2} = \rho {n_{im2}}^2 {D_2}^2 A_{disk2} \left(\frac{\eta_{NET\ im2} PQA_{im2}}{J_{im2}}\right) \qquad \text{[Eq. 49]}$$

where $\eta_{NET\ im2}$ is read from the map using J_{im2} and PQA_{im2}, and corrected for compressibility losses using Eq. 25 and Eq. 26 (M_0 is calculated as V_{im2}/c and J_{im2} is used instead of J_2 in Eq. 26).

Finally, the total CRP thrust can be obtain as

$$Fn_{CRP} = Fn_1 + Fn_2 \qquad \text{[Eq. 50]}$$

Step 4: Calculate $Vind_{21A}$

Once the operation of the rear propeller is known, its auto-induced velocity can be calculated using Eq. 32

$$Vind_{22A@2} = \frac{\sqrt{{V_{0im2}}^2 + \frac{2Fn_2}{\rho A_{disk2}}} - V_{0im2}}{2} \qquad \text{[Eq. 51]}$$

$Vind_{21A}$ is then obtained from $Vind_{22A@2}$ and the stream contraction as defined in Eq. 35. Note that $Vind_{21A} < Vind_{22A@2}$ since the stream contraction occurs in the direction of the flow.

$$Vind_{21A} = Vind_{22A@2}\left(1+\frac{-z_{12}/r_2}{\sqrt{1+\left(\frac{-z_{12}}{r_2}\right)^2}}\right) \quad \text{[Eq. 52]}$$

The CRP calculation process can be repeated using the obtained value of Vind21A in an iterative process (E.g. return to “Forward propeller calculation” in page 63).

2.2.3.2.3 Implementation

The CRP model described in section 2.2.3.2.2 was implemented in two separate PROOSIS components as shown in Figure 36. Specific “CRP ports” were created to transfer the variables of the forward propeller used on the rear propeller ($A_{disk1,}$ $Vind_{11A,}$ $F_{1,}$ $n_{1,}$ $D_{1,}$ $Q_{1,}$ Pw_{mech1}, V_0, ρ, c). Additionally a thrust and an information port were created to transfer Fn_{CRP} and $KEincrease_{CRP}$ (defined in Eq. 53) to the performance monitor.

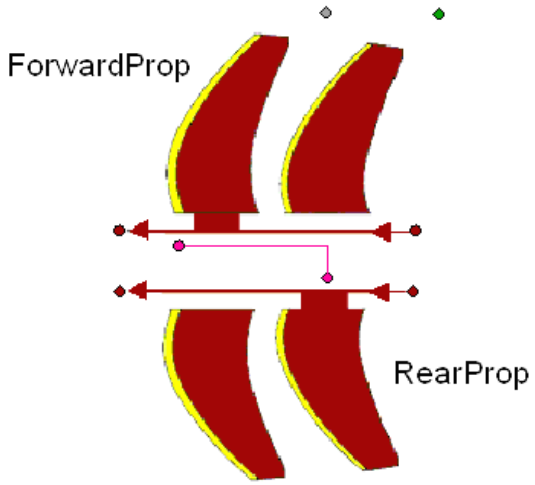

Figure 36: CRP components schematic view

In addition to the equations mentioned in section 2.2.3.2.2, the PROOSIS CRP component model comprises:

- a torque balance and conservation of rotational speeds in mechanical shafts
- a definition of the inertia of the propellers and extra equations required for transient calculations
- unit conversions
- scaling of the SRP maps. One scalar and one adder are included for each of the following map variables: J, PQA and efficiency.
- an alternative calculation of the induced velocities required for the verification of the model (detailed in section 2.2.3.2.4)

- a calculation of the increase in kinetic energy of the flow through the CRP, which is required by the performance monitors (described in section 2.2.3.5) to estimate the propulsive efficiency.

  $KEincrease_{CRP} = KEincrease_1 + KEincrease_2$ [Eq. 53]

  According to momentum theory, the increase in kinetic energy of the flow through each propeller can be estimated as [Ref. 135]

  $KEincrease_i = (V_{0imi} + Vind_{Aii})\, Fn_i$ [Eq. 54]

Two sets of PROOSIS components were created:

- *CRP-e* (used for the engine calculations).

  These components use the equations presented in section 2.2.3.2.2 together with the aforementioned equations. One table of the form η_{NET}=f(J,PQA) (where the blade angle setting is not an explicit variable) is used to represent the propeller characteristics. These components are useful for engine cycle calculations because the rotational speeds of the propellers are used as engine control variables and Pw_{mech1} and Pw_{mech2} are set by the engine core operation.

- *CRP-v* (used for the model verification calculations).

  These components use the equations presented in section 2.2.3.2.2 but C_P and C_T are used instead of PQA and TQA respectively. These equations are only valid for constant hub to tip ratios. This does not represent a limitation since the hub to tip ratios are not varied during the verification simulations. Two tables of the form $C_P = f(J, \beta_{0.75})$ and $\eta_{NET} = f(J, \beta_{0.75})$ are used to represent the propeller characteristics. These components are useful for the model verification calculations because the available propeller experimental tests were produced and tabulated at constant blade angle settings and presented in terms of C_P and C_T.

Both the forward and the rear propeller maps can be displayed. The verification components display C_P in the y axis and the engine components display $\frac{A_{disk}}{D^2}PQA$ in the y axis. This was done so that the maps plotted by CRP-v and CRP-e components are identical for the hub to tip ratio at which they were produced.

PROOSIS components can be used in isolation or together with other components in order to simulate part of an engine or a complete engine. It is not necessary to code equations sequentially in PROOSIS, as it has the capability of sorting the equations to suit any valid set of inputs. For example:

- *Model inputs*: flight conditions, n_1, n_2, Pw_{mech1}, Pw_{mech2}.

  A mathematical model is generated using the equations in the same order and as they appear in section 2.2.3.2.2.

- *Model inputs*: flight conditions, J_1, J_2, $\beta_{0.75\,1,}$ $\beta_{0.75\,2}$.

  The equations are sorted so that n_1 and n_2 are first obtained from J_1, J_2 and Eq. 17. Then, $J_{im\,1}$ and $J_{im\,2}$ are calculated, and $PQA_{im\,1}$ and $PQA_{im\,2}$ (or C_{P1} and C_{P2} for the CRPv model) are obtained from the propeller maps using $J_{im\,1}$, $\beta_{0.75\,1}$, $J_{im\,2}$, $\beta_{0.75\,2}$. Finally the powers of the forward and rear propellers are obtained respectively by rearranging Eq. 29 and Eq. 47. This specific arrangement of the equations is used for the verification of the model since the available experimental data is tabulated for J and $\beta_{0.75}$.

In a similar manner, PROOSIS allows a flexible definition of the guesses to be used in an iteration process. An appropriate selection of the guesses is required to produce numerically stable models (this subject is presented in more depth in Appendix I).

2.2.3.2.4 Verification against existing CRP experimental data

Experimental CRP performance data found in the public domain was used to verify the capability of the proposed CRP model to predict:

- the CRP performance from SRP performance characteristics
- the effect of propeller spacing on the CRP performance

2.2.3.2.4.1 Calculation of the CRP performance from SRP characteristics

In order to verify the capability of the model to predict the CRP performance from the performance of the CRPs, the maps of the forward and rear propellers (operating in isolation) and some CRP operating points are required.

An extensive literature review on CRP wind tunnel tests was conducted. The largest source of CRP performance data comes from a series of CRP investigations carried out during the 1940s in the NACA Propeller-Research Wind Tunnel. Other tests carried out by NACA and Stanford University were also found. Ref. 146, and Ref. 161 - Ref. 163 contain CRP performance data for which the SRP performance is not known and therefore can not be used in a verification process. Ref. 150[24], Ref. 151 and Ref. 152[25] contain CRP performance maps for different CRP configurations and their corresponding SRP maps. The wind tunnel tests reported in these references were done at a maximum speed of 110mph (~50 m/s) and the tip Mach numbers were lower than 0.4 in all cases. Consequently the CRP maps found in Ref. 150 - Ref. 152 are low speed maps in which compressibility effects are negligible. These low speed maps are the type of maps

[24] Ref. 154 - Ref. 160 contain the same information as Ref. 150. Ref. 150 presents the performance data in a clearer manner and it was consequently used for the model verification.

[25] The SRP performance data of the propellers used the tests reported in Ref. 152 can be found in Ref. 153.

required by the CRP model. All the reported CRP operating points were produced at $n_1 = -n_2$ and therefore $J_1 = -J_2$ and a unique J is used within this section for expressing overall (total) CRP variables.

The SRP and CRP maps available in Ref. 150 and Ref. 152 were digitised in the form of $C_P = f(J, \beta_{0.75})$ and $\eta_{NET} = f(J, \beta_{0.75})$ tables. The maps of Ref. 151 are already provided in the form of tables. The CRPv PROOSIS components[26], the digitised SRP maps and the reported test conditions (V_0, D_1, D_2, D_h, z_{12}, $\beta_{0.75\ 1}$, $\beta_{0.75\ 2}$, n_1 and n_2) were used to simulate the CRP operation. The following paragraphs present the results of these simulations and the comparisons with respect to the experimental CRP measurements.

NACA TN-689 (Ref. 151)

Figure 37 shows the forward propeller map and Figure 38 the rear propeller map reported in NACA TN-689. They are both two blade propellers. The operating lines (in green) in these figures correspond to the operation of both propellers in a CRP configuration at the wind-tunnel tested blade angle settings ($\beta_{0.75\ 1}/\beta_{0.75\ 2}$ = 45º/43.9º, 35º/34.4º, 25º/24.7º and 15º/15º). These operating lines cover the complete range of advance ratios that can be simulated in CRP arrangement with the SRP maps provided in the report.

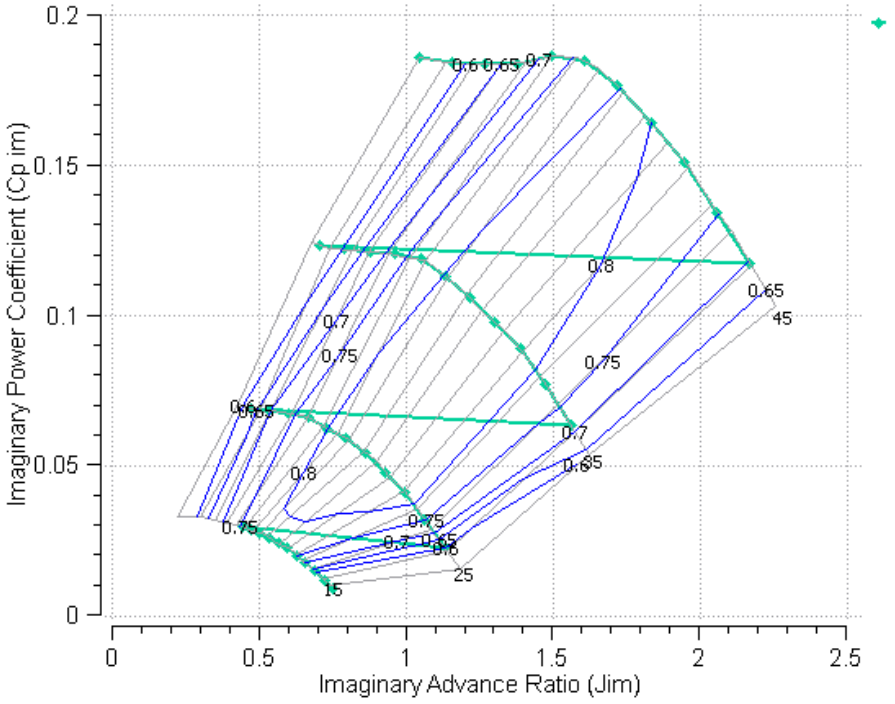

Figure 37: Operation of the forward propeller in CRP arrangement (Map from Ref. 151)

[26] The Atmosphere and General PROOSIS components were also required for these simulations. Shaft end components were also connected to the output mechanical ports of the CRP. These components are described in Ref. 130.

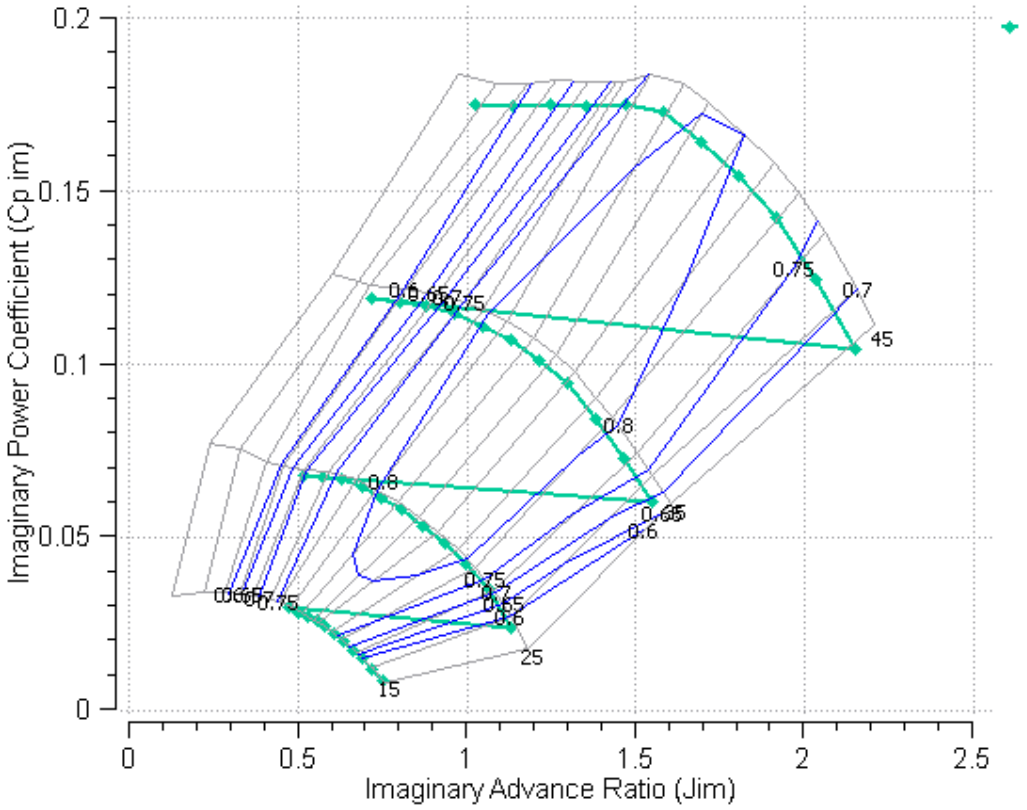

Figure 38: Operation of the rear propeller in CRP arrangement (Map from Ref. 151)

Figure 39 and Figure 40 present the experimental and simulated $\eta_{NET\ CRP}$[27] and $C_{P\ TOT}$[28] against J for all the reported combinations of propeller blade angles in Ref. 151. The prediction of both the consumed power (represented by $C_{P\ TOT}$) and the produced thrust (represented by $\eta_{NET\ CRP}$) is in agreement with the experiments. The maximum difference between the experimental and simulated $\eta_{NET\ CRP}$ is lower than 1% for $\beta_{0.75\ 1}/\beta_{0.75\ 2}$ = 35º/34.4º, 25º/24.7º and 15º/15º, and 2.5% for $\beta_{0.75\ 1}/\beta_{0.75\ 2}$ = 45º/43.9º. The maximum difference between the experimental and simulated $C_{P\ TOT}$ is lower than 2.5% for $\beta_{0.75\ 1}/\beta_{0.75\ 2}$ = 35º/34.4º, 25º/24.7º and 15º/15º, and 3.2% for $\beta_{0.75\ 1}/\beta_{0.75\ 2}$ = 45º/43.9º. The highest differences are observed in the regions where the propellers operate with some sections in stall. The errors are smaller than 1% for the operating points which are far from the stall regions.

It is not possible to find out whether the main differences come from the forward or rear propeller, because the only available CRP performance data are $C_{P\ TOT}$ and $\eta_{NET\ CRP}$.

---

[27] $\eta_{NET\ CRP}$ is the overall CRP net efficiency defined using the total CRP thrust and power (F_1+F_2 and Pw_1+Pw_2)

[28] $C_{P\ TOT}$ is the overall CRP power coefficient defined by Pw_1+Pw_2

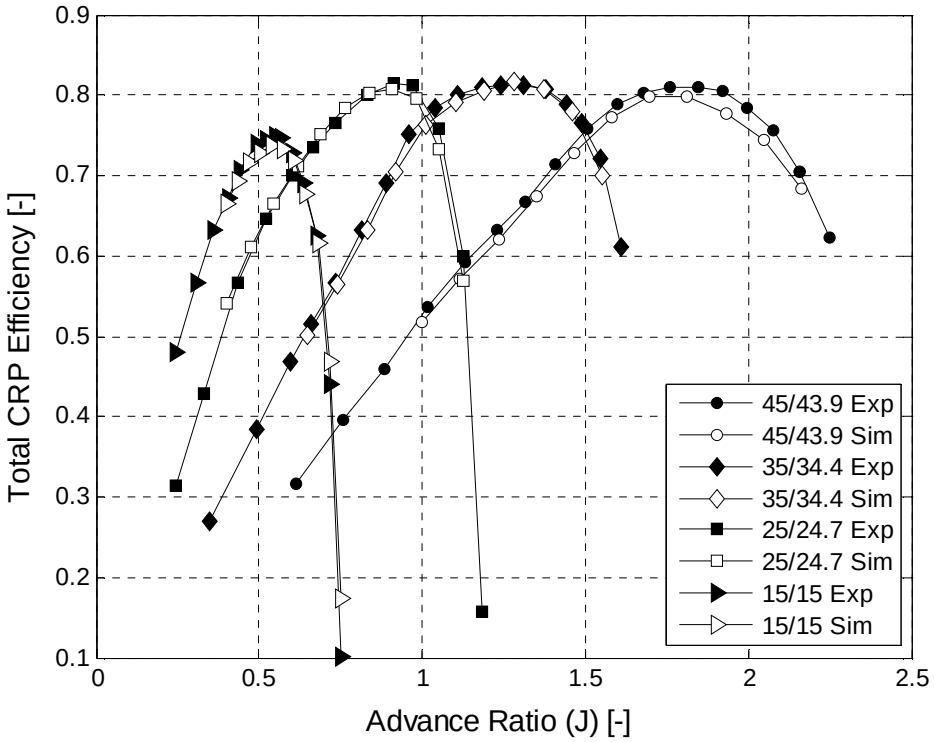

Figure 39: Experimental and simulated CRP $\eta_{NET\ CRP}$ vs. J and blade settings

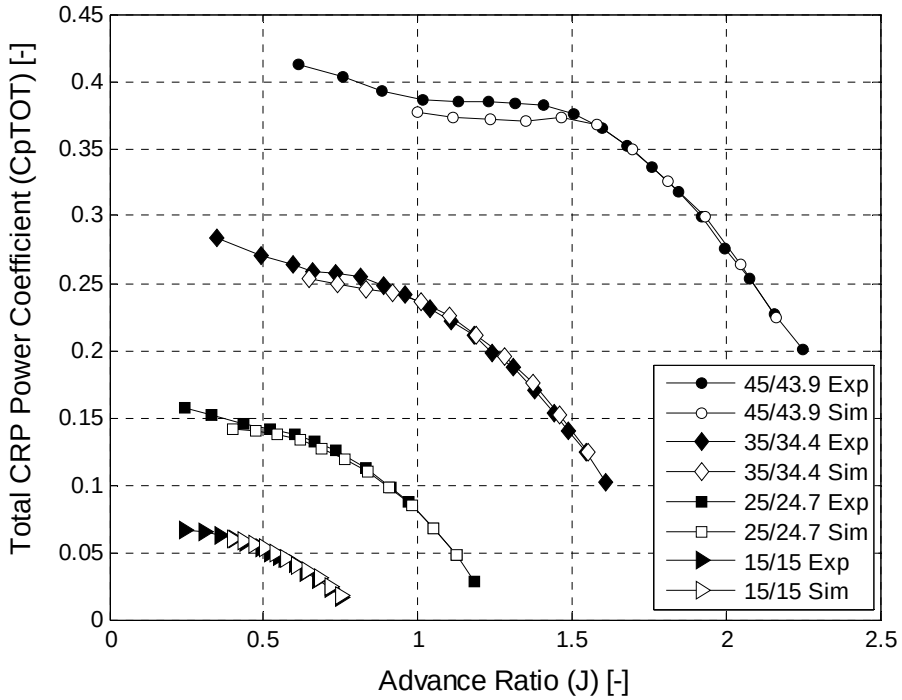

Figure 40: Experimental and simulated $C_{P\ TOT}$ vs. J and blade settings

NACA TN-1634 (Ref. 152)

Figure 41 and Figure 42 present the experimental and simulated CRP $\eta_{NET\ CRP}$ and $C_{P\ TOT}$ of the 30D[29] propeller against J for four of the reported combinations of propeller blade angles in NACA TN-1634. This propeller is formed by a pair of three blade 30S[29] propellers. Their definition and performance can be found in Ref. 153.

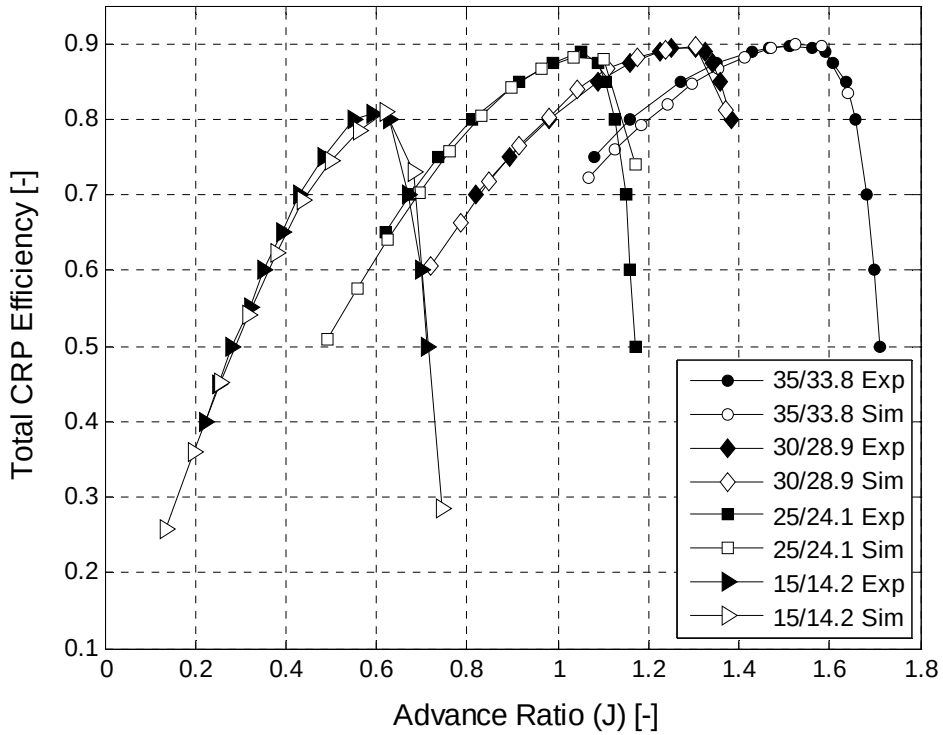

Figure 41: Experimental and simulated CRP $\eta_{NET\ CRP}$ vs. J and blade settings

Both the efficiency and consumed power trends were correctly predicted by the model. The maximum difference between the experimental and simulated $\eta_{NET\ CRP}$ is approximately 1% for $\beta_{0.75\ 1}/\beta_{0.75\ 2}$ = 25/24.1 and 30/28.9, and 2.5% for the $\beta_{0.75\ 1}/\beta_{0.75\ 2}$ = 15/14.2 and 35/33.8. The maximum difference between the experimental and simulated $C_{P\ TOT}$ is approximately 7% for $\beta_{0.75\ 1}/\beta_{0.75\ 2}$ = 30/28.9 and 35/33.8, and 4% for $\beta_{0.75\ 1}/\beta_{0.75\ 2}$ = 25/24.1 and 15/14.2.

[29] 30D and 30S are the names given to the CRP and SRP respectively reported in NACA TN-1634.

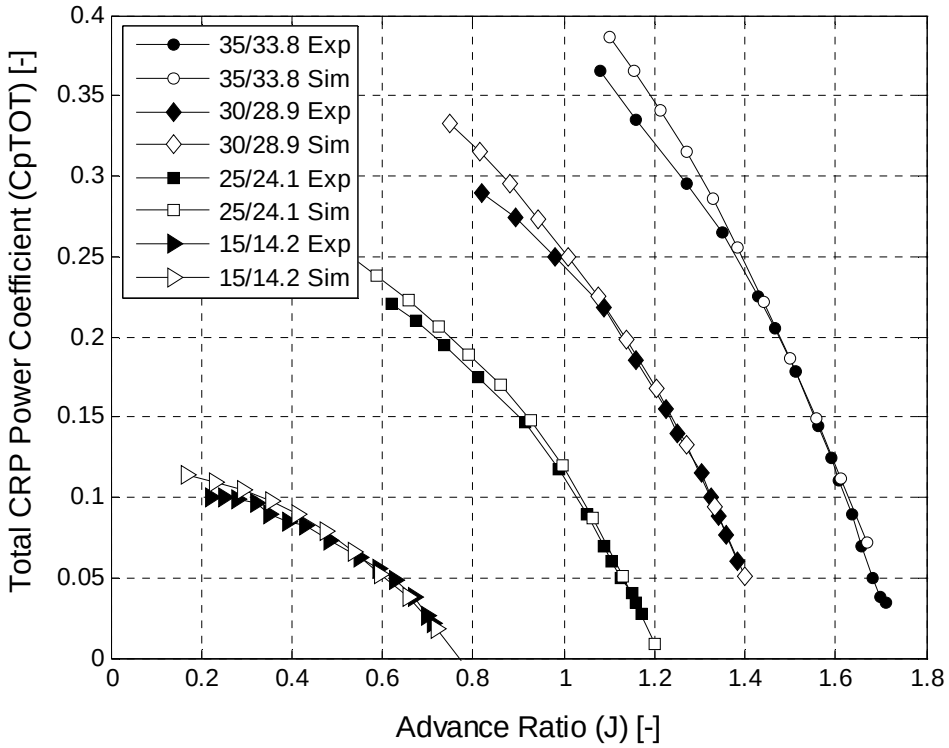

Figure 42: Experimental and simulated $C_{P\,TOT}$ vs. J and blade settings

In addition to the modelling assumptions and methods, the following two possible sources of errors were identified:

- the SRP performance map was digitised from a poor quality image. It was not available in the form of a table.
- the $\beta_{0.75\ 1}/\beta_{0.75\ 2}$ = 15/14.2 line was created extrapolating the rear propeller map since no SRP information is available for angles below 15º.

Similarly to what was observed in the NACA NT-689 calculations, the power predictions are relatively accurate for low values of $C_{P\,TOT}$ and the errors increase with $C_{P\,TOT}$. Conversely, relative to the NACA NT-689 calculations, in this case the $C_{P\,TOT}$ was over predicted for all the blade angle settings.

NACA WR-L-359 (Ref. 150)

NACA WR-L-359 presents the performance of CRPs with 2, 3 and 4 blades in each propeller. The 4 blade configuration was selected for the verification since 2 and 3 blade propellers had already been analysed (see above). Figure 43 and Figure 44 present the experimental and simulated CRP $\eta_{NET\ CRP}$ and $C_{P\,TOT}$ against J for four of the reported combinations of propeller blade angles.

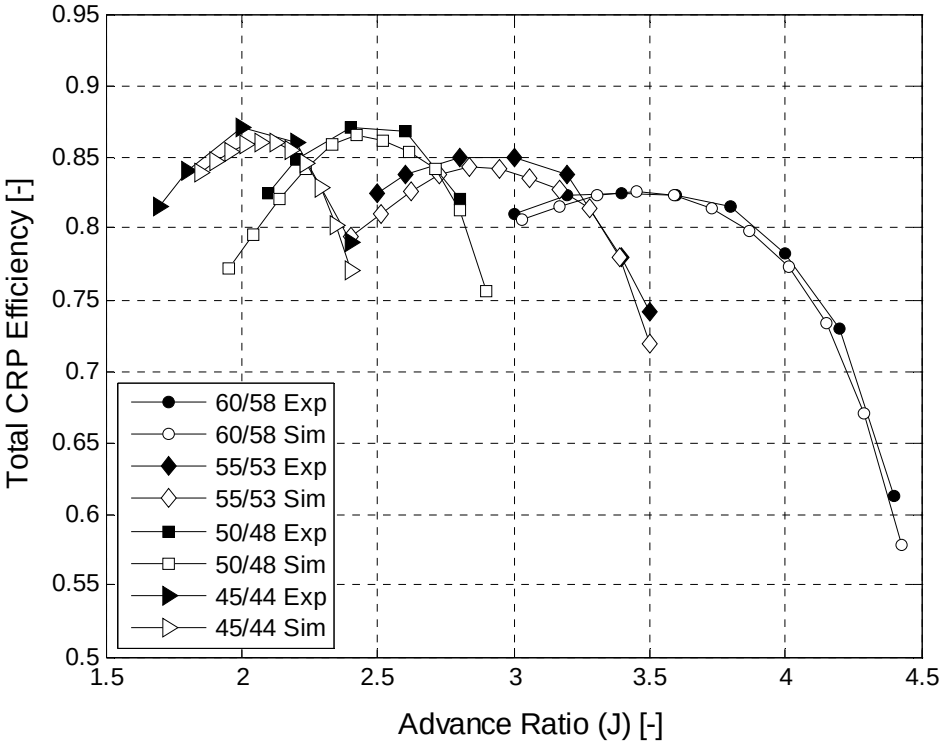

Figure 43: Experimental and simulated CRP $\eta_{NET\ CRP}$ vs. J and blade settings

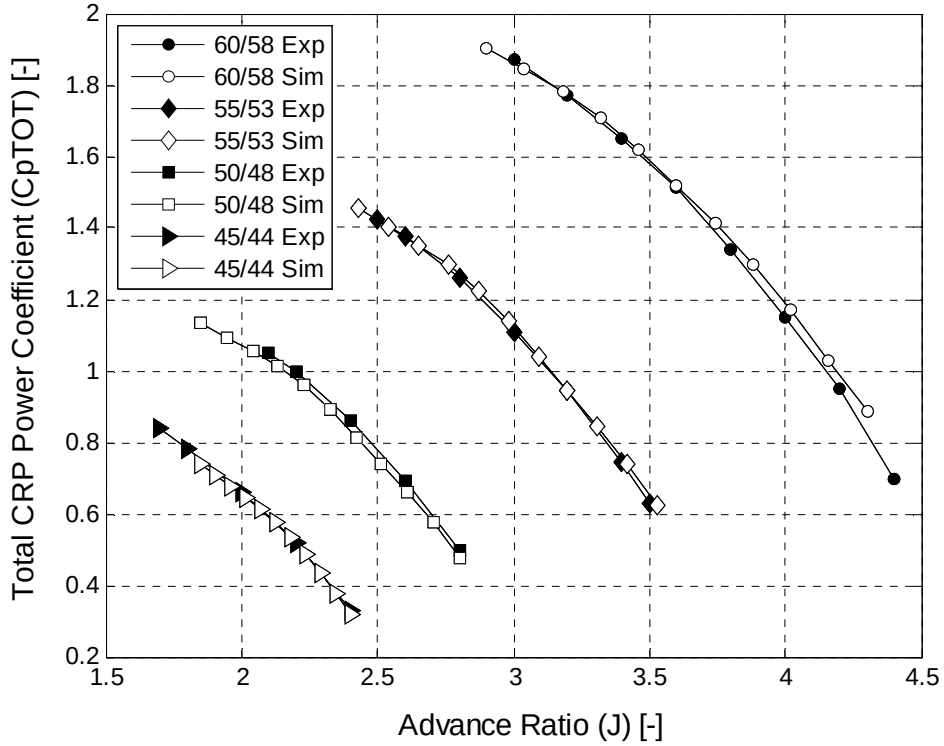

Figure 44: Experimental and simulated $C_{P\ TOT}$ vs. J and blade settings

Both the efficiency and consumed power trends were correctly predicted by the model. The maximum difference between the experimental and simulated $\eta_{NET\ CRP}$ is approximately 1.5% for all the blade angle settings. The maximum difference between the experimental and simulated $C_{P\ TOT}$ is approximately 3% for all the blade angle settings. In this case the $C_{P\ TOT}$ was over predicted for the high blade angle settings and under predicted for the low blade angle settings.

Figure 45 shows the individual power coefficients (C_{P1} and C_{P2}) obtained experimentally, for the previously presented blade angle settings [Ref. 150]. Figure 46 shows the individual power coefficients obtained from the simulations. It can be observed that:

- the differences between the predicted and measured power coefficients for the $\beta_{0.75\ 1}/\beta_{0.75\ 2}$ = 45/44 blade angle setting are negligible.
- the differences between the predicted and measured C_{P2} for the $\beta_{0.75\ 1}/\beta_{0.75\ 2}$ = 60/58.2 and 55/53.5 blade angle settings are negligible. In these cases, the C_{P1} is over predicted being responsible for the over prediction of the C_{PTOT}.
- for the $\beta_{0.75\ 1}/\beta_{0.75\ 2}$ = 50/48 blade angle setting, the C_{P1} is under predicted, and the C_{P2} is over predicted.

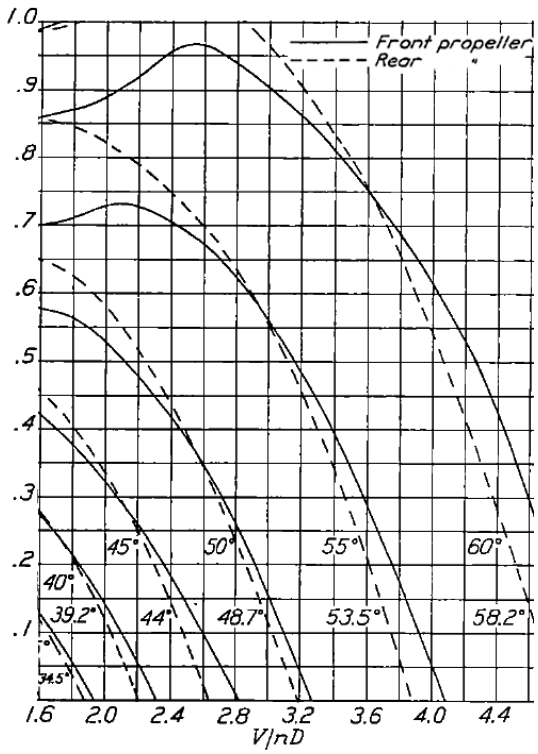

Figure 45: Experimental individual propeller C_P vs. J and blade settings [Ref. 150]

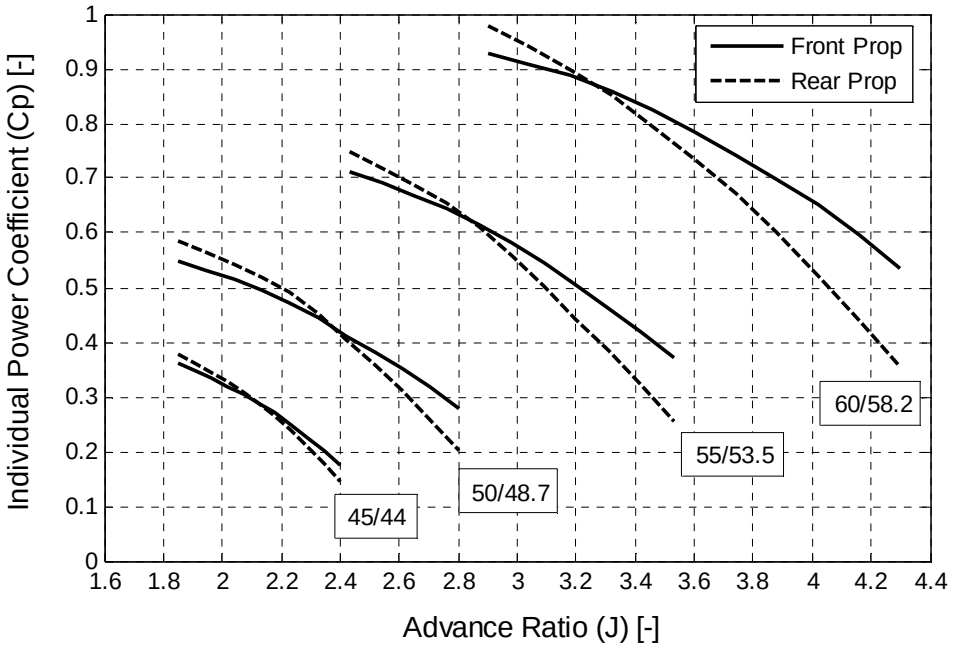

Figure 46: Simulated individual propeller C_P vs. J and blade settings

Model validity at high flight speeds

The experiments of the three analysed CRPs were carried out at constant n_1 and n_2 and V_0 was varied to obtain the desired values of J. V_0 was varied between 13 mph and 110 mph which correspond to approximately M 0.017 to 0.15 at ISA SL conditions. The induced velocities (the interactions between propellers) at low forward speeds are larger than at high forward speeds both in absolute value and relative to V_0. Consequently, the induced velocities have more influence on the operation of CRPs at low forward speeds than at high forward speeds. The simulations previously presented show good agreement between the predicted and the measured operation of CRPs at low forward speed. Although no experimental data of CRPs with their corresponding SRP characteristics at high flight speeds are available, it is expected that the model may produce results with possibly the same level of accuracy as for low speeds.

2.2.3.2.4.2 Effect of propeller spacing on the CRP performance

No reference with SRP and CRP performance data for different spacing between propellers was found in the public domain. Ref. 164 contains performance data for different spacing for the F7/A7 propeller (shown in Figure 47), but the characteristics of the isolated SRP are not presented. For this reason only a qualitative verification is possible. The SR-7 is probably the most similar propeller design for which SRP data is available. The F7/A7 and the SR-7 were developed by the same team, at the same period of time and for the same DP flight conditions.

Figure 48 presents the simulated CRP performance at the operating conditions of the experiments presented in Figure 47. Figure 48 was obtained using the CRPv PROOSIS components together with scaled SR-7 maps[30] and the geometric definition of the CRP and operating conditions provided in Ref. 164. Although the obtained values were not the same (because the propeller map was not known), the trends and orders of magnitude of the variation of PQA, torque ratio and efficiency with respect to the propeller spacing are in agreement with the experimental data.

The previously performed simulations were repeated using the following definition of Ωind_{12} instead of assuming $\Omega ind_{12} = \Omega ind_{11}$ (see *Tangential induced velocity calculation* on page 65):

$$\Omega ind_{12} = \frac{Q_1}{\frac{2}{4}\pi\rho\left(V_{0im2} + Vind_{A22@2}\right)\left(r_{1COR}{}^4 - r_h{}^4\right)} \qquad \text{[Eq. 55[31]]}$$

with

$$r_{1COR} = \sqrt{\frac{2\left(A_{1disk}V_{0im1} + Vind_{A11@1}\right)}{\pi\left(V_{0im2} + Vind_{A22@2}\right)} + r_h{}^2} \qquad \text{[Eq. 56[32]]}$$

Figure 49 presents the results of these simulations. It can be seen that the effect of spacing is not correctly captured. Ωind_{12} calculated using Eq. 55 is greater than Ωind_{11} because the flow is contracting. Consequently n_{im2} obtained with Eq.55 is greater than n_{im2} obtained with Ωind_{11}. The increase in n_{im2} with the spacing produces an increase of the Pw_{im2}, Q_2 and Fn_2 and consequently an increase in Q_2/Q_1 and efficiency. As a result, the increase of Pw_{im2}, Q_2/Q_1 and efficiency with axial spacing produced by Eq. 55 cancel the decrease in the same magnitudes produced by the changes in axial velocity with spacing.

[30] The SR-7 maps were scaled so that for the design conditions of the F7/A7 CRP, the imaginary operaing points on both propeller maps coincide with the DP of SR-7.

[31] Momentum balance (analogous to Eq. 39) applied to the plane of the rear propeller.

[32] Mass flow balance to calculate the radius of the flow that passes through the forward propeller and reaches the rear propeller.

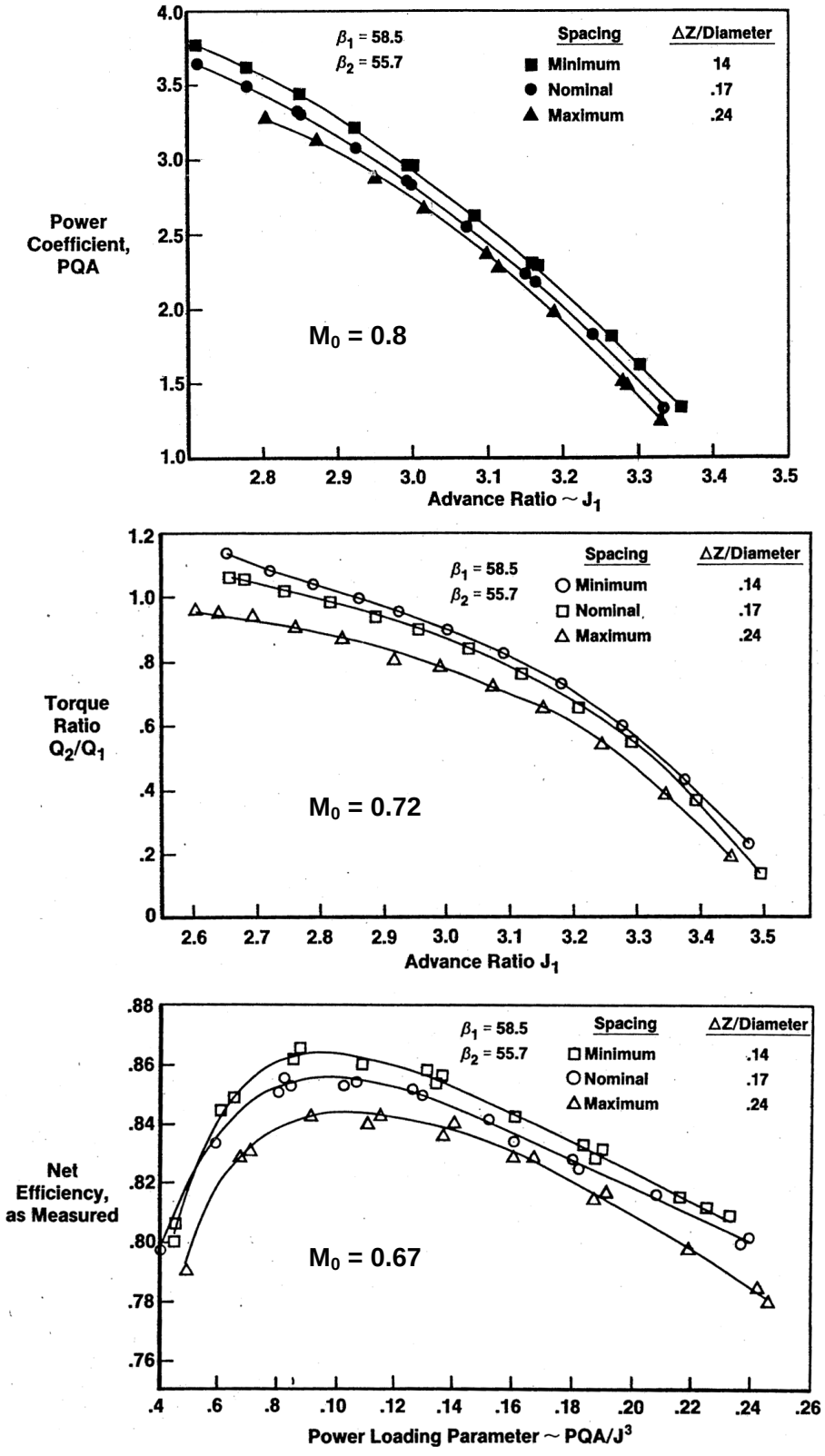

Figure 47: Effect on spacing on CRP performance (experimental data [Ref. 164])

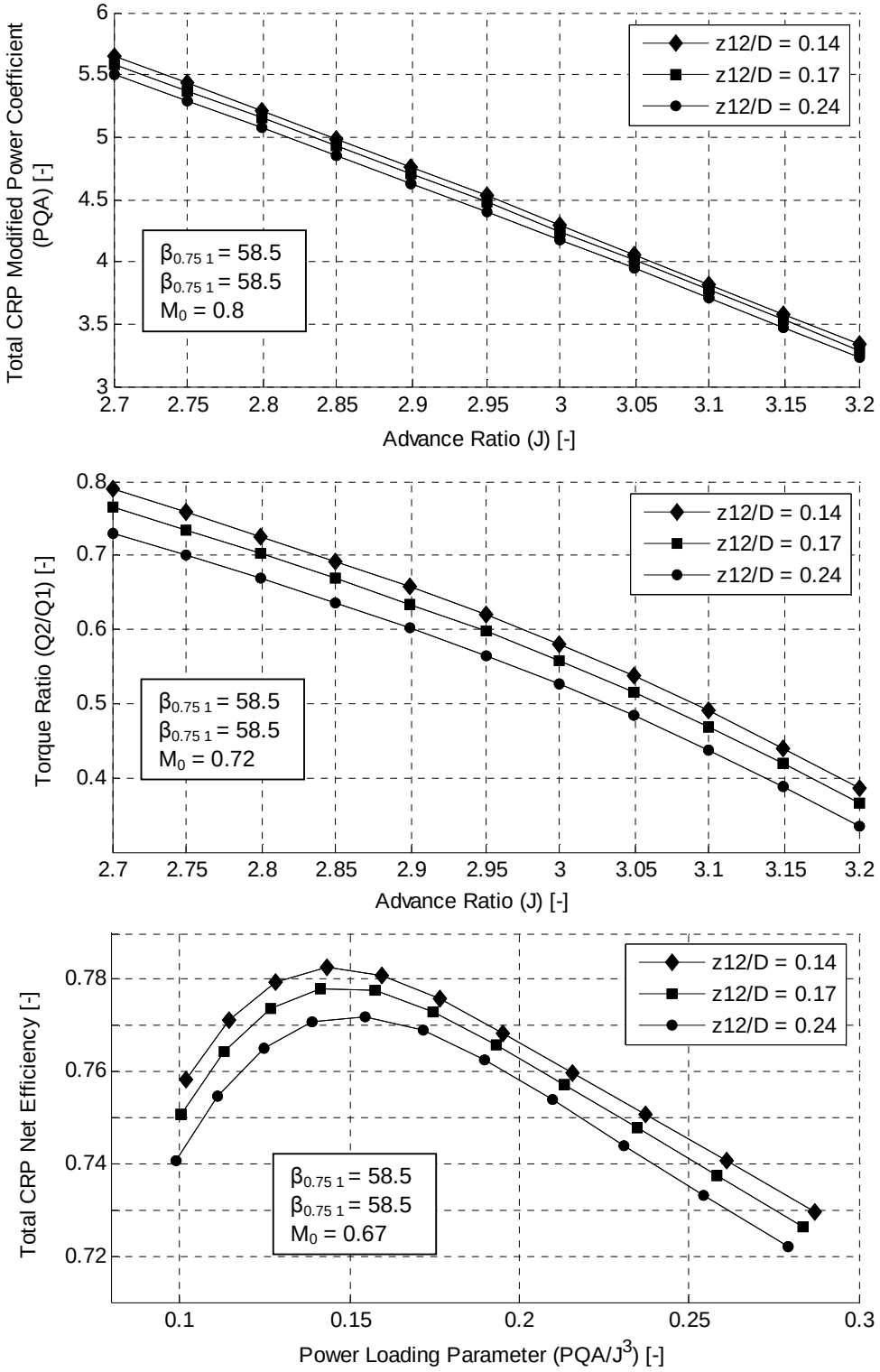

Figure 48: Effect on spacing on CRP performance (proposed CRP model)

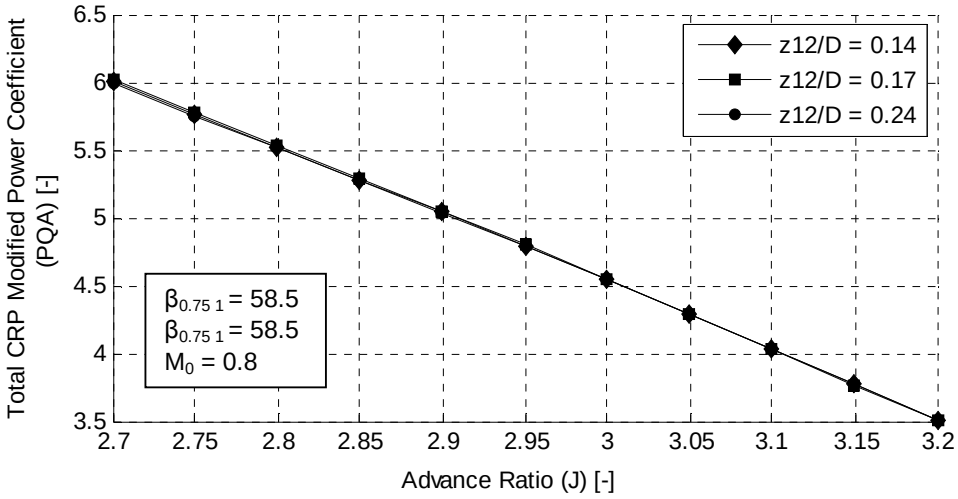

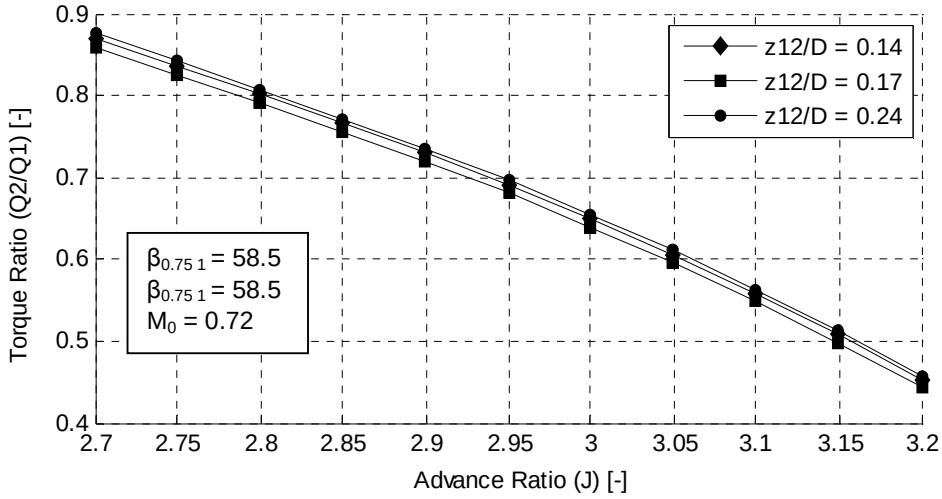

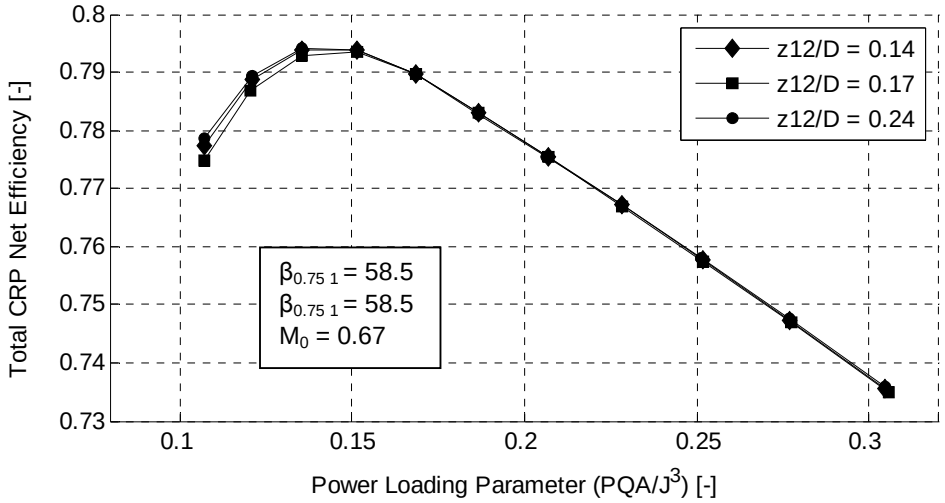

Figure 49: Effect on spacing on CRP performance (model with Eq. 55)

Figure 50 shows the tangential velocity at 0.75 radius with respect to the distance to the propeller plane for the SR-3 propeller at its DP[33]. It was obtained through CFD calculations and the modelling description can be found in Ref. 167[34]. It can be seen that the tangential velocity decreases with the axial distance which is the opposite of what Eq. 55 produces.

The simulations presented in section 2.2.3.2.4.1 were repeated using Eq. 55 and the errors with respect to the experimental data were larger. As a consequence, Eq. 55 is not used ($\Omega ind_{12} = \Omega ind_{11}$ is used instead) in the CRP model despite expressing the correct definition of Ωind_{12} according to the model assumptions.

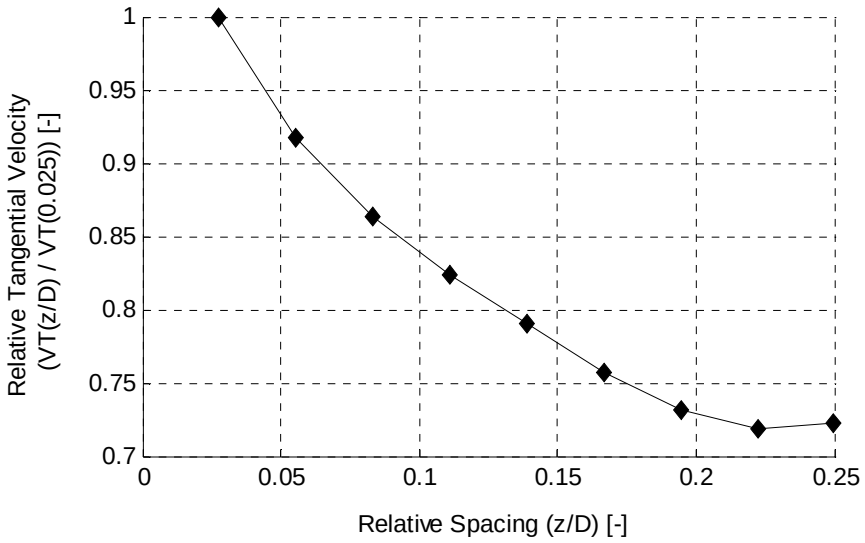

Figure 50: Tangential velocity vs. axial distance to propeller (SR-3 at 0.75r at DP)

Summary of CRP verification

Three different propeller designs were simulated in CRP configuration and the results of the simulations are in agreement with the available experimental data. It is not possible to identify potential improvements to the model with the limited available experimental data. The level of accuracy of the CRP model was judged to be suitable for preliminary design space exploration assessments.

[33] CFD results were only available for the SR-3 propeller. The results were used to demonstrate a representative trend.

[34] This plot is not available in Ref. 167. It was produced from the CFD results files of the calculations described in Ref. 167.

2.2.3.2.5 DP CRP efficiency estimation

The DP CRP efficiency ($\eta_{NET\ CRP}$) is calculated using the CRP model presented in section 2.2.3.2.2, but instead of reading the individual propeller efficiencies from their maps, they are estimated from a technology curve. The ideal[35] DP efficiency of a SRP at constant tip speed and flight conditions (speed altitude and temperature) is a function of

- the number of blades of the propeller (N_b)
- the power loading ($L_P = Pw_{mech} / A_{disk}$) [Ref. 14].

Figure 51 shows the variation of ideal SRP DP efficiency with respect to L_P for 8 and 10 blade propellers (at 10668m, ISA conditions, M_0 = 0.8 and a tip speed of 244 m/s). Ref. 14 also provides the same information for propellers with 2, 4 and infinite number of blades.

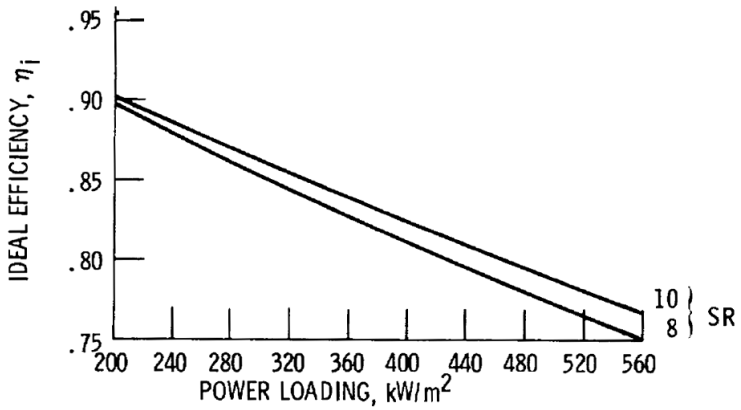

Figure 51: Ideal SRP efficiency vs. power loading (Alt = 10668 m, ISA, M_0 = 0.8, Tip speed = 244 m/s) [Ref. 14]

It was observed that for a given loading, $\eta_{8blade} - \eta_{4blade} \approx ½ (\eta_{4blade} - \eta_{2blade})$. The efficiency of a 16 blade propeller at L_P = 560kW/m^2 was guessed as

$$\eta_{16blade@560} = \eta_{8blade@560} + \frac{1}{2}\left(\eta_{8blade@560} - \eta_{4blade@560}\right) \qquad \text{[Eq. 57]}$$

The reported efficiencies of the 2, 4 and 8 blade at 560kW/m^2 together with the estimated $\eta_{16blade@560}$ were used to build a piecewise cubic Hermite interpolating polynomial. Figure 52 shows the aforementioned function. This polynomial was used to estimate $\eta_{10blade@560}$. The error between the estimated and the reported value of $\eta_{10blade@560}$ was 0.35%. This polynomial was also used to estimate the efficiencies of propellers with 9 to 15 blades at L_P = 560kW/m^2.

[35] Only losses associated to the acceleration of the fluid in the axial directions are considered. Viscous losses are not considered.

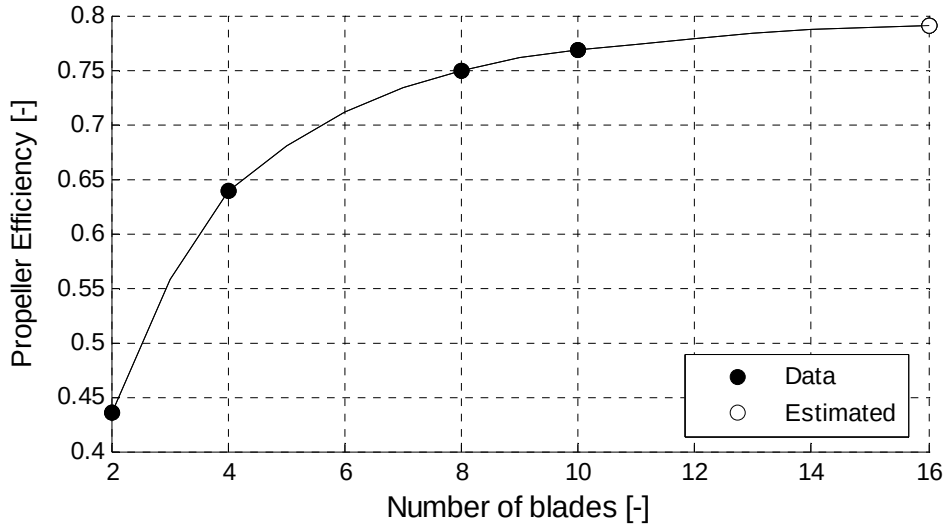

Figure 52: Ideal SRP efficiency vs. number of blades (Loading = 560 kW/m^2, Alt = 10668 m, ISA, M_0 = 0.8, Tip speed = 244 m/s)

The efficiency vs. L_P curves (Figure 51) between 200 and 560 kW/m^2 were approximated as straight lines passing through the 200 and 560 kW/m^2 points for 2, 4, 8 and 10 blade propellers (data available in Ref. 14). These lines converged to η_{NET} = 0.975 for L_P = 0 kW/m^2.

It was assumed that for a given DP flight condition and propeller tip speed, the variation in real DP efficiency (for a given blade design technology), is a function of the number of blades and L_P and follows the same trends as the ideal efficiency. Consequently the real DP propeller efficiencies were estimated as follows

$$\eta_{NET}(N_b, L_P) = 0.975 - \frac{(0.975 - \eta_{Nb@560})K_{LP}}{560} L_P \qquad \text{[Eq. 58]}$$

where the values of $\eta_{Nb@560}$ are those presented in Figure 52, and K_{LP}[36] is a technology factor. The effects of compressibility are already included in the CRP model. The value of $M^*_{h0.75}$ and $Slope_{corrM}$ [37]used in Eq. 25 are part of the propeller technology curve since they represent the level of technology and the design choices.

2.2.3.2.6 Feasibility criteria

During the engine assessment studies, the obtained values of L_P were lower than 400 kW/m^2. Ref. 169 contains the characteristics of advanced high speed propellers by Hamilton Standard. The reported DP loading for specific 8 blade

[36] K_{LP} reflects the technology level of a particular propeller design and is calculated from known efficiency values of that design.

[37] $M^*_{h0.75}$ and $Slope_{corrM}$ are calculated from data available for a particular propeller design

propeller designs range from 260 to 560 kW/m^2. Only 8 to 16 blade propellers were considered in this PhD research project and consequently all the studied propeller designs were judged to be feasible.

2.2.3.3 CRT

A description of the LP CRT and the challenges associated to its use in the DDOR are provided in sections 1.1.2.3 and 1.1.2.5 respectively. This type of LPT was used in the GE-UDF, but very little information about its performance was made public. Figure 53 shows the only available GE-UDF CRT performance map. It has efficiency contours, but the mass flow rate lines were omitted and the power split between the two parts of the CRT is not known. Consequently this map is not a complete representation of the performance of a CRT.

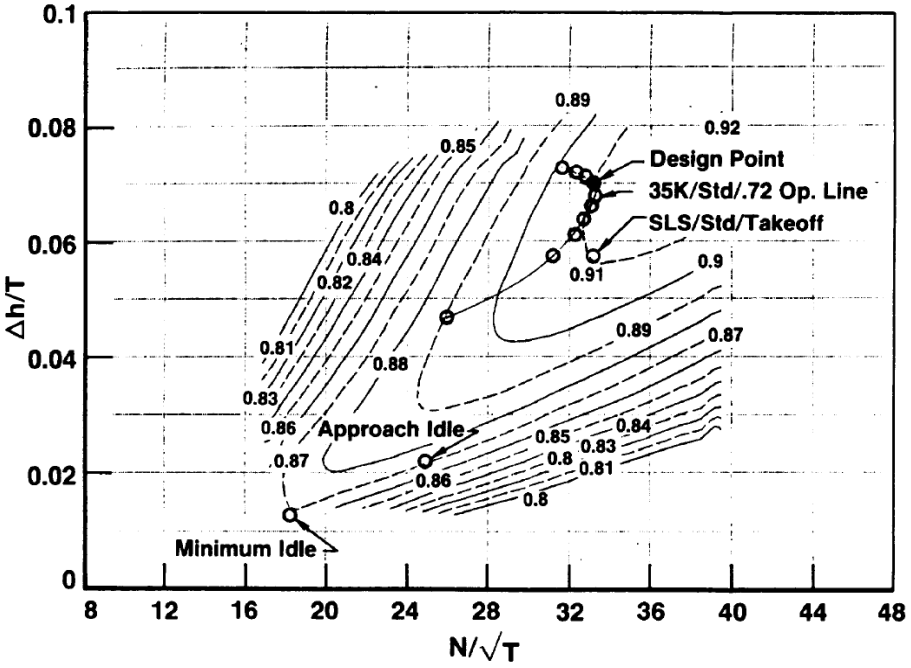

Figure 53: GE-UDF CRT map (n_1=n_2)[Ref. 33]

The use of counter rotating HP and IP turbines is reported in more detail in the public domain. In this configuration, the HP and IP shafts rotate in opposite directions, and there is no stator between the HP and IP turbine blades. Figure 54 shows the two typical HP-IP counter rotating arrangements found in literature. Ref. 170 - Ref. 173 expose the advantages of these turbine configurations. Appendix C presents a thorough bibliography of the challenges and design considerations of HP-IP counter rotating turbines.

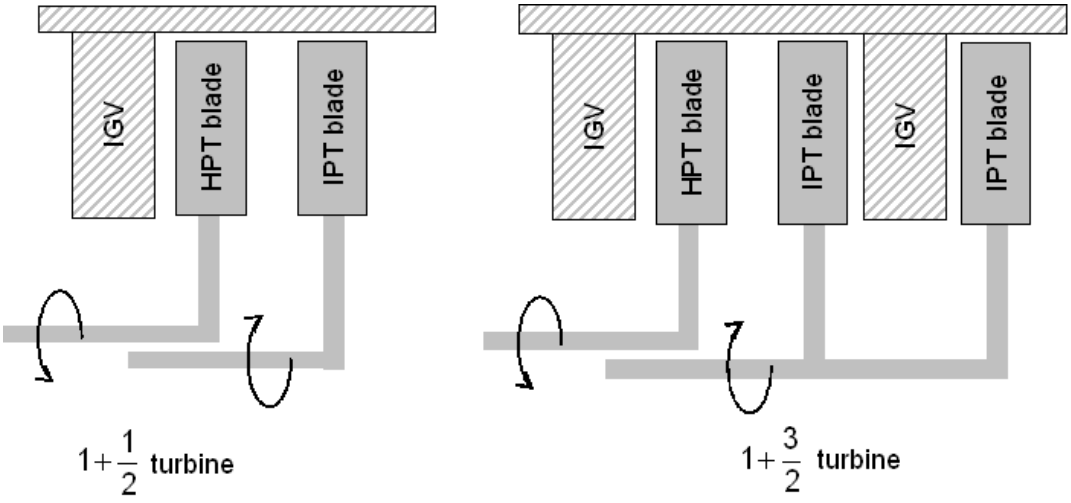

Figure 54: Typical HP-IP counter rotating turbine arrangements

No reference proposing a performance modelling methodology or presenting performance maps for these types of turbines was found in the public domain at the beginning of this PhD research project (refer to foot note 15 in page 42).

The complete design of a turbine is a complex engineering project which requires detailed design tools. The exact performance characteristics of a turbine design are only known after it is manufactured and tested. 1-D mean line predictions are used at preliminary design stages to estimate and optimise the gas path, velocity triangles and airfoil-count [Ref. 175]. These types of methods provide valid trends and a first insight into the design of a turbine [Ref. 175]. The performance of a turbine can be predicted to an accuracy of approximately 2% [Ref. 176] using these type of methods.

The 1-D mean line analysis was selected to calculate the DP and OD performance of the CRT for the present preliminary design studies. A literature review on the existing 1-D turbine calculation codes was conducted. None of the reported codes are capable of calculating the performance CRTs. Ref. 177 presents a review of the 1-D codes developed by NASA for compressors and turbines. Two NASA 1-D codes exist for the design of conventional axial turbines:

- TURBAN [Ref. 178, Ref. 179]: It is a very simplified calculation code in which a stage by stage definition of the extracted power and velocity diagrams is not possible.
- TD2-2 [Ref. 180, Ref. 181]: It is a stream tube calculation code in which the gas path is divided in sections (minimum of 3: hub, mean radius and tip sections) and all the flow magnitudes (including radial velocities) are calculated along the blade span. This methodology is closer to a 2-D calculation and it is an order of magnitude more costly than mean line 1-D methods from a computational point of view [Ref. 180].

Only one OD 1-D code developed by NASA is available in the public domain:

- AXOD [Ref. 182, Ref. 183]: It follows the same approach as TD2-2 dividing the gas path in stream tubes and a minimum of 3 sections is required. These two pieces of software were designed to be compatible and the output of TD2-2 is used as input to AXOD [Ref. 186]. AXOD is reported to be numerically unstable [Ref. 182].

Ref. 184 mentions a 1-D mean line code for axial turbines which is proprietary of the von Karman Institute of Fluid Dynamics, but the reference describing this code is not available in the public domain. Ref. 132 also mentions a 1-D calculation but no details are provided apart from the loss model used. TURBGEO [Ref. 185] is a 1-D turbine analysis code developed at CU. Only constant axial velocity designs can be calculated. It does not allow a flexible definition of the gas path and power extraction per stage. Ref. 187 - Ref. 189 describe another 1-D mean line design calculation. This model is not appropriate to calculate LP CRTs because it assumes a choked IGV which is not the case. Furthermore, the axial velocity is considered constant across the turbine and all the relative inlet and outlet Mach numbers of every stage are used as inputs. This methodology can not use geometrical features of the gas path as input and therefore does not have the required flexibility. Following a review of the existing 1-D codes and their limitations, it was concluded that it was necessary to develop a dedicated 1-D mean line code for CRTs.

First, 1-D mean line DP and OD calculation methodologies for a CRT were developed and coded in Matlab. Subsequently, both the DP and OD calculation methodologies were verified against a known CRT design (named CRT-k). Different CRT designs were then studied with both 1-D models. The performance of the CRT of the baseline DDOR used in the assessments is presented in detail. Finally, a 0-D methodology to estimate the DP and OD performance of different CRT designs was derived from the 1-D models. The 0-D model was necessary in order to comply with the calculation time requirements of the platform.

The following sections present the requirements for the 1-D and 0-D CRT performance models, as well as the developed models, their verification and the implementation of the 0-D model used in PROOSIS for the DDOR assessments.

2.2.3.3.1 CRT models requirements

2.2.3.3.1.1 1-D mean line model

Three main tasks were performed:

1 - development of a 1-D mean line modelling methodology for both DP and OD performance calculations
2 - verification with respect to the performance of a known CRT design
3 - study of the performance of different CRT designs.

Three 1-D mean line CRT codes were required to perform these three tasks: CRT-DPe, CRT-DPv, CRT-OD. The following paragraphs present the requirements of these three codes.

CRT-DPe calculation code: used to estimate the design of a CRT from its performance requirements. It was envisaged that this code would calculate the:

- power extraction per stage: $Pw_{stage\ i}$
- gas path geometrical definition: $r_{h\ in}$, $r_{tip\ in}$, $r_{mean\ in,}$ $r_{h\ out}$, $r_{tip\ out}$ and $r_{mean\ out}$ for every stage
- velocity triangles of each stage: $Vabs_{in}$, V_{inA}, $Vabs_{inT}$, α_{in}, $Vrel_{in}$, $Vrel_{inT}$, $\beta_{in,}$ $Vabs_{out}$, V_{outA}, $Vabs_{outT}$, α_{out}, $Vrel_{out}$, $Vrel_{outT}$ and β_{out} at every stage (see definitions in Figure 56)
- blade metal angles of each stage: $\beta_{metal\ in}$ and $\beta_{metal\ out}$
- turbine outlet conditions: Tt_{out} and Pt_{out} of the last stage
- overall CRT isentropic efficiency: $\eta_{is\ CRT}$

from the:

- gas properties: γ and R (ideal gas is assumed, refer to section 2.2.3.3.2.1)
- flow conditions at the inlet of the turbine: $\dot{m}_{in\,1}$,$Pt_{in\ 1}$, $Tt_{in\ 1}$ and $\alpha_{in\,1}$ (IGV angle)
- rotational speeds of both drums: n_1 and n_2
- number of stages: NbStages
- blading geometrical characteristics: detailed in section D1 in Appendix D
- required overall CRT power extraction and design torque ratio: $Pw_{CRT\ Des}$ and $TR_{CRT\ Des}$
- CRT inlet and outlet hub and tip radii: $r_{h\ in\ 1}$, $r_{tip\ in\ 1}$, $r_{mean\ in\ 1,}$ $r_{h\ out\ NbStages}$, $r_{tip\ out\ NbStages}$ and $r_{mean\ out\ NbStages}$

This code includes simplified preliminary design rules to distribute the power extraction between the turbine stages and size the gas path. It was judged not to be appropriate for a verification of the 1-D mean line methodology against the known CRT design which was the result of a detailed design effort. Consequently, a dedicated code (CRT-DPv) was developed to verify the modelling methodologies.

CRT-DPv calculation code: used to verify the design calculation methodology with respect to a known CRT design. It was envisaged that this code would calculate the:

- velocity triangles of each stage: $Vabs_{in}$, V_{inA}, $Vabs_{inT}$, α_{in}, $Vrel_{in}$, $Vrel_{inT}$, $\beta_{in,}$ $Vabs_{out}$, V_{outA}, $Vabs_{outT}$, α_{out}, $Vrel_{out}$, $Vrel_{outT}$ and β_{out} at every stage
- blade metal angles of each stage: $\beta_{metal\ in}$ and $\beta_{metal\ out}$
- turbine outlet conditions: Tt_{out} and Pt_{out} of the last stage
- overall CRT isentropic efficiency: $\eta_{is\ CRT}$

from the:

- gas properties: γ and R (ideal gas is assumed, refer to section 2.2.3.3.2.1)
- flow conditions at the inlet of the turbine: $\dot{m}$,$Pt_{in\ 1}$, $Tt_{in\ 1}$ and $\alpha_{in\,1}$ (IGV angle)
- rotational speeds of both drums: n_1 and n_2
- number of stages: NbStages

- gas path geometrical definition: $r_{h\ in}$, $r_{tip\ in}$, $r_{mean\ in}$, $r_{h\ out}$, $r_{tip\ out}$ and $r_{mean\ out}$ for every stage
- blading geometrical characteristics: detailed in section D1 in Appendix D
- required power extraction in each stage: $Pw_{stage\ i}$

In order to perform a valid comparison between the calculated and known CRT design, it is necessary to impose the exact design criteria of the known CRT on the calculations. These design criteria are represented by the power extraction per stage, the geometrical definition of the gas path and the blade characteristics. The calculated blade angles, velocities and efficiencies are compared to those of the known design. The blade angles could have been used as inputs instead of the power extraction per stage and the simulated and the real extracted power could have then been compared. It was preferred to use the power extraction of each stage as an input in order to minimise the differences between CRT-DPv and CRT-DPe codes.

CRT-OD calculation code: used to calculate the OD performance of a known CRT design. It was verified with the performance data of the known CRT design and then used to predict the performance of new CRT designs. It was envisaged that this code would calculate the:

- turbine outlet conditions: Tt_{out} and Pt_{out} of the last stage
- extracted power and torque ratio: Pw_{CRT}, $Pw_{drum\ 1}$, $Pw_{drum\ 2}$ and TR_{CRT}
- overall CRT isentropic efficiency: $\eta_{is\ CRT}$
- velocity triangles of each stage: $Vabs_{in}$, V_{inA}, $Vabs_{inT}$, α_{in}, $Vrel_{in}$, $Vrel_{inT}$, β_{in}, $Vabs_{out}$, V_{outA}, $Vabs_{outT}$, α_{out}, $Vrel_{out}$, $Vrel_{outT}$ and β_{out} at every stage

from the:

- gas properties: γ and R (ideal gas is assumed, refer to section 2.2.3.3.2.1)
- flow conditions at the inlet of the turbine: $\dot{m}$, $Pt_{in\ 1}$, $Tt_{in\ 1}$ and $\alpha_{in\ 1}$ (IGV angle)
- rotational speeds of both drums: n_1 and n_2
- number of stages: NbStages
- blade metal angles of each stage: $\beta_{metal\ in}$ and $\beta_{metal\ out}$
- gas path geometrical definition: $r_{h\ in}$, $r_{tip\ in}$, $r_{mean\ in}$, $r_{h\ out}$, $r_{tip\ out}$ and $r_{mean\ out}$ for every stage
- blading geometrical characteristics: detailed in section D1 in Appendix D

This code was required to simulate a wide range of OD operating conditions:

- pressure ratios from lower than 1, (details in section 2.2.3.3.2.6) to the choke PR. It was not required to simulate the performance of the CRT operating in sonic or super sonic conditions.
- corrected rotational speed of the external drum relative to the design corrected rotational speed ($N_{COR\ Rdes\ 1}$) from 0.7 to 1.3
- rotational speed ratio ($nR_{CRT} = -n_1 / n_2$) from 0.8 to 1.2

2.2.3.3.1.2 0-D model

It was envisaged that the 0-D CRT model would calculate the performance of a known CRT (for which an appropriate 0-D representation is available) allowing a flexible and independent definition of the:

- inlet flow conditions: $\dot{m}$, $Pt_{in\,1}$, $Tt_{in\,1}$
- rotational speeds of both drums: n_1 and n_2

A technology curve was also required to calculate the DP efficiency of the CRT with respect to the DP inlet flow conditions, stage count, rotational speeds of both drums and power extraction. A performance feasibility criterion for the CRT was also needed.

2.2.3.3.2 1-D CRT model

2.2.3.3.2.1 Model assumptions, nomenclature and general considerations

General assumptions

1 - The performance of the CRT is only calculated at its mean line. The accuracy of mean line methods is approximately 2% [Ref. 176].

2 - The working fluid is considered to be an ideal gas with constant γ and Cp. The air properties are used for the present model. The implications of these assumptions for performance calculations can be found in Ref. 109.

3- The expansion process occurring between the inlet and the outlet of the stage is assumed to be adiabatic.

Gas Path geometry assumptions

1 - The outlet conditions (Pt, Ps, Tt, Ts, velocities) and gas path geometry of a stage are equal to the inlet conditions and gas path geometry of the following stage (no inter stage duct considered). This was assumed in order to obtain a continuous gas path shape on the design code avoiding nested iterations while calculating an unknown stage with an unknown inter stage duct. A rigorous calculation should consider the real starting and ending point of each blade row and model the inter stage region as a duct considering its shape. The errors introduced by this assumption were calculated for the known CRT (for which the inter stage ducts are known) and were found to be smaller than 0.3% in all the calculated parameters at DP. Figure 55 presents the gas path geometry of CRT-k (a known CRT design) based on this assumption.

Each blade row is considered as a turbine stage. According to this definition, CRT-k has 20 stages. Note that the first and last stages have larger axial chords because of the mechanical functions they perform.

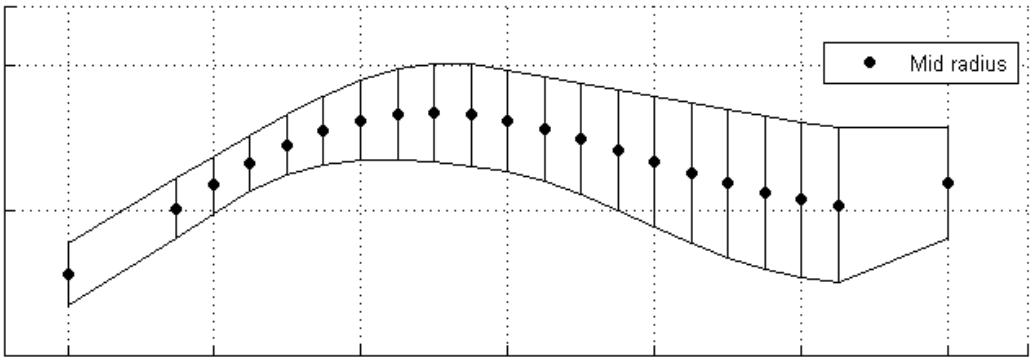

Figure 55: Gas path geometry of CRT-k (same scale for x and y axis).

2 - The studied CRT designs have the blade rows perpendicular to the axis of rotation (as in Figure 55).

3 - The mid radius at any stage inlet may not be equal to the mid radius at the stage outlet. In fact, the studied designs have large variations in mid stage radius as can be seen in Figure 55. For this reason, the difference between the inlet and outlet mean blade tangential velocities (U_{in} and U_{out}) has an impact on the mean line calculations, and is therefore considered in the velocity triangles. Figure 56 presents the velocity triangles of a turbine stage as well as the nomenclature used and sign convention. Blade speeds of consecutive stages have opposite directions and there is no fixed stage apart from the IGV. Mabs and Mrel are the Mach numbers corresponding to the absolute (Vabs) and relative velocities (Vrel) respectively.

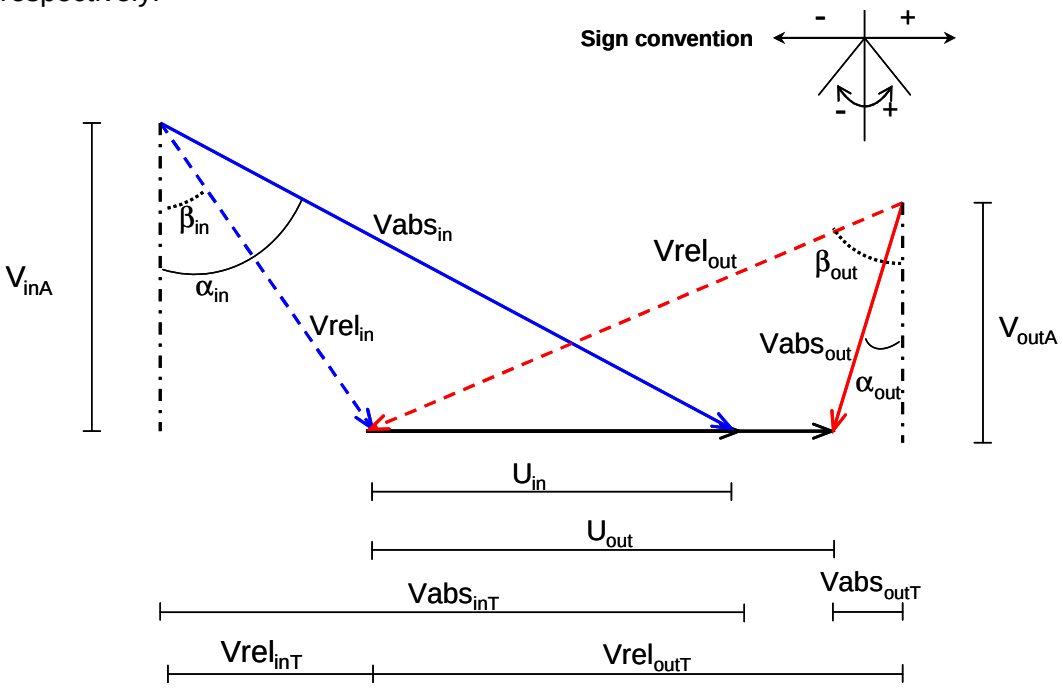

Figure 56: Stage velocity triangles, definitions and sign convention

Blade geometrical design assumptions

1 – The channel between two blades is convergent and the throat of the convergent channel is located at the rear part of the blade (segment AB on Figure 57). This is the appropriate blade design for low speed CRTs.

Figure 57: Cascade geometry assumptions

2 – The blades are designed to have zero incidence at DP (the inlet blade metal angle ($\beta_{metal\ in}$) is equal to the DP β_{in}).

3 – The flow deviation model proposed in Ref. 194 is used to provide a relationship between β_{out} and $\beta_{metal\ out}$ for both DP and OD operation.

4 – The inlet and outlet effective absolute and relative flow areas are calculated using Eq. 59 and Eq. 60 respectively.

$$Aeff = A_{disk}\, cos\left(\frac{\pi}{180}\alpha\right) \qquad \text{[Eq. 59]}$$

$$Aeff\ rel = A_{disk}\, cos\left(\frac{\pi}{180}\beta\right) \qquad \text{[Eq. 60]}$$

This assumption is reasonable as there is only a small variation in relative exit angles (< 5º) and the dimensions of the trailing edges are relatively small compared to the blade spacing.

Losses calculation methods

1 - 1-D mean line methods are based on the calculation of the velocity triangles at the stage inlet and outlet and require loss correlations to model the stage efficiency. Ref. 190 and Ref. 191 are two theses which review and compare all the loss models for axial turbines available in the public domain. The most accurate of the reviewed models allowing DP and OD calculations and not requiring a detailed geometrical definition of the blade is the one proposed in Ref. 192 and Ref. 193. Ref. 192 proposes a method for calculating the losses at zero incidence ($\beta_{in} = \beta_{metal\ in}$). Ref. 193 provides a method to correct the losses calculated by Ref. 192 for $\beta_{in} \neq \beta_{metal\ in}$.

The correlations presented in Ref. 193 were verified for incidences between -50º and +70º. This incidence range allows the evaluation of severe OD operations. Consequently, the aforementioned loss model was selected for the present mean line code.

The different losses calculated with the selected method are first expressed as total pressure loss coefficients. Then they are added into an overall total pressure loss coefficient (Yt), which for a cascade is defined as

$$Yt = \frac{Pt_{in} - Pt_{out}}{Pt_{out} - Ps_{out}} \qquad \text{[Eq. 61a]}$$

for a rotating cascade with equal inlet and outlet diameter is defined as

$$Yt = \frac{Pt\,rel_{in} - Pt\,rel_{out}}{Pt\,rel_{out} - Ps_{out}} \qquad \text{[Eq. 61b]}$$

For a rotating cascade with different inlet and outlet diameters the Yt is defined as

$$Yt = \frac{Pt\,rel_{out\,is} - Pt\,rel_{out}}{Pt\,rel_{out} - Ps_{out}} \qquad \text{[Eq. 61c]}$$

since the Pt rel varies from the inlet to the outlet due to the change in stage radius and it is no longer possible to relate directly the outlet conditions with the inlet conditions using Yt.

General considerations

1 - The used isentropic efficiency, both for the turbine and for the stages is the *total-to-total* isentropic efficiency (defined in Eq. 62). This is because the velocity in the flow is “useful” for the downstream component which can be either the exit nozzle or the subsequent turbine stage[38].

$$\eta_{is} = \frac{ht_{in} - ht_{out}}{ht_{in} - ht_{out\ is}} \qquad \text{[Eq. 62]}$$

2 - Two main calculation bricks are used in the three developed 1-D mean line CRT codes in order to calculate the expansion process occurring in a stage:

- ***Stage-DP*** calculation brick, used in CRT-DPv and CRT-DPe.
- ***Stage-OD*** calculation brick, used in CRT-OD

These two calculation bricks are first described and subsequently the complete CRT codes are presented.

---

[38] A detailed discussion about the use of total-to-total, total-to-static and static-to-static isentropic eficiencies can be found in Ref. 194.

2.2.3.3.2.2 *Stage-DP* calculation brick

Stage-DP used in CRT-DPv, CRT-DPe to calculate the exit conditions of a turbine stage, from the inlet conditions, exit geometry and required power extraction.

Input

- gas properties: γ, R, Cp
- inlet gas path geometry: $r_{h\ in}$, $r_{tip\ in}$, $r_{mean\ in}$ and $A_{disk\ in}$
- outlet gas path geometry: $r_{h\ out}$, $r_{tip\ out}$, $r_{mean\ out}$ and $A_{disk\ out}$
- blading geometrical characteristics: detailed in section D1 in Appendix D
- rotational speed of the stage: n
- inlet flow conditions: $\dot{m}$, Ts_{in}, $Tt\ abs_{in}$, Ps_{in}, $Pt\ abs_{in}$, $Mabs_{in}$, $Pt\ rel_{in}$, $Tt\ rel_{in}$ and $Mrel_{in}$
- inlet velocities: $Vabs_{in}$, $Vabs_{inT}$, V_{inA}, α_{in}, $Vrel_{in}$, $Vrel_{inT}$ and β_{in}
- required power extraction: Pw_{stage}

Output

- outlet flow conditions: Ts_{out}, $Tt\ abs_{out}$, Ps_{out}, $Pt\ abs_{out}$, ρ_{out}, $Mabs_{out}$, $Pt\ rel_{out}$ and $Mrel_{out}$
- outlet velocities: $Vabs_{out}$, V_{outA}, $Vabs_{outT}$, α_{out}, $Vrel_{out}$, $Vrel_{outT}$ and β_{out}
- Blade metal angles: $\beta_{metal\ in}$ and $\beta_{metal\ out}$
- stage isentropic efficiency: $\eta_{is\ stage}$

NOTA: Some of the input can be obtained from other input variables (E.g. $r_{mean\ in}$ from $r_{h\ in}$ and $r_{tip\ in}$). These variables are calculated in the main codes (CRT-DPv, CRT-DPe and CRT-OD), and used as inputs to the calculation bricks to avoid the repetition of calculations and minimise the calculation time. The same comment applies to the output variables.

The outline of this calculation is the following:

Step 1 - calculate Tt_{out} from Tt_{in} and Pw_{stage}, as well as $Vabs_{outT}$ from $Vabs_{inT}$, the annulus geometry, n and Pw_{stage}.

Step 2 - guess $\eta_{is\ stage}$ (guessed value noted as $\eta^*_{is\ stage}$)

Step 3 - calculate the exit velocity triangle

Step 4 - calculate the stage losses

Step 5 - calculate $\eta_{is\ stage}$ from the inlet conditions and the losses

Step 6 – repeat steps 3 to 5 until $(\eta^*_{is\ stage} - \eta_{is\ stage})/ \eta_{is\ stage} <$ tolerance. The calculated $\eta_{is\ stage}$ is used as $\eta^*_{is\ stage}$ for the next iteration.

Step 1: calculate Tt_{out} and $Vabs_{outT}$

$$\Delta ht = ht_{out} - ht_{in} = \frac{Pw_{stage}}{\dot{m}} \quad \text{[Eq. 63]}$$

Note that Pw_{stage} is expressed from the point of view of the fluid, being negative for turbines since the power is extracted from the fluid.

$$\Delta Tt = Tt_{out} - Tt_{in} = \frac{\Delta ht}{Cp} \quad \text{[Eq. 64]}$$

$$Tt_{out} = Tt_{in} + \Delta Tt \quad \text{[Eq. 65]}$$

$Vabs_{outT}$ is calculated from a momentum balance (deduction available in Ref. 195, page 213)

$$Vabs_{outT} = \frac{\Delta ht + U_{out} Vabs_{inT}}{U_{out}} \quad \text{[Eq. 66]}$$

where U_{out} is calculated as

$$U_{out} = r_{mean\ out} 2\pi n \quad \text{[Eq. 67]}$$

***Step 2:* guess $\eta_{is\ stage}$**

At this step, $Vabs_{outT}$ is known, but $Vabs_{out}$ and the static conditions at the outlet of the stage are not known. These magnitudes depend on the stage efficiency. In order to calculate the exit conditions, $\eta_{is\ stage}$ is guessed (guessed value noted as $\eta^*_{is\ stage}$). The calculated exit conditions are subsequently used to calculate the stage losses and their corresponding $\eta_{is\ stage}$ which is checked against $\eta^*_{is\ stage}$ in Step 6. An initial guess of $\eta^*_{is\ stage} = 0.9$ is used for all the stages.

***Step 3:* calculate the exit velocity triangle using $\eta^*_{is\ stage}$**

Using ideal gas equations, $Pt\ abs_{out}$ can be calculated as

$$Pt\,abs_{out} = Pt\ abs_{in} \left(1 - \frac{1 - \frac{Tt\ abs_{out}}{Tt\ abs_{in}}}{\eta^*_{is\ stage}} \right)^{\frac{\gamma}{\gamma - 1}} \quad \text{[Eq. 68]}$$

V_{outA} is calculated iteratively using Eq. 69 to Eq. 74. V_{outA} is used as a guess, and a Newton-Raphson solver is used to minimise the error defined in Eq. 75 (tolerance 10^{-8}).

$$\alpha_{out} = \frac{180}{\pi} arctan\left(\frac{Vabs_{outT}}{V_{outA}} \right) \quad \text{[Eq. 69]}$$

$$Vabs_{out} = \frac{V_{outA}}{cos\left(\frac{\pi}{180}\alpha_{out}\right)} \quad \text{[Eq. 70]}$$

$Mabs_{out}$ is obtained solving Eq. 71 (equation 1.11 in Ref. 196) with a Newton-Raphson solver.

$$\frac{Vabs_{out}}{\sqrt{Tt_{out}}} = Mabs_{out}\sqrt{\gamma R}\left(1+\frac{\gamma-1}{2}Mabs_{out}^{\ 2}\right)^{-0.5} \quad \text{[Eq. 71]}$$

The capacity (q_{out}) and the effective outlet area are calculated using Eq. 72 and Eq. 73 respectively (equation 1.9 in Ref. 196)

$$q_{out} = Mabs_{out}\sqrt{\gamma R}\left(1+\frac{\gamma-1}{2}Mabs_{out}^{\ 2}\right)^{\frac{-(\gamma+1)}{2(\gamma-1)}} \quad \text{[Eq. 72]}$$

$$Aeff_{out} = \frac{\dot{m}\sqrt{Tt_{out}}}{q_{out}Pt_{out}} \quad \text{[Eq. 73]}$$

An outlet flow area ($A^*_{disk\ out}$) can be calculated and compared to the real outlet area. These two magnitudes are equal for the correct V_{outA}.

$$A^*_{disk\ out} = \frac{Aeff_{out}}{cos\left(\frac{\pi}{180}\alpha_{out}\right)} \quad \text{[Eq. 74]}$$

$$ErrorA_{disk} = \frac{\left(A^*_{disk\ out} - A_{disk\ out}\right)}{A_{disk\ out}} \quad \text{[Eq. 75]}$$

Once the absolute outlet velocities are known, the relative outlet velocities can be calculated as

$$Vrel_{outT} = Vabs_{outT} - U_{out} \quad \text{[Eq. 76]}$$

$$\beta_{out} = \frac{180}{\pi}arctan\left(\frac{Vrel_{outT}}{V_{outA}}\right) \quad \text{[Eq. 77]}$$

$$Vrel_{out} = \frac{V_{outA}}{cos\left(\frac{\pi}{180}\beta_{out}\right)} \quad \text{[Eq. 78]}$$

The outlet static pressure and temperature are calculated as (equation 1.7 and 1.8 in Ref. 196)

$$Ps_{out} = \frac{Pt_{out}}{\left(1 + \frac{\gamma - 1}{2} Mabs_{out}^{\ 2}\right)^{\frac{\gamma}{\gamma - 1}}} \quad \text{[Eq. 79]}$$

$$Ts_{out} = \frac{Tt_{out}}{1 + \frac{\gamma - 1}{2} Mabs_{out}^{\ 2}} \quad \text{[Eq. 80]}$$

and the outlet density as

$$\rho_{out} = \frac{Ps_{out}}{Ts_{out} R} \quad \text{[Eq. 81]}$$

The relative outlet total temperature and pressure are calculated as

$$Tt\,rel_{out} = Ts_{out} + \frac{Vrel_{out}^{\ 2}}{2Cp} \quad \text{[Eq. 82]}$$

$$Pt\,rel_{out} = Ps_{out}\left(\frac{Tt\,rel_{out}}{Ts_{out}}\right)^{\frac{\gamma}{\gamma - 1}} \quad \text{[Eq. 83]}$$

and the relative outlet Mach number as

$$c_{out} = \frac{Vabs_{out}}{Mabs_{out}} \quad \text{[Eq. 84]}$$

$$Mrel_{out} = \frac{Vrel_{out}}{c_{out}} \quad \text{[Eq. 85]}$$

Step 4: **Calculate the stage losses**

The loss calculation requires the blade metal angles, which are calculated as follows

$\beta_{metal\ in} = \beta_{\ in}$ [Eq. 86][39]

$\beta_{metal\ out}$ is obtained solving the following equation with the calculated values of $\beta_{\ out}$ and $Mrel_{out}$ (deviation model proposed in Ref. 194 including the adequate blade geometric definition).

[39] Blade geometrical design assumption 2, page 93

$\beta_{out} = \beta_{metal\ out}$ for $Mrel_{out}=1$

$\beta_{out} = 1.154\ \beta_{metal\ out} - 11.5 + 0.615\ Chord$ for $0 < Mrel_{out} < 0.5$

Linear variation between both for $0.5 < Mrel_{out} < 1$

[Eq. 87]

$Mrel_{out}$ at the design point is lower than 0.5 for all the stages of the studied CRTs and the solution of this equation does not require iterations.

The total stage pressure loss Yt (defined in Eq. 61) is calculated following the procedure indicated in Ref. 192 and Ref. 193. This procedure, customised for the sign convention defined in Figure 56 and the used blade geometric design, is detailed in Appendix D.

***Step 5:* calculate $\eta_{is\ stage}$ from the inlet conditions and the losses**

In order to evaluate the efficiency of a stage, the ideal and real outlet conditions are required. First of all, the ideal $Pt\ rel_{out\ is}$ of the stage is calculated from the real outlet conditions (obtained in Eq. 83) and the definition of the total loss coefficient (Eq. 61c).

$$Pt\ rel_{out\ is} = Yt\left(Pt\ rel_{out} - Ps_{out}\right) + Pt\ rel_{out} \qquad \text{[Eq. 88]}$$

Finally, using the relationships between total and static magnitudes, $Ts_{out\ is}$ and $Tt_{out\ is}$ can be calculated as

$$Ts_{out\ is} = Tt\ rel_{out}\left(\frac{Ps_{out}}{Pt\ rel_{out\ is}}\right)^{\frac{\gamma-1}{\gamma}} \qquad \text{[Eq. 89]}$$

$$Tt_{out\ is} = Ts_{out\ is}\left(\frac{Pt_{out}}{Ps_{out}}\right)^{\frac{\gamma-1}{\gamma}} \qquad \text{[Eq. 90]}$$

After calculating $Tt_{out\ is}$, the isentropic efficiency of a stage with a total pressure loss coefficient Yt can be obtained as

$$\eta_{is\ stage} = \frac{Tt_{in} - Tt_{out}}{Tt_{in} - Tt_{out\ is}} \qquad \text{[Eq. 91]}$$

***Step 6:* Check the error in $\eta_{is\ stage}$ and iterate accordingly**

The calculated $\eta_{is\ stage}$ is used as $\eta^*_{is\ stage}$ in step 2 for the next iteration. This iteration scheme proved to be numerically robust for the studied CRTs.

2.2.3.3.2.3 *Stage-OD* calculation brick

Stage-OD used in CRT-OD to calculate the exit conditions of a turbine stage, from the inlet conditions, exit geometry and blade geometrical definition.

Input

- gas properties: γ, R, Cp
- inlet gas path geometry: $r_{h\ in}$, $r_{tip\ in}$, $r_{mean\ in}$ and $A_{disk\ in}$
- outlet gas path geometry: $r_{h\ out}$, $r_{tip\ out}$, $r_{mean\ out}$ and $A_{disk\ out}$
- blading geometrical characteristics: detailed in section D1 in Appendix D
- blade metal angles: $\beta_{metal\ in}$ and $\beta_{metal\ out}$
- rotational speed of the stage: n
- inlet flow conditions: $\dot{m}$, Ts_{in}, $Tt\ abs_{in}$, Ps_{in}, $Pt\ abs_{in}$, $Mabs_{in}$, $Pt\ rel_{in}$ and $Mrel_{in}$
- inlet velocities: $Vabs_{in,}$ $Vabs_{inT}$, V_{inA}, α_{in}, $Vrel_{in}$, $Vrel_{inT}$ and β_{in}

Output

- outlet flow conditions: Ts_{out}, $Tt\ abs_{out}$, Ps_{out}, $Pt\ abs_{out}$, ρ_{out}, $Mabs_{out}$, $Pt\ rel_{out}$ and $Mrel_{out}$
- outlet velocities: $Vabs_{out}$, V_{outA}, $Vabs_{outT}$, α_{out}, $Vrel_{out}$, $Vrel_{outT}$ and β_{out}
- stage isentropic efficiency: $\eta_{is\ stage}$

NOTA: Some of the input can be obtained from other input variables (E.g. $r_{mean\ in}$ from $r_{h\ in}$ and $r_{tip\ in}$). These variables are calculated in the main codes (CRT-DPv, CRT-DPe and CRT-OD), and used as inputs to the calculation bricks to avoid the repetition of calculations and minimise the calculation time. The same comment applies to the output variables.

The outline of this calculation is the following:

Step 1 - calculate the ideal stage exit conditions

Step 2 - guess $Mrel_{out}$ (guessed value noted as M^*rel_{out})

Step 3 - calculate the stage losses

Step 4 - calculate the $Mrel_{out}$ from the losses and ideal exit conditions

Step 5 - repeat steps 3 and 4 until $(M^*rel_{out} - Mrel_{out})/ Mrel_{out} <$ tolerance. The calculated $Mrel_{out}$ is used as M^*rel_{out} for the next iteration.

Step 6 - calculate the exit velocity triangles and exit flow properties

***Step 1*: calculate the ideal stage exit conditions**

First, the outlet isentropic conditions in a rotor are calculated using the conservation of rothalpy (expressed in the relative frame) and the equations of an isentropic expansion of an ideal gas (Eq. 93).

$$Tt\,rel_{out} = Tt\,rel_{in} + \frac{U_{out}^{\,2} - U_{in}^{\,2}}{2Cp} \qquad \text{[Eq. 92]}$$

$$Pt\,rel_{out\ is} = Pt\,rel_{in}\left(\frac{Tt\,rel_{out}}{Tt\,rel_{in}}\right)^{\frac{\gamma}{\gamma-1}} \qquad \text{[Eq. 93]}$$

Then $Mrel_{out\ is}$ is calculated in an iterative process. $M^*rel_{out\ is}$ is guessed, then the exit relative angle $\beta_{out\ is}$ is calculated from Eq. 87 using the guessed $M^*rel_{out\ is,}$ and $Mrel_{out\ is}$ is obtained solving Eq. 94 and Eq. 95 with a Newton-Raphson solver.

$$Aeff\,rel_{out\,is} = A_{disk\,out}\,cos\left(\frac{\pi}{180}\beta_{out\,is}\right) \qquad \text{[Eq. 94]}$$

$$\frac{\dot{m}\sqrt{Tt\,rel_{out}}}{Aeff\,rel_{out\,is}Pt\,rel_{out\,is}} = Mrel_{out\,is}\sqrt{\gamma R}\left(1+\frac{\gamma-1}{2}Mrel_{out\,is}^{\,2}\right)^{\frac{-(\gamma+1)}{2(\gamma-1)}} \qquad \text{[Eq. 95]}$$

the obtained $Mrel_{out\ is}$ is used as guess for subsequent iteration steps until

$(M^*rel_{out\ is}- Mrel_{out\ is})/ Mrel_{out\ is}$ is smaller than a fixed tolerance value.

Finally, the static isentropic outlet conditions are calculated using the relationships between static, total conditions and M.

$$Ts_{out\ is} = \frac{Tt\,rel_{out}}{1+\frac{\gamma-1}{2}Mrel_{out\,is}^{\,2}} \qquad \text{[Eq. 96]}$$

$$Ps_{out\ is} = \frac{Pt\,rel_{out\,is}}{\left(1+\frac{\gamma-1}{2}Mrel_{out\,is}^{\,2}\right)^{\frac{\gamma}{\gamma-1}}} \qquad \text{[Eq. 97]}$$

The real expansion taking place in the rotor would reach the same static pressure as the ideal expansion. Consequently

$$Ps_{out} = Ps_{out\,is} \qquad \text{[Eq. 98]}$$

Step 2: **guess $Mrel_{out}$** (guessed value noted as M^*rel_{out})

The real outlet conditions are a function of the ideal outlet conditions and the stage losses. At the same time, the losses are a function of the outlet conditions. For this reason, the solution of the real expansion requires an iterative process. M^*rel_{out} is used as a guess. Subsequently the stage losses are calculated as well as the real exit conditions. The obtained $Mrel_{out}$ is compared against the guessed M^*rel_{out}. $Mrel_{out\ is}$ is used as initial value for M^*rel_{out}

***Step 3:* calculate the stage losses**

First the exit relative angle β_{out} is calculated from Eq. 87 using the guessed M^*rel_{out}. Then the stage losses are evaluated following the procedure described in Appendix D (using M^*rel_{out}).

***Step 4:* calculate $Mrel_{out}$ from the losses and ideal exit conditions**

$Pt\ rel_{out}$ is obtained from the ideal outlet conditions and the loss coefficient (using the definition of Eq. 61)

$$Pt\,rel_{out} = \frac{Pt\,rel_{out\_is} + Ps_{out}\,Yt}{1 + Yt} \qquad \text{[Eq. 99]}$$

$Mrel_{out}$ is subsequently calculated solving Eq. 101 (capacity equation). The relative effective area is first calculated using β_{out} (obtained in step 3).

$$Aeff\,rel_{out} = A_{disk\,out}\,cos\left(\frac{\pi}{180}\beta_{out}\right) \qquad \text{[Eq. 100]}$$

$$\frac{\dot{m}\sqrt{Tt\,rel_{out}}}{Aeff\,rel_{out}\,Pt\,rel_{out}} = Mrel_{out}\sqrt{\gamma R}\left(1 + \frac{\gamma - 1}{2}Mrel_{out}^{\,2}\right)^{\frac{-(\gamma+1)}{2(\gamma-1)}} \qquad \text{[Eq. 101]}$$

***Step 5 - c*heck the error in $Mrel_{out}$ and iterate accordingly**

The obtained $Mrel_{out}$ is used as guess for subsequent iteration steps until $(M^*rel_{out} - Mrel_{out}) / Mrel_{out}$ is smaller than a fixed tolerance value. This iteration scheme proved to be numerically robust for the studied CRTs.

***Step 6* - calculate the exit velocity triangles and exit flow properties**

Once the relative outlet conditions are defined, the static and absolute magnitudes are determined, as well as the velocity triangles. First the static temperature, air density and speed of sound are evaluated as

$$Ts_{out} = \frac{Tt\,rel_{out}}{1 + \frac{\gamma - 1}{2}Mrel_{out}^{\,2}} \qquad \text{[Eq. 102]}$$

$$\rho_{out} = \frac{Ps_{out}}{Ts_{out}R} \qquad \text{[Eq. 103]}$$

$$c_{out} = \sqrt{\gamma R Ts_{out}} \qquad \text{[Eq. 104]}$$

Then, the relative exit velocity triangle is calculated as

$$Vrel_{out} = \frac{Mrel_{out}}{C_{out}} \qquad \text{[Eq. 105]}$$

$$V_{outA} = Vrel_{out}\, cos\left(\frac{\pi}{180}\beta_{out}\right) \quad \text{[Eq. 106]}$$

$$Vrel_{outT} = Vrel_{out}\, sin\left(\frac{\pi}{180}\beta_{out}\right) \quad \text{[Eq. 107]}$$

Then, the absolute exit velocity triangle is calculated as

$$Vabs_{outT} = Vrel_{outT} + U_{out} \quad \text{[Eq. 108]}$$

$$\alpha_{out} = \frac{180}{\pi} arctan\left(\frac{Vabs_{outT}}{V_{outA}}\right) \quad \text{[Eq. 109]}$$

$$Vabs_{out} = V_{outA}\, cos\left(\frac{\pi}{180}\alpha_{out}\right) \quad \text{[Eq. 110]}$$

$$Mabs_{out} = \frac{Vabs_{out}}{c_{out}} \quad \text{[Eq. 111]}$$

The total outlet temperature and pressure are subsequently calculated as

$$Tt_{out} = Ts_{out} \frac{Vabs_{out}^{\,2}}{2Cp} \quad \text{[Eq. 112]}$$

$$Pt_{out} = Ps_{out}\left(\frac{Tt_{out}}{Ts_{out}}\right)^{\frac{\gamma}{\gamma-1}} \quad \text{[Eq. 113]}$$

Finally, ΔTt and $\eta_{is\ stage}$ are calculated

$$\Delta Tt = Tt_{out} - Tt_{in} = \frac{\Delta ht}{Cp} \quad \text{[Eq. 114]}$$

$$\eta_{is\ stage} = \frac{1 - \frac{Tt_{out}}{Tt_{in}}}{1 - \left(\frac{Pt_{out}}{Pt_{in}}\right)^{\frac{\gamma-1}{\gamma}}} \quad \text{[Eq. 115]}$$

2.2.3.3.2.4 CRT-DPv code

A brief description of *CRT-DPv* as well as the complete list of input and output variables can be found in section 2.2.3.3.1.1. This code uses Stage-DP calculation brick described in section 2.2.3.3.2.2.

Outline of the calculation:

Step 1 - calculate the inlet conditions to the first stage

Step 2 - use Stage-DP to calculate the outlet conditions and blade metal angles

Step 3 - store the absolute outlet conditions of the stage as inlet absolute conditions of the following stage, and calculate the inlet conditions relative to the following stage

Step 4 - repeat steps 2 and 3 for all the turbine stages

Step 5 - calculate the overall turbine isentropic efficiency ($\eta_{is\ CRT}$) and pressure ratio (PR_{CRT})

Steps 1, 3 and 5 are described in Appendix E.

2.2.3.3.2.5 CRT-OD code

A brief description of *CRT-OD* as well as the complete list of input and output variables can be found in section 2.2.3.3.1.1. This code uses Stage-OD calculation brick described in section2.2.3.3.2.3.

Outline of the calculation:

Step 1 - calculate the inlet conditions to the first stage

Step 2 - use Stage-OD to calculate the outlet conditions

Step 3 - store the absolute outlet conditions of the stage as inlet absolute conditions of the following stage, and calculate the inlet conditions relative to the following stage

Step 4 - repeat steps 2 and 3 for all the turbine stages

Step 5 - calculate $\eta_{is\ CRT}$, PR_{CRT}, Pw_{CRT}, $Pw_{drum\ 1}$, $Pw_{drum\ 2}$, TR_{CRT} and the power ratio of the CRT (PwR_{CRT} defined in Eq. 120)

Steps 1 and 3 of CRT-OD are identical to steps 1 and 3 of CRT-DPv described in Appendix D. Step 5 of CRT-OD comprises the following calculations in addition to those of step 5 of CRT-DPv.

$$Pw_{drum\,1} = \dot{m}Cp \sum_{i=odd\ stages} \Delta Tt_i \qquad \text{[Eq. 116]}$$

$$Pw_{drum\,2} = \dot{m}Cp \sum_{i=even\ stages} \Delta Tt_i \qquad \text{[Eq. 117]}$$

$$Pw_{CRT} = \dot{m}Cp\left(Tt_{out\,NbStages} - Tt_{in\,1}\right) \qquad \text{[Eq. 118]}$$

$$Q_{drum\,1} = \frac{-Pw_{drum\,1}}{n_1 \frac{\pi}{30}} \qquad Q_{drum\,2} = \frac{-Pw_{drum\,2}}{n_2 \frac{\pi}{30}} \qquad \text{[Eq. 119]}$$

note that n_1 is positive and n_2 is negative and $Q_{drum\ 1}$ and $Q_{drum\ 2}$ have opposite signs.

$$TR_{CRT} = \frac{-Q_{drum\,1}}{Q_{drum\,2}} \quad \text{and} \quad PwR_{CRT} = \frac{Pw_{drum\,1}}{Pw_{drum\,2}} \qquad \text{[Eq. 120]}$$

2.2.3.3.2.6 Verification of the 1-D mean line modelling methodology.

The developed 1-D mean line DP and OD methodologies were verified against a known 20 stage CRT design (CRT-k). ***Only limited information about CRT-k can be presented in this thesis due to non disclosure agreements. Consequently, the values on the axes are sometimes omitted.***

CRT-DPv was executed using the input corresponding to the DP of CRT-k (gas path geometry presented in Figure 55). The conservation of mass flow rate and rothalpy was verified for each stage. The calculated $\beta_{metal\ out}$ and $Mrel_{out}$ were verified with respect to those of CRT-k (Figure 58). The obtained values and trends are close to those of CRT-k.

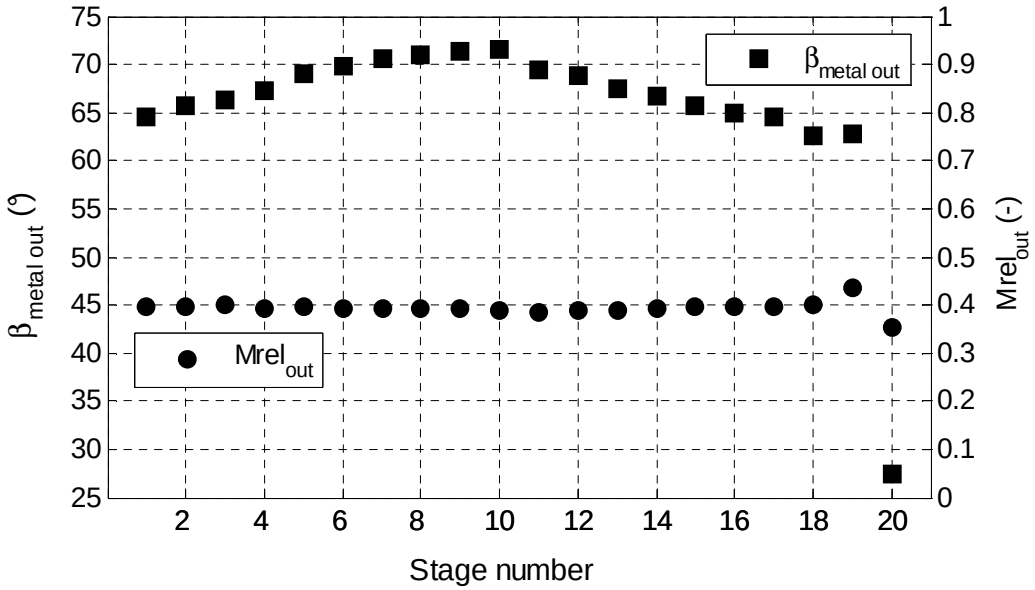

Figure 58: Calculated $\beta_{metal\ out}$ and $Mrel_{out}$ for CRT-k

Figure 59 shows the DP velocity triangles of the first and last four stages. The inlet velocities are plotted in blue while the outlet velocities are plotted in red. The full lines represent the absolute velocities and the dotted lines represent the relative velocities.

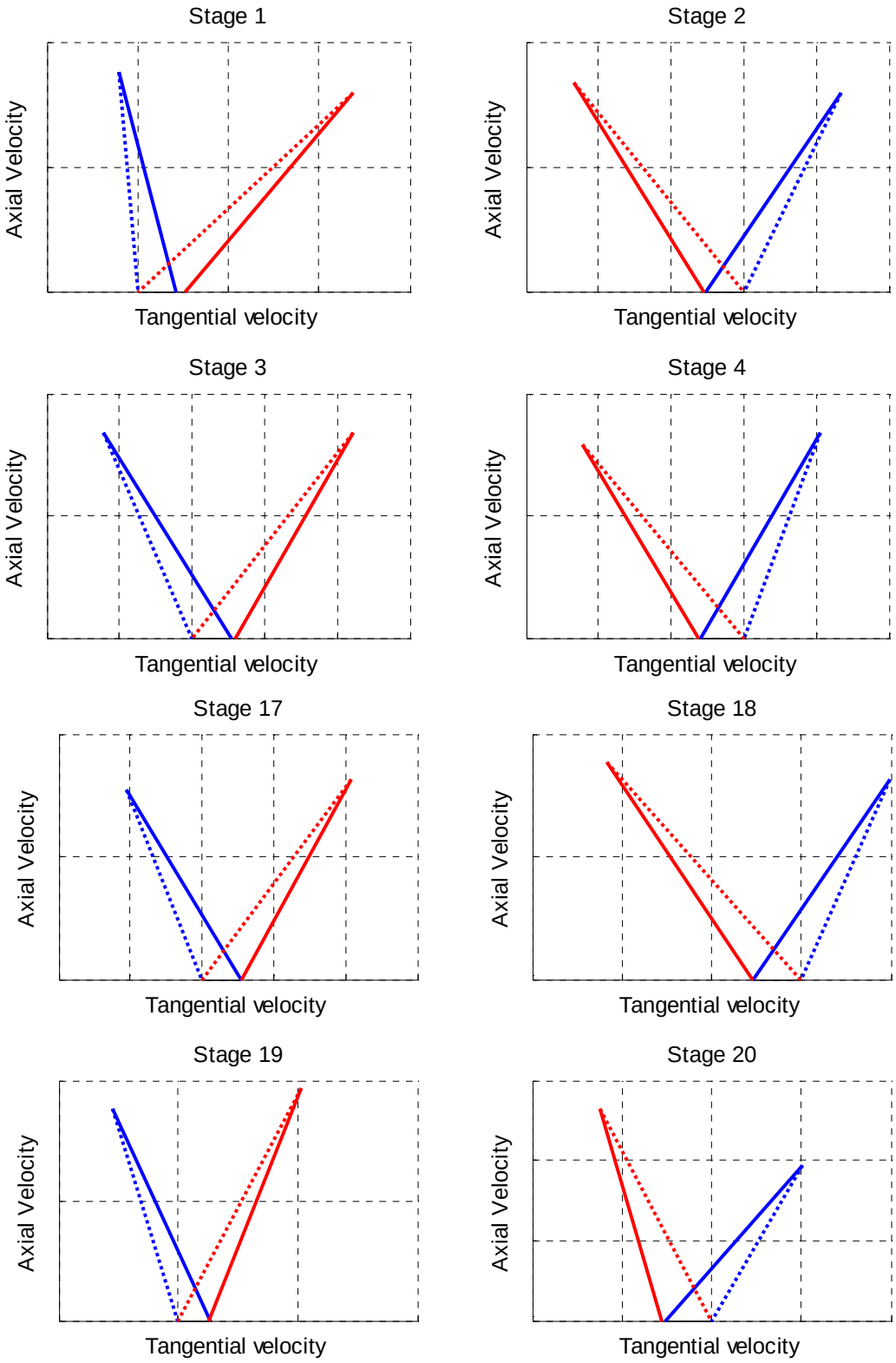

Figure 59: Estimated DP velocity triangles of CRT-k (first and last 4 stages)

The value of one division in the y axis is the same for all the plots. The value of one division in the x axis is the same for all the plots (but not the same as the y division). The difference between U_{in} and U_{out} can only be seen in the first stage due to the used scale.

Despite the fact that the torque delivered to both parts of the turbine is equal, it can be seen that the outlet swirl is lower than the inlet swirl[40]. This is due to the increased axial velocity in the last stages. Reduced outlet swirls are desired in this type of turbine to reduce losses in the nozzle (note that there is no outlet guide vane). The calculated exit swirl is close to that of CRT-k as is the calculated efficiency (88.8%).

OD calculations were performed using CRT-OD, the input data corresponding to CRT-k and the calculated blade metal angles. The difference between the performance obtained with CRT-DPv and CRT-OD using the DP inlet conditions and rotational speeds as inputs is of the order magnitude of the numerical tolerances set in both codes. This shows that the methods used in both codes are consistent. The performance predictions at reference cruise and take-off points are close to those of CRT-k.

2.2.3.3.2.7 CRT-DPe code

A brief description of *CRT-DPe* as well as the complete list of input and output variables can be found in section 2.2.3.3.1.1. This code uses Stage-DP calculation brick described in section 2.2.3.3.2.2 and includes preliminary design criteria to split the power between the stages and size the gas path.

Outline of the calculation:

Step 1 - calculate the inlet conditions to the first stage

Step 2 – calculate the power extracted in each stage

Step 3 – guess the stage $r_{mean\ out}$ and calculate $r_{h\ out}$ following the gas path design criteria.

Step 4 – use Stage-DP to calculate the outlet conditions and blade metal angles

Step 5 – repeat steps 3 and 4 until getting a target $Mrel_{out}$

Step 6 - store the absolute outlet conditions of the stage as inlet absolute conditions of the following stage, and calculate the inlet conditions relative to the following stage

Step 7 - repeat steps 3 and 6 for all the turbine stages

Step 8 - calculate $\eta_{is\ CRT}$, PR_{CRT}

[40] Note that the maximum y value of the last plot is 50% higher than the maximum value of the other plots

Steps 1, 6 and 8 of CRT-DPe are identical to steps 1, 3 and 5 of CRT-DPv described in Appendix E. Steps 2, 3 and 5 contain the CRT preliminary design criteria and are described below.

Before describing the used preliminary design criteria, three design considerations are presented:

Consideration 1: number of stages

The mechanical design of a CRT with two drums (Figure 60) requires an even number of stages. In that case, the first and the last stages are used to transmit the power to the propellers and as structural support of each drum. An odd number of stages requires highly complex structures in order to ensure the mechanical integrity of the CRT and transmit the power to the CRP[41]. For this reason only even number of stages are considered in this PhD research project.

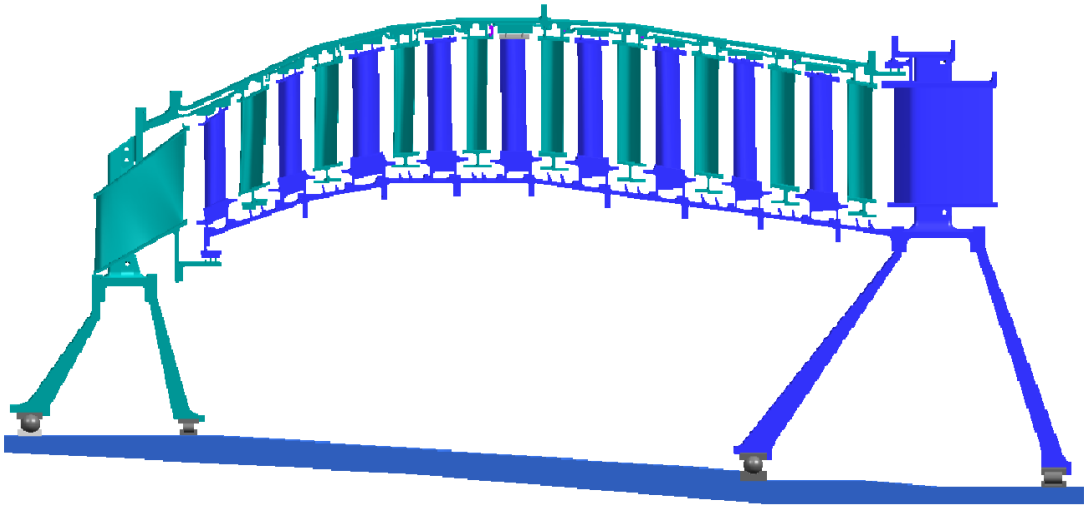

Figure 60: CRT cross sectional drawing [Ref. 34]

Consideration 2: gas path geometry

1 - Both parts of the CRT share the same gas path with both the internal and external drums following a smooth, continuous curve. The changes in cross sectional area are relatively small from one stage to another (except for the first and last ones). At the same time, variations in Ts are relatively small across the turbine (~2.5% change in each stage). As a consequence, the changes in axial velocity are relatively small from one stage to the following one. This can be seen in

[41] In order to understand the mechanical complexity of having an odd number of stages, the reader is challenged to find a mechanical arrangement allowing the installation of a further turbine stage at the front or at the back of the CRT of Figure 60. Note that the connections of the extra stages are not possible thought the top of the CRT since the propellers are directly linked to the first and last stages.

the velocity triangles of Figure 59. The mean line of the CRT also follows a smooth curve.

2 - The inlet hub and tip radius of the first stage are set by the mid frame which is located between the IPT and CRT. The outlet hub and tip radius of the last stage are set by the exit nozzle.

3 – It can be observed that r_{tip} and r_h are rapidly increased in the first stages. This is done in order to increase U_{in} and U_{out} and reduce the loading of the stages. Once the maximum r_{tip} is achieved, it is gradually reduced so that the outlet constraints can be satisfied. r_{tip} is constrained by the hub diameter of the propellers and the equipment required on the blade roots.

4 - Three preliminary design criteria are used in CRT-DPe to define the gas path:

- The axial chords of the first and last stages are known ($AxialChord_1$ and $AxialChord_{NbStages}$). The axial chord of the rest of the stages is the same for every stage and for every CRT design ($AxialChord_{int}$).
- r_{tip} is defined as follows:
    - for stages 1 to 10, $r_{tip\ in}$ equals the $r_{tip\ in}$ of CRT-k (Figure 55). According to the model assumptions, $r_{tip\ out\ i} = r_{tip\ in\ i+1}$.
    - for the last stage (NbStages), $r_{tip\ in\ NbStages} = r_{tip\ out\ NbStages}$
    - for all the stages from 11 to NbStages-1, $r_{tip\ in}$ is defined by the straight line between $r_{tip\ in\ 10}$ and $r_{tip\ in\ NbStages}$.

  Figure 61 shows the definition of the outer drum, according to the aforementioned design criteria, for two CRTs with 18 and 24 stages respectively. The dotted vertical lines delimit two consecutive stages.
- r_h for every stage is calculated so as to obtain $Mrel_{out} = 0.4$ (except for the last one because the outlet geometry is defined by the nozzle requirements). This is done to obtain low compressibility losses and similar outlet blade angles across the turbine (this point is explained in the paragraph below).

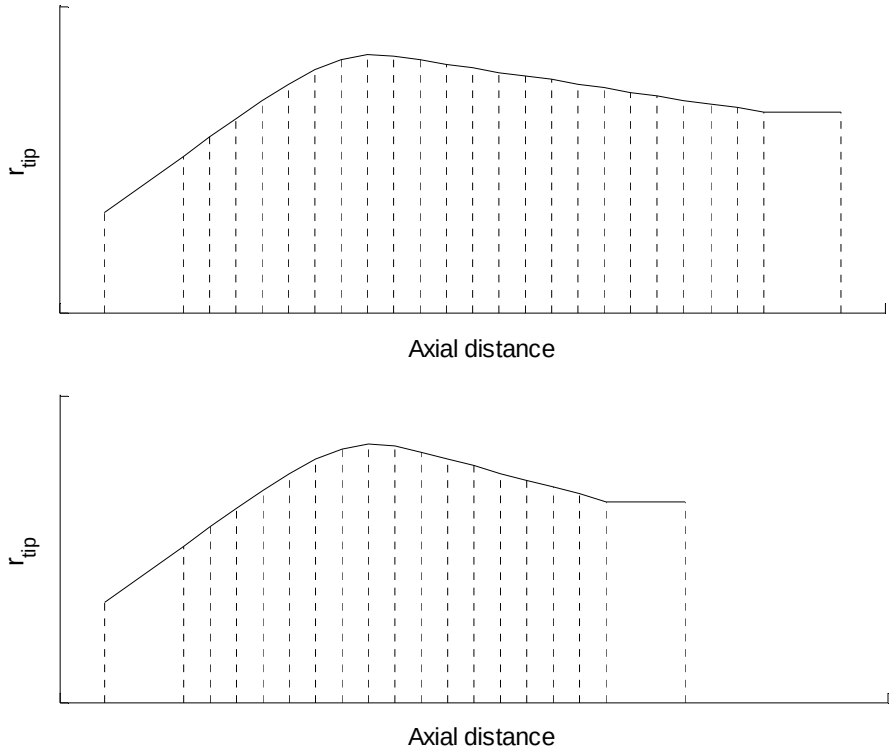

Figure 61: Tip radius definition of two CRT designs with 18 and 24 stages

Consideration 3: velocity triangles

1 – TR_{CRT} has a large impact on the design feasibility of a highly loaded CRT with large number of stages. The impact of TR_{CRT} on the velocity triangles of a highly loaded CRT is shown in the following two examples:

Example 1: $TR_{CRT} = 1$

Figure 62 shows the velocity triangles of the first six stages of a CRT defined by the following parameters at DP:

- IGV angle = 35º
- constant and equal axial velocity for all stages: V_A = 100 m/s
- constant and equal mean radius for all stages: r_{mean} = 45 m
- n_1 = 900 rpm and n_2 = 1000 rpm
- NbStages = 16
- TR_{CRT} = 1
- first stage enthalpy change: Δht_1 = -7.15 kJ/kg
- last stage enthalpy change: Δht_{16} = -7.15*(10/9) kJ/kg
- enthalpy change for even stages: Δht_{even} =10 kJ/kg
- enthalpy change for odd stages: Δht_{odd} =9 kJ/kg

Note that this is a relatively highly loaded design which requires a flow turning angle close to 100º. It can be seen from Figure 62 that the even stages have the

same absolute and relative angles (except for stage 16 which is not shown). The same repetition is observed for the odd stages apart for the first one. This is because $TR_{CRT} = 1$ and V_A and r_{mean} are conserved across the turbine. In the case of a real turbine with $TR_{CRT} = 1$, the variations in V_A and r_{mean} produce relatively small variations in the flow angles, but the similarity of the angles amongst even and odd stages is maintained (see Figure 58 and Figure 59)

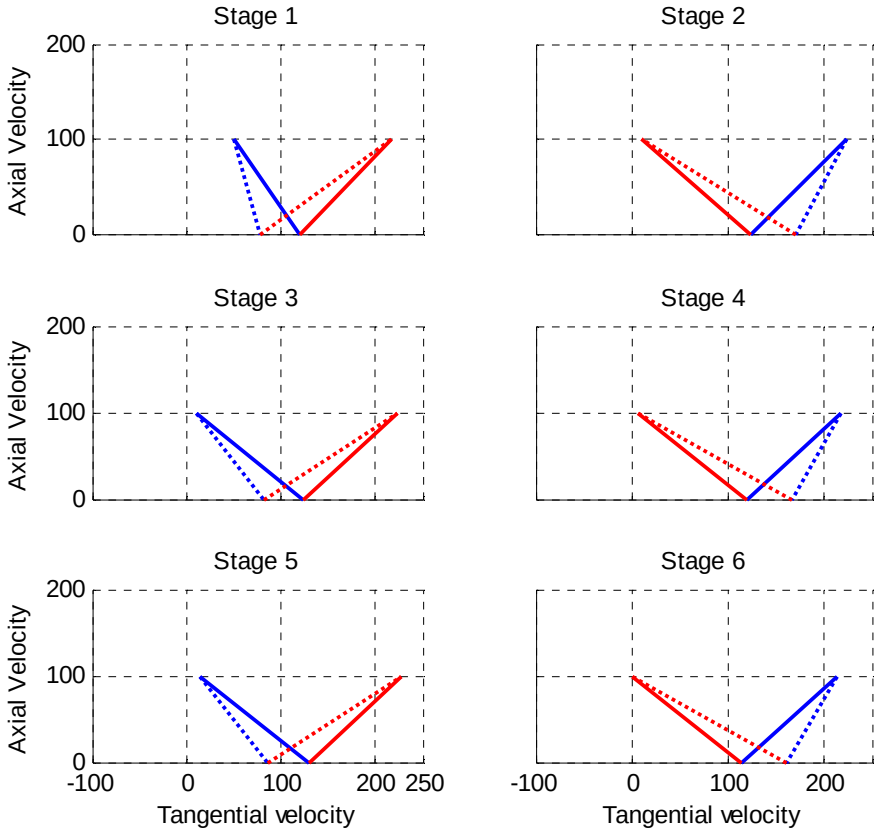

Figure 62: Mid radius velocity triangles of a CRT with $TR_{CRT} = 1$

Example 2: $TR_{CRT} = 0.9$

Figure 63 shows the velocity triangles of the first six stages of a CRT defined by the same DP parameters as the CRT of Example 1, except from n_2. In this case, n_2 = 900 rpm, and in consequence $TR_{CRT} = 0.9$. It can be seen that the angles vary from stage to stage. This is due to the fact that $TR_{CRT} \neq 1$ and V_A and r_{mean} are conserved across the turbine.

The distance between the two higher vertices of the velocity triangles is proportional to the torque of the stage (Δht/U). The outlet velocity of a stage is the inlet velocity of the following stage. This means that two consecutive velocity triangles share one of the two higher vertices. As a consequence, if the torque of two consecutive stages is the same, the triangles have their two vertices in the same place. If $TR_{CRT} \neq 1$ the vertex of the exit velocity triangle changes from stage

to stage and the inclination of the velocity triangles increases from stage to stage. If $TR_{CRT} < 1$ the triangles are inclined to the left, while if $TR_{CRT} > 1$ the triangles are inclined to the right.

In a real CRT, r_{mean} and V_A change from stage to stage, but the inclination of the velocity triangles is required in order to achieve $TR_{CRT} \neq 1$. $\beta_{out\ 6}$ in example 2 ($TR_{CRT} = 0.9$) is approximately 15º higher than $\beta_{out\ 6}$ in example 1 ($TR_{CRT} = 1$). It is also important to highlight that the velocity triangles vary along the blade span to maintain the radial equilibrium in the flow. As a consequence, the outlet angles at the tip are higher than at the hub. This makes stage 6, the last feasible stage of this CRT. Stage 8 would result in an exit angle at the tip close to 85º which is non feasible (Ref. 199).

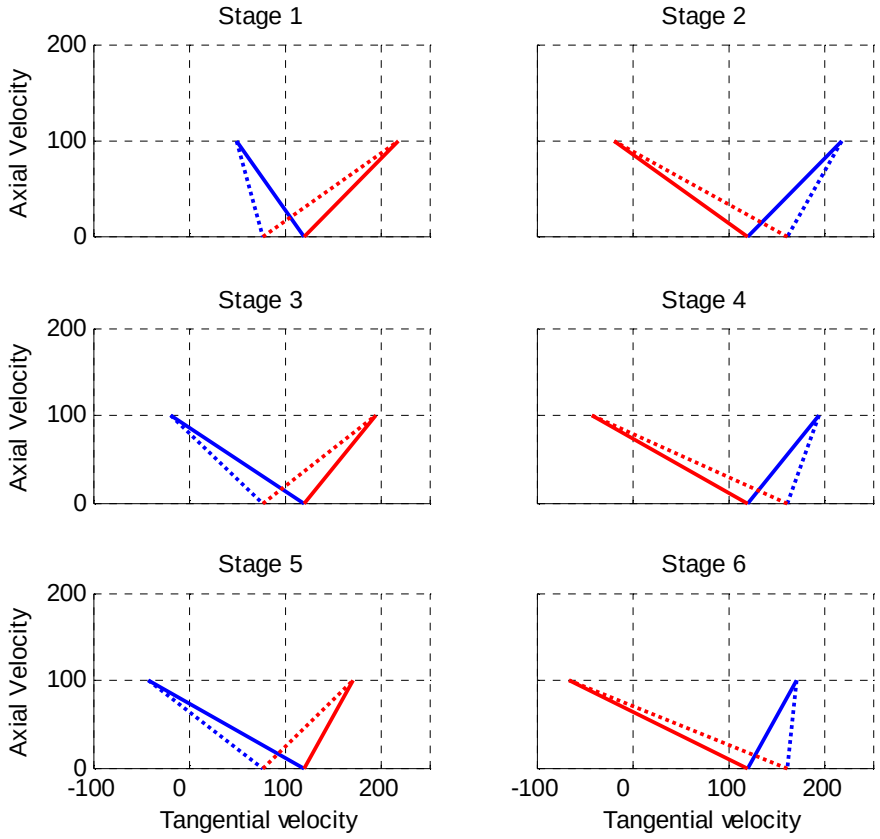

Figure 63: Mid radius velocity triangles of a CRT with TR = 0.9

It is concluded that for highly loaded CRTs with large number of stages, the feasibility of the blading design may be jeopardised, as the difference between $Q_{drum\ 1}$ and $Q_{drum\ 2}$ is increased. For this reason, only CRTs with $TR_{CRT} = 1$ were considered for the assessments.

2 – The shape of the velocity triangles has an impact on the blade feasibility (see above) and the stage losses. The stage reaction is used in conventional turbines to establish the shape of velocity triangles. This factor can not be defined for a CRT

since there is no stator. A form factor (FF) can be defined to establish the shape of the velocity triangles of two consecutive stages:

FF = 0 => inlet relative velocity to stage 1 is axial

FF = 1 => outlet relative velocity stage 2 is axial

Figure 64 shows three pairs of velocity triangles corresponding to two consecutive stages of a CRT with TR_{CRT} = 1 and FF = 0, 0.5 and 1 respectively (the blade speeds at inlet and outlet were considered equal for simplicity of the drawings). Point C is defined as the point where $U_{out\ 1}$ and $U_{in\ 2}$ coincide. A and B are the upper vertices of the velocity triangles

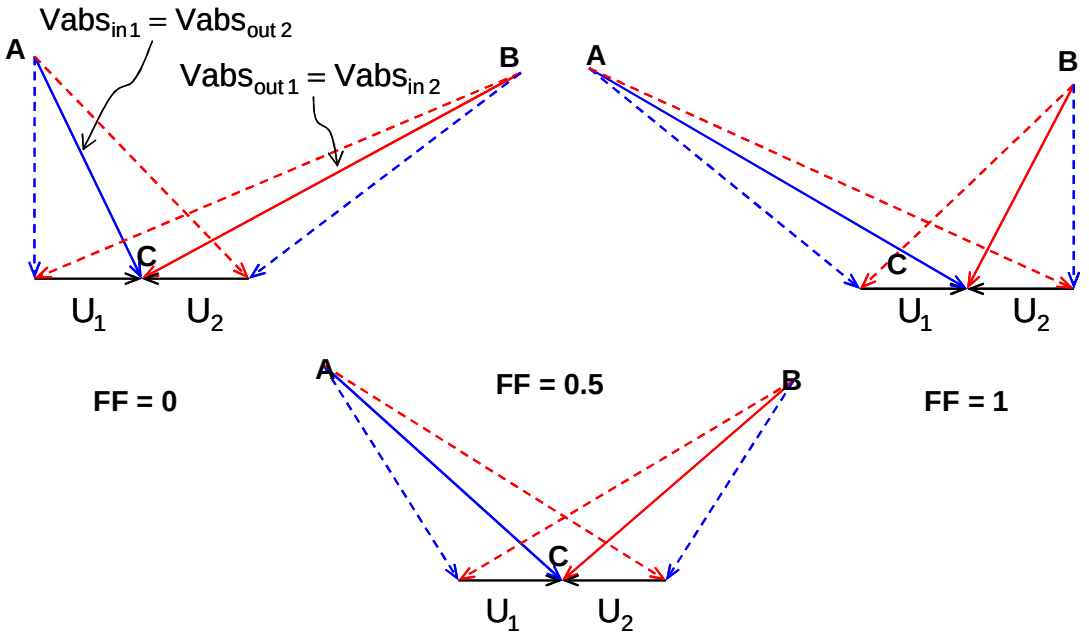

Figure 64: Form factor definition for CRT consecutive stages

For two consecutive stages with TR_{CRT} = 1, $U_{in\ 1} = U_{out\ 1} = U_{in\ 2} = U_{out\ 2}$ and constant V_A, FF = 0.5 minimises the losses and the maximum blade metal angles in both stages. In this particular case, the velocity triangles of stage 1 are symmetric to those of stage 2 (the inlet and outlet velocity triangles of a stage are not symmetric). In the case, of different rotational speeds (consequently different blade tangential velocities), the losses in both stages and the maximum blade metal angles are minimised with point C centred with respect to A and B.

In real CRTs, U and V_A vary from stage to stage, and so does FF. The variations in FF across the CRT are relatively small since the variations of V_A and U are relatively small and TR_{CRT} = 1 (refer to Consideration 3 1 in page 110). Although the FF is not maintained constant across the CRT, FFs close to 0.5 (or with C centred with respect to A and B for $n_1 \neq n_2$) are desirable in order to ensure the feasibility of the blade design and minimise stage losses.

After having introduced some design considerations, Steps 2, 3 and 5 of CRP-DPe are described.

Step 2: calculate the power extracted in each stage

Four preliminary design criteria are used in Step 2:

1 – $Pw_{stage\ 1}$ is defined so that C for stage 2 is centred with respect to A and B. Since TR_{CRT} = 1, this criteria implies that C is approximately centred for all the following stages (refer to Consideration 3 1 and 3 2 in pages 110 - 114).

2 – Constant ΔTt is considered for even and odd stages from 2 to 10 (ΔTt_{even} may not be equal to ΔTt_{odd}). The stage pressure ratio increases from stage to stage, and so does V_A (for constant $Mrel_{out}$). At the same time, r_{mean} increases and therefore the increase in turning angles is relatively small.

3 – Constant $\Delta Tt/Tt_{in}$ is considered for even and odd stages from 11 to NbStages-1 ($\Delta Tt/Tt_{in\ even}$ may not be equal to $\Delta Tt/Tt_{in\ odd}$). At stage 10, r_{mean} starts reducing, Tt has been considerably reduced in the first 10 stages (~200 K), and constant ΔTt would result in increasing turnings and cross sectional areas (for constant relative exit Mach numbers). For this reason a constant $\Delta Tt/Tt_{in}$ (which also corresponds to constant pressure ratio) is more appropriate.

4 - $Pw_{stage\ NbStages}$ is defined as to satisfy the required power extraction in drum 2.

The power extracted in each stage ($Pw_{stage\ i}$) is calculated from:

- inlet absolute tangential velocity: $Vabs_{in\ 1\ T}$
- inlet mass flow rate: $\dot{m}$
- number of stages of the CRT: NbStages
- total temperature at the inlet of the CRT: $Tt_{in\ 1}$
- both drums rotational speeds: n_1 and n_2
- required overall CRT power extraction: Pw_{CRT} (negative magnitude)
- mean radius at the inlet of the CRT: $r_{mean\ in\ 1}$
- assumed values of: $r_{out\ 1}$ and $r_{mean\ 2}$ (those of CRT-k are used)

Outline of the calculation:

Step 2.1 – calculate the required temperature drop in each of the two drums of the CRT ($\Delta Tt_{req\ drum\ 1}$ and $\Delta Tt_{req\ drum\ 2}$)

Step 2.2 – calculate the blade tangential velocities for the first two stages

Step 2.3 – guess ΔTt_2

Step 2.4 – calculate the power extracted in each stage using the guess value of ΔTt_2 and the established preliminary design criteria

Step 2.5 – calculate the temperature drop in each of the two drums of the CRT ($\Delta Tt_{drum\ 1}$ and $\Delta Tt_{drum\ 2}$)

Step 2.6 – repeat steps 3 to 5 until

$$(\Delta Tt_{drum\ 1} - \Delta Tt_{req\ drum\ 1}) / \Delta Tt_{req\ drum\ 1} < \text{tolerance}$$

Steps 2.1 to 2.6 are described in detail in Appendix F. A discussion about the geometrical assumptions done in Step 2.2 is provided below.

Discussion about assumptions of Step 2.2

$r_{in\ 1}$ is known before designing the CRT, but $r_{out\ 1}$ and $r_{mean\ 2}$ are not. A rigorous calculation to obtain the point C centred for the second stage would first require to solve the power distribution, then solve the two first turbine stages, and finally verify the radius assumptions. These nested iterations are computational costly and doing them does not grant that the C points of all the velocity triangles are centred. To avoid this complexity, values of $r_{out\ 1}$ and $r_{mean\ 2}$ of CRT-k are assumed for this calculation.

In order to obtain the point C centred for every velocity triangle, further more costly iteration schemes and more sophisticated design rules to split the power across stages and shape the gas path are required.

Example of application of the power distribution function

Figure 65 shows an example of the power distribution obtained for a CRT defined by

- Pw_{CRT} = -8.4 MW
- $Vabs_{inT\ 1}$ = 60 m/s
- $\dot{m}$ = 20 kg/s
- NbStages = 24
- Tin_1 = 1200 K
- N_1 = 800 rpm and N_2 = -900 rpm

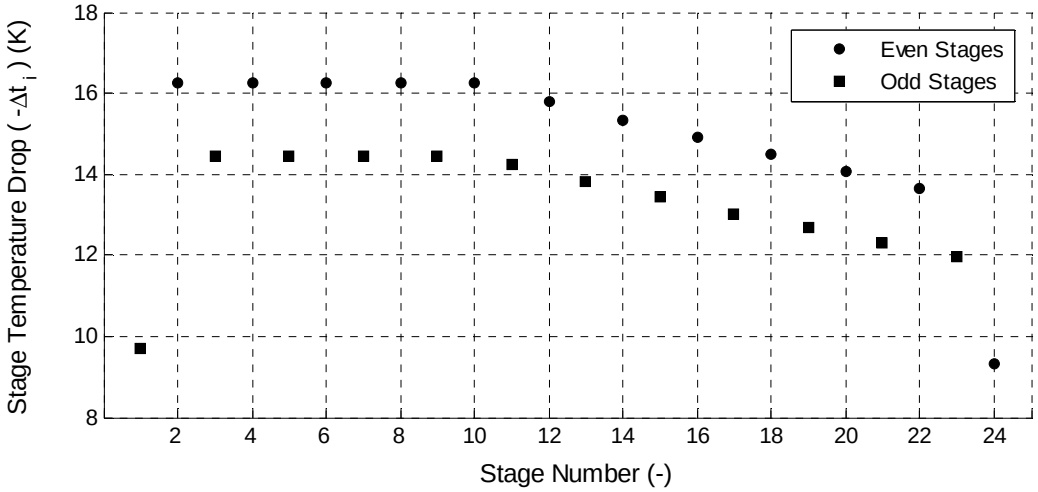

Figure 65: Power distribution for CRT ($n_1 \neq n_2$)

It can be seen that the Pw_{CRT}, TR_{CRT} and preliminary design criteria are satisfied. The velocity triangles can not be drawn before solving completely the CRT.

Step 3: guess the stage $r_{mean\ out}$ and calculate $r_{h\ out}$ following the gas path design criteria

The gas path design criteria detailed in pages 108 – 110 are used to determine $t_{tip\ out}$ for every stage. $r_{mean\ out}$ is guessed, and $r_{h\ out}$ is calculated as

$$r_{h\ out\ i} = r_{mean\ out\ i} - (r_{tip\ out\ i} - r_{mean\ out\ i}) \quad \text{[Eq. 121]}$$

This allows the calculation of $A_{disk\ out}$, and subsequently all the required input to Stage-DP calculation brick are known.

$$A_{disk\ out\ i} = \pi\left(r_{tip\ in\ i}^{\ 2} - r_{h\ in\ i}^{\ 2}\right) \quad \text{[Eq. 122]}$$

Step 5: repeat steps 3 and 4 until getting a target $Mrel_{out}$

$Mrel_{out}$ = 0.4 was selected as design criteria for all the stages (except for the last one for which the $Mrel_{out}$ is calculated from the input outlet geometry). The value of $r_{mean\ out}$ which results in $Mrel_{out}$ = 0.4 is obtained with a Newton-Raphson solver (not with a direct iteration as in the calculation bricks). The feasible range of $r_{mean\ out}$ was constrained to [0, r_{tip} - 0.05]. The maximum limit was set to r_{tip} - 0.05 to avoid small areas which result in M > 1 (the 1-D mean line model was developed for subsonic speeds).

2.2.3.3.2.8 Baseline CRT evaluation

CRT-DPe and CRT-OD were used to predict the DP and OD operation of the CRT of the baseline DDOR engine design used for the assessment studies. The following DP requirements for the CRT were obtained from the engine requirements (described in section 3.1.2), the baseline design choices (detailed in section 3.3.1) and preliminary performance calculations at DP:

- Inlet flow: $\dot{m}$=13.7 kg/s, $Pt_{in\ 1}$ = 226.5 kPa and $Tt_{in\ 1}$ = 1068 K
- IGV angle: $\alpha_{in\ 1}$ = 35º
- required power extraction: Pw_{CRT} = -5.8 MW
- TR_{CRT} = 1
- rotational speeds: $N_1 = -N_2$ = 860 rpm
- number of stages: NbStages = 20
- gas properties: γ = 1.338 and R = 287 J/(kg K) based on the mean CRT temperature

Figure 66 shows the obtained power distribution across the 20 stages. Unlike the example of Figure 65, ΔTt for stages 2 - 10 is equal because PwR_{CRT} = 1.

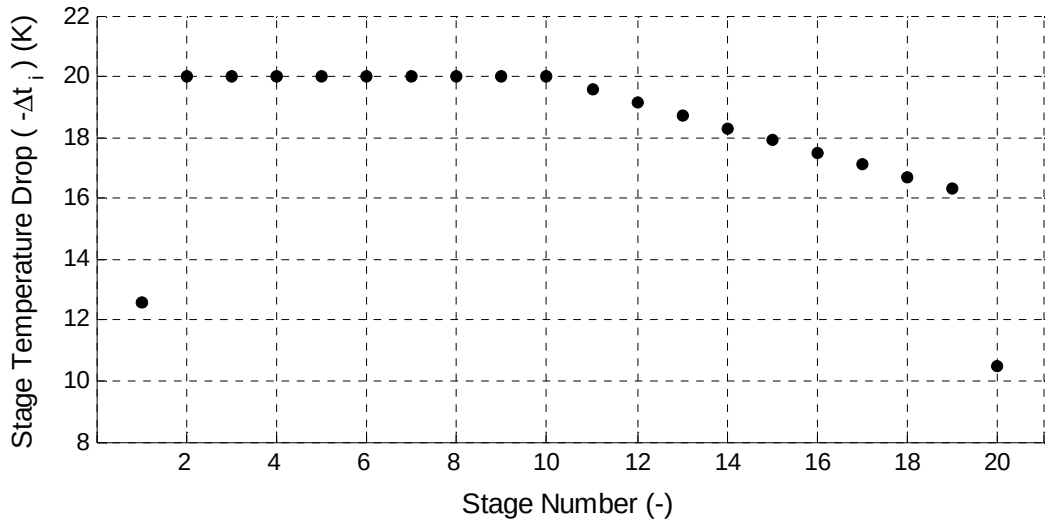

Figure 66: DP power distribution with stages (baseline CRT)

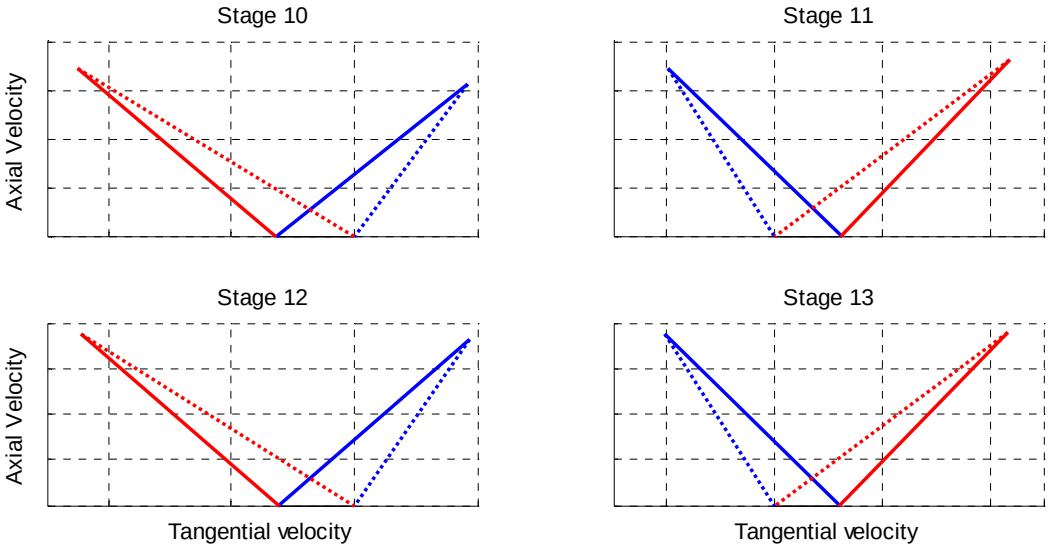

Figure 67: DP velocity triangles of stages 10-13 (baseline CRT)

Figure 67 shows the velocity triangles of stages 10 – 13. It can be seen that although the axial velocity increases and tangential velocity decreases from stage to stage, the C point is approximately centred with respect to A and B for all the velocity triangles.

The calculated DP $\eta_{is\ CRT}$ was 0.881. This value was judged to be representative of a year 2020 CRT design[42].

[42] Although the loss correlations correspond to year 1990 technology levels, the obtained $\eta_{is\ CRT}$ was judged to be representative of a year 2020 CRT design. It is important to note that the loss model used does not consider mechanical and windage losses (no correlations to estimate these two types of losses for CRTs were found in the public domain). This may be the reason

Figure 68 - Figure 70 present the OD performance of the baseline CRT at speed ratios 1, 0.8 and 1.2 respectively. The speed ratio (nR_{CRT}) is defined as

$$nR_{CRT} = \frac{-n_1}{n_2} = \frac{-N_1}{N_2} \quad \text{[Eq. 123]}$$

The corrected rotational speed relative to the design corrected rotational speed is defined as

$$n_{i\ COR\,Rdes} = \frac{n_{i\ COR}}{n_{i\ COR\,Des}} = \frac{N_{i\ COR}}{N_{i\ COR\,Des}} \quad \text{[Eq. 124]}$$

where $n_{i\ COR}$ is calculated using Eq. 7. The corrected mass flow rate is obtained using Eq. 6, and PR_{CRT} is obtained using Eq. E 35 (Appendix E). The selection of the variables presented in the performance maps of a CRT is provided in 2.2.3.3.3.2.

The dotted rectangle in the efficiency chart of Figure 68 highlights the approximate region for which the correlation of secondary losses is used outside the limits for which it was validated. This region corresponds to very low idle settings which are only used during some segments of the descent. The incidence angles are within the limits of the correlations for the rest of the map.

why the overall turbine efficiency is over predicted with respect to the level of technology of 1990.

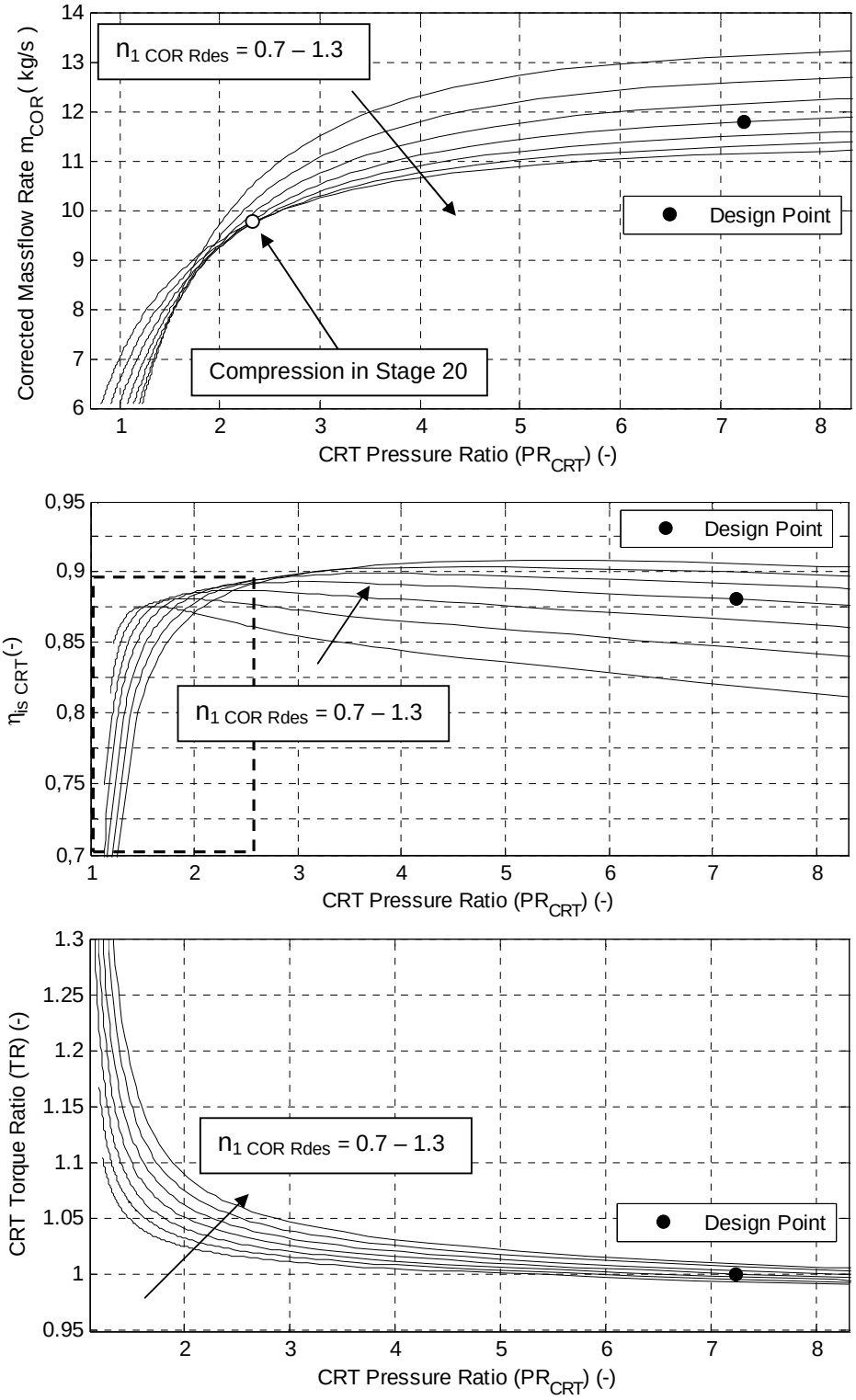

Figure 68: Baseline CRT performance maps at nR_{CRT} = 1

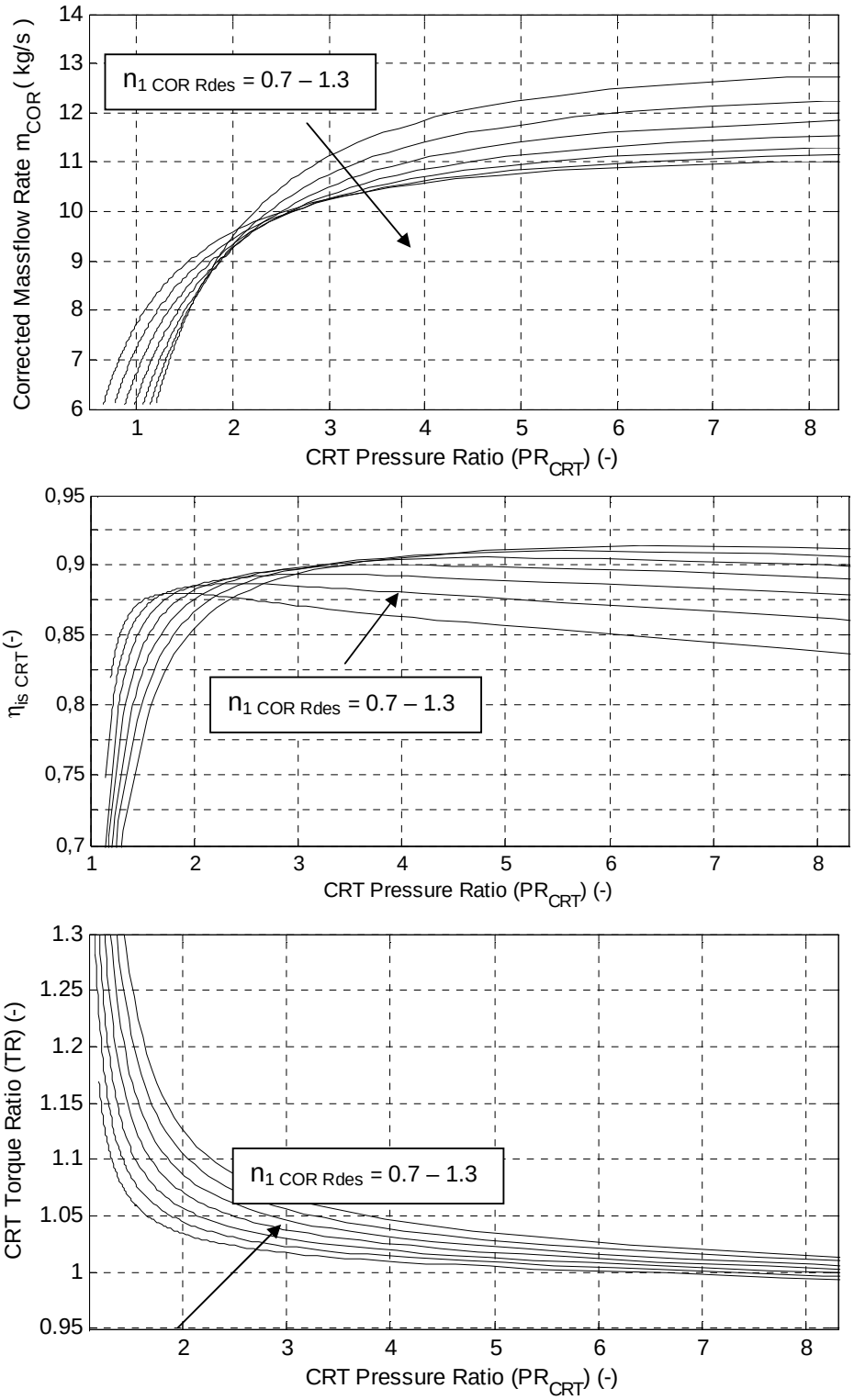

Figure 69: Baseline CRT performance maps at nR_{CRT} = 0.8

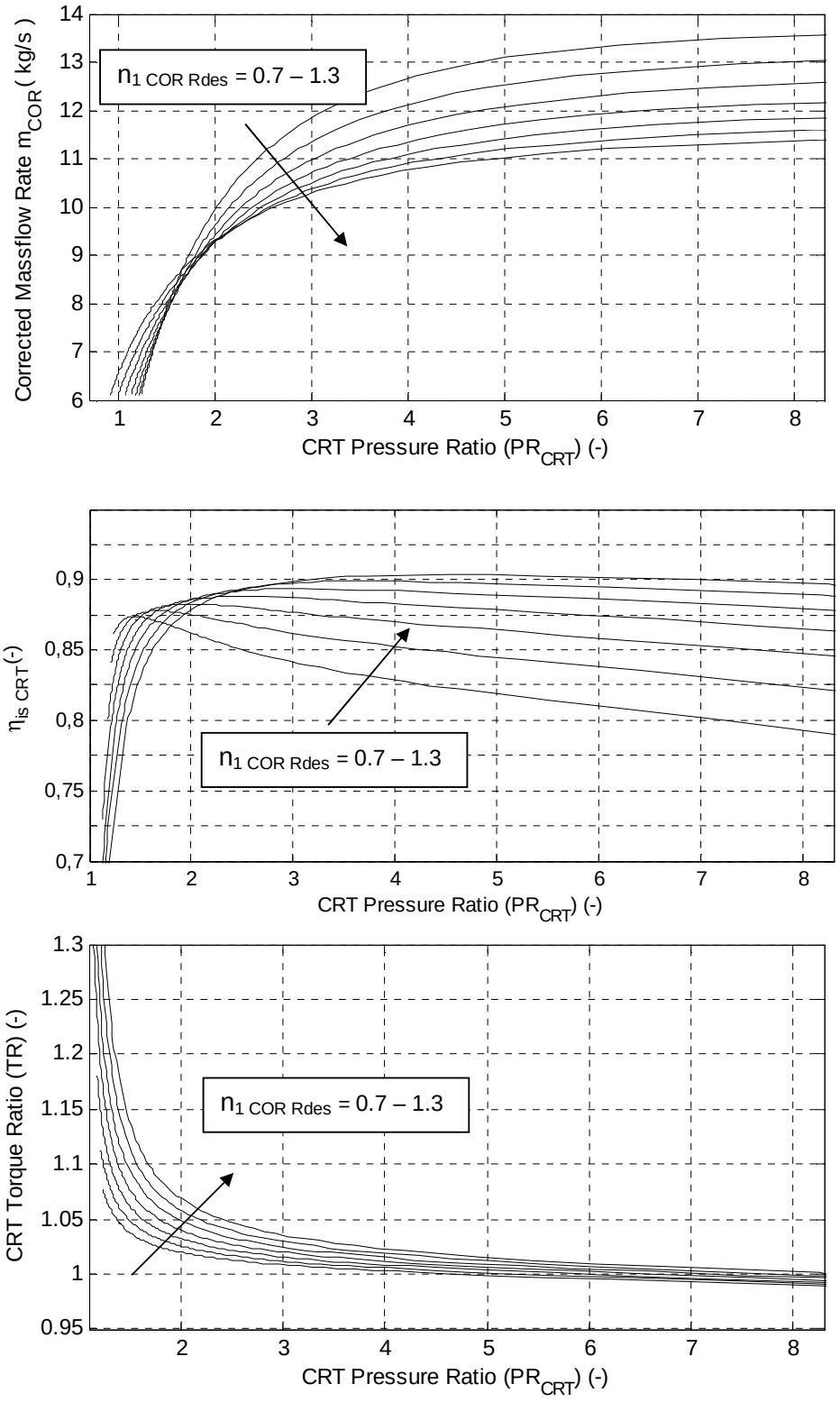

Figure 70: Baseline CRT performance maps at nR_{CRT} = 1.2

It can be seen that $\dot{m}_{COR}$ at the DP PR_{CRT} varies by approximately 20% for $n_{1COR\ Rdes}$ between 0.7 and 1.3. Such large variations in $\dot{m}_{COR}$ are characteristic of turbines with unchoked nozzle guide vanes (the only guide vane in a CRT is the IGV which is unchoked). Even when the turbine is choked, $\dot{m}_{COR}$ varies with n_1 and n_2 because choke occurs in a rotating stage and this phenomenon is largely affected by n_1 and n_2. It is interesting to note, that although at DP $Mrel_{out}$ = 0.4 for all the stages, an increase in $\dot{m}_{COR}$ of approximately 2% results in $Mrel_{out}$ = 1 (choke condition) in stage 19 and PR_{CRT} = 14.5. Figure 71 shows the total pressure loss coefficients (Yt) for every stage at the choke condition for $n_{1COR\ Rdes}$ = 1. It can be seen that the losses increase exponentially across the turbine and this is due to the increase in incidence angle from stage to stage. The exponential increase of Yt across the turbine and the relationship between $Mrel_{out}$ and $Prel_{out}$ (Eq. 95) explain that a only a 2% increase in $\dot{m}_{COR}$ results in $Mrel_{out}$ = 1 at the back of the CRT.

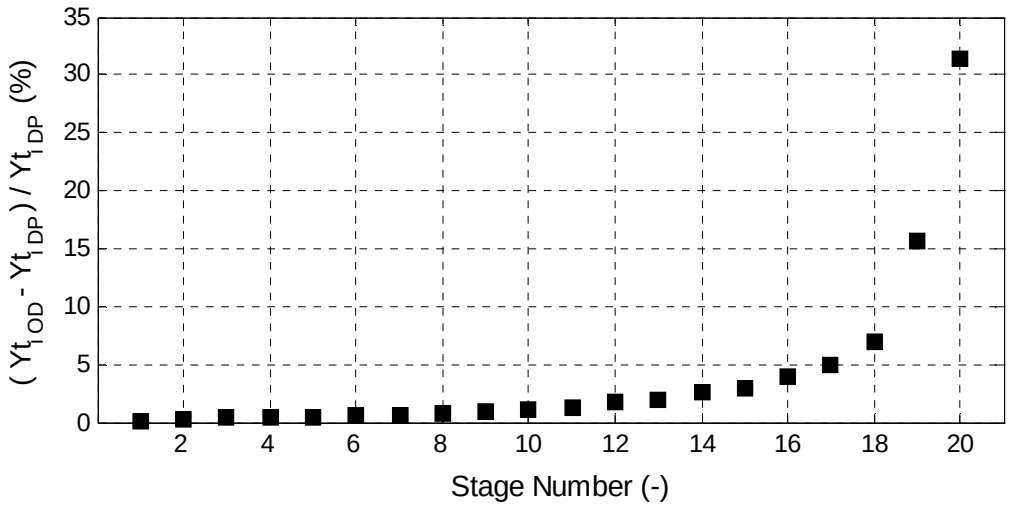

Figure 71: Stage Yt at choke condition as % of DP Yt

Figure 68 - Figure 70 show that some operating points have PR_{CRT} < 1. At these operating conditions, the CRT behaves as a compressor rather than as a turbine. In fact, for severe OD conditions, the last stages of the CRT may act as compressing stages. The white dot in the mass flow chart of Figure 68 indicates the first point of the $n_{1COR\ Rdes}$ = 1 line for which Stage 20 acts as a compressor stage. Figure 72 shows the velocity triangle at this operating point (values of velocities omitted). It can be seen that $Vabs_{out\ T}$ is larger than $Vabs_{in\ T}$ and therefore the flow absorbs energy and is compressed. All the operating points of the $n_{1COR\ Rdes}$ = 1 line which have lower PR_{CRT} than the white dot, represent OD conditions for which at least one stage acts a compressor.

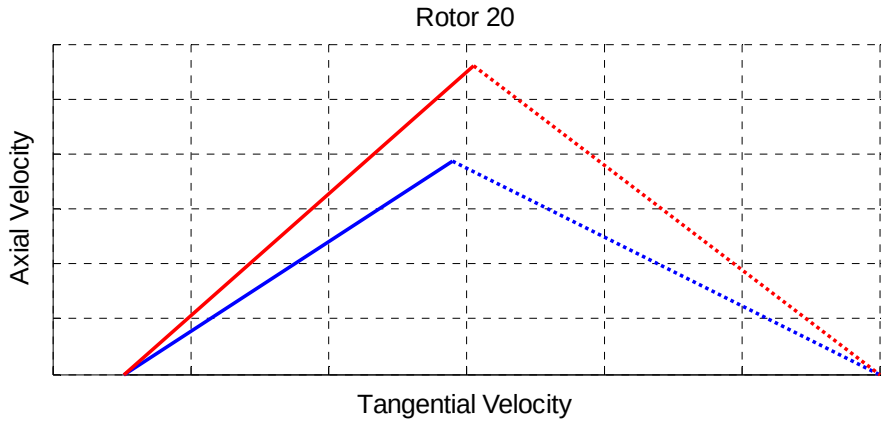

Figure 72: Velocity triangles of Stage 20 operating as a compressor stage

It can be seen from the maps, that variations in TR_{CRT} are smaller than 5% for $PR_{CRT} > 3$. For $PR_{CRT} < 2.5$ the variations in TR_{CRT} increase and this is due to the propagation of losses across the turbine and the torque unbalance produced by the compressing stages.

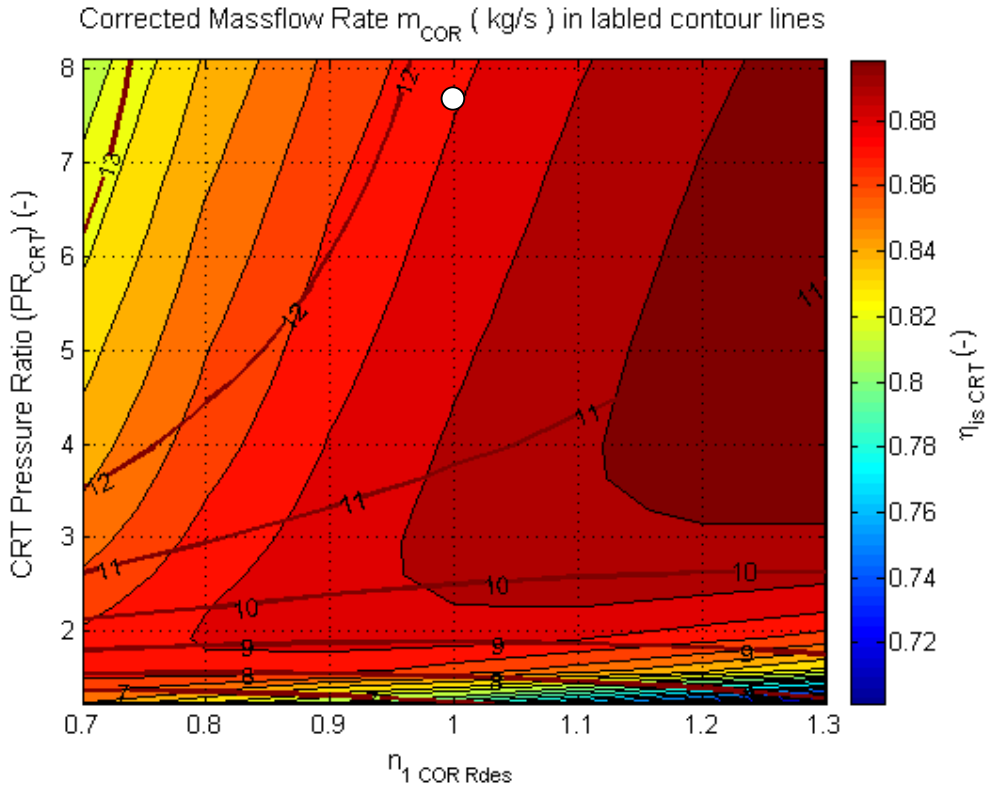

Figure 73: Baseline CRT performance map (in format of UDF CRT map, $nR_{CRT} = 1$)

Figure 73 shows a performance map of the baseline CRT (TR_{CRT} not included) in the format of the available CRT map from the UDF (Figure 53)[43]. It can be seen that the efficiency contours of both figures have similar shapes.

2.2.3.3.3 0-D model

Different CRT designs can be studied with CRT-DPe and CRT-OD. The variation of the performance with respect to the number of stages, rotational speeds, required power and inlet conditions can be quantified both at DP and OD conditions. The impact of the main preliminary design criteria on the overall performance of the CRT could also be assessed by including minor modifications to CRE-DPe. For example, the power distribution and velocity criteria could be modified so that the relative exit speed of the last stage of the CRT is axial. The resultant CRT would have lower efficiency, but the exit flow would rotate at the same speed as the exit nozzle and afterbody, and therefore reduce the losses of these components. Trade-off studies of the impact of CRT design choices at engine and mission levels are possible if the 1-D codes are integrated within the engine performance code. This integration was performed, but the calculations proved to be numerically unstable and approximately 3 hours were required for an engine DP calculation[44].

In order to comply with the time requirements of the simulation platform, a 0-D methodology to calculate DP and OD performance of CRTs was derived from the 1-D analysis. The 0-D methodology does not have the same level of fidelity as the 1-D methodology. This limitation is acknowledged and it is recommended that further work is performed to integrate the 1-D codes within the engine performance code and use them for the DDOR assessments[45]. The following paragraphs describe the developed 0-D methodology for both DP and OD performance calculations.

2.2.3.3.3.1 0-D DP performance modelling methodology

A 0-D methodology to estimate the DP $\eta_{is\ CRT}$ of a given CRT design was developed. It requires the following input:

- gas properties: γ and R

---

[43] $n_{1\ COR\ Rdes}$ is used instead of $n/\sqrt{Tt_{in}}$. The difference between these two magnitudes is a multiplication by a constant. Analogously, PR_{CRT} is used instead of $\Delta h/T_{in}$.

[44] 3 hours were required for a DP calculation because all the engine design parameters are solved simultaneously, and approximately 130 CRT designs were performed. A parametric study where two parameters are varied in 10 steps would require 2 weeks of calculations.

[45] Extensive work on numerical methods is required in order to achieve a stable engine calculation including the 1-D codes.

- flow conditions at the inlet of the turbine: $\dot{m}$, $Pt_{in\,1}$, $Tt_{in\,1}$
- rotational speeds of both drums: n_1 and n_2
- number of stages: NbStages
- required overall CRT power extraction: Pw_{CRT}

Outline of the calculation:

Step 1 - define two *representative* stages. One, representative of drum 1 and the other one representative of drum 2.

Step 2 - obtain the η_{is} for the two representative stages

Step 3 - calculate η_{is} of a turbine comprising NbStages/2 repetitions of the two representative stages.

The following paragraphs describe steps 1 to 3.

Step - 1: **define two representative stages.**

Two representative stages (rd1 and rd2) of each drum are defined. Δht_{dr1} and Δht_{dr1} are calculated as

$$\Delta ht_{rd1} = \frac{\Delta ht_{CRT}}{(1+PwR)NbStages/2} \qquad \text{[Eq. 125]}$$

$$\Delta ht_{rd2} = \Delta ht_{CRT} - \Delta ht_{rd1} \qquad \text{[Eq. 126]}$$

where

$$\Delta ht_{CRT} = \frac{Pw_{CRT}}{\dot{m}} \qquad \text{[Eq. 127]}$$

$$PwR = \frac{Pw_{drum\,1}}{Pw_{drum\,2}} = \frac{-n_1}{n_2} \qquad \text{[Eq. 128]}$$

Note that only designs with $TR_{CRT} = 1$ are considered.

The velocity triangles of a representative stage are defined as follows

- the point C is centred with respect to A and B
- $V_{in\,rd1\,A} = V_{out\,rd1\,A} = V_{in\,rd2\,A} = V_{out\,rd2\,A} = V_A$
- $r_{mean\ in\ rd1} = r_{mean\ out\ rd1} = r_{mean\ in\ rd2} = r_{mean\ out\ rd2} = r_{mean\ rd}$ and consequently $U_{rd1} = r_{mean\ rd}\ 2\pi n_1$ and $U_{rd2} = r_{mean\ rd}\ 2\pi n_2$ [Eq. 129]

Figure 74 shows the velocity triangles of two representative stages (with $n_1 \neq n_2$) according to the previous definition. The red and blue triangles correspond to rd1 and the dotted grey triangles to rd2.

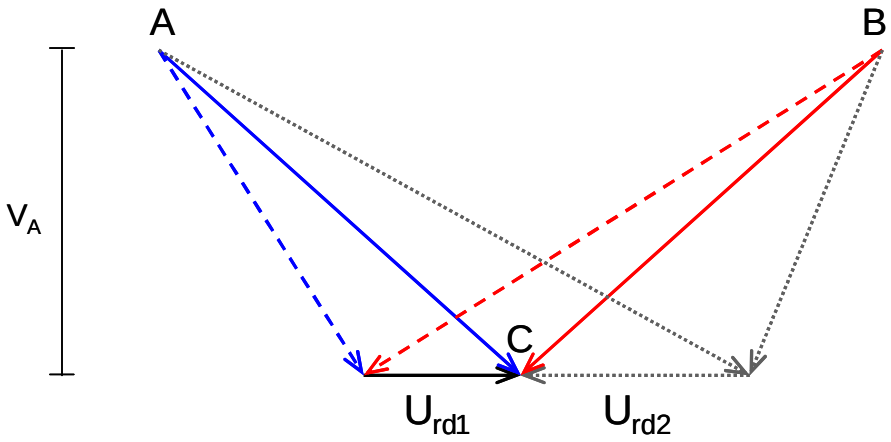

Figure 74: Velocity triangles for a CRT representative stage

The used values of V_A and $r_{mean\ rd}$ are the average of axial velocities and mean radii of all the stages of the baseline CRT.

The stage loading coefficient ($\psi = \Delta h / U^2$) and flow coefficient ($\Phi = v_A / U$) can be calculated for the two representative stages as

$$\psi_{rd1} = \frac{-\Delta h_{rd1}}{U_{rd1}^{\ 2}} \quad \text{and} \quad \psi_{rd2} = \frac{-\Delta h_{rd2}}{U_{rd2}^{\ 2}} \qquad \text{[Eq. 130]}^{46}$$

$$\Phi_{rd1} = \frac{V_A}{U_{rd1}} \quad \text{and} \quad \Phi_{rd2} = \frac{V_A}{U_{rd2}} \qquad \text{[Eq. 131]}$$

Step – 2: **obtain the η_{is} for each the two representative stages**

Ref. 171 proposes a methodology to calculate the $\eta_{is\ stage}$ of a CRT stage from its stage loading and flow coefficient. Figure 75 shows the results of these calculations in the form of a Smith chart. The majority of the stages of the baseline CRT are located inside the dotted rectangle in Figure 75. It can be seen that in this region a reduction in ψ would result in an increase in stage efficiency. The maximum increase in stage efficiency for any of the stages of the baseline CRT is of the order of 1%, even if the loading is halved. Larger variations in efficiency are expected knowing that the baseline CRT is a highly loaded design. Moreover, this result is not in agreement with the 1-D simulations which suggest larger changes in efficiency. As a consequence, the methodology proposed in Ref. 171 was judged not adequate and a novel method was required.

[46] Note that $\Delta ht = \Delta h$ since $Vabs_{in} = Vabs_{out}$

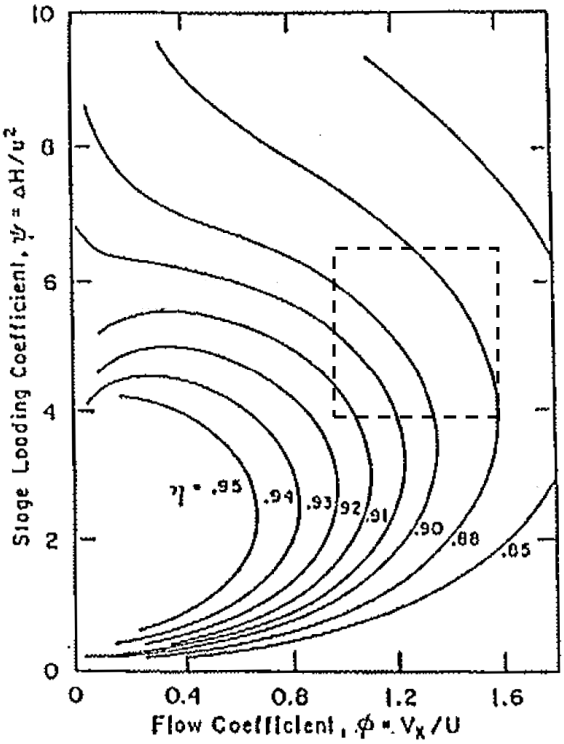

Figure 75: CRT stage Smith chart from Ref. 171

The following paragraphs describe a methodology to calculate $\eta_{is\ stage}$ from ψ and Φ, for a CRT stage with the velocity triangles defined in Step 1.

The isentropic efficiency of a rotating turbine stage can be defined as[47]

$$\eta_{is\,stage} = \frac{h_{in} - h_{out}}{h_{in} - h_{out\ is}} = \frac{h_{in} - h_{out}}{(h_{in} - h_{out}) + (h_{out} - h_{out\ is})} \qquad \text{[Eq. 132]}$$

The enthalpy loss coefficient is defined as [Ref. 176]

$$\zeta = \frac{h_{out} - h_{out\ is}}{ht\,rel_{out} - h_{out}} \qquad \text{[Eq. 133]}$$

Using the definition of total enthalpy, ζ can be expressed as

$$\zeta = \frac{h_{out} - h_{out\ is}}{ht\,rel_{out} - h_{out}} = \frac{h_{out} - h_{out\ is}}{\left(h_{out} + \frac{1}{2}Vrel_{out}^{\ 2}\right) - h_{out}} = \frac{h_{out} - h_{out\ is}}{\frac{1}{2}Vrel_{out}^{\ 2}} \qquad \text{[Eq. 134]}$$

[47] Total-to-total efficiency is equal to static-to-static efficiency since Vabsin = Vabsout.

and therefore

$$h_{out} - h_{out\ is} = \frac{1}{2} Vrel_{out}{}^2 \zeta \qquad \text{[Eq. 135]}$$

Combining Eq. 132 and Eq. 135 the stage efficiency can be written in terms of enthalpy change, enthalpy loss coefficient and relative outlet velocity

$$\eta_{is\ stage} = \frac{-\Delta h}{-\Delta h + \frac{1}{2} Vrel_{out}{}^2 \zeta} = \frac{1}{1 + \frac{Vrel_{out}{}^2 \zeta}{-2\Delta h}} \qquad \text{[Eq. 136]}$$

$Vrel_{out}$ and Δh can be written in terms of the stage loading and flow coefficients.

$$Vrel_{out}{}^2 = \left(\frac{v_A}{cos(\beta_{out})} \right)^2 = v_A{}^2 \frac{1}{cos^2(\beta_{out})} = v_A{}^2 \left(1 + tan^2(\beta_{out})\right) \qquad \text{[Eq. 137]}$$

The stage loading coefficient (Ψ) and flow coefficient (Φ) are defined as

$$\psi = \frac{-\Delta h}{U^2} \qquad \text{[Eq. 138]}[48]$$

$$\Phi = \frac{v_A}{U} \qquad \text{[Eq. 139]}$$

and a relationship between Δh and V_A can be obtained using the previously defined coefficients.

$$\frac{\Phi^2}{\psi} = \frac{v_A{}^2}{-\Delta h} \qquad \text{[Eq. 140]}$$

Combining Eq. 136, Eq. 137 and Eq. 140, η_{is} can be written as a function of Ψ, Φ and β_{out}.

$$\eta_{is\ stage} = \left[1 + \frac{Vrel_{out}{}^2 \zeta}{-2\Delta h} \right]^{-1} = \left[1 + \frac{v_A{}^2 \left(1 + tan^2(\beta_{out})\right)\zeta}{-2\Delta h} \right]^{-1} = \left[1 + \frac{\Phi^2 \left(1 + tan^2(\beta_{out})\right)\zeta}{2\psi} \right]^{-1}$$

[Eq. 141]

Finally a simple correlation to obtain ζ from the flow parameters is required. Ref. 200 proposes the following correlation to predict both profile and secondary losses from the blade turning angle and blade chord to height ratio:

---

[48] Note that $\Delta ht = \Delta h$ since $Vabs_{in} = Vabs_{out}$

$$\zeta = 0.025\left(1+\left(\frac{\beta_{in}+\beta_{out}}{90}\right)^2\right)\left(1+3.2\frac{\text{AxialChord}}{\text{blade}_h}\right) \quad \text{[Eq. 142]}$$

The baseline CRT has an average chord to height ratio of 0.3. The constant (0.025) of the correlation was adjusted in order to obtain the levels of efficiency predicted by the 1-D code. The used loss correlation is

$$\zeta = 0.018\left(1+\left(\frac{\beta_{in}+\beta_{out}}{90}\right)^2\right)(1+3.2(0.3)). \quad \text{[Eq. 143]}$$

Finally, β_{in} and β_{out} are obtained from ψ and Φ (the deduction of Eq. 144 and Eq. 145 is presented in Appendix G).

$$\beta_{in} = \frac{180}{\pi} arctan\left(\frac{\frac{\psi}{2}-1}{\Phi}\right) \quad \text{[Eq. 144]}$$

$$\beta_{out} = \frac{180}{\pi} arctan\left(\frac{\frac{\psi}{2}+1}{\Phi}\right) \quad \text{[Eq. 145]}^{49}$$

$\eta_{is\ rd1}$ and $\eta_{is\ rd2}$ are calculated using Eq. 141 , Eq. 143 - 145 and Eq. 130 -131.

Figure 76 shows $\eta_{is\ stage}$ as a function of ψ and Φ according to the previously described calculation method. The dotted rectangle highlights the region where the stages of the baseline CRT are located. It can be seen that a reduction in Pw_{CRT} or in rotational speeds would result in an increase in $\eta_{is\ stage}$.

[49] β_{in} and β_{out} obtained from Eq. 144 and 145 are both positive for the studied CRTs. This does not respect the sign convention defined for 1-D calculations, but it is not required for 0-D calculations.

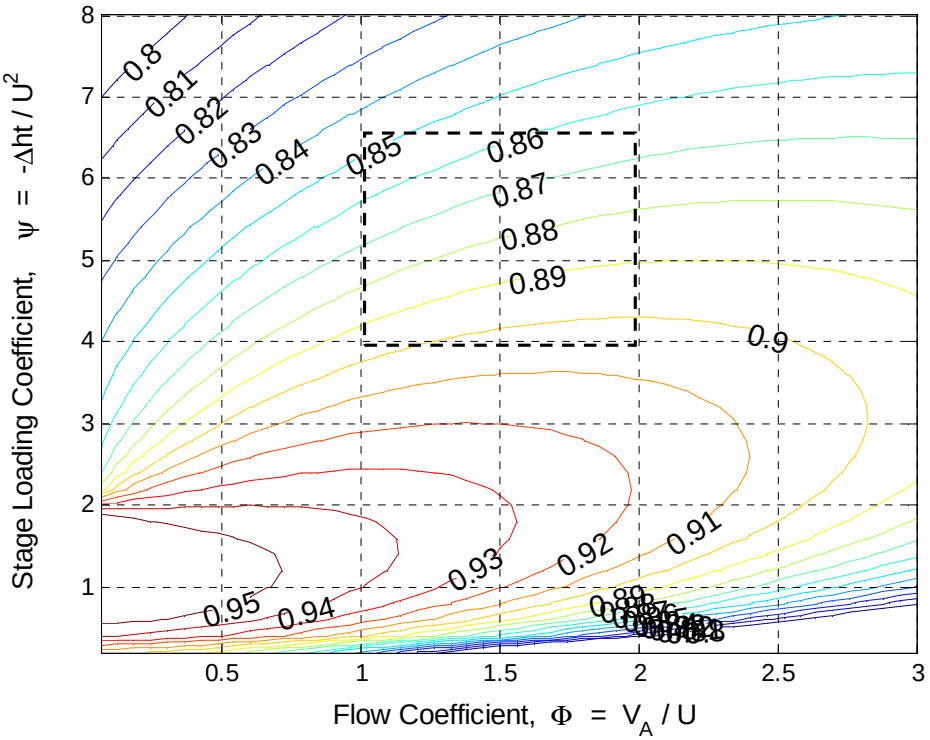

Figure 76: Smith chart for CRT stage

Step – 3: **calculate η_{is} of a turbine formed by NbStages/2 repetitions of the two representative stages.**

The temperature drop in the two representative stages is calculated as

$$\Delta Tt_{rd1} = \frac{\Delta ht_{rd1}}{Cp} \quad \text{and} \quad \Delta Tt_{rd2} = \frac{\Delta ht_{rd2}}{Cp} \qquad \text{[Eq. 146]}^{50}$$

The CRT is assumed to be formed by NbStages/2 repetitions of the two representative stages. The outlet conditions of each stage are calculated from $Tt_{in\,i}$, $\Delta Tt_{rd\,i}$ and $\eta_{is\,rd\,i}$ (rd i correspond to rd1 for odd and rd2 for even stages) using the following equations.

$$Tt_{out\,i} = Tt_{in\,i} + \Delta Tt_{rd\,i} \qquad \text{[Eq. 147]}$$

[50] Note that Δh and ΔT are negative since power is extracted from the flow.

$$Pt_{out_i} = Pt_{in_i}\left(1-\frac{\left(1-\frac{Tt_{out_i}}{Tt_{in_i}}\right)}{\eta_{is\,rd\,i}}\right)^{\frac{\gamma}{\gamma-1}} \quad \text{[Eq. 148]}$$

$$Tt_{in_{i+1}} = Tt_{out_i} \quad \text{[Eq. 149]}$$

$$Pt_{in_{i+1}} = Pt_{out_i} \quad \text{[Eq. 150]}$$

Finally, $\eta_{is\ CRT}$ is calculated as

$$\eta_{is\,CRT} = \frac{1-\frac{Tt_{out\ NbStages}}{Tt_{in\,1}}}{1-\left(\frac{Pt_{out\ NbStages}}{Pt_{in\,1}}\right)^{\frac{\gamma-1}{\gamma}}} \quad \text{[Eq. 151]}$$

Verification of the 0-D DP calculation against 1-D calculations

The 0-D DP $\eta_{is\ CRT}$ calculation methodology was extensively verified against the results of CRT-DPe. The change in $\eta_{is\ CRT}$ with respect to the changes in design parameters of the baseline CRT design (defined in section 2.2.3.3.2.8) were studied with the 0-D and 1-D methods. Two examples are presented below.

Figure 77 shows the variation of $\eta_{is\ CRT}$ with respect to the rotational speed (keeping $n_1 = -n_2$) predicted with both methods. Figure 78 shows the variation of $\eta_{is\ CRT}$ with respect to the number of stages.

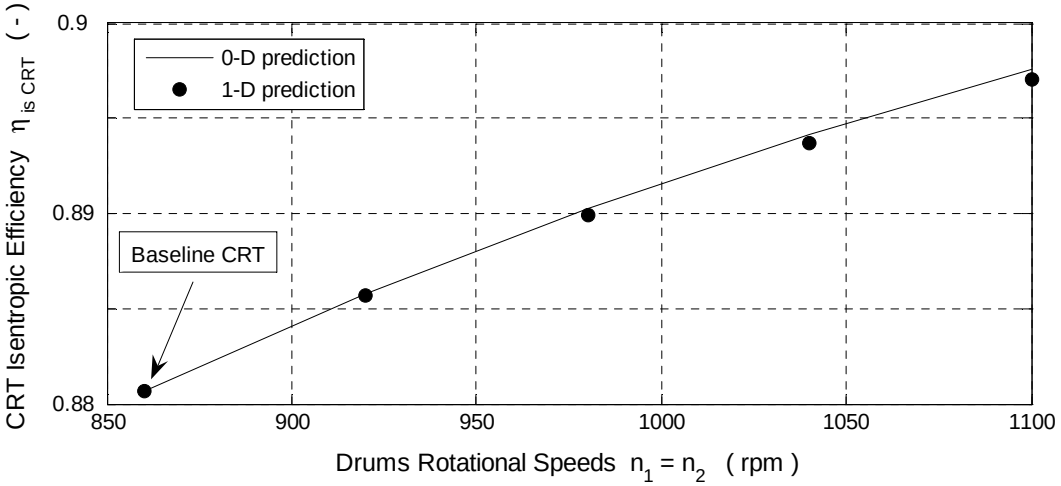

Figure 77: Impact of rotational speed on DP $\eta_{is\ CRT}$ (1-D and 0-D predictions)

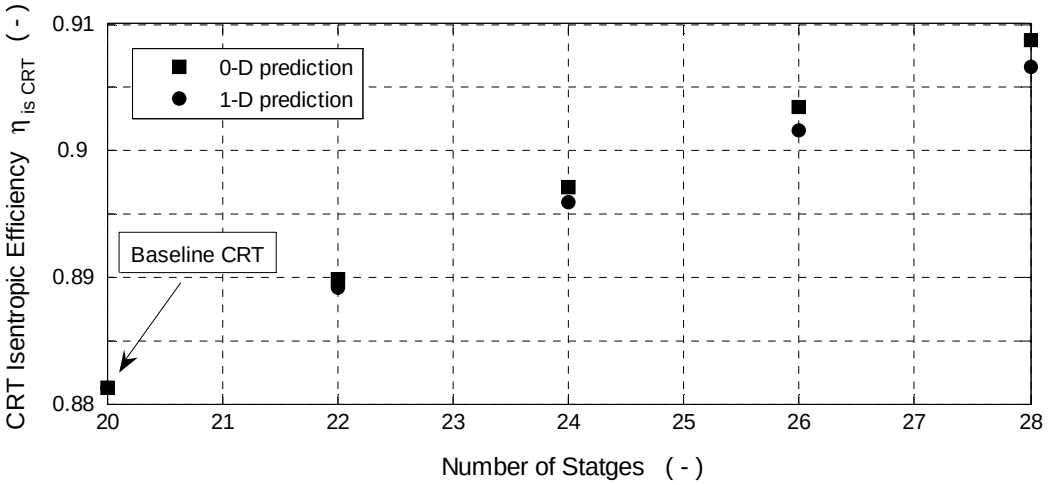

Figure 78: Impact of NbStages on DP $\eta_{is\ CRT}$ (1-D and 0-D predictions)

It can be seen that for these two examples, the 0-D method produces the same trends as the 1-D method, and that absolute errors are smaller than 0.2%. In both cases the 0-D model over predicted $\eta_{is\ CRT}$. This is due to the simplified loss estimations and gas path assumptions. In the case of the change in the number of stages, the average r_{mean} predicted by the 1-D code was smaller than the r_{mean} assumed for the 0-D calculations.

The same level of agreement between the 1-D and 0-D DP predictions were obtained for changes in Pw_{CRT}, $Tt_{in\ 1}$ and $\dot{m}$.

Feasibility criteria

The CRT design is judged feasible if both representative stages have turning angles < 120º (turning angle = $\beta_{in} + \beta_{out}$ calculated using Eq. 144 and Eq. 145). This is due to geometric limitations in the design of the turbine channels with turnings above 120º [Ref. 168].

2.2.3.3.3.2 0-D OD performance modelling methodology

Considering constant gas properties (γ and R), and ignoring Reynolds effects, the OD performance of a given CRT design (with no variable geometry and no cooling flows) which operates unchoked is defined by three parameters:

- $\dot{m}_{COR} = \dfrac{\dot{m}\sqrt{Tt_{in\ 1}}}{Pt_{in\ 1}}$
- $n_{1\ COR} = \dfrac{n_1}{\sqrt{Tt_{in\ 1}}}$
- $nR_{CRT} = \dfrac{-n_1}{n_2}$

This is because:

- at a given $\dot{m}_{COR}$, $Mabs_{in\ 1}$ is fixed because $Aeff_{in\ 1}$ is fixed (see Eq. E1 in Appendix E)
- at a given $n_{1\ COR}$, the Mach number of $U_{in\ 1}$ is fixed since $r_{mean\ in\ 1}$ is fixed, and $\sqrt{Tt_{in\ 1}}$ reflects the speed of sound at the inlet.
- with Mach numbers fixed for both the inlet air and mean blade speed, the incidence to the blades in stage 1 and $Mrel_{in\ 1}$ is fixed. Consequently, the total pressure loss coefficient (Yt) (not considering Reynolds effects) and the power output is fixed (by similar velocity triangles).
- with fixed power output, and fixed Mach number corresponding to $U_{out\ 1}$, $Mrel_{out\ 1}$ and $Mabs_{out\ 1}$ are fixed
- with fixed Yt and static to relative total inlet pressure (function of $Mrel_{in\ 1}$), pressure losses are a fixed fraction of $Pt\ rel_{\ in\ 1.}$ Consequently, given that the power extraction is fixed, PR across the stage is fixed.
- with fixed PR in stage 1 and $Pw_{stage\ 1}$, $Tt_{in\ 1}/Tt_{out\ 1}$ and $\eta_{is\ 1}$ are fixed.
- with fixed $Tt_{in\ 1}/Tt_{out\ 1}$ and considering $Tt_{out\ 1} = Tt_{in\ 2}$, $Tt_{in\ 2}$ can be written as K $Tt_{in\ 1}$ and $n_{2\ COR} = \frac{n_2}{\sqrt{Tt_{in\ 1} K}}$. Consequently a fixed nR_{CRT} and $n_{1\ COR}$ result in a fixed $n_{2\ COR}$.
- A fixed $n_{2\ COR}$ results in a fixed Mach number for $U_{in\ 2}$ as for $U_{in\ 1}$
- following the same argument as for stage 1, with fixed inlet flow and blade Mach numbers in stage 2, PR in stage 2, $Pw_{stage\ 2}$, $Tt_{in\ 2}/Tt_{out\ 2}$ and $\eta_{is\ 2}$ are fixed.
- this is repeated for all stages, and finally PR_{CRT}, $\eta_{is\ CRT}$ and TR are fixed.

Gamma and Reynolds corrections are required to account for changes in the fluid properties and viscous effects (which change with temperature and fuel to air ratio). The corrections defined in sections 5.2.3 and 5.2.4 of Ref. 109 were used. These corrections were already implemented in the conventional turbine component in PROOSIS.

For different CRT designs, the baseline CRT maps are scaled making the real cycle DP coincide with the DP of the CRT map. The use of a scaled map to represent the performance of an unknown turbine design for preliminary design calculations is discussed in Ref. 109 (section 5.10.9). The conventional turbine scaling factors (F5.10.4 in Ref. 109) were used and an additional one was defined for nR_{CRT} as

$$nR_{CRT} = nR_{CRT\ map} \cdot SF_{nR} \qquad \text{[Eq. 152]}$$

It was not necessary to define a scaling factor for TR_{CRT} because only designs with $TR_{CRT} = 1$ were considered.

2.2.3.3.4 Implementation

The CRT model described in section 2.2.3.3.3 was implemented in a single PROOSIS component as shown in Figure 79.

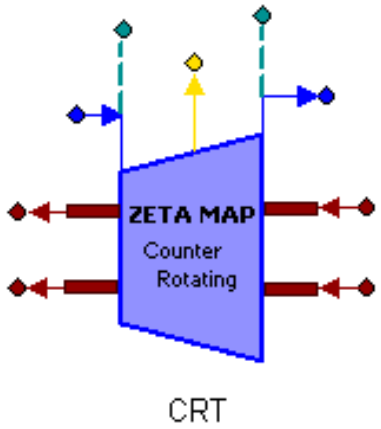

Figure 79: CRT component schematic view

The existing TurbineBasicMapZETA component of the TURBO V1.0 library was used as a basis for the implementation of the CRT (described in Ref. 130 and Ref. 131). This component models a conventional un-cooled turbine and uses a ZETA map[51]. Figure 80 shows the inheritance tree for the conventional un-cooled turbine component of the TURBO V1.0 library.

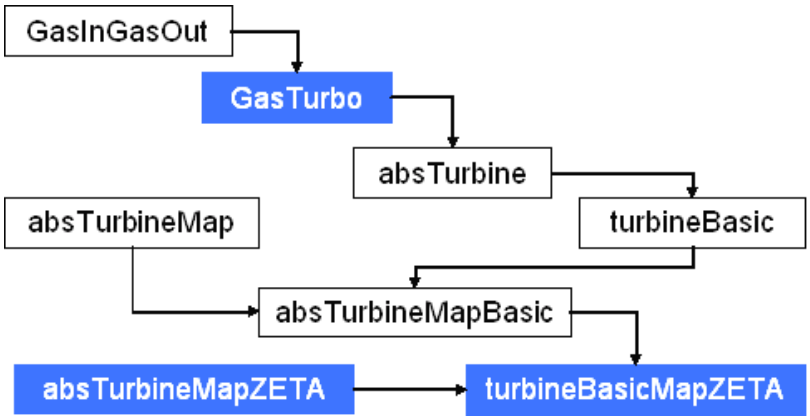

Figure 80: Conventional un-cooled turbine inheritance tree (TURBO V1.0 Library)

An analogous set of components with the same inheritance structure was created for the CRT. The required modifications were introduced in the components

[51] Ref. 130 and Ref. 131 describe the ZETA map format. ZETA is a parameter used to define the position of a point in a constant speed line of a turbine map

highlighted in blue in Figure 80. The second shaft was added in the GasTurbo component creating a GasTurbo2 component. The definition of TR_{CRT} (Eq. 120) and nR_{CRT} (Eq. 123) together with the torque balance, conservation of rotational speed and continuity of inertia of the second shaft were included in GasTurbo2. absTurbine2, turbineBasic2, absTurbineBasic2 and AbsturbineMap2 contain the same equations as the conventional turbine components. The additional scaling factor for nR_{CRT} (Eq. 152) was included in absTurbineMapZETA2 together with the variables defined in absTurbineMapZETA. TurbineBasicMapZETA2 has the equations of TurbineBasicMapZETA (nR_{CRT} added to the map reading functions) as well as an additional equation to obtain TR_{CRT} from the CRT maps.

The CRT maps shown in Figure 68 - Figure 70 were implemented in PROOSIS in the form of four tables:

- $\eta_{is\ CRT} = f\ (\ nR_{CRT\ map},\ n_{1\ COR\ Rdes},\ ZETA)$
- $\dot{m}_{COR} = f\ (\ nR_{CRT\ map},\ n_{1\ COR\ Rdes},\ ZETA)$
- $TR = f\ (\ nR_{CRT\ map},\ n_{1\ COR\ Rdes},\ ZETA)$
- $-\Delta ht_{CRT}/T_{in\ 1} = f\ (\ nR_{CRT\ map},\ n_{1\ COR\ Rdes},\ ZETA)$

$-\Delta ht_{CRT}/T_{in\ 1}$ is used instead of PR_{CRT} to maximise the similarities with the existing conventional turbine models in PROOSIS. These two parameters have the same physical meaning and a univocal relationship between them can be established [Ref. 109 section 5.10].

$n_{1\ COR\ Rdes}$ is used instead of $n_{1\ COR}$ for practical reasons

A non physical parameter, ZETA, was used to divide the corrected speed lines in equal intervals. This was done for numerical stability purposes.

The CRT maps are not displayed because PROOSIS does not allow the visualisation of a collection of maps for a single component. Even if this was possible, it would only have been possible to plot the operating points with nR_{CRT} values for which there is a map.

The DP efficiency calculation (technology curve) described in section 2.2.3.3.3.1 was implemented as a function which is used to scale the efficiency map during the engine DP calculation.

2.2.3.4 DPGB

The GOR uses a DPGB to transmit the power from the LPT to the CRP as described in section 1.1.2.2. This allows the use of a high speed (and consequently highly efficient) conventional LPT while keeping low rotational speeds on the propellers. However, there is a weight penalty and mechanical complexity associated with this system.

A complete description of the mechanical configuration of a DPGB is provided in Ref. 202. Figure 81 shows the general arrangement of a DPGB. It has the following three shafts:

- Sun shaft (connected to the Sun gear)
- Carrier shaft (connected to the centre of all the planet gears)
- Ring shaft (connected to the exterior ring)

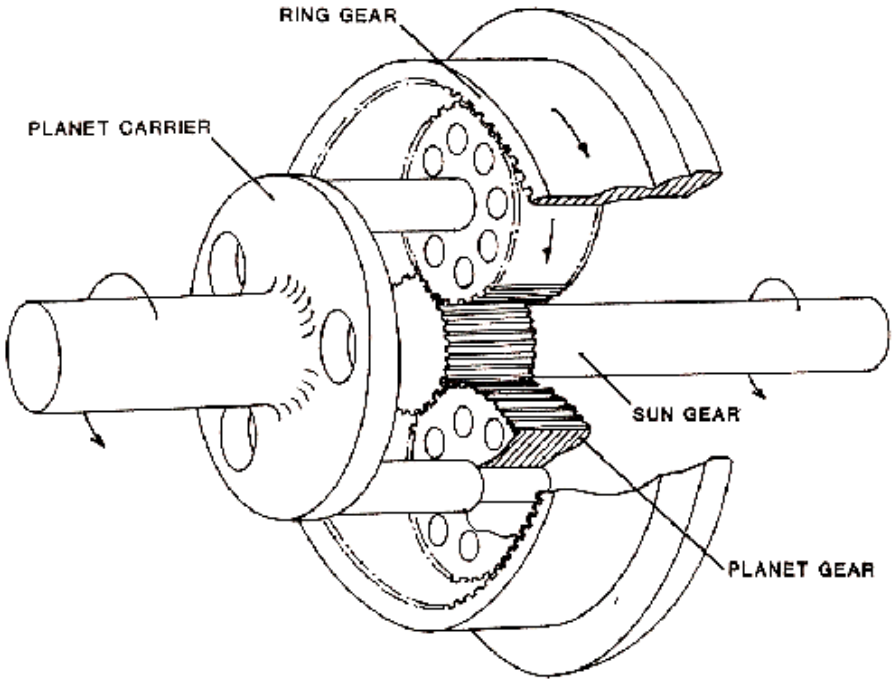

Figure 81: DPGB mechanical arrangement [Ref. 202]

A three free shaft DPGB differs from a conventional two shaft gearbox in the following ways:

- A conventional two shaft gearbox has one input shaft and one output shaft. A DPG however, may have one input shaft and two output shafts or two input shafts and one output shaft.
- A conventional two shaft gearbox has a fixed input/output shaft rotational speed ratio imposed by the relative diameters of the gears. Conversely, the three shafts of a DPG have fixed torque ratios imposed by the relative diameters of the gears. The rotational speeds of two of the shafts can be independently imposed and the rotational speed of the third shaft is an outcome of the energy balance of the DPGB.

As a consequence, the operation of a DPGB is defined by the rotational speeds of two of the shafts and the torque of one shaft[52]. In the case of the GOR engine, the sun shaft is used as input and the ring and carrier shafts are used to drive the CRP. The rotational speeds of the propellers (ring and carrier) are imposed by the control of the engine, and the torque of the sun is imposed by the operation of the LPT.

The DPGB requires a dedicated oil system since it operates at a much lower temperature than the oil of the gas turbine (~100ºC difference) [Ref. 201]. It also requires a dedicated oil-air cooling system, because the fuel (usually used to cool the engine oil) can not absorb the amount of heat generated by the gas turbine and the gearbox[53] [Ref. 203]. This air-oil cooling system is installed in the nacelle of the GOR. It requires an air intake (called scoop) and a blower (small compressor powered by the HP shaft) to ensure a minimum air flow at low flight speeds. The exit of the cooling air is radial (it can not reach the exhaust nozzle) and therefore does not generate useful thrust. This system generates ram drag at all flight speeds and consumes mechanical power at low flight speeds.

2.2.3.4.1 Model requirements

It was envisaged that the DPGB model would calculate

- the unknown rotational speed: either n_{Sun} or n_{Ring} or $n_{Carrier}$
- the two unknown torques: either Q_{Ring} $Q_{Carrier}$ or Q_{Ring} Q_{Sun} or $Q_{Carrier}$ Q_{Sun}

from:

- two rotational speeds: either n_{Ring} $n_{Carrier}$ or n_{Ring} n_{Sun} or $n_{Carrier}$ n_{Sun}
- one torque: either Q_{Sun} or Q_{Ring} or $Q_{Carrier}$
- the gearbox torque ratio: $TR_{DPGB} = \frac{Q_{Carrier}}{-Q_{Ring}}$
- the design rotational speed of the Sun shaft: $n_{Sun\ Des}$
- the design torque of the Sun shaft: $Q_{Sun\ Des}$

It was also envisaged that the model would include the air cooling system and calculate

- the ram drag produced by the cooling air flow: RAM_{Scoop}
- the kinetic energy of the air flow at the inlet and outlet of the cooling system: $KE_{Scoop\ in}$ $KE_{Scoop\ out}$

from:

- the flight conditions: Alt, M_0, deviation from ISA conditions (dISA)
- power consumed by the blower: Pw_{Blower}

---

[52] The rotational speed of any two shafts can be imposed and the torque of any of the three shafts can be imposed.

[53] Note that fuel efficient engines have a lower fuel flow requirement and therefore a lower fuel cooling capacity.

A technology curve and feasibility criteria were also required for the DPGB performance model.

2.2.3.4.2 DPGB performance model

Ref. 204 presents the force equilibrium equations of an ideal DPGB (equations 1.60 a-c in Ref. 204). Eq. 153 and Eq. 154 are derived from the force equilibrium equations. The mechanical efficiency is included to reflect the real operation of the DPGB.

$$Q_{Ring} = -Q_{Sun}(1+2rR)\eta_{mech\,DPGB} \quad \text{[Eq. 153]}$$

$$Q_{Carrier} = 2Q_{Sun}(1+rR)\eta_{mech\,DPGB} \quad \text{[Eq. 154]}$$

with

$$rR = \frac{r_{Planet}}{r_{Sun}} \quad \text{[Eq. 155]}$$

It can be seen that the relative size of the gears impose a torque ratio rather than a speed ratio as in conventional 2 shaft gearboxes. The torque ratio of the gearbox can be calculated as

$$TR_{DPGB} = \frac{Q_{Carrier}}{-Q_{Ring}} = \frac{2Q_{sun}(1+rR)\eta_{Mech\ DPGB}}{Q_{sun}(1+2rR)\eta_{Mech\ DPGB}} = \frac{2+2rR}{1+2rR} \quad \text{[Eq. 156]}$$

The power balance on the DPGB is

$$\eta_{mech\ DPGB}Pw_{Sun} + Pw_{Carrier} + Pw_{Ring} = 0 \quad \text{[Eq. 157]}$$

with

$$Pw_i = Q_i\, n_i 2\pi \quad \text{[Eq. 158]}$$

Equations 153, 154,156 and 157 enable the calculation of the output variables from the input. First rR is obtained from TR_{DPGB} using Eq. 156, then the unknown torques can be calculated from Eq. 153 and Eq. 154, and finally the unknown rotational speed is calculated from Eq. 157. Note that PROOSIS is capable of arranging the equations to suit any valid combinations of known and unknown variables.

The mechanical efficiency of a DPGB operating with the sun as input and the ring and carrier as output (as in the GOR engine), is a function of Q_{Sun} and n_{Sun} [Ref. 203]. Figure 82 presents the efficiency map for a 12000 HP (~9MW) DPGB as a function of the $Q_{Sun\ Rdes}$ and $n_{Sun\ Rdes}$ (digitised from Figure 12 Ref. 203).

$$Q_{Sun\ Rdes} = \frac{Q_{Sun}}{Q_{Sun\ des}} \quad \text{[Eq. 159]}$$

$$n_{Sun\ Rdes} = \frac{n_{Sun}}{n_{Sun\ des}} = \frac{N_{Sun}}{N_{Sun\ des}} \qquad \text{[Eq. 160]}$$

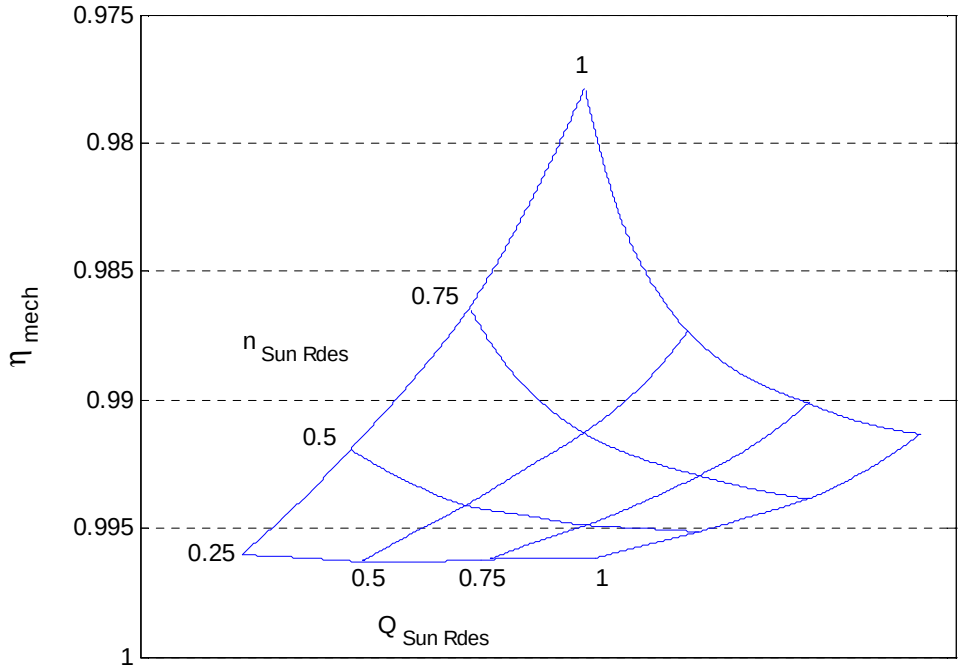

Figure 82: $\eta_{mech\ DPGB}$ as function of $Q_{Sun\ Rdes}$ and $n_{Sun\ Rdes}$ [Ref. 203]

This efficiency map was used for the assessment studies.

The heat rejected by the DPGB is calculated as

$$Heat_{DPGB} = Pw_{Sun}\left(1 - \eta_{mech\ DPGB}\right) \qquad \text{[Eq. 161]}$$

2.2.3.4.3 DPGB cooling system model

The cooling system was modelled using an intake, a compressor with no map (to simulate the blower), a duct (to simulate the heat exchanger) and a convergent nozzle. The existing components in the PROOSIS TURBO V1.0 library were used (described in Ref. 130 and Ref. 131). The efficiency of the compressor and the pressure loss in the duct were kept constant for all the operating conditions. The blower is activated below a specific flight speed and it consumes a constant fraction of the HP shaft power. RAM_{Scoop} and $KE_{Scoop\ in}$ are calculated by the inlet component, and $KE_{Scoop\ out}$ is calculated by the nozzle component. The mass flow rate through the system is a function of the flight conditions and the power consumed by the blower.

This simplified approach was judged acceptable because the ram drag of the cooling system was evaluated to be lower than 0.5% of the thrust of the engine at any condition. A rigorous modelling would require:

- simulating the blower as a compressor with an associated map, and its rotational speed linked to the rotational speed of the HP shaft.
- knowing the fraction of the total heat generated by the DPGB that is cooled by the air (the rest is cooled by the fuel).
- modelling the heat exchanger using a pressure loss correlations such as the ones described in Ref. 205.
- calculating the geometry of the heat exchanger for each evaluated engine design.

2.2.3.4.4 Technology curves

The mechanical efficiency of the DPGB at TOC was considered 0.99 for all the studied engine designs. According to Ref. 201 and Ref. 206, the efficiency of large high speed DPGBs for geared aero engines is governed by the lubrication system and meshing losses are negligible. Ref. 206 lists the key aspects of the design of the lubrication system that influence the efficiency of this type of gearboxes. Ref. 201 suggests that using modern lubrication techniques the mechanical efficiency of a DPGB is expected to be 0.99 at TOC. Note that the DPGB is designed at take-off, where the transmitted torque is approximately double than that at TOC (which is the DP for the aerodynamic design of turbomachinery components).

The following parameters of the cooling system of the DPGB were considered fixed for all studied designs:

- efficiency of the blower
- fraction of HP power consumed by the blower
- flight speed range for which the blower operates
- pressure drop in the heat exchanger
- the nozzle area

2.2.3.4.5 Feasibility criteria

A DPGB design is considered feasible if its external diameter is smaller than the hub diameter of the last stage of the LPT. This allows the installation of the DPGB inside the LPT exhaust duct (see Figure 11).

The dimensions of the DPGB are calculated by WeiCo using the rotational speeds and torques of each of the three shafts at take-off (see details in section 2.3). The gears are designed with standard modules and teeth. Mechanical failure criteria (pitting and tooth breakage) are used to ensure their integrity.

The mechanical design of the DPGB and its maximum diameter fixes both the maximum and minimum feasible values of TR_{DPBG}. This can be deduced from the relationship between rR and TR_{DPGB} (Eq. 156 plotted in Figure 83).

- *Minimum TR_{DPGB} limit:* For a given r_{Sun} (designed for a given Q_{Sun} and n_{Sun}), r_{Planet} increases (and consequently the diameter of the DPGB increases) as TR_{DPGB} decreases. The minimum TR_{DPGB} is determined by the maximum diameter set to the DPGB.
- *Maximum TR_{DPGB} limit:* For a minimum r_{Planet} (designed for a given $Q_{Carrier}$ and $n_{Carrier}$), r_{Sun} increases (and consequently the diameter of the DPGB increases) as TR_{DPGB} increases. The maximum TR_{DPGB} is determined by the maximum diameter set to the DPGB.

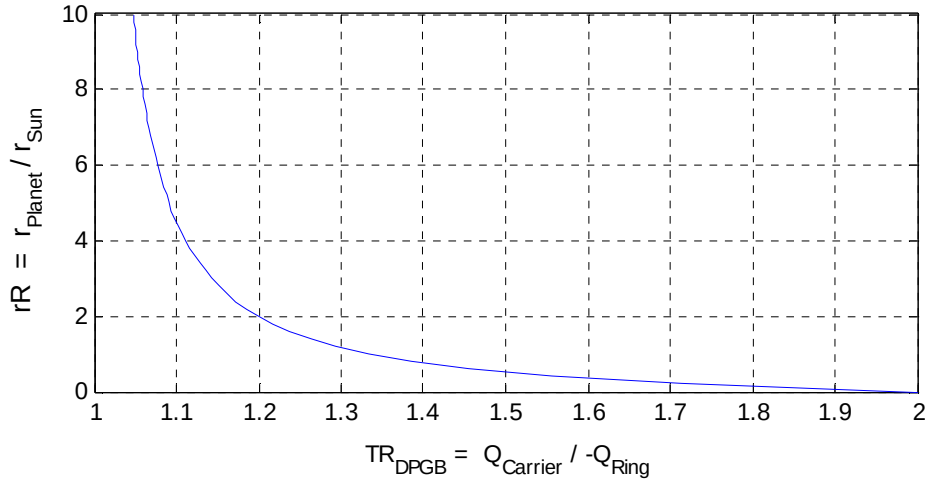

Figure 83: rR vs. TR_{DPGB} for a DPGB (Eq. 156)

The cooling system has a fixed design which is judged feasible. Its installation in the nacelle is also judged feasible for all the studied GOR engines. The intake is located next to the intake of the core flow (as on the P&W Allison 578-DX see Figure 22), and the heat exchanger is located between the IPC and the nacelle where there is enough space.

2.2.3.4.6 Implementation

DPGB

Figure 84 shows the schematic view of the DPGB component in PROOSIS. The component contains the equations presented in section 2.2.3.4.2. Eq. 157 was substituted by Eq. 162 (which is obtained from Eq. 157, Eq. 153, Eq. 154 and 158) in order to improve the numerical stability of the simulations.

$$n_{Sun} = n_{Ring}\left(1+2\frac{2-TR_{DPGB}}{-2+2TR_{DPGB}}\right) - n_{Carrier}\left(2+2\frac{2-TR_{DPGB}}{-2+2TR_{DPGB}}\right) \qquad \text{[Eq. 162]}$$

In addition to the aforementioned equations, the inertial equations required for transient calculations as well as an efficiency map reading function were included. The efficiency map is a table of the form $\eta_{mech} = f\ (Q_{Sun\ Rdes}, n_{Sun\ Rdes})$. The yellow dot in Figure 84 indicates the heat rejection port.

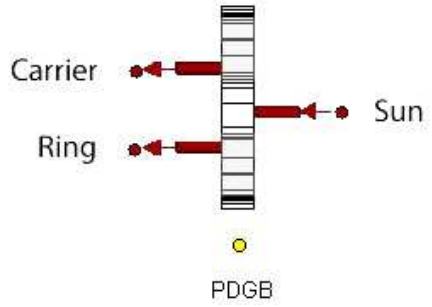

Figure 84: DPGB PROOSIS component schematic view

DPGB cooling system

Figure 85 shows the air cooling system for the DPGB. The following components from TURBO V1.0 library were used: InletAtm, Duct0SasP and Nozzle (complete descriptions available in Ref. 130 and Ref. 131). Two components were created for this specific application:

- *ShaftBlower:* It contains all the equations of the Shaft component of TURBO V1.0 library (Ref. 130 and Ref. 131) and an additional fractional power off-take which is activated below a given flight speed.
- *Blower:* It contains the equations of the Compressor component of TURBO V1.0 library (Ref. 130 and Ref. 131) apart from those related to the mechanical and heat ports which were deleted to simplify the calculations. The white port on the blower and ShaftBlower transmits the value of the power (in kW) to be used by the blower.

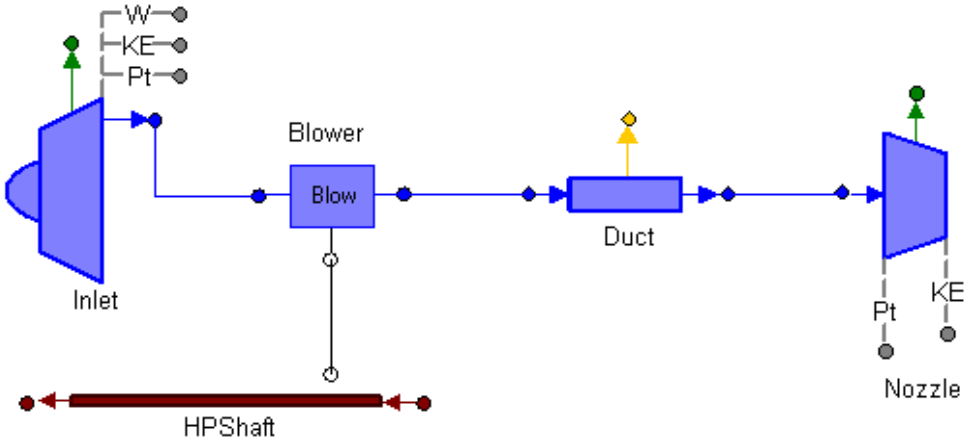

Figure 85: PROOSIS schematic view of the air cooling system for the DPGB

2.2.3.5 Performance monitors

2.2.3.5.1 Requirements

Two different performance monitors were required, one for the DDOR and another one for the GOR. This is because the GOR has two separate air flows (core flow and DPGB cooling flow) and the DDOR has only one air flow (core flow).

It was envisaged that the performance monitors would calculate:

- overall engine pressure ratio, overall compression ratio, overall expansion ratio and overall compression and expansion efficiencies
- core net thrust: Fn_{Core}
- engine net thrust: Fn
- SFC
- thermal, propulsive and overall engine efficiencies: η_{Th}, η_{Prop}, η_{Ov}

from:

- flow properties at stages 2, 3, 4, 5 and 7[54].
- engine inlet mass flow rate: $\dot{m}_{inlet}$
- fuel flow rate and fuel low heating value: $\dot{m}_{fuel}$ and LHV_{fuel}
- nozzle gross thrust and inlet momentum drag: Fg_{nozzle} and RAM_{inlet}
- CRP thrust: F_{CRP}
- inlet flow and exhaust nozzle kinetic energy: KE_{inlet} and KE_{nozzle}
- increase in flow kinetic energy due to the CRP: $KE_{increase\ CRP}$

In the case of the GOR, the following inputs were also required:

- DPGB cooling system scoop momentum drag: RAM_{Scoop}
- kinetic energy at the inlet and outlet of the DPGB cooling system: $KE_{Scoop\ in}$ and $KE_{Scoop\ in}$

2.2.3.5.2 Performance monitor for the DDOR

The performance monitor for the DDOR includes all the equations from the absMONITOR component of the TURBO V1.0 library (Ref. 130 and Ref. 131). This component contains all the equations to calculate overall engine pressure ratio, overall compression ratio, overall expansion ratio and overall compression and expansion efficiencies.

The core and engine net thrusts are calculated as

$$Fn_{engine} = Fg_{nozzle} + RAM_{inlet} + Fn_{CRP} \quad \text{[Eq. 163]}$$

$$Fn_{core} = Fg_{nozzle} + RAM_{inlet} \quad \text{[Eq. 164]}$$

---

[54] Stage 2 = first compressor inlet. Stage 3 = last compressor outlet. Stage 4 = first turbine inlet. Stage 5 = last turbine outlet. Stage 7 = exhaust nozzle inlet.

SFC is calculated as

$$SFC = 10^6 \frac{\dot{m}_{fuel}}{Fn_{engine}} \qquad \text{for} \quad Fn \neq 0$$

$$SFC = 0 \qquad \text{for} \quad Fn = 0 \qquad \text{[Eq. 165]}$$

A specific definition for $Fn_{engine} = 0$ is required to avoid a division by zero which would result in an error. The 10^6 factor is required to obtain SFC in g/(kN s)

The thermal and propulsive efficiencies are calculated as

$$\eta_{Th} = \frac{KE_{nozzle} - KE_{inlet} + KE_{increaseCRP}}{\dot{m}_{fuel}\ LHV_{fuel}} \qquad \text{[Eq. 166]}$$

$$\eta_{Prop} = \frac{Fn_{engine} V_0}{KE_{nozzle} - KE_{inlet} + KE_{increaseCRP}} \qquad \text{[Eq. 167]}$$

with

$$V_0 = \frac{-RAM_{inlet}}{\dot{m}_{inlet}} \qquad \text{[Eq. 168]}$$

Finally the overall engine efficiency is calculated as

$$\eta_{Ov} = \eta_{Th}\ \eta_{Prop} \qquad \text{[Eq. 169]}$$

Figure 86 shows the PROOSIS schematic view of the DDOR monitor component.

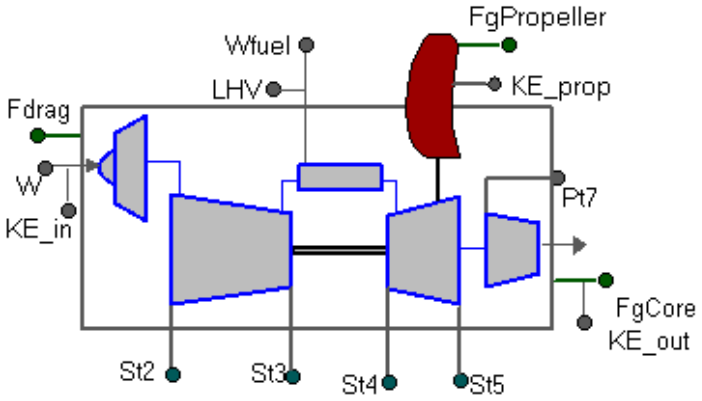

Figure 86: DDOR performance monitor PROOSIS schematic

2.2.3.5.3 Performance monitor for the GOR

The performance monitor for the GOR contains the same equations as the monitor of the DDOR, except from Eq. 163, Eq. 166 and Eq. 167 which are replaced by Eq. 170, Eq. 171 and Eq. 172 respectively.

$$Fn_{engine} = Fg_{nozzle} + RAM_{inlet} + F_{CRP} + RAM_{Scoop} \quad \text{[Eq. 170]}$$

$$\eta_{Th} = \frac{KE_{nozzle} - KE_{inlet} + KE_{increaseCRP} - KE_{Scoop\ in} + KE_{Scoop\ out}}{\dot{m}_{fuel}\ LHV_{fuel}} \quad \text{[Eq. 171]}$$

$$\eta_{Prop} = \frac{Fn_{engine} V_0}{KE_{nozzle} - KE_{inlet} + KE_{increaseCRP} - KE_{Scoop\ in} + KE_{Scoop\ out}} \quad \text{[Eq. 172]}$$

These equations take into account the effect of the air flow of the DPGB cooling system on the overall engine performance.

Figure 87 shows the PROOSIS schematic view of the GOR monitor component.

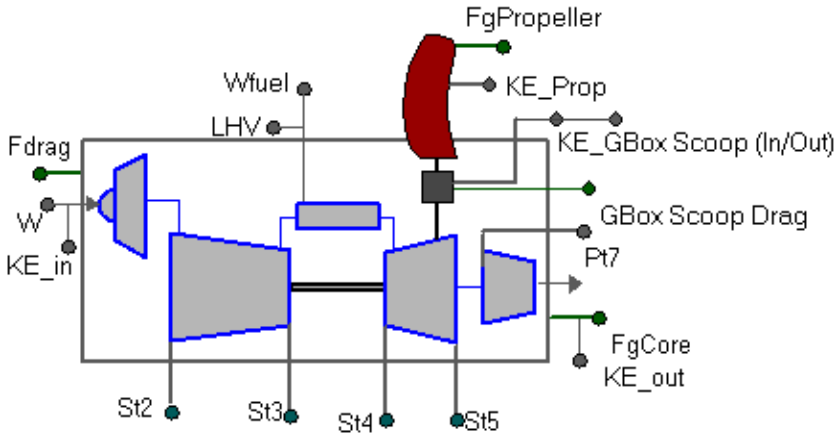

Figure 87: GOR performance monitor PROOSIS schematic

2.2.4 GOR engine model

A PROOSIS GOR engine model was created using the developed CRPe, DPGB, Blower, ShaftBlower and GOR performance monitor components as well as the existing conventional components listed in Table 2 (section 2.2.3.1). Figure 88 shows the GOR engine schematic. The GOR performance monitor is omitted from Figure 88 for visualisation purposes.

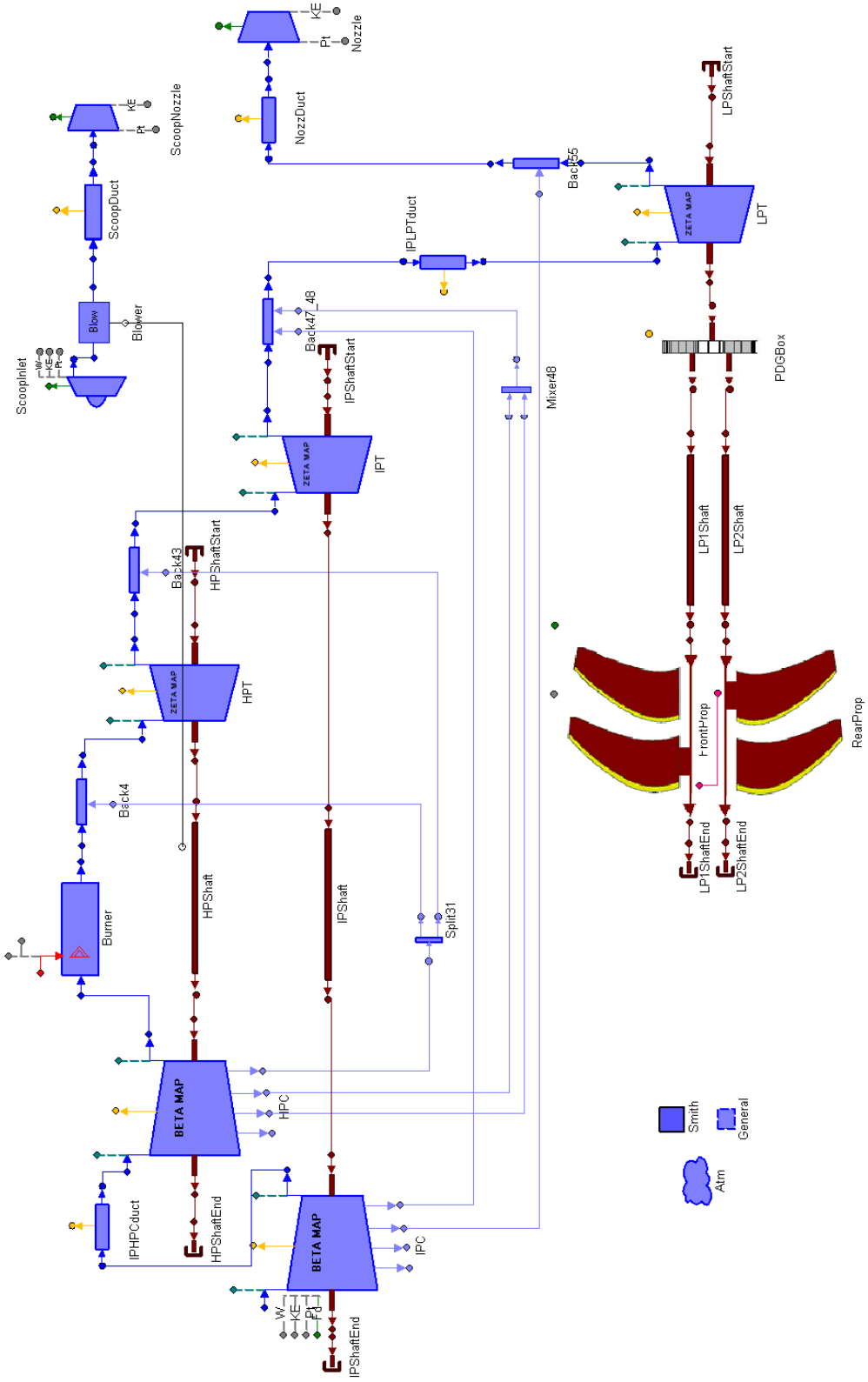

Figure 88: GOR engine schematic

It can be seen that there is no inlet component for the engine core. The inlet and compressor components were modelled as a single component which included the equations of both components. This was done to eliminate the need for guessing a mass flow rate and improve the numerical stability of the model. Although PROOSIS is capable of rearranging the equations of the model, it was observed PROOSIS required 8 guess to match the engine core when an Inlet component was used. Appendix H shows a matching procedure for the core of a CROR (valid for a GOR and DDOR using fuel flow or TET and the rotational speeds of the propellers as handles) showing the 7 required guesses and checks. The additional guess required by PROOSIS was the mass flow rate of a component of the core. This introduced strong numerical instabilities, since the mass flow rate of the core was also determined by the rotational speed of the IPC and the BETA[55] parameter of the IPC, which PROOSIS also required as guesses. Appendix I presents good practices to improve the stability of performance calculations in PROOSIS comprising the elimination of unnecessary guesses.

The rectangular component located next to the atmosphere and general components contains the Smith chart used to estimate the efficiency of the LPT stages at DP.

The heat ports of the DPGB and the duct of the air cooling system (ScoopDuct) were not connected. This is because the fraction of heat generated in the DPGB which is cooled by the fuel system is not known. A rigorous approach to model the impact of heat exchanges on engine performance would require modelling the engine and DPGB oil systems together with the air cooling and fuel cooling system (including a precise model of the fuel tanks in order to calculate the temperature of the fuel).

One of the unconnected bleeds of the IPC is used to cool the propeller environment and is also used as variable bleed to ensure a minimum surge margin at low power settings. The bled mass flow is discharged directly to the atmosphere, and for this reason the bleed port is unconnected.

As it was explained in section 2.2.3.4, the rotational speeds of two shafts of the DPGB have to be fixed in order to obtain the rotational speed of the third shaft. For this reason two rotational speeds have to be independently controlled in the GOR engine. The selected control variables are both propellers rotational speeds and these are adjusted by changing the pitch angles of the propellers (and therefore their power consumption). Consequently, the GOR engine has three main control parameters: TET and n_1 and n_2. This is not the case in turbofan engines with fixed pitch fans where only the TET is controlled (apart from variable bleeds and IGVs). This additional 2 degrees of freedom can be used to implement fuel burn and noise

[55] BETA is a parameter used to define the position of a point in a constant speed line of a compressor map.

reduction control strategies. This was investigated during this PhD research project and is reported in Chapter 3.

All the shaft components were set to “Steady State Calculation” because only steady state performance calculations are required by the OR-TERA2020 platform.

A mathematical model was created using the following set of input.

Input:

- heat loss of compressors, turbines and ducts
- rotational speeds of the propellers: n_1 and n_2
- fuel flow and fuel conditions: $\dot{m}_{fuel}$, Pt_{fuel}, Tt_{fuel}
- flight conditions: Alt, M_0 and dISA

The solution of this model requires three main iteration blocks with the following set of guesses

Engine core

- BETA parameters of the compressors: $BETA_{IPC}$ and $BETA_{HPC}$
- corrected rotational speeds of the compressors relative to their design values: $n_{COR\ Rdes\ IPC}$ and $n_{COR\ Rdes\ HPC}$
- ZETA parameters of the turbines: $ZETA_{IPT}$, $ZETA_{HPT}$ and $ZETA_{LPT}$

CRP

- induced velocity of the rear propeller on the forward propeller: $Vind_{21A}$

DPGB cooling system

- corrected mass flow rate of the DPGB cooling system: $\dot{m}_{COR\ Scoop}$

2.2.5 DDOR engine model

A PROOSIS DDOR engine model was created using the developed CRPe, CRT-0D and DDOR performance monitor components as well as the existing conventional components listed in Table 2 (section 2.2.3.1). Figure 89 shows the DDOR engine schematic. The DDOR performance monitor was omitted from Figure 89 for visualisation purposes.

The merged inlet and compressor component was also used in the DDOR to improve the stability of the model (refer to page 147).

The consideration presented in section 2.2.4 regarding the heat management system of the GOR also applies to the DDOR.

A variable bleed on the IPC is required to ensure its stable operation at low power settings, as for the GOR engine. It is modelled in the same manner as for the GOR (refer to page 147).

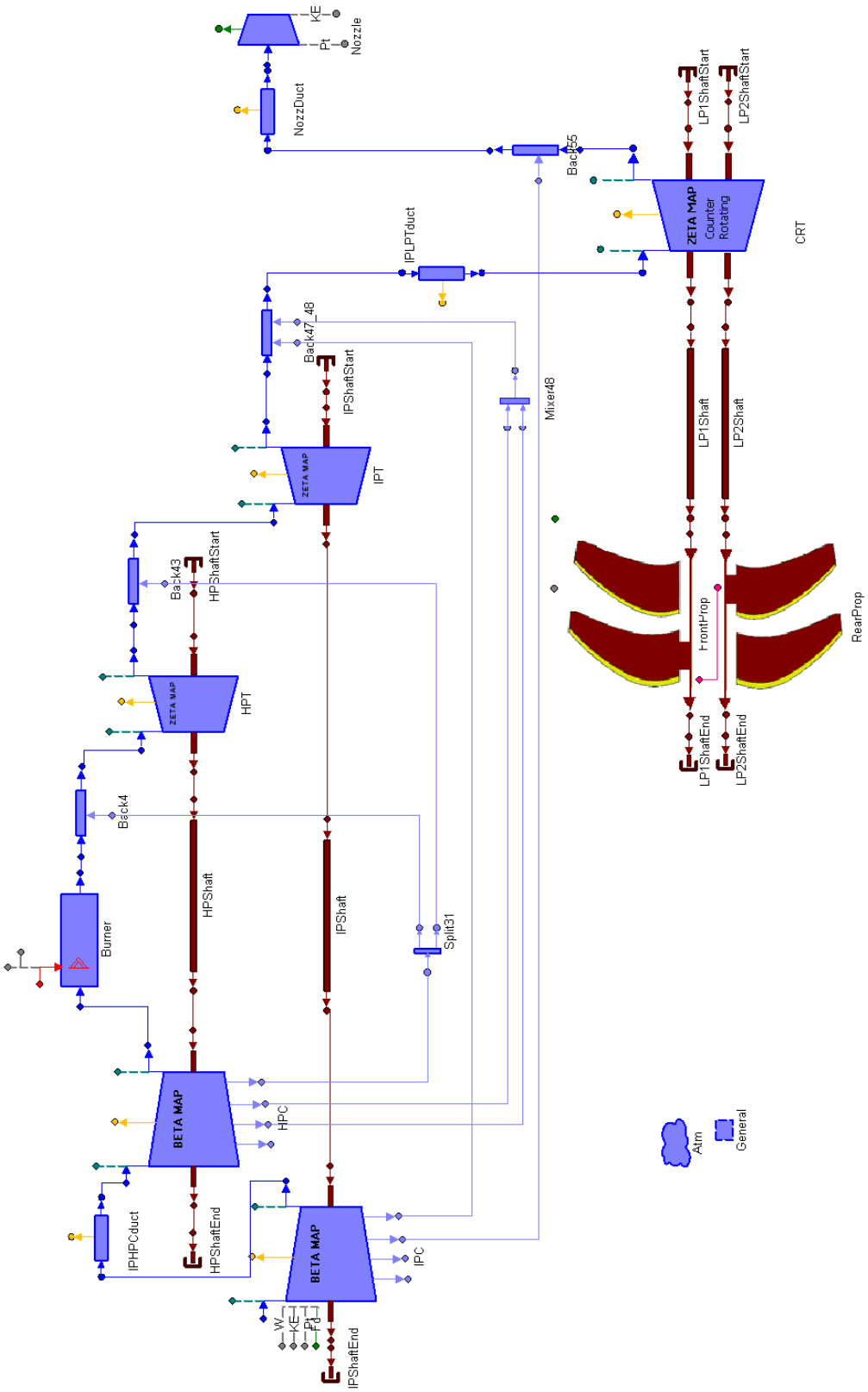

Figure 89: DDOR engine schematic

Although the two parts of the CRT are aerodynamically coupled, both can rotate at different speeds. The rotational speeds of the CRT drums are equal to the rotational speeds of the CRP. n_1 and n_2 can be adjusted by changing the pitch angle of the propellers and therefore their power consumption. For this reason the DDOR engine has three main control variables: TET, n_1 and n_2. This is not the case in turbofan engines with fixed pitch fans where only the TET is controlled (apart from variable bleeds and IGVs). This additional 2 degrees of freedom can be used to implement fuel burn and noise reduction control strategies. This was investigated during this PhD research project and is reported in Chapter 3.

A mathematical model was created using the same inputs as for the GOR engine model. The solution of this model requires two main iteration blocks, one for the engine core and another one for the CRP. These two iteration blocks use the same guesses as in the GOR engine model[56].

2.2.6 OR-TERA2020 performance decks

Two engine performance decks, one for the GOR model and another for the DDOR model, were produced for the OR-TERA2020 platform. They are stand alone executables generated by PROOSIS and they can run in any PC with a Windows 32 bit operating system. The two decks perform the same series of calculations but for the different engine models (GOR and DDOR). They read three input files (which define the engine design and mission points to be simulated) and write four output files (3 input files for other OR-TERA2020 modules and a log file). The definition of the input and output files can be found in Ref. 207 and an overview is provided in section 2.7.

The performance decks do the following calculations:

1 - Engine sizing at DP

The DP performance for the CROR engines is TOC. It is defined as Alt = 35kft (10668m), dISA = 10 and M_0 = 0.73 according to the definition of the aircraft used for the assessments [Ref. 208]. A TET of 1725 K is used at this point (see section 3.2.1.1). At TOC, the aircraft requires 5 400 lbf (24.03 kN) thrust per engine and 250hp (~186.4 kW) of mechanical power off-take per engine [Ref. 208]. During this first calculation the core is sized to meet the thrust requirement while the component maps are scaled to suit the engine definition and match the DP efficiencies calculated by the technology curves. This is an iterative process and all the variables are solved simultaneously since they are all very closely linked. The standard procedure to calculate a DP in PROOSIS[57] was found numerically unstable. It did not converge if the initial values of the guesses of the engine model,

[56] $ZETA_{CRT}$ is used in the DDOR model instead of $ZETA_{LPT}$.

[57] The standard procedure to calculate a DP in PROOISIS is produced by the wizzards available in the software and examples can be seen in the ENGINE V1.0 library.

scaling factors and areas were not close enough to the final solution (~5% difference was the maximum limit). For some other DP variables (design rotational speeds and design powers) the behaviour was random, for some engine designs, the calculation converged if the initial values were close enough to the solution and for other engine designs it only converged if the initial values were far enough from the final values. This problem was solved in previous TERA projects by creating a function to initialise all the variables to be solved at DP. The creation of this function requires a large effort which involves solving all the engines to be assessed, starting with the baseline and making small changes in the design parameters so that the calculation is initialised close to the solution. This process can not be done automatically, and manual changes have to be done to the initial values because some of the variables (design rotational speeds and design powers) cause instabilities if they are initialised too close to the solution. A different approach was taken in this PhD research project, which consists in defining a novel DP calculation method and not using the conventional method available in PROOSIS. This method is described in detail in Appendix I together with further good practices to improve the stability of performance calculations in PROOSIS. The developed DP calculation method converged for all the assessed CROR engines in less than 2s, using a unique set of initialisation values. The proposed DP calculation method and good practices are also part of the contribution of this PhD project because they enable the creation of flexible and robust performance simulation models with PROOSIS, which was not possible before.

The performance feasibility criteria of the components are checked once the DP calculation has been completed. If the design is judged non feasible, the deck stops the calculations and writes on the log file that the design is non feasible. If the engine is judged feasible, the calculations are continued.

2 – Calculation of take-off TET

Take-off TET is calculated imposing the engine thrust and power off-take requirements at the take-off point: 22 000lbf (~97.8kN) of thrust, Alt = 1150ft (~350.5m), M_0 = 0.20, dISA = 28K and HP-shaft power off-take 250hp (~186.4kW) [Ref. 208]. The CROR engines are flat rated for temperatures below ISA+15. Consequently, all the take-off and climb performance calculations for ambient temperatures below ISA+15 are first carried out at ISA+15 (“corner point” condition) using the appropriate value of TET and then repeated at the appropriate ambient temperature maintaining the thrust levels obtained at the corner point.

3 – Calculation of engine performance at the noise certification points

The engine performance is calculated at the following three points:

- Sideline: M_0 = 0.2, dISA = 10, Alt = 0m, take-off power setting
- Cutback: M_0 = 0.2, dISA=10, Alt = 500m, climb power setting

- Approach: M_0 = 0.2, dISA=10, Alt = 120m, Fn_{engine} = 31 kN[58]

The engine performance at these three points is used by the noise prediction module to estimate the engine certification noise. The definition of Alt and M_0 for these three points was provided by the developers of the noise module. At the approach point, the variable bleed of the IPC is controlled to ensure a minimum IPC surge margin of 10%.

4 - Calculation of engine performance at the ICAO emissions certification points

100%, 85%, 30% and 7% take-off thrust settings are simulated at Alt = 0, M_0 = 0.1 and dISA = 0. The 100% take off-thrust is obtained using the previously calculated take-off TET and considering that the engine is flat rated for dISA < 15. Although emissions regulations do not yet exist for CROR engines, these calculations were not performed at static conditions as the ICAO regulations require for turbofan engines. This is because the installed static thrust of a CROR is highly dependent on installation effects, and therefore the uninstalled static thrust of a CROR may not reflect directly the installed levels of emissions.

5 - Calculation of engine performance at the climb points of the mission

The engine performance is calculated for the climb points defined in the mission input file. The specific mission profile used for the CROR assessments is presented in section 3.1.3. The first 1000 ft of the climb are calculated at take-off power setting (using take-off TET and flat rated for dISA < 15) and all the points above 1000 ft are calculated at climb power setting (using TOC TET and flat rated for dISA < 15)

6 - Calculation of engine performance at the cruise points of the mission

The engine performance is calculated at the cruise M_0 for a range of desired cruise thrusts and altitudes. The aircraft performance module selects the most efficient altitude to cruise (see details in sections 2.4.1 and 3.1.4.1), and the required thrust to maintain the flight level at every cruise point. The simulation of a range of altitudes and thrust levels avoids the iterations between the engine performance and aircraft performance modules (which would be numerically costly).

7 - Calculation of engine performance at the descent points of the mission

The engine performance is calculated for the descent points of the mission defined in the mission input file. For these points, the fuel flow is controlled to obtain a fixed

[58] 31 kN per engine is the estimated thrust required to keep a constant approach speed at maximum landing weight and M_0 = 0.2, dISA = 10, Alt = 120m.

rotational speed of the HP shaft[59], instead of a TET or thrust level. The IPC bleed is also controlled during descent points to ensure a 10% surge margin.

8 - Calculation of engine performance at the points required for the mechanical preliminary design

The preliminary mechanical design of the engine components is done taking into consideration the operation of the engine at TOC, take-off and mid cruise:

- TOC: as defined for the DP calculation
- take-off: Take-off TET, Alt = 0, M_0 = 0.25 and dISA = 15
- mid cruise: Alt = 35 kft (10668 m), M_0 = 0.75 and Fn_{engine} = 4000lbf (~17.8 kN)

The engine performance at these three points is simulated.

Engine control for performance calculations

The engine control strategy used at every mission point and power setting is an input to the performance decks. The used control for the GOR and the DDOR are presented and discussed in sections 3.2.2 and 3.3.2 respectively.

2.3 Engine preliminary mechanical design and weight

The engine mechanical preliminary design and weight module used in the OR-TERA2020 platform was developed by Chalmers University and the University of Stuttgart. It follows the approach proposed by Ref. 209. It consists in estimating the engine components dimensions from performance operating data and appropriate design criteria and the weight from the dimensions and materials properties. The turbomachinery and mechanical components are sized in consistency with the choices done in the performance module (technology curves and gas path definitions for the LPT and CRT). The performance operation of the engine at TOC, take-off and mid cruise are used as input for the mechanical preliminary design of the engine. The definition of the input and output files of WeiCo can be found in Ref. 207 and an overview is provided in section 2.7.

The design strategies of the various engine components suggested in Ref. 209 have been extensively updated during the VITAL and NEWAC projects based on the state of the art design criteria and engine data. Containments, discs, CRTs, hot and cold structures models (not reported in Ref. 209) were included in order to increase the accuracy of the predictions.

In order to predict the weight of GORs and DDORs, three main tasks were performed:

[59] A minimum rotational speed is required to ensure the required levels of transient performance, to ensure the correct operation of the seccondary air system and to maintain the auxiliary equipment (driven by the HP shaft) in operation.

- development of a preliminary design methodology for DPGBs
- implementation of a propeller weight estimation method
- set up the engine architectures in WeiCo

Development of a preliminary design methodology for DPGBs

This model was developed by the University of Stuttgart. A description of this model is available in Ref. 211(confidential document), and a summary is provided below.

This module estimates the dimensions and weight of a DPGB, the shafts that link it with the LPT and propellers as well as the cooling system for the DPGB. It requires the following input:

- rotational speeds of the propellers and LPT at take-off
- sun power at take-off
- maximum gearbox diameter (hub diameter of the last stage of the LPT)
- diameter of the sun shaft (calculated by WeiCo as LP shaft)
- Distance between LPT and forward and rear propellers

The gearbox is designed at take-off (Alt = 0, dISA = 15 and M_0 = 0.25) because torques are maximum at this operating condition. The mechanical preliminary design of the DPGB is based on the calculation of the mechanical strength of the gears. The geometry of the gears is determined iteratively by guessing the module (only standard modules are used) and number of teeth in the sun gear, and verifying the margin with respect to pitting and tooth breakage criteria. The weights of the remaining components of the DPGB (bearings, casing, oil system and internal structures) are calculated in proportion to the weight of the gears. The required coefficients of proportionality are obtained from data available in Ref. 212. This preliminary design model also calculates the length of the DPGB. This is used to calculate the length of the Sun, Carrier and Ring shafts which are used to estimate their weights.

The design of the DPGB is considered feasible if its diameter is inferior to the hub diameter of the last stage of the LPT.

Implementation of a propeller weight estimation method

Ref. 99 suggests a method for estimating the weight of advanced propellers. The weight of a propeller is first calculated for a reference propeller with a reference number of blades, reference tip speed and reference maximum absorbed power. The weight of the reference propeller is a function of its diameter, and this function is provided for puller propellers with 8 and 10 blades. Then the weight of the reference propeller is corrected with respect to the real tip speed, and real maximum absorbed power. The weight obtained with this method includes the weight of the retentions, actuators, pitch control system and anti-icing system.

This method was updated to reflect the weight of puller propellers which have relatively large hub diameters. The weight of each blade of the reference puller propeller is calculated as suggested in Ref. 210.

$$m_{blade\,1Ref} = 4.552(D_1 - D_{h1})^{2.6} \quad \text{[Eq. 173]}$$

$$m_{blade\,2Ref} = 4.552(D_2 - D_{h2})^{2.6} \quad \text{[Eq. 174]}$$

Then the weight of each blade is corrected for tip speed and maximum power loading as suggested in Ref. 99[60].

$$m_1 = m_{blade\,1Ref} N_{b1} \left(\frac{\pi n_1 D_1}{192}\right)^{0.3} \left(\frac{L_{P1@take-off} / N_{b1}}{55}\right)^{0.3} \quad \text{[Eq. 175]}$$

$$m_2 = m_{blade\,2Ref} N_{b2} \left(\frac{\pi n_2 D_2}{192}\right)^{0.3} \left(\frac{L_{P2@take-off} / N_{b2}}{55}\right)^{0.3} \quad \text{[Eq. 176]}$$

The propeller power loading (L_P) is calculated using the power of the propellers at the mechanical design take-off point (Alt = 0, dISA = 15 and M_0 = 0.25)

Finally the mass of the CRP is calculated as

$$m_{CRP} = m_1 + m_2$$

GOR and DDOR engine architecture in WeiCo

The following mechanical components were configured in WeiCo to model the DDOR:

IPC	HPT
Intermediate frame	HPT transition duct
HPC	IPT
Combustor	Rear frame
HPT	CRT
HPT transition duct	CRP
IPT	Hot nozzle
Intermediate frame	HP and IP shafts
HPC	Accessories
Combustor	Nacelle

The GOR engine was configured with the same mechanical components except from the CRT which was substituted by a conventional LPT. The DPGB and the LP and propeller shafts were also included in the GOR engine.

[60] Note that the loading correction in Ref. 99 does not include the number of blades, but it can be seen that the 8 blade propeller weight can be obtained from the 10 blade propeller weight applying Eq. 175.

2.4 Aircraft performance

The aircraft performance module used in the OR-TERA2020 simulation platform is Hermes V5D, a customised version of Hermes V5 (user manual Ref. 224). It calculates the aircraft performance in a discrete form using the aircraft definition (mass and geometry or drag polars), engine performance tables and mission profile as inputs. Its main outputs are the time, covered distance, fuel consumed and engine operation for every mission segment. The definition of the input and output files of Hermes V5D can be found in Ref. 207.

The following paragraphs provide a description of the used modelling methodology and the outline of the calculations performed by Hermes V5D. The differences between Hermes V5 and Hermes V5D are highlighted.

2.4.1 Modelling methodology

The aircraft performance modelling methodology used to calculate take-off, climb, cruise, descent and approach phases is described in Ref. 225 (chapter 10). It is based on the following main assumptions:

- pitching, rolling and yawing moments are null and therefore the aircraft can be considered as a punctual mass.
- the climb angle and the angle between the thrust vector and the aircraft fuselage are small. Consequently their cosines are approximated to 1 and their sines are approximated to 0.
- only changes in altitude and horizontal position are considered (2-D trajectory).
- the mission is defined in a discrete manner and the motion equations are integrated numerically. The accuracy of the performance calculations is a function of the time steps used to define the mission.

These assumptions are acceptable and commonly used at preliminary design level for civil aircraft which do not perform “violent” manoeuvres [Ref. 227]. Rigorous aircraft performance calculations considering the 6 degrees of freedom of the aircraft are described in Ref. 227.

The landing performance calculation method described in Ref. 225 is also used in Hermes V5D. It is based on the estimation of the landing time and a constant engine operation during this phase.

Ref. 225 proposes to calculate the fuel consumption during the taxiing phases using an input taxing time and fuel flow. This simplification does not reflect the variations in taxing fuel consumption with respect to the aircraft load. Hermes V5D calculates the taxing phases as ground rolls at 3 m/s (using the same methodology as the take-off ground roll). The engine fuel consumption is calculated from the required thrust for the ground roll and the input engine performance table at taxing rating.

Figure 90 shows the generic form of a mission as it can be defined in Hermes V5D. The mission profile and fuel planning calculations follow the requirements for international flights as defined by FAR 121, JAR OPS 1. Note that the range is equal to the distance covered during climb, cruise and descent.

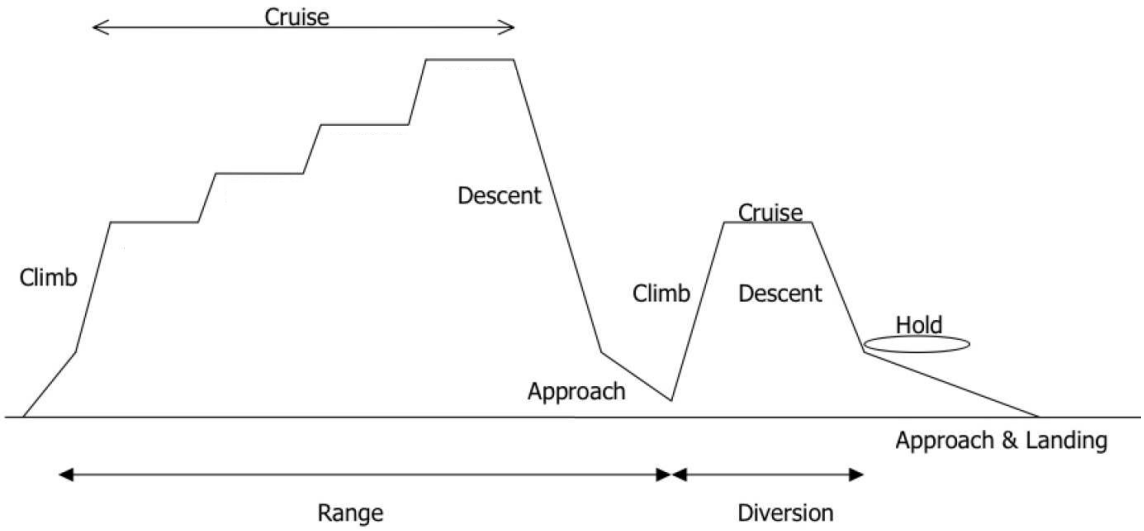

Figure 90: Generic form of a mission in Hermes V5D [Ref. 224]

The following paragraphs describe some specific details of the implementation of the performance modelling methodologies proposed in Ref. 225 for the different mission phases.

General calculations

The atmospheric conditions are evaluated for every point of the mission using the international standard atmosphere definition.

The aerodynamic characteristics of the aircraft (drag polars) can be calculated from its geometric definition following the procedure described in Ref. 226 or can be included in the input files (this is not possible in Hermes V5). A fixed aircraft design is used for the assessments of the present PhD research project (refer to sections 3 and 3.1.1). Its drag polars (at different aircraft configurations) were included in the code of Hermes V5D and can be selected using a flag in the input file.

Take-off, climb, descent and approach calculations

The take-off, climb and approach profiles are defined in Hermes V5D following the FAR and JAR procedures.

The climb and descent profiles are defined in terms of altitude (Alt) in meters and flight equivalent air speed (EAS) in knots. The engine thrust for every climb and descent point is an input to the aircraft performance module (calculated by the engine performance module). Consequently, the range covered in a climb or descent segment, the spent time and the rate of climb or rate of descent are

obtained integrating the motion equations along the segment. Note that the exact trajectory of the aircraft can not be defined in Hermes V5D[61]. In order to avoid iterations in the integration of the motion equations, the weight of the aircraft is considered constant along any segment. The rate of climb or descent ($\partial Alt/\partial t$) and the change in velocity with altitude ($\partial V_0/\partial h$) are considered constant along a segment. The rate of climb is calculated using the average velocity, lift and drag of the segment. According to the model and the aforementioned assumptions, the rate of climb or descent can be calculated as

$$\left.\frac{\partial Alt}{\partial t}\right|_i = \frac{\left[\frac{(Fn_i + Fn_{i+1}) - (Drag_i + Drag_{i+1})}{2}\right]\frac{(V_{0\,i} + V_{0\,i+1})}{2Weight_i}}{1 + \frac{(V_{0\,i} + V_{0\,i+1})}{2g}\frac{(V_{0\,i+1} - V_{0\,i})}{(Alt_{i+1} - Alt_i)}} \qquad \text{[Eq. 177]}^{62}$$

where Weight is the weight of the aircraft and the sub indices i and i+1 correspond to the climb or descent points.

The error introduced by the constant derivates and aircraft weight and average velocity, drag and lift assumptions was calculated for the reference mission using the baseline GOR (defined in sections 3.1.3 and 3.2.1 respectively). Errors in rate of climb were < 0.03%, and errors in rate of descent were < 0.01%.

Hermes V5 calculates the rate of climb (or descent) considering three points and averaging the rate of climb (or descent) of two consecutive segments. As a consequence the performance of a climb or descent segment depends on the performance of the following segment. This requires the definition of additional segments at the end of the climb and the descent which do not correspond to the flown mission.

Cruise calculations

The cruise segments are specified in terms of M_0, possible cruise altitudes and duration. The number of cruise segments is calculated from the cruise time and the duration of the cruise segments. The duration of the last cruise segment is calculated in order to obtain the exact guessed cruise time[63]. At every cruise point,

---

[61] The definition of the trajectory of the aircraft would require a table of engine performance at different thrust levels for every climb and descent point. In this way, a rate of climb or descent can be imposed, the required thrust is calculated, and the fuel consumption is obtained from the engine performance tables.

[62] Eq. 177 is Eq. 10.16 of Ref. 224 considering constant derivates along a segment as well as average velocity, lift and drag.

[63] In Hermes V5, apart from the first and last segments, all the cruise segments have the input duration. The first and last segments have half of the input duration. As a consequence, the total duration of the cruise is a discrete variable and this produces numerical instabilities in the mission calculation because the total cruise duration is used as a guess.

the aircraft aerodynamic efficiency[64] is calculated at the current flight altitude and at a higher allowed cruise altitude. The aircraft would climb to a higher altitude if it provides a higher aerodynamic efficiency and a minimum climb rate of 300 ft/min can be achieved[65].

In order to avoid iterations in the integration of the motion equations of the aircraft, the weight of the aircraft is assumed to be constant along any cruise segment. The calculated variations in aircraft weight along cruise segments were smaller than 0.05% for all the simulations performed (1min cruise duration used). For an average cruise segment, a 0.05% variation in aircraft weight results in a 0.045% variation in required thrust and 0.019% variation in the segment fuel consumption.

Steady state level flight conditions are assumed for the cruise segments. Consequently the lift of the aircraft is equal to its weight and the required thrust of the engines is equal to the drag of the aircraft. The fuel consumption and operation of the engines for a cruise segment are calculated by linear interpolation of the cruise engine performance tables (input to the aircraft module) using the required thrust.

2.4.2 Outline of the calculations

Hermes V5D can perform two different calculations:

a) obtain the maximum range (and the corresponding mission performance) for a given payload and fuel load

b) obtain the fuel load (and the corresponding mission performance) for a given payload and mission range

In the present PhD research project, a fixed mission range (calculation b) is used to assess the variation in mission fuel burn produced by changes in engine preliminary design parameters. Consequently, only the calculation b is presented in this section. In this case, the aircraft performance along a mission is calculated iteratively because the required fuel load, distance and time to TOC as well as the descent distance and time are not known. The fuel load and cruise time are guessed and the calculated mission range and required fuel load are used as checks. The two guesses are solved simultaneously using a Newton-Raphson solver. The calculation procedure is as follows:

1. Guess fuel load and cruise time using a Newton-Raphson solver
2. Verify if (aircraft weight + payload + fuel load) < MTOW
3. Perform taxi-out and take-off calculations (take-off field length, consumed fuel and time)

---

[64] The aircraft aerodynamic efficiency is defined as lift/drag ratio. For a given aircraft configuration, the maximum efficiency altitude is a function of the aircraft weight.

[65] The minimum climb rate criteria is not verified in Hermes V5.

4. Perform climb calculations for every climb segment:
    a. Evaluate aircraft weight. Calculate lift and drag as well as read the engine thrust from the engine input file for the two points defining the segment.
    b. Calculate the average rate of climb (Eq. 177), distance and time needed to cover the segment.
    c. Calculate the fuel burnt during the segment.
5. Calculate the overall climb time, range and fuel burn.
6. Calculate the number of cruise segments from the guessed cruise time and input cruise segment time. The duration of the last cruise segment is calculated in order to obtain the exact guessed cruise time.
7. Perform cruise calculations for every cruise segment:
    a. Evaluate aircraft weight, drag and lift
        i. Evaluate drag/lift for a higher altitude and decide which altitude to fly (the allowed cruise flight levels are input).
    b. Calculate the required thrust to maintain cruise speed (from the force balance).
    c. Interpolate the engine cruise table to calculate the operating point of the engine (SFC as well as Tt, Pt, mass flow rate and FAR at the engine sections required by the emissions model)
    d. Calculate the fuel burned and distance covered during the segment.
8. Calculate overall cruise time, range and fuel burn
9. Obtain the altitudes of every descent point as (final cruise altitude – landing altitude) / number of descent segments. Note that the final cruise altitude is not known a priori.
10. Perform descent calculations for every descent segment:
    a. Evaluate aircraft weight. Calculate lift and drag as well as read the engine thrust from the engine input file for the two points defining the segment.
    b. Calculate the average rate of descent (Eq. 177), distance and time needed to cover the segment.
    c. Calculate the fuel burnt during the segment.
11. Calculate overall descent time, range and fuel burn.
12. Perform the landing and taxi-in calculations or diversion mission calculations which are done as additional climb cruise and descent phases.
13. Obtain the mission totals and required fuel load from the mission fuel and reserve requirements.
14. Calculate the errors to be used in the Newton-Raphson solver:
    a. (calculated range - specified range)/ specified range
    b. (calculated fuel load - guessed fuel load)/ calculated fuel load

Points 1-14 are repeated until the errors are smaller than a defined tolerance.

2.5 Engine gaseous emissions

The emissions and environmental impact module used in the OR-TERA2020 framework is the same as in NEWAC TERA2020 [Ref. 213]. It is capable of calculating emissions at ground level and altitude for burner designs with known emissions index characteristics (defined below) based on the P3T3 or Boeing 2 [66] methods[67]. The following paragraphs provide a summary of the modelling methodology used in this PhD research project and the outline of the calculations performed by the emissions module. The definition of the input and output files of the emissions model can be found in Ref. 207.

2.5.1 Modelling methodology

The P3T3 method [Ref. 216] is used in the present PhD research project because it predicts emissions more precisely than the Boeing 2 method for a known combustor technology [Ref. 214 and Ref. 215]. The P3T3 is a method to predict the emissions index (EI) of different gaseous species at any engine operating condition. Eq. 178 defines the EI for NOx (EINOx). The EI of the other gaseous species are defined analogously.

$$EINOx = \frac{NOx_{Emitted}}{\dot{m}_{fuel} t} = \frac{(kg)}{(kg/s)(s)} \qquad \text{[Eq. 178]}$$

The mass of the various gaseous species are calculated from the emissions indexes the fuel flow and the time that the engine operates at a given regime. According to the P3T3 method, the EIs of the different gaseous species at a given engine operating condition are calculated as [Ref. 216]:

$$EI = EI_{SLS\ ISA@T3} \left(\frac{P3}{P3_{SLS\ ISA@T3}} \right)^{n} \left(\frac{FAR}{FAR_{SLS\ ISA@T3}} \right)^{m} e^{(19(hum_{SL\ ISA} - hum))}$$

[Eq. 179]

[66] The Boeing 2 method is not described in this thesis because it is not used. This method is described in detail in Appendicees C and D of Ref. Ref. 217

[67] The emissions model also has the capability of of estimating the EI characteristics for lean burners from engine performance data. This capability is not used in this PhD research project since lean burners are not assessed.

The required data is:

- combustor inlet Pt: P3
- combustor inlet Tt: T3
- fuel to air ratio in the combustor: $FAR = \frac{\dot{m}_{fuel}}{\dot{m}_{air\ 3}}$
- specific humidity of the air: hum (kg water / kg dry air)
- m and n coefficients (characteristics of the combustor technology)[68]
- $EI_{SLS\ ISA\ @T3}$, $P3_{SLS\ ISA\ @T3}$ and $FAR_{SLS\ ISA\ @T3}$, which are obtained substituting $T3_{SLS\ ISA}$ by T3 in the following characteristic curves of the combustor and engine technology:
  - $EI_{SLS\ ISA}$ vs. $T3_{SLS\ ISA}$ (one for every gaseous specie to be predicted)
  - $P3_{SLS\ ISA}$ vs. $T3_{SLS\ ISA}$
  - $FAR_{SLS\ ISA}$ vs. $T3_{SLS\ ISA}$

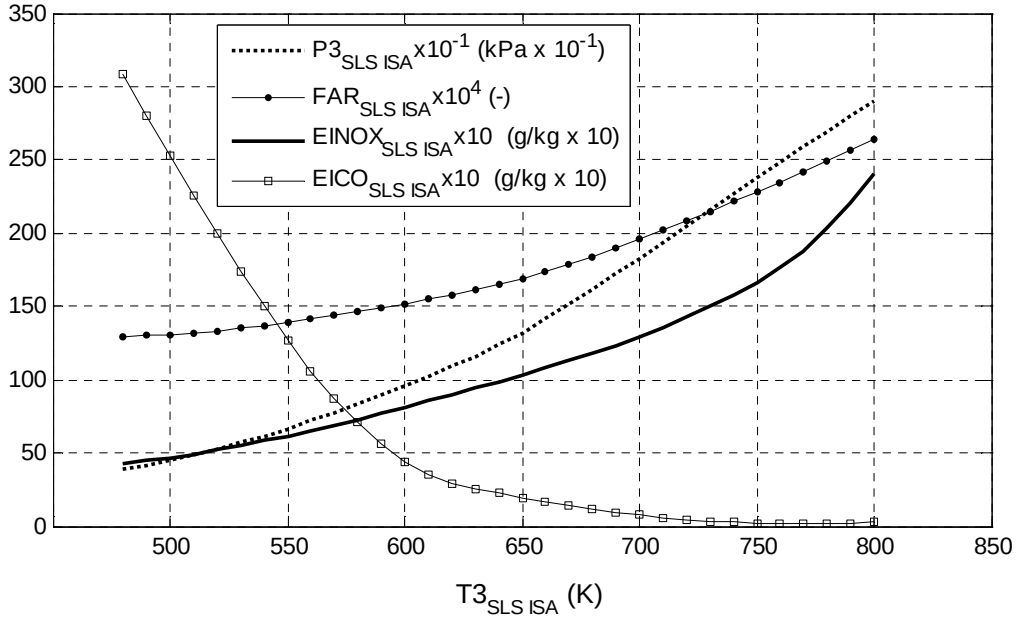

Figure 91: Estimated P3T3 NOx and CO characteristic curves for the CFM56-7B27/3

The CFM56-7B27/3 burner characteristic curves were used for the CROR assessments. This combustor and engine technology was chosen because it was the latest engine certified by CFM at the beginning of the present PhD project (June 2006 [Ref. 218]). The characteristic curves were produced using the ICAO data base and the engine performance model for the baseline short range turbofan engine model in NEWAC TERA2020 (developed by National Technical University of Athens matching the performance of the CFM56-7B27/3 available in the public domain). Figure 91 shows the three characteristic curves used to predict NOx

[68] Ref. 216 proposes values of m and n for various combustors technologies.

emissions in the present assessment studies. The EI curves of CO and unburned hydrocarbons (UHC) were also included in the emissions module.

2.5.2 Outline of the calculations

First the CO_2, CO, NOx, H_2O and UHC emissions at the certification points are calculated. Then, they are integrated to calculate the totals emitted throughout the LTO cycle (defined in Figure 92). Then NOx, CO and UHC are compared to the ICAO regulations. Finally the CO_2, CO, NOx, H_2O and UHC emissions are evaluated for all the mission points using the performance data produced by the aircraft performance module.

ICAO Reference LTO Cycle

Operating Mode	Thrust setting	Time in operating mode, minutes
Take-off	100 % F_{oo}	0.7
Climb	85 % F_{oo}	2.2
Approach	30 % F_{oo}	4.0
Taxi/ground idle	7 % F_{oo}	26.0

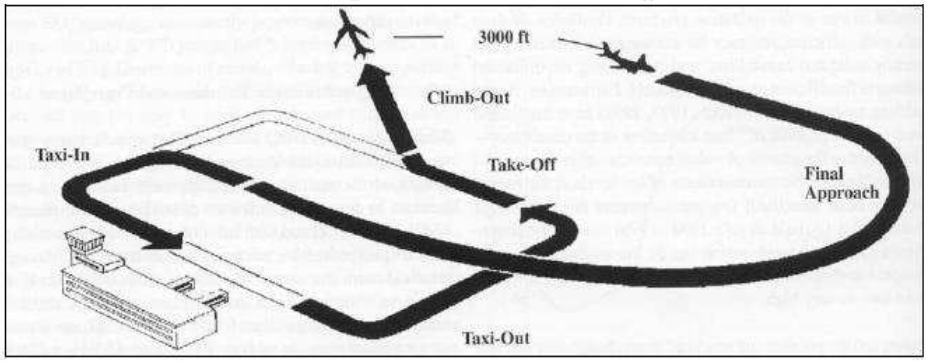

Figure 92: ICAO LTO cycle definition

2.6 Engine noise

The noise module of the OR-TERA2020 was developed by the Aristotle University of Thessaloniki and is called TENOR (TEra Noise module for Open Rotor). It estimates the effective perceived noise levels (EPNL) produced by the two propellers and their interaction, at the three certification points (sideline, cutback and approach). The definition of the input and output files of TENOR can be found in Ref. 207.

2.6.1 Modelling methodology

TENOR is a continuous model produced by fitting a Kirging approximation [Ref. 239] to the estimated certification noise of 51 different CRP designs with:

- diameter of the forward propeller (from 3.66 to 4.88 m)
- clipping of the rear propeller (from 10 to 20 %)
- spacing between the propellers (from 0.61 to 1.4 m)

- number of blades in each propeller (from 8 to 14)
- rotational speeds of the propellers ($730 < n_1 < 1210$ and $630 < n_2 < 1450$)

The 51 CRP designs were selected to suit the Kriging approximation method requirements. The geometrical definition of the 51 CRP designs was generated from a baseline blade geometry (provided by the OEMs involved in the DREAM project) which was scaled to meet the required diameters. The scaled blades were repeated equally spaced around the hub (fixed hub diameter) to meet the required number of blades. The certification noise for each CRP design was evaluated following the procedure described below:

A) The fluctuation in pressure field at a surface located close to the CRP was obtained from unsteady CFD calculations. This was computed using the non-linear harmonics method existent in the NUMECA CFD package. A fixed blade angle setting was used for all take-off CFD simulations and another one for all the approach simulations. It is important to highlight that no mixing plane was used (see Figure 93) therefore the simulations capture all the interaction effects between the propellers.

B) The results of the CFD simulations were used as inputs of the Ffowcs Williams-Hawkings module implemented in the NUMECA software. This module was used to estimate the pressure field variation and noise spectrum produced by the CRP at a series of points following the ICAO noise flight path.

C) The EPNL at the certification points were calculated by simulating the certification measurement procedure.

This module was verified by the Aristotle University of Thessaloniki and OEMs during the DREAM project, but this process was not reported in the public domain.

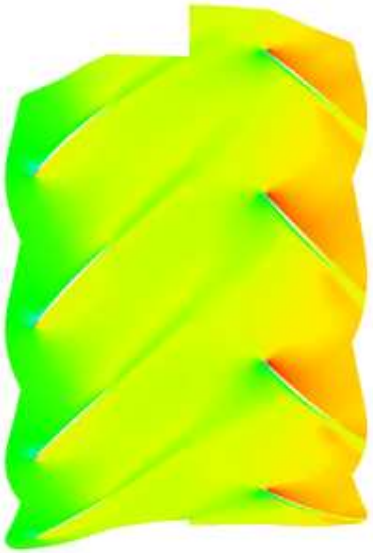

Figure 93: Absolute Pt field around CRP obtained with NUMECA [Ref. 223]

The required inputs to TENOR are:

- Geometric definition of the propeller
  - diameter of the forward propeller
  - clipping of the rear propeller
  - spacing between the propellers
  - number of blades in the forward and rear propeller
- Engine performance data on the three representative noise certification points defined in section 2.2.6 – 3:
  - rotational speeds of the propellers
  - thrust produced by the CRP
  - torque ratio of the CRP
- Aircraft incidence angle

The outputs of TENOR are the EPNL of the sideline, cutback and approach certification points (in EPNdB) as well as the margins with respect to the ICAO regulations (Ref. 7 Annex 16 Chapter 4).

TENOR is a preliminary design noise evaluation tool to rapidly explore the design space of CROR engines. It only evaluates the noise of the CRP. A rigorous calculation should include the noise evaluation of aircraft and other engine noise sources. The following paragraphs demonstrate that the changes in certification noise levels of a CROR are dominated by the changes in noise levels of the CRP. Consequently TENOR can be used to obtain representative certification noise trends for preliminary design studies.

2.6.2 Noise assessment of the engine core

A full engine noise assessment of the baseline GOR was performed using SOPRANO [Ref. 219 and Ref. 220]. SOPRANO is an aircraft and engine noise prediction code developed by Anotec during the SilenceR EU project. It estimates the noise produced independently by the aircraft and engine components (fan, combustor, LPT and jet) based on correlations available in the public domain (based on geometrical definition of components and performance data). The perceived noise levels at the three certification points are calculated from the noise contributions of individual components by simulating the certification measurement procedure (accounting for the propagation and installation effects).

Performance data from the baseline GOR (defined in section 3.2) and its geometrical definition (obtained from WeiCo) were used to predict the noise contribution of the burner, LPT and jet at the three certification points. Figure 94 presents the result of these simulations together with the CRP noise predicted by TENOR. It can be seen that the CRP noise level is more than 10dB higher than the noise levels of the other sources for the three certification points. This result is consistent with the work presented by DREAM-WP.2.5 where the LPT noise contribution was estimated to be lower than 0.5dB in all certification points [Ref.

221]. A similar noise level split between components is expected for the DDOR architecture [Ref. 222]. This suggests that the changes in total engine noise are dominated by the changes in CRP noise levels.

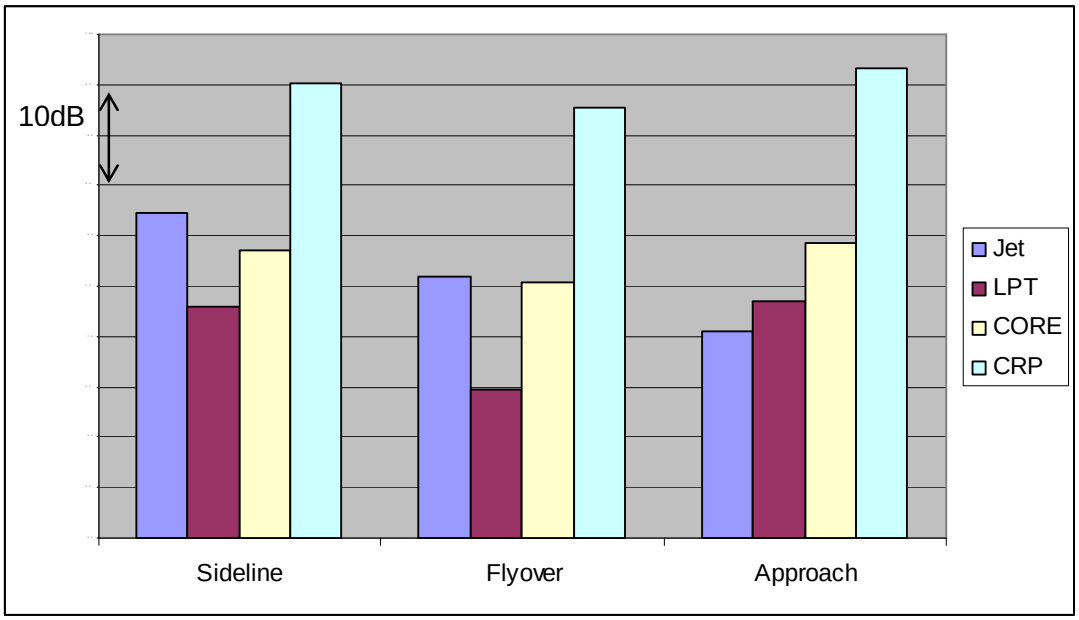

Figure 94: Engine noise sources contribution at certification points (ENPL)

2.6.3 Recommendations for noise model enhancement

TENOR was built from the evaluation of 51 CRP designs. These designs were obtained by changing the geometric design parameters listed in section 2.6 and the rotational speeds of the propellers. The same blade design was used for all the studied CRPs. The blade angle setting at each certification point was kept constant for all the studied CRPs. Consequently, the power absorbed by the CRP and TR_{CRP} were obtained from the CFD simulations. For example, as the diameter of the rear propeller is reduced (keeping all the other parameters fixed), the power absorbed by the rear propeller (Pw_{CRP}) is reduced, the total CRP thrust (Fn_{CRP}) is reduced and the TR_{CRP} is increased.

A Kriging approximation was fitted to the estimated noise levels, which are a function of the propeller definition and rotational speeds. Fn_{CRP} and TR_{CRP} were also modelled using a Kriging approximation. Finally TENOR was built using the geometrical definition of the CRP, n_1 and n_2, Fn_{CRP} and TR_{CRP} as inputs to the Kriging approximation. Although the Kriging approximation can be used with Fn_{CRP} and TR_{CRP} as inputs (because it is a function), it can not reflect the variation of

noise with respect to these parameters because they were not varied independently within the test cases used to build the model[69].

It is recommended to extend the CFD calculations to include different blade angle settings or different blade geometrical definitions in order to capture the independent variation of noise with respect to Fn_{CRP} and TR_{CRP}. However, this was not feasible within the time constraints of the DREAM project. This additional capability would increase the fidelity of the model and allow engine optimisation studies with noise as one the objectives.

2.7 OR-TERA2020 platform

The described simulation modules were integrated in a commercial optimiser (ISIGHT) to form the OR-TERA2020 simulation platform. ISIGHT contains mathematical algorithms which enable the user to perform sensitivity analyses, design space explorations, optimisations among other analyses using all or some of the OR-TERA2020 modules. It also manages the data transfer between modules and provides a graphic interface to the platform. A detailed description of the structure of the OR-TERA2020 platform, the implementation in ISIGHT and a description of the input and output files is provided in Ref. 207. The following paragraphs provide a summary of the OR-TERA2020 structure, execution sequence and data flow as well as a description of the type of studies that can be performed using this platform.

Figure 95 shows the structure of the OR-TERA2020 platform, the main input and output files, the information flows and the execution sequence. Every module is a stand alone executable that reads one or several input files, and writes one or several output files. The input file of a module can be the output file of a previously executed module, or it can be created by ISIGHT using previously obtained variables. The following paragraphs describe the sequence of events that take place during one OR-TERA2020 calculation.

[69] For example, noise levels obtained with TENOR are insensitive to TR and this is not the expected behaviour.

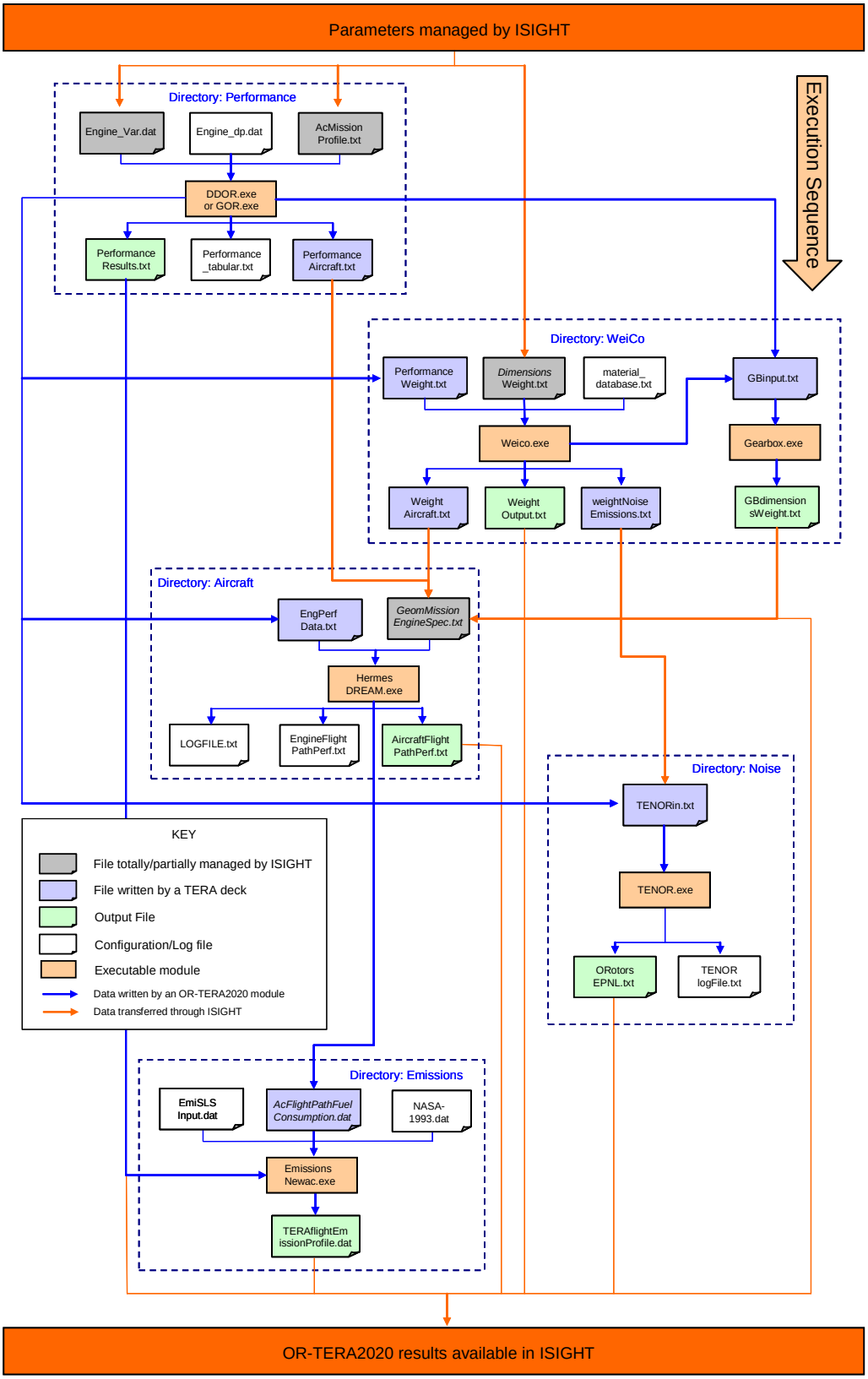

Figure 95: OR-TERA2020 file structure and data flow

Step 1 - ISIGHT creates the input files which contain the engine preliminary design variables (Engine_Var.dat and DimensionsWeight.txt), engine control (AcMissionProfile.txt) variables and mission profile (AcMissionProfile.txt and GeomMissionEngineSpec.txt). The definition of these variables depends on the type of performed assessment (optimisation or design space exploration).

Step 2 - The engine performance module is executed. It sizes the engine to meet the DP requirements. It simulates the operation of the engine along the specified mission and writes the performance tables required by the aircraft module (EngPerfData.txt). It calculates the engine performance at the noise and gaseous emissions certification points and writes the corresponding output files (TENORin.txt and PerformanceResults.txt). It also simulates the mechanical preliminary design operating points and writes the results in PerformanceWeight.txt and the gearbox performance at take-off in GBinput.txt.

Step 3 - The engine preliminary mechanical design module sizes the engine components and writes the total engine weight in GeomMissionEngineSpec.txt.

Step 4 - The aircraft performance module simulates the desired mission and outputs the mission performance (AcFlightPathPerf.txt) as well as the flight path and engine operation at all the mission points (AcFlightPathFuelConsumption.txt).

Step 5 - The noise module calculates the noise levels at the three certification points.

Step 6 - The emissions module calculates the gaseous emissions at the certification points, LTO cycle and along the mission.

Note that the simulation modules are executed in sequence and no iteration loops are required to assess a particular engine design with a given control strategy performing a given mission. This calculation sequence can be repeated for the different engine designs, engine control strategies or mission profiles to be assessed. It is important to highlight that only the engine (design and control) and mission definitions can be modified in OR-TERA2020. The aircraft definition as well as the engine performance requirements are fixed for the present CROR engine assessments (see details in section 2.1). The aircraft definition (and consequently the engine performance requirements) could be varied if an aircraft preliminary design module was available and iterations between the engine performance, engine preliminary mechanical design and aircraft performance were possible.

The feasibility of the engine design is evaluated by the feasibility criteria included in the performance and in the mechanical preliminary design modules. If an engine design is judged non feasible, the aircraft performance, emissions and noise modules are not executed, and the following engine design is assessed. Additional feasibility criteria can be included in ISIGHT based on the available variables (E.g.: maximum take-off TET).

The following studies can be performed with the OR-TERA2020 platform:

- Engine design space exploration for a fixed mission: The impact of the engine preliminary design variables on the mission fuel burn, noise and emissions (and all variables available in the platform) can be can be assessed.
- Engine preliminary design optimisation studies for a fixed mission: Any of the calculated variables can be minimised or maximised by changing the engine preliminary design variables[70]. Any of the calculated variables and the engine preliminary design variables variable in ISIGHT can be used as constraints in the optimisation process.
- Mission profile optimisation studies for a fixed engine design. The climb, cruise and descent profiles can be modified in order to minimise the mission fuel burn, time or the gaseous emissions.
- Evaluation of a fixed engine design flying different missions. The mission profile, payload and range can be varied to assess the performance of a given engine design along different missions.
- Simultaneous optimisation of the engine preliminary design and mission profile for a fixed mission duty (pay load and range).
- Isolated module optimisations: Single modules or groups of modules can be used to optimise specific aspects of the engine design. For example:
    - the engine performance module can be used in isolation to find the minimum fuel burn control strategy of the propellers for a given set of operating requirements.
    - the engine performance and preliminary mechanical design modules can be used together to find minimum weight engine design regions.

It is important to highlight that the results of the OR-TERA2020 assessments are based on preliminary design methods. This information can be used to identify optimum design regions to be explored in more detail with dedicated design tools and to assist the design process when compromises should be performed as a consequence of design, operational or regulatory constraints.

[70] Note that the certification noise can not be used as an optimisation criterion (refer to section 2.6.3).

3 ENGINE ASSESSMENTS

CRORs have significant potential to reduce aircraft fuel burn, however there are challenges that need to be addressed both at aircraft and at engine level (described in section 1.1.2.5). Multi disciplinary preliminary design space exploration assessments can be used to identify optimum design regions to be explored in more detail with dedicated design tools and to assist the design process when compromises should be performed as a consequence of design, operating or regulatory constraints.

This chapter presents the variation in fuel burn, noise and emissions for pusher GORs and DDORs with respect to:

- the control of the rotational speeds of the propellers
- the following LP preliminary design variables:
    - IPC bleed mass flow rate (for cooling and noise reduction techniques)
    - Nozzle pressure ratio at DP
    - Spacing between propellers
    - Hub diameters of the propellers
    - Number of blades of the forward and rear propeller
    - Diameter of the forward and rear propeller
    - Forward and rear propeller rotational speeds at top of climb (TOC) and take-off (design variables)
    - Number of stages of the LPT and CRT
    - DPGB torque ratio (for the GOR)

The sensitivity of the mission fuel burn with respect to the DP efficiencies of core compressors, turbines and DPGB (for the GOR) is also presented.

These assessments focused on the design and control of the specific CROR LP components. Consequently, a fixed gas generator technology level (overall pressure ratio and DP TET) was used both for the GOR and DDOR.

A fixed reference aircraft was used to assess the performance of the different OR engine designs. This is consistent with the current aircraft manufacturer and engine OEM approach. An alternative approach is discussed in section 2.1. A fixed reference mission (maximum payload and 500 NM) was also used[71]. A weighted average of different missions could have been used to compare engine designs, but the interpretation of the results would have been more complex and the calculation time significantly increased.

[71] Ref. 234 presents overall mission performance studies and mission profile optimisation studies of the reference aircraft with the baseline GOR coverign different ranges. This work is the result of a collaborative effort between the author of this thesis and an M.Sc. researcher.

The LTO emissions analyses mainly focus on NOx because:

- NOx emissions have been the focus of the ICAO gaseous emissions certification standards (regulatory limits have been reduced three times: 1995 203 and 2007 [Ref. 6])
- CO_2 and H_2O emissions are proportional to the amount of fuel burned
- the methods to calculate emissions produce relatively less accurate estimations for CO and UHC than for the rest of the species. This is because the formation of CO and the presence of UHC are highly dependant on the dynamics of the combustion process.

The presented results are expressed as differences relative to a baseline design (a baseline GOR defined in section 3.2.1 and a baseline DDOR described in section 3.3.1). This approach is consistent with the level of fidelity of the tools used for the assessments.

The direct comparison of different type of engines (DDOR, GOR or even turbofans) based on preliminary design methods may be misleading since the modelling methodologies and assumptions are different for the various engine specific components (as well as the aircraft). Consequently the DDOR and GOR engines are not compared quantitatively.

First the reference aircraft is defined and its main performance characteristics are presented. The reference mission is subsequently defined. Then the multidisciplinary assessments of the GOR and DDOR engines are presented.

Format of the presentation of the results

The variation of the performance parameters of the CROR engines presented in the engine control and design space exploration studies are expressed as a percentage change relative to a reference value. This reference value is represented in the plots with a white dot. If the reference value lies outside the range of the plot, it is explicitly defined in the text.

3.1 Reference aircraft and mission

3.1.1 Definition of the reference aircraft

Ref. 208 defines the following top level requirements of the reference OR aircraft used for the engine assessments of the DREAM project.

- Design PAX: 160. No additional payload is considered
- Maximum take-off weight (MTOW): 83500 kg
- The aircraft is designed to take-off at full payload and full fuel load.
- The design and operation of the aircraft should take advantage of the fuel burn benefits of flying slower.
- Design TOC speed: $M_{0\ TOC} = 0.73$
- Design cruise speed: $M_{0\ Cruise} = 0.75$

- Take-off field length (TOFL) < 2500 m
- Time to initial cruise altitude < 30 min
- Minimum initial cruise altitude: 31000 ft (9448.8 m)
- Rear fuselage mounted pusher CROR engines
- CRP diameter < 14 ft (4.26 m)
- Both the aircraft and engine technologies correspond to an entry into service of 2020.

These requirements were used to define the reference OR aircraft used for this PhD research project. Table 3 presents the mass break down of the reference aircraft. Figure 96 shows its low speed (M_0 < 0.5) aerodynamic characteristics for the different aircraft configurations defined in Table 4. Figure 97 presents its aerodynamic characteristics at the clean configuration for different flight speeds[72]. Table 3, Figure 96 and Figure 97 contain all the required data to define an aircraft in Hermes V5D.

MTOW	83500 kg
Useful Payload = Max payload	14400 kg
Operating empty weight	45700 kg
Fuel load	23400 kg
Maximum landing weight	76500 kg

Table 3: Reference OR aircraft weight break down

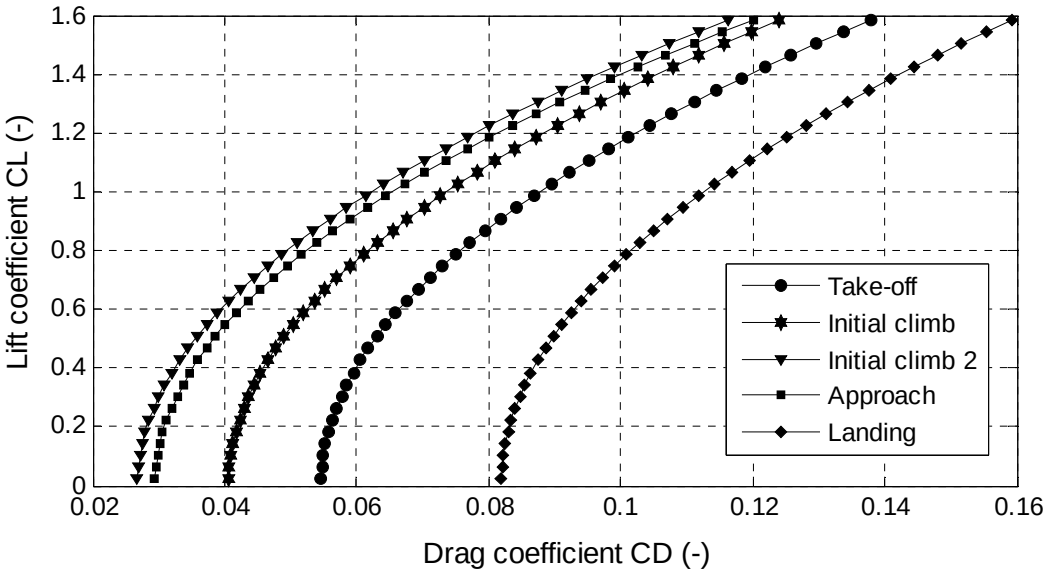

Figure 96: Drag polars of the reference OR aircraft (non clean configurations, M_0 < 0.5)

[72] The aerodynamic characteristics of the aircraft at the clean configuration and M_0 < 0.6 are considered equal to the aerodynamic characteristics of the aircraft at the clean configuration and M_0 = 0.6.

Configuration Name	Flaps Angle (º)	Landing Gear position
Take-off	15	Down
Initial climb	15	Up
Initial climb 2	5	Up
Clean	0	Up
Approach	10	Up
Landing	30	Down

Table 4: Definition of configurations of the reference OR aircraft

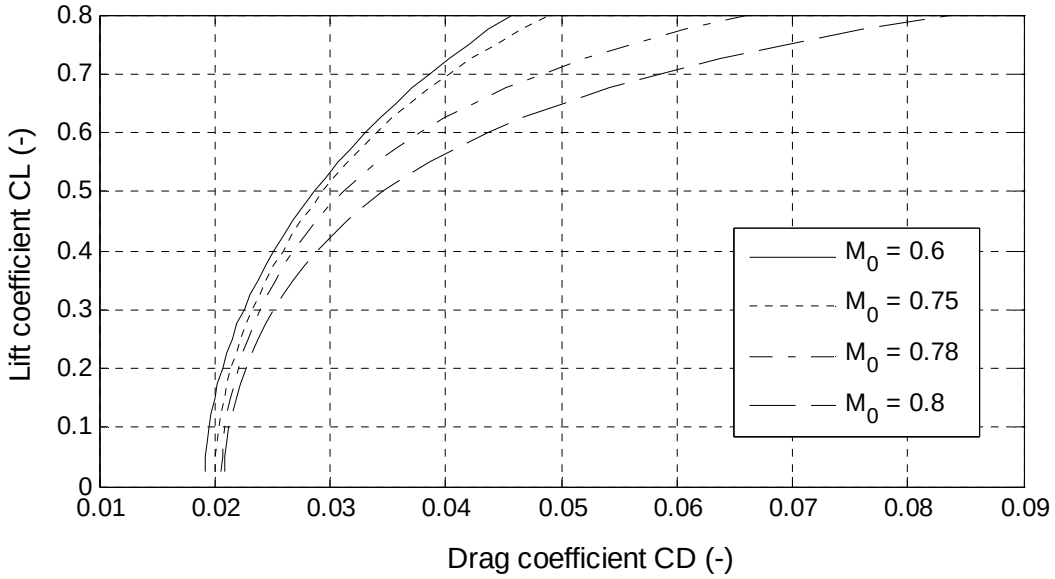

Figure 97: Drag polars of the reference OR aircraft (clean configuration)

The methods used to obtain the mass break down and aerodynamic characteristics can not be described in this thesis due to non disclosure agreements[73].

The engine pylon and nacelle drag were included in the aircraft drag and therefore they are equal for all the studied engine designs. A rigorous calculation would require preliminary design methods to obtain the pylon and the engine nacelle geometry and to calculate their drag for each studied CROR engine. This limitation is acknowledged and it is recommended that further work is performed on this area.

[73] Initially, the aircraft preliminary design methods presented in Ref. 230, Ref. 231, Ref. 232 and Ref. 233 were used to estimate these magnitudes. The difference between the required TOC thrust calculated with the different methods was approximately 20%. Consequently, it was decided to use a higher fidelity methodology.

3.1.2 Engine performance requirements

The thrust requirements (per engine) of the reference aircraft presented in section 3.1.1 are the following:

- Take-off: 1150 ft (~457 m), M_0 = 0.20, dISA = 28 → 97.86 kN
- TOC: 35 000 ft (~10666 m), M_0 = 0.73, dISA = 10 → 24.02 kN
- Cruise: 35 000 ft (~10666 m), M_0 = 0.75, ISA → 15.57 – 22.5 kN

These thrust levels ensure the correct values of take-off field length, residual rate of climb at TOC and cruise level flight at maximum load.

The reference aircraft requires 250 hp (~186.4 kW) of mechanical power from each engine (bleed air is not required) [Ref. 208].

All the assessed CROR engines were sized at TOC in order to satisfy the TOC thrust requirement. The take-off TET was calculated imposing the take-off thrust requirement. Finally a check was done to verify that an acceptable surge margin of the IPC at minimum cruise thrust could be achieved without opening the IPC discharge valve.

3.1.3 Definition of the reference mission

A 500 NM range business mission is used for the engine assessments. It corresponds to an average mission covered by a 160 PAX class aircraft in Europe. The following paragraphs define the different aspects of the reference mission.

Payload: Maximum payload (160 PAX = 14400 kg)

Range: 500 NM from lift-off to touch down.

Atmospheric temperature: ISA for all the mission points

Take-off and landing altitudes: Sea level (0 m)

Contingency fuel: 5 min level flight at 1500ft plus 5% of mission fuel (as defined in JAR OPS)

Taxi-out duration: 12 min

Taxi-in duration: 6 min

Climb profile: Table 5 presents the climb profile of the reference mission as well as the aircraft configuration at every phase of the climb. The input climb profile for the performance module is defined in steps of 500ft for Alt < 2000ft and in steps of 1000 ft for Alt < 2000 ft.

AC Configuration	Alt[m]	Alt [ft]	CAS[kt]	M[-]
Take-off	TAKE-OFF	0	153.0	0.231
	152.4	500	153.0	0.233
Initial climb	304.8	1000	153.0	0.235
	457.2	1500	158.0	0.245
	609.6	2000	158.0	0.248
Initial climb 2	914.4	3000	178.0	0.284
Clean	1219.2	4000	208.0	0.338
	1524	5000	248.0	0.410
	1828.8	6000	250.0	0.420
	3045	10000	250.0	0.452
	3048	10000	260.0	0.470
	9753.6	32000	260.0	0.721
	10058.4	33000	257.7	0.730
	10363.2	34000	251.9	0.730
	10666	35000	246.2	0.730
	10666	35000	253.6	0.750

Table 5: Climb profile definition

Note that TOC is achieved at $M_0 = 0.73$ and then the aircraft is accelerated to $M_0 = 0.75$ at cruise altitude.

Cruise: Cruise is done at $M_0 = 0.75$ and 35000 ft. The choice of the cruise altitude is justified in section 3.1.4.3.

Descent profile: Table 6 presents the descent profile of the reference mission as well as the aircraft configuration at every descent segment. The input descent profile for the aircraft performance module is defined in steps of 1000ft.

AC Configuration	Alt[m]	Alt [ft]	CAS[kt]	M[-]
Clean	10668.0	35000	253.6	0.750
	9448.8	31000	277.5	0.750
	9144.0	30000	280.0	0.741
	3048.0	10000	280.0	0.505
	2743.2	9000	250.0	0.444
	2438.4	8000	250.0	0.436
	2133.6	7000	250.0	0.428
	1828.8	6000	250.0	0.420
	1524.0	5000	220.0	0.364
	1219.2	4000	220.0	0.357
	914.4	3000	220.0	0.351
Approach	609.6	2000	181.3	0.284
Landing	304.8	1000	141.3	0.217
	LANDING	0	136.3	0.206

Table 6: Descent profile definition

It is important to highlight that climb and descent speeds above 10000 ft are lower than those of conventional turbofan aircraft (300-310 kt). This is done to reduce the

mission fuel burn and take full advantage of the CROR engines as it is indicated in the aircraft top level requirements (section 3.1.1). Ref. 234 presents a study of the impact of the climb and descent speeds on mission fuel burn and time of the reference mission using the baseline GOR engine (defined in section 3.2.1). Climb speeds between 250 and 310 kt and descent speeds between 260 and 300 were evaluated (steps of 10 kt were considered in order to satisfy current air traffic control practices). The minimum mission fuel burn is obtained climbing at 260 kt and descending at 280 kt. Climbing and descending at the minimum fuel burn speeds results in a 5 min longer mission than climbing at 310 kt and descending at 300 kt.

3.1.4 Performance of the reference aircraft

This section presents the main performance characteristics of the reference OR aircraft using the baseline GOR engine defined in section 3.2.1.

3.1.4.1 Step cruise performance

The reference OR aircraft was simulated in cruise at M_0 = 0.75. Its initial weight was set to 85 tons and its altitude was automatically selected by the performance module to maximise the aerodynamic efficiency of the aircraft (lift/drag). The possible altitudes were 31, 33, 35, 37 and 39 kft. The aircraft module also verified that a minimum climb rate of 300 ft/min could be achieved for every step cruise climb. Figure 98 presents the obtained aerodynamic efficiency along the simulated cruise and Table 7 the adopted cruise altitudes for different aircraft weights. The peaks in Figure 98 correspond to changes in cruise altitude.

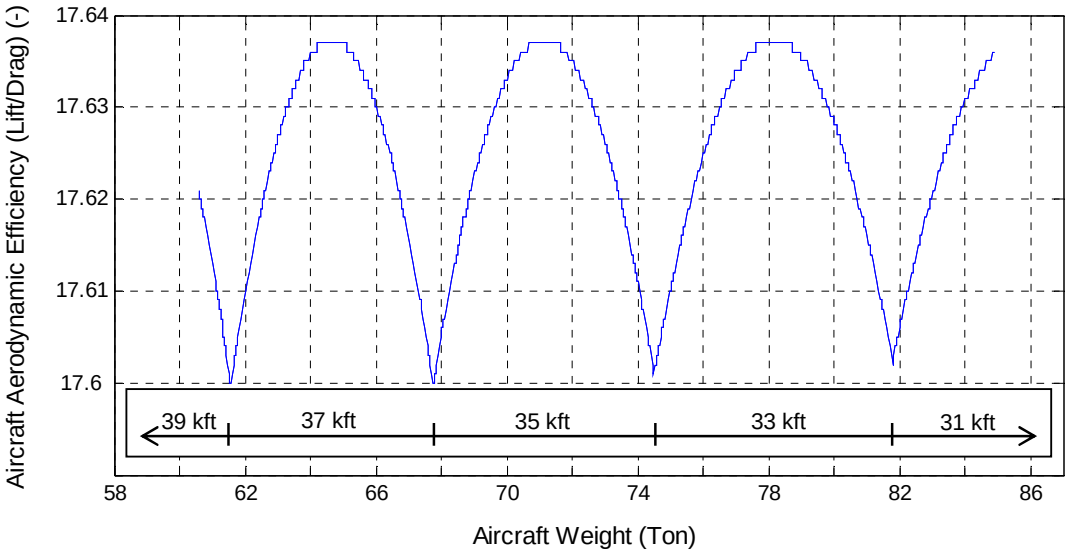

Figure 98: Cruise altitude selection based on aircraft weight

Alt (kft)	(tons)
31	AC Weight > 81.8
33	81.8 > AC Weight > 74.5
35	74.5 > AC Weight > 67.7
37	67.7 > AC Weight > 61.6
39	AC Weight < 61.6

Table 7: Adopted cruise altitudes vs. aircraft weight

Note that for missions at ISA temperature, the 31kft cruise altitude is not used. This is because when the aircraft takes off at its MTOW (83.5 tons), its weight at 31kft is lower than 81.8 tons and the baseline GOR can provide a rate of climb higher than 300 ft/min.

3.1.4.2 500 to 3000NM missions

The aircraft module, together with the baseline GOR engine performance (summary provided in Table 8) were used to simulate 500, 1000, 2000 and 3000 NM missions with maximum payload (14.4 tons).

	Take-off	Mid-Climb	TOC	Mid-Cruise	Mid-descent
Alt (kft)	0	18	35	35	18
M_0 (-)	0.23	0.545	0.73	0.75	0.586
dISA (-)	0	0	10	0	0
Fn (kN)	108.54	39.43	24.03	17.79	2.36
SFC (kg/(daN*h))	0.256	0.367	0.430	0.437	1.479
SFC (g/(kN*s))	7.11	10.2	11.94	12.14	41.07

Table 8: Summary of baseline GOR engine performance

The four missions were simulated using the reference mission profile defined in section 3.1.3 but allowing the optimum selection of the TOC and cruise altitude as described in the previous section. In order to select the most efficient TOC altitude, the aircraft performance module evaluates the most efficient start of cruise altitude. In order to estimate the mass of the aircraft at the different possible start of cruise points, it calculates the climb up to the different allowed cruise levels.

Table 9 presents the obtained fuel burn, distance and time for every phase of the 500, 1000, 2000 and 3000 NM missions.

	Mission Range (NM)			
	500	**1000**	**2000**	**3000**
TOC Altitude (kft)	39	37	37	35
FUEL BURN (Kg)				
Taxi-Out:	190	196	208	220
Take-Off (Ground Roll):	46	48	53	58
Climb:	1166	1098	1261	1299
Cruise:	583	2412	5954	9837
Descent:	372	372	372	372
Taxi-In:	95	98	104	110
Mission	2166	3929	7640	11565
Mission + Taxing	2452	4223	7952	11896
DISTANCE (km)				
Taxi-Out:	2.2	2.2	2.2	2.2
Take-Off (Ground Roll):	1.2	1.3	1.4	1.6
Climb:	324.0	280.7	331.1	323.1
Cruise:	317.2	1286.7	3089.2	4948.8
Descent:	283.8	283.9	284.0	284.1
Taxi-In:	1.1	1.1	1.1	1.1
TIME (min)				
Taxi-Out:	12.0	12.0	12.0	12.0
Take-Off (Ground Roll):	0.5	0.5	0.6	0.6
Climb:	28.4	25.2	29.4	29.2
Cruise:	23.9	96.9	232.6	372.0
Descent:	29.5	29.5	29.5	29.5
Taxi-In:	6.0	6.0	6.0	6.0
Mission time	81.8	151.6	291.5	430.7

Table 9: 500 to 3000NM mission fuel, distance and time

Figure 99 presents the obtained mission + taxing fuel burn as a function of the mission range.

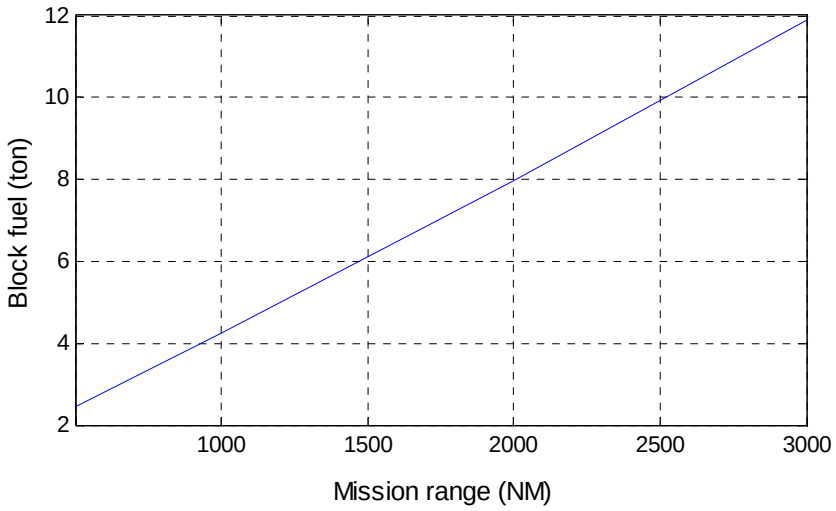

Figure 99: Fuel consumption vs. Mission Range at max payload

The time to TOC is lower than 30 minutes for the four studied missions. It is important to note that the time to TOC is smaller than the climb time, since the climb also includes the acceleration from M_0 = 0.73 to 0.75 which is performed after reaching TOC. In the case of the 500NM mission (Figure 100) the time to TOC is approximately 26.5 minutes.

3.1.4.3 Reference mission analysis

The 500 NM mission obtained allowing the aircraft module to select the optimum TOC and cruise altitudes, has a 24 minutes cruise. This does not leave enough time for two members of the crew to serve 160 passengers. In order to increase the cruise time a lower TOC altitude can be adopted but with an associated fuel burn penalty. Table 10 summarises the effects of imposing the TOC and cruise altitude on mission time and fuel burn.

TOC and cruise altitude (Alt_{TOC}) (kft)	**39**	**37**	**35**	**33**
Mission + taxing fuel (kg)	2451	2456	2475	2510
Mission time (min)	81.7	81.4	81	80.3
Cruise time (min)	24	29	33	35

Table 10: 500 NM mission for different imposed TOC altitudes

Alt_{TOC} = 35 kft provides 9 more minutes of cruise and imposes a 1% fuel burn penalty compared to Alt_{TOC} = 39 kft. Alt_{TOC} = 33 kft would only provide 2 extra cruise minutes at a cost of 1.5% extra fuel burn compared to Alt_{TOC} = 35 kft. Consequently the best compromise between increase of cruise duration and fuel burn penalty is achieved at Alt_{TOC} = 35 kft. For this reason the reference mission defined in section 3.1.3 and used for the CROR assessments has a TOC altitude of 35 kft and the step cruise is not allowed.

Figure 100 and Figure 101 present the 500 NM mission profiles for Alt_{TOC} = 39 kft and Alt_{TOC} = 35 kft respectively.

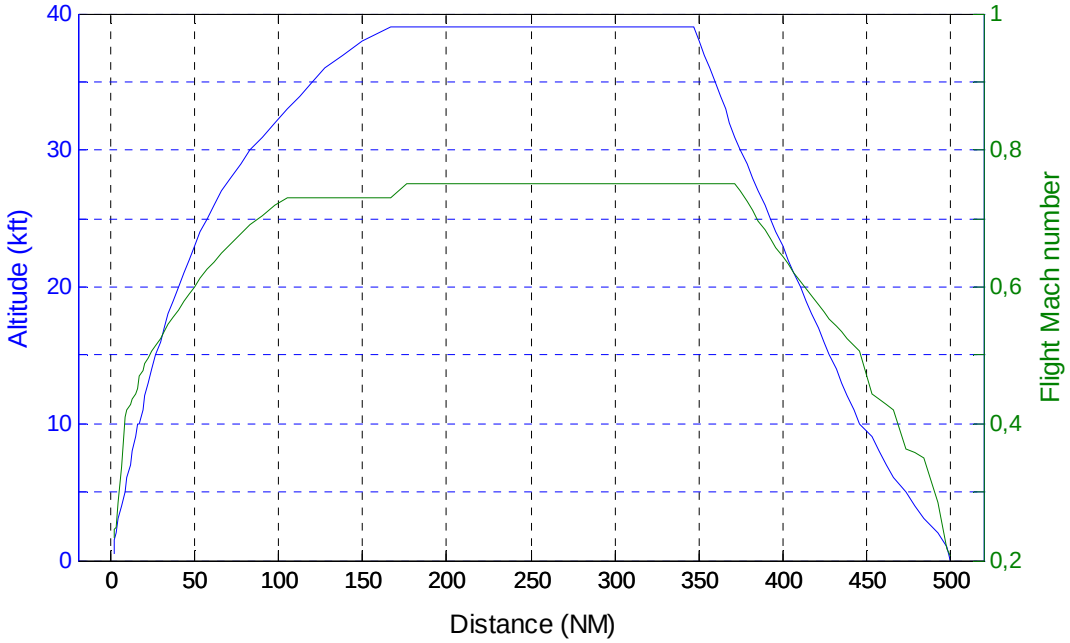

Figure 100: 500NM baseline mission profile (Alt_{TOC} = 39kft)

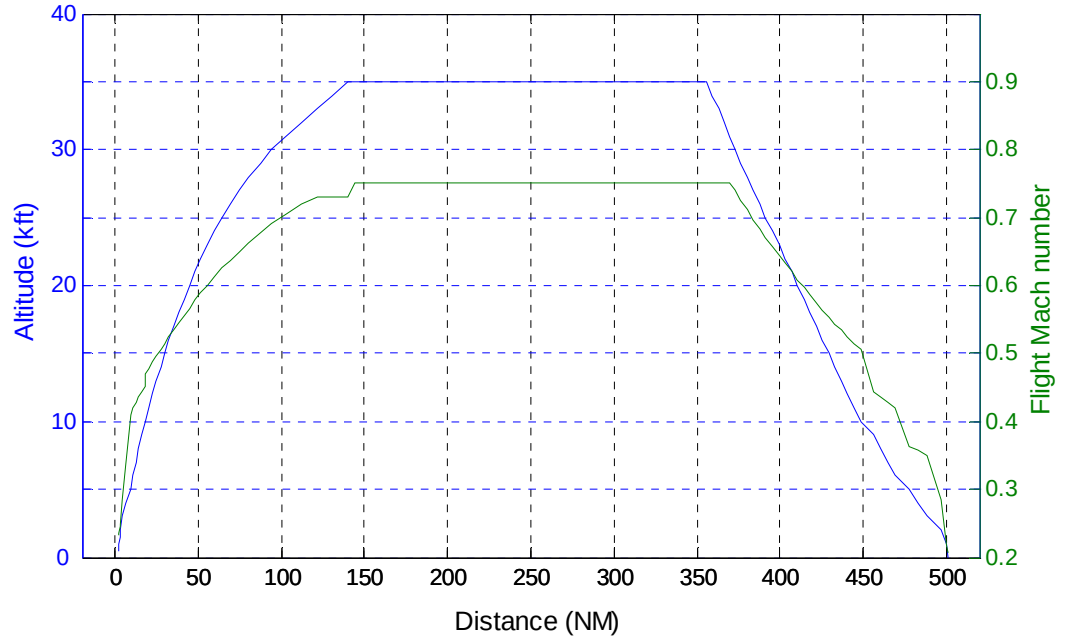

Figure 101: 500NM TERA baseline mission profile (Alt_{TOC} = 35kft)

3.1.4.4 Payload-range diagram

Figure 102 shows the payload-range diagram of the reference OR aircraft. It has only one diagonal line because the aircraft is designed to take-off with its maximum payload and maximum fuel load. Point A represents the mission flown at maximum fuel and maximum payload. Point B represents the mission flown at maximum fuel

load and no payload. Both missions were simulated using the reference mission profile defined in section 3.1.3 but allowing the optimum selection of the cruise altitude and not including contingency fuel. The profiles of missions A and B are presented in Appendix J.

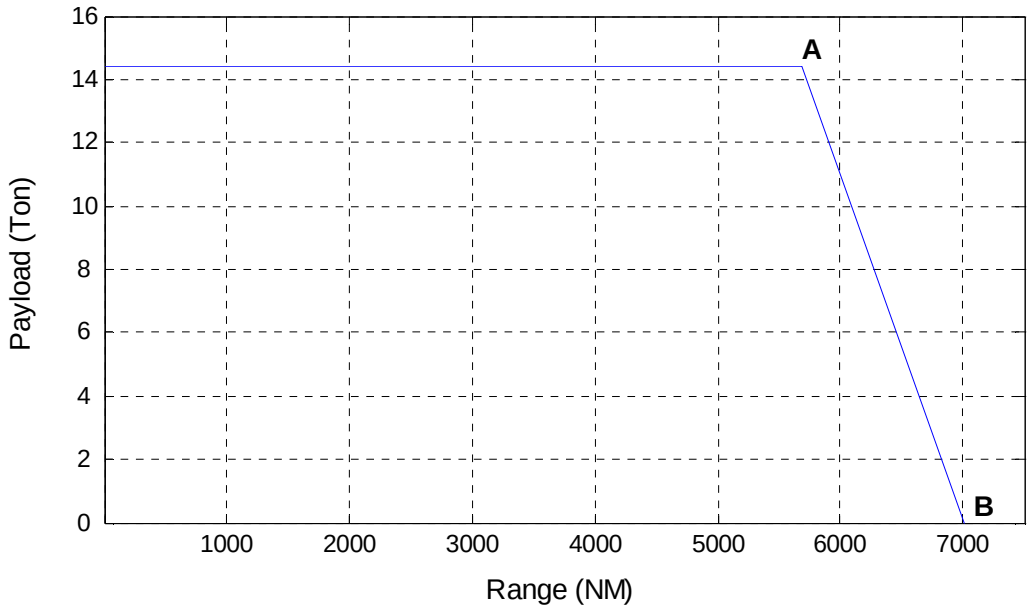

Figure 102: Reference aircraft payload-range diagram (baseline GOR engine)

3.2 GOR assessments

First the baseline GOR is defined, and then the engine control assessments and design space exploration are presented.

3.2.1 Baseline GOR engine definition

The following paragraphs describe the preliminary design definition of the baseline GOR. The schematic of the engine performance model of the GOR is presented in section 2.2.4. This engine was sized to meet the engine performance requirements described in section 3.1.2.

3.2.1.1 Core definition

Single stages HPT and IPT were chosen for the baseline GOR. This sets the maximum achievable compressors pressure ratio. Table 11 summarises the choices of PR and NbStages for compressors and turbines (expressed at TOC: Alt = 35 kft, M_0 = 0.73 and dISA = 28K).

Component	TOC PR	NbStages
IPC	7	6
HPC	6.5	6
HPT	-	1
IPT	-	1
LPT	-	3
Nozzle	1.3	-

Table 11: Baseline GOR core components PR and NbStages choices

The overall compressors pressure ratio (OPR) is 45.5 and the optimum TOC TET was estimated to be 1725 K (following the procedure described in Ref. 21 and discussions with experts from OEMs).

The nozzle pressure ratio (NPR) is a design parameter in an OR. It sets the pressure ratio across the LPT and consequently its extracted power. A NPR of 1.3 was chosen to maximise the LPT power extraction while ensuring positive core thrust for the lowest thrust cruise point (required to cover nacelle vent needs).

The reference GOR engine has a 3 stage LPT. Ref. 134 indicates that an LPT with 2 stages can also satisfy the GOR engine requirements but the 3 stages design offers a higher isentropic efficiency.

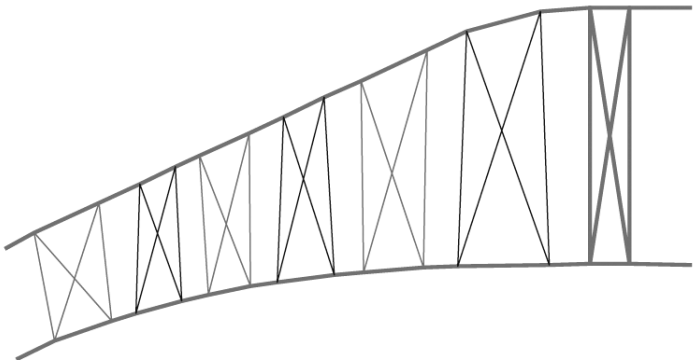

Figure 103: 3 stage LPT gas path [Ref. 134]

The DP efficiencies for the turbomachinery components of the GOR, reflecting a year 2020 level of technology, are presented in Table 12. $\eta_{is\ LPT}$ was calculated using the methodology presented in section 2.2.3.1.1. The isentropic efficiency of the rest of the components was estimated by industrial experts.

Component	Isentropic Efficiency (-)
IPC	0.87
HPC	0.87
HPT	0.9
IPT	0.9
LPT	0.925

Table 12: Efficiency of baseline GOR turbomachinery components

Table 13 presents the estimated pressure losses in the baseline GOR ducts reflecting a year 2020 level of technology.

Component	Pressure Loss (%)
Burner	4
IPC - HPC	0.75
IPT – LPT	0.75
Nozzle Duct	2

Table 13: Baseline GOR pressure losses

Note that the nozzle duct of the GOR engine has the same length as the CRP module (see Figure 104) and the shafts that drive the propellers pass through this duct. Consequently, relatively high pressure losses are expected.

The burner is an annular design and its estimated efficiency is 99%.

3.2.1.2 Secondary Air System

The SAS of the baseline GOR engine was designed to satisfy its cooling and sealing requirements. The description of the SAS is omitted due to non disclosure agreements.

3.2.1.3 Propellers

The diameter of the two propellers of the baseline GOR is 14 ft (4.26 m). Consequently the clipping of this propeller design is 0%.

$$\text{Clipping} = 100\frac{D_1 - D_2}{D_1 - D_h} \qquad \text{[Eq. 180]}$$

$N_1 = -N_2 = 860$ rpm were selected at DP so that the propellers helical tip Mach numbers are lower than 0.88 at DP.

The hub diameter of both propellers is 1.6 m.

The spacing between the roots of the propellers is 1.06 m (0.25 D).

DP η_{NET} of each propeller was calculated using the methodology presented in section 2.2.3.2.5. DP $\eta_{NET\ CRP}$ is approximately 0.86.

The baseline CRP has 12 blades in the forward propeller and 9 blades in the rear propeller. Note that the power loading of the forward propeller is higher than the power loading of the rear propeller (see section 3.2.1.4). The number of blades was selected in order to have approximately equal power loading per blade in both propellers.

3.2.1.4 Gearbox

Figure 104 shows the arrangement and connections of the DPGB. The carrier is connected to the forward propeller and the ring to the rear propeller. This

configuration is adopted for all the studied GOR engines. Eq. 181 defines the TR_{CRP}[74].

$$TR_{CRP} = Q_1 / Q_2 \quad \text{[Eq. 181]}$$

Note that the specific connection of the DPGB with the CRP selected for the GOR results in $TR_{CRP} = TR_{DPGB}$ (TR_{DPGB} defined in Eq. 156). Theoretically, TR_{DPGB} can vary between 1 and 2 (refer to section 2.2.3.4.5), and consequently $Q_1 \geq Q_2$ for all the studied GOR engines.

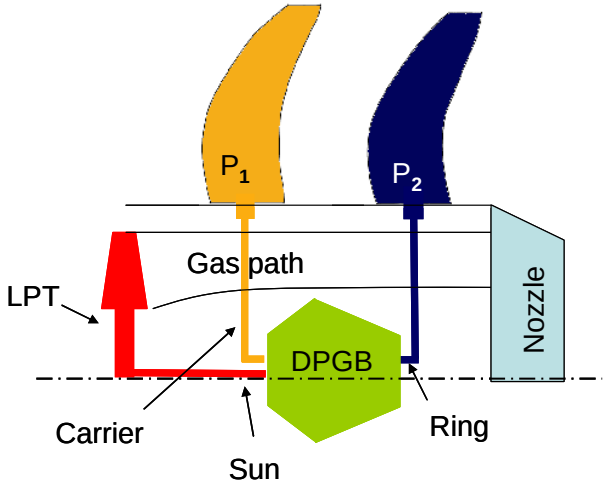

Figure 104: DPGB arrangement

TR_{DPGB} is 1.33. This value was selected in order to obtain the reported DP N_{LPT} [Ref. 134] for the selected DP N_1 and N_2.

DP $\eta_{mech\ DPGB}$ = 99% (refer to section 2.2.3.4.4).

3.2.1.5 Gearbox air cooling system

The air cooling system of the DPGB is described in section 2.2.3.4.3. $\eta_{is\ Blower}$ = 0.88, the heat exchanger and duct pressure losses are 6% and the exit area is 65 cm^2. The blower is activated for $M_0 < 0.35$ and it consumes 0.25% of the HP spool power. For $M_0 > 0.35$, the blower is not used as the ram-compression provides the required air mass flow rate. Table 14 shows the power consumed by the blower and the mass flow rate of air through the cooling system at different altitudes and flight speeds at ISA +10 conditions.

[74] This definition results in $TR_{CRP} = TR_{CRT}$ for the DDOR engine.

Alt (m)	M_0	Engine power setting	Blower power (kW)	Air mass flow rate (kg/s)
0	0	Take-off	27.4	1.25
500	0.25	Take-off	27.0	1.31
1200	0.34	Climb	26.1	1.31
1800	0.42	Climb	0	0.63
10668	0.73	Climb	0	0.46

Table 14: DPGB air cooling system operation

3.2.1.6 Auxiliary power extraction

The mechanical power required by the aircraft (250 hp at all operating regimes) is extracted from the HP shaft. This is done in order to have a unique auxiliary gearbox covering the power extraction and starting requirements.

3.2.1.7 Components maps

Appendix K shows the IPC, HPC, HPT, IPT, LPT and propeller maps for the baseline GOR. The IPC, HPC, HPT and IPT maps of the GOR are those used for the 3 spool engine models in NEWAC.

The LPT map corresponds to a 3-stage high speed and highly loaded LPT, designed for a geared turbofan (available in Ref. 235). This is the latest map corresponding to a high speed 3-stage turbine of a geared engine for the A320/B737 class, found in the public domain.

The map presented Ref. 203 (Figure 82) is used for the DPGB.

The SR-7 propeller map (available in Ref. 169[75]) is used for both propellers because it is the latest map of an advanced high speed propeller available in the public domain. The difference in DP power loading (L_P) between SR-7 and the forward propeller of the baseline GOR is ~10%. The critical helical Mach number ($M^*_{h0.75}$) of the propellers is 0.89 and the compressibility correction factor ($Slope_{corrM}$) is 0.4 as suggested in Ref. 139.

3.2.1.8 Technology curves

The DP efficiencies of the LPT and propellers were calculated using the methodologies described in sections 2.2.3.1.1 and 2.2.3.2.5 respectively.

The mean radii of the LPT stages were obtained from Ref. 134.

The technology factor used in the technology curve of the propellers (K_{LP}) is 1.56. The CRP efficiency obtained with K_{LP} = 1.56 is approximately 4% lower than the

[75] Two SR-7 propellers are reported in the open literature: SR-7A and SR-7L. The geometrical designs of both propellers are the same and therefore they have the same performance [Ref. 31]. SR-7L is the metalic propeller used for wind tunnel tests, and SR-7A is the composite propeller used for the flight tests [Ref. 31].

CRP efficiency obtained using K_{LP} = 1 (note that the propeller efficiency decreases as K_{LP} increases, see Eq. 58). K_{LP} was selected to reflect the reduction in propeller efficiency produced by low noise blade designs.

3.2.1.9 Baseline for noise studies

The noise module was designed to predict the noise of CRPs with clippings between 10 and 20%. The baseline GOR and DDOR used for these assessments are defined with equal propeller diameters (0% clipping) and it is not possible to obtain the noise levels for the baseline engines. Consequently, the noise trends are presented for various levels of clipping (explicitly mentioned in the text). In these cases, all the engine preliminary design parameters are equal to those of the baseline engine except for the diameter of the rear propeller.

3.2.2 Engine control assessments

The rotational speed of the propellers of a GOR engine can be independently controlled (see section 2.2.4). This can be used to implement noise, emissions or fuel burn reduction control strategies. The potential benefits of flexible propeller control were not exploited in the most recent GOR demonstrators, the Allison 578-DX, and the Ivchenko Progress D-236, which were operated at constant N_1 and N_2 [Ref. 236 and Ref. 46].

This section presents the influence of the control of the CRP on fuel burn, noise and emissions for the baseline GOR. Each flight phase is analysed independently.

3.2.2.1 Climb

Figure 105 presents the variation of Fn and SFC with respect to Alt and M_0 for an average climb TET, ISA conditions and $N_1 = -N_2 = n_{1Des}$ (reference point to express variations: Alt = 35 kft and M_0 = 0.75). The trends are similar to those of a turbofan. The relative variation of Fn, SFC and the aircraft performance characteristics define the optimum fuel burn climb speeds and the trade-off between climb fuel and time. Above 10kft of altitude, a constant CAS of 260kt is used for the assessments because it minimises the fuel consumption of the reference mission (see section 3.1.3).

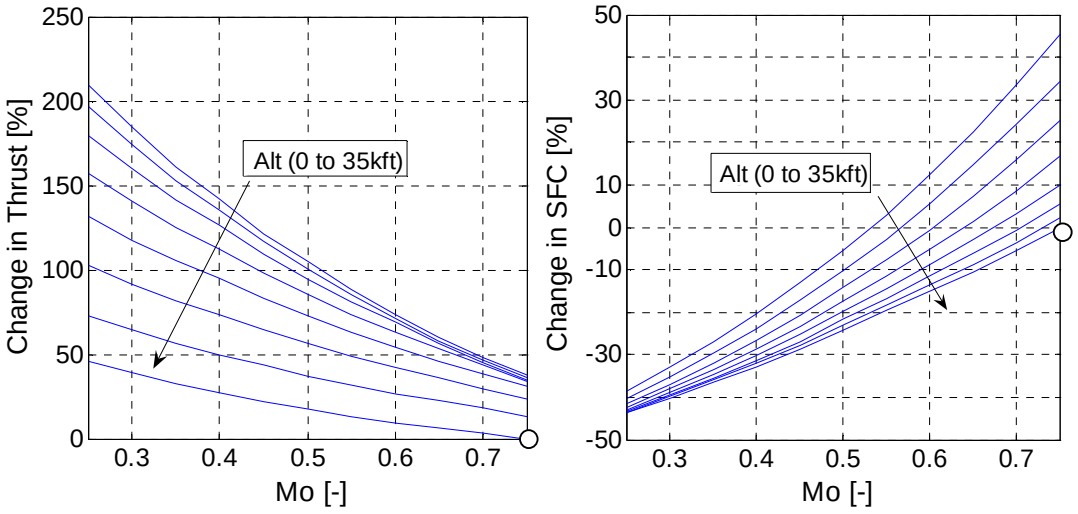

Figure 105: Fn and SFC vs. M_0 and Alt (dISA = 0, TET = 1640K and $N_1 = -N_2 = N_{1Des}$)

The variation of SFC with respect to N_1 and N_2 is different for every climb condition, and it follows the same trends as the cruise, take-off and descent which are presented below.

3.2.2.2 Cruise

The cruise phase is done at $M_0 = 0.75$. The thrust requirement decreases along the cruise as the aircraft becomes lighter. The reference aircraft at full load requires 22.4 kN of thrust at the start of cruise and 17kN at cruise end. Figure 106a presents the change in SFC with respect to Fn and N_1 (with $N_1 = -N_2$ for simplicity). Note that the Fn vs. SFC curve of the GOR is different from the traditional "U" shape curve for a turbofan. This is because the variations in η_{Prop} of a CROR are small and therefore the changes in η_{Ov} are dominated by the changes in η_{Th}.

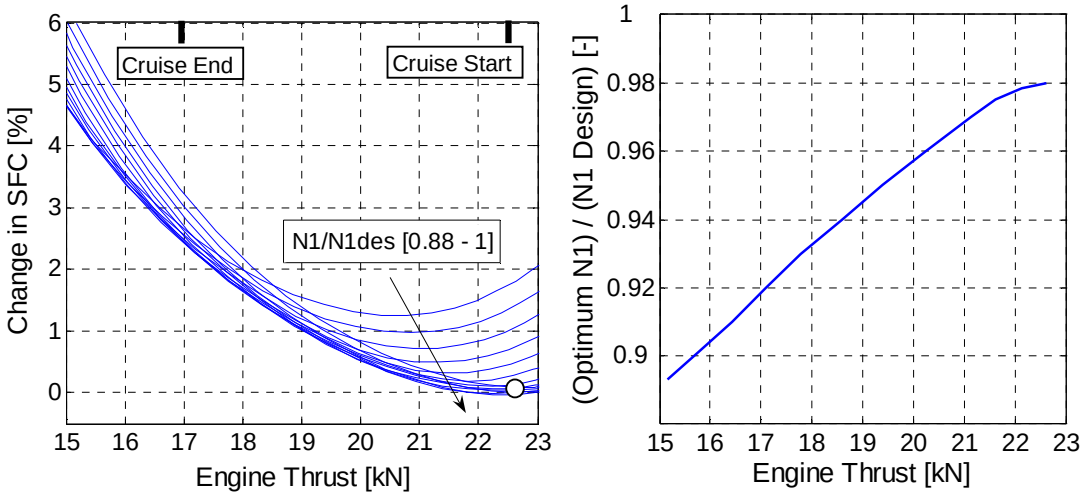

Figure 106a: SFC vs. Fn (cruise) **b: Optimum cruise N_1 vs. Fn**

(dISA = 0, Alt = 35kft, $M_0 = 0.75$, $N_1 = -N_2$)

The results shown in Figure 106a suggest that a fuel saving of approximately 1-2% can be achieved by using the optimum propeller rotational speeds as opposed to constant rotational speeds. Figure 106b presents an optimum N_1 schedule to minimise fuel consumption for this flight condition (with $N_1 = -N_2$). It can be seen that low rotational speeds minimise SFC for low power settings and high rotational speeds minimise SFC for high power settings.

The speed ratio of the propellers ($nR = -N_1/N_2$) can also be varied and an optimum bi-dimensional schedule of N_1 and N_2 can be produced. Figure 107 and Figure 108 show the change in SFC with N_1 and N_2 for the thrust requirements at the start and end of cruise respectively.

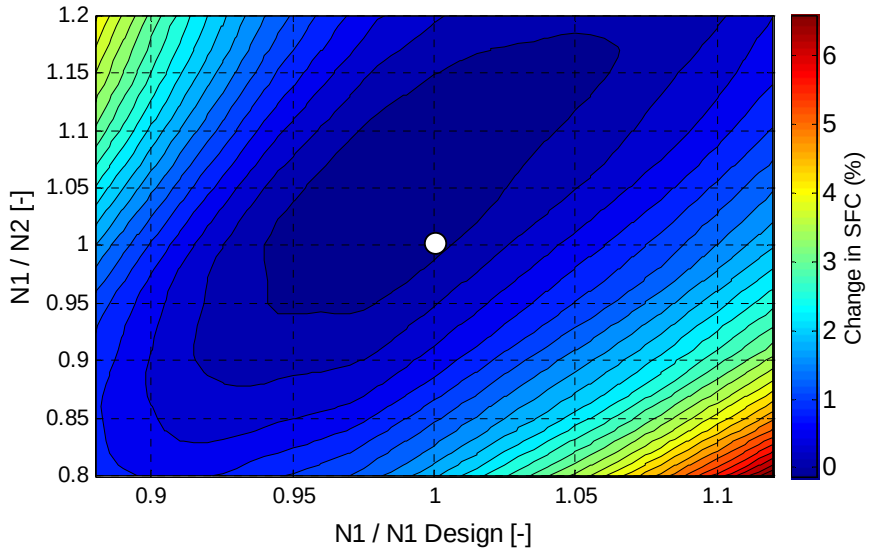

Figure 107: SFC vs. N_1 and nR (Fn = 22.4 kN dISA = 0, Alt = 35kft, M_0 = 0.75)

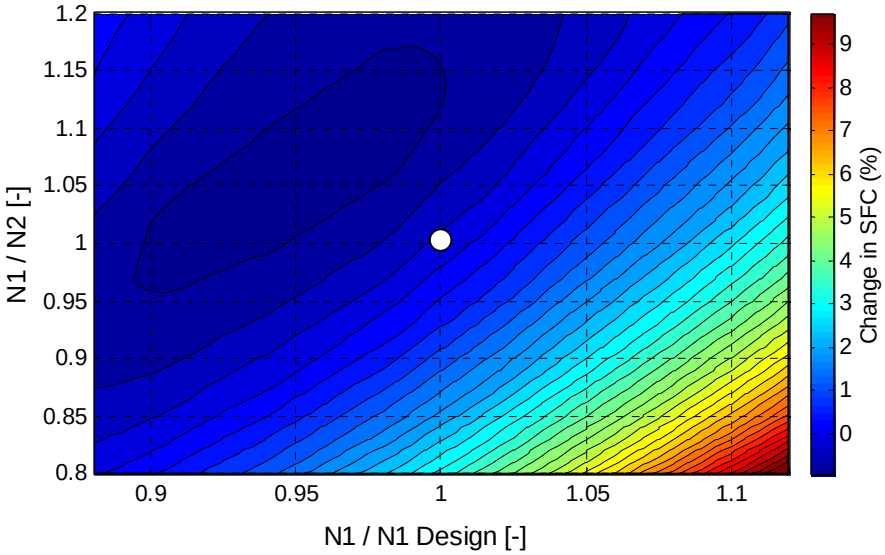

Figure 108: SFC vs. N_1 and nR (Fn = 17 kN dISA = 0, Alt = 35kft, M_0 = 0.75)

The shapes of the contours of the two previously presented plots are mainly dominated by the changes in $\eta_{NET\ CRP}$ and $\eta_{is\ LPT}$ as it can be seen in Figure 109. The variations in $\eta_{NET\ CRP}$ and $\eta_{is\ LPT}$ are different for different engine designs, and consequently different GOR designs have different minimum fuel control strategies. In order to do a fair comparison between the fuel consumption of different engine designs they should be operated at their optimum control speeds. In the same way, in an optimisation process, both the design and control should be optimised simultaneously. This process is very computationally expensive and for this reason the reference minimum SFC control strategy was used for all the studied engine designs.

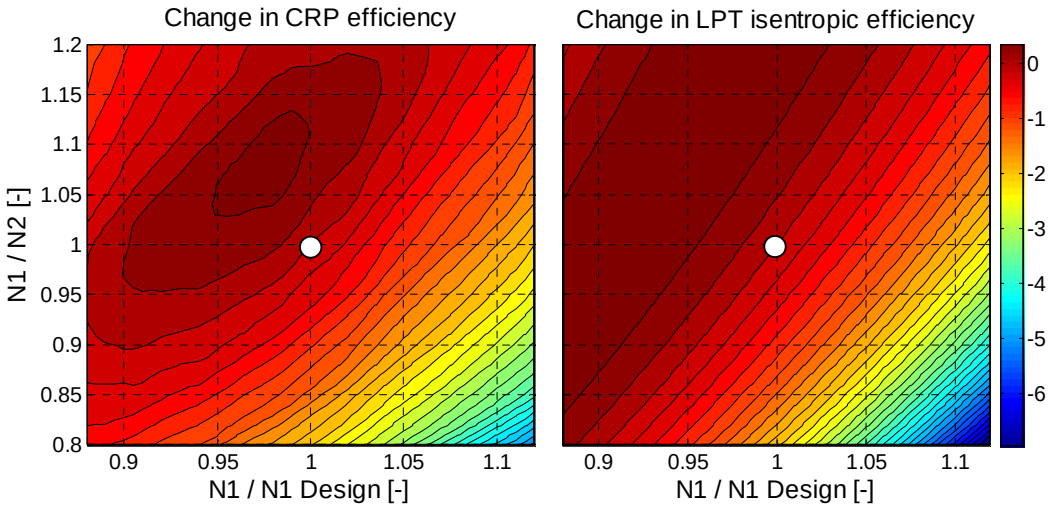

Figure 109: $\eta_{NET\ CRP}$ and $\eta_{is\ LPT}$ vs. N_1 and nR (Fn=17 kN, dISA=0, Alt=35kft, M_0 =0.75)

Figure 110 shows the change in SFC with respect to N_1 and N_2 for an engine design with 20% propeller clipping (radically different from the baseline). The red dot is located in the minimum SFC point for the baseline engine. It can be seen that the iso-SFC contours and the minimum SFC speeds of the 20% clipped GOR and the baseline GOR are different. Despite these differences, the use of the reference optimum control as opposed to its customised optimum control results in a 0.1% SFC penalty. This suggests that the use of the reference control strategy is a valid simplification to enable the comparison of different engine designs.

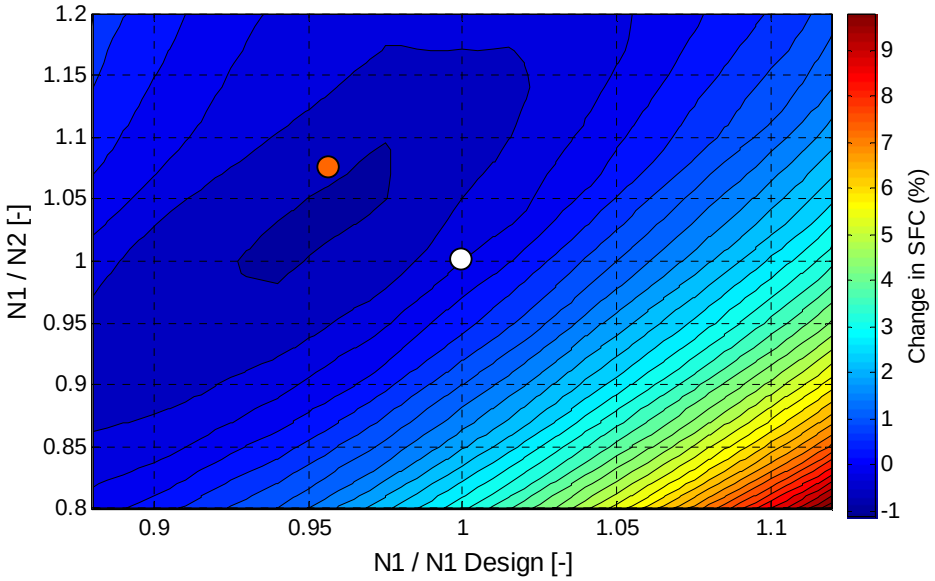

Figure 110: SFC vs. N1 and nR (Fn = 17 kN dISA = 0, Alt = 35kft, M0 = 0.75) (Engine design with 20% clipping)

3.2.2.3 Descent

Figure 111 presents the change in SFC for a mid descent point with respect to N_1 and N_2. The reference point used to express variations is $N_1 = N_{1Des}$ and $N_1 = -N_2$ (as in the previous figures). In consistence with the cruise trends, the minimum SFC is achieved at low rotational speeds. Although the changes in SFC with N_1 and N_2 are higher than for cruise (~20%), the potential mission fuel savings offered by an optimised descent control strategy are of the same order of magnitude than for cruise. This is because the thrust levels at descent are considerably lower than at cruise and the fuel consumption of the descent is relatively a small portion of the mission fuel burn (~10% for the reference mission).

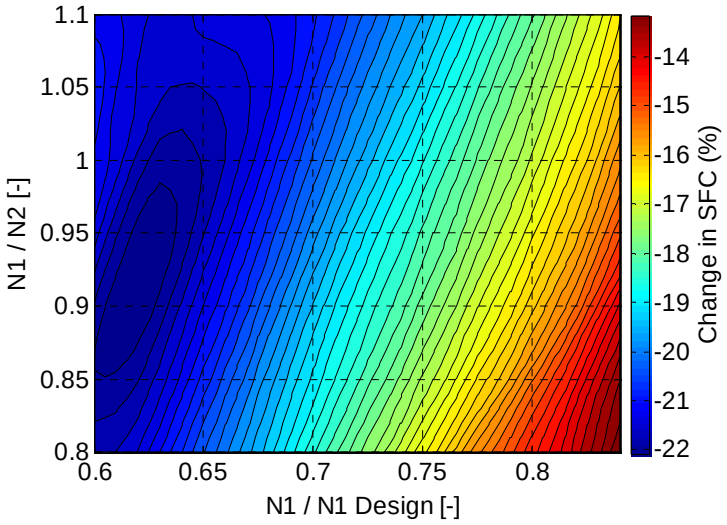

Figure 111: SFC vs. N_1 and nR @ mid descent point (Fn=3kN, dISA=0, Alt=17 kft, M_0=0.57)

3.2.2.4 Landing and take-off cycle

The control strategy used along the LTO cycle has an impact on the LTO fuel consumption as well as on the certification noise and emissions. The take-off control strategy has an impact on the fuel burn even outside the LTO cycle because the DPGB is designed at take-off.

3.2.2.4.1 Take-off

Figure 112 presents the variation in SFC with respect to N_1 and nR for a fixed take-off thrust (M_0 = 0.2, Alt = 0, dISA = 0, Fn = 107 kN). It is dominated by the changes in $\eta_{NET\ CRP}$ and $\eta_{is\ LPT}$. Note that compressibility effects on the propellers are relatively low at take-off flight speed.

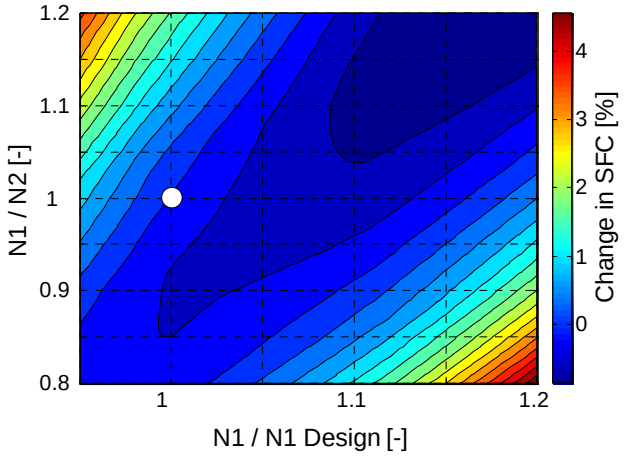

Figure 112: SFC vs. N_1 and nR at Take-off (M_0 = 0.2, Alt = 0, dISA = 0, Fn = 107 kN)

Figure 113 shows the change in DPGB and engine weight with respect to the N_1 and nR. The gearbox is designed at take-off, where the transmitted torques are at a maximum. In this study, the take-off thrust requirement was kept fixed and as N_1 and N_2 increase, Q_1, Q_2, Q_{LPT} and the weight of the DPGB decrease. The change in gearbox weight is not continuous because the gears are designed using standard teeth sizes which are not continuous.

For some rotational speeds in the central part of Figure 113, the DPGB weight increases as N_1 and/or N_2 increase. In these cases, the torques decrease and the size of the teeth of the gears decrease[76]. At the same time, the width of the gears has to be increased in order to satisfy the mechanical integrity criteria, resulting in a heavier DPGB design. It is recommended that further work is done on the mechanical preliminary design model of the DPGB so that it calculates the lightest feasible DPGB design as opposed to the minimum diameter DPGB design.

[76] The DPGB mechanical preliminary design model calculates a DPGB with the smallest feasible diameter.

Figure 114 shows the change in mission fuel burn with respect to the control of the CRP at take-off. It can be seen that it is dominated by the change in gearbox weight. Within the studied range (except for the central part of the chart), an increase in take-off propeller rotational speeds results in a reduction in mission fuel burn, and the impact of N_1 is approximately double the impact of N_2.

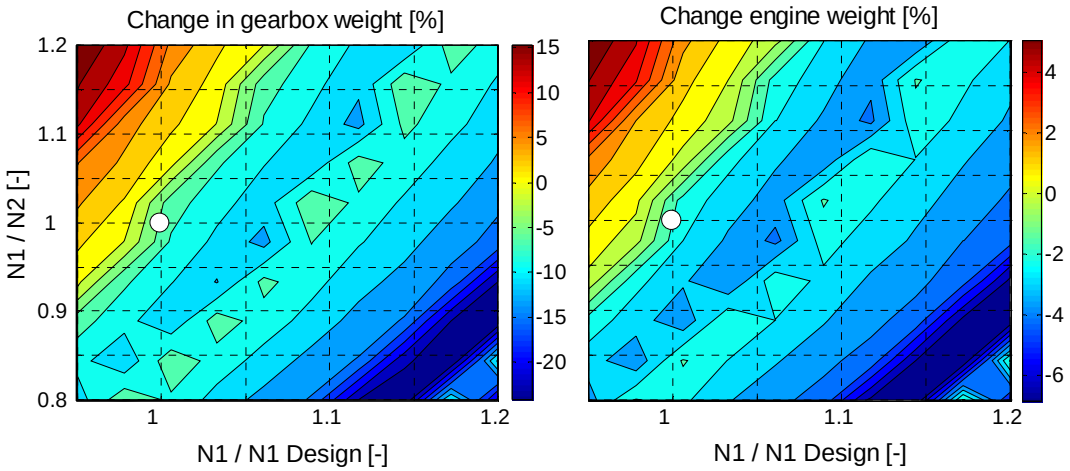

Figure 113: DPGB and engine weight vs. Take-off N_1 and nR

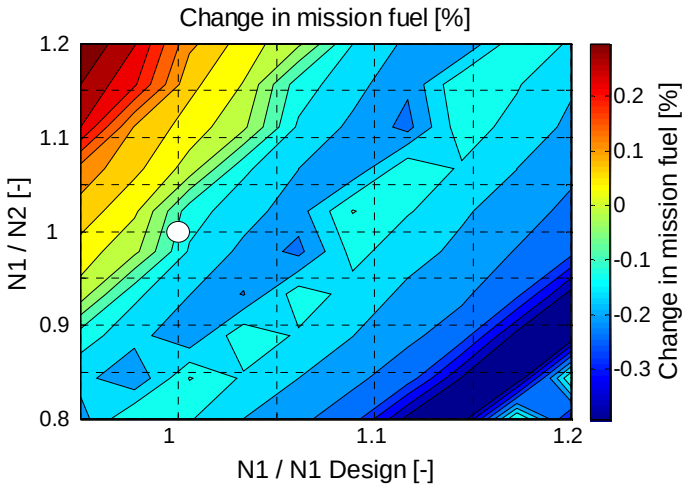

Figure 114: Mission fuel vs. Take-off N_1 and nR

However, as N_1 and N_2 increase, both the sideline and flyover noise levels increase as shown in Figure 115. Note that due to model limitations, the ranges of these figures are different to the ranges of previous figures. At sideline, N_2 dominates the noise level at relatively low N_1, and N_1 dominates the noise level at relatively high N_1. At flyover, N_1 dominates the noise level at relatively low N_1, and N_2 dominates the noise level at relatively high N_1.

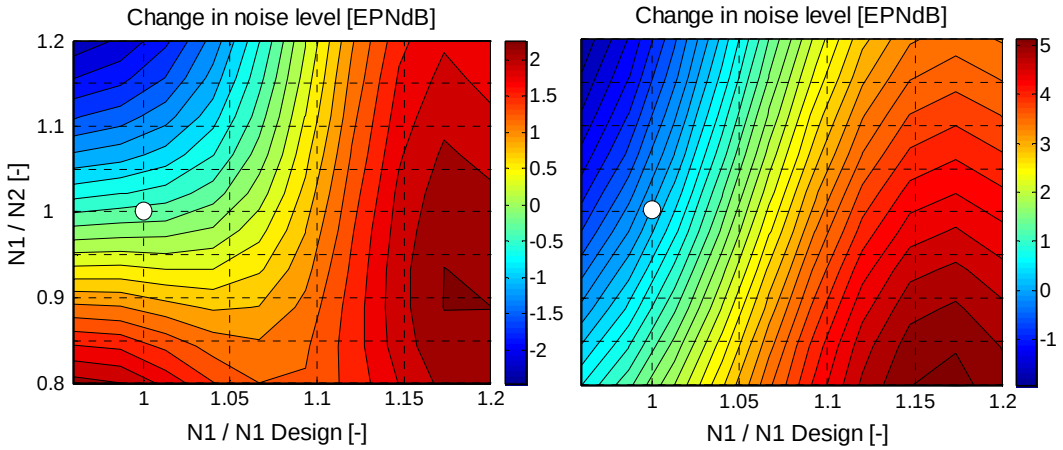

Figure 115a: Sideline Noise vs. N_1 and nR **b: Flyover Noise vs. N_1 and nR**

Figure 116 presents the variation in NOx emissions for the take-off point with respect to the control of the CRP. The variations in LTO NOx and CO_2 emissions follow the trends of SFC. The magnitudes of the variations of NOx are higher than those of SFC due to the required changes in TET. The total mission CO_2 emissions follow the mission fuel burn trends.

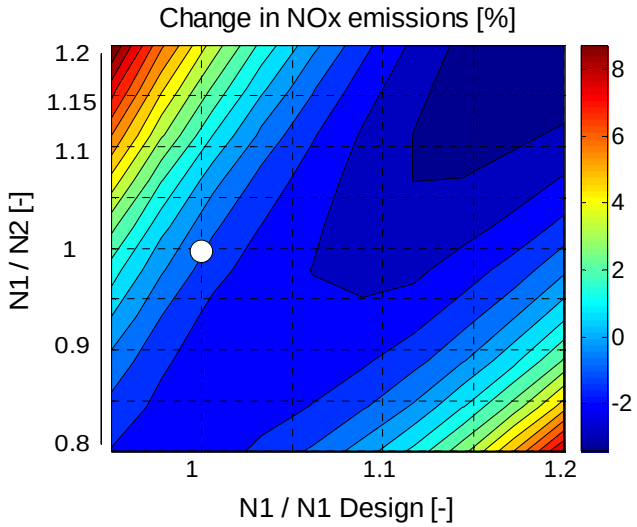

Figure 116: Take-off NOx emissions vs. N_1 and nR

The most fuel efficient take-off control strategies are at high rotational speeds because the DPGBs are lighter. N_1/N_{1Des} = 1.15 and nR = 0.85 result in a 20% reduction in DPGB weight and 0.4% reduction in mission fuel with respect to the reference control strategy, but requires 13 K higher take-off TET. N_1/N_{1Des} = 1.15 and nR = 0.85 results in a 4.5% penalty in LTO NOx emissions[77] and a noise penalty of approximately 2 EPNdB for sideline and 5 EPNdB for flyover with respect to the reference control.

[77] Note that take-off + climb-out NOx is approximately 65% of the LTO NOx.

Both sideline and flyover noise can be reduced by 2 EPNdB with respect to the reference control strategy by operating the CRP at relatively lower rotational speeds (N_1/N_{1Des} = 0.95 and nR = 1.2). This would be at a cost of 0.3% increase in mission fuel, 5.5% increase in LTO NOx emissions, and 10 K increase in take-off TET with respect to the reference control.

At take-off, the engine operates at the highest TET and thrust levels and therefore at the highest mechanical stresses. Consequently, mechanical integrity criteria of every component should be considered when optimising the take-off control.

3.2.2.4.2 Approach

Figure 117a shows the change in SFC of the baseline GOR with respect to N_1 and nR for the approach condition used for noise calculations. In consistence with the previously presented SFC trends, the minimum SFC is achieved at low rotational speeds.

Figure 117b presents the change in approach noise level with respect to N_1 and nR. Low rotational speeds appear to be more appropriate for the approach since they result in low fuel bun, emissions and noise. Note that for this engine design, the noise module did not allow the calculation below 0.97 N_{1Des} and for this reason it is not possible to establish the exact trade-offs between noise and fuel burn.

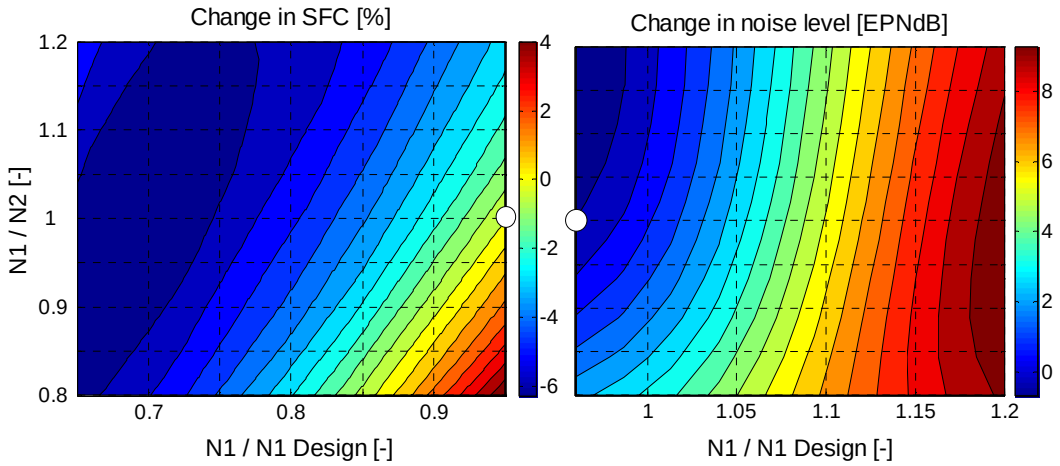

Figure 117a: Approach SFC vs. N_1 and nR b: Approach Noise vs. N_1 and nR (M_0 = 0.2 , alt = 120 m Thrust = 31 kN)

Figure 118 presents the changes in NOx emissions for the approach phase with respect to N_1 and nR. Low rotational speeds result in low emissions. It should be noted that the NOx emissions during the approach phase, are approximately 12% of the LTO NOx and therefore the impact of the approach control strategy on LTO NOx is expected to be lower than 1%.

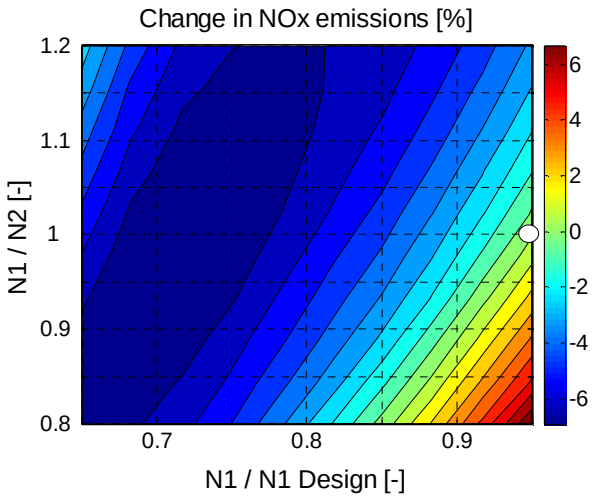

Figure 118 : Approach NOx emissions

3.2.3 Design space exploration

This section presents the influence of the following LP preliminary design variables on fuel burn, noise and emissions for a pusher GOR:

- IPC bleed mass flow rate used for cooling and noise reduction techniques
- Spacing between propellers
- Hub diameters of the propellers
- Nozzle pressure ratio at DP
- Number of blades of the forward and rear propellers
- DPGB torque ratio
- Number of stages of the LPT
- Diameter of the forward propeller
- Rotational speed of the forward propeller at DP (TOC)
- Propeller clipping
- Speed ratio of the propellers at DP (TOC)

The sensitivity of the mission fuel burn with respect to the DP efficiencies of compressors, turbines and DPGB is also presented.

The variations are expressed as differences relative to the baseline GOR. In each of the following studies, one or two design parameters are varied and all the rest are kept equal to those of the baseline GOR.

The previously presented minimum fuel burn control is used for the performance calculations of all the engine designs. The noise simulations at sideline and flyover are also performed at the minimum fuel burn propeller speeds. The noise simulations corresponding to approach are performed at N_1 = 1.1 N_{1Des} due to a limitation in the minimum rotational speed that the noise module can simulate. For clarity, the real propeller rotational speeds are shown on all the noise plots.

3.2.3.1 IPC bleed mass flow rate used for cooling and noise reduction techniques

One of the bleeds of the IPC is used to cool LP components such as the CRP pitch changing mechanisms and seals. This cooling flow is discharged to the atmosphere and does not contribute to the engine thrust. The bleed requirements may increase (with respect to the baseline value) due to higher cooling requirements or for CRP noise reduction techniques[78]. Figure 119a shows the change in mission fuel burn (Mission Fuel 1) and engine weight with respect to the extra IPC bleed requirement (expressed as a % of the IPC inlet mass flow rate). The mission fuel burn increases with the bleed mass flow rate, both because the engine weight and SFC increase. The changes in engine weight are mainly due to changes in the weight of the IPC, IPT, LPT (its inlet conditions are modified) and nacelle. Figure 119b shows the change in the mass of pollutants emitted during the ICAO LTO cycle with respect to the extra IPC bleed mass flow rate.

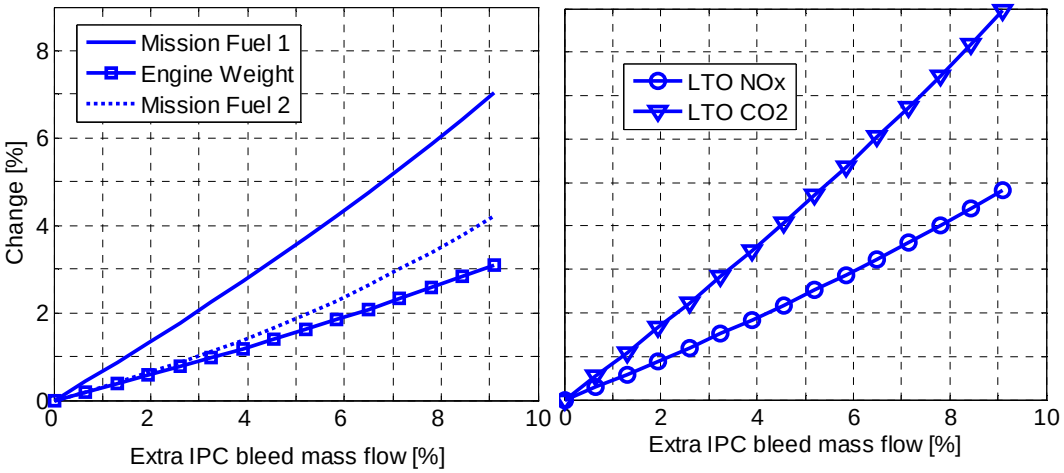

Figure 119 a: Mission fuel & eng. weight **b: ICAO LTO emissions vs. extra IPC bleed**

If the extra IPC bleed is only required during the LTO cycle to reduce the certification noise, the bleed mass flow rate could be reduced to the baseline value during the rest of the mission. The dotted line in Figure 119a (Mission Fuel 2) depicts the change in fuel burn that results of operating this bleed only during the LTO cycle. Although air is bled during a very small part of the mission, the fuel penalty is relatively large due to a heavier engine that operates far from its design conditions along the entire mission.

Ref. 237 presents the changes in installed noise levels of a GOR with respect to the amount of pylon blowing (work carried out under WP 2.3 of the DREAM project). The results provided in Ref. 237 together with the presented mission fuel

[78] One noise reduction technique for CRORs may be to blow air through the trailing edge of the pylon. This reduces the vorticity of the flow behind the pylon (which is ingested by the CRP) and reduces the noise of installed pusher CRPs [Ref. 237].

burn trends (Figure 119), provide the trade-off between fuel burn and noise. For example, a pylon blowing of 8% of the IPC inlet mass flow rate reduces the installed noise by approximately 5dB in all certification points [Ref. 237] at a cost of 3.5% or 6% increase in mission fuel burn (depending on the portion of the mission during which blowing is used).

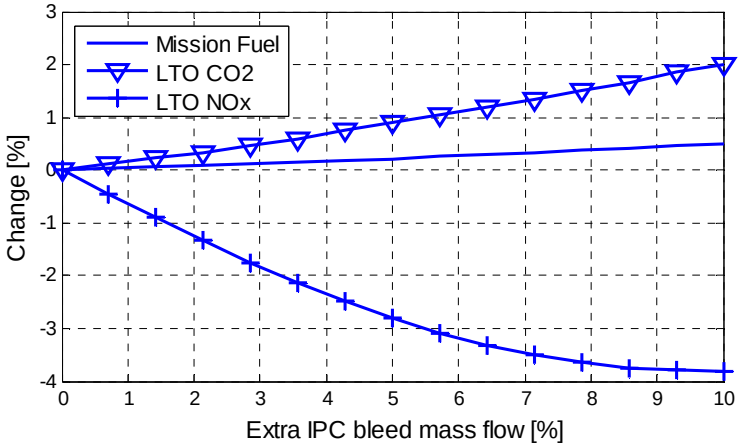

Figure 120: Effects of bleeding IPC air during the LTO cycle (baseline GOR)

If the extra bleed is only required during the LTO cycle, the core turbomachinery components could be sized without considering this bleed requirement. Figure 120 shows the impact of the extra IPC bleed mass flow rate (expressed as a % of the IPC inlet mass flow rate) on the mission fuel burn and ICAO LTO emissions for this design choice. The penalties in terms of fuel burn are low since the engine weight is not increased and it is operated far from its design running line only during the LTO cycle which is a relatively small part of the mission. As the extra bleed mass flow rate increases, CO_2 emissions increase since the fuel burnt is increased, but NOx emissions reduce since P3 reduces for this type of OD operation. As the extra bleed mass flow rate increases, take-off TET increases. 10% extra IPC bleed results in approximately 90 K increase in take-off TET and this may not be acceptable. A detailed evaluation of the impact of take-off TET on turbine cooling, components mechanical integrity and lifing is required to complete the trade-off studies of this specific bleed operation.

3.2.3.2 Spacing between propellers

The spacing between propellers is defined as the distance (in meters) between the roots of the blades of the forward propeller and roots of the blades of the rear propeller. Note that for a spacing of 0.65m the distance between the forward blade trailing edge and the rear blade leading edge is close to 0.15 m. This minimum space is needed to ensure that the blades of the two propellers do not touch each other at any possible blade pitch angle. The reference value used to express variations in this study is the minimum feasible spacing. The spacing between propellers has a relatively large impact on CRP noise levels as shown in Figure 121. Both for 10% and 20% clipped CRP designs, noise level reductions of the order of 6 EPNdB in the three certification points can be achieved by increasing the

spacing between the propellers to 1.35 m. The changes in approach noise of the 20% clipped are larger than for the 10% clipped design.

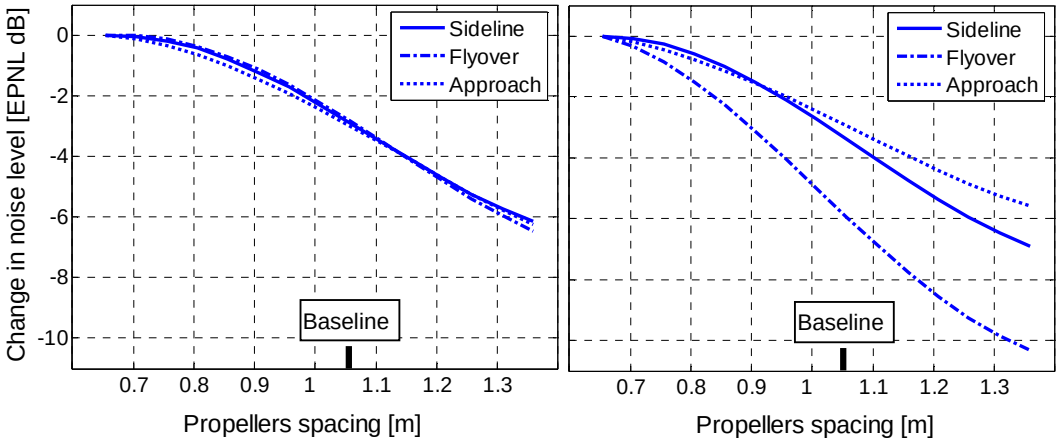

Figure 121a: Noise vs. prop. spacing (10% clipping) **b: (20% clipping)**

The spacing between the propellers has also an effect on the performance of the CRP. Close propellers are more efficient at DP mainly due to lower local mach numbers and a more uniform inlet flow to the rear blades. Figure 122 shows the impact of the spacing between the propellers on the mission fuel burn for 0%, 10% and 20% clipped CRP designs. In order to show only the difference caused by the spacing and not the differences caused by the clipping[79], the fuel burn of the minimum spacing design for each clipping was used as a reference. For clippings between 0 and 20%, the increase in spacing between propellers of 0.1 m results in a mission fuel burn penalty of ~0.07%.

The spacing between the propellers also impacts the size and weight of the output shafts of the gearbox, and the drag of the engine nacelle, but these differences are not accounted in the simulations.

Changes in LTO emissions are lower than 1% for CO_2, NOx and CO for the studied spacing range.

[79] The variations in fuel burn with respect to clipping for a fixed spacing are presented in section 3.2.3.7.2.

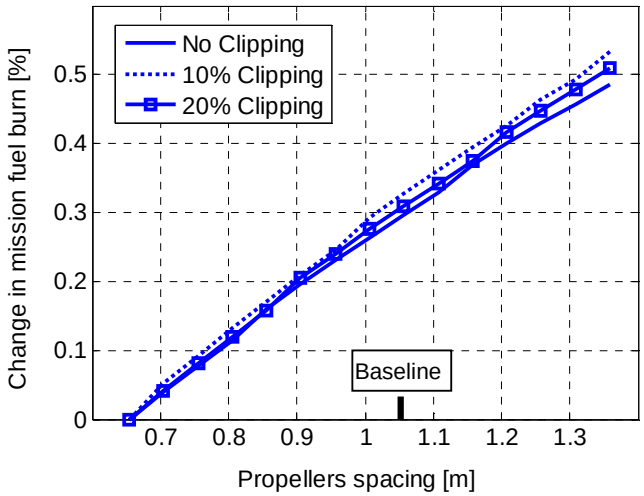

Figure 122: Mission fuel burn vs. spacing between propellers

3.2.3.3 Hub diameter of the propellers

Figure 123 presents the influence of the hub diameters of the propellers on mission fuel burn and engine weight (note that both propellers have the same hub diameter). As the hub diameter is increased, the propeller blades are smaller and consequently lighter[80], but their efficiency decreases due to an increase in power loading (L_P). The reduction in propeller efficiency with the increase in hub diameter has a larger impact on the mission fuel burn than the reduction of engine weight.

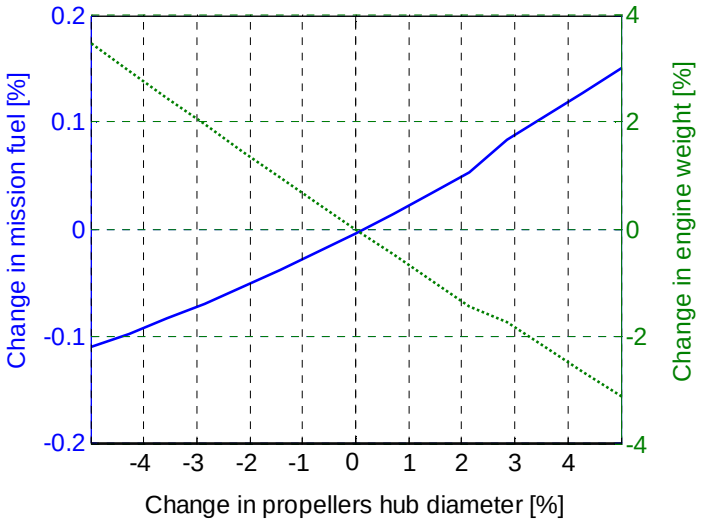

Figure 123: Mission fuel burn and engine weight vs. hub diameter of the propellers

[80] For example, a 5% increase in the hub diameter results in a 4 cm blade length reduction.

The changes in LTO emissions with respect to the hub diameter of the propellers are of the same order of magnitude as the changes in fuel burn. It is not possible to asses the changes in certification noise with respect to the hub diameter using TENOR.

It is expected that higher hub diameters would result in higher nacelle drag and higher fuel burn penalties than those shown in Figure 123. This effect is not considered in this study (refer to sections 3.1.1). For this reason only small changes in hub diameter were assessed. It is also relevant to mention that the diameter of the LPT was not changed with the hub diameter.

3.2.3.4 Nozzle pressure ratio

The DP NPR defines the pressure drop across the LPT and consequently the power of the propellers. Figure 124 shows the change in propeller thrust at DP (as a percentage of the overall engine thrust) with respect to DP NPR. Even for relatively high nozzle pressure ratios (~1.6), the propeller produces almost 90% of the overall engine thrust. Figure 124 also presents the change in DP $\eta_{NET\ CRP}$ and $\eta_{is\ LPT}$ with respect to DP NPR. As DP NPR increases, the power extracted in the turbine decreases and consequently the stage loading of the LPT ($\Delta h/U^2$) and the power loading of the propellers (L_P) decrease. This results in an increase in both components efficiencies. $\eta_{is\ LPT}$ reaches a maximum value at a NPR = 1.48 and it is constant for designs with lower loadings.

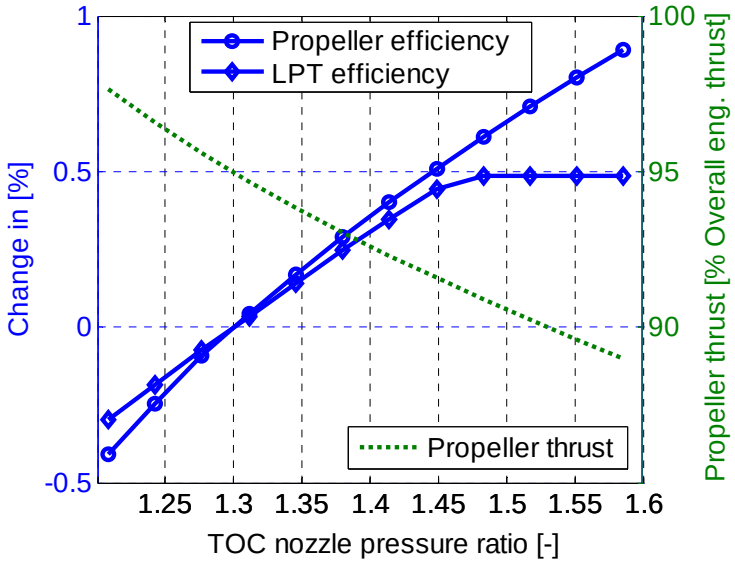

Figure 124: Propeller thrust, $\eta_{NET\ CRP}$ and $\eta_{is\ LPT}$ vs. NPR at DP

The increase in DP $\eta_{NET\ CRP}$ and $\eta_{is\ LPT}$ as well as the nozzle exit flow velocity produced by the increase in DP NPR, result in an increase in η_{Th} as presented in Figure 125. This figure also shows the variation in DP η_{Prop} caused by the change in DP NPR. As a consequence of the changes in η_{Th} and η_{Prop}, η_{Ov} has a parabolic shape with a maximum at NPR = 1.42.

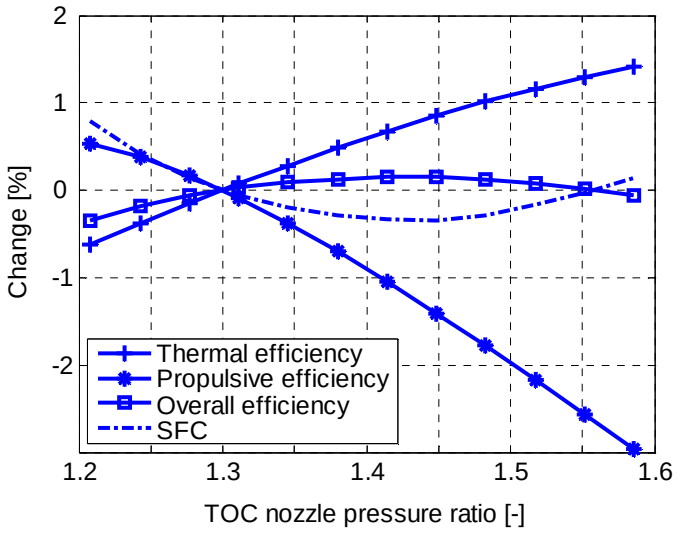

Figure 125: DP engine efficiencies and SFC vs. NPR

Figure 126 shows the change in mission fuel burn with respect to DP NPR. Changes in mission fuel burn are larger than those of SFC due to the change in engine weight. As DP NPR increases, the power extracted in the LPT decreases and the weight of the LPT and CRP decrease. The change in engine weight is the main reason why the minimum mission fuel DP NPR (~1.53) is higher than the minimum SFC DP NPR (1.42). A DP NPR of approximately 1.53 would result in a mission fuel saving of 1% with respect to the baseline DP NPT, but at a cost of higher jet noise.

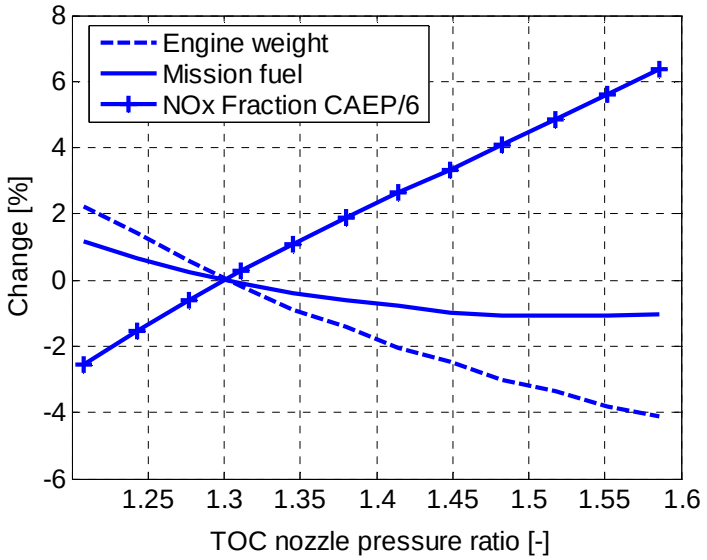

Figure 126: Mission fuel burn, engine weight and NOx emissions vs. DP NPR

Emissions increase as DP NPR increases since the reduction in η_{Prop} with NPR is larger for low flight speeds. Figure 126 shows the variation of fractional LTO NOx

with respect to CAEP/6 regulations. Variations in the other gaseous species are smaller than those of NOx.

It is not possible to asses the changes in certification noise with respect to NPR using TENOR (see section 2.6.3).

3.2.3.5 Number of blades of the forward and rear propellers

As the number of blades of the CRP increases, $\eta_{NET\ CRP}$ increases (as the blades are less loaded), SFC reduces, but the weight and mechanical complexity of the engine increase. Figure 127 presents the variation of DP SFC and engine weight with respect to the number of blades in the forward and rear propellers (from 8 to 16 blades).

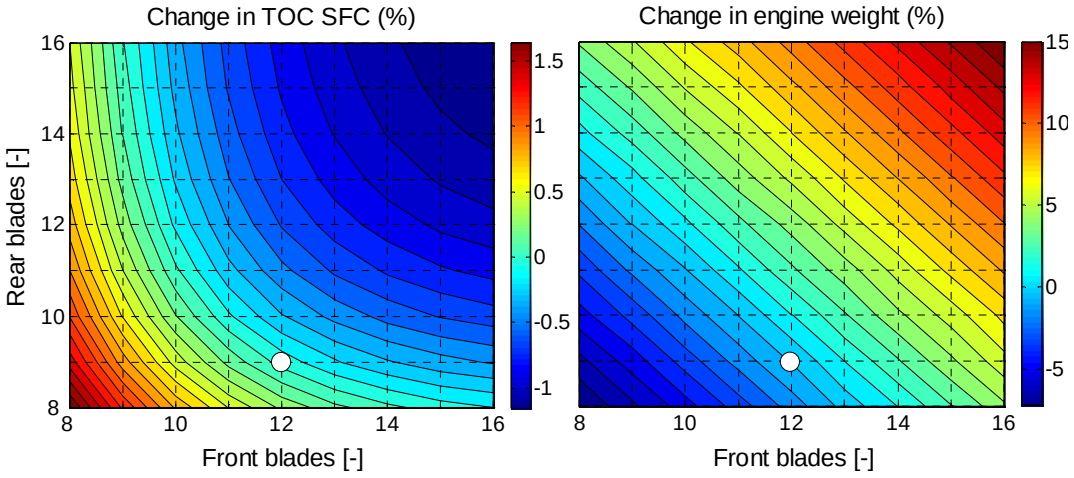

Figure 127a: DP SFC vs. N_b **b: engine weight vs. N_b**

Figure 128 presents the change in mission fuel burn with respect to the number of blades of the forward and rear propeller for a 0% clipped CRP design (baseline). The minimum fuel burn design has 14 blades in the forward and 13 blades in the rear propeller (denoted as 14x13). For propeller designs with more than 14 blades, the efficiency benefit of an extra blade is smaller than the associated weight penalty. Figure 129 presents the variation in mission fuel burn for 10% and 20% clipped CRP designs. Note that the contours of Figure 128 and Figure 129 do not have smooth shapes due to the discontinuous changes in DPGB weight. The optimum number of blades for the forward propeller does not change with the propeller clipping. The optimum number of blades of the rear propeller increases with clipping. This is because the penalty of an extra blade is reduced for clipped rear propeller (smaller and therefore lighter blades) and the efficiency improvement for an extra blade is higher (clipped propellers are more loaded).

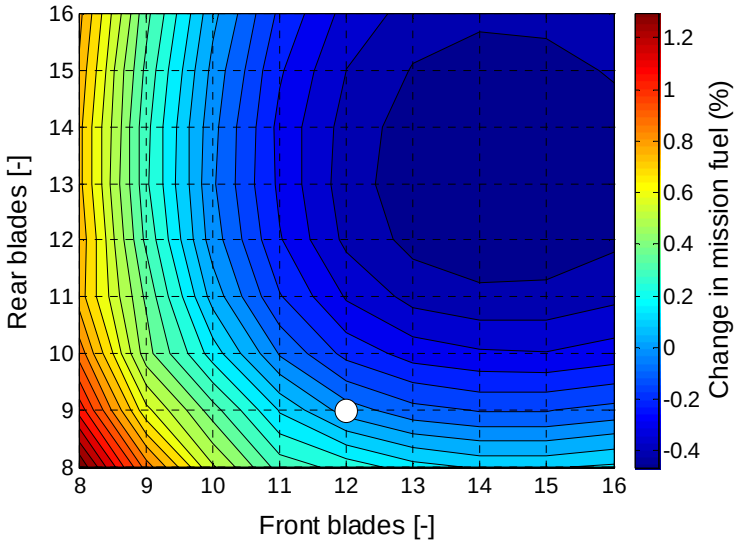

Figure 128: Mission fuel burn vs. N_b

The number of blades of the propellers has also an impact on the engine manufacturing and maintenance cost, as well as on its mechanical complexity. These elements have to be considered when selecting the number of blades of the CRP.

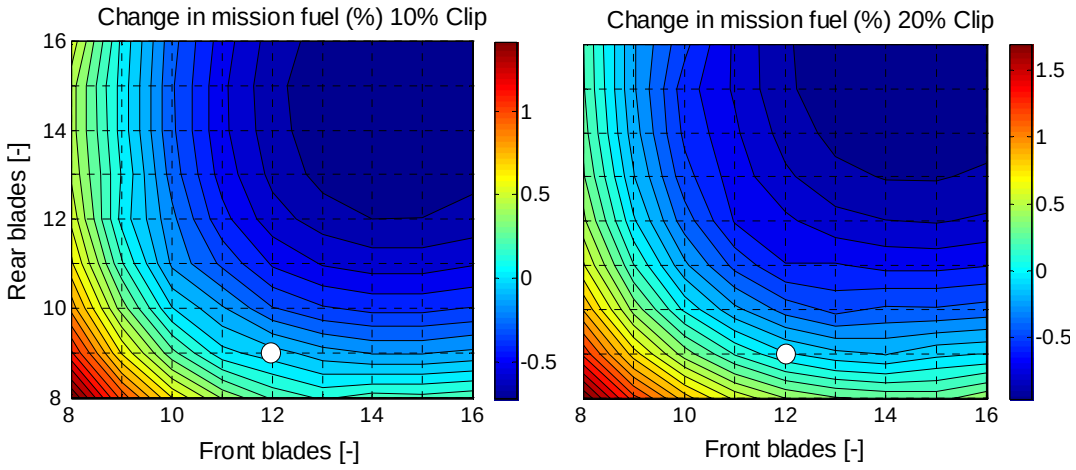

Figure 129: Mission fuel vs. N_b for clipped CRPs[81]

Changes in emissions follow the same trends as SFC and the variations are of the same order of magnitudes as those of the SFC.

Figure 130 and Figure 131 show the change in noise for the three certification points with respect to the number of blades of the propellers for a 10% clipped

[81] The white dots represent the engine designs which have 10% and 20% clipped CRP designs and the rest of the design parameters equal to the baseline GOR

CRP. Note that the noise module is capable of assessing propellers with 8 to 14 blades. Sideline and flyover noise are dominated by the number of blades of the rear propeller while approach noise is dominated by the number of blades of the forward propeller. These figures together with Figure 129a present the trade-off between mission fuel burn and certification noise for changes in N_b, for a 10% clipped CRP GOR. For example: the $N_{b1}xN_{b2}$ = 14x13 design (minimum fuel burn design) is 1.4 EPNdB louder in sideline, 1.7 EPNdB louder in flyover and 4 EPNdB louder in approach than the 8x8 design. The cost of using an 8x8 design (quieter) with respect to the 14x13 design is 2.2% in mission fuel burn.

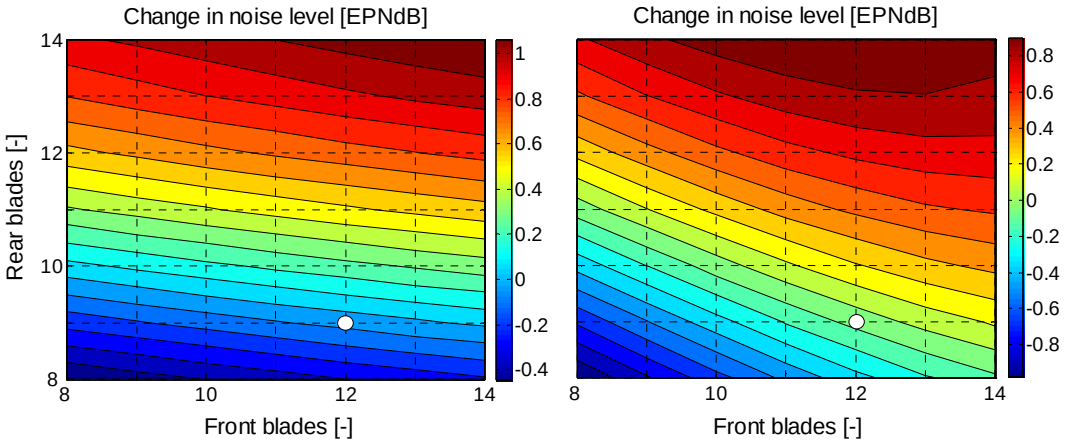

Figure 130a: Sideline noise vs. N_b (10% clipping) b: Flyover noise vs. N_b (10% clipping)

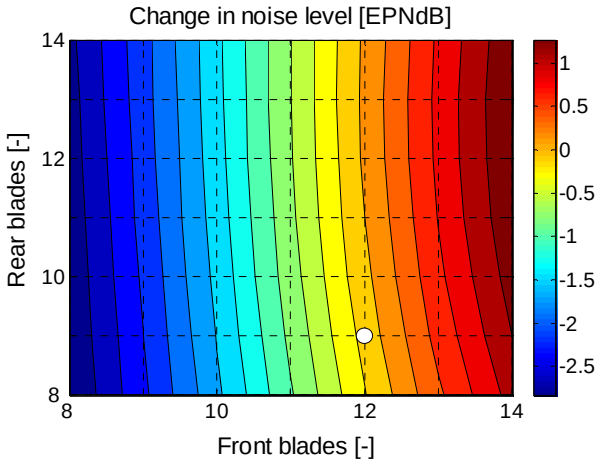

Figure 131: Approach noise vs. N_b (10% clipping)

Figure 132 and Figure 133 present the changes in noise with respect to the number of blades of the propellers for a 20% clipped CRP design. The number of blades in the rear propeller of a 20% clipped design has a larger impact on approach noise than for the 10% clipped design. These figures together with Figure 129b present the trade-off between mission fuel burn and certification noise for changes in N_b of a 20% clipped CRP GOR. For example: the 14x14 design (minimum fuel burn design within the range of the noise predictions) is 1.4 EPNdB louder in sideline,

1.2 EPNdB louder in flyover and 5 EPNdB louder in approach than the 8x8 design. The cost of using an 8x8 design (quieter) with respect to the 14x14 design is 2.6% in mission fuel burn.

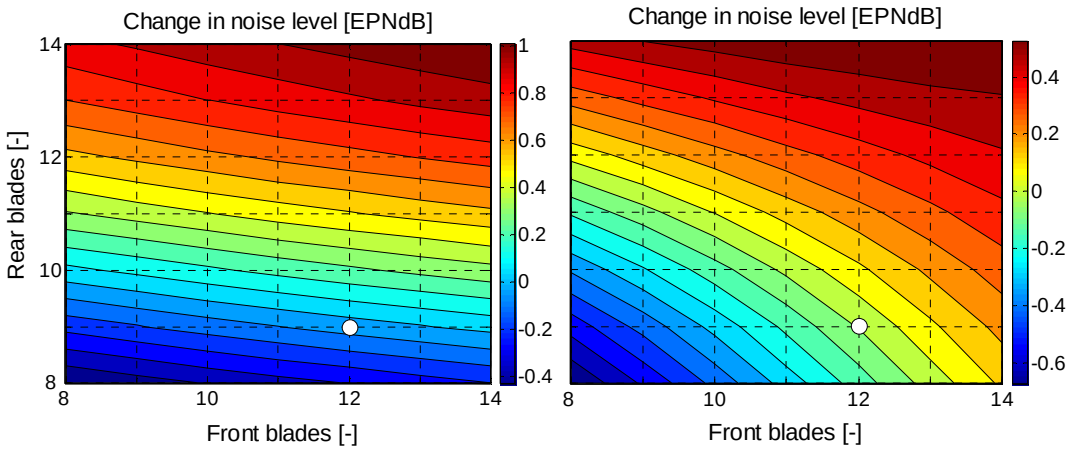

Figure 132a: Sideline noise vs. N_b (20% clipping) **b: Flyover noise vs. N_b (20% clipping)**

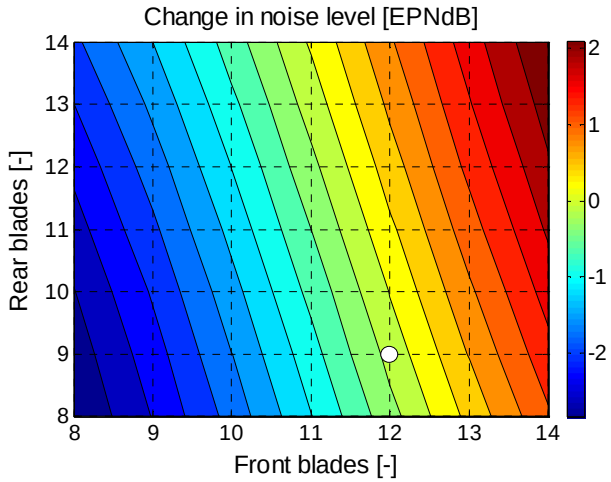

Figure 133: Approach noise vs. N_b (20% clipping)

Both for the 10% and 20% clipped CRP GORs, the noise increases with the number of blades in both propellers. This suggests that the increase in interaction noise produced by an additional blade is not compensated by the reduction in loading noise (even for highly clipped designs). These preliminary results need to be further investigated with an enhanced noise prediction module as suggested in section 2.6.3.

3.2.3.6 Gearbox torque ratio

This section describes the impact of TR_{DPGB} on mission fuel burn, certification noise and emissions for different propeller rotational speeds (using $N_1 = -N_2 = N$). TR_{DPGB} has a large influence on the speed ratios of the different shafts of the DPGB (refer

to section 2.2.3.4.2). Since N_1 and N_2 are fixed by the control of the CRP, TR_{DPGB} sets N_{LPT}. The study is first carried out for a 3 stages LPT design (baseline LPT design) and then for a 2 stages LPT design.

3.2.3.6.1 3 stages LPT (baseline GOR design)

Figure 134a shows the change of CRP efficiency due to the change in TR_{DPGB} for different values of DP N_1. Within the studied range of N_1, $\eta_{NET\ CRP}$ increases as TR_{DPGB} decreases. This is due to a better distribution of the power loading between the forward and rear propeller and a reduction of the CRP exit swirl. The order of magnitude of the change in DP $\eta_{NET\ CRP}$ with TR_{DPGB} for a fixed N_1 is consistent with the aerodynamic design predictions presented in Ref. 15.

Figure 134b presents the change in $\eta_{is\ LPT}$ due to the change in TR_{DPGB} for different values of DP N_1. For a given CRP rotational speed, $\eta_{is\ LPT}$ increases as the TR_{DPGB} decreases due to an increase in N_{LPT} (see Eq. 162) and a reduction in the extracted power (produced by the increase in $\eta_{NET\ CRP}$). A maximum achievable LPT isentropic efficiency was set to the LPT technology curve (see details in section 2.2.3.1.1) and it is the cause of the constant efficiency area in this figure.

The white regions in the figures of this analysis correspond to non feasible LPT designs (the boundaries between the feasible and non feasible regions on the figures do not appear to be smooth due to the limited number of simulated designs). The lower-right non feasible area corresponds to mechanically non feasible LPT designs due to high rotational speeds. The upper-left non feasible area corresponds to aerodynamically non feasible LPT designs due to low rotational speeds and consequently high aerodynamic loading. A DPGB design with TR_{DPGB} below 1.235 is not feasible because it would require a larger diameter than the hub diameter of the last stage of the LPT.

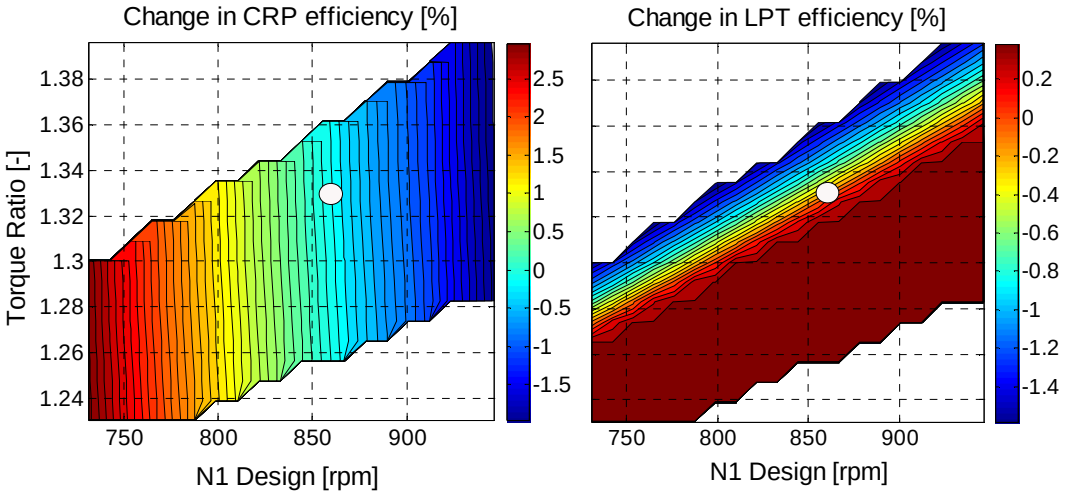

Figure 134a: $\eta_{NET\ CRP}$ vs. TR_{DPGB} and N_1 **b: $\eta_{is\ LPT}$ vs. TR_{DPGB} and N_1**

Figure 135 presents the variation in DPGB and engine weight with respect to TR_{DPGB} and N_1. The discontinuities in the contours correspond to changes in the size of the teeth of the gears (standard sizes used). The DPGB weight decreases as N_1 increases, but the engine weight is relatively unaffected due to the increase in LPT and CRP weight.

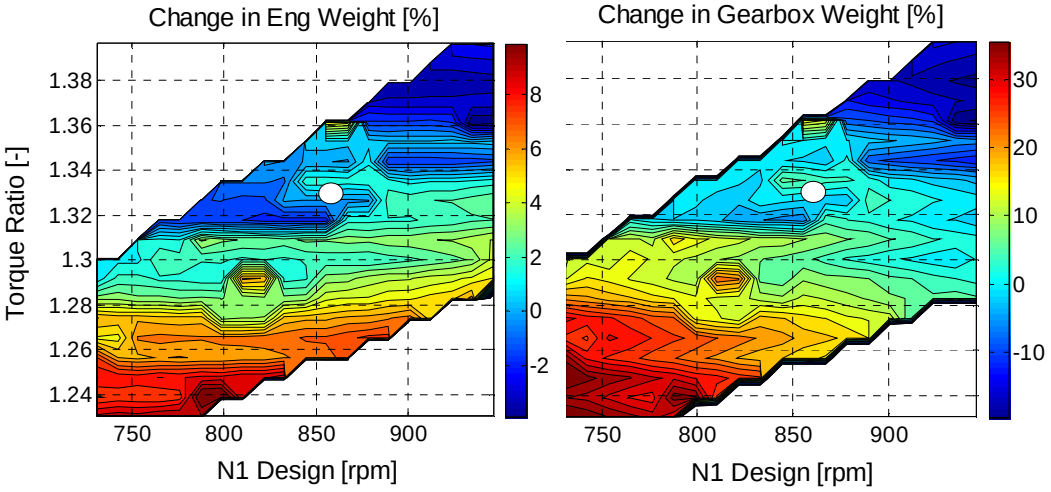

Figure 135a: Engine weight vs. TR_{DPGB} and N_1 **b: DPGB weight vs. TR_{DPGB} and N_1**

Figure 136 shows the change in mission fuel burn with respect to TR_{DPGB} and N_1. For any given rotational speed, the minimum fuel burn TR_{DPGB} coincides with the TR_{DPGB} at which the maximum $\eta_{is\ LPT}$ is achieved. A reduction in TR_{DPGB} below the optimum value, results in an increase in engine weight which has a larger influence on mission fuel burn than the increase in $\eta_{NET\ CRP}$ (no increase in $\eta_{is\ LPT}$).

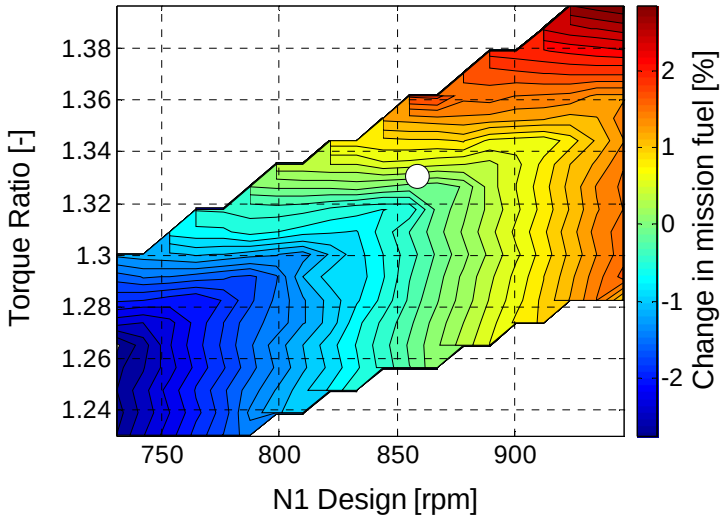

Figure 136: Mission fuel burn vs. TR_{DPGB} and N_1

Changes in certification emissions follow the same trends as SFC (which are dominated by changes in $\eta_{NET\ CRP}$ and $\eta_{is\ LPT}$) and the variations are of the same order of magnitudes as those of SFC.

It is not possible to asses the changes in certification noise with respect to TR_{DPGB} using TENOR (refer to section 2.6.1).

3.2.3.6.2 2 stages LPT

A 2 stage LPT can also satisfy the power extraction requirements of the GOR [Ref. 134]. The 2 stage LPT requires a higher rotational speed than the 3 stage LPT which is achieved with a lower TR_{DPGB} at a given N_1. Figure 137 shows the gas path geometry of a 2 stage LPT for the GOR application [Ref. 134]. The dimensions of this design [Ref. 134] were used in the technology curve to predict the DP $\eta_{is\ LPT}$ at different TR_{DPGB} and N_1. The design N_{LPT} of this LPT is obtained with TR_{DPGB} = 1.257 at N_1 = 860 rpm (baseline value).

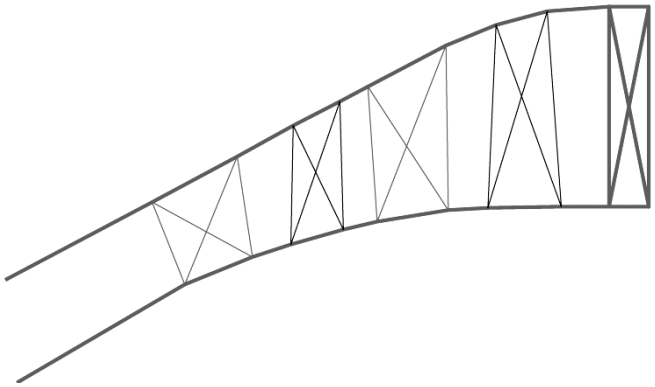

Figure 137: 2 stage LPT gas path [Ref. 134]

The reference values of efficiencies, weight and mission fuel used to express the variations in this section are those of the baseline GOR. This is done to facilitate the comparison between both engine design options.

Figure 138 presents the change in $\eta_{NET\ CRP}$ and $\eta_{is\ LPT}$ due to the change in TR_{DPGB} for different values of DP N_1. The trends are similar to those of the 3 stage LPT GOR design apart from the fact that the maximum LPT isentropic efficiency level is not achieved in this case. The LPT feasibility region is smaller than for the 3 stage LPT design due to higher stage aerodynamic loadings.

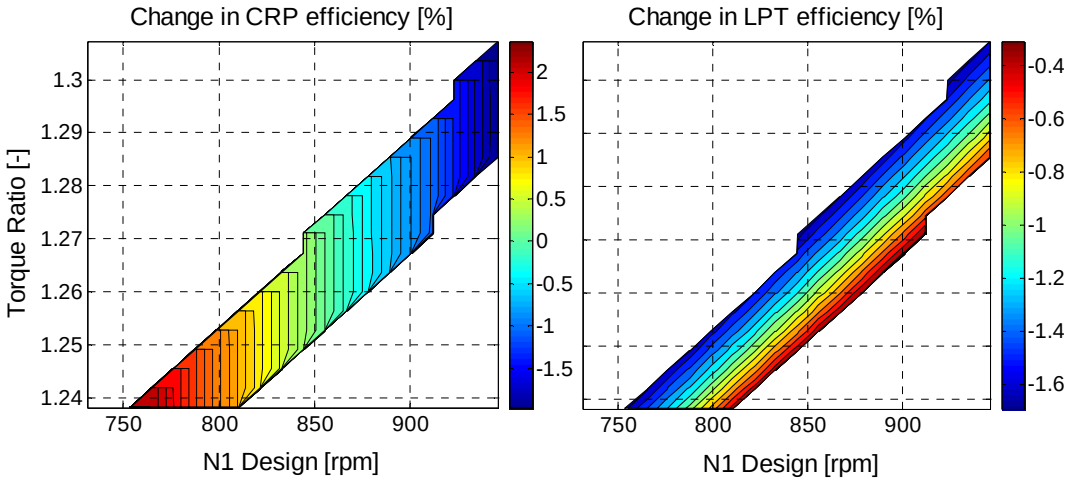

Figure 138a: $\eta_{NET\ CRP}$ vs. TR_{DPGB} and N_1 **b: $\eta_{is\ LPT}$ vs. TR_{DPGB} and N_1**

Figure 139 shows the change in DPGB and engine weight with respect to TR_{DPGB} and N_1. For the baseline N_1 (860 rpm), the GOR with a 2 stages LPT and TR_{DPGB} = 1.257[82] is ~ 3.5% heavier than the GOR with a 3 stages LPT and TR_{DPGB} = 1.33[81]. This is because the 2 stages LPT requires a heavier DPGB than the 3 stages LPT GOR, and the difference in DPGB weight is larger than the weight of an additional stage.

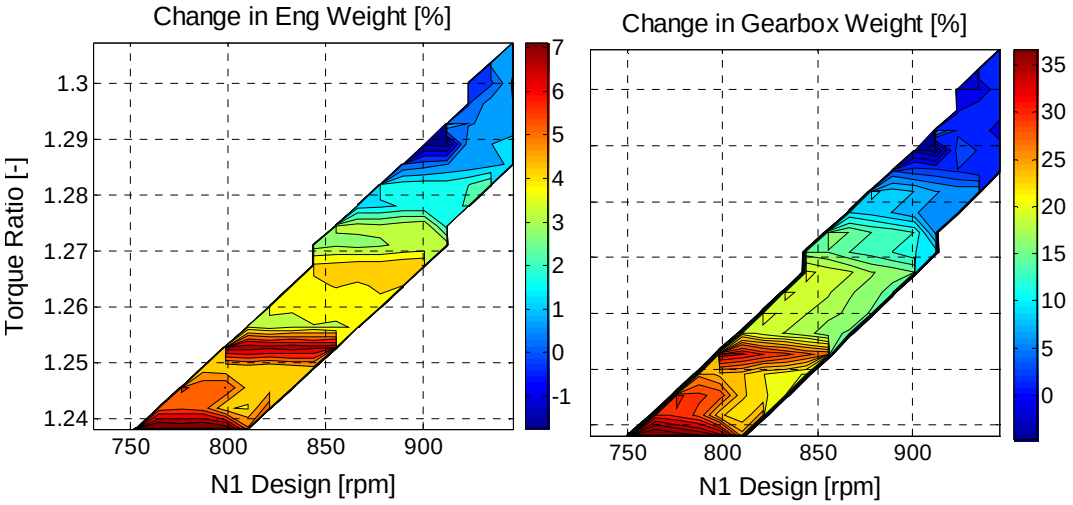

Figure 139a: Engine weight vs. TR_{DPGB} and N_1 **b: DPGB weight vs. TR_{DPGB} and N_1**

Figure 140 shows the variation in mission fuel burn with respect to TR_{DPGB} and N_1. For the studied range of N_1, a reduction in TR_{DPGB} results in a reduction in mission fuel burn. This is because the increase in $\eta_{NET\ CRP}$ and $\eta_{is\ LPT}$ produced by the reduction in TR_{DPGB}, overwhelm the gearbox weight penalty. For the reference N_1 (860rpm), the GOR with a 2 stages LPT and the minimum fuel burn TR_{DPGB}

[82] These values of TR_{DPGB} together with N_1 = 860 rpm, result in the DP N_{LPT} of the LPTs reported in Ref. 134.

consumes 0.8% more than the GOR with a 3 stages LPT and the minimum fuel burn TR_{DPGB}. The presented trade-offs together with manufacturing and maintenance cost analyses can be used to identify the most economically attractive number of stages of the LPT.

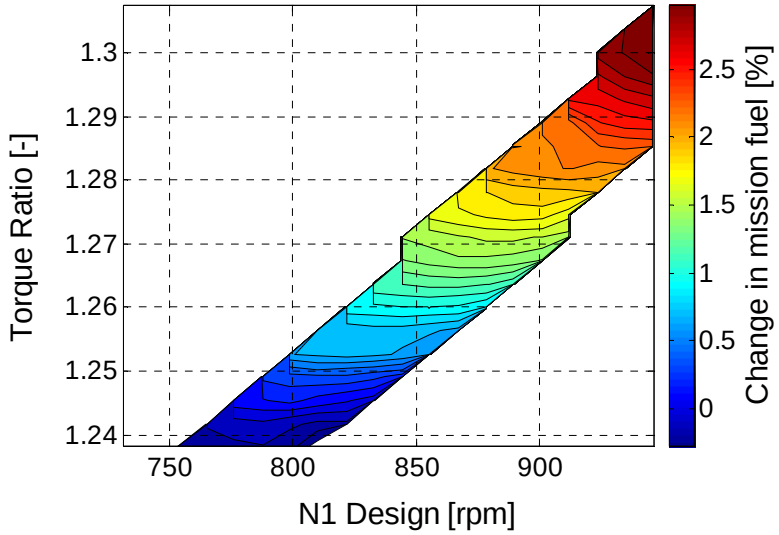

Figure 140: Mission fuel burn vs. TR_{DPGB} and N_1

3.2.3.7 Diameters and rotational speeds of the propellers

This section presents the effects of changing the diameters and rotational speeds of the propellers. In order to present the results in 2-D charts, it was decided to divide the study in two sub-sections:

- Diameter and rotational speed: the diameters and rotational speeds of both propellers are varied keeping $N_1 = -N_2 = N$ and $D_1 = D_2 = D$.
- Clipping and speed ratio: different clippings and speed ratios of the propellers are assessed using D_1 and N_1 of the baseline GOR.

As presented in section 3.2.3.6.1 and 3.2.3.6.2, the feasible range of CRP rotational speeds depends on TR_{DPGB}. A 3 stages LPT and a $TR_{DPGB} = 1.29$ were used for these studies in order to maximise the range of feasible propeller rotational speeds that could be investigated. The variations are expressed relative to this GOR design. The mission fuel burn of this design is 0.3% higher than that of the baseline.

3.2.3.7.1 Diameter and rotational speed

Figure 141 presents the change in mission fuel burn with respect to the CRP diameter ($D = D_1 = D_2$) and rotational speed ($N = N_1 = -N_2$). The CRP diameter corresponding to the minimum fuel burn design is larger than 4.26 m for the studied range of rotational speeds. The diameter of the CRP was constrained to 4.26 m to comply with installation requirements. Figure 142 shows an extended version of Figure 141 (D between 3.5 and 5.3 m) for a 10% clipped CRP design (weight and

drag penalties associated with a longer pylon not considered). The CRP diameter corresponding to the minimum fuel burn design is approximately 4.73 m for all the studied rotational speeds. The estimated mission fuel burn reduction for a D = 4.73 m design relative to a D = 4.26 m design, is less than 0.4% and it would be even lower if the associated installation penalties were considered. Consequently, the CRP diameter corresponding to the minimum fuel burn is between 4.26 and 4.73 m. This result is equally valid for unclipped CRPs.

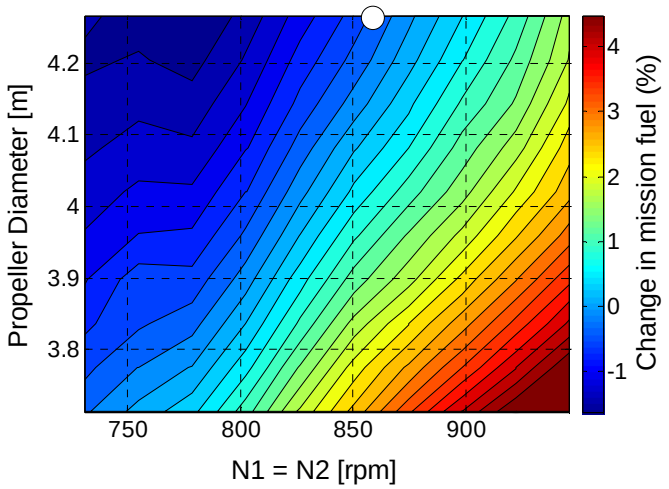

Figure 141: Mission fuel burn vs. N and D ($N = N_1 = -N_2$ and $D = D_1 = D_2$)

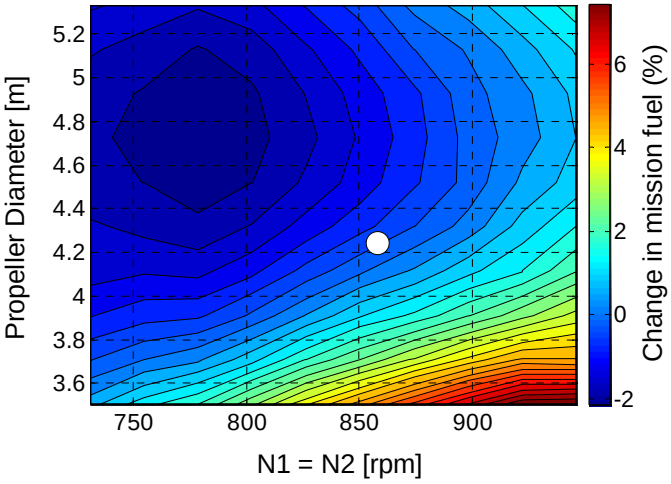

Figure 142: Mission fuel burn vs. N and D for 10% clipped CRP (extended not considering aircraft level penalties)

Figure 143 shows the change in SFC with respect to D and N for the TOC and take-off points. These two operating conditions are taken as representative examples of high and low flight speeds and will be used to explain the trends of Figure 141 and Figure 142. Figure 144 presents the change in engine weight with respect to D and N.

The trends presented in Figure 141 and Figure 142 are mainly dominated by the changes in $\eta_{NET\ CRP}$ and $\eta_{is\ LPT}$ (which determine the SFC) and the changes in engine weight. For example, the mission fuel burn of engine design with D = 3.8 m and N = 950 rpm is approximately 4.3% higher than the fuel burn of the reference design[83]. It can be seen in Figure 143 that the SFC of the D = 3.8 m and N = 950 rpm design is almost 5% higher at TOC and 6% higher at take-off relative to the SFC of the reference design. Figure 144 indicates that the D = 3.8 m and N = 950 rpm design is approximately 12% lighter than the reference design. The 5-6% SFC penalty overwhelms the 12% reduction in engine weight resulting in a 4.3% increase in mission fuel burn.

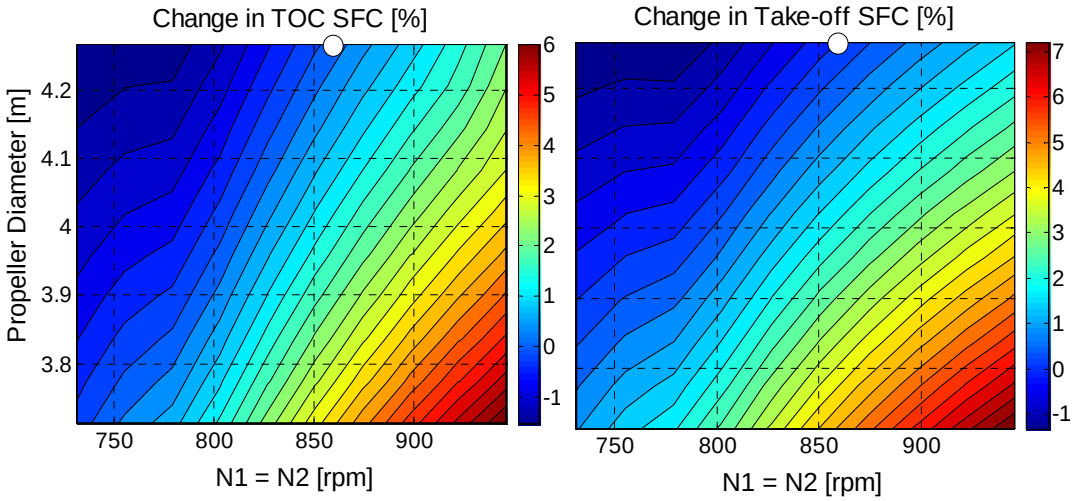

Figure 143: TOC and take-off SFC vs. N and D (take-off: M_0 = 0.25, dISA = 0, Alt = 0)

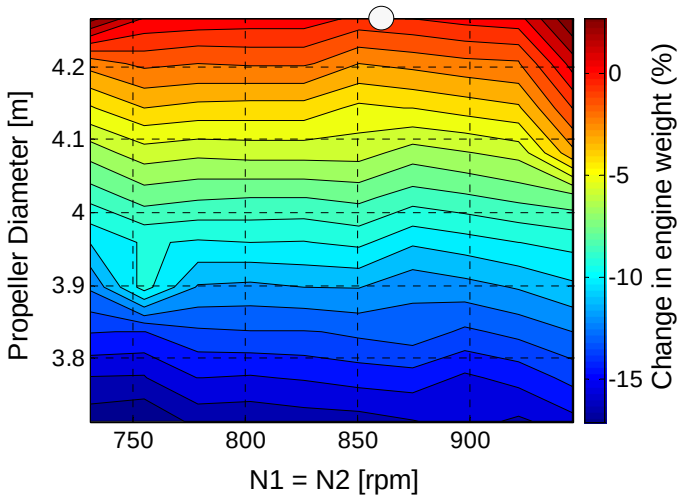

Figure 144: Engine weight vs. N and D

[83] The reference GOR used for this studies has TR_{DPGB} = 1.29 and the rest of the design parameters equal to those of the baseline GOR

Note that the variation in the engine weight with N is smaller than 1% for any D within the studied range of N (see Figure 144). This is because the weight penalty associated with a faster LPT and CRP is balanced by the weight reduction of a faster DPGB (see Figure 145).

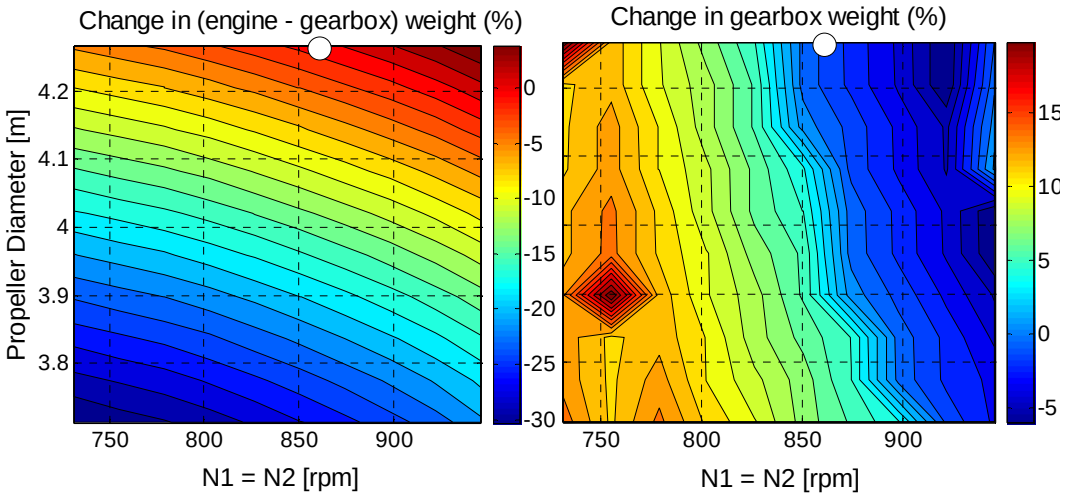

Figure 145: Engine and DPGB weight vs. N and D

The following paragraphs present the main factors which influence the variations in TOC SFC with D and N (Figure 146a). Figure 147a shows the variation in TOC $\eta_{NET\ CRP}$ and Figure 146b shows the variation in $\eta_{is\ LPT}$. It can be seen that the iso-SFC contours are similar to the iso- $\eta_{NET\ CRP}$ contours but with a reduced slope in the region where $\eta_{is\ LPT}$ varies with N.

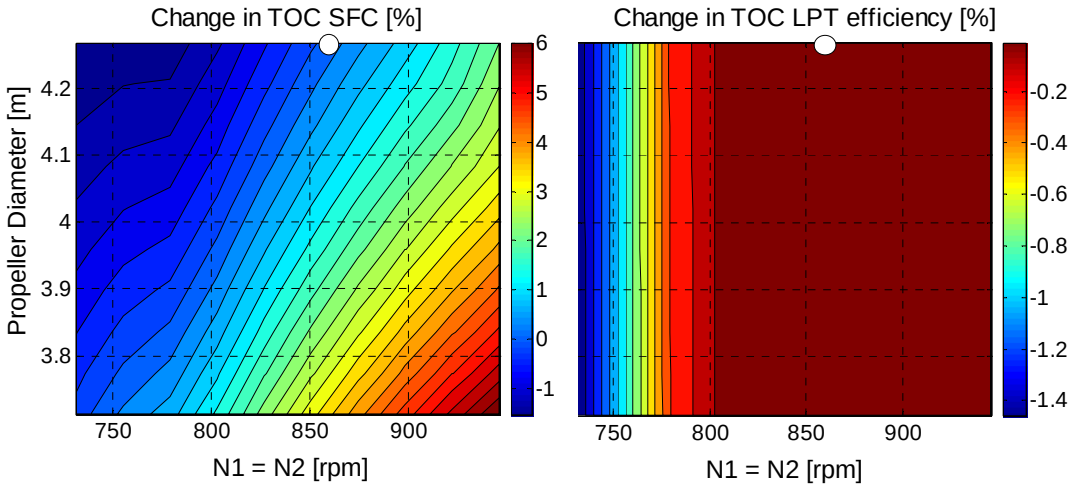

Figure 146a: TOC SFC vs. N and D

b: TOC $\eta_{is\ LPT}$ vs. N and D

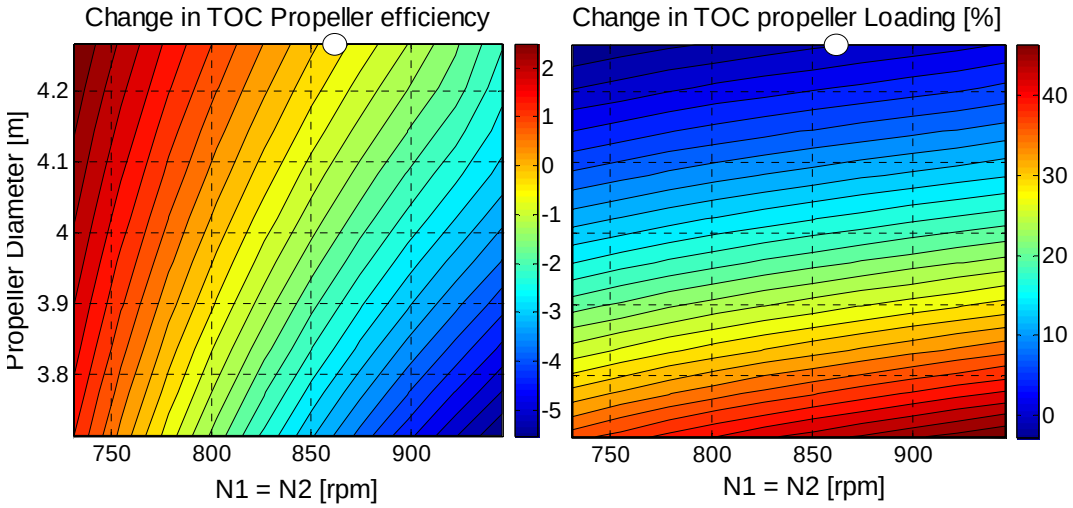

Figure 147a: TOC $\eta_{NET\ CRP}$ vs. N and D b: TOC L_P vs. N and D[84]

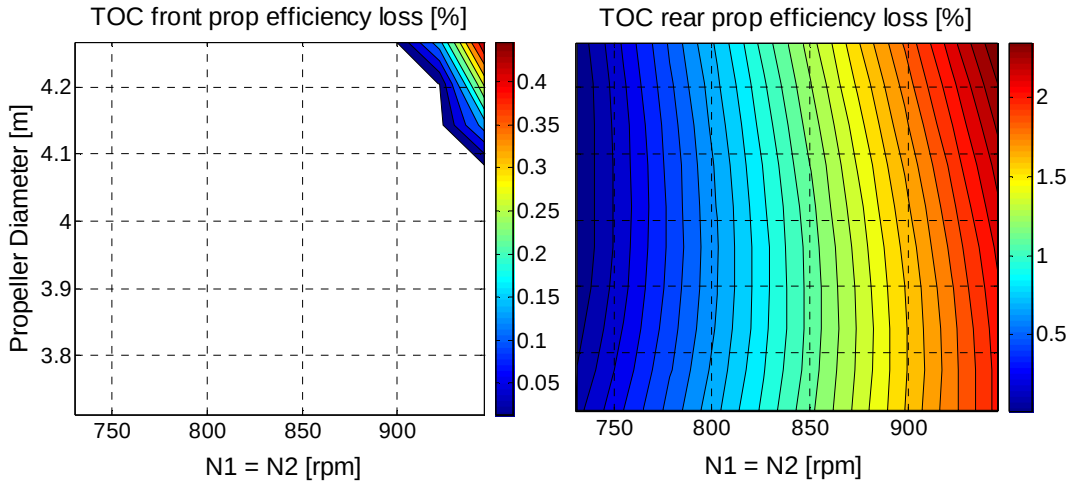

Figure 148: Propeller efficiency losses due to compressibility effects (TOC)

The changes in TOC $\eta_{NET\ CRP}$ (Figure 147a) are dominated by the changes in power loading (L_P) (Figure 147b) and compressibility losses (Figure 148):

- As D reduces, L_P increases and as a result $\eta_{NET\ CRP}$ decreases. Additionally, as D reduces, the compressibility losses decrease but this change is relatively smaller than the changes in efficiency due to the increase in L_P.
- As N increases, the compressibility losses in both propellers increase (apart from the region where they are zero for the forward propeller) making the propeller less efficient. As the propeller is less efficient, more power is required to produce the TOC thrust, resulting in a higher L_P and a further reduction in $\eta_{NET\ CRP}$.

[84] Note that the variation in L_{P1} is equal to the variation in L_{P2} because TR_{DPGB} is fixed and $N_1 = -N_2$ and $D_1 = D_2$

The forward propeller compressibility losses are dominated by its tip speed (Figure 148). If the relative tip helical Mach number is smaller than 0.89, there are no compressibility losses (white region in Figure 148). The compressibility losses of the rear propeller are higher than those of the forward propeller. This is because the flow reaching the rear propeller has higher axial and rotational speeds resulting in higher relative tip helical Mach numbers. The variation of the induced velocities has a major influence on the shape of the contours of the rear propeller compressibility losses (Figure 148). The effects of compressibility losses of the forward propeller on $\eta_{NET\ CRP}$ and SFC can be seen in Figure 147 and Figure 146 respectively (change in slope of the contours). The effects of the rear propeller compressibility losses on $\eta_{NET\ CRP}$ and SFC are more difficult visualise because they affect all the plotted designs.

Figure 149 and Figure 150 present the variations in certification noise with respect to the propeller diameters and design rotational speeds for a 10% clipped CRP design. It should be noted that due to limitations in the noise module, the propeller is operated at 1.1 N_{1Des} at the three certification points. These limitations are also responsible for the absence of values in white regions of the plots. The propeller rotational speeds indicated in these figures correspond to the real rotational speeds of the propellers at the certification points. The maximum simulated diameter is 4.7 m which corresponds approximately to the minimum mission fuel burn propeller diameter identified in Figure 142. These figures together with Figure 142 present the trade-off between noise and fuel burn with respect to N and D for a 10% clipped CRP GOR. The emissions follow the same trends as the changes in SFC for each operating point.

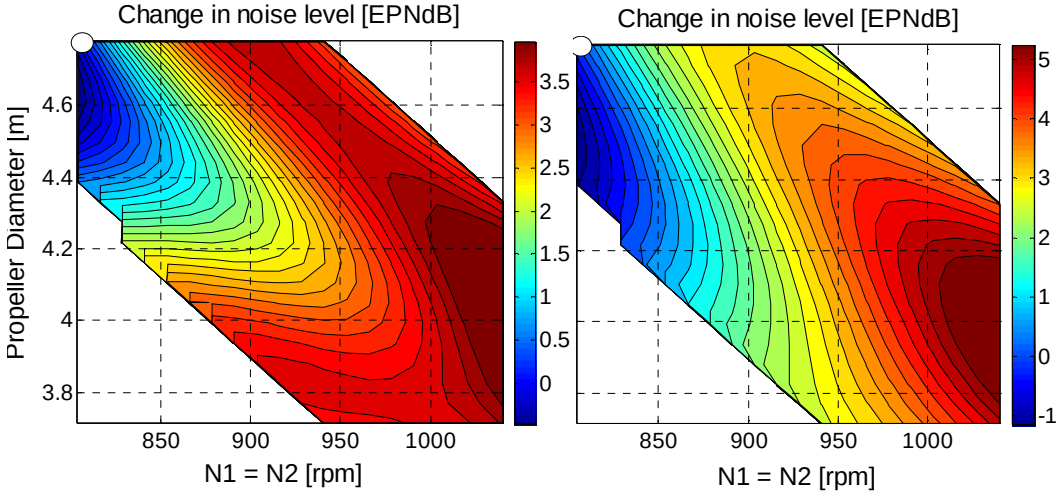

Figure 149a: Sideline noise vs. N and D **b: Flyover noise vs. design N and D**

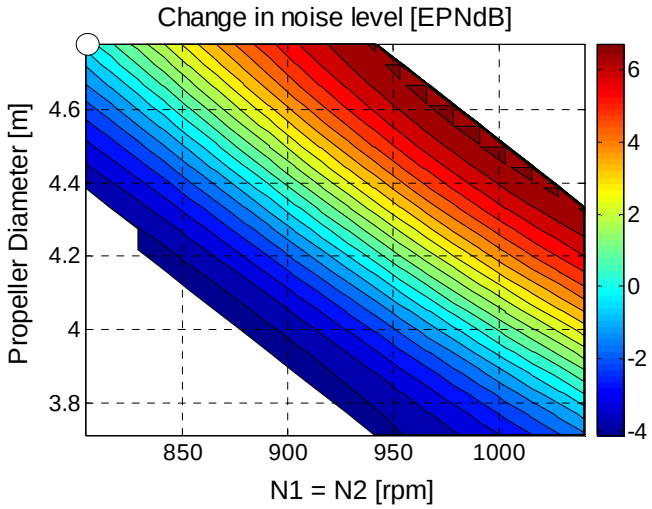

Figure 150: Approach noise vs. design N and D

As a general conclusion, sideline and flyover noise can be reduced by increasing D and operating the CRP at the appropriate rotational speeds. For any D there is a minimum sideline noise N. This is due to the relative variations in loading and interaction noise of both propellers. As N is reduced, the interaction noise is reduced, but the loading noise is increased as the thrust is kept constant. At high N, the reduction in interaction noise produced by the reduction in N is higher than the increase in loading noise. At low N, the increase in loading noise produced by the reduction in N is higher than the reduction in interaction noise.

The minimum noise rotational speeds for the 10% clipped GOR with D = 4.26 m is between 850 and 900 rpm.

The propeller tip speed corresponding to the minimum sideline noise decreases as D increases. In reality, the variations in minimum noise tip speed with D are likely to be larger than those obtained because of the reasons described in section 2.6.3.

The flyover noise follows the same trends as sideline noise, but the minimum N for every D is lower in the case of flyover, as the aerodynamic loading of the propeller is lower than that for sideline.

The approach noise is dominated by the interactions between the propellers as the aerodynamic loadings are considerably reduced. It can be seen in Figure 150 that the approach noise increases as D increase for a constant tip speed (function of D and N). Consequently, the reduction in sideline and flyover noise that could be achieved by increasing D at constant tip speed would result in a noise penalty during approach. The trade-off between noise levels at the three certification points is of paramount relevance since the regulations impose maximum allowed levels for (sideline + flyover + approach) as well as for (sideline + flyover), (sideline + approach) and (approach + flyover).

The shapes of the noise vs. N and D contours of a 20% clipped design are analogous to those of the 10% clipped design. The variations in sideline EPNdB

with respect to N and D of a 20% clipped design are of the same order of magnitude than those of the 10% clipped design. The variations in flyover and approach EPNdB with respect to N and D of a 20% clipped design are approximately half of those of the 10% clipped design.

3.2.3.7.2 Clipping and speed ratio of the propellers

The CRP can be clipped (D_2 smaller than D_1) to reduce the effects of the tip vortex produced by the forward propeller on the rear propeller. This reduces the propeller noise but also reduces its efficiency since part of the swirl of the forward propeller is not recovered by the rear propeller. The definition of clipping is provided in Eq. 180 (section 3.2.1.3)

Figure 151 and Figure 152 present the variations in mission fuel burn and engine weight with respect to propeller clipping and N_2 for the reference values of D_1, N_1 and $TR_{DPGB\,=}$ 1.29.

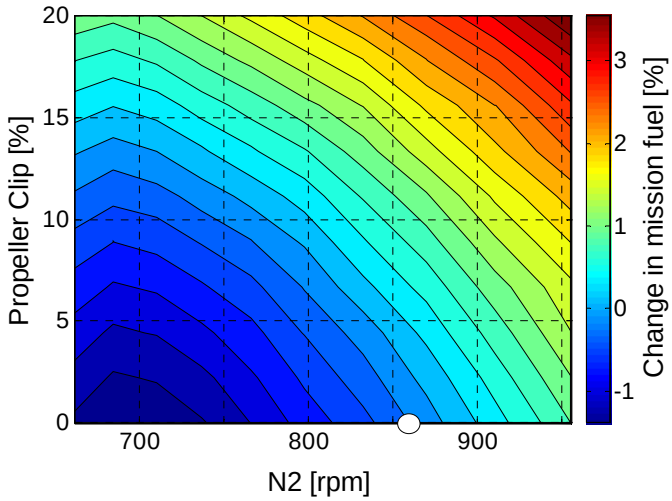

Figure 151: Mission fuel burn vs. Clipping and N_2 (reference D_1 and N_1, $TR_{DPGB\,=}$ 1.29)

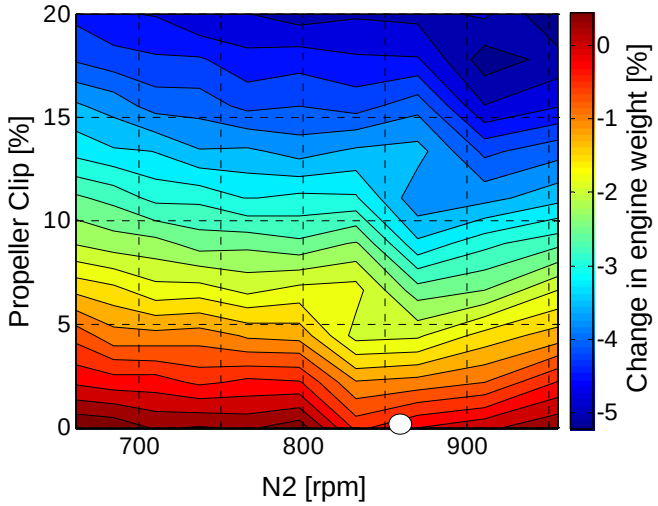

Figure 152: Engine weight vs. Clipping and N_2 (reference D_1 and N_1, $TR_{DPGB\,=}$ 1.29)

Changes in engine weight are dominated by the clipping, and the influence of N_2 is relatively small. This is because the increase in LPT and CRP weight with N_2 is balanced by the reduction in DPGB weight. Although the engine weight decreases with clipping, mission fuel burn increases. For all the studied values of N_2, the unclipped CRP design offers the lowest mission fuel burn. It can be seen that a reduction in N_2 offers a reduction in mission fuel burn up to a certain point. The minimum mission fuel burn for the unclipped design is achieved at N_2 = 700 rpm.

The following paragraphs present the main factors which influence the variations in DP SFC with respect to clipping and N_2 (Figure 153a). The TOC iso-SFC contours follow the iso- $\eta_{NET\ CRP}$ contours (Figure 153b) modified by the changes in $\eta_{is\ LPT}$ (Figure 154a) in the low N_2 region. It can be seen that the iso- $\eta_{NET\ CRP}$ contours have a change in slope due to the variation in compressibility losses of the rear propeller (Figure 154b). The variations in compressibility losses of the forward propeller are relatively smaller.

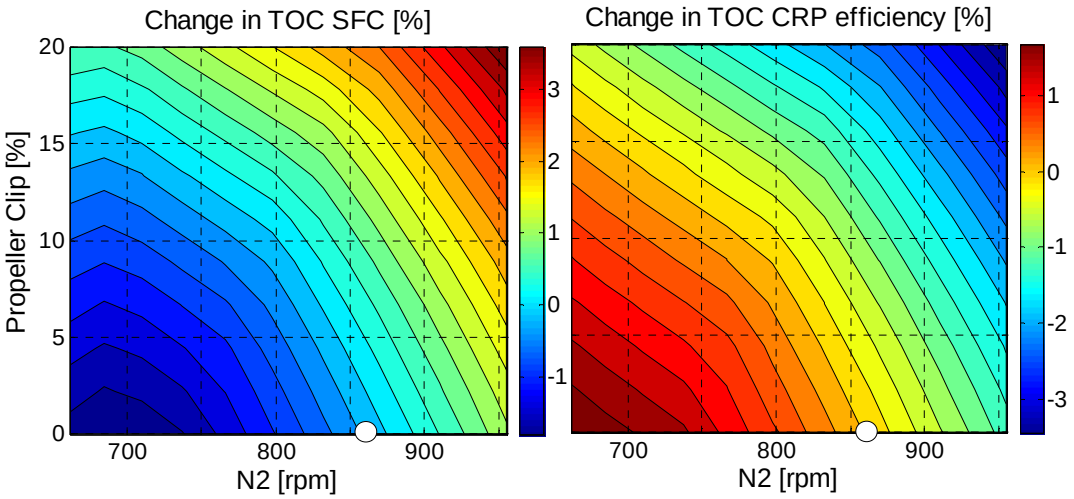

Figure 153a: TOC SFC vs. Clipping and N_2 **b: TOC CRP η_{NET} vs. Clipping and N_2**

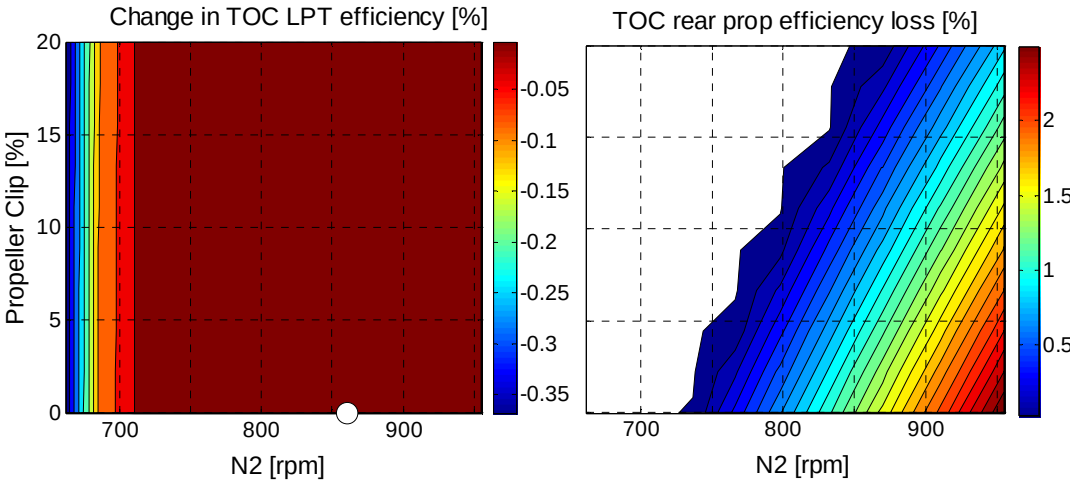

Figure 154a: TOC $\eta_{is\ LPT}$ vs. Clipping and N_2 b: compressibility losses vs. Clipping and N_2

The changes in $\eta_{is\ LPT}$ with respect to N_2 are relatively smaller than those obtained for changes in N_1 and N_2 (Figure 146b). This is because a simultaneous variation in N_1 and N_2 produces a higher change in N_{LPT} than a variation in N_2. Moreover, for TR_{DPGB} = 1.29 (value used for the current analysis) and the selected connections between the DPGB and propellers, a change in N_1 has 30% more influence on N_{LPT} than a change in N_2 (see Eq. 162).

Figure 155 shows the changes in the forward and rear propeller power loading (L_P) at DP. Changes in N_2 result in a variation in the power ratio of the propellers because the DPGB produces a constant torque split between the two propellers. For constant clipping, a quasi linear variation of L_P with N_2 can be observed for the rear propeller, denoting the quasi linear variation in power[85] (the area is fixed). For constant N_2, L_P of the rear propeller varies aproximately[85] in proportion to change in area. The forward propeller power (which is proportional to L_P since it has a constant area) varies in order to compensate for the changes in CRP power ratio (and changes in the efficiency of components).

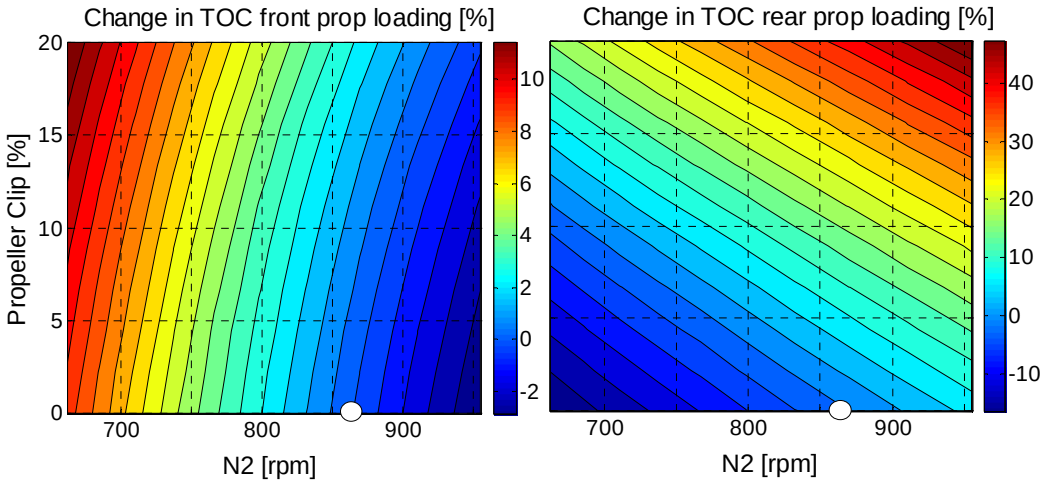

Figure 155: TOC L_P vs. Clipping and N_2

Figure 156 and Figure 157 present the change in certification noise with respect to the propeller clipping and N_2. Note that the propeller rotational speeds indicated in the noise figures correspond to the real rotational speed at the corresponding operating point (1.1 N_{1Des}) and the white dots are located at the reference N_2 used to express the variations. According to TENOR, clipping has a very limited influence (less than 1dB in the studied range) on sideline noise but has a relevant effect on both flyover and approach noise levels. Flyover noise level can be reduced 1.5 EPNdB by clipping 20% the rear propeller at the reference N_2. Approach noise can be reduced almost 2.5 EPNdB with the same amount of clipping. This relevant reduction in noise would be achieved at a cost of 2% of mission fuel burn. Figure 151, Figure 156 and Figure 157 present the trade-off

[85] The variation is not linear because the total power absorbed by the CRP varies as $\eta_{NET\ CRP}$ and $\eta_{is\ LPT}$ vary.

between noise and mission fuel burn for any combination of clipping and N_2. A reduction in N_2 appears to be beneficial both from the noise and the fuel consumption point of view for the GOR with TR_{DPGB} = 1.29. The emissions follow the same trends as the changes in SFC for each operating point.

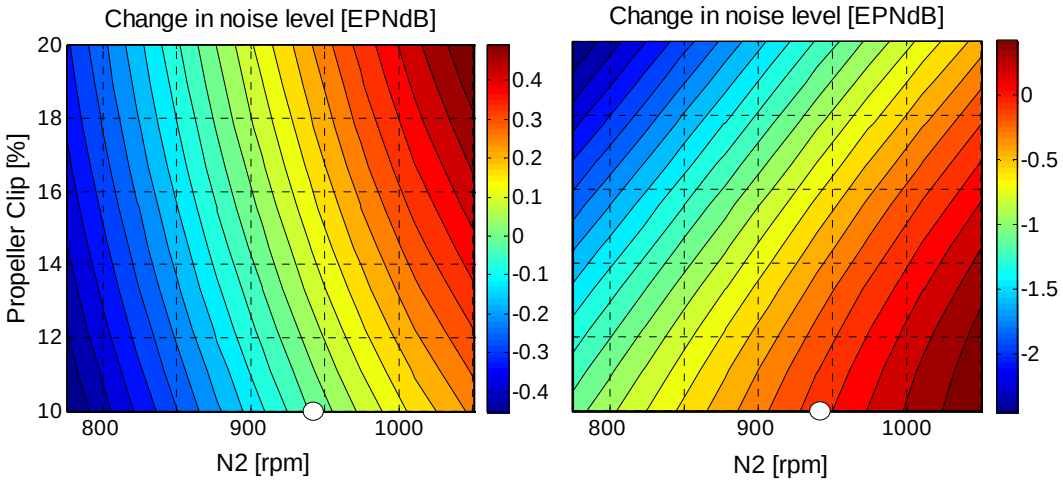

Figure 156a: Sideline noise vs. Clipping and N_2 b: Flyover noise vs. Clipping and N_2

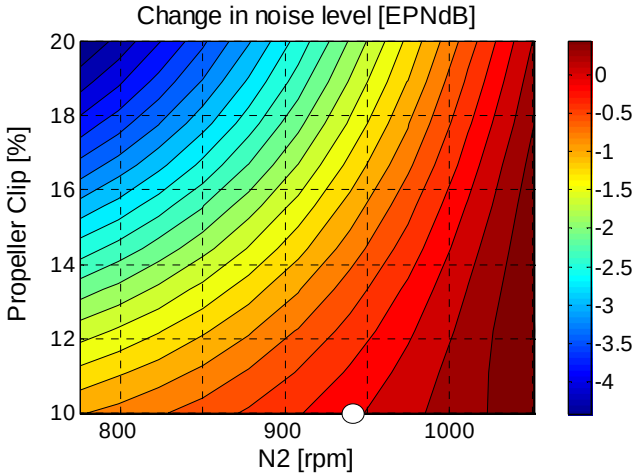

Figure 157: Approach noise vs. Clipping and N_2

3.2.3.8 Efficiencies of compressors, turbines and DPGB

The IPC, IPT, HPC, HPT and DPGB efficiencies were estimated for a 2020 level of technology and were kept constant for all the studied GOR designs. The LPT efficiency was estimated using the methodology described in section 2.2.3.1.1. Table 15 summarises the effects of not achieving the estimated efficiency levels on mission fuel burn.

Change in component efficiency	Change in mission fuel burn [%]
-1% IPC poly. eff.	+ 0.55
-1% IPT is. eff.	+ 0.28
-1% HPC poly. eff.	+ 0.46
-1% HPT is. eff.	+ 0.41
-1% LPT is. eff.	+ 0.89
-1% Gearbox eff.	+ 1.04

Table 15: Mission fuel burn penalty vs. change in efficiency of components

3.2.3.9 Minimum fuel burn design region

Within the assumptions of the study, the GOR design which offers the minimum fuel consumption for the reference mission lies in the following region of the design space:

- DP NPR ~ 1.5
- 3 stage LPT
- TR_{DPGB} ~ 1.27
- D_1 between 4.26 and 4.7
- Clipping = 0
- Nb_1 = 14 and Nb_2 = 13
- DP N_1 between 730 and 750
- DP N_2 between 700 and 730
- Minimum hub diameter
- Minimum spacing between propellers

Table 16 presents the results of a mission fuel burn minimisation performed with ISIGHT. The optimiser was allowed to modify all the low pressure preliminary design variables listed in section 3.2.3, except for the IPC bleed mass flow rate which was set to zero. The minimum SFC control strategy for the baseline GOR was used and the following constraints were imposed.

- maximum dimaters of the propellers = 4.26 m (the pylon considered in the aircraft model does not allow larger propeller diameters)
- minimum spacing between propellers = 0.65 m (refer to section 3.2.3.2)
- minimum hub diameter = 1.5 m (limited by the exit diameter of the LPT, the size of the pitch change mechanisms and the thickness of the nacelle)

Engine Design	
Core	Baseline
$D_1 = D_2$	4.26 m
Spacing between propellers	0.65 m
Hub diameters of the propellers	1.5 m
Nb_1	14
Nb_2	13
DP N_1	740
DP N_2	715

LPT number of stages	3
TR_{DPGB}	1.27
DP NPR	1.47

Changes relative to the baseline GOR	
Mission fuel burn	- 3.7 %
LTO NOx	- 4 %
Engine weight	+ 8.7 %

Table 16: Minimum mission fuel burn GOR design

The certification noise of this GOR design can not be evaluated with TENOR because the clipping of the rear propeller is smaller than 10% (refer to section 2.6). Minimum noise GOR designs could be identified with an enhanced noise module (refer to section 2.6.3).

3.3 DDOR assessments

First the baseline DDOR is defined, and then the engine control assessments and design space exploration are presented.

3.3.1 Baseline DDOR definition

The following paragraphs describe the preliminary design definition of the baseline DDOR. The schematic of the engine performance model of the DDOR is presented in section 2.2.5. This engine was sized to meet the engine performance requirements described in section 3.1.2.

3.3.1.1 Core definition

The baseline DDOR has the same number of stages and PRs in the core components as the baseline GOR (presented in Table 11). The DP TET and DP efficiencies of the IPC HPC HPT and IPT are the same as for the baseline GOR (presented in Table 12)

Table 17 presents the estimated pressure losses in the baseline DDOR ducts reflecting a year 2020 level of technology.

Component	**Pressure Loss (%)**
Burner	4
IPC - HPC	0.75
IPT – CRT	1
Nozzle Duct	1

Table 17: Baseline DDOR pressure losses

Note that the IPT-CRT duct has a relatively high pressure loss for an inter turbine duct. This is a consequence of the relatively large difference in mean radii of the IPT and CRT and the presence of the relatively thick struts of the mid frame which pass through it.

The burner is an annular design and its estimated efficiency is 99%.

3.3.1.2 CRT

The CRT of the baseline engine is described in section 2.2.3.3.2.8. It has 20 stages. The first stage is connected to the external drum and the forward propeller. The last stage is connected to the internal drum and to the rear propeller similarly to the CRT of Figure 60. This connection between the CRT and the CRP results in $TR_{CRT} = TR_{CRP}$ (defined in Eq. 120 and Eq. 180 respectively) and $nR_{CRT} = nR_{CRP} = -n_1/n_2 = -N_1/N_2$.

DP $TR_{CRT} = 1$ for all the studied DDOR engines (refer to Consideration 3 in section 2.2.3.3.2.7). DP $\eta_{is\ CRT}$ was calculated using CRT-DPe (described in section 2.2.3.3.2.7) and is approximately 0.88.

3.3.1.3 Secondary Air System

The SAS of the baseline DDOR engine was designed to satisfy its cooling and sealing requirements. The description of the SAS is omitted due to non disclosure agreements.

3.3.1.4 Propellers

The propellers of the DDOR have the same diameters, spacing between propellers, DP rotational speeds and number of blades as those of the baseline GOR.

DP η_{NET} of each propeller was calculated using the methodology presented in section 2.2.3.2.5. DP $\eta_{NET\ CRP}$ is approximately 0.86.

3.3.1.5 Auxiliary power extraction

The mechanical power required by the aircraft (250 hp at all operating regimes) is extracted from the HP shaft. This is done in order to have a unique auxiliary gearbox covering the power extraction and starting requirements.

3.3.1.6 Components maps

The maps used for the IPC, HPC, HPT, IPT and propellers are the same as for the GOR. They were scaled so that the location of the DP in the maps was the same as for the GOR.

The used CRT map is presented in Figure 68 - Figure 70. It was obtained using CRT-DPe as described in section 2.2.3.3.2.8.

3.3.1.7 Technology curves

The technology curve of the CRT is described in section 2.2.3.3.3.1 and gives the same result as the 1-D mean line code (described in section 2.2.3.3.2.7) for the baseline CRT.

The technology curve used for the propellers is described in section 2.2.3.2.5 and the used technology factor (K_{LP}) is 1.56 as for the GOR.

3.3.1.8 Baseline for noise studies

The noise module was designed to predict the noise of CRPs with clippings between 10 and 20%. The baseline GOR and DDOR used for these assessments are defined with equal propeller diameters (0% clipping) and it is not possible to obtain the noise levels for the baseline engines. Consequently, the noise trends are presented for various levels of clipping (explicitly mentioned in the text). In these cases, all the engine preliminary design parameters are equal to those of the baseline engine except for the diameter of the rear propeller.

3.3.2 Engine control assessments

The rotational speed of the propellers of a DDOR engine can be independently controlled (see section 2.2.5). The control system of the GE-UDF demonstrator allowed a flexible definition of N_1 and N_2 in order to enable the investigation of noise and SFC reduction control strategies during the ground and flight tests [Ref. 33]. The only results of these investigations found in the public domain, are the variations in SFC at take-off (operating conditions not reported) with respect to N_1 with $N_1 = -N_2$ (figures 7.14 and 7.15 in Ref. 238). The SFC Vs. N_1 trends obtained with the engine performance model developed for this research project are consistent with those presented in Ref. 238.

This section presents the influence of the control of the CRP on fuel burn, noise and emissions for the baseline DDOR. Each flight phase is analysed independently.

3.3.2.1 Climb

Figure 158 presents the variation of Fn and SFC with respect to Alt and M_0 for an average climb TET, ISA conditions and $N_1 = -N_2 = N_{1Des}$ (reference point to express variations: Alt = 35 kft and M_0 = 0.75). The trends are similar to those of the GOR. The relative variation of Fn, SFC and the aircraft performance characteristics define the optimum fuel burn climb speeds and the trade-off between climb fuel and time. Above 10kft of altitude, a constant CAS of 260 kt is used for the assessments because it minimises the fuel consumption of the reference mission. This was calculated following the same procedure used for the studies presented in Ref. 234 (variations in CAS of 10 kt were considered).

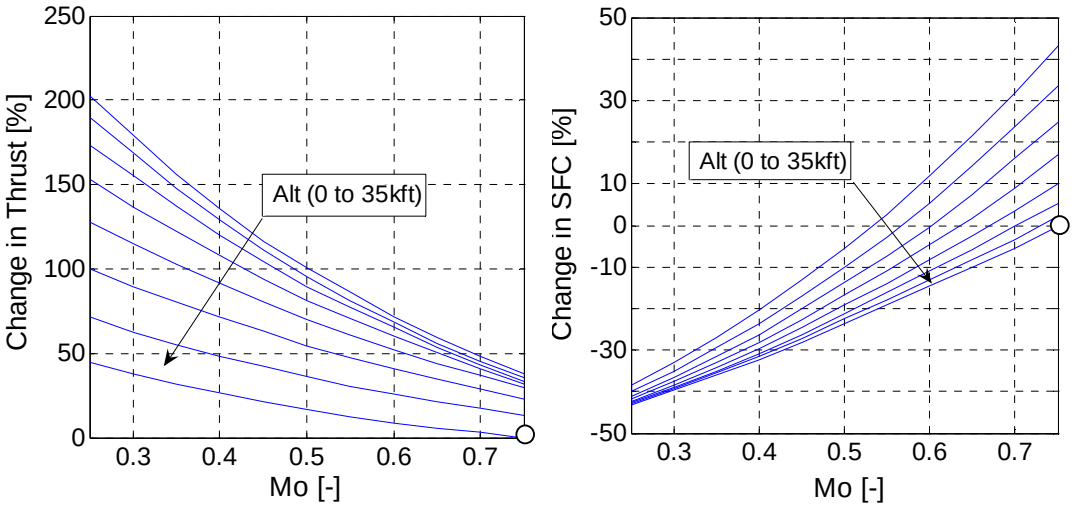

Figure 158: Fn and SFC vs. M_0 and Alt (dISA = 0, TET = 1640K and $n_1 = -n_2 = n_{1Des}$)

The variation of SFC with respect to N_1 and N_2 is different for every climb condition, and it follows the same trends as the cruise, take-off and descent which are presented below.

3.3.2.2 Cruise

The cruise phase is done at $M_0 = 0.75$. The thrust requirement decreases along the cruise as the aircraft becomes lighter. The reference aircraft at full load requires 22.4 kN of thrust at the start of cruise and 17 kN at cruise end. Figure 159a presents the change in SFC with respect to Fn and N_1 (with $N_1 = -N_2$ for simplicity). Note that the Fn vs. SFC curve of the DDOR is different from the traditional "U" shape curve for a turbofan. This is because the variations in η_{Prop} of a CROR are small and therefore the changes in η_{Ov} are dominated by the changes in η_{Th}.

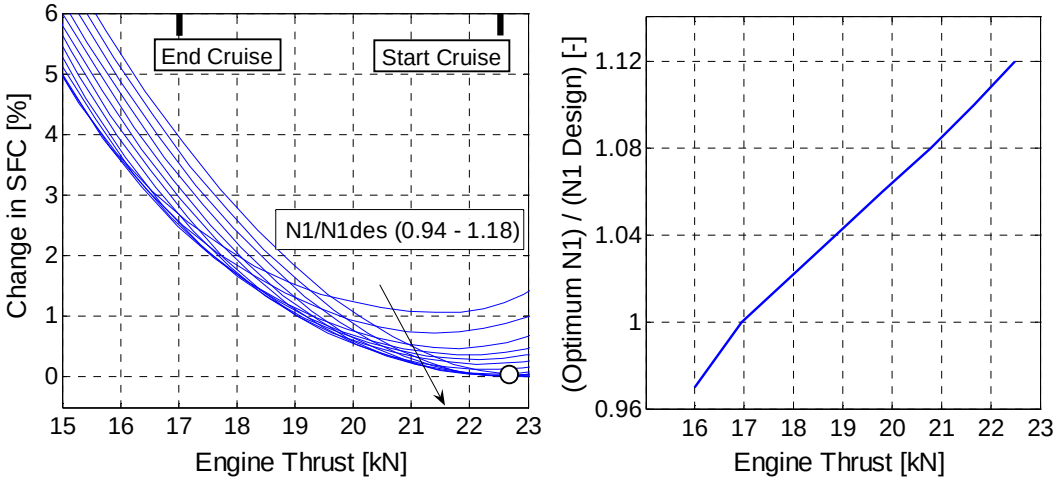

Figure 159a: SFC vs. Fn (cruise) **b: Optimum cruise N_1 vs. Fn**

(dISA = 0, Alt = 35kft, $M_0 = 0.75$, $N_1 = -N_2$)

The results shown in Figure 158a suggest that approximately 1-2% fuel saving can be achieved by using the optimum propeller rotational speeds as opposed to constant rotational speeds. Figure 159b presents an optimum N_1 schedule to minimise fuel consumption for this flight condition (with $N_1 = -N_2$). It can be seen that low rotational speeds minimise SFC for low power settings and high rotational speeds minimise SFC for high power settings.

The speed ratio of the propellers ($nR = -N_1/N_2$) can also be varied and an optimum bi-dimensional schedule of N_1 and N_2 can be produced. Figure 160 shows the change in SFC with N_1 and N_2 for the start of cruise thrust.

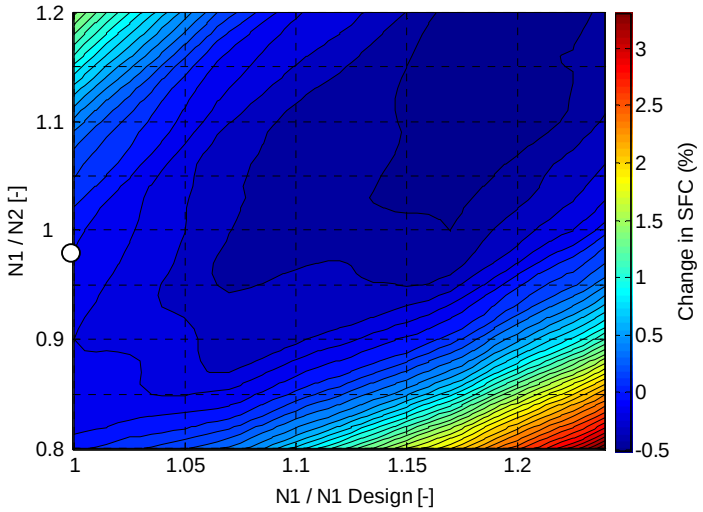

Figure 160: SFC vs. N_1 and nR (Fn = 22.4 kN dISA = 0, Alt = 35kft, M_0 = 0.75)

The shapes of the contours of Figure 160 are mainly dominated by the changes in $\eta_{NET\ CRP}$ and $\eta_{is\ CRT}$. For the studied ranges of N_1 and N_2, $\eta_{NET\ CRP}$ decreases and $\eta_{is\ CRT}$ increases as N_1 or N_2 increase. There is a trade-off between both efficiencies, and for this particular design and cruise operating condition the minimum SFC is achieved at higher rotational speeds than the optimum propeller efficiency rotational speeds.

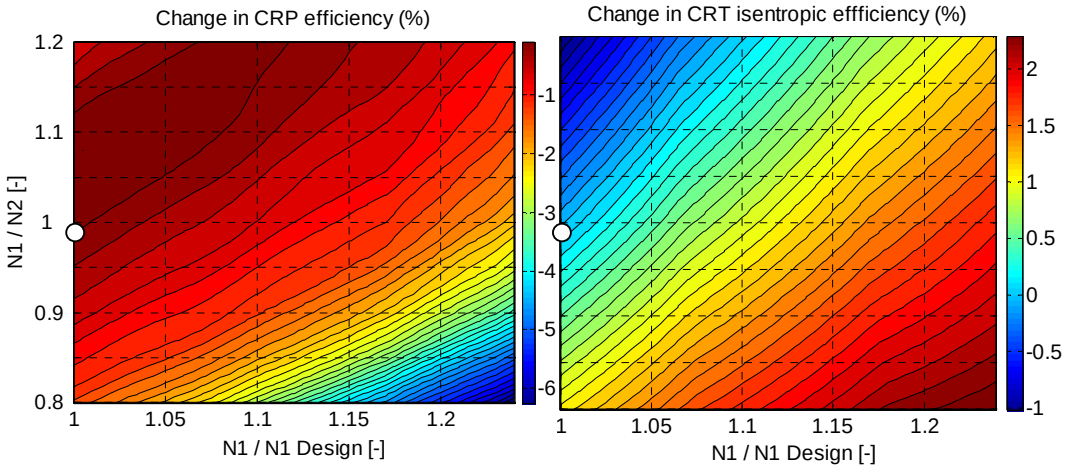

Figure 161: CRP & LPT efficiencies vs. N_1 and nR (Fn=22.4kN, dISA=0, Alt=35kft, M_0=0.75)

The variations in $\eta_{NET\ CRP}$ and $\eta_{is\ LPT}$ are different for different engine designs, and consequently different DDOR designs have different minimum fuel control strategies. In order to do a fair comparison between the fuel consumption of different engine designs they should be operated at their optimum control speeds. In the same way, in an optimisation process, both the design and control should be optimised simultaneously. This process is very computationally expensive and for this reason the reference minimum SFC control strategy was used for all the studied engine designs. The evaluation of the control of different DDOR designs showed that the use of the baseline control as opposed to a dedicated optimum control can lead to differences of the order of 0.2% in fuel burn. This suggests that the use of the reference control strategy is a valid simplification that enables the comparison of different engine designs.

3.3.2.3 Descent

The minimum SFC is achieved at low rotational speeds, as descent thrust is relatively small. The optimum N_1/N_{1Des} values for the different descent points are close to 0.7. Although the changes in SFC with N_1 and N_2 are higher than for cruise (~20%), the potential mission fuel savings offered by an optimised descent control strategy are of the same order of magnitude than for cruise. This is because the thrust levels at descent are considerably lower than at cruise and the fuel consumption of the descent is a small portion of the mission fuel burn (~10% for the reference mission).

3.3.2.4 Landing and take-off cycle

The control strategy used along the LTO cycle has an impact on the LTO fuel consumption as well as on the certification noise and emissions.

3.3.2.4.1 Take-off

Figure 162 presents the variation in SFC with respect to N_1 and nR for a fixed take-off thrust (M_0 = 0.2, Alt = 0, dISA = 0, Fn = 107 kN). Within the studied ranges of N_1 and N_2, high rotational speeds result in a reduction of SFC due to the increase in $\eta_{is\ CRT}$. Note that compressibility effects on the propellers are relatively low at take-off flight speed.

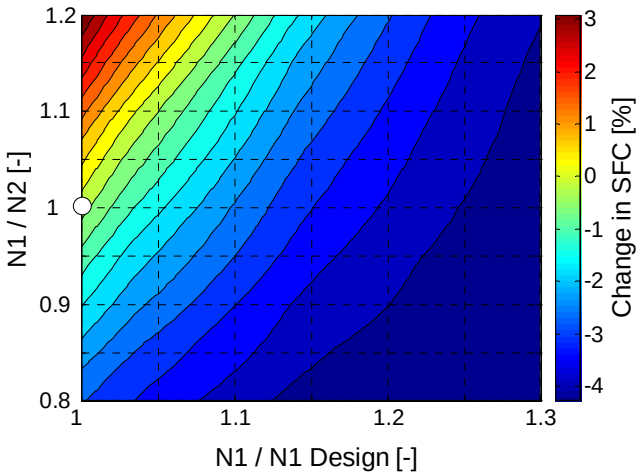

Figure 162: SFC vs. N_1 and nR at Take-off (M_0 = 0.2, Alt = 0, dISA = 0, Fn = 107 kN)

However, as N_1 and N_2 increase, both the sideline and flyover noise levels increase as shown in Figure 163. Note that due to model limitations, the ranges of these figures are different to the ranges of previous figures. At sideline, N_2 dominates the noise level at relatively low N_1, and N_1 dominates the noise level at relatively high N_1. At flyover, N_1 dominates the noise level at relatively low N_1, and N_2 dominates the noise level at relatively high N_1.

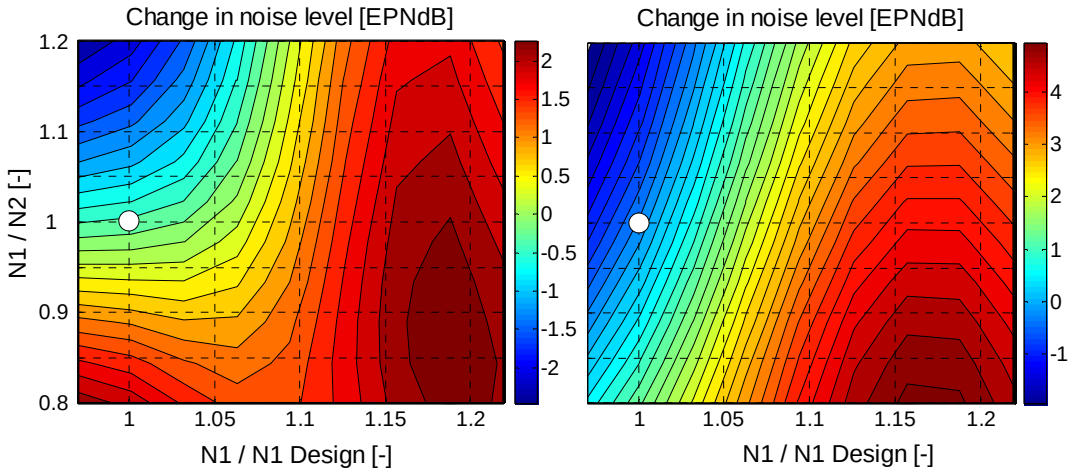

Figure 163a: Sideline Noise vs. N_1 and nR **b: Flyover Noise vs. N_1 and nR**

Figure 164 presents the variation in NOx emissions for the take-off point with respect to the control of the CRP. The variations in LTO NOx and CO_2 emissions follow the trends of SFC. The magnitudes of the variations of NOx are higher than those of SFC due to the required changes in TET. The total mission CO_2 emissions follow the mission fuel burn trends.

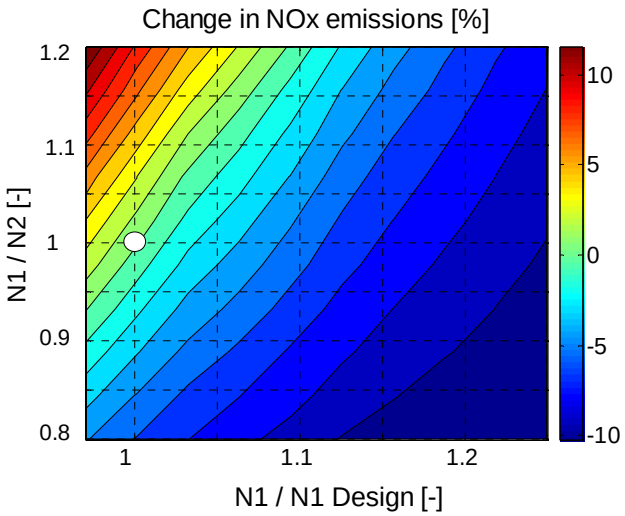

Figure 164: Take-off NOx emissions vs. N_1 and nR

The most fuel efficient and less pollutant take-off control strategies are at high rotational speeds. N_1/N_{1Des} = 1.3 and N_1/N_2 = 0.8 result in a 0.9% reduction in mission fuel burn and 6.5% reduction in LTO NOx emissions[86] with respect to the reference control. On the contrary, N_1/N_{1Des} = 1.3 and N_1/N_2 = 0.8 penalises the certification noise by approximately 2 EPNdB for sideline and 4 EPNdB for flyover with respect to the reference control.

Both sideline and flyover noise can be reduced by 2 EPNdB with respect to the reference control strategy by operating the engine at relatively lower rotational speeds (N_1/N_{1Des} = 0.95 and nR = 1.2). This would be at a cost of 0.3% increase in mission fuel, 7% increase in LTO NOx emissions, and 10 K increase in TET with respect to the reference control.

At take-off, the engine operates at the highest TET and thrust levels and therefore at the highest mechanical stresses. Consequently, the mechanical integrity criteria of every component should be considered when optimising the take-off control.

3.3.2.4.2 Approach

Figure 165a shows the change in SFC of the baseline DDOR with respect to N_1 and nR for the approach condition used for noise calculations. In consistence with the previously presented SFC trends, the minimum SFC is achieved at low rotational speeds. The non uniformity in the SFC contours is due to the linear interpolation used in the CRT map (PROOSIS only allows linear interpolation for 3-D tables).

Figure 165b presents the change in approach noise level with respect to N_1 and nR. Low rotational speeds appear to be more appropriate for the approach since they result in low fuel bun emissions and noise. Note that for this engine design, the

[86] Note that take-off + climb-out NOx is approximately 65% of the LTO NOx.

noise module did not allow the calculation below 0.97 N_{1Des} and for this reason it is not possible to establish the exact trade-offs between noise and fuel burn.

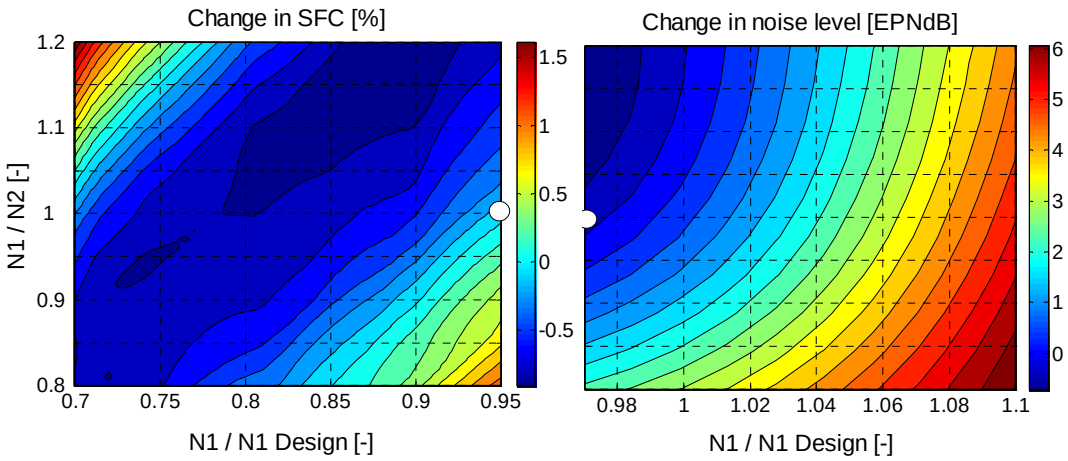

Figure 165a: Approach SFC vs. N_1 and nR b: Approach Noise vs. N_1 and nR (M_0 = 0.2 , alt = 120 m Thrust = 31 kN)

Figure 166 presents the changes in NOx emissions for the approach phase with respect to N_1 and nR. Low rotational speeds result in low emissions. It should be noted that the NOx emissions during the approach phase, are approximately 12% of the LTO NOx and therefore the impact of the approach control strategy on LTO NOx is expected to be lower than 1%.

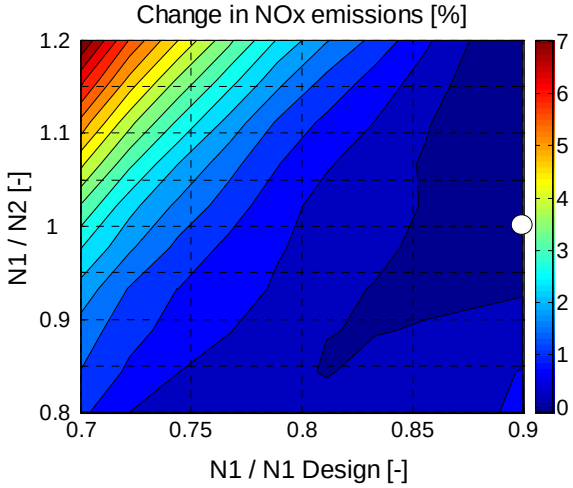

Figure 166 Approach NOx emissions

3.3.3 Design space exploration

This section presents the influence of the following LP preliminary design variables on fuel burn, noise and emissions for a pusher DDOR:

- IPC bleed mass flow rate used for cooling and noise reduction techniques
- Spacing between propellers
- Hub diameters of the propellers
- Nozzle pressure ratio at DP
- Number of blades of the forward and rear propellers
- Number of stages of the CRT
- Diameter of the forward propeller
- Rotational speed of the forward propeller at DP (TOC)
- Propeller clipping
- Speed ratio of the propellers at DP (TOC)

The sensitivity of the mission fuel burn with respect to the DP efficiencies of compressors, turbines is also presented.

The variations are expressed as a difference relative to the baseline DDOR. In each of the following studies, one or two design parameters are varied and all the rest are kept equal to those of the baseline DDOR.

The previously presented minimum fuel burn control is used for the performance calculations of all the engine designs. The noise simulations at sideline and flyover are also performed at the minimum fuel burn propeller speeds. The noise simulations corresponding to approach are performed at 1.15 N_{1Des} due to a limitation in the minimum rotational speed that the noise module can simulate. For clarity, the real propeller rotational speeds are shown on all the noise plots.

3.3.3.1 IPC bleed mass flow rate used for cooling and noise reduction techniques

One of the bleeds of the IPC is used to cool LP components such as the CRP pitch changing mechanisms and seals. This cooling flow is discharged to the atmosphere and does not contribute to the engine thrust. The bleed requirements may increase (with respect to the baseline value) due to higher cooling requirements or for CRP noise reduction techniques[87]. Figure 167a shows the change in mission fuel burn (Mission Fuel 1) and engine weight with respect to the extra IPC bleed requirement (expressed as a % of the IPC inlet mass flow rate). The mission fuel burn increases with the bleed mass flow rate, both because the engine weight and SFC increase. The changes in engine weight are mainly due to changes in the weight of the IPC,

[87] One noise reduction technique for CRORs may be to blow air through the trailing edge of the pylon. This reduces the vorticity of the flow behind the pylon (which is ingested by the CRP) and reduces the noise of installed pusher CRPs [Ref. 237]

IPT, CRT (its inlet conditions are modified) and nacelle. Figure 167b shows the change in the mass of pollutants emitted during the ICAO LTO cycle with respect to the extra IPC bleed mass flow rate.

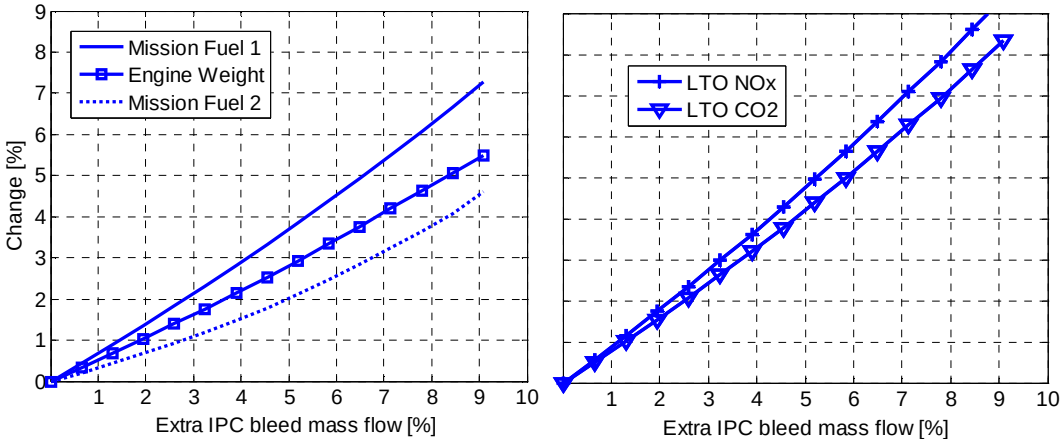

Figure 167a: Mission fuel & eng. weight b: ICAO LTO emissions vs. extra IPC bleed

If the extra IPC bleed is only required during the LTO cycle to reduce the certification noise, the bleed mass flow rate could be reduced to the baseline value during the rest of the mission. The dotted line in Figure 167a (Mission Fuel 2) depicts the change in fuel burn that results of operating this bleed only during the LTO cycle. Although air is bled during a very small part of the mission, the fuel penalty is relatively large due to a heavier engine that operates far from its design conditions along the entire mission. These curves together with the variation of certification noise of a DDOR with respect to the pylon blowing can be used to show the trade-off between fuel burn and noise.

If the extra bleed is only required during the LTO cycle, the core turbomachinery components could be sized without considering this bleed requirement. Figure 168 shows the impact of the extra IPC bleed mass flow (expressed as a % of the IPC inlet mass flow rate) on the mission fuel burn and ICAO LTO emissions for this design choice. The penalties in terms of fuel burn are low since the engine weight is not increased and it is operated far from its design running line only during the LTO cycle which is a relatively small part of the mission. As the extra bleed mass flow rate increases, CO_2 emissions increase since the fuel burnt is increased, but NOx emissions reduce since P3 reduces for this type of OD operation. As the extra bleed mass flow rate increases, take-off TET increases. 10% extra IPC bleed results in approximately 80 K increase in take-off TET and this may not be acceptable. A detailed evaluation of the impact of take-off TET on turbine cooling, components mechanical integrity and lifing is required to complete the trade-off studies of this specific bleed operation.

A detailed evaluation of the impact of take-off TET on turbine cooling, components mechanical integrity and lifing is required to complete the trade-off studies of this specific bleed operation.

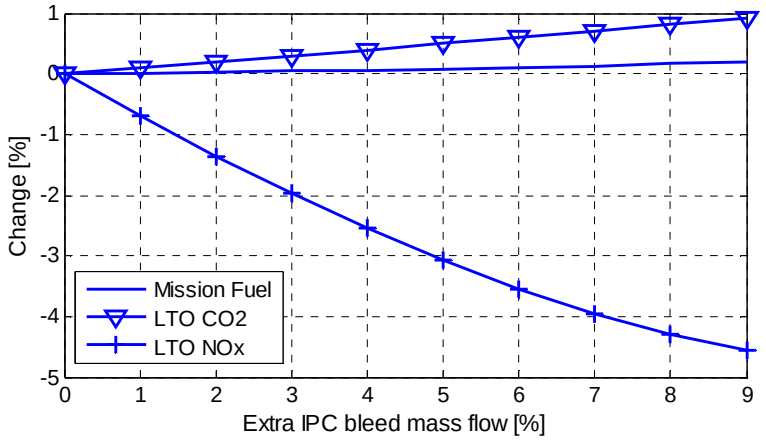

Figure 168: Effects of bleeding IPC air during the LTO cycle (baseline DDOR)

3.3.3.2 Spacing between propellers

The spacing between propellers is defined as the distance (in meters) between the roots of the blades of the forward propeller and the roots of the blades of the rear propeller. Note that for a spacing of 0.65m, the distance between the forward blade trailing edge and the rear blade leading edge is close to 0.15 m. This minimum space is needed to ensure that the blades of the two propellers do not touch each other at any possible blade pitch angle. The reference value used to express variations in this study is the minimum feasible spacing. The spacing between propellers has a relatively large impact on CRP noise levels as shown in Figure 121. Both for 10% and 20% clipped CRP designs, noise level reductions of the order of 6 EPNdB in the three certification points can be achieved by increasing the spacing between the propellers to 1.35 m. The changes in approach noise of the 20% clipped are larger than for the 10% clipped design.

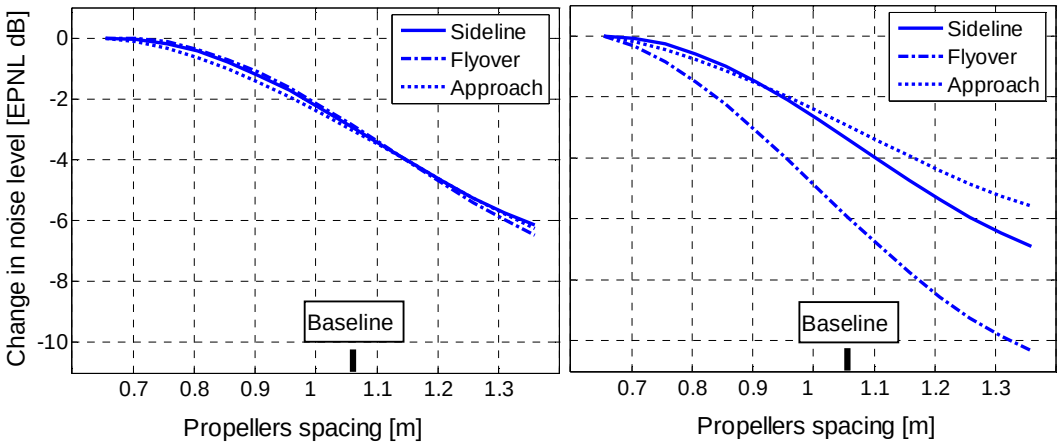

Figure 169a: Noise vs. prop. spacing (10% clipping) **b: (20% clipping)**

The spacing between the propellers has also an effect on the performance of the CRP. Close propellers are more efficient at DP mainly due to lower local mach

numbers and a more uniform inlet flow to the rear blades. Figure 170 shows the impact of the spacing between the propellers on the mission fuel burn for 0%, 10% and 20% clipped CRP designs. In order to show only the difference caused by the spacing and not the differences caused by the clipping[88], the fuel burn of the minimum spacing design for each clipping was used as a reference. Highly clipped designs are less affected by the spacing than less clipped designs, and the trends are dominated by the relative changes in propeller loading, operating points on the propeller maps and compressibility losses. The increase in spacing between propellers of 0.1 m results in a mission fuel burn penalty of ~0.07% for clippings between 0 and 10% and a mission fuel burn penalty of ~0.04% for 20% clipped designs.

The spacing between the propellers also impacts the size and weight of the mechanisms that link the CRT with the CRP, and the drag of the engine nacelle, but these differences are not accounted in the simulations.

Changes in LTO emissions are lower than 1% for CO_2, NOx and CO for the studied spacing range.

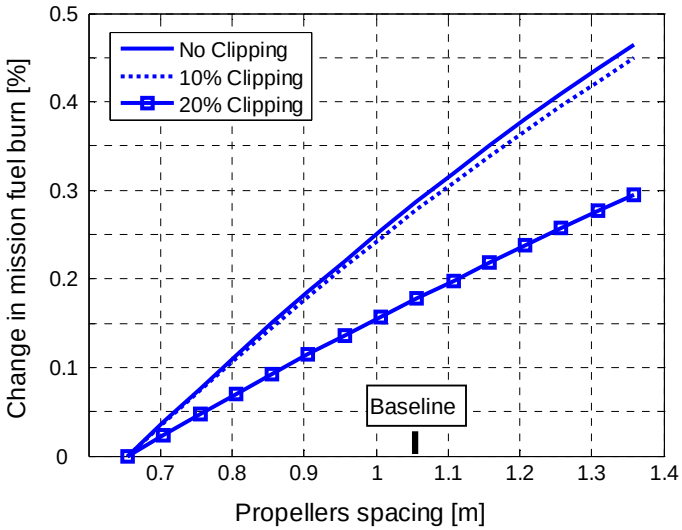

Figure 170: Mission fuel burn vs. spacing between propellers

3.3.3.3 Hub diameter of the propellers

Figure 171 presents the influence of propellers hub diameter on mission fuel burn and engine weight (note that both propellers have the same hub diameter). As the hub diameter is increased, the propeller blades are smaller and consequently lighter[89], but their efficiency decreases due to an increase in power loading (L_P).

[88] The variations in fuel burn with respect to clipping for a fixed spacing are presented in section 3.3.3.7.2.

[89] For example, a 5% increase in the hub diameter results in a 4 cm blade length reduction.

The reduction in propeller efficiency with the increase in hub diameter has a larger impact on the mission fuel burn than the reduction of the engine weight.

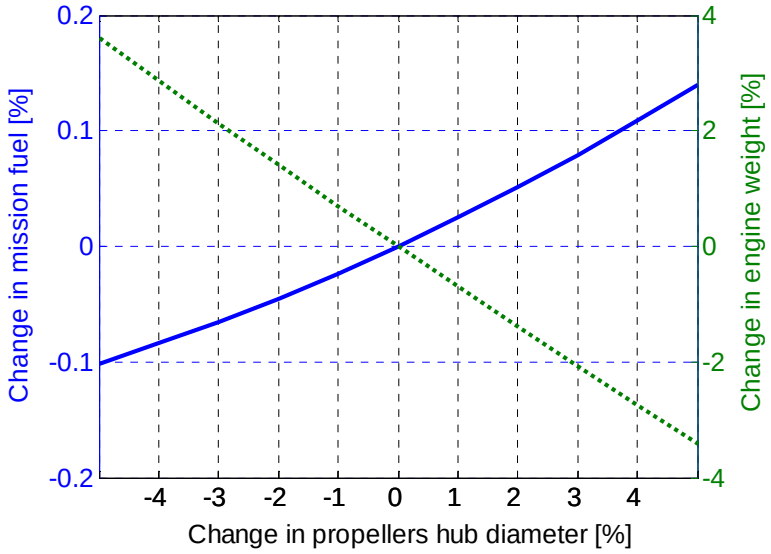

Figure 171: Mission fuel burn and engine weight vs. hub diameter of the propellers

The changes in LTO emissions with respect to the hub diameter of the propellers are of the same order of magnitude as the changes in fuel burn. It is not possible to asses the changes in certification noise with respect to the hub diameter using TENOR.

It is expected that higher hub diameters would result in higher nacelle drag and higher fuel burn penalties than those shown in Figure 171. This effect is not considered in this study (refer to sections 3.1.1). For this reason only small changes in hub diameter were assessed. It is also relevant to mention that the diameter of the CRT was not changed with the hub diameter.

3.3.3.4 Nozzle pressure ratio

The DP NPR defines the pressure drop across the LPT and consequently the power of the propellers. Figure 172 shows the change in propeller thrust at DP (as a percentage of the overall engine thrust) with respect to NPR. Even for relatively high nozzle pressure ratios (~1.6), the propeller produces almost 90% of the overall engine thrust. Figure 172 also presents the change in DP $\eta_{NET\ CRP}$ and $\eta_{is\ CRT}$ with respect to DP NPR. As DP NPR increases, the power extracted in the turbine decreases and consequently the stage loading of the CRT ($\Delta h/U^2$) and the power loading of the propellers (L_P) decrease.

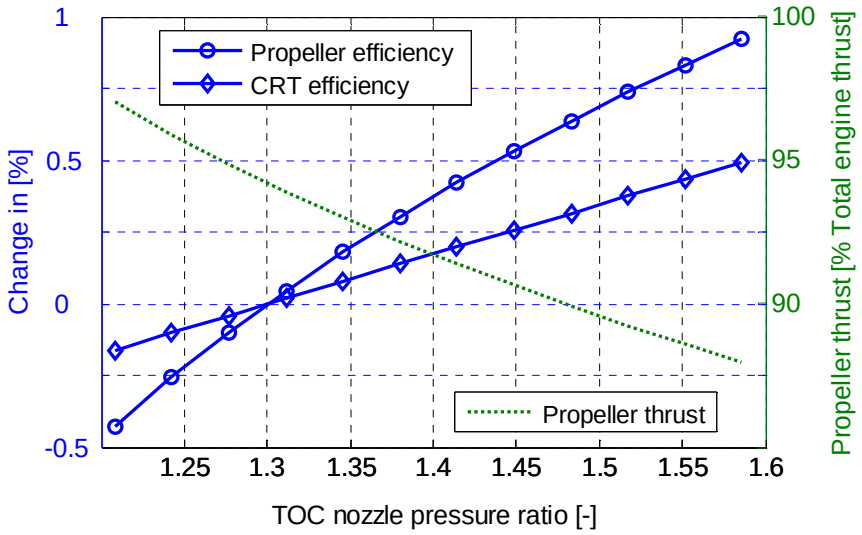

Figure 172: Propeller thrust, $\eta_{NET\ CRP}$ and $\eta_{is\ CRT}$ vs. NPR at DP

The increase in DP $\eta_{NET\ CRP}$ and $\eta_{is\ CRT}$ as well as the nozzle exit flow velocity produced by the increase in DP NPR, result in an increase in DP η_{Th} as presented in Figure 173. This figure also shows the variation in DP η_{Prop} caused by the change in DP NPR. As a consequence of the changes in η_{Th} and η_{Prop}, η_{Ov} has a parabolic shape with a maximum in NPR = 1.45.

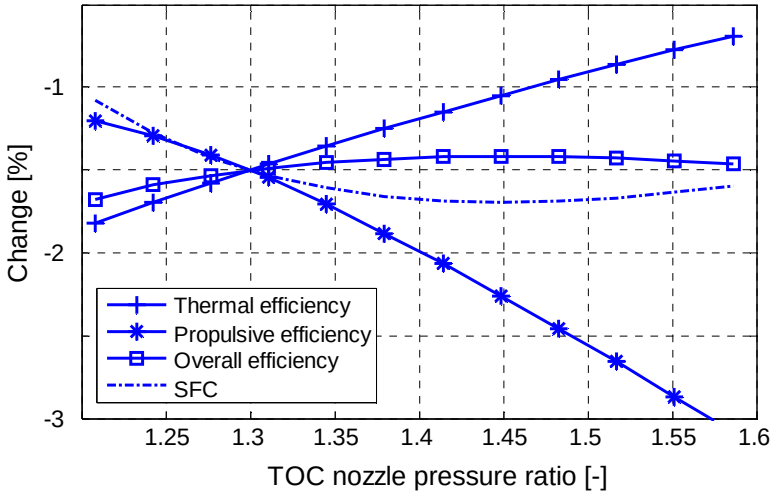

Figure 173: DP engine efficiencies and SFC vs. NPR

Figure 174 shows the change in mission fuel burn with respect to DP NPR. Changes in mission fuel burn are larger than those of SFC due to the change in engine weight. As DP NPR increases, the power extracted in the CRT decreases and the weights of the CRT and CRP decrease. The change in engine weight is the main reason why the minimum mission fuel NPR is higher than the minimum SFC DP NPR (1.45). A DP NPR of approximately 1.6 would result in a mission fuel

saving of 1% with respect to the baseline DDOR, but at a cost of higher jet noise and a longer nozzle which is undesired for installation purposes.

As the DP NPR increases, the power extracted in the CRT decreases and the CRT and CRP weights decrease. The change in engine weight also shifts the minimum fuel (with respect to the DP minimum) to a higher value of NPR (~1.6). A DP NPR of 1.6 would result in a mission fuel saving of 1.15% but at the cost of higher jet noise and a longer nozzle which is undesired for installation purposes.

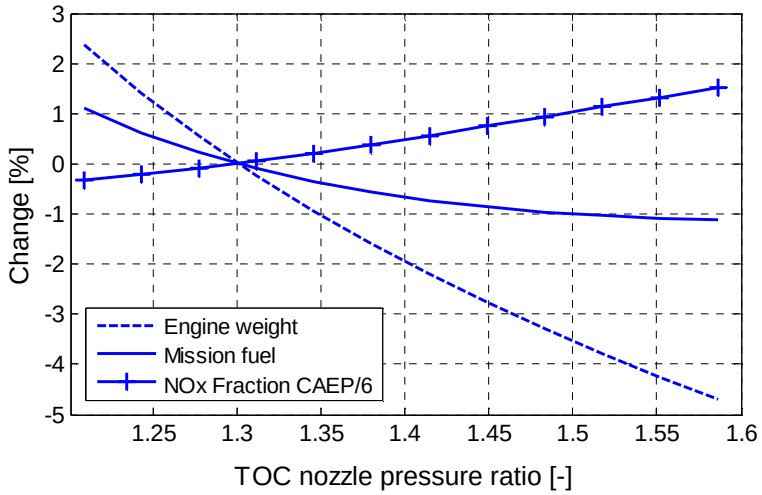

Figure 174: Mission fuel burn, engine weight and NOx emissions vs. DP NPR

Emissions increase as DP NPR increases since the reduction in η_{Prop} with NPR is larger for low flight speeds. Figure 174 shows the variation of fractional LTO NOx with respect to CAEP/6. Variations in the other gaseous species are smaller than those of NOx.

It is not possible to asses the changes in certification noise with respect to NPR using TENOR (see section 2.6.3).

3.3.3.5 Number of blades of the forward and rear propellers

As the number of blades of the CRP increases, $\eta_{NET\ CRP}$ increases (as the blades are less loaded), SFC reduces, but the weight and mechanical complexity of the engine increases. Figure 175 presents the variation of DP SFC and engine weight with respect to the number of blades in the forward and rear propellers (from 8 to 16 blades).

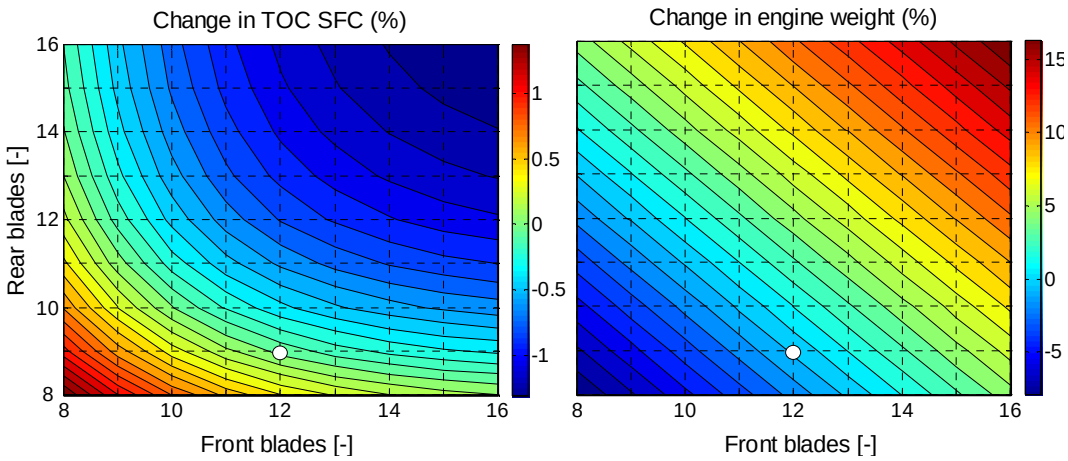

Figure 175a: DP SFC vs. N_b **b: engine weight vs. N_b**

Figure 176 presents the change in mission fuel burn with respect to the number of blades of the forward and rear propeller for a 0% clipped CRP design (baseline). The minimum fuel burn design has 13 blades in the forward and 14 in the rear propeller (denoted as 13x14). For propeller designs with more than 14 blades, the efficiency benefit of an extra blade is smaller than the associated weight penalty. Figure 177 presents the variation in mission fuel burn for 10% and 20% clipped CRP designs. The optimum number of blades for the forward propeller does not change with the propeller clipping. The optimum number of blades of the rear propeller increases with clipping. This is because the penalty of an extra blade is reduced for clipped rear propeller (smaller and therefore lighter blades) and the efficiency improvement for an extra blade is higher (clipped propellers are more loaded).

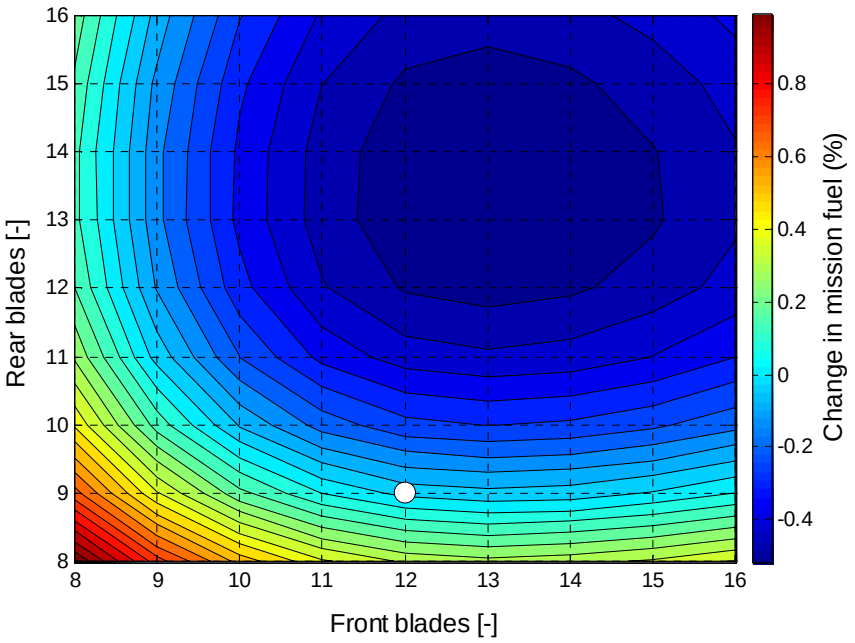

Figure 176: Mission fuel burn vs. N_b

The number of blades of the propellers has also an impact on the engine manufacturing and maintenance cost, as well as on its mechanical complexity. These elements have to be considered when selecting the number of blades of the CRP.

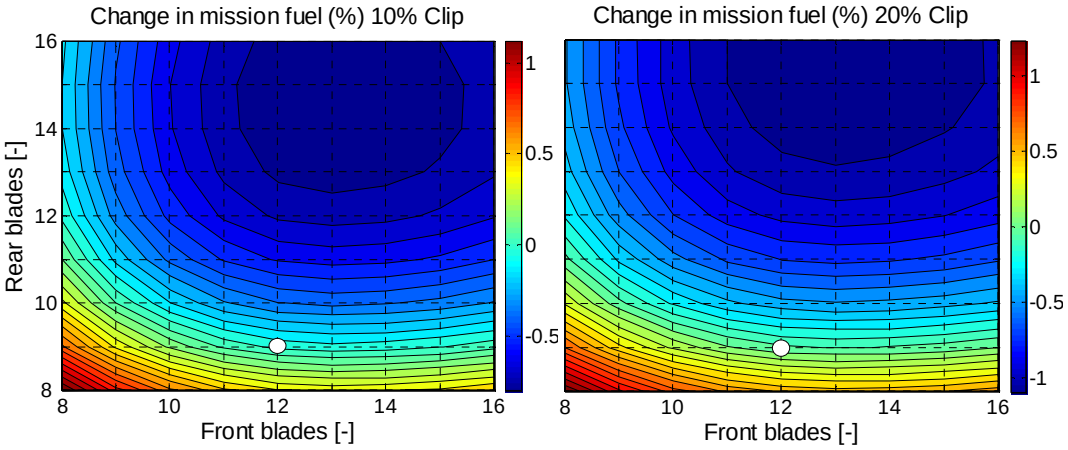

Figure 177: Mission fuel vs. N_b for clipped CRPs[90]

Changes in emissions follow the same trends as SFC and the variations are of the same order of magnitudes as those of the SFC.

Figure 178 and Figure 179 show the change in noise for the three certification points with respect to the number of blades of the propellers for a 10% clipped CRP. Note that the noise module is capable of assessing propellers with 8 to 14 blades. Sideline and flyover noise are dominated by the number of blades of the rear propeller while approach noise is dominated by the number of blades of the forward propeller. These figures together with Figure 177a present the trade-off between mission fuel burn and certification noise for changes in N_b of a 10% clipped CRP DDOR. For example: the $N_{b1}xN_{b2}$ = 13x14 design (minimum fuel burn design within the limits of the noise simulations) is 1.4 EPNdB louder in sideline, 1.7 EPNdB louder in flyover and 3.5 EPNdB louder in approach than the 8x8 design. The cost of using an 8x8 design (quieter) with respect to the 13x14 design is 1.9% in mission fuel burn.

[90] The white dots represent the engine designs which have 10% and 20% clipped CRP designs and the rest of the design parameters equal to the baseline DDOR

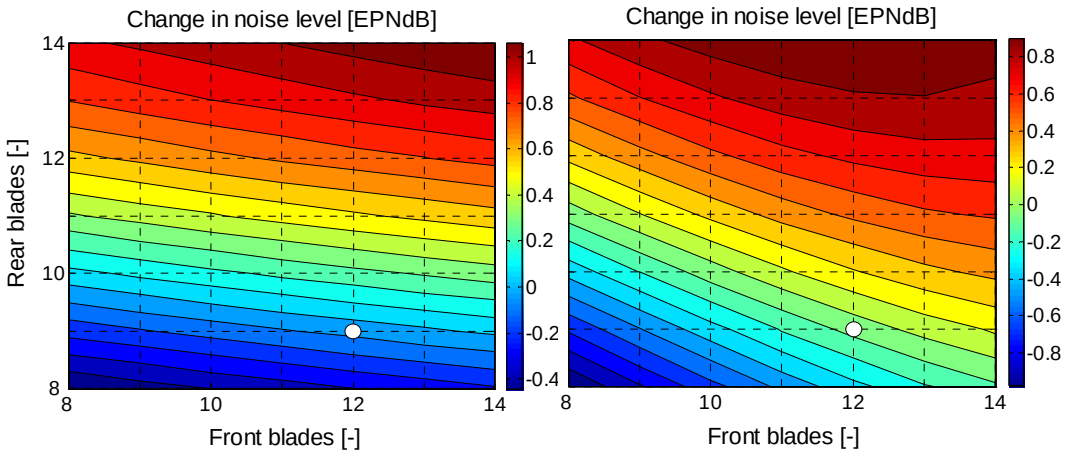

Figure 178a: Sideline noise vs. N_b (10% clipping) b: Flyover noise vs. N_b (10% clipping)

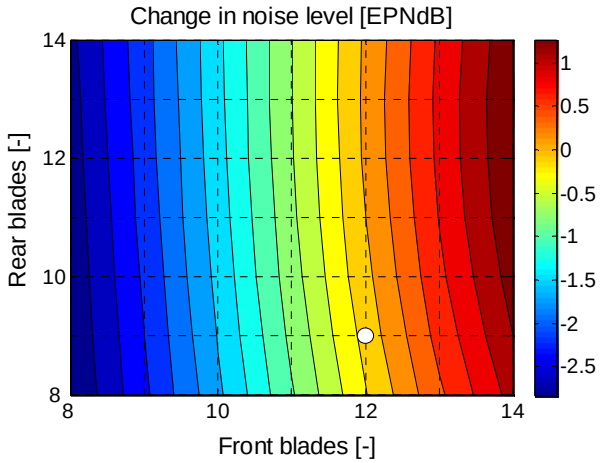

Figure 179: Approach noise vs. N_b (10% clipping)

Figure 180 and Figure 181 present the change in noise with respect to the number of blades of the propellers for a 20% clipped CRP design. The number of blades in the rear propeller of a 20% clipped design has a larger impact on approach noise than for the 10% clipped design. These figures together with Figure 177 present the trade-off between mission fuel burn and certification noise for changes in N_b of a 20% clipped CRP DDOR. For example: the 13x14 design (minimum fuel burn design within the limits of the noise simulations) is 1.4 EPNdB louder in sideline, 1.2 EPNdB louder in flyover and 4.5 EPNdB louder in approach than the 8x8 design. The cost of using an 8x8 design (quieter) with respect to the 13x14 design is 2.3% in mission fuel burn.

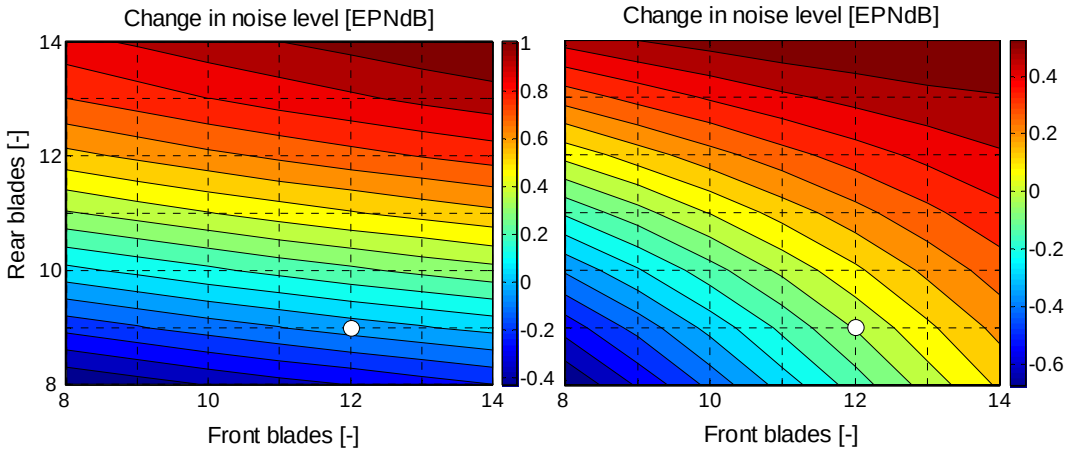

Figure 180a: Sideline noise vs. N_b (20% clipping) b: Flyover noise vs. N_b (20% clipping)

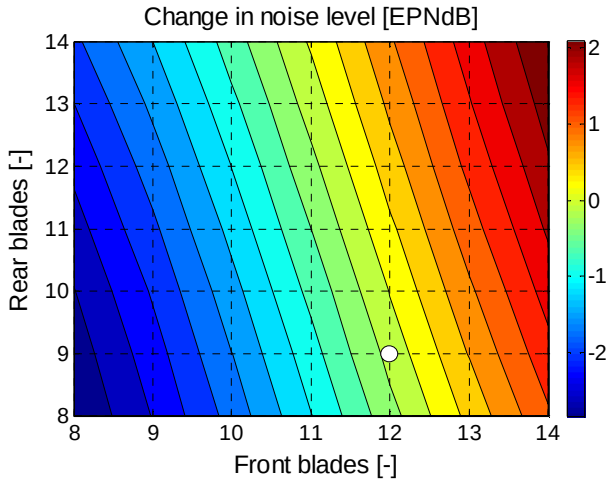

Figure 181: Approach noise vs. N_b (20% clipping)

Both for the 10% and 20% clipped CRP DDORs, the noise increases with the number of blades in both propellers. This suggests that the increase in interaction noise produced by an additional blade is not compensated by the reduction in loading noise (even for highly clipped designs). These preliminary results need to be further investigated with an enhanced noise prediction module as suggested in section 2.6.3.

3.3.3.6 Number of stages and rotational speeds of the CRT

The CRT can be designed with different number of stages (NbStages). Only even NbStages are considered in this study (see Consideration 1 in section 2.2.3.3.2.7). Given the CRT power requirement, N_1, N_2 and inlet flow conditions, there is a minimum NbStages required in the CRT (set by the maximum achievable stage turning (see section 2.2.3.3.3.1). Figure 182 presents the minimum required NbStages of the baseline DDOR for a range of forward and rear propeller rotational speeds (maintaining $N_1 = -N_2 = N$). The same plot was produced for DDORs with CRP diameters ranging from 4.26 to 3.5 m. The rotational speeds at which the

minimum required NbStages change, varied by less than 1% for all the studied CRP diameters. This is because the specific power of the CRT ($Pw_{CRT}/\dot{m}_{in\ CRT}$) is almost constant (given that the core PR and the NPR are fixed) and the variations in CRT inlet temperatures are relatively small. DDORs with different core and/or NPR definitions have different feasibility charts.

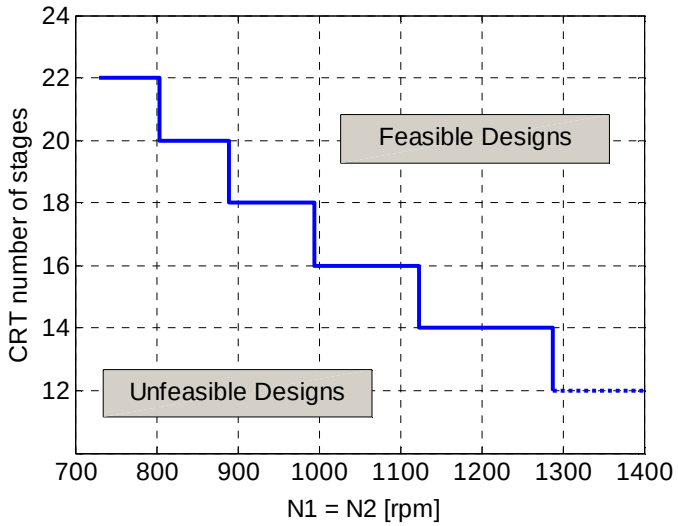

Figure 182: CRT feasibility chart

Figure 183 shows the change in mission fuel burn with respect to NbStages for different values of N. Within the studied range of N, the increase in NbStages reduces the mission fuel burn. This is because the increase in $\eta_{is\ CRT}$ obtained by adding an extra couple of CRT stages is higher than the weight penalty of the extra stages.

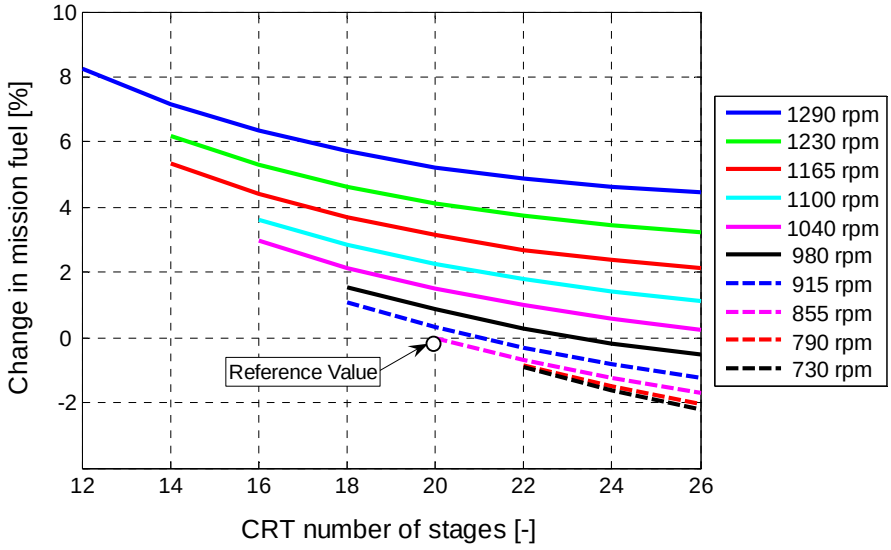

Figure 183: Mission fuel burn vs. NbStages and N ($N_1 = -N_2$)

Figure 184 presents the change in $\eta_{is\ CRT}$ and engine weight for all the cases presented in Figure 183. The change in $\eta_{NET\ CRP}$ with NbStages is minimum (the propeller loading varies less than 1%) and therefore not presented. The changes in $\eta_{NET\ CRP}$ with N_i are presented in the section 3.3.3.7.

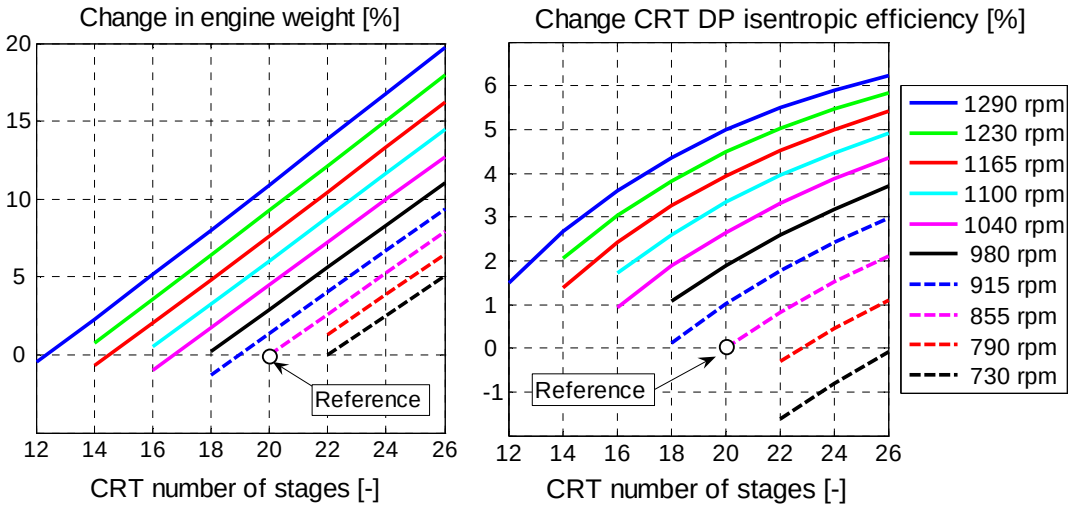

Figure 184: Engine weight and $\eta_{is\ CRT}$ vs. NbStages and N ($N_1 = -N_2$)

It should be noted that the present results do not consider the change in the aircraft structures weight required to fit a heavier engine and the changes in nacelle drag of a longer engine. This would reduce the benefit offered by an extra pair of CRT stages. Manufacturing and maintenance costs associated to the extra CRT stages also need to be considered during the optimisation process.

Figure 185 presents the changes in gaseous emissions for the baseline DDOR with respect to NbStages. The emissions follow the trends of the changes in SFC, which are almost identical to those of $\eta_{is\ CRT}$ (dashed pink line in Figure 184).

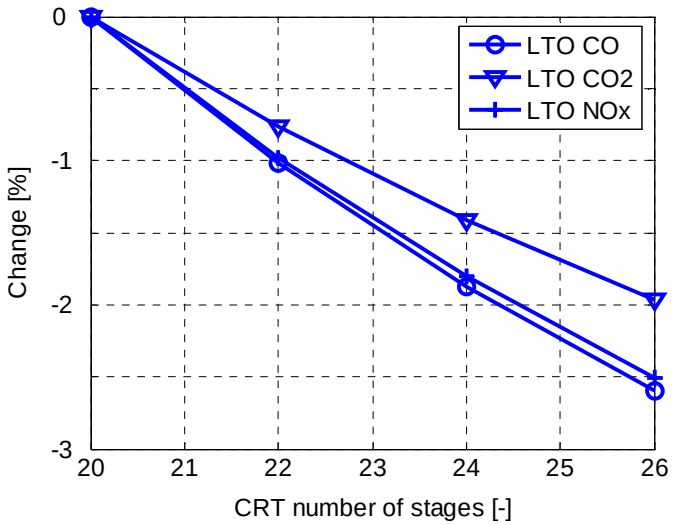

Figure 185: LTO emissions vs. CRT number of stages for the reference DDOR design

3.3.3.7 Diameters and rotational speeds of the propellers

This section presents the effects of changing the diameters and rotational speeds of the propellers. In order to present the results in 2-D charts, it was decided to divide the study in two sub-sections:

- Diameter and rotational speed: the diameter and rotational speeds of both propellers are varied keeping $N_1 = -N_2 = N$ and $D_1 = D_2 = D$.
- Clipping and speed ratio: different clippings and speed ratios of the propellers are assessed using D_1 and N_1 of the baseline DDOR.

As presented in section 3.3.3.6, the feasible range of CRP rotational speeds depends on the number of stages of the CRT. A 22 stages CRT is used in the following sections in order to increase the range of feasible propeller rotational speeds that could be investigated. The mission fuel burn of this design is 0.6% lower than that of the baseline.

3.3.3.7.1 Diameter and rotational speed

Figure 186 presents the change in mission fuel with the CRP diameter ($D = D_1 = D_2$) and rotational speed ($N = N_1 = -N_2$). The minimum fuel design for all the studied rotational speeds is higher than 4.26 m. The diameter of the CRP was constrained to 4.26 m to comply with installation requirements. For the baseline N, the estimated minimum mission fuel burn D (weight and drag penalties associated with a longer pylon not considered) is approximately 4.7 m. The estimated mission fuel burn reduction of a D = 4.7 m design relative to a D = 4.26 m design, is less than 0.4% and it would be even lower if the associated installation penalties were considered.

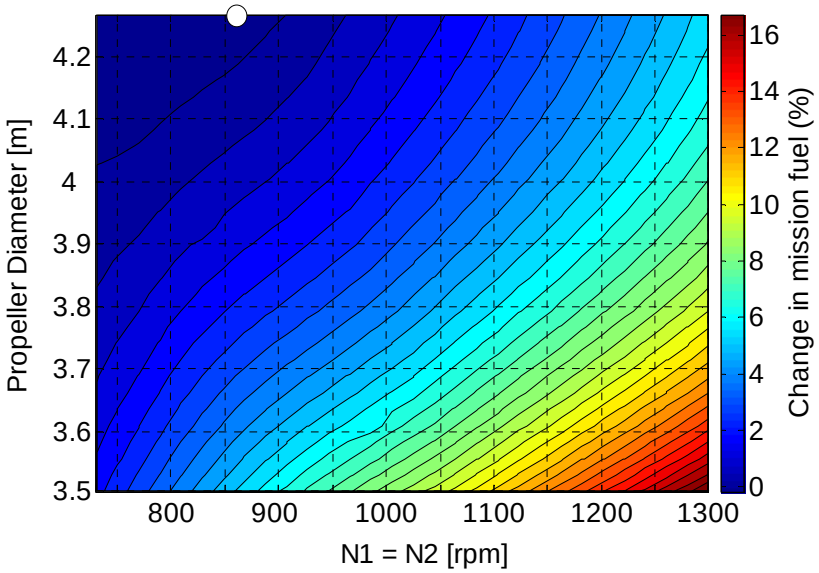

Figure 186: Mission fuel burn vs. N and D ($N = N_1 = -N_2$ and $D = D_1 = D_2$)

The variation in mission fuel burn vs. N and D for a 10% clipped CRP design was also plotted for a 10% clipped design (using D_1 = 4.26 m and N = 860 rpm as a

reference). It was not possible to distinguish visually the difference between this plot and Figure 186, and it is consequently omitted.

Figure 187 shows the change in SFC with respect to D and N for the TOC and take-off points. These two operating conditions are taken as representative examples of high and low flight speeds and will be used to explain the trends of Figure 186. Figure 188 presents the change in engine weight with respect to D and N.

The trends presented in Figure 186 are mainly dominated by the changes in $\eta_{NET\ CRP}$ and $\eta_{is\ CRT}$ (that determine the SFC) and the changes in engine weight. For example, the fuel burn of the engine design with D = 4.26 m and N = 1300 rpm is approximately 5.5% higher than the fuel burn of the reference design[91]. It can be seen in Figure 187 that the SFC for the D = 4.26 m and N = 1300 rpm design is almost 8% higher at TOC and 1.5% higher at take-off relative to the SFC of the reference design. Figure 188 indicates the D = 4.26 m and N = 1300 rpm design is approximately 10% heavier than the baseline. The combined effect of 1.5 - 8% SFC penalty and 10% engine weight penalty result in 5.5% increase in mission fuel burn.

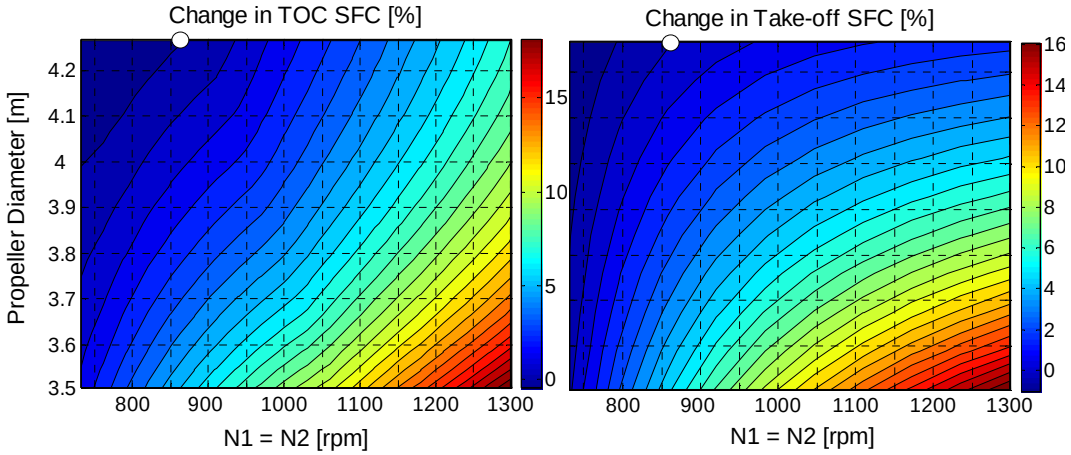

Figure 187: TOC and take-off SFC vs. D and N (take-off: M_0 = 0.25, dISA = 0, Alt = 0)

Engine weight increases with increases in both D and N. This is because CRPs and CRTs with higher rotational speeds are heavier (higher stresses). Furthermore, the engine core weight increases as DP N increases because CRPs are less efficient and a higher core mass flow rate is required.

[91] The reference DDOR used for this studies has a 22 stages CRTand the rest of the design parameters equal to those of the baseline DDOR

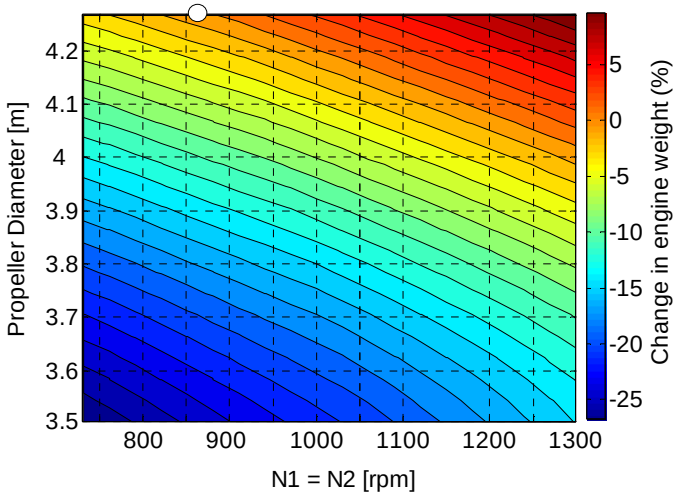

Figure 188: Engine weight vs. N and D

The following paragraphs present the main factors which influence the variations in TOC SFC with D and N (Figure 189a). Figure 190a shows the variation in TOC $\eta_{NET\ CRP}$ and Figure 190b shows the variation in $\eta_{is\ CRT}$. It can be seen that the iso-SFC contours are similar to the iso- $\eta_{NET\ CRP}$ contours but with a reduction in the slope due to the increase of $\eta_{is\ CRT}$ with increasing N.

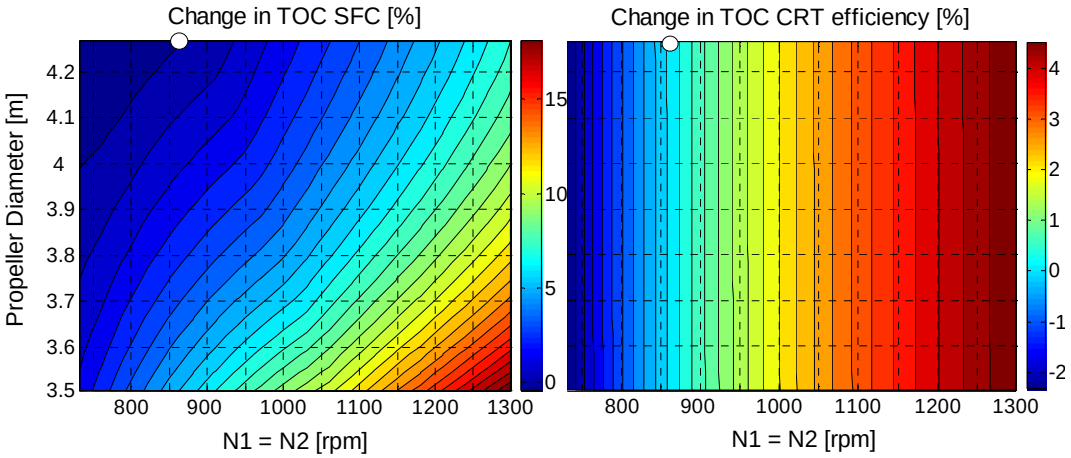

Figure 189a: TOC SFC vs. D and N

b: TOC $\eta_{is\ CRT}$ vs. D and N

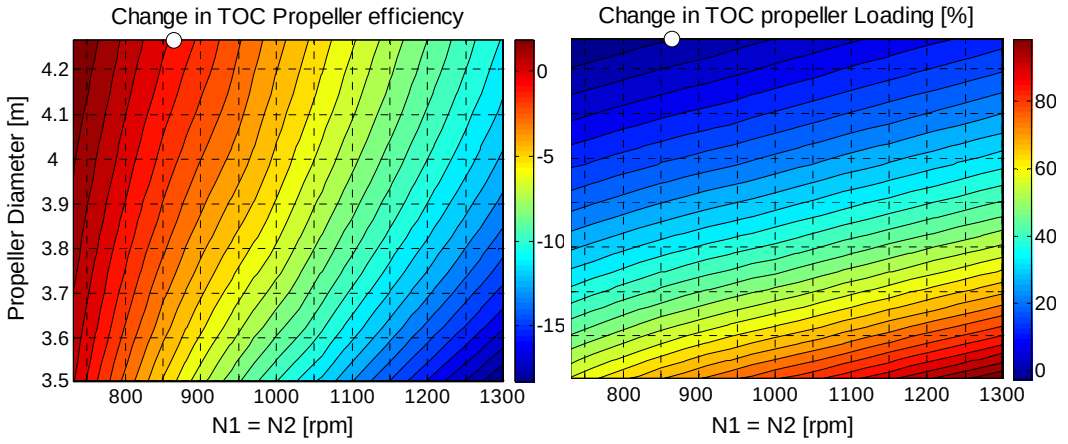

Figure 190a: TOC $\eta_{NET\ CRP}$ vs. D and N b: TOC L_P vs. D and N[92]

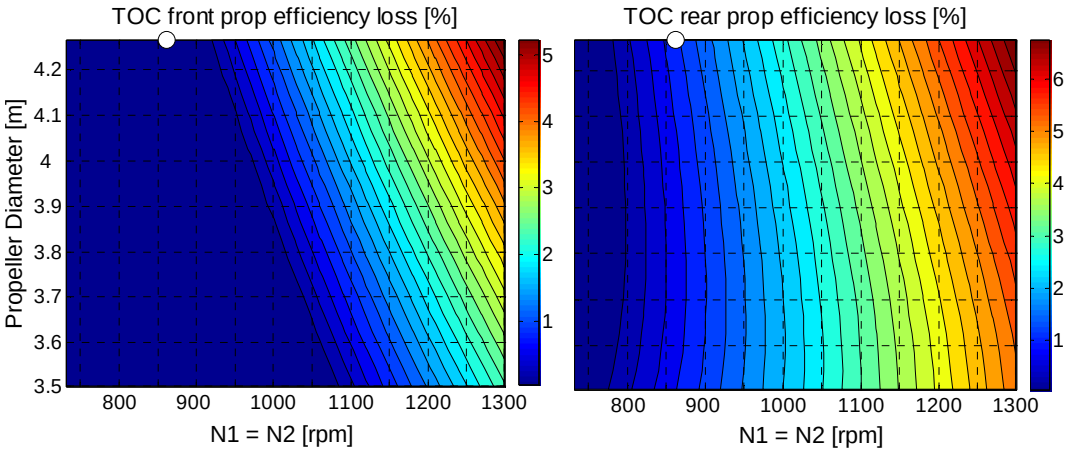

Figure 191: Propeller efficiency losses due to compressibility effects

The changes in $\eta_{NET\ CRP}$ (Figure 190a) are dominated by the changes in power loading (LP) (Figure 190b) and compressibility losses (Figure 191):

- As D reduces, L_P increases and as a result η_{NET} decreases. Additionally, as D reduces, the compressibility losses decrease, but this change is relatively smaller than the changes in efficiency due to the increase in L_P.
- As N increases, the compressibility losses in both propellers increase (apart from the region where they are zero for the forward propeller) making the propeller less efficient. As the propeller is less efficient, more power is required to produce the TOC thrust, resulting in a higher L_P and a further reduction in $\eta_{NET\ CRP}$.

The forward propeller compressibility losses are dominated by its tip speed (Figure 191). If the relative tip helical Mach number is smaller than 0.89, there are no transonic losses (dark blue region in Figure 191). The compressibility losses of the

[92] Note that the variation in L_{P1} is equal to the variation in L_{P2} because TR_{CRT} is fixed and $N_1 = -N_2$ and $D_1 = D_2$

rear propeller are higher than those of the forward propeller. This is because the flow reaching the rear propeller has higher axial and rotational speeds resulting in higher relative tip helical Mach numbers. The variation of the induced velocities has a major influence on the shape of the contours of Figure 191. The effects of the compressibility losses of the forward propeller on $\eta_{NET\ CRP}$ and on SFC can be seen in Figure 189a and Figure 190 respectively (change in slope of the contours). The effects of the rear propeller compressibility losses on $\eta_{NET\ CRP}$ and SFC are more difficult visualise because they affect all the plotted designs.

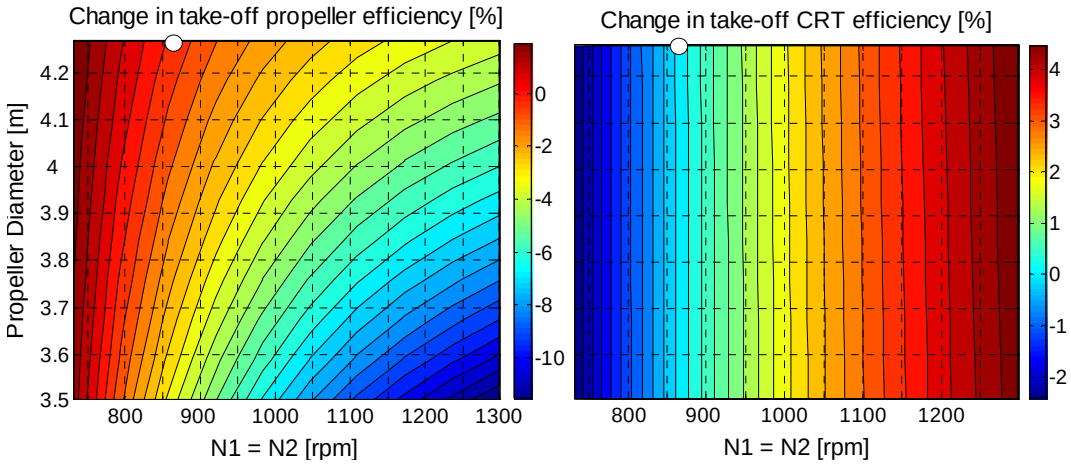

Figure 192: Take-off $\eta_{NET\ CRP}$ vs. D and N b: Take-off $\eta_{is\ CRT}$ vs. D and N

(M_0 = 0.25, dISA = 0, Alt = 0)

Figure 192 presents the change in take-off CRP and CRT efficiencies with D and N. The trends are similar to those of TOC with the difference that no compressibility losses take place due to the low flight speed.

Figure 193 and Figure 194 present the variations in certification noise with respect to D and N for a 10% clipped CRP design. It should be noted that due to limitations in the noise module, the propeller is operated at 1.15 N_{1Des} at the three certification points. These limitations are also responsible for the absence of values in white regions of the plots. The propeller rotational speeds indicated in these figures correspond to the real rotational speeds of the propellers at the certification points. These figures together with Figure 186 present the trade-off between noise and fuel burn with respect to N and D. The emissions follow the same trends as the changes in SFC for each operating point.

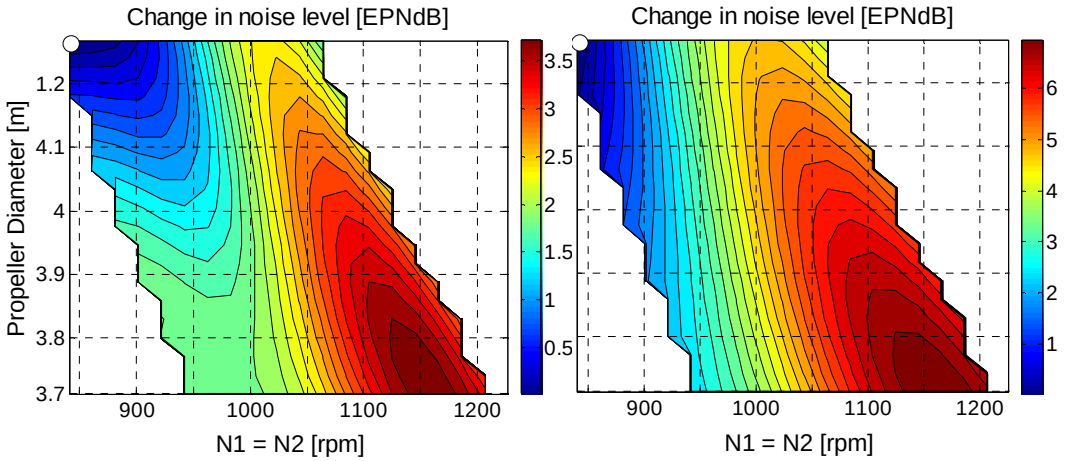

Figure 193a: Sideline noise vs. D and N **b: Flyover noise vs. design D and N**

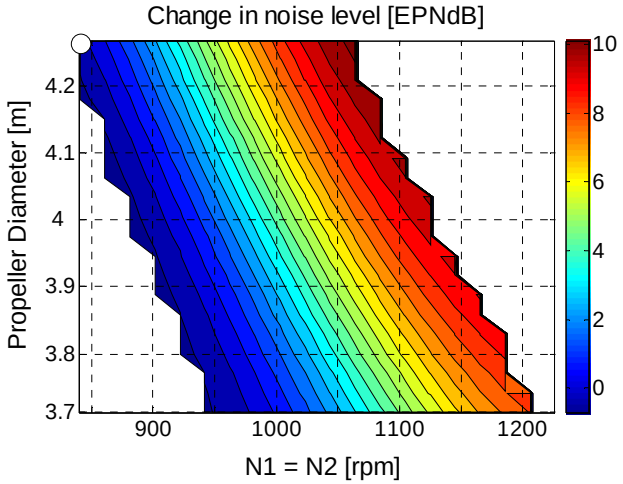

Figure 194: Approach noise vs. design D and N

As a general conclusion, sideline and flyover noise can be reduced by increasing D and operating the CRP at the appropriate rotational speeds. For any D there is a minimum sideline noise N. This is due to the relative variations in loading and interaction noise of both propellers. As N is reduced, the interaction noise is reduced, but the loading noise is increased as the thrust is kept constant. At high N, the reduction in interaction noise produced by the reduction in N is higher than the increase in loading noise. At low N, the increase in loading noise produced by the reduction in N is higher than the reduction in interaction noise.

The minimum noise rotational speeds for the 10% clipped DDOR with D = 4.26 m is between 850 and 900 rpm.

The propeller tip speed corresponding to the minimum sideline noise decreases as D increases. In reality, the variations in minimum noise tip speed with D are likely to be larger than those obtained because of the reasons described in section 2.6.3.

The flyover noise follows the same trends as sideline noise, but the minimum N for every D is lower in the case of flyover, as the aerodynamic loading of the propeller is lower than that for sideline.

The approach noise is dominated by the interactions between the propellers as the aerodynamic loadings are considerably reduced. It can be seen in Figure 194 that the approach noise increases as D increase for a constant tip speed (function of D and N). Consequently, the reduction in sideline and flyover noise that could be achieved by increasing D at constant tip speed would result in a noise penalty during approach. The trade-off between noise levels at the three certification points is of paramount relevance since the regulations impose maximum allowed levels for (sideline + flyover + approach) as well as for (sideline + flyover), (sideline + approach) and (approach + flyover).

The shapes of the noise vs. N and D contours of a 20% clipped design are analogous to those of the 10% clipped design. The variations in sideline EPNdB with respect to N and D of a 20% clipped design are of the same order of magnitude than those of the 10% clipped design. The variations in flyover and approach EPNdB with respect to N and D of a 20% clipped design are approximately half of those of the 10% clipped design.

3.3.3.7.2 Clipping and speed ratio of the propellers

The CRP can be clipped (D_2 smaller than D_1) to reduce the effects of the ingestion of the forward propeller tip vortex by the rear propeller. This reduces the propeller noise but also reduces its efficiency since part of the swirl of the forward propeller is not recovered by the rear propeller. The definition of clipping is provided in Eq. 180 (section 3.2.1.3)

Figure 195 and Figure 196 present the variations in mission fuel burn and engine weight with respect to the propeller clipping and N_2 for the baseline value of D_1 and N_1 (NbStages = 22).

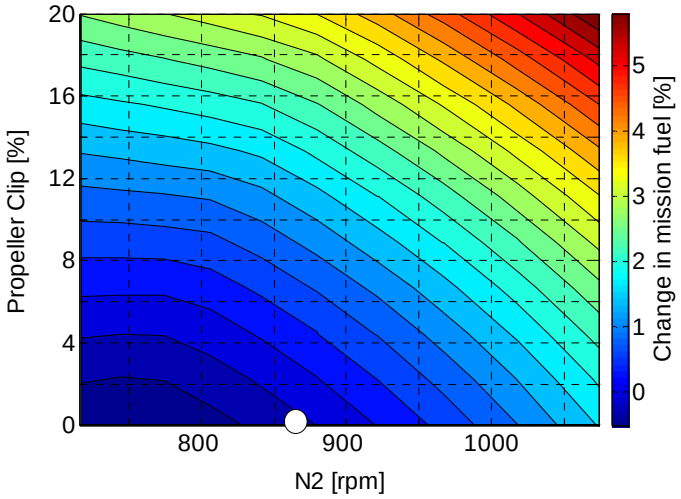

Figure 195: Mission fuel burn vs. Clipping and N_2 (baseline D_1 and N_1, NbStages = 22)

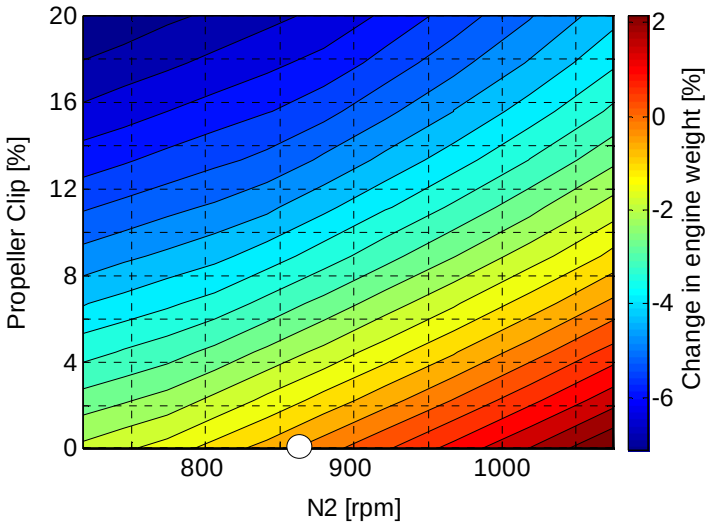

Figure 196: Engine weight vs. Clipping and N_2 (baseline D_1 and N_1, NbStages = 22)

Although the engine weight decreases with clipping, mission fuel burn increases. For all the studied values of N_2, the unclipped CRP design offers the lowest mission fuel burn. A reduction in N_2 offers a reduction in mission fuel burn up to a certain point. The minimum mission fuel burn for the unclipped design is achieved at N_2 = 750 rpm.

The following paragraphs present the main factors which influence the variations in DP SFC with respect to clipping and N_2 (Figure 197a). The TOC iso-SFC contours are similar to the iso- $\eta_{NET\ CRP}$ contours (Figure 197b) with the slopes modified by the change in $\eta_{is\ CRT}$ (Figure 198a). It can be seen that the iso- $\eta_{NET\ CRP}$ contours have a change in slope due to the compressibility losses of the rear propeller (Figure 198b). The variations in compressibility losses of the forward propeller are relatively smaller.

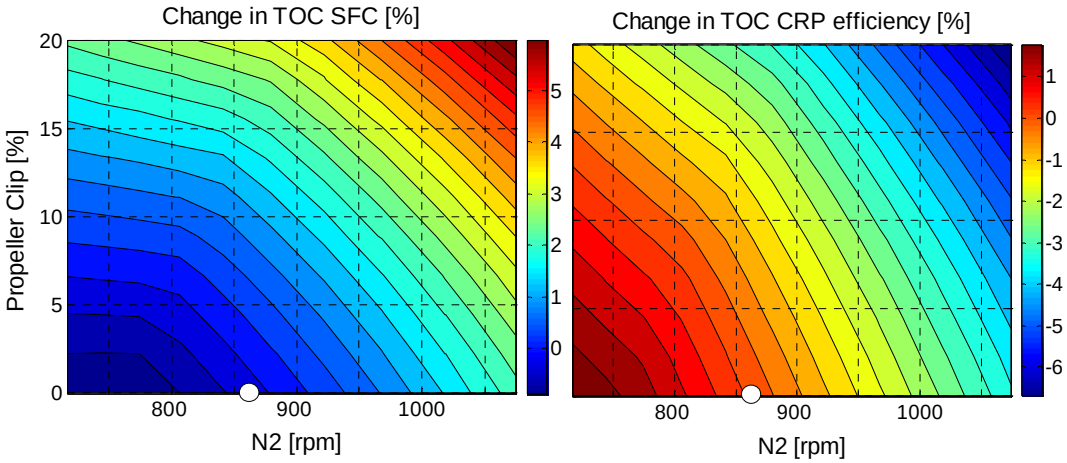

Figure 197a: TOC SFC vs. Clipping and N_2 **b: TOC CRP η_{NET} vs. Clipping and N_2**

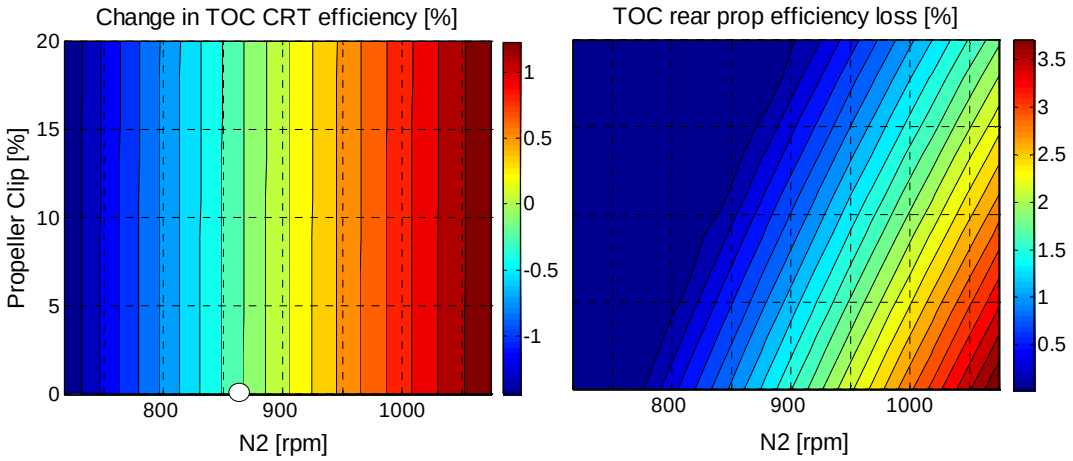

Figure 198a: TOC $\eta_{is\ LPT}$ vs. Clipping and N_2 b: compressibility losses vs. Clipping and N_2

The changes in $\eta_{is\ CRT}$ with respect to N_2 are relatively smaller than those obtained for changes in N_1 and N2 (Figure 189b). This is because a simultaneous variation in N_1 and N_2 reduces the aerodynamic loading of all CRT stages, while a change in N_2 only affects half of the CRT stages. Furthermore, a simultaneous change in N_1 and N_2 results in a quadratic change of the aerodynamic loading of the stages ($\Delta h/U^2$), while a variation in N_2 only results in a linear change. This is due to the fact that the CRT provides equal torque to both drums. In the case of an increase in N_1 and N_2, the forward and rear propeller powers remain almost constant, and therefore the loading ($\Delta h/U^2$) is reduced quadratically for both rotors. In the case of an increase in N_2, the power of the rear propeller increases almost linearly with N_2 (maintaining a constant torque ratio), and therefore the aerodynamic loading ($\Delta h/U^2$) of the stages rotating at N_2 decrease linearly.

Figure 199 shows the changes in the forward and rear propeller power loading (L_P) at DP. Changes in N_2 result in a variation in the power ratio of the propellers because DP TR_{CRT} = 1. For constant clipping, a quasi linear variation of L_P with N_2 can be observer for the rear propeller, denoting the quasi linear variation in power[93] (the area is fixed). For constant N_2, L_P of the rear propeller varies aproximately[93] in proportion to change in area. The forward propeller power (which is proportional to L_P since it has a constant area) varies to compensate for the changes in CRP power ratio (and changes in the efficiency of components).

[93] The variation is not linear because the total power absorbed by the CRP varies as the efficiency of the CRP and CRT vary.

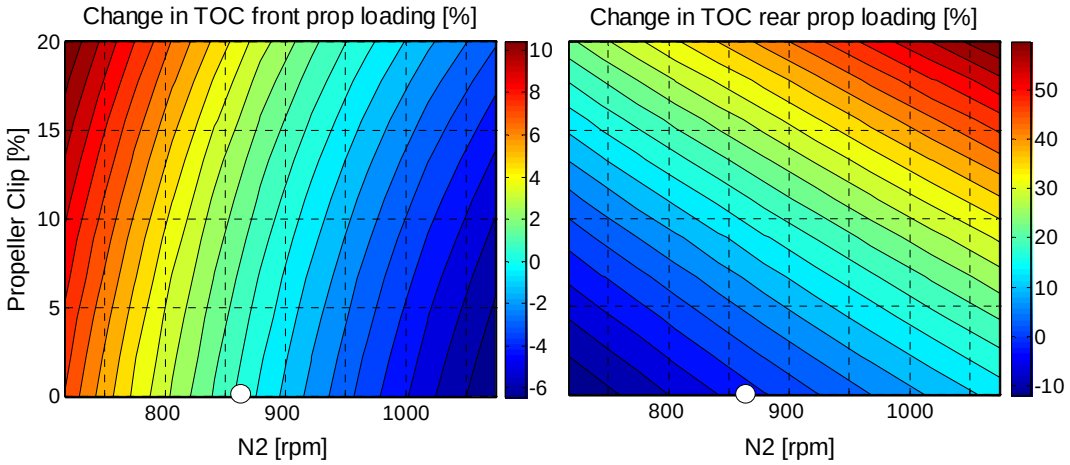

Figure 199: TOC L_P vs. clipping and N_2

Figure 200 and Figure 201 present the changes in certification noise with respect to the propeller clipping and N_2. Note that the propeller rotational speeds indicated in the noise figures correspond to the real rotational speed (1.15 N_{1Des}) at the corresponding operating point and the white dots are located at the reference N_2 used to express the variations. According to TENOR, clipping has a very limited influence (less than 0.5 dB within the studied range) on sideline noise but has a relevant effect on both flyover and approach noise levels. Flyover noise level can be reduced 2.5 EPNdB by clipping 20% the rear propeller at the reference N_2. Approach noise can be reduced almost 3.5 EPNdB with the same amount of clipping. This relevant reduction in noise would be achieved at a cost of 3.5% of mission fuel burn. Figure 195, Figure 200 and Figure 201 show the trade-off between noise and mission fuel burn for any combination of clipping and N_2 for a DDOR with a 22 stages CRT. A reduction in N_2 appears to be beneficial both from the noise and the fuel consumption point of view. The emissions follow the same trends as the changes in SFC for each operating point.

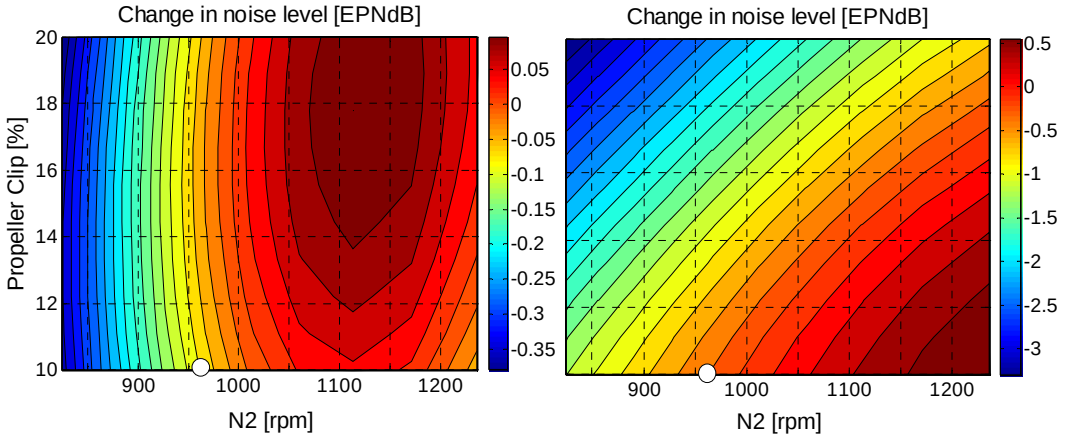

Figure 200a: Sideline noise vs. Clipping and N_2 b: Flyover noise vs. Clipping and N_2

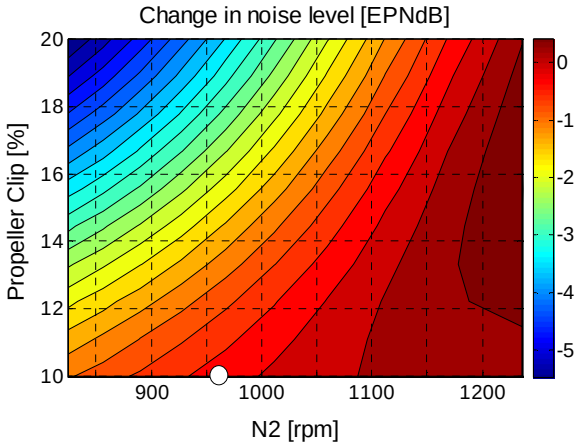

Figure 201: Approach noise vs. Clipping and N_2

3.3.3.8 Efficiencies of compressors and turbines

The IPC, IPT, HPC and HPT efficiencies were estimated for a 2020 level of technology and were kept constant for all the studied DDOR designs. The CRT efficiency was estimated using the methodology described in section 2.2.3.3.3.1. Table 18 summarises the effects of not achieving the estimated efficiency levels on mission fuel burn.

Change in component efficiency	Change in mission fuel burn [%]
-1% IPC poly. eff.	+ 0.65
-1% IPT is. eff.	+ 0.32
-1% HPC poly. eff.	+ 0.51
-1% HPT is. eff.	+ 0.46
-1% CRT is. eff.	+ 1.00

Table 18: Mission fuel penalty vs. change in efficiency of turbomachinery components

3.3.3.9 Minimum fuel burn design region

Within the assumptions of the study, the number of stages of the CRT which minimises the fuel burn of the reference mission is approximately 30. A DDOR engine with such a large CRT was judged to be non feasible. A 22 stages CRT was judged to be acceptable from a mechanical integration point of view (based on discussions with OEM experts) and used as a limit in the optimisation study. The DDOR design with a 22 stages CRT which offers the minimum fuel consumption for the reference mission lies in the following region of the design space:

- DP NPR ~ 1.6
- D_1 between 4.26 and 4.7
- Clipping = 0
- Nb_1 = 13 and Nb_2 = 14
- DP N_1 and N_2 ~ 750

- Minimum hub diameter
- Minimum spacing between propellers

Table 19 presents the results of a mission fuel burn minimisation performed with ISIGHT. The optimiser was allowed to modify all the low pressure preliminary design variables listed in section 3.3.3, except for the IPC bleed mass flow rate which was set to zero. The minimum SFC control strategy for the baseline DDOR was used and the following constraints were imposed.

- maximum dimaters of the propellers = 4.26 m (the pylon considered in the aircraft model does not allow larger propeller diameters)
- minimum spacing between propellers = 0.65 m (refer to section 3.2.3.2)
- minimum hub diameter = 1.55 m (limited by the diameter of the CRT at stage 11 and the thickness of the nacelle)
- maximum number of stages of the CRT = 22

Engine Design	
Core	Baseline
$D_1 = D_2$	4.26 m
Spacing between propellers	0.65 m
Hub diameters of the propellers	1.55 m
Nb_1	13
Nb_2	14
DP N_1	750
DP N_2	750
CRT number of stages	22
DP NPR	1.57

Changes w.r.t. the baseline DDOR	
Mission fuel burn	- 2.8 %
LTO NOx	- 2.4 %
Engine weight	+ 7.4 %

Table 19: Minimum mission fuel burn DDOR design

The certification noise of this DDOR design can not be evaluated with TENOR because the clipping of the rear propeller is smaller than 10% (refer to section 2.6). Minimum noise DDOR designs could be identified with an enhanced noise module (refer to section 2.6.3).

4 CONCLUSIONS AND RECOMMENDATIONS FOR FURTHER WORK

4.1 Conclusions

CRORs have significant potential to reduce aircraft fuel burn (see section 1.1.2.5), however there are challenges that need to be addressed both at aircraft and at engine level (see section 1.1.2.5). Currently, diverse efforts (see section 1.1.2.6) are being devoted to develop novel solutions in order to overcome the main challenges. Some of these solutions may impact different aspects of the engine and aircraft design, operation and performance.

The assessment of the impact of the main low pressure preliminary design and control parameters of CRORs on mission fuel burn, certification noise and emissions is necessary to identify optimum design regions and to assist the development process when compromises need to be performed as a consequence of design, operational or regulatory constraints.

Novel methodologies to model the performance of CRPs (0-D) and CRTs (1-D and 0-D) were developed. These models were verified using available data (see sections 2.2.3.2.4 and 2.2.3.3.2.6). Additionally, a performance model of a DPGB was developed. Using these component models, novel CROR engine performance models were developed which allow the independent definition of the design and operation of the two parts of the CRP and CRT. This is not possible with other state of the art modelling tools.

A multi-disciplinary preliminary design simulation framework (TERA-OR 2020) was built using the novel engine performance modules together with dedicated CROR aircraft performance, engine geometry and weight, gaseous emissions and certification noise simulation modules. These simulation modules were also verified with available data.

The trade-offs between fuel burn, noise and emissions with respect to the main LP preliminary design and control variables of a pusher GOR and DDOR (160 PAX aircraft flying a 500 NM mission and cruising at M 0.75) were presented. Minimum fuel burn regions were identified on the GOR and DDOR design spaces.

The following sections summarise some of the main conclusions:

4.1.1 General conclusions

- The CROR architecture offers 2 additional degrees of freedom in engine control (N_1 and N_2) compared to turbofans. The minimum fuel burn control strategies for a GOR and a DDOR were presented (rotational speeds for minimum SFC increase with an increase in required thrust). These strategies provide 1 - 2% mission fuel burn savings relative to a fixed N_1 and N_2 control. Significant noise reductions can also be achieved by adequately controlling the rotational speeds

of the propellers during the LTO cycle. Sideline and flyover noise can be reduced by 2 EPNdB by reducing N_1 and N_2, at a cost of 0.3% in mission fuel burn, 5.5-7% increase in LTO NOx emissions and 10-15 K increase in take-off TET. During approach, reductions in N_1 and N_2 (relative to the design values) have a positive effect on noise, fuel burn and emissions.

- Air from the IPC can be bled and blown through the engine pylon to reduce the noise of the CRP. A permanent extra bleed of 10% of the IPC inlet mass flow rate results in an 8% increase in mission fuel burn. If the extra bleed is only used during the LTO cycle and is not considered for the top of climb aerodynamic sizing of turbomachinery components, it has a negligible impact on fuel burn, but a large impact on take-off TET (~80-90 K increase in take-off TET for 10% extra IPC bleed) and therefore NOx.

- The spacing between the propellers has a large influence on certification noise levels and a relatively small influence on mission fuel burn both for clipped and unclipped CRP designs. A CROR with a propeller spacing of 1.35 m produces 6 EPNdB less noise for all certification points and consumes 0.3-0.5% more fuel than a CROR with a propeller spacing of 0.65 m.

- As the diameter of the propellers (D) increases, their power loading reduce but the compressibility losses and weight increase. D was limited to a maximum of 4.26 m due to installation constraints. For the studied range of CRP rotational speeds (725–950 rpm for the GOR and 730-1300 rpm for the DDOR), D = 4.26 m grants the minimum mission fuel burn. Larger values of D were simulated (not considering the weight and drag penalty associated with a longer pylon) and the fuel burn optimum was found at 4.7 m, offering a fuel burn reduction of 0.4%. This reduction would be even smaller if the corresponding installation penalties were to be considered.

- Sideline and flyover noise can be reduced by increasing D and operating the propellers at the appropriate rotational speeds. For a given D, there is a combination of rotational speeds (N_1 and N_2) that produces minimum sideline and flyover noise. The minimum noise tip speeds (sideline and flyover) decrease as D increases. The rotational speeds for minimum sideline noise, for 10% clipped CRPs with D = 4.26 m, are between 850 and 900 rpm for both engines. The rotational speeds for minimum flyover noise are lower than those for sideline. These rotational speeds lie outside of the range of the noise module predictions.

- At a constant propeller tip speed, approach noise is increased with an increase in D. The noise during approach can be reduced by reducing either D, N_1 or N_2. The trade-off between noise levels at the three certification points is of paramount relevance since the regulations impose maximum allowed levels for (sideline + flyover + approach) as well as for (sideline + flyover), (sideline + approach) and (approach + flyover).

- Propeller clipping is an effective technique to reduce certification noise levels. 20% clipped designs are 2.5 EPNdB quieter at flyover and 4.5 EPNdB quieter at

approach than 10% clipped designs. The mission fuel burn penalty of 20% clipped CRPs relative to unclipped CRPs is ~2 % for a GOR and ~3.5% for a DDOR. Unclipped propellers offer minimum mission fuel burn for all the studied range of CRP rotational speeds.

- The reduction of N_2 reduces both noise and fuel burn up to a certain value of N_2 (function of the engine design). A further reduction in N_2 reduces noise, but increases the mission fuel burn.

- The number of propeller blades has a significant impact on the certification noise levels. The number of blades of the rear propeller dominates the sideline and flyover noise, while the number of blades of the forward propeller dominates the approach noise. An increase in the number of blades results in an increase in certification noise for all the studied CRP designs.

- The minimum fuel consumption is achieved with a 13x14 CRP (13 blades in the forward and 14 blades in the rear propeller) for the DDOR and a 14x13 CRP for the GOR. These engine designs are ~0.5% more fuel efficient than the baseline engines (12x9 CRP) but require 6 extra blades. An increased number of blades in the rear propeller is required to minimise the mission fuel burn for clipped designs. For both engine architectures, 2 extra rear blades are required to minimise the fuel burn for 20% clipped designs achieving a fuel reduction of ~0.1%. The presented trends together with mechanical and cost considerations can be used to determine the optimum number of blades of the propellers.

- The minimum SFC DP NPR is approximately 1.45 (trade-off between propulsive and thermal efficiency) while the minimum mission fuel burn DP NPR lies between 1.55 and 1.6. This is due do the engine weight reduction (LPT or CRT and CRP) associated with the increase in DP NPR.

- A 5% increase in hub diameter results in a 0.15% increase in mission fuel burn.

4.1.2 GOR conclusions

- The gearbox is designed at take-off and its weight depends on the transmitted torque. Consequently, the take-off propeller control strategy has an impact on the fuel consumption outside the LTO cycle. A 15% increase in take-off N_1 and N_2, relative to the design values, results in a 0.4% reduction in mission fuel burn (but noise levels are increased).

- For fixed N_1 and N_2, the rotational speed of the LPT (N_{LPT}) is a function of TR_{DPGB}. The range of TR_{DPGB} which results in feasible LPT designs (beyond this range the turbine rotates either too fast or too slowly) for different CRP rotational speeds (with $N_1 = N_2 = N$) was presented for 2 and 3 stages LPTs (Figure 138 and Figure 134 respectively). For any value of N, the difference between the minimum and maximum feasible TR_{DPGB} is approximately 0.1 and 0.02 for GORs with 3 stage and 2 stage LPTs respectively.

- The diameter of the DPGB increases as N_1, N_2 and TR_{DPGB} decrease. The DPGB design is considered feasible if its diameter is smaller than the hub diameter of the last stage of the LPT. For the 3 stage LPT GOR, the minimum feasible N_1 is ~730 rpm, the minimum feasible N_2 is ~660 rpm and the minimum feasible TR_{DPGB} is ~1.23. For the 2 stage LPT GOR, the minimum feasible N_1 is ~750 rpm, the minimum feasible N_2 is ~690 rpm and the minimum feasible TR_{DPGB} is ~1.24

- At constant N_1 and N_2, a reduction in TR_{DPGB} results in an increase of N_{LPT} and $\eta_{is\ LPT}$ (within certain limits) but both the LPT and the DPGB become heavier (larger turbine disks and planet gears required). For low clipped CRP designs, a reduction in TR_{DPGB} also results in an increase of $\eta_{NET\ CRP}$ due to a more favourable power loading distribution. As a consequence, a reduction in TR_{DPGB} reduces the mission fuel burn, provided $\eta_{is\ LPT}$ improves. This is the case for all the studied 2 stage LPT designs, but it is not the case for some of the studied 3 stage LPT designs (above a certain limit of N_{LPT} compressibility losses are higher than the potential gains associated with the reduction in aerodynamic loading).

- A simultaneous reduction of N_1, N_2 and TR_{DPGB} (within the limits presented in the previous point) reduces the mission fuel burn.

- The increase in CRP and LPT weight produced by the increase in design N_1 and N_2 (at a constant $N_{1\ take\text{-}off}$ / $N_{1\ Des}$, within the studied ranges) is approximately equal to the weight reduction of the DPGB. As a consequence, the weight of the GOR is practically unaffected by the design values of N_1 and N_2.

- Within the assumptions of the study, the GOR design which offers the minimum fuel consumption for the reference mission lies in the following region of the design space:
    - DP NPR ~ 1.5
    - 3 stage LPT
    - TR_{DPGB} ~ 1.27
    - D_1 between 4.26 and 4.7
    - Clipping = 0
    - Nb_1 = 14 and Nb_2 = 13
    - DP N_1 between 730 and 750
    - DP N_2 between 700 and 730
    - Minimum hub diameter and spacing between propellers

4.1.3 DDOR conclusions

- A chart showing the minimum required number of stages of the CRT for different CRP rotational speeds was presented (Figure 182).

- For the studied range of rotational speeds (730 to 1300 rpm) and number of stages of the CRT (12 to 26), an additional pair of CRT stages results in a mission fuel burn reduction. The fuel burn reduction due to additional CRT stages reduces as the number of stages of the CRT increase. The presented results can

be used together with turbine integration, mechanical integrity and economical considerations to select the appropriate number of CRT stages.

- Within the assumptions of the study, DDOR design with a 22 stages CRT which offers the minimum fuel consumption for the reference mission lies in the following region of the design space:
    - DP NPR ~ 1.6
    - D_1 between 4.26 and 4.7
    - Clipping = 0
    - Nb_1 = 13 and Nb_2 = 14
    - DP N_1 and N_2 ~ 750
    - Minimum hub diameter and spacing between propellers

4.2 Contribution to knowledge

The overall contribution to knowledge is the assessment of the impact of the main LP GOR and DDOR preliminary design and control parameters on mission fuel burn, certification noise and emissions. These assessments identify the optimum design regions to be explored in further detail with dedicated design tools. Additionally, they aid the design process when compromises need to be performed as a consequence of design, operational or regulatory constraints.

Novel methodologies to model the performance of CRPs (0-D) and CRTs (1-D and 0-D) were developed. Additionally, a performance model of a DPGB was developed. Using these component models, novel CROR engine performance models were developed which allow the independent definition of the design and operation of the two parts of the CRP and CRT. This is not possible with other state of the art modelling tools.

4.3 Recommendations for further work

Further work can be done to refine the engine, aircraft and noise modules, in order to improve the level of fidelity of the assessments. The following areas of work have been identified.

CRP model

- Verifying the CRP modelling methodology with further experimental data corresponding to advanced propeller designs at high forward speeds and refining the methodologies used to estimate the induced velocities.

CRT model

- Using a fully rigorous fluid model (such as those reported in Ref. 241) instead of ideal gas equations with constant fluid properties.

- Verifying the predictions of the 1-D mean line code in low pressure ratio regions where the loss correlations used were extrapolated.

- Using a more detailed loss evaluation method such as the one proposed in Ref. 242 and Ref. 243. Note that this method requires a more detailed definition of the blade geometry and a refined 1-D blade geometry design methodology is also required.

Engine performance models

- Integrating the 1-D mean line CRT calculation codes (both DP and OD) with the performance code in order to assess the impact of different CRT design criteria at engine and mission level. This requires:
  - optimisation of the numerical methods used in the 1-D codes in order to reduce the calculation time
  - the design of a numerically stable procedure to solve the engine design and the CRT design simultaneously.
- Improving the level of fidelity of the DPGB cooling system including:
  - the simulation of the blower as a compressor with a suitable map, and linking its rotational speed to the rotational speed of the HP shaft.
  - the calculation of the geometry of the heat exchanger for each evaluated engine design taking into consideration the fuel cooling system.
  - the simulation of the heat exchange and pressure losses of the air flow through the heat exchanger (using correlations such as the ones described in Ref. 205).
- Including a model to account for the variations in engine nacelle drag with respect to the geometrical definition of the components of the core.

Engine mechanical preliminary design model

- Modifying the mechanical preliminary design criteria of the differential planetary gearbox so that it finds the lightest design as opposed to the smallest design.
- Using the CRT gas path and blading obtained with the 1-D design methodology (integrated into the performance module) as input to the CRT preliminary mechanical design model.

Noise model

- Extending the data base of simulated CRPs including different blade designs or independent variations in blade pitch angles of both propellers. This would enable the noise module to predict the changes in noise with respect to the thrust and torque ratio of the CRP.
- Extending the ranges of simulated rotational speeds.
- Including the calculation of aircraft noise as well as ground and installation effects.

- Including cabin noise models in order to estimate cabin acoustic treatment requirements.

Aircraft model

- Including a preliminary design routine in the aircraft performance module to account for the changes in aircraft weight and aerodynamic characteristics due to:
  - changes in engine weight and propeller diameter which impact the design of engine mounting structures and aerodynamic control surfaces
  - changes in engine noise which impact the cabin acoustic treatment requirements

  The use of such a preliminary design aircraft module requires the iteration between the aircraft performance, engine performance and noise modules and is computationally costly.

Assessments

- Comparing each CROR engine design using its minimum fuel burn control strategy. This requires the use of an optimiser within the performance module in order to find the minimum SFC control strategy for every simulated point.
- Repeating the engine design space exploration using the enhanced engine, aircraft and noise modules.
- Using the enhanced noise estimation module to identify the minimum noise designs and control strategies.
- Developing and integrating additional simulation modules to assess the influence of preliminary design variables on environmental impact, acquisition costs and direct operating costs for CRORs.

REFERENCES

Ref. 1 Boeing Commercial Airplanes, (2011), "*Current Market Outlook 2011 to 2030"*.

Ref. 2 Low cost & Regional Airline Business (2008), "Jet Propulsion: Market Outlook", *Low cost & Regional Airline Business,* October 2008.

Ref. 3 European Commission (2001), "*European transport policy for 2010: time to decide",* European Commission.

Ref. 4 Airlines for America, (2012), *"Toward Global Competitiveness, Economic Empowerment and Sustained Profitability"*, January 2012, Airlines for America.

Ref. 5 Association of European Airlines, (2007), *"Operating Economy of AEA airlines 2007"*, Association of European Airlines, December 2007.

Ref. 6 ICAO organisation, (2008), *"ICAO Annex 16, International standards and recommended practices, Environmental protection, Volume II, Aircraft engine emissions"*, 3rd ed, July 2008.

Ref. 7 ICAO organisation, (2002), *"ICAO Annex 16 Volume 1, Environmental Protection, Aircraft Noise"*, amendment 7, 21 March 2002.

Ref. 8 European Parliament (2008), *"Directive 2008/101/EC of the European Parliament and of the Council"*, 19 November 2008.

Ref. 9 Clarke, J. P., (2003), *"The Role of Advanced Air Traffic Management in Reducing the Impact of Aircraft Noise and Enabling Aviation Growth"*, Journal of Air Transport Management, Vol. 9, No. 3, pp. 161-165, May 2003.

Ref. 10 Guy Norris, (2008), *"Core Values"*, Aviation Week & Space Technology, 14th July 2008.

Ref. 11 P. Seidenman, D. J. Spanovich, (2009), *"Powerplant Performance"*, Aviation Week, Overhaul & Maintenance, November 2009.

Ref. 12 A.L. Weisbrich, J. Godston,E. Bradley, (1982), *"Technology and Benefits of Aircraft Counter-Rotation Propellers"*, NASA CR-168258, 1982.

Ref. 13 R. H. Langue, (1986), *"A review of advanced turboprop transport aircraft"*, Progress in Aerospace Sciences, Volume 23, Issue 2, Pages 151–166, 1986.

Ref. 14 D. C. Mikkelson, G. A. Mitchell, L. J Bober, (1984) "Summary of recent NASA propeller research", NASA-TM-8373, January 1984.

Ref. 15 H. Zimmer, (1988), "*Overview of high speed propeller investigation at Dornier*", Advanced propellers and their installation on aircraft, International conference proceedings, The Royal Aeronautical Society, 26th-27th September 1988.

Ref. 16 A. J. Evans, G. Liner, (1958), "*A wind-tunnel investigation of the aerodynamic characteristics of a full-scale supersonic-type three-blade propeller at Mach numbers to 0.96*", NACA-TR-1375, 1958.

Ref. 17 A. J. Evans, E. B. Klunker, (1947), "*Preliminary investigation of two full-scale propellers to determine the effect of swept-back blade tips on propeller aerodynamic characteristics*", NACA-RM-L6J21, 1947.

Ref. 18 A. J. Evans, G. Liner, (1951), "*A wind-tunnel investigation of the aerodynamic characteristics of a full-scale sweptback propeller and two related straight propellers*", NACA-RM-L50J05, 1951.

Ref. 19 C. Rohrback, F. B. Metzger, (1975) "*The Prop-Fan, a New Look at Propulsors*", Proceedings of the AIAA/SAE 11th Propulsion Conference, AIAA 75-1208, Anaheim, California, USA, 29th September-1 October 1975.

Ref. 20 R. D. Hager, D. Vrabel, (1988), "*Advanced Turboprop Project"*, NASA SP-495, January 1988.

Ref. 21 J. Kurzke, (2003), "*Achieving maximum thermal efficiency with the simple gas turbine cycle*", 9th CEAS European Propulsion Forum: Virtual Engine - A Challenge for Integrated Computer Modelling, Roma, Italy, 15-17 October 2003.

Ref. 22 S. Boggia, K. Rüd, (2004), "*Intercooled recuperated aero engine*", Advanced Project Design, MTU Aero Engines, München, Germany, 2004.

Ref. 23 M. W. Whellens, (2003), "*Multidisciplinary Optimisation of Aero-engines using Genetic Algorithms and Preliminary Design Tools",* PhD Thesis, Cranfield University, United Kingdom, 2003.

Ref. 24 M. Plohr, A. Dopelheuer, M. Lecht, (1999), "*The Gas Turbine Heat Cycle and its Influence on Fuel Efficiency and Emissions*", Proceedings of NATO/RTO Air Vehicle Technology Symposium, Ottawa, Canada, October 1999.

Ref. 25 P. Akbari, R. Nalim, N. Mueller, (2006), "*A review of wave rotor technology and its applications"*, Journal of Engineering for Gas Turbines and Power, Vol. 128, p 717-735, 2006.

Ref. 26 A. J. B. Jackson, (2009), "Optimisation of aero and industrial gas turbine design for the environment", PhD Thesis, Cranfield University, United Kingdom, 2009

Ref. 27 Zimbrick R.A. and Colehour J.L., 1998, "An Investigation of Very High Bypass Ratio Engines for Subsonic Transports", Proceedings of AIAA/AMSE/SAE/ASEE 24th Joint Propulsion Conference, Boston, Massachusetts, USA, 11-13 July 1998

Ref. 28 J. A. Borradaile, (1988), "Towards the optimum ducted UHBR engine", Proceedings of AIAA/SAE/ASME/ASEE 24th Joint Propulsion Conference, AIAA-89-2954, Boston, Massachusetts, USA, July 11-13 1988.

Ref. 29 N. D. Kuznetsov, (1993), "*Propfan engines*", Proceedings of AIAA/SAE/ASME/ASEE 19th Joint propulsion conference and exhibit, AIAA-93-1981, Monterey, Canada, 28-30 June 1993.

Ref. 30 H. Grieb, D. Eckardt, (1986), "*Propfan and Turbofan, Antagonism or Synthesis*", Proceedings of 15th Congress of the International Council of the Aeronautical Sciences, Vol. 1, ICAS- 86-3.8.2, London, UK, 7-12 September 1986.

Ref. 31 F. Metzger (1988), "*Prop-Fan design and test experience*", Advanced propellers and their installation on aircraft, International conference proceedings, The Royal Aeronautical Society, 26th-27th September 1988.

Ref. 32 A. Bradley, (2010), "Engine design for the environment", Lecture to the Royal Aeronautical Society - Hamburg, DGLR and VDI, Hamburg, 24th June 2010.

Ref. 33 GE Aircraft Engines, (1987), "*Full scale technology demonstration of a modern counterrotating unducted fan engine concept, Design report*", NASA CR-180867, December 1987.

Ref. 34 G. Amato, (2011), "*Strut design for contra-rotating turbine*", MSc Thesis, Politecnico di Torino, 2011.

Ref. 35 G. A. Charier, F. Gallet, W. Balk, (2010), "*Device for controlling the pitch of fan blades of a turboprop*", US Patent: US2010/0104438, 29th April 2010.

Ref. 36 J. S. Vanderover, K. D. Visser, (2006), "*Analysis of a Contra-Rotating Propeller Driven Transport Aircraft*", AIAA 2006.

Ref. 37 W.C. Strack, G. Knip, J. Godston, E. Bradley, (1982), "*Technology and Benefits of Aircraft Counter Rotation Propellers*", NASA TM-82983, 1982.

Ref. 38 B. H. Little, D. T. Poland, H. W. Bartel and C. C. Withers, "*Propfan test assessment (PTA): Final project report*", NASA CR-185138.

Ref. 39 R. Harris and R.D. Cuthebertson, (1987), "*UDF TM / 727 Flight Test Program*", Proceedings of AIAA/SAE/ASME 23rd Joint Propulsion Conference, AIAA-87/1733, San Diego, California, USA, 29 June – 2 July 1987.

Ref. 40 C. Reid, (1988), "*Overview of flight testing of GE aircraft engines UDF engine*", Proceedings of AIAA/SAE/ASME/ASEE 24th Joint Propulsion Conference, AIAA-88-3082, Boston, Massachusetts, USA, July 11-13 1988.

Ref. 41 D. C. Chapman, J. Godston, D. E. Smith, (1988), "Testing of the 578-DX propfan propulsion system", Proceedings of AIAA/SAE/ASME/ASEE 24th Joint Propulsion Conference, AIAA-88-2804, Boston, Massachusetts, USA, July 11-13 1988.

Ref. 42 D. C. Chapman, R. E. Fleury, D.E. Smith, (1989), "Testing of the 578-DX propfan propulsion system", Proceedings of AIAA/ASME/SAE/ASEE 25th Joint Propulsion Conference, AIAA-89-2954, Monterey, Canada, July 10-12 1989.

Ref. 43 J. M. Bosquet, (1987), "*Etude de l'aerodynamique des helices pour avions rapides*", AGARD 69th Symposium of the propulsion and energetic panel, Paris, France, 4-8th May 1987.

Ref. 44 P. Gardarein, (1991), "*Calculs aerodynamiques des helices rapides transoniques*", 28eme Colloque d'Aerodynamique Appliquee, ISA, Saint-Louis, France, 21-23 October 1991.

Ref. 45 T. J. Kirker, (1990), "*Procurement and testing of a 1/5 scale advanced counter rotating propfan model*", Proceedings of AIAA 13th Aeroacoustics Conference, AIAA-90-3975, Tallahassee, Florida, USA, October 22-24 1990.

Ref. 46 M. Daly, B Gunston, (2002), "*Jane's Aero-Engines*", IHS Janes, September 2002.

Ref. 47 Advisory Council for Aeronautics Research in Europe, (2001), "European aeronautics: a vision for 2020", Publications Office of the European Union, January 2001.

Ref. 48 Advisory Council for Aeronautics Research in Europe, (2011), "*Flightpath 2050 Europe's Vision for Aviation*", Publications Office of the European Union, 2011.

Ref. 49 DREAM project, "*Grant agreement for: Collaborative project – Large-scale Integrating Project , Annex I - Description of Work",* R2.3 April 2011.

Ref. 50 G. Norris, (2008), "*Open return*", Aviation Week & Space Technology, 14 July 2008.

Ref. 51 G. Norris, (2009), "*Rotor revival*", Aviation Week & Space Technology, 14 December 2009.

Ref. 52 A. Peters, (2010), "*Assessment of propfan propulsion systems for reduced environmental impact*", Massachusetts Institute of Technology MSc Thesis, 29 January 2010.

Ref. 53 B. H. Little (1988), "Flight test of the propfan test assessment (PTA) aircraft", Advanced propellers and their installation on aircraft, International conference proceedings, The Royal Aeronautical Society, 26th-27th September 1988

Ref. 54 G.A. Swift, (1987), "Advanced propfan analysis for the family of commuter airplanes", NASA-CR-182566, May 1987.

Ref. 55 G Norris, (2008), "*Push or Pull*", Aviation Week & Space Technology, 24 November 2008.

Ref. 56 J. Morris, (1986), "A p*ropfan stauts report*", Proceedings of 15th Congress of the International Council of the Aeronautical Sciences, Vol 1, ICAS- 86-3.8.1, London, UK, 7-12 September 1986.

Ref. 57 Innovation Analysis Group, 2009, "*Engine Thoughts*", available at: http://www.iag-inc.com/2009/09/22/engine-thoughts-2/, September 2009, (Accessed 5th May 2011).

Ref. 58 A. Bleythe (1988), "*Design considerations for open rotor installation on transport aircraft*", Advanced propellers and their installation on aircraft, International conference proceedings, The Royal Aeronautical Society, 26th-27th September 1988

Ref. 59 B. Sweetman, (2005), "*The Short, Happy Life of the Prop-fan*", *Air & Space* magazine, September 2005

Ref. 60 G. Thomasson (1988), "*Advanced Propellers, some airworthyness considerations*", Advanced propellers and their installation on aircraft, International conference proceedings, The Royal Aeronautical Society, 26th-27th September 1988

Ref. 61 N. J. Peacock, (1976), "*The propfan, a fuel efficient propulsor*", Aeronautical Research Council, ARC.38-164, December 1976.

Ref. 62 C. E. Hughes, J. A. Gazzaniga, (1988), "*Summary of low-speed wind tunnel results of several high-speed counterrotation propeller configurations*", Proceedings of AIAA/SAE/ASME/ASEE 24th Joint Propulsion Conference, AIAA 88-3149, Boston, Massachusetts, USA, 11-13 July 1988.

Ref. 63 D. C. Reemsnyder, D. A. Sagerser, (1979), *"Effect of forward velocity and cross-wind on the reverse-thrust performance of a variable pitch fan engine*", NASA TM-79059, January 1979

Ref. 64 D. G. M. Davis, D. C. Miller, (1976), "*A variable pitch fan for ultra quiet demonstrator engine*", RAeS Spring Symposium, May 1976.

Ref. 65 D. Tanner, T. Wynosky, (1984), "Engine Inlet Interaction with a Prop-Fan Propulsion System," SAE Technical Paper 841478, 1984.

Ref. 66 I. M. Goldsmith, (1981), "A study to define the research and technology requirements for advanced turbo/propfan transport aircraft", NASA CR-166138, February 1981.

Ref. 67 C. P. Stolp, J. A. Baum, (1977), "*Advanced turboprop propulsion system reliability and maintenance cost*", Proceedings of SAE Aerospace engineering and manufacturing meeting, SAE-771009, Los Angeles, California, USA, 14-17 November 1977.

Ref. 68 J. F. Dugan, D. P. Bencze, L. J. Williams, (1977), "*Advanced turboprop technology development*", Proceedings of AIAA Aircraft systems and technology meeting, AIAA-77-1223, Seattle, USA, 22-24 August 1977.

Ref. 69 International Bureau of Aviation, (2008), "*Engine Values Book*", International Bureau of Aviation, Surrey, UK, 2008.

Ref. 70 Clean Sky Joint Undertaking, (2012), "Clean sky at a glance", Clean Sky Joint Undertaking publication, Brussels, Belgium, February 2012.

Ref. 71 M. D. Guynn, J. J. Berton, E. S. Hendricks, M. T. Tong, W. J. Haller, D. R. Thurman, (2011), "*Initial assessment of open rotor propulsion applied to an advanced single-aisle aircraft*", Proceedings of 11th AIAA Aviation Technology, Integration, and Operations (ATIO) Conference; Virginia Beach, VA; United States, 20-22 September 2011.

Ref. 72 E. S. Hendricks, (2011), "*Development of an open rotor cycle model in NPSS using a multi-design point approach*", Proceedings of Turbo Expo 2011, GT-2011-46694, Vancouver, BC, Canada, 6-10 June 2011.

Ref. 73 L. Larson, T. Grönstedt, K. G. Kyprianidis, (2011), "*Conceptual design and mission analysis for a geared turbofan and an open rotor configuration*", Proceedings of Turbo Expo 2011, GT-2011-46451, Vancouver, BC, Canada, 6-10 June 2011.

Ref. 74 L. McCullers, (1984), "*Aircraft configuration optimization including optimized flight profiles*", NASA CP 2327, April 1984.

Ref. 75 M. D. Ardema, M. C. Chambers, A. P. Patron, A. S. Hahn, H. Miura, M. D. Moore, (1996), "*Analytical fuselage and wing weight estimation of transport aircraft*" NASA TM-110392, May 1996.

Ref. 76 J. K. Lytle , (2000), "*The numerical propulsion system simulation: an overview*", NASA TM-2000-209915, June 2000.

Ref. 77 M. D. Guynn, J. J. Berton, K. L. Fisher, W. J. Haller, M. T. Tong, D. R. Thurman, (2009), "*Engine concept study for an advanced single-aisle transport*" NASA TM-2009-215784, 2009.

Ref. 78 E. Onat, G. Klees, (1979), "A Method to Estimate Weight and Dimensions of Large and Small Gas Turbine Engines", NASA CR 159481, January 1979.

Ref. 79 M.T. Tong, B. A. Naylor, (2009), "An Object-Oriented Computer Code for Aircraft Engine Weight Estimation", NASA/TM-2009-215656, December 2009.

Ref. 80 R.E. Gillian, (1983), "*Aircraft Noise Prediction Program User's Manual*", NASA TM-84486, January 1983.

Ref. 81 K.G. Kyprianidis, R.F. Colmenares Quintero, D.S. Pascovici, S.O.T. Ogaji, P Pilidis, and A.I Kalfas, (2008), "*EVA - A Tool for Environmental Assessment of Novel Propulsion Cycles*", Proceedings of ASME Turbo Expo, GT2008-50602, 9-13 June 2008.

Ref. 82 NEWAC WP1.3 partners, (2008), "D1.3.1A – NEWAC TERA2020 Module Specifications", NEWAC Project deliverable, December 2008.

Ref. 83 DAR Corp, http://www.darcorp.com/Software/AAA/, (Accessed 11 May 2011)

Ref. 84 J. Roskam, (2003), "*Airplane design"*, Volumes I-VIII, Design, Analysis and Research Corporation, Lawrence, Kansas, USA, 2003.

Ref. 85 F. C. Newton, R. H. Liebeck, G. H. Mitchell, A. Mooiweer, M. M. Platte, T. L. Toogood, R. A. Wright, (1986), "*Multiple Application Propfan Study (MAPS): Advanced tactical transport*", NASA-CR-175003, March 1986.

Ref. 86 N. F. Dannenhoffer, J. S. Herzberg, J. R. Kretzing, J. P. Landfield, C. L. Mahoney, R. A. Mahoney, H. C. Potonides, (1986), "*Multiple Purpose Subsonic Naval Aircraft (MPSNA) Multiple Application Propfan Study (MAPS)*", NASA-CR-179452, July 1986.

Ref. 87 D. M. Winkeljohn, C. H. Mayrand, (1986), "*Multiple-Purpose Subsonic Naval Aircraft (MPSNA) Multiple Application Propfan Study (MAPS)*", NASA-CR-175096, March 1986.

Ref. 88 A. L Weisbrich, J. Godston, E. Bradley, (1982), "*Technology and benefits of aircraft counter rotation propellers*", NASA-CR-168258, December 1982 (thesis authors date of birth).

Ref. 89 T. A. Egolf, O. L. Anderson, D. E. Edwards, A. J. Landgrebe, (1988), "*An analysis for high speed propeller-nacelle aerodynamic performance prediction. Volume 1: Theory and application*", NASA-CR-4199 , December 1988.

Ref. 90 R. W. Awker, (1986), "*Evaluation of propfan propulsion applied to general aviation*", NASA-CR-175020, March, 1986

Ref. 91 Boeing Commercial Aircraft Corp, Preliminary Design Department, (1976), "*Energy consumption characteristics of transports using the prop-fan concept*", NASA-CR-137937, October 1976.

Ref. 92 E. F. Kraus, J. C. Vanabkoude, (1976), "*Cost/benefit tradeoffs for reducing the energy consumption of the commercial air transportation system*", NASA-CR-137925, June 1976.

Ref. 93 J. P. Hopkins, (1976), "*Study of the cost/benefit tradeoffs for reducing the energy consumption of the commercial air transportation system*", NASA-CR-137926, August 1976.

Ref. 94 J. P. Hopkins, H. E. Wharton, "*Study of the cost/benefit tradeoffs for reducing the energy consumption of the commercial air transportation system*", NASA-CR-137927, August 1976.

Ref. 95 J. F. Dugan, D. P. Bencze, L. J. Williams, (1977), "*Advanced turboprop technology development*", Proceedings of AIAA Aircraft systems and technology meeting, AIAA-77-1223, Seattle, USA, 22-24 August 1977.

Ref. 96 V. S. Johnson, (1983), "*Parametric study of factors affecting the fuel efficiency of advanced turboprop airplanes*", Proceedings of the AIAA Applied Aerodynamics Conference, AIAA PAPER 83-1823, Danvers, MA, USA, 13-15 July 1983.

Ref. 97 C. N. Reynolds, (1985), "*Advanced Prop-fan Engine Technology (APET) single- and counter-rotation gearbox/pitch change mechanism*", NASA CR-168114 Vol2, July 1985.

Ref. 98 C. E. Whitfield, R. Mani, P. R. Gliebe, (1990), "*High Speed Turboprop Aeroacoustic Study, (Counterrotation), Volume I and II*", NASA CR 185241, July 1990.

Ref. 99 D. Parzych,A. Shenkman, S. Cohen, (1984), "*Large-scale Advanced Propfan (LAP) performance, acoustic and weight estimation*", NASA CR-174782, January 1984.

Ref. 100 Joachim Kurzke, (2007), "*Gasturb 11*", Dachau, Germany, 2007.

Ref. 101 The GSP Development Team, (2010), "*GSP 11 User Manual, Version 11.1.0*", National Aerospace Laboratory NLR, October 2010.

Ref. 102 J. Dominy, (1987), "*Transmission efficiency in advanced aerospace powerplant*", AIAA/SAE/ASME/ASEE 23rd Joint Propulsion Conference, AIAA-87-2043, San Diego, Calufornia, USA, 29 June – 2 July 1987.

Ref. 103 K. A. Geiselhart, (1994), "*A technique for integrating engine cycle and aircraft configuration optimization*", NASA-CR-19160, February 1994.

Ref. 104 R. K. Michelle, (2010), "*Environmental design space (EDS)*", Aviation Environmental Tools Colloquium, 1 December 2010.

Ref. 105 K. Kyprianidis, T. Grönstedt, S. Ogaji, P. Pilidis, R. Singh, (2010), "*Assessment of future aero engine designs with intercooled and intercooled recuperated cores*", Proceedings of ASME Turbo Expo 2010, GT-2010-23621.

Ref. 106 P.D. Norman, D.H. Lister, M. Lecht,P. Madden, K. Park, O. Penanhoat, C. Plaisance, K. Renger, (2003), "*Development of the Technical Basis for a New Emissions Parameter Covering the Whole Aircraft Operation: NEPAIR*", Final Technical Report, NEPAIR/WP4/WPR/01, September 2003.

Ref. 107 IHS Engineering Science Data Unit, "Estimation of airframe drag by summation of components: principles and examples", ESDU 97016.

Ref. 108 G. Doulgeris, P. Giannakakis, (2008), "*Hermes V5 & TmatchCalls V3 User Manual*", School of Engineering, Cranfield University, October 2008.

Ref. 109 P. Walch, P. Fletcher, (2004), "*Gas turbine performance, Second Edition*", Blackwell Science, 2004.

Ref. 110 V. Pachidis, (2008), "*Gas turbine performance simulation*", Simulation and diagnostics course notes: School of Engineering, Cranfield University, 2008.

Ref. 111 Gas Turbine Engineering Group, (2008) "*The TURBOMATCH scheme*", Turbomatch User's Manual, School of Engineering, Cranfield University, 2008.

Ref. 112 Empresarios Agrupados, (2011), "*PROOSIS 2.6.0 User manual*", EA International, Madrid, Spain, 2011.

Ref. 113 A. Alexiou, T. Tsalavoutas, (2011) "*Introduction to gas turbine modelling with PROOOSIS*", EA International, Madrid, Spain, 2011.

Ref. 114 C. N. Reynolds, (1985), "*Advanced Prop-fan Engine Technology (APET) single- and counter-rotation gearbox/pitch change mechanism*", NASA CR-168114 Vol1, July 1985.

Ref. 115 J. Yin, A. Stuermer, (2011), "*Pylon blowing for the reduction of installation-associated noise of CROR engines*", Journal of Sound and Vibration 330, p. 4974-75, 2011.

Ref. 116 http://www.2747.com, (Accessed 1 May 2012).

Ref. 117 http://www.airliners.net, (Accessed 1 May 2012).

Ref. 118 Rolls Royce plc, (1996), "*The jet engine*", Fifth edition, Renault Printing Co Ltd, UK, 1996.

Ref. 119 http://www.airwar.ru/enc/engines/nk-93.html, (Accessed 3 May 2012).

Ref. 120 http://www.econologie.com, (Accessed 3 May 2012).

Ref. 121 http://www.globalsecurity.org/military/systems/aircraft/p-9.htm, (Accessed 5 May 2012).

Ref. 122 http://www.antonov.com, (Accessed 5 May 2012), English version is not available; navigate through the website in Russian.

Ref. 123 http://en.wikipedia.org/wiki/Westland_Wyvern, (Accessed 5 May 2012).

Ref. 124 http://www.britannica.com, (Accessed 5 May 2012).

Ref. 125 V. MOORE, (2007), "*Pratt & Whitney considers geared open rotor concept*", Flight Global, 3 July 2007.

Ref. 126 http://dautremont.perso.libertysurf.fr/Cargo/Cargos.html, (Accessed 5 May 2012).

Ref. 127 Dassault Systems, (2010), "*ISIGHT 4.5, User's guide*", 2010.

Ref. 128 VITAL Project web site,
http://ec.europa.eu/research/transport/projects/items/vital_en.htm.

Ref. 129 NEWAC Project web site, www.newac.eu.

Ref. 130 VIVACE WP2.4 partners, (2007), "*PROOSIS TURBO library: Physical modelling specifications, all components*", VIVACE project, December 2007.

Ref. 131 VIVACE WP2.4 partners, (2007), "*PROOSIS standard components library*", VIVACE project, December 2007.

Ref. 132 A. Alexiou, I. Roumeliotis, N. Aretakis, A. Tsalavoutas, K. Mathioudakis, (2012), "*Modelling contra-rotating turbomachinery components for engine performance simulations: The geared turbofan with contra-rotating core*

case", Proceedings of ASME Turbo Expo 2012, GT-2012-69433, Copenhagen, Denmark, 11-15 June 2012.

Ref. 133 C. A. Perullo, J. C. M. Tai, D. N. Mavris, (2012), "*Effects of advanced engine technology on open rotor cycle selection and performance*", Proceedings of ASME Turbo Expo 2012, GT2012-69331, Copenhagen, Denmark, 11-15 June 2012.

Ref. 134 M. Morales, (2010), "*WP2.5 High Speed Low Pressure Turbine Design*", DREAM project M30 Review presentation, September 21-22 2010, TURBOMECA, Pau.

Ref. 135 W. C. Nelson, (1944), "*Airplane propeller principles*", New York, J. Wiley & Sons, Inc.; London, Chapman & Hall, Ltd. 1944.

Ref. 136 G. Eiffel, (1914), "*Nouvelles recherches sur la resistence de l´air et l´aviation*", H. Dunod et E. Pinat Editeurs, Paris, France, 1914.

Ref. 137 R. J. Jeracki, D.C. Mikkelson, (1979), "*Wind Tunnel Performance of Four Energy Efficient Propellers Designed for Mach 0.8 Cruise*", NASA TM-79124, 1979.

Ref. 138 J. Gilman, (1946), "*Wind-tunnel tests and analysis of three 10-foot-diameter three-blade tractor propellers differing in pitch distribution*", NACA WR-L-712, 1946.

Ref. 139 G. A. Mitchell, (1988), "*Experimental aerodynamic performance of advanced 40 deg-swept 10-blade propeller model at Mach 0.6 to 0.85*", NASA TM-88969, 1988.

Ref. 140 G. K. Yamauchi, W. Johnson, (1983), "*Trends of Reynolds number effects on two-dimensional airfoil characteristics for helicopter rotor analyses*", NASA TM-84363, 1983.

Ref. 141 M.A. Lock, (1941), "*Interference velocity for a close pair of contra-rotating airscrews*", Aeronautical Research Council Reports and Memoranda, Reports and Memoranda No. 2084, 22nd July 1941.

Ref. 142 B. W. Denner, (1989), "*An approximate model for the performance and acoustic predictions of counterrotating propeller configurations*", NASA CR-180667, 1989.

Ref. 143 S. C. Playle, K. D. Korkan, E Von Lavante, (1986), "*A numerical method for the design and analysis of counter-rotating propellers*", Journal of Propulsion, Vol. 2. No.1, pp. 57-63, January-February 1986.

Ref. 144 F. Ginzel, (1949), "*Calculation of counterrotating propellers*", NACA TM-1208, 1949.

Ref. 145 R. E. Davidson, (1981), "*Optimization and performance calculation of dual-rotation propellers*", NASA TP-1948, 1981

Ref. 146 I. Naiman, (1943), "*Method of calculating performance of dual-rotating propellers from airfoil characteristics*", NACA WR-L-330, 1943.

Ref. 147 A. R. Collar, (1941), "*On the static thrust of contra-rotating airscrews*", Aeronautical Research Council Reports and Memoranda, Reports and Memoranda No. 1994, 27th May 1941.

Ref. 148 O. Gur, A. Rosen, (2008),"*Comparison between blade-element models of propellers*", The Aeronautical Journal, Vol. 112, No. 1138, pp. 689-104, December 2008.

Ref. 149 B. Chandrasekaran, (1985), "*Method for the prediction of the installation aerodynamics of a propfan at subsonic speeds*", NASA CR-3887, 1985.

Ref. 150 H.W. Gray, (1942), "*Wind-tunnel tests of single- and dual-rotating pusher propellers having from three to eight blades*", NACA WR-L-359, 1942.

Ref. 151 E. P. Lesley, (1939), "*Tandem Air Propellers*", NACA TN-689, 1939.

Ref. 152 J. Gilman, (1948), "*Wind-tunnel tests and analysis of two 10-foot-diameter six-blade dual-rotating tractor propeller differing in pitch distribution*", NACA TN-1634, 1948.

Ref. 153 J. Gilman, (1946), "*Wind-tunnel tests and analysis of three 10-foot-diameter three-blade tractor propellers differing in pitch distribution*", NACA WR-L-712.

Ref. 154 D. Biermann, E. P. Hartman, (1942), "*Wind-tunnel tests of four- and six-blade single- and dual-rotating tractor propellers*", NACA TR-747, 1942.

Ref. 155 W. H. Gray, D. Biermann, (1941), "*Wind-Tunnel Tests of Eight-Blade Single and Dual-Rotating Propellers in the Tractor Position*", NACA WR-L-384, 1941.

Ref. 156 D. Biermann, R. N. Conway, (1942), "*Propeller charts for the determination of the rotational speed for the maximum ratio of the propulsive efficiency to the specific fuel consumption*", NACA TR-749, 1942.

Ref. 157 J. D. Maynard, (1942), "*Wind-tunnel tests of single- and dual-rotating tractor propellers of large blade width*", NACA WR-L-385, 1942.

Ref. 158 W. H. Gray, N. Mastrocola, (1943), "*Representative operating charts of propellers tested in the NACA 20-foot propeller-research tunnel*", NACA WR-L-286, 1943.

Ref. 159 W. H. Gray, (1944), "*Wind-tunnel tests of dual-rotating propellers with systematic differences in number of blades, blade setting, and rotational speed of front and rear propellers*", NACA WR-L-80, 1944.

Ref. 160 W. H. Gray, (1943), "*Wind-tunnel tests of single and dual-rotating tractor propellers at low blade angles and of two-and three-blade tractor propellers at blade angles up to 65 degrees*", NACA WR-L-316, 1943.

Ref. 161 R. M. Reynolds, J. H. Walker, (1954), "*Investigation of the NACA 4-(5)(05)-037 six- and eight-blade, dual-rotation propellers at positive and negative thrust at Mach numbers up to 0.90, including some aerodynamic characteristics of the NACA 4-(5)(05)-041 two- and four-blade, single-rotat*", NACA RM-A54G13, 1954.

Ref. 162 R. J. Platt, R. A. Shumaker, (1950), "*Investigation of the NACA 3-(3)(05)-05 eight-blade dual-rotating propeller at forward Mach numbers to 0.925*", NACA RM-L50D21, 1950.

Ref. 163 E. Pepper, J.G McHugh, (1942), "*The Characteristics of Two Model Six-Blade Counterrotating Pusher Propellers of Conventional and Improved Aerodynamic Design*", NACA WR-L-404, 1942.

Ref. 164 T. J. Sullivan, (1990), "*Aerodynamic performance of a scale-model, counterrotating unducted fan*", Journal of Turbomachinery, Vol. 112, pp. 579-586, October 1990.

Ref. 165 L. L. M. Veldhuis, (2005), "*Propeller wing aerodynamic interference*", PhD Thesis, Technische Universiteit Delft, 28th June 2005.

Ref. 166 J.M. Bousquet, P. Gardarein, (2003), "*Improvements on computations of high speed propeller unsteady aerodynamics*", Aerospace Science and Technology Vol.7 pp.465–472, 2003.

Ref. 167 C. Mateos Borrego, (2009), "*CFM56 core fitted with a new propfan designed usign CFD*", Cranfield University, Department of Power and Propulsion, MSc Thesis, September 2009.

Ref. 168 R. H. Cavicchi, A. B. Constantine, (1955), "*Analysis of Limitations Imposed on One-Spool Turbojet-Engine Designs by Turbines Having Downstream Stators at 0, 2.0 and 2.8 Flight Mach Numbers*", NACA RM-E54J14, 1955.

Ref. 169 D. Parzych, A. Shenkman, S. Cohen, (1985), "*Large-scale Advanced Propfan (LAP) performance, acoustic and weight estimation*", NASA CR-174782, 1985.

Ref. 170 B. A. Ponomarev, Y. V. Sotsenko, (1986), "*Turbines with counter-rotating rotors for aircraft powerplants*", Izvestiya VUZ, Aviatsionnaya Tekhnika, Vol. 29, No. 2, pp. 50-53, 1986.

Ref. 171 J. F. Louis, (1985), "*Axial flow contra-rotating turbines*", ASME-85-GT-218, Proceedings of the 30th ASME International Gas Turbine Conference and Exhibit, Houston, TX, USA, 18-21 March 1985.

Ref. 172 R. Cai, W. Wu, G. Fang, (1990), "*Basic analysis of counter-rotating turbines*", ASME-90-GT-108, Proceedings of the 35th ASME International Gas Turbine and Aeroengine Congress and Exposition, Brussels, Belgium, 11-14 June 1990

Ref. 173 J. Lucheng, (2007), "*Analysis of technical challenges in vaneless counter-rotating turbomachinery*", GT2007-27617, Proceedings of ASME Turbo Expo 2007: Power for land, sea and air, Montreal, Canada, 14-17 May 2007.

Ref. 174 D. G. Ainley, G. C. R. Mathieson, (1951), "*A method of performance estimation for axial flow turbines*" British Aeronautical Research Council, Reports and memoranda Nº 2974, 1951.

Ref. 175 M. W. Benner, S. A. Sjolander, S. H. Moustapha, (2006), "*An empirical prediction method for secondary losses in turbines: Part I — A new loss breakdown scheme and penetration depth correlation*", Journal of Turbomachinery, Vol. 128, pp. 273-280, April 2006.

Ref. 176 J. D. Denton, (1993),"*Loss mechanisms in turbomachines*", Journal of Turbomachinery, Vol. 115, pp. 621-656, October 1993.

Ref. 177 A. J. Glassman, (1995), "*Design geometry and design/off-design performance computer codes for compressors and turbines*", NASA CR-198433, 1995.

Ref. 178 A. J. Glassman, (1992), "*Computer code for preliminary sizing analysis of axial-flow turbines*", NASA CR-4430, 1992.

Ref. 179 A. J. Glassman, (1972), "*Computer program for preliminary design analysis of axial-flow turbines*", NASA TN-D-6702, 1972.

Ref. 180 A. F. Carter, F. K. Lenherr, (1969), "*Analysis of geometry and design-point performance of axial-flow turbines using specified meridional velocity gradients*", NASA CR-1456, 1969.

Ref. 181 A. J. Glassman, (1992), "*Users manual and modeling improvements for axial turbine design and performance computer code TD2-2*", NASA CR-189118, 1992.

Ref. 182 E. E. Flagg, (1967), "*Analytical procedure and computer program for determining the off-design performance of axial flow turbines*", NASA CR-710, 1967.

Ref. 183 A. J. Glassman, (1994), "*Modeling improvements and users manual for axial-flow turbine off-design computer code AXOD*", NASA CR-195370, 1994.

Ref. 184 G. Paniagua, S. Szokol, R. Varvill, (2008), "*Contrarotating Turbine Aerodesign for an Advanced Hypersonic Propulsion System*", Journal of Propulsion and Power, Vol. 24, No. 6, pp. 1269-1277, November-December 2008.

Ref. 185 M. T. Basurto, (1995), "*Conversion of a military turbofan to a civil aero-engine*", M.Sc. Thesis, Department of Power and Propulsion, Cranfield University, 1995.

Ref. 186 C. S. Shu-cheng, (2009), "*Preliminary axial flow turbine design and off-design performance analysis methods for rotary wing aircraft engines*", NASA TM 2009-215651/PART1, 2009.

Ref. 187 J. D. Mattingly, W. H. Heiser, D. T. Pratt, (2002), "*Aircraft engine design*", Second edition, AIAA Education Series, Reston, VA, 2002. ***Older versions of software in this book are available on the web at www.aircraftenginedesign.com.***

Ref. 188 J. D. Mattingly, (2005), "*Elements of gas turbine propulsion*", McGraw-Hill, AIAA Education Series, Reston, VA, 2005.

Ref. 189 M. G. Turner, A. Merchant, D. Bruna, (2006), "*A turbomachinery design tool for teaching design concepts for axial-flow fans, compressors and turbines*", GT2006-90105, Proceedings of GT2006, ASME Turbo Expo 2006: Power for Land, Sea and Air, Barcelona, Spain, 8-11 May, 2006.

Ref. 190 N. Wei, (2000), "*Significance of loss models in aerothermodynamic simulation for axial turbines*", PhD Thesis, Department of Energy Technology, Division of Heat and Power Technology, Royal Institute of Technology KTH, 2000.

Ref. 191 A. N. Dahlquist, (2008), "*Investigation of losses prediction, Methods in 1D for axial gas turbines*", MsC Thesis, Division of Thermal Power Engineering, Department of Energy Sciences, Lund University, 2008.

Ref. 192 S. C. Kacker, U. Okapuu, (1982), "*A mean line prediction method for axial flow turbine efficeincy*", Journal of Engineering for Power, Vol. 104, pp. 111 – 119, January 1982.

Ref. 193 S. H. Moustapha, S. C. Cacker, B. Tremblay, (1990), "*An improved incidence losses prediction method for turbine airfoils*", Journal of Turbomachinery, Vol. 112, pp. 267 – 276, April 1990.

Ref. 194 S. L. Dixon, (1998),"*Fluid mechanics and thermodynamics of turbomachinery*", Fourth Edition, Butterworth-Heinemann, 1998.

Ref. 195 D. G. Wilson, T. Korakianitis, (1998), "*The design of high efficiency turbomachinery and gas turbines*", Second edition, Prentice Hall, 1998.

Ref. 196 K. W. Ramsden, (2008), "*Thermofluids, Turbomachinery course notes*", Department of Power and Propulsion, School of engineering, Cranfield University, 2008.

Ref. 197 P. Gorlier, G. Germain, (1998), *http://philippe.gorlier.voila.net/Documents/Viscosite.pdf*, (Accessed 2 March 2010).

Ref. 198 A. J. Glassman, (1993), "*Blading models for TURBAN and CSPAN turbomachine design codes*", NASA CR-191164, 1993.

Ref. 199 A. J. Glassman, (1994), "*Turbine design and application, Volume 1*", NASA SP-290, 1994.

Ref. 200 J. H. Horlock, (1966), "*Axial flow turbines – Fluid mechanics and thermodynamics*", Butterworths, London, 1966.

Ref. 201 J. Dominy, R. A. Midgley, (1984),"*A Transmission for the Contra-Rotating Prop-Fan Powerplant*", AIAA-84-1196, Proceedings of the AIAA/SAE/ASME 20th Joint Propulsion Conference, San Diego, California, USA, 11-13 June 1984.

Ref. 202 P. Lynwander, (1983), "*Gear Drive Systems: Design and Application*", Published by Marcel Dekker, 1983.

Ref. 203 J. Dominy, (1987) "*Transmission Efficiency in Advanced Aerospace Powerplant*", Proceedings of the AIAA/SAE/ASME/ASEE 23rd Joint Propulsion Conference, Paper AIAA-87-2043, Cincinnati, Ohio, USA, 29 June – 2 July 1987.

Ref. 204 D. B. Dooner, (1995), "Kinematic geometry of gearing", First Edition, Published by John Wiley, New York, 1995.

Ref. 205 S. K Ramesh, S. P. Dusan, (2003), "*Fundamentals of heat exchanger design*", Published by John Wiley, New York, 2003.

Ref. 206 C. M. Toraason, C. L. Broman, (1984) "*Advanced gearboxes for a modern single rotation turboprop engine*", AIAA-84-1197 Proceedings of the AIAA/SAE/ASME 20th Joint Propulsion Conference, Cincinnati, Ohio, USA, 11-13 June 1984.

Ref. 207 P. Bellocq, E. Giordano, T. Gronstedt, (2010), "*Updated TERA model description*", DREAM project delivreble D1.2.2A, August 2010.

Ref. 208 N. Tantot, (2008), "*Open rotor aircraft guidelines for WP1.2 activities*", DREAM Engineering Coordination memo DREAM-SN-ECM-0100, October 2008.

Ref. 209 E. Onat, G. W. Klees, (1979), "A method to estimate weight and dimensions of large and small gas turbine engines", NASA CR-159481, 1979.

Ref. 210 D. Christo, (2009), “Load analysis of open rotor aircraft engines”, MSc thesis, Space Engineering, Luea University of Technology, 2009.

Ref. 211 O. Argo, H. Lipowsky, J. Heidemarie, (2008), “*DREAM gearbox weight model specification*”, DREAM WP1.2 Coordination memo, May 2009.

Ref. 212 D.C. Howe, C.V. Sundt and A.H. McKibbon, (1988), “AGBT, Advanced counter-rotating gearbox detailed design report”, NASA CR-180883, 1988.

Ref. 213 NEWAC WP 1.3, (2008), “*NEWAC TERA2020 module specifications - R 0.2*”, NEWAC deliverable D1.3.1A, December 2008.

Ref. 214 D. DuBois, G. Paynter, (2006), *“”Fuel flow method2” for estimating aircraft emissions*", SAE Technical Paper 2006-01-1987, December 2006.

Ref. 215 Deutschen Zentrums für Luft- und Raumfahrt (DLR), (2000), “*Aviation emissions and evaluation of reduction options (AERO), Main Report, Part I: Description of the AERO Modelling System*”, December 2000.

Ref. 216 P. D. Norman, D. H. Lister, K. Lecht, P. Madden, K. Park, O. Penanhoat, C. Plaisance, K. Renger, (2003), “*Development of the technical basis for a new emissions parameter covering the whole aircraft operation: NEPAIR*”, Final Technical Report, NEPAIR/WP4/WPR/01, September 2003.

Ref. 217 S. L. Baughcum, T. G. Tritz, S. C. Henderson, and D. C. Pickett, (1996), “*Scheduled civil aircraft emission inventories for 1992: Database development and analysis*”, NASA CR-4700, April 1996.

Ref. 218 European Aviation Safety Agency (EASA), (2010), "Type certificate data sheet E.004, Issue 03, Type CFM International SA CFM56-7B series engines", July 2010.

Ref. 219 N.Van Oosten, (2007), "*SOPRANO Presentation*", SOPRANO Workshop, Madrid, Spain, 21 - 22 June 2007.

Ref. 220 F. de Roo, E. Salomons, N. van Oosten, P. Hullah, "*Reference and engineering models for aircraft noise sources*", INAGINE project, Deliverable 9 Volume 2 - Validation, February 2002.

Ref. 221 M. Morales, "*WP2.5 High speed low pressure turbine design*", M30 DREAM project Review presentation, Pau, 21-22 September 2010.

Ref. 222 L. Pinelli, (2011), “*Development of a computational method for turbomachinery tone noise analysis*”, Tesi di Dottorato, Dip. Energetica, Università degli Studi di Firenze, 2011.

Ref. 223 E. Giordano, K. Kritikos, A. I. Kalfas, (2011), "Counter rotating propeller noise model based on NLH approach and parametric study", DREAM project final workshop presentation, Derby, UK, 21-22 September 2011

Ref. 224 P. Gianakakis, (2009), "*Hermes V5 & TmatchCalls V3 user manual*", Department of Power and Propulsion, Cranfield University, September 2009.

Ref. 225 L. R. Jenkinson, P. Simpkin, D. Rhodes, (2003) “*Civil Jet Aircraft Design”,* Butterworth Heinemann Publications, 2003.

Ref. 226 Engineering Sciences Data Unit, (2009), "Estimation of airframe drag by summation of componentsÑ principles and examples", ESDU-97016, 2009

Ref. 227 J. Roskam, C-T. Edward Lan, (1997), "*Airplane aerodynamics and performance*", DARcorporation, 1997.

Ref. 228 Empresarios Agrupados, (2011), "*EL manual*", EA International, Madrid, Spain, 2011.

Ref. 229 Empresarios Agrupados, (2011), "*Mathematical algorithms & simulation guide*", EA International, Madrid, Spain, 2011.

Ref. 230 E. Torenbeek, (1982), "*Synthesis of subsonic airplane design*", Delft University Press, Delft, Netherlands, 1982.

Ref. 231 D. P. Raymer, (2006), "*Aircraft design: a conceptual approach*", 4th Edition, American Institute of Aeronautics and Astronautics, 2006.

Ref. 232 J. Roskam, (1986), "*Airplane design*", Roskam Aviation and Engineering Corporation, Kansas, USA, 1986

Ref. 233 D. Howe, (2000), "*Aircraft conceptual design synthesis*", Professional Engineering Publishing, UK, 2000.

Ref. 234 S. Capodanno, (2010),"*Multidisciplinary assessments of novel geared open rotor engines*", M.Sc. Thesis, Department of Power and Propulsion, Cranfield University, UK, 2010.

Ref. 235 G. Wilfert, B. Kriegl, L. Wald, O. Johanssen, (2005), "*CLEAN - Validation of a GTF high speed turbine and integration of heat exchanger technology in an environmental friendly engine concept*", ISABE – 2005 – 1156, XVII International Symposium on air breathing engines (ISABE), Munich, Germany, 4-9 September 2005.

Ref. 236 N. E. Anderson, L. Nightingale, D. A. Wagner, (1989), "·*Design and test of a propfan gear system*", Journal of propulsion, Vol. 5 No. 1, pp. 95-102, January -February 1989.

Ref. 237 J. Ricouard, E. Julliard, M. Omais, V. Regnier, A. Parry, S. Baralon, (2010), "*Installation effects on contra-rotating open rotor noise*", AIAA 2010-3795, Proceedings of the 16th AIAA/CEAS Aeroacoustics Conference, Stockolm, Sweeden, 7-9 June 2010.

Ref. 238 GE Aircraft Engines, (1987), "*Full scale technology demonstration of a modern counterrotating unducted fan engine concept, Engine test*", NASA CR-180869, December 1987.

Ref. 239 T. Simpson, T. Mauery, J. Korte, F. Mistree, (2001), "*Kriging models for global approximation in simulation-based multidisciplinary design optimization*", AIAA Journal, Vol. 39, No. 12, pp. 2233-2241, December 2001.

Ref. 240 T. Robinson, (2008), "*Prize flight*", Aerospace International, Royal Aeronautical Society, July 2008.

Ref. 241 K. Kyprianidis, V. Sethi, S. O. T. Ogaji, P. Pilidis, R. Singh, A. Kalfas, (2009), "*Thermo-Fluid Modelling for Gas Turbines – Part I: Theoretical Foundation and Uncertainty Analysis*", Proceedings of ASME TURBO EXPO 2009: Power for Land, Sea and Air, GT-2009-60092, Orlando, FL, USA, 8-12 June 2009.

Ref. 242 M. W. Benner, S. A. Sjolander, S. H. Moustapha, (2006), "*An empirical prediction method for secondary losses in turbines: Part I — A new loss breakdown scheme and penetration depth correlation*", Journal of Turbomachinery, Vol. 128, pp. 273-280, April 2006.

Ref. 243 M. W. Benner, S. A. Sjolander, S. H. Moustapha, (2006), "*An empirical prediction method for secondary losses in turbines: Part II — A new secondary loss correlation*", Journal of Turbomachinery, Vol. 128, pp. 281-291, April 2006.

Ref. 244 N. Tantot, J. Julliard, "*From turbojet to innovative architectures: open rotor and contra rotative fan engines*", VKI Series Lectures, Aero-engine design: from state-of-the-art turbofans towards innovative architectures, von Karman Institute, 3-7 March 2008.

Ref. 245 C. Dejeu, M. Vernet, J. Talbotec, "*Reverse thrust tests: An experimental approach based on numerics*", 47th International Symposium of Applied Aerodynamics Wind tunnel and computation: a joint strategy for flow prediction, Paris, 26-28 March 2012.

Appendix A – Recent patents related to CROR engines

Engine architecture

Adrien J. P. Fabre, SNECMA, "*TURBINE ENGINE WITH CONTRA-ROTATING NON-DUCTED PROPELLERS*", WO 201 1/033204, March 2011.

Francois Gallet, SNECMA, "*ARCHITECTURE DE TURBOMACHINE AMELIORANT L'ADMISSION D'AIR*", FR 2 951 502, October 2009.

Bruno A. Beutin, Antoine O. F. Colin, Clarisse S. M. Reaux, Didier J. L. Yvon, SNECMA, "*TURBOMACHINE A TURBINE LIBRE ENTRAINANT UN GENERATEUR ELECTRIQUE DE PUISSANCE*", FR 2 941 493, January 2009.

Bruno A. Beutin, Antoine O. F. Colin, Clarisse S. M. Reaux, Didier J. L. Yvon, SNECMA, "*TURBOMACHINE A TURBINE DE PUISSANCE EQUIPEE D'UN GENERATEUR ELECTRIQUE DE PUISSANCE*", FR 2 941 494, January 2009.

Dimitrie Negulescu, ROLLS-ROYCE DEUTSCHLAND LTD, "*TURBOPROP PROPULSION UNIT WITH PUSHER PROPELLER*", US 2010/0212285, August 2010.

CRP mechanical design

Francois Gallet, Gilles A. Charier, SNECMA, "*SYSTEM OF COMPACT COUNTRA-ROTATING PROPELLERS*", WO 2010/092094, August 2010.

Francois Gallet, SNECMA, "*SYSTEME D'HELICES CONTRAROTATIVES A HELICES ENTRAINEES PAR UN TRAIN EPICYCLOIDAL AMELIORE*", FR *2 928 976*, March 2008.

PCM design

M Poucher, DOWTY ROTOL, "*A BLADE ROTOR ASSEMBLY AND A CONTROL SYSTEM THEREFORE*", GB2180892, April 1989.

Paul A. Carvalho, David R. Danielson, Robert H. Perkinson, HAMILTON SUNDSTRAND CORP., "*COUNTER-ROTATINF OPEN-ROTOR (CROR)*", EP 2 388 192, November 2011.

Gilles A. Charier, Francois Gallet, Wouter Balk, SNECMA, "*DEVICE FOR CONTROLLING THE PITCH OF FAN BLADES OF A TURBOPROP*", US 2010/0104438, April 2010.

Francois Gallet, SNECMA, "*TURBOPROPULSEUR COMPROTANT UN ENSEMBLE DE PALES A ORIENTATION REGLABLE*", EP 1 921 325, November 2007.

Francois Gallet, SNECMA, "*TURBOPROP HAVING A PROPELLER MADE UP OF VARIABLE-PITCH BLADES*", US 2008/0247877, October 2008

CRP blades design and control for noise reduction

Matthew D. Moore, Kelly L. Boren, Robin B. Langtry, THE BOEING COMPANY, "*COUNTER ROTATING FAN DESIGN AND VARIABLE BLADE ROW SPACING OPTIMIZATION FOR LOW ENVIRONMENTAL IMPACT*", US 2010/0206982, August 2010.

Cedric Morel, SNECMA, "*TURBOMACHINE WITH UNDUCTED PROPELLERS*", US 2010/0054913, March 2010.

Maxime Leburn, SNECMA, "*TURBOMACHINE HAVING AN UNDUCTED FAN PROVIDED WITH AIR GUIDE MEANS*", US 2010/0124500, May 2010.

Benoit G. Farvacque, Philippe J. P. Fessou, SNECMA, "*TURBOMACHINE A HELICES NON CARENEES*", FR 2 935 348, August 2008.

Anthony B. Parry, Nicholas Howarth, Mark D. Taylor, ROLLS-ROYCE plc, "*AEROENGINE*", US 2010/0047068, February 2010.

Propellers anti icing

Guillaume Bulin, Jean Michel Rogero, Christian Fabre, AIRBUS, "*DEICING DEVICE FOR PROPFAN-TYPE PROPELLER BLADES*", WO 2010/128240, May 2010.

Eric De Wergifosse, Cedric Duval, *HISPQNO-SUIZA FR, "ALIMENTATION ELECTRIQUE DES EQUIPEMENTS PORTES PAR LE ROTOR D'UN MOTEUR D'AERONEF*", *2 961 176, June 2010.*

Bruno Albert Beutin, Antoine Olivier Francois Colin, Clarisse Savine Mathilde Reaux, Didier Jean-Louis Yvon, SNECMA, "*TURBINE ENGINE WITH A POWER TURBINE EQUIPPED WITH AN ELECTRIC POWER GENERATOR CENTERED ON THE AXIS OF THE TURBINE ENGINE*", US 2010/0186418, July 2010.

Bruno Albert Beutin, Antoine Olivier Francois Colin, Clarisse Savine Mathilde Reaux, Didier Jean-Louis Yvon, SNECMA, "*TURBINE ENGINE WITH A POWER TURBINE EQUIPPED WITH AN ELECTRIC POWER GENERATO* ", US 2011/0167835, July 2011.

Claude M. Mons, SNECMA, "*PROCEDE DE DEGIVRAGE D'UNE PIECE OU DE PREVENTION DE FORMATION DE GIVRE SUR CELLE-CI*", FR 2 941 918, February 2009.

Paul D. Hopewell, Alan S. Kinson, Rolls Royce plc, "ELECTRICAL GENERATOR ARRANGEMENT", US 8,008,822, Aug. 30, 2011.

Cooling for structural components

Dimitrie Negulescu, ROLLS-ROYCE DEUTSCHLAND, "*AIRCRAFT GAS TURBINE ENGINE*", US 2011/0209458, September 2011.

Timothy P. Keating, ROLLS-ROYCE plc, "*COOLING SYSTEM*", US 2011/0083417, April 2011.

Gearbox oil cooling

Guillaume Bulin, Ralf-Henning Stolte, AIRBUS, "*FLUID-COOLING DEVICE FOR A TURBINE ENGINE PROPULSIVE UNIT*", WO 2010/136710, May 2010

Christelle Rinjonneau, Pierre Guillaume, AIRBUS FR, "*PROPULSEUR A TURBOMACHINE POUR AERONEF AVEC REFROIDISSEUR INSTALE DANS LA NACELLE*", EP 2 348 211, January 2011.

Philippe G. Chanez , Gaetan J. Mab-Boux , Philippe G. Minot, SNECMA, "*ENTREE D AIR DE MOTEUR A TURBINE A GAZ DANS UNE NACELLE*", FR *2 951 503*, October 2009.

Philippe G. Minot, Thomas A. C. Vincent, Didier J. L. Yvon , SNECMA, "*ENTREE D AIR DE MOTEUR A TURBINE A GAZ DANS UNE NACELLE*", FR *2 951 504*, October 2009.

Richard G. Stretton, ROLLS-ROYCE plc, "*A GAS TURBINE ENGINE*", EP 2 383 441, November 2011.

CRT mechanical design

Thomas Ory Moniz, Robert Joseph Orlando, GENERAL ELECTRIC COMPANY, "*COUNTER-ROTATING GAS TURBINE ENGINE AND METHOD OF ASSEMBLING SAME*", US 2006/0093469, May 2006.

Thomas O. Moniz, Anant P. Singh, Daniel M. Allen, Donald R. Bond, GENERAL ELECTRIC COMPANY, "*COUNTER-ROTATING TURBINE ENGINE AND METHOD OF ASSEMBLING SAME*", US 2006/0090450, May 2006

Robert Joseph Orlando, Thomas Ory Moniz, GENERAL ELECTRIC COMPANY, "*COUNTER-ROTATING GAS TURBINE ENGINE AND METHOD OF ASSEMBLING SAME*", US 2006/0093468, May 2006.

Thomas Ory Moniz, Robert Joseph Orlando, GENERAL ELECTRIC COMPANY, "*COUNTER-ROTATING GAS TURBINE ENGINE AND METHOD OF ASSEMBLING SAME*", US 2006/0093464, May 2006.

Thomas Ory Moniz, Robert Joseph Orlando, GENERAL ELECTRIC COMPANY, "*COUNTER-ROTATING GAS TURBINE ENGINE AND METHOD OF ASSEMBLING SAME*", US 2006/0093451, May 2006.

Rollin George Giffin, William James Morrow, GENERAL ELECTRIC COMPANY, "*METHODS AND APPARATUS FOR ASSEMBLING A GAS TURBINE ENGINE*", US 2006/0032210, February 2006.

Jorge Francisco Seda, GENERAL ELECTRIC COMPANY, "*COUNTER-ROTATING TURBINE ENGINE*", EP 1 655 475, May 2006.

Core flow exhaust

Robert H. Perkinson, "HAMILTON SUNDSTRAND CORP., "*PROPELLER WITH THERMALLY PROTECTED BLADES*", EP 2 233 394, September 2010.

Alfred M. Stern, UNITED TECHNOLOGIES CORPORATION, "*COOLED PUSHER PROPELLER SYSTEM AND METHOD OF DIRECTING AN EXHAUST FLOW FROM A PROPULSION SYSTEM*", EP 2 090 765, August 2009.

Kenneth Mackie, Richard Standing, ROLLS-ROYCE plc, "*PROPFAN ENGINE*", EP 2 253 817, October 2010.

Kenneth Udall, ROLLS-ROYCE plc, "*FLOW MIXER AND CORRESPONDING GAS TURBINE ENGINE*", WO 2011/107320, October 2010.

Vibration monitoring

Daniel Edward Mollmann, GENERAL ELECTRIC COMPANY, "*DUAL ROTOR VIBRATION MONITORING*", US 2009/0263247, October 2009.

Pylon design

Christelle Rinjonneau, Pierre Guillaume, AIRBUS FR, "*TURBOMACHINE SUPPORT PYLON FOR AIRCRAFT*", US 2011/0315813, December 2011.

Daniel Kent Vetters, Robert Wayne Cedoz, David Eames, ROLLS-ROYCE US, "*DUAL ROTOR VIBRATION MONITORING*", US 2010/0259996, October 2011.

Peter K. Beardsley, ROLLS-ROYCE plc, "*MOUNTING SYSTEM FOR USE IN MOUNTING A GAS TURBINE ENGINE*", US 2008/0105782, May 2008.

Engine installation on the aircraft

Christophe Cros, AIRBUS FR, "*AIRCRAFT WITH LOW NOISE, SUCH AS DURING TAKE-OFF AND LANDING*", US 2008/0179465, July 2008.

Christophe Cros, AIRBUS FR, "*LOW-NOISE AIRCRAFT, PARTICULARLY AT TAKE-OFF AND LANDING*", US 2008/0191087, August 2008.

Pierre-Emmanuel Gall, Christophe Cros, AIRBUS FR, "*AIRCRAFT HAVING A REDUCED ENVIRONMENTAL IMPACT*", US 2008/0258005, October 2008

Pierre-Emmanuel Gall, Christophe Cros, AIRBUS FR, "AIRCRAFT HAVING REDUCED ENVIRONMENTAL IMPACT", US 2009/0020643, January 2009.

Jorge Pablo Verde Preckler, Maria Caballero Asensio, AIRBUS ES, "*ACOUSTICALLY ATTENUATED FUSELAGE FOR AIRCRAFT*", US 2009/0152400, June 2009.

Jorge Pablo Verde Preckler, AIRBUS ES, "*IMPACT RESISTANT AIRCRAFT FUSELAGE*", US 2009/0140096, June 2009.

Laurent Lafont, AIRBUS FR, "*PROCEDE POUR L'AMELIORATION DES PERFORMANCES D'UN AERONEF*", *FR 2 942 772, March 2009.*

Pierre-Emmanuel Gall, Julien Ricouard, AIRBUS FR, "*METHOD FOR PRODUCING AN AIRCRAFT WITH REDUCED ENVRIONMENTAL IMPACT AND THE AIRCRAFT THUS OBTAINED*", US 2010/0264264, October 2010.

Bruno Saint-Jalmes, Jason Zaneboni, Mathieu Belleville, AIRBUS FR, "*AIRCRAFT FUSELAGE*", US 2010/0032518, February 2010.

Dimitrie Negule, ROLLS-ROYCE DEUTSCHLAND, "*AIRCRAFT WITH TAIL PROPELLER-ENGINE LAYOUT*", US 2010/0155526, June 2010.

Appendix B – Bibliography of 2-D and 3-D SR and CR propeller design and performance calculation methodologies

Review papers of 2-D and 3-D methods

M. Laban, J.C. Kok, B.B. Prananta, (2010), "*Numerical tools for contra-rotating open-rotor performance, noise and vibration assessment*", ICAS 2010-4.4.2, Proceedings of the 27th Congress of International Council of the Aeronautical Sciences, Nice, France, 19 - 24 September 2010.

Q. R. Wald, (2006), "*The aerodynamics of propellers*", Progress in Aerospace Sciences, Vol. 42, Issue 2, pp. 85-128, 2006

O. Gur, A. Rosen, (2008),"*Comparison between blade-element models of propellers*", The Aeronautical Journal, Vol. 112, No. 1138, pp. 689-104, December 2008.

T. A. Egolf, O. L. Anderson, D. E. Edwards, A. J. Landgrebe, (1988), "*An Analysis for High Speed Propeller-Nacelle Aerodynamic Performance Prediction, Volume I - Theory an Application*", NASA CR-4199, 1988.

K. D. Korkan, G. M. Gregorek, (1980), "*A Theoretical and experimental investigation of propeller performance methodologies*", AIAA 80-1240, Proceedings of AIAA/SAE/ASME 16th Joint Propulsion Conference, Hartford, Connecticut, USA, 30 June - 2 July 1980.

A. J. Bocci, J. I. Morrison, (1985), "*A review of ARA research into propeller aerodynamic prediction methods*", AGARD Conference Proceedings No.366, Aerodynamics and Acoustics of Propellers, February 1985.

2-D methods

M. H. Williams, (1990), "*An Unsteady Lifting Surface Method for Single Rotation Propellers*", NASA CR-4302, 1990.

R. E. Davidson, (1981), "*Optimization and performance calculation of dual-rotation propellers*", NASA TP-1948, 1981

C. N. Adkins, R. H. Liebeck, (1994), "*Design of optimum propellers*", Journal of Propulsion and Power, Vol. 10 No. 5, Sept. Oct. 1994.

K. Nasu, S. Saito, Y. Nakamura, (1987), "*Extension of local circulation method to counter rotation propeller*", AIAA-1987-1891, Proceedings of the 23rd AIAA/SAE/ASME/ASEE Joint Propulsion Conference, San Diego, CA, USA, 29 Jne - 2 July 1987.

K. D. Korkan, J. A. Gazzaniga, (1987), "*Off-design analysis of counter-rotating propeller configurations*", Journal of Propulsion, Vol. 3. No.1, pp. 91-93, January-February 1987.

S. C. Playle, K. D. Korkan, E Von Lavante, (1986), "*A numerical method for the design and analysis of counter-rotating propellers*", Journal of Propulsion, Vol. 2. No.1, pp. 57-63, January-February 1986.

Thoai-Sum Luu, R. Collercandy, (1985), “*Design concept and performance prediction technic for potential flows around advanced propellers*”, AGARD Conference Proceedings No.366, Aerodynamics and Acoustics of Propellers, February 1985.

B. W. Denner, (1989), "*An Approximate Model for the Performance and Acoustic Predictions of Counterrotating Propeller Configurations*", NASA CR-180667, 1989.

D.J. Lesieutre, J.P. Sullivan, (1985), "*The Analysis of Counter-Rotating. Propeller Systems*", SAE Technical Paper 850869, April 1985

L. J. Bober, L.K. Chang, (1981), “*Factors influencing the predicted performance of advanced propellers*”, AIAA-1981-1564, Proceedings of the 17th SAE and ASME Joint Propulsion Conference, Colorado Springs, USA, 27-29 July 1981.

J. Gilman, (1951), "*Application of Theodorsen's propeller theory to the calculation of the performance of dual-rotating propellers*", NACA RM-L51A17, 1951.

F. Ginzel, (1949), "*Calculation of Counterrotating Propellers*", NACA TM-1208, 1949.

M.A. Lock, (1941), "*Interference velocity for a close pair of contra-rotating airscrews*", Aeronautical Research Council Reports and Memoranda, Reports and Memoranda No. 2084, 22nd July 1941.

I. Naiman, (1943), "*Method of calculating performance of dual-rotating propellers from airfoil characteristics*", NACA WR-L-330, 1943.

T. Theodorsen, (1944), "*The theory of propellers I : determination of the circulation function and the mass coefficient for dual-rotating propellers*", NACA WR-L-490, 1944.

T. Theodorsen, (1944), "*The theory of propellers II : method for calculating the axial interference velocity*", NACA WR-L-157, 1944.

T. Theodorsen, (1944), "*The theory of propellers III : the slipstream contraction with numerical values for two-blade and four-blade propellers*", NACA WR-L-155, 1944.

T. Theodorsen, (1944), "*The theory of propellers IV : thrust, energy, and efficiency formulas for single and dual rotating propellers with ideal circulation distribution*", NACA TR-778, 1944.

S. Goldstein , (1929), “*On the vortex theory of screw propellers*”, Proc. of the Royal Society (A) 123, 440, 1929.

L. Prandtl, A. Betz, *"Schraubenpropeller mit geringstem Energieverlust"*, Göttinger Nachrichten, 1919.

3-D methods

R. Boisard, F. Falissard, G. Delattre, (2012), "*HPC capabilities of the elsA CFD software applied to a counter rotating open rotor test rig*", Paper FP08-2012-boisard, Proceedings of the 47th Symposium of Applied Aerodynamics, Paris, France, 26-28 March 2012.

R. Schnell, J. Yin, C. Voss, E. Nicke, (2010), "*Assessment and optimisation of the aerodynamic and acoustic characteristics of a counter rotating open rotor*", GT2010-22076, Proceedings of the ASME Turbo Expo 2010, Glasgow, UK, 14-18 June 2010.

A. Zachariadis, C. A. Hall, (2009), "*Application of a Navier-Stokes solver to the study of open rotor aerodynamics*", GT2009-59332, Proceedings of ASME Turbo Expo 2009: Power for Land, Sea and Air GT2009, Orlando, Florida, USA, 8-12 June, 2009.

A. Stuermer, J. Yiny, (2009), "*Low-speed aerodynamics and aeroacoustics of CROR propulsion systems*", Proceedings of the 15th AIAA/CEAS Aeroacoustics Conference, Miami, Florida, USA, 11 - 13 May 2009.

C. J. Miller, G. G. Podboy, (1990), "*Euler analysis comparison with LDV data for an advanced counter-rotation propfan at cruise*", NASA TM-103249, 1990.

J.M. Bousquet , P. Gardarein, (2003), "*Improvements on computations of high speed propeller unsteady aerodynamics*", Aerospace Science and Technology Vol. 7, pp. 465–472, 2003.

T. E. Hannigan, H. S. Wainauski, (1991), *"Wind tunnel results of counter rotating prop-fans designed with lifting line and euler code methods*", AIAA-91-2499, Proceedings of the AIAA/SAE/ASME/ASEE 27th Joint Propulsion Conference, Sacramento, CA, USA, 24-26 June 1991.

R. Srivasta, L. N. Sankar, (1993), "*Efficient hybrid scheme for the analysis of counter-rotating propellers*", Journal of Propulsion and Power, Vol. 9, No. 3, pp. 382-388, May-June 1993.

J. Cho, M. H. Williams, (1990), "*Counter-rotating propeller analysis using a frequency domain panel method*", Journal of Propulsion, Vol. 6, No. 4, pp. 426-433, July –August 1990.

N. Kroll,D. Lohmann, J. Schone, (1987), "*Numerical methods for propeller aerodynamics and acoustics at DFVLR*", Proceedings of the 69th Symposium of the AGARD Propulsion and Energetics Panel on Technology for Advanced Aero Engine Components, pp. 24.1-24.15, Paris, France, May 4-8, 1987

L. H. Smith, (1987), "*Unducted fan aerodynamic design*", Journal of Turbomachinery. Vol. 109, pp. 313-324, 1987.

J. M. Bousquet, (1987), "*Analysis of high speed propellers aerodynamics*", Proceedings of the 69th Symposium of the AGARD Propulsion and Energetics Panel on Technology for Advanced Aero Engine Components, pp. 25.1-25.12, Paris, France, May 4-8, 1987.

Appendix C – Bibliography of challenges and design considerations of HP-IP counter rotating turbines

Ref. 172 and Ref. 173

H. Zhang, H-S. Wang, F. Tang, J-Z. Xu, X-L.Zhao, (2007), "*Research of the performance of a vaneless counter-rotating turbine on the off-design conditions*", Journal of Engineering Thermophysics, Vol. 28 No. 4, pp. 571-573, July 2007.

Q-J.Zhao, H-S. Wang, X-L. Zhao, J-Z. Xu, (2007), "*Influence of rotor speed on flow characteristics in a vaneless counter-rotating turbine*", Journal of Engineering Thermophysics, Vol. 28 No. 6, pp. 925-928, November 2007.

L-C. Ji, J. Chen, L. Xiang, J-Z. Xu, (2003), "*Aerodynamic design of the vaneless counter-rotating turbine*", Journal of Engineering Thermophysics, Vol. 24 No. 6, pp. 943-946, November 2003.

L-C. Ji, J. Chen, H-B. Huang, J-Z. Xu, (2003), "*Key techniques in utilizing vaneless counter-rotating turbine*", Journal of Engineering Thermophysics, Vol. 24 No. 1, pp. 35-38, January 2003.

X-J. Fang, S-Y. Liu, P. Wang, W-J Zang, (2005), "*Design and analysis of LP-vaneless contra-rotating turbine*", Journal of Propulsion Technology, Vol. 26 No. 3, pp. 234-238, June 2005.

L-C. Ji, X-B. Quan, J-Z. Xu, (2001), "*A primary design of one counter-rotating turbine*", Journal of Engineering Thermophysics, Vol. 22 No. 4, pp. 438-440, July 2001.

L-C. Ji, W-T. Zhong, J-Z. Xu, (2001), "*Primary analysis and design of a vaneless counter-rotating turbine*", Journal of Engineering Thermophysics, Vol. 22 No. 2, pp. 167-170, March 2001.

X-J. Fang, S-Y. Liu, P. Wang, (2003), "*Aerodynamic characteristic study of axial transonic highly loaded contra-rotating turbine*", Journal of Baijing University of Aeronautics and Astronautics, Vol 29. N0. 6, pp. 475-479, June 2003.

R-J. Cai, (2001), "*Consideration on the basic design and application of counter-rotating turbines*", Journal of Aerospace Power, Vol. 16, No. 3,pp. 193-198 ,July 2001.

R-J. Cai, X-G. Wei, (2001), "*Triple counter-rotating turbine and its basic analysis*", Journal of Aerospace Power, Vol. 7, No. 1,pp. 72-76 ,January 1992.

L-C. Ji, W-W. Shao, B-C. Wang, (2008), "*Basic analysis of a counter-rotating turbine*", Journal of Propulsion Technology, Vol. 29 No. 1, pp. 62-66, February 2008.

L-C. Ji, (2007), "*Basic analysis on 1+3/2 and 1+1/2 counter-rotating turbines*", Journal of Engineering Thermophysics, Vol. 28 No. 1, pp. 113-116, June 2007.

H-S. Wang, K. Yang, Q-J. Zhao, Z-Z Zhang, X-L. Zhao, J-Z. Xu, "*Influence of rotor tip clearance on performance of caneless counter-rotating turbine*", Journal of Engineering Thermophysics, Vol. 27 No. 3, pp. 399-401, May 2006.

L-C. Ji, J. Chen, H-B. Huang, J. Chen, H-L. Yu, J-Z. Xu, "*Design and test of a supersonic cascade used for the vaneless counter-rotating turbine*", Journal of Engineering Thermophysics, Vol. 25 No. 1, pp. 45-48, January 2004.

K. Yang, H-S Wang, X-L. Zhao, J-Z. Xu, J-Y. Du, "*Numerical sinmulation of improving ration of output work by curbing low pressure rotor of caneless counter-rotating turbine*", Journal of Engineering Thermophysics, Vol. 27 No. 5, pp. 757-759, September 2006.

Appendix D – Turbine stage loss calculation method

D.1 Blading model and blade geometrical data

This section presents the blade geometrical parameters used for the loss calculations.

1- Stagger angle

Following the preliminary design blading estimation method of Ref. 198, the blade stagger angle (Stagger) is calculated as

$$\text{Stagger} = \frac{180}{\pi} arctan\left(\frac{c_\theta}{\sigma_x}\right) \quad \text{[Eq. D 1]}$$

where

$$\sigma_x = \frac{2\cos\left(\frac{\pi}{180}\beta_{out}\right)}{0.8\cos\left(\frac{\pi}{180}\beta_{in}\right)} \sin\left(\frac{\pi}{180}(\beta_{in} - \beta_{out})\right) \quad \text{[Eq. D 2]}$$

and

$$c_\theta = \sin^2\left(\frac{\pi}{180}\beta_{in}\right) - a\left(\cos\left(\frac{\pi}{180}\beta_{in}\right) - \cos\left(\frac{\pi}{180}\beta_{out}\right)\right) - \sin^2\left(\frac{\pi}{180}\beta_{out}\right) \quad \text{[Eq. D 3]}$$

with

$$a = \frac{\sigma_x - \sin\left(\frac{\pi}{180}\beta_{in}\right)\cos\left(\frac{\pi}{180}\beta_{in}\right) + \sin\left(\frac{\pi}{180}\beta_{out}\right)\cos\left(\frac{\pi}{180}\beta_{out}\right)}{\sin\left(\frac{\pi}{180}\beta_{in}\right) - \sin\left(\frac{\pi}{180}\beta_{out}\right)} \quad \text{[Eq. D 4]}$$

2 – Blade height, space, chord and number of blades

$$\text{Mean blade height: } blade_h = \frac{(r_{tip\ out} + r_{tip\ in}) - (r_{h\,out} + r_{h\ in})}{2} \quad \text{[Eq. D 5]}$$

The blade axial chord is obtained from the gas path and the inter stage spacing.

$$\text{AxialChord} = \text{AxialChord}_{Path} - 0.022 \quad \text{[Eq. D 6]}$$

The blade chord (Chord) is calculated from the axial chord and the stagger angle as

$$\text{Chord} = \frac{\text{AxialChord}}{cos\left(\text{Stagger}\frac{\pi}{180}\right)} \qquad \text{[Eq. D 7]}$$

The spacing between two blades (Space) at mean radius is calculated as

$$\text{Space} = \frac{\text{AxialChord}}{|\sigma_x|} \qquad \text{[Eq. D 8]}$$

The first and the last stages have 35 blades. This is to comply with the structural requirements of these stages. The number of blades of all the other stages are calculated as

$$\text{Nb} = int\,\text{eger}\left(\frac{2\pi r_{mean}}{\text{Space}}\right) \qquad \text{[Eq. D 9]}$$

and the spacing is re calculated for the integer number of blades as

$$\text{Space} = \frac{2\pi r_{mean}}{\text{Nb}} \qquad \text{[Eq. D 10]}$$

3 – Blade geometrical features

The following blade geometrical features were assumed for the CRT designs:

Diameter of the leading edge: $D_{LE} = 0.03$ Chord [Eq. D 12]

Maximum blade thickness (t_{MAX}) divided by the chord: $\frac{t_{MAX}}{\text{Chord}} = 0.1$ [Eq. D 13]

SE coefficient, used for the deviation model: $\text{SE} = \frac{\text{Space}}{6.25}$ [Eq. D 14]

Trailing edge thickness: $t_{TE} = 0.01$ Chord [Eq. D 15]

Number of seals in the shroud: NbSeals = 2 [Eq. D 16]

Shroud seal clearance: $k = 0.3$ mm [Eq. D 17]

D.2 Sign convention for angles in the loss model

D.2.1 Blade and flow angles

The following conversion is required to adapt the sign convention of angles defined in Figure 56, to the sign convention of angles used in Ref. 192 for loss calculations:

for odd stages

$\beta'_{in} = \beta_{in}$ and $\beta'_{out} = -\beta_{out}$

$\beta'_{metal\ in} = \beta_{metal\ in}$ $\beta'_{metal\ out} = -\beta_{metal\ out}$

for even stages

$$\beta'_{in} = -\beta_{in} \qquad \text{and} \qquad \beta'_{out} = \beta_{out}$$
$$\beta'_{metal\ in} = -\beta_{metal\ in} \qquad \beta'_{metal\ out} = \beta_{metal\ out}$$

[Eq. D 18]

α' and β' are the angles adapted to the sign convention used in Ref. 192.

D.2.2 Incidence

The definition of incidence (i) provided in Ref. 193 was extended to both counter rotating stages which have different signs of $\beta_{metal\ in}$.

$i = \beta_{in} - \beta_{metal\ in}$ for odd stages

$i = \beta_{metal\ in} - \beta_{in}$ for even stages [Eq. D 19]

Figure D1 shows the sign convention for the incidence extended for CRTs using the sign convention for angles defined in Figure 56.

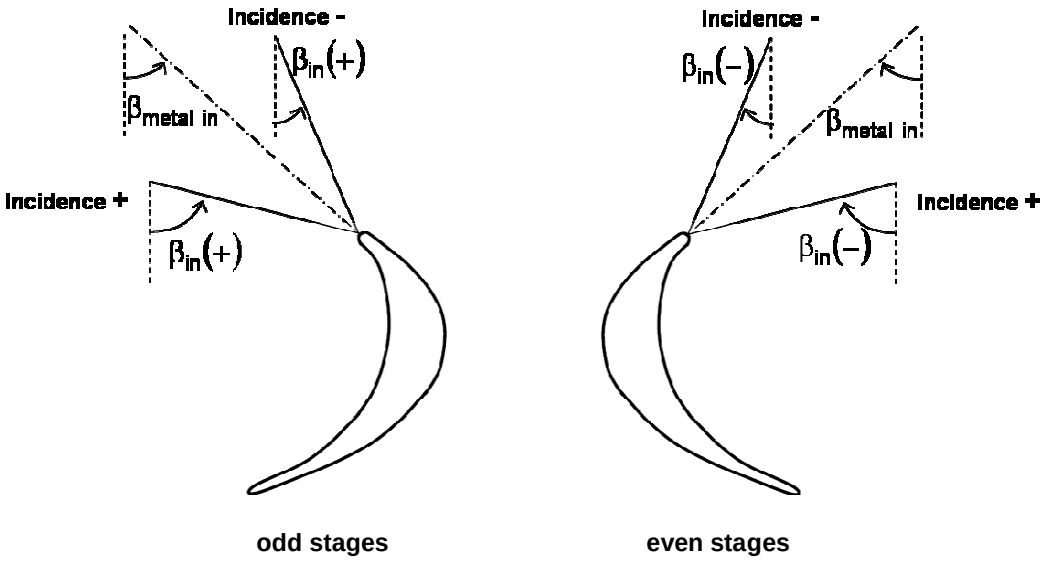

Figure D1: Incidence sign convention of the used loss model extended to CRTs

D.3 Losses calculation procedure

At cero incidence, the total pressure loss coefficient is calculated as

$$Yt = Y_P C_{Re} + Y_S + Y_{TE} + Y_{TC}$$ [Eq. D 20]

where:

$Y_P C_{Re}$ is the profile loss coefficient corrected with respect to Reynolds number

Y_S is the secondary loss coefficient

Y_{TE} is the railing edge loss coefficient

Y_{TC} is the tip clearance loss coefficient

These independent loss coefficients are calculated as follows.

NOTA: The majority of the equations presented in section D.5 can be found in Ref. 192 and Ref. 193 . References are provided for all the equations which are not found in Ref. 192 and Ref. 193.

D.3.1 Profile loss coefficient

The low subsonic speed and cero incidence profile loss coefficient (Y_{PA}) is calculated as

$$Y_{PA} = \left(Y_{P1} + \left| \frac{\beta'_{metal\,in}}{\beta'_{out}} \right| \left(\frac{\beta'_{metal\,in}}{\beta'_{out}} \right) [Y_{P2} - Y_{P1}] \right) \left(\frac{t_{MAX} / Chord}{0.2} \right)^{\frac{\beta'_{metal\,in}}{\beta'_{out}}} \qquad \text{[Eq. D 21]}$$

Where Y_{P1} and Y_{P2} are read from Figure D2

These figures were digitised and functions with appropriate interpolation methods were created to obtain Y_{P1} and Y_{P2} in the calculation code.

K_P is used to correct the estimated profile losses at different Mach numbers.

$$K_1 = 1 \qquad \text{for } Mrel_{out} < 0.2$$

$$K_1 = 1 - 1.25(Mrel_{out} - 0.2) \qquad \text{for } Mrel_{out} > 0.2 \qquad \text{[Eq. D 22]}$$

$$K_2 = \left(\frac{Mrel_{in}}{Mrel_{out}} \right)^2 \qquad \text{[Eq. D 23]}$$

$$K_P = 1 - K_2(1 - K_1) \qquad \text{[Eq. D 24]}$$

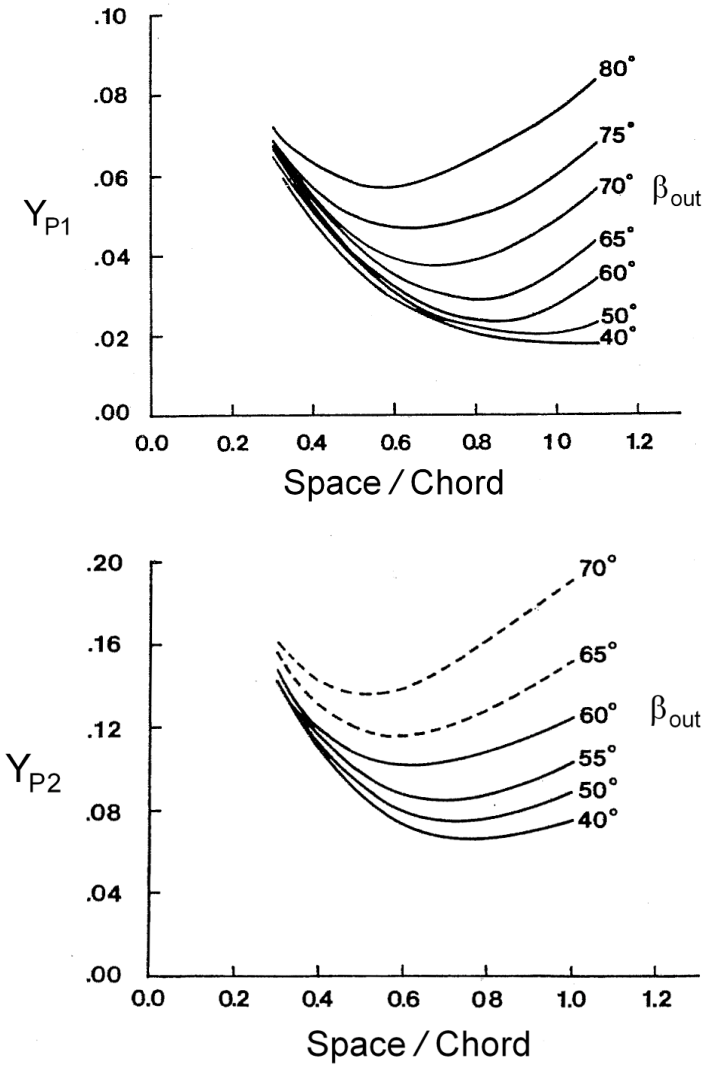

Figure D2: Y_{P1} and Y_{P2} [Ref. 192]

The loss coefficient accounting for shock the leading edge losses (Y_{SHOCK}) is calculated as

$$Y'_{hub} = 0 \qquad \text{for } Mrel_{in\,hub} < 0.4$$

$$Y'_{hub} = 0.75\left(Mrel_{in\ hub} - 0.4\right)^{1.75} \qquad \text{for } Mrel_{in\,hub} > 0.4 \qquad \text{[Eq. D 25]}$$

(Eq. D 25 is extracted from Ref. 190, equation 2.5.7, page 44)

$$Mrel_{in\,hub} = Mrel_{in}\left(1 + 5.2\left|\frac{r_{hub}}{r_{tip}} - 1\right|^{2.2}\right) \qquad \text{[Eq. D 26]}$$

$$Y'_{SHOCK} = \left(\frac{r_{hub}}{r_{tip}}\right) Y'_{hub} \qquad \text{[Eq. D 27]}$$

$$Y_{SHOCK} = Y'_{SHOCK}\left(\frac{Ps_{in}}{Ps_{out}}\right)\frac{1-\left(1+\frac{\gamma-1}{2}Mrel_{in}{}^{2}\right)^{\frac{\gamma}{\gamma-1}}}{1-\left(1+\frac{\gamma-1}{2}Mrel_{out}{}^{2}\right)^{\frac{\gamma}{\gamma-1}}} \qquad \text{[Eq. D 28]}$$

The profile loss coefficient at cero incidence ($Y_{P\,i=0}$) is calculated as

$$Y_{Pi=0} = 0.914\left(\tfrac{2}{3} Y_{PA} K_P + Y_{SHOCK}\right) \qquad \text{[Eq. D 29]}$$

This profile loss coefficient is subsequently corrected for incidence. This requires to convert $Y_{P\,i=0}$ to a kinetic energy loss coefficient ($\phi_{Pi=0}$) solving Eq. D 30

$$Y_{Pi=0} = \frac{\left[1-\frac{\gamma-1}{2}Mrel_{out}{}^{2}\left(\frac{1}{\phi_{Pi=0}{}^{2}}-1\right)\right]^{-\frac{\gamma}{\gamma-1}}-1}{1-\left(1+\frac{\gamma-1}{2}Mrel_{out}{}^{2}\right)^{-\frac{\gamma}{\gamma-1}}} \qquad \text{[Eq. D 30]}$$

The change in kinetic energy loss coefficient due to incidence is calculated as

$$\Delta\phi_P{}^{2} = 0.778x10^{-5}\chi_1 + 0.56x10^{-7}\chi_1{}^{2} + 0.4x10^{-10}\chi_1{}^{3} + 2.054x10^{-19}\chi_1{}^{6}$$

for 800 χ_1 > 0

$$\Delta\phi_P{}^{2} = -5.1734x10^{-6}\chi_1 + 7.6902x10^{-9}\chi_1{}^{2}$$

for 0 > χ_1> -1000

[Eq. D 31]

where

$$\chi_1 = (i)\left(\frac{D_{LE}}{Space}\right)^{-1.6}\left(\frac{cos\left(\frac{\pi}{180}\beta'_{metal\ in}\right)}{cos\left(\frac{\pi}{180}\beta'_{metal\ out}\right)}\right)^{-2} \qquad \text{[Eq. D 32]}$$

and the incidence (i) is calculated using Eq. D 19. This correlation was produced with data within the range of 800 > χ_1> -1000, and all the OD conditions simulated in this PhD research project where within this range.

The total profile kinetic energy loss coefficient is calculated and converted to a pressure loss coefficient

$$\phi_P{}^2 = \phi_{Pi=0}{}^2 + \Delta\phi_P{}^2 \qquad \text{[Eq. D 33]}$$

$$Y_P = \frac{\left[1-\frac{\gamma-1}{2}\text{Mrel}_{out}{}^2\left(\frac{1}{\phi_P{}^2}-1\right)\right]^{-\frac{\gamma}{\gamma-1}}-1}{1-\left(1+\frac{\gamma-1}{2}\text{Mrel}_{out}{}^2\right)^{-\frac{\gamma}{\gamma-1}}} \qquad \text{[Eq. D 34]}$$

Y_P is the profile loss at Re = 2 x 10^2. For any other Reynolds number, the following correction factor (C_{Re}) is used.

$$C_{Re} = \left(\frac{Re}{2\text{x}10^5}\right)^{-0.4} \qquad \text{for} \quad \text{Re} \le 2\text{x}10^5$$

$$C_{Re} = 1 \qquad \text{for} \quad 2\text{x}10^5 < \text{Re} < 10^6$$

$$C_{Re} = \left(\frac{Re}{10^6}\right)^{-0.2} \qquad \text{for} \quad \text{Re} > 10^6 \qquad \text{[Eq. D 35]}$$

Where Re is calculated as

$$Re = \frac{\rho_{out}\text{Vrel}_{out}\text{Chord}}{\mu_{out}} \qquad \text{[Eq. D 36]}$$

with [Ref. 197]

$$\mu_{out} = (17.1)(10^{-6})\sqrt{\frac{\text{Ts}_{out}}{273}}\,\frac{\left(1+\frac{114}{273}\right)}{\left(1+\frac{114}{\text{Ts}_{out}}\right)} \qquad \text{[Eq. D 37]}$$

D.3.2 Secondary losses coefficient

The low subsonic speed secondary loss coefficient at cero incidence Y_{SA} is first calculated as

$$Y_{SA} = 0.0334(\text{AR})\left(\frac{cos\left(\frac{\pi}{180}\beta'_{out}\right)}{cos\left(\frac{\pi}{180}\beta'_{metal\,in}\right)}\right)\left(\frac{C_L}{\text{Space}/\text{Chord}}\right)^2\left(\frac{cos\left(\frac{\pi}{180}\beta'_{out}\right)^2}{cos\left(\frac{\pi}{180}\beta'_{m}\right)^3}\right)$$

[Eq. D 33]

where

$$\frac{C_L}{\text{Space / Chord}} = 2\left(tan\left(\frac{\pi}{180}\beta'_{in}\right) + tan\left(\frac{\pi}{180}\beta'_{out}\right)\right) cos\left(\frac{\pi}{180}\beta'_{m}\right) \qquad \text{[Eq. D 34]}$$

$$\frac{180}{\pi}\beta'_{m} = arctan\left(tan\left(\frac{\pi}{180}\beta'_{in}\right) - tan\left(\frac{\pi}{180}\beta'_{out}\right)\right) \qquad \text{[Eq. D 35]}$$

and

$$AR = \frac{1 - 0.25\sqrt{2 - \text{blade}_h / \text{Chord}}}{\text{blade}_h / \text{Chord}} \qquad \text{for blade}_h\text{/Chord} \leq 2$$

$$AR = \frac{1}{\text{blade}_h / \text{Chord}} \qquad \text{for blade}_h\text{/Chord} > 2 \qquad \text{[Eq. D 36]}$$

Finally the secondary loss coefficient at zero incidence ($Y_{S\ i=0}$) is calculated from Y_{SA} and the following Mach number corrections

$$Y_{S\,i=0} = 1.2 Y_{SA} K_S \qquad \text{[Eq. D 37]}$$

where

$$K3 = \left(\frac{\text{AxialChord}}{\text{blade}_h}\right)^2 \qquad \text{[Eq. D 38]}$$

$$K_S = 1 - K_3(1 - K_P) \qquad \text{[Eq. D 39]}$$

and K_P is the one calculated in Eq. D 24.

The secondary loss coefficient $Y_{S\,i=0}$ is subsequently corrected for incidence.

$$Y_S = Y_{S\,i=0}\left(exp\,(\chi_2) + 13\,\chi_2{}^2 + 400\,\chi_2{}^4\right) \qquad \text{for } 0.3 > \chi_2 > 0$$

$$Y_S = Y_{S\,i=0}\,exp(\chi_2) \qquad \text{for } 0 > \chi_2 > -0.4$$

[Eq. D 40]

where

$$\chi_2 = \frac{i}{180 - \left(\frac{\pi}{180}\left(\beta'_{\text{metal in}} + \beta'_{\text{metal out}}\right)\right)} \left(\frac{D_{LE}}{\text{Chord}}\right)^{-0.3} \left(\frac{cos\left(\frac{\pi}{180}\beta'_{\text{metal in}}\right)}{cos\left(\frac{\pi}{180}\beta'_{\text{metal out}}\right)}\right)^{-1.5}$$

[Eq. D 41]

This correlation was produced with data within the range of 0.3 > χ_2 > -0.4. Its use was allowed outside the aforementioned range to obtain the performance of extreme OD cases and obtain complete CRT maps. The zone of the CRT map for which this correlation is extrapolated is indicated in Figure 68. In this region the incidences are negative and it can be seen in figure 10 of Ref. 193 that the variations in the loss coefficient are relatively small and linear with respect to i. It is important to note that although these extreme points were included in the CRT map, they do not have a significant influence on the assessment studies since the CRT operates in this region only for some low idle descent points.

D.3.3 Trailing edge loss coefficient

The trailing edge loss coefficient is calculated as

$$Y_{TE} = \frac{\left[1 - \frac{\gamma-1}{2} Mrel_{out}^{\,2}\left(\frac{1}{1-\Delta\phi_{TE}^{\,2}} - 1\right)\right]^{-\frac{\gamma}{\gamma-1}} - 1}{1 - \left(1 + \frac{\gamma-1}{2} Mrel_{out}^{\,2}\right)^{-\frac{\gamma}{\gamma-1}}} \qquad \text{[Eq. D 42]}$$

where

$$\Delta\phi_{TE}^{\,2} = \Delta\phi_{Ax}^{\,2}\left|\frac{\beta'_{metal\,in}}{\beta'_{out}}\right|\left(\frac{\beta'_{metal\,in}}{\beta'_{out}}\right)\left(\Delta\phi_{Imp}^{\,2} - \Delta\phi_{Ax}^{\,2}\right) \qquad \text{[Eq. D 43]}$$

and $\Delta\phi^2_{Ax}$ and $\Delta\phi^2_{Imp}$ are obtained from Figure D.

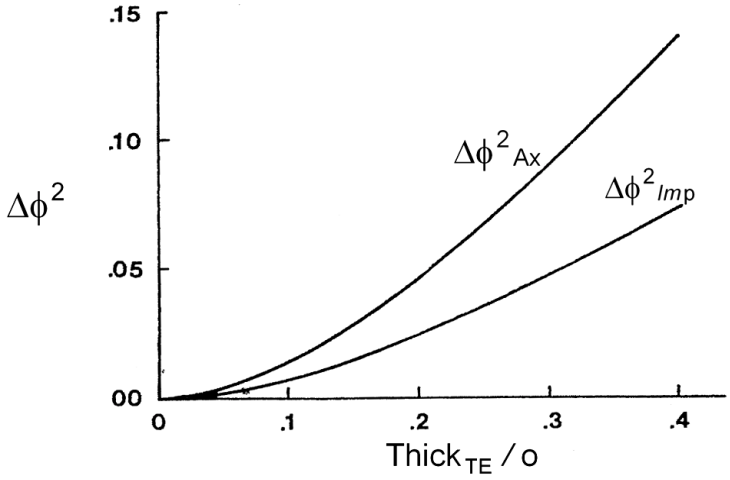

Figure D3: $\Delta\phi^2_{Ax}$ and $\Delta\phi^2_{Imp}$ vs. t_{TE}/o [Ref. 192]

the throat opening (o) is calculated as

$$o = \text{Space}\, cos\left(\frac{\pi}{180}\beta_{\text{metal out}}\right)$$ [Eq. D 44]

D.3.4 Tip clearance loss coefficient

The studied CRTs have shrouded rotors. The tip clearance loss coefficient is estimated as

$$Y_{TC} = 0.37\frac{\text{Chord}}{\text{blade}_h}\left(\frac{k}{\text{NbSeals}^{0.42}\,\text{Chord}}\right)^{0.78}\left(\frac{C_L}{\text{Space}/\text{Chord}}\right)^2\left(\frac{cos\left(\frac{\pi}{180}\beta'_{\text{out}}\right)^2}{cos\left(\frac{\pi}{180}\beta'_m\right)^3}\right)$$ [Eq. D 45]

Appendix E – CRT-DPv code

A brief description of *CRT-DPv* as well as the complete list of input and output variables can be found in section 2.2.3.3.1.1. This code uses Stage-DP calculation brick described in section 2.2.3.3.2.2.

Outline of the calculation:

Step 1 – calculate the inlet conditions to the first stage

Step 2 – use Stage-DP to calculate the outlet conditions and blade metal angles

Step 3 – store the absolute outlet conditions of the stage as inlet absolute conditions of the following stage, and calculate the inlet conditions relative to the following stage

Step 4 – repeat steps 2 and 3 for all the turbine stages

Step 5 – calculate the overall turbine isentropic efficiency

Steps 1, 3 and 5 are described below.

Step 1: calculate the inlet conditions to the first stage

First $Mabs_{in\,1}$ is obtained solving Eq. E1 (the subscript 1 denotes the first stage of the CRT)

$$\frac{\dot{m}\sqrt{Tt_{in1}}}{Aeff_{in1}\,Pt_{in1}} = Mabs_{in1}\sqrt{\gamma R}\left(1+\frac{\gamma-1}{2}Mabs_{in1}{}^{2}\right)^{\frac{-(\gamma+1)}{2(\gamma-1)}} \qquad \text{[Eq. E1]}$$

where

$$Aeff_{in1} = A_{disk\,in1}\,cos\left(\frac{\pi}{180}\alpha_{in1}\right) \quad \text{and} \quad A_{disk\,in1} = \pi\left(r_{tip\,in1}{}^{2} - r_{h\,in1}{}^{2}\right) \qquad \text{[Eq. E2]}$$

Then the static conditions are calculated as

$$Ps_{in1} = \frac{Pt_{in1}}{\left(1+\frac{\gamma-1}{2}Mabs_{in1}{}^{2}\right)^{\frac{\gamma}{\gamma-1}}} \qquad \text{[Eq. E3]}$$

$$Ts_{in1} = \frac{Tt_{in1}}{1+\frac{\gamma-1}{2}Mabs_{in1}{}^{2}} \qquad \text{[Eq. E4]}$$

$$\rho_{in1} = \frac{Ps_{in1}}{Ts_{in1}R} \qquad \text{[Eq. E5]}$$

The absolute and relative velocity triangles are calculated as

$$Vabs_{in1} = \frac{\dot{m}}{\rho_{in1} Aeff_{in1}} \qquad \text{[Eq. E6]}$$

$$V_{in1A} = Vabs_{in1} \cos\left(\frac{\pi}{180}\alpha_{in1}\right) \qquad \text{[Eq. E7]}$$

$$Vabs_{in1T} = Vabs_{in1} \sin\left(\frac{\pi}{180}\alpha_{in1}\right) \qquad \text{[Eq. E8]}$$

$$U_{in1} = 2\pi r_{mean\,in1} n_1 \qquad \text{[Eq. E9]}$$

$$Vrel_{in1T} = Vabs_{in1T} - U_{in1} \qquad \text{[Eq. E10]}$$

$$\beta_{in1} = \frac{180}{\pi} \arctan\left(\frac{Vrel_{in1T}}{V_{in1A}}\right) \qquad \text{[Eq. E11]}$$

$$Vrel_{in1} = \frac{V_{in1A}}{\cos\left(\frac{\pi}{180}\beta_{in1}\right)} \qquad \text{[Eq. E12]}$$

$$Mrel_{in1} = \frac{Vrel_{in1}}{\sqrt{\gamma R Ts_{in1}}} \qquad \text{[Eq. E13]}$$

Finally, the relative total temperature and pressure are calculated as

$$Tt\,rel_{in1} = Ts_{in1} + \frac{Vrel_{in1}^{\,2}}{2Cp} \qquad \text{where} \qquad Cp = \frac{\gamma R}{\gamma - 1} \qquad \text{[Eq. E14]}$$

$$Pt\,rel_{in1} = Ps_{in1}\left(\frac{Tt\,rel_{in1}}{Ts_{in1}}\right)^{\frac{\gamma}{\gamma-1}} \qquad \text{[Eq. E15]}$$

Step 3: store the absolute outlet conditions of the stage as inlet absolute conditions of the following stage, and calculate the inlet conditions relative to the following stage

The following outlet variables of to the stage i are stored as inlet for the stage i+1:

$Ps_{in\,i+1} = Ps_{out\,i}$ [Eq. E16]

$Ts_{in\,i+1} = Ts_{out\,i}$ [Eq. E17]

$Tt_{in\,i+1} = Tt_{out\,i}$ [Eq. E18]

$Pt_{in\,i+1} = Pt_{out\,i}$ [Eq. E19]

$\rho_{in\ i+1} = \rho_{out\ i}$ [Eq. E20]

$Vabs_{in\ i+1} = Vabs_{out\ i}$ [Eq. E21]

$V_{in\ i+1\ A} = V_{out\ i\ A}$ [Eq. E22]

$Vabs_{in\ i+1\ T} = Vabs_{out\ i\ T}$ [Eq. E23]

$\alpha_{in\ i+1} = \alpha_{out\ i}$ [Eq. E24]

$Mabs_{in\ i+1} = Mabs_{out\ i}$ [Eq. E25]

$Aeff_{in\ i+1} = Aeff_{out\ i}$ [Eq. E2]6

The relative inlet velocity triangle is calculated as

$U_{in\ i+1} = 2\pi r_{mean\ in\ i+1}\ n_{i+1}$ [Eq. E27]

where n_{i+1} is the rotational speed corresponding to the following stage (n_1 or n_2)

$$Vrel_{in\ i+1T} = Vabs_{in\ i+1T} - U_{in\ i+1}$$ [Eq. E28]

$$\beta_{in\ i+1} = \frac{180}{\pi} arctan\left(\frac{Vrel_{in\ i+1T}}{V_{in\ i+1A}}\right)$$ [Eq. E29]

$$Vrel_{in\ i+1} = \frac{V_{in\ i+1A}}{cos\left(\frac{\pi}{180}\beta_{in\ i+1}\right)}$$ [Eq. E30]

$$Mrel_{in\ i+1} = \frac{Vrel_{in\ i+1}}{\sqrt{\gamma RTs_{in\ i+1}}}$$ [Eq. E31]

The relative inlet total temperature and pressure are calculated as

$$Tt\ rel_{in\ i+1} = Ts_{in\ i+1} + \frac{Vrel_{in\ i+1}^{\ 2}}{2Cp}$$ [Eq. E32]

$$Pt\ rel_{in\ i+1} = Ps_{in\ i+1}\left(\frac{Tt\ rel_{in\ i+1}}{Ts_{in\ i+1}}\right)^{\frac{\gamma}{\gamma-1}}$$ [Eq. E33]

Step 5 – calculate the overall turbine isentropic efficiency and pressure ratio

$\eta_{is\,CRT}$ and PR_{CRT} are calculated as

$$\eta_{is\,CRT} = \frac{1 - \frac{Tt_{out\ NbStages}}{Tt_{in\ 1}}}{1 - \left(\frac{Pt_{out\,NbStages}}{Pt_{in\ 1}} \right)^{\frac{\gamma - 1}{\gamma}}} \qquad \text{[Eq. E34]}$$

$$PR_{CRT} = \frac{Pt_{in\ 1}}{Pt_{out\ NbStages}} \qquad \text{[Eq. E35]}$$

Appendix F – Method to calculate the stage power distribution for a CRT in CRT-DPe

The four preliminary design criteria used in this calculation are described in page 114.

The power extracted in each stage ($Pw_{stage\ i}$) is calculated from:

- inlet absolute tangential velocity: $Vabs_{in\ 1\ T}$
- inlet mass flow rate: $\dot{m}$
- number of stages of the CRT: NbStages
- total temperature at the inlet of the CRT: $Tt_{in\ 1}$
- both drums rotational speeds: n_1 and n_2
- required overall CRT power extraction: Pw_{CRT} (negative magnitude)
- mean radius at the inlet of the CRT: $r_{mean\ in\ 1}$
- baseline values of: $r_{out\ 1}$ and $r_{mean\ 2}$

Outline of the calculation:

Step 1 – calculate the required temperature drop in each of the two drums of the CRT ($\Delta Tt_{req\ drum\ 1}$ and $\Delta Tt_{req\ drum\ 2}$)

Step 2 – calculate the blade tangential velocities for the first two stages

Step 3 – guess ΔTt_2

Step 4 – calculate the power extracted in each stage using the guess value of ΔTt_2 and the established preliminary design criteria

Step 5 – calculate the temperature drop in each of the two drums of the CRT ($\Delta Tt_{drum\ 1}$ and $\Delta Tt_{drum\ 2}$)

Step 6 – repeat steps 3 to 5 until

$$(\Delta Tt_{drum\ 1} - \Delta Tt_{req\ drum\ 1}) / \Delta Tt_{req\ drum\ 1} < \text{tolerance}$$

Step 1: calculate the required temperature drop in each of the two drums of the CRT ($\Delta Tt_{req\ drum\ 1}$ and $\Delta Tt_{req\ drum\ 2}$)

The overall change in Tt across the turbine is calculated as

$$\Delta Tt_{CRT} = \frac{Pw_{CRT}}{\dot{m} Cp} \qquad \text{[Eq. F1]}$$

and the ratio of the power extracted in each drum of the CRT (PwR_{CRT}) is calculated as

$$PwR_{CRT} = \frac{Pw_{drum\,1}}{Pw_{drum\,2}} = \frac{-n_1}{n_2} \qquad \text{[Eq. F2]}$$

Note that only designs with TR_{CRT} = 1 are considered. Then the required change in Tt across each of the two drums are obtained as

$$\Delta Tt_{req\,drum\,1} = \frac{\Delta Tt_{CRT}}{1 + PwR_{CRT}} \qquad \text{[Eq. F3]}$$

$$\Delta Tt_{req\,drum\,2} = \Delta Tt_{CRT} - \Delta Tt_{req\,drum\,1} \qquad \text{[Eq. F4]}$$

Step 2: calculate the blade tangential velocities for the first two stages

The blade tangential velocities at the inlet and outlet of stages 1 and 3 ($U_{in\,1}$, $U_{out\,1}$, U_2 assumed equal for inlet and outlet) are calculated as

$$U_i = r_i 2\pi n_i \qquad \text{[Eq. F5]}$$

where $r_{in\,1}$ is an input, while $r_{out\,1}$ and $r_{mean\,2}$ are assumed (see discussion about the limitations of this assumptions in page 115).

Step 4: calculate the power extracted in each stage using the guess value of ΔTt_2 and the established preliminary design criteria

Δht_1 is calculated so that the C point of the velocity triangle of stage 2 is centred. A momentum balance (analogous to Eq. 66) applied to stage 1 together with the desired geometric condition of stage 2, results in

$$\Delta ht_1 = \left(\frac{U_2}{2} - \frac{\Delta ht_2}{2U_2} \right) U_{out\,1} - Vabs_{in\,1T}\, U_{in\,1} \qquad \text{[Eq. F6]}$$

where

$$\Delta ht_2 = Cp \Delta Tt_2 \quad \text{and} \quad Cp = \frac{\gamma R}{\gamma - 1} \qquad \text{[Eq. F7]}$$

ΔTt_1 is obtained from Δht_1

$$\Delta Tt_1 = \frac{\Delta ht_1}{Cp} \qquad \text{[Eq. F8]}$$

ΔTt for 1< i < 10 is calculated following a constant ΔTt_i for each drum and satisfying the PwR

$$\Delta t_{i=\text{even}\ \le 10} = \Delta Tt_2$$

$$\Delta Tt_{1<i=odd<10} = \Delta Tt_2\, PwR_{CRT} \qquad \text{[Eq. F9]}$$

The ΔTt for 10< i < NbStages is calculated following a constant $\Delta Tt_i/Tin_i$ for each drum and satisfying the PwR

$$\Delta Tt_{10<i=even<NbStages} = \frac{\Delta Tt_{10}}{Tt_{in\ 10}} Tt_{in\ i}$$

$$\Delta Tt_{i=odd>10} = \frac{\Delta Tt_{10}}{Tt_{in\ 10}} Tt_{in\ i}\, PwR_{CRT} \qquad \text{[Eq. F10]}$$

where

$$Tt_{in\,i+1} = Tt_{in\ i} + \Delta Tt_i \qquad \text{[Eq. F11]}$$

Step 5: calculate the temperature drop in each of the two drums of the CRT

The temperature change across the odd stages is first calculated

$$\Delta Tt_{drum\,1} = \sum_{i=odd} \Delta Tt_i \qquad \text{[Eq. F12]}$$

$\Delta Tt_{NbStages}$ is calculated to satisfy $\Delta Tt_{drum\,2} = \Delta Tt_{req\,drum\,2}$

$$\Delta Tt_{NbStages} = \Delta Tt_{req\,drum\,2} - \Delta Tt_{partial\,drum\,2} \qquad \text{[Eq. F13]}$$

with

$$\Delta Tt_{partial\,drum\,2} = \sum_{i=even<NbStages} \Delta Tt_i \qquad \text{[Eq. F14]}$$

Step 6: repeat steps 3 - 5 until ($\Delta Tt_{drum\,1}$ - $\Delta Tt_{req\,drum\,1}$)/$\Delta Tt_{req\,drum\,1}$ < tolerance

The iteration is performed with a Newton-Raphson solver and proved to be numerically stable.

Appendix G – Velocity triangle calculations for 0-D CRT DP efficiency calculation

This appendix presents the deduction of Eq. 144 and Eq. 145 in which β_{in} and β_{out} for a CRT stage are expressed as a function of ψ and Φ. The presented equations are valid for a velocity triangle in which (example Figure G1):

- the point C is centred with respect to A and B
- $V_{A\,in} = V_{A\,out} = V_A$
- $U_{in} = U_{out} = U$

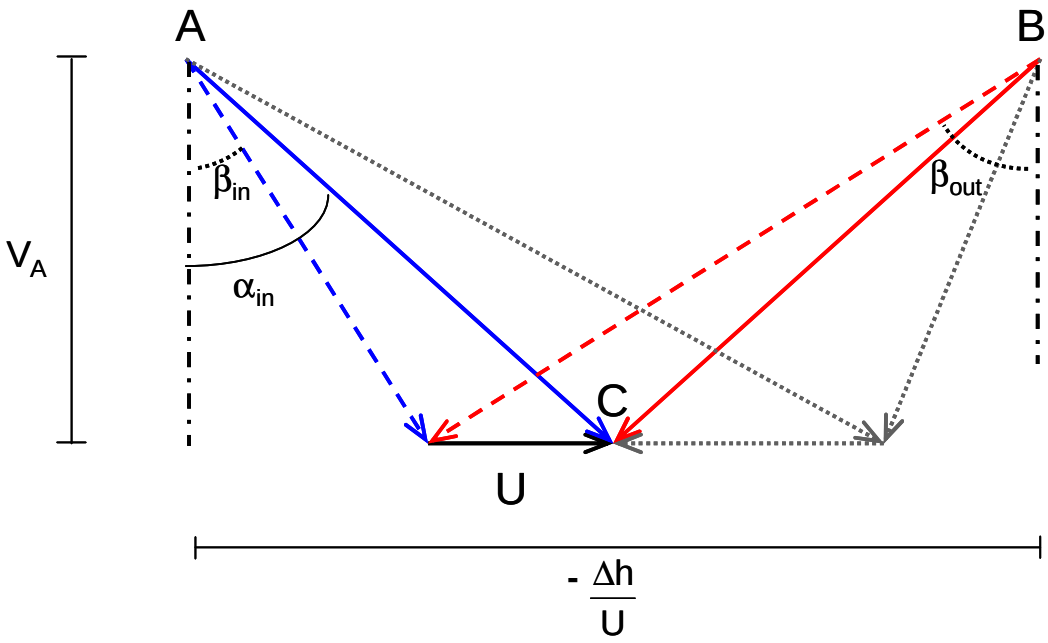

Figure G1: Velocity triangles for a CRT stage (C centred, $V_{A\,in} = V_{A\,in} = V_A$ and $U_{in} = U_{out} = U$)

β_{out} is calculated considering that C is centred with respect to A and B

$$\frac{1}{2}\frac{-\Delta h}{U} = v_A \, tan(\beta_{out}) - U \qquad \text{[Eq. G1]}$$

dividing all the terms by U and using $\psi = \frac{-\Delta h}{U^2}$ and $\Phi = \frac{v_A}{U}$

$$\frac{1}{2}\frac{-\Delta h}{UU} = \frac{v_A}{U} tan(\beta_{out}) - \frac{U}{U} = \frac{1}{2}\psi = \Phi\, tan(\beta_{out}) - 1 \qquad \text{[Eq. G2]}$$

Consequently

$$\psi = 2(\Phi\, tan(\beta_{out}) - 1) \qquad \text{and} \qquad \beta_{out} = \frac{180}{\pi} arctan\left(\frac{\frac{\psi}{2}+1}{\Phi}\right) \qquad \text{[Eq. G3]}$$

In a similar manner, β_{in} is calculated considering that C is centred with respect to A and B.

$$\frac{1}{2}\frac{-\Delta h}{U} = v_A\, tan(\beta_{in}) + U \qquad \text{[Eq. G4]}$$

dividing all the terms by U and using $\psi = \frac{-\Delta h}{U^2}$ and $\Phi = \frac{v_A}{U}$

$$\frac{1}{2}\frac{-\Delta h}{UU} = \frac{v_A}{U} tan(\beta_{in}) + \frac{U}{U} = \frac{1}{2}\psi = \Phi\, tan(\beta_{in}) + 1 \qquad \text{[Eq. G5]}$$

Consequently

$$\psi = 2(\Phi\, tan(\beta_{in}) + 1) \qquad \text{and} \qquad \beta_{in} = \frac{180}{\pi} arctan\left(\frac{\frac{\psi}{2}-1}{\Phi}\right) \qquad \text{[Eq. G6]}$$

Appendix H – Matching procedure for CROR engines using fuel flow or TET and the rotational speeds of the propellers as handles

The figure below shows the matching procedure for a CROR engine with fuel flow or TET and the rotational speeds of the propellers as handles. This matching procedure can be used to solve the engine with a direct iterative procedure. The majority of the performance codes use solvers (Newton-Raphson, Minipack, etc) instead of direct iterations. In this case, the same guesses are used and they are solved simultaneously. The differences between the two variables in each rhombic box are used as errors to be minimised by the solver.

Note that the guess of the induced velocity of the rear propeller on the forward propeller was not mentioned. This is because this iteration is only required inside the CRP model and does not affect the operation of the engine core.

If TET is used as a handle, the injected fuel is used as a guess inside the burner component in order to match the required TET. It was not included in the engine matching scheme because it is a component internal iteration.

In the case of the GOR, the mass flow rate of the DPGB cooling system is required as a guess. It was not included in the engine matching scheme because it does not affect the operation of the engine core.

The following specific nomenclature is used in the figure below:

- PWT: power turbine which can be a LPT or a CRT
- eff: isentropic efficiency
- NDMF: corrected mass flow rate
- HPTW, HPCW, IPTW and IPCW: power of the HPT, HPC, IPT and IPC respectively
- Ma_0: flight Mach number

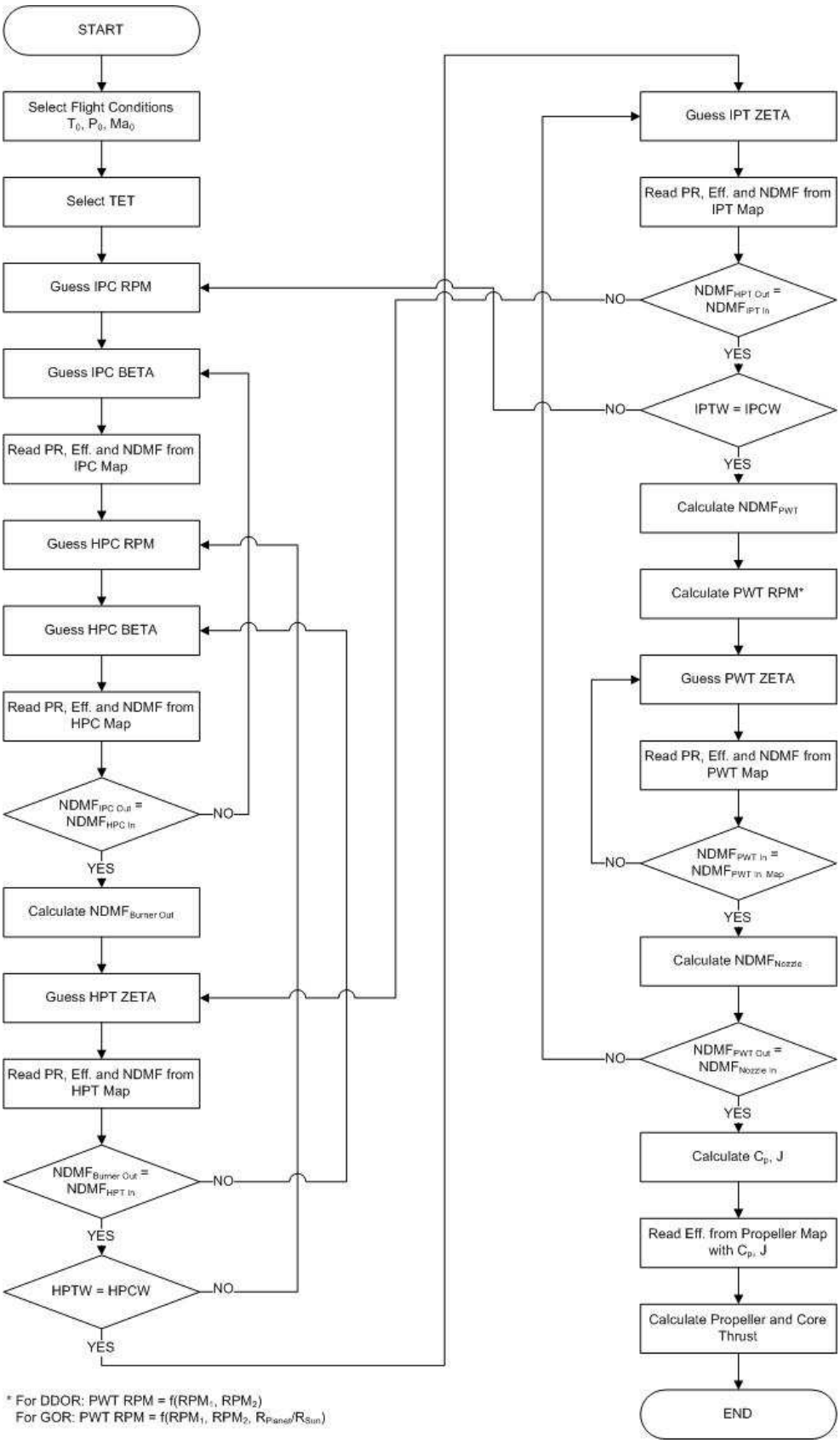
START
Select Flight Conditions
T_0, P_0, Ma_0
Select TET
Guess IPC RPM
Guess IPC BETA
Read PR, Eff. and NDMF from IPC Map
Guess HPC RPM
Guess HPC BETA
Read PR, Eff. and NDMF from HPC Map
$NDMF_{IPC\ Out}$ = $NDMF_{HPC\ In}$
NO
YES
Calculate $NDMF_{Burner\ Out}$
Guess HPT ZETA
Read PR, Eff. and NDMF from HPT Map
$NDMF_{Burner\ Out}$ = $NDMF_{HPT\ In}$
NO
YES
HPTW = HPCW
NO
YES
Guess IPT ZETA
Read PR, Eff. and NDMF from IPT Map
$NDMF_{HPT\ Out}$ = $NDMF_{IPT\ In}$
NO
YES
IPTW = IPCW
NO
YES
Calculate $NDMF_{PWT}$
Calculate PWT RPM*
Guess PWT ZETA
Read PR, Eff. and NDMF from PWT Map
$NDMF_{PWT\ In}$ = $NDMF_{PWT\ In\ Map}$
NO
YES
Calculate $NDMF_{Nozzle}$
$NDMF_{PWT\ Out}$ = $NDMF_{Nozzle\ In}$
NO
YES
Calculate C_p, J
Read Eff. from Propeller Map with C_p, J
Calculate Propeller and Core Thrust
END
* For DDOR: PWT RPM = f(RPM_1, RPM_2)
For GOR: PWT RPM = f(RPM_1, RPM_2, R_{Planet}/R_{Sun})

Appendix I – Methods to improve the numerical stability of steady state engine performance calculations in PROOSIS

The targeted readers for this appendix are PROOSIS users and developers. Consequently the PROOSIS nomenclature and vocabulary is used.

PROOSIS is a gas turbine performance simulation code. It is capable of calculating the steady state and transient operation of a gas turbine engine or a group of engine components. PROOSIS documentation provides a complete description of the software including its modelling language, mathematical algorithms and capabilities as well as the models of the engine components available in the TURBO V1.0 library [Ref. 112, Ref. 113, Ref. 130, Ref. 131 and Ref. 228 Ref. 229].

The DP and OD calculations methodologies proposed by the wizards of the software and included in the sample engine library (ENGINE V1.0 library) proved to be numerically unstable for the two CROR engines defined in sections 2.2.4 and 2.2.5. A very particular initialisation of the unknown variables was required which could only be calculated once the final solution was known (see details in sections 2.2.6 and 2.2.4). The same difficulty was observed for all the engines in the ENGINE library V1.0, and was also reported by other PROOSIS users. In order to simulate different engine designs at various OD conditions (take-off, climb, cruise, descent idle, and certification points), an initialisation function was required. The creation of this function requires a large effort which involves solving the DP and OD performance, for all the required conditions, for all the engines to be assessed. First the DP of the baseline engine has to be solved using an engine model which comprises components with no maps. Then the engine design variables have to be varied in small steps to solve the DP of other engine designs. Finally all the OD conditions of all the engine designs have to be solved varying the operating conditions (Alt, M_0, dISA, $\dot{m}_{fuel}$, n_1 and n_2) in small steps. This process can not be done automatically, and manual changes to the initial values have to be done because sometimes the calculations do not converge if some of the initial values (especially design rotational speeds and design powers) are too close to the solution.

During the course of this PhD research project, an alternative methodology and good practices (GPs) were developed to produce numerically stable steady state:

- engine performance mathematical models
- OD calculations
- single point and multi point DP calculations to size engine components from performance requirements

They enabled the calculation of DP and OD performance of a wide range of CROR designs for a wide range of operating conditions (take-off, climb, cruise, descent idle, and certification points) without the need of a customised initialisation. The following paragraphs describe the developed methodology and GPs. A brief

description of the process required to perform an engine simulation in PROOSIS is first provided.

Three main steps are required to simulate an engine (or part of an engine) in PROOSIS.

1. *Creation of an engine schematic.* The schematic of an engine is created using the existing components and connecting them in the appropriate order. Then, the properties of every component (E.g.: pressure loss of the ducts and burner, maps of the various components, exit area of the nozzle, diameters of the propellers, torque ratio of the gearbox, DP enthalpy drop of the turbines and rotational speeds of the shafts, etc.) have to be defined. The properties of the components are called "data". If a component is not available in the libraries, it can be created by defining the ports[94] and data of the component and the equations which model the performance of the component.

2. *Creation of a mathematical model (called partition)*. A partition of an engine is a system of equations that contains all the equations and variables of the engine components (n equations and m variables). Normally m > n and it is required to define m-n variables which are called "boundaries". The boundaries represent external conditions which are required to be known in order to solve the system of equations[95]. The system of equations may have non linear equations, or tables (typically component characteristics and fluid properties), and consequently it is not possible to establish an explicit solution sequence. In these cases, the system has to be solved iteratively and the user has to define the guesses (called "algebraics") and PROOSIS defines the checks in the form of errors to be minimised (called "residues"). It is important to note that unlike other gas turbine performance codes (E.g.: Gasturb and Turbomatch); there is no specific mathematical model for the DP calculation. During DP calculations, the unknown data of the different components is calculated with a numerical solver at the same time as the mathematical model is solved (details are presented in sections I.2 and I.3 of this appendix).

3. *Creation of an experiment*. An experiment is a sequence of calculations to be performed using the previously defined mathematical model. DP and OD calculations can be done on the same experiment, but only one mathematical model can be used in an experiment. For example, an experiment which calculate the OD performance of a known engine in different operating points

[94] Ports are the interfaces of the components which contain the variables to be transmitted to other components.

[95] E.g.: for the CROR engines defined in section 2.2.4 and 2.2.5 the selected boundaries were: the heat rejected by the engine components, the fuel inlet conditions (Tt and Pt) the fuel flow and the rotational speed of the propellers.

Note that flight conditions are not boundaries, but data of the atmospheric component.

would contain several blocks in which the operating conditions are defined and subsequently the mathematical model of the engine is solved.

I.1 GPs to obtain stable mathematical models

I.1.1 Definition of the boundaries

It is recommended to use the fuel flow rate ($\dot{m}_{fuel}$) as a boundary as opposed to TET. This increases the model stability especially at low idle settings.

The mass flow rate of the core ($\dot{m}_{core}$) decreases as $\dot{m}_{fuel}$ decreases. At relatively high power settings, the reduction in $\dot{m}_{fuel}$ is relatively larger than the reduction in $\dot{m}_{core}$, and TET decreases as $\dot{m}_{fuel}$ decreases. At low power settings, the reduction in $\dot{m}_{core}$ may be relatively larger than the reduction in $\dot{m}_{fuel}$. In these cases TET increases as $\dot{m}_{fuel}$ is reduced. Consequently, two operating points may have the same TET and different values of $\dot{m}_{fuel}$. If TET is used as a boundary, it may not define the operation of the engine at very low power settings. For low power settings where the operating point can still be defined with TET, the choice of TET as a boundary makes the model unstable at low power settings.

I.1.2 Definition of the algebraics

It is recommended to device a physically and numerically sound matching procedure for the engine or part of an engine (such as the one presented in Appendix H) before creating a mathematical model in PROOSIS. The mathematical model in PROOSIS should have the same algebraics as guesses in the devised matching procedure. If PROOSIS can not set up a valid mathematical model with the exact algebraics required in the matching procedure, it means that it can not manipulate correctly the equations. In this case, the equations should be manipulated by the user until achieving a valid mathematical model which uses the desired algebraics. If this is not done, and the amount of algebraics is higher than the theoretically required, the mathematical model is likely to be unstable.

It is recommended not to use mass flow rate ($\dot{m}$) as an algebraic if the simulated engine (or part of an engine) has components with maps which define the mass flow rate (e.g.: compressors and turbines). In these cases, the map reading variables (such as rotational speeds, BETA and ZETA parameters) should be used as algebraics. This is the main reason why all the engine OD simulations proposed in the ENGINE V1.0 library are highly unstable. There are two common cases in which $\dot{m}$ is required as an algebraic:

Case 1: Engines (or part of engines) with components with no maps (e.g.: the air cooling system of the GOR, described in sections 2.2.3.4.3 and 2.2.3.4.6).

Case 2: Engines in which the pressure losses of the intake are a function of $\dot{m}$ or M (this is not the case in the engines of the ENGINE V1.0 library).

In both cases, it is recommended to use $\dot{m}_{COR}$ as algebraic instead of $\dot{m}$ because the variations of $\dot{m}_{COR}$ are relatively smaller than the variations of $\dot{m}$. For the engines models corresponding to Case 2, it is recommended to modify the equations of the compressor and the format of the compressor map so that the only required algebraic from the compressors are their pressure ratio (since their $\dot{m}_{COR}$ can be caluclated using the equations of the previous components and the inlet $\dot{m}_{COR}$ which is used as algebraic).

In order to avoid the mass flow rate as an algebraic in the GOR and DDOR engines models produced for this PhD research project ,the inlet and IPC components had to be merged. In the case of the GOR, the equations of the DPGB had to be manipulated because PROOSIS did not manage to obtain the rotational speed of the Sun from the rotational speeds of the Ring and Carrier shafts (which were used as boundaries). Eq. 162 (obtained from Eq. 157, Eq. 153, Eq. 154 and 158) had to be used instead of Eq. 157. The equations of the duct and secondary air system components were also manipulated to avoid unnecessary algebraics in the GOR and DDOR engine models.

I.1.3 Extrapolation in the characteristics of the components

For some simulations, the solver may require to do large variations in the algebraics before finding the final solution[96]. In these cases, some component maps are read outside the domain for which they were defined, and

- if the extrapolation of the characteristic is set to “forbidden”, the simulation is aborted.
- if the extrapolation of the characteristic is set to “constant”, the solver may probably not find a solution since changes in the algebraics do not modify the residues of the model.

In order to avoid these two situations, it is recommended to select a linear extrapolation in all the characteristics of the engine components. In this case, the model residues can always be defined and they always vary when the algebraics are varied.

Additional variables can be included in the model of the components to inform the user if the simulated points are inside the defined map or they correspond to extrapolated points.

The same recommendation applies to the fluid properties.

[96] It was observed that large steps were required for some simulations despite the fact that the initialisation of the algebraics was close to the final solution.

I.2 GPs to define stable OD calculations

It is often required to calculate the performance of an engine at a particular regime defined by operating parameters such as thrust, power, TET, rotational speed of a shaft or surge margin. In these cases, $\dot{m}_{fuel}$ and some other boundaries or data (such as bleed valve flows) are not known and have to be solved together with the algebraics. In order to obtain the unknown boundaries or component data, PROOSIS builds a function that solves the mathematical model of the engine for a given set of the unknown boundaries and data, and calculates the error with respect to the desired criteria. This function is used in a solver to find the boundaries, data and algebraics that produce the desired OD operation. This procedure is slow and can be unstable because the mathematical model may not have a solution for a given set of boundaries and data imposed by the solver.

Instead of using the method proposed by PROOSIS it is recommended to solve all the unknown variables (boundaries, data and algebraics) at the same time with an nlSolver. This requires the definition of a function that:

- has the unknown variables as input
- calculates the residues of the mathematical model using the FRES() command. This command calculates all the variables of the mathematical model (including the residues) using the latest defined boundaries, algebraics and data (it does not solve the mathematical model). FRES() does not produce execution errors and calculates all the variables of the model, provided that the map extrapolation is allowed and the functions called by the model (such as fluid functions) converge[97].
- has the residues of the mathematical model and the errors of the additional required conditions as output.

This methodology proved to be numerically stable for all the simulated engines and OD conditions. No specific initialisation is required. Very low idle OD conditions converge with the initialisation of high power settings and vice versa. Convergence can also be achieved with initialisations outside the maps of the components.

Two examples of such a function and their corresponding solvers are provided below.

Example 1

For the gaseous emissions calculations at idle setting (Alt = 0 m, dISA=0 and M_0 = 0.1), it is required to impose a level of thrust (6% of take-off thrust) and a surge margin in the IPC (10%). The following function and solver are used to solve this OD calculation for the GOR defined in section 2.2.4.

[97] The stability and ranges of the used fluid models affect the stability of the engine models. If the used fluid functions do not converge for some cases, they should be revised. An apropriate extrapolation of these functions may be required, especially those using Mach numbers.

Solver:

```
TOLERANCE=1.e-8
nlsolver(fcnID, 11, idAlg, fresID, info)
```

Function:

```
FUNCTION NO_TYPE fcnID
(OUT INTEGER n, OUT REAL idAlg[], OUT REAL fresID[], OUT INTEGER iflag)
DECLS
BODY

-- Store the variables to be solved
-- FIRST, store algebraics of the model
HPC.BETA = idAlg[1]
HPC.NcRdesMap = idAlg[2]
HPT.ZETA = idAlg[3]
IPC.BETA = idAlg[4]
IPC.NcRdesMap = idAlg[5]
IPT.ZETA = idAlg[6]
LPT.ZETA = idAlg[7]
RearProp.Prop_in.Vind = idAlg[8]
ScoopInlet.WcStd = idAlg[9]
-- THEN, store data: in this case the IPC bleed
IPC.W_bld[2] = idAlg[10]
-- THEN, store boundaries: in this case the fuel flow
Burner.Fu_in.W = idAlg[11]

FRES()  --Calculate the model variables including residues

-- Store the residues of the model
fresID[1] = getResidueValue(1)
fresID[2] = getResidueValue(2)
fresID[3] = getResidueValue(3)
fresID[4] = getResidueValue(4)
fresID[5] = getResidueValue(5)
fresID[6] = getResidueValue(6)
fresID[7] = getResidueValue(7)
fresID[8] = getResidueValue(8)
fresID[9] = getResidueValue(9)
-- Store the errors with respect to the additional criteria
fresID[10] = (10 - IPC.SMpct ) / 10
fresID[11] = (FnTarget - Perf.Fn) / FnTarget

END FUNCTION
```

The order of the definition of the variables to be solved (idAlg in this example) and the calculated errors (fresID in this example) proved to have an influence on the

numerical stability of the solver. It is recommended to use as input variable in the "position i" (idAlg[i]) the variable that has a stronger influence on the error in the "position i" (fresID[i]). For example, idAlg[1] is the HPC BETA and fresID[1] is the error in the mass flow balance on the inlet of the HPT[98]. Following the same criterion, idAlg[10] is the IPC bleed mass flow rate, and fresID[10] is the error with respect to the surge margin target. This would result in a "more diagonal" Jacobian matrix which improves the stability of the numerical solver.

Note that it may be required to execute all the initialisation bricks (Exec_Init() command) of the components and/or to reset all the events of the model (Reset_Events() command) before calling the solver or inside the function (before calling FRES()). The need for the use of these commands is related to the nature of the models. Details of the use of these commands are presented in Ref. 228 (chapter 10, Initialisation Issues).

Also note that this model has WAR set to zero in the atmosphere component and does not require WAR as an algebraic.

Example 2

For the descent points of the mission, it is required to impose a corrected rotational speed of the HP shaft and a surge margin in the IPC (10%). In this case, one of the algebraics of the mathematical model is used as a criterion to define the desired operating point. Consequently, it is a known variable and it is not required to be solved. The following function and solver are used to solve this OD calculation for the GOR defined in section 2.2.4.

Solver:

```
TOLERANCE=1.e-8
nlsolver(fcnID2, 10, idAlg2, fresID2, info)
```

Function:

```
FUNCTION NO_TYPE fcnID2
(OUT INTEGER n, OUT REAL idAlg[], OUT REAL fresID[], OUT INTEGER iflag)
DECLS
BODY

-- Store the variables to be solved
-- FIRST, store algebraics of the model
HPC.BETA = idAlg2[1]
-- THEN, store boundaries: in this case the fuel flow
Burner.Fu_in.W = idAlg2[2]
-- THEN, store algebraics of the model
```

[98] Note that at low power settings the corrected rotational speeds tend to be flat and a change in BETA results in a relatively small change in PR and a relatively large change in mass flow rate.

```
HPT.ZETA = idAlg2[3]
IPC.BETA = idAlg2[4]
IPC.NcRdesMap = idAlg2[5]
IPT.ZETA = idAlg2[6]
LPT.ZETA = idAlg2[7]
RearProp.Prop_in.Vind = idAlg2[8]
ScoopInlet.WcStd = idAlg2[9]
-- FINALLY, store data: in this case the IPC bleed
IPC.W_bld[2] = idAlg2[10]

FRES()  --Calculate the model variables including residues

-- Store the residues of the model
fresID2[1] = getResidueValue(1)
fresID2[2] = getResidueValue(2)
fresID2[3] = getResidueValue(3)
fresID2[4] = getResidueValue(4)
fresID2[5] = getResidueValue(5)
fresID2[6] = getResidueValue(6)
fresID2[7] = getResidueValue(7)
fresID2[8] = getResidueValue(8)
fresID2[9] = getResidueValue(9)
-- Store the errors with respect to the additional criteria
fresID2[10] = (10 - IPC.SMpct ) / 10

END FUNCTION
```

Note that idAlg2[2] is the fuel flow and fresID2[2] is the power balance of the HP shaft.

I.3 GPs to define stable DP calculations

The aim of a DP calculation is to obtain some unknown data of the engine components (scaling factors of the maps, areas, efficiencies and design rotational speeds) imposing some design criteria (E.g.: position of the DP on the maps of the components, TET) and performance requirements (E.g.: thrust). Technology curves may be used to estimate the efficiency of certain components during the DP calculation. The engine operates at steady state at the DP and consequently the mathematical model of the engine has to be solved. Some of the boundaries and algebraics may also be unknown[99].

[99] In the case of the GOR engine defined in section 2.2.4, the unknown algebraics at a DP calculation are: propeller induced velocity and mass flow rate through the gearbox cooling system.

For this type of calculations, PROOSIS generates a function that solves the mathematical model of the engine for a given set of the unknown data and boundaries, and calculates the error with respect to the design criteria. This function is used in a solver to find the data, boundaries and algebraics that produce the desired DP operation. This procedure is slow and can be unstable because the mathematical model may not have a solution for a given set of data and boundaries imposed by the solver.

It is recommended to calculate the DP using the same GPs as for the OD calculations. Note that as in the example 2 of the OD calculations, some of the algebraics are known at DP ($N_{COR\ Rdes}$ and BETA of compressors and ZETA for turbines), and therefore it is not required to calculate them.

Multi point design calculations were also tested using the presented methodology (setting the efficiency of the gearbox at take-off). The function that implements a multi point design performs the following tasks:

1. store the data of the components (defined in the input vector)
2. store the flight conditions, boundaries and algebraics of the first point (defined in the input vector)
3. use the command FRES() (with the appropriate initialisation) to calculate all the variables of the model at the first point.
4. calculate the errors with respect to the design criteria of the first point, and get the residues of the mathematical model at the first point.
5. store the flight conditions, boundaries and algebraics of the second point (defined in the input vector)
6. use the command FRES() (with the appropriate initialisation) to calculate all the variables of the model at the second point.
7. calculate the errors with respect to the design criteria of the second point, and get the residues of the mathematical model at the second point.
8. steps 5 – 7 can be repeated for further operating points.

This function is used together with a solver as presented in the previous examples to find the unknown data of the components and define the design of the engine. These calculations also proved to be numerically stable.

Example

The DP calculation of the GOR engine defined in section 2.2.4 is presented below. It is a single design point calculation at TOC in which the TET and thrust are imposed as well as the position of the DP on the component maps. The efficiency of the LPT and propellers are calculated using the technology curves described in sections 2.2.3.1.1 and 2.2.3.2.5 respectively. Some of the input variables and errors are omitted and replaced by "…" to avoid repetition.

The effect of the order of the unknowns and errors on the numerical stability of this type of calculation is stronger than in the previously presented OD calculations. For example, if the following changes in the definition of errors are done in the function presented below, the solver is unable to find a valid solution to the DP calculation.

fresDP[1] = (Thrust_DP - Perf.Fn)/Perf.Fn ⟶ fresDP[35] = (Thrust_DP - Perf.Fn) / Perf.Fn

fresDP[35] = 1- LPT.NcRdes ⟶ fresDP[1] = 1- LPT.NcRdes

Note that in the function of the example:

- the residues of the model which correspond to mass flow balances are defined in the same “position” as the mass flow scaling factors.
- the residues of the model which correspond to power balances in the shafts are defined in the same “position” as the design pressure ratio of the turbines.
- the area of the nozzle is defined in the same “position” as the thrust of the engine since it imposes the size of the core.
- the fuel flow is defined in the same “position” as TET.

Solver:

TOLERANCE=1.e-8
nlsolver(fcnDP, 46, z, fresDP, info)

Function:

```
FUNCTION NO_TYPE fcnDP
(OUT INTEGER n, OUT REAL z[], OUT REAL fresDP[], OUT INTEGER iflag )
DECLS
BODY

Nozzle.Aexit          = z[1]
IPC.s_mapWc_in        = z[2]
IPC.s_mapEff_in       = z[3]
IPC.s_NcRdes_in       = z[4]
IPC.s_mapPR_in        = z[5]
HPC.s_mapWc_in        = z[6]
HPC.s_mapEff_in       = z[7]
HPC.s_NcRdes_in       = z[8]
HPC.s_mapPR_in        = z[9]
HPT.s_mapWc_in        = z[10]
HPT.s_mapEff_in       = z[11]
HPT.s_mapNc_in        = z[12]
HPT.s_mapDhqT_in      = z[13]
IPT.s_mapWc_in        = z[14]
IPT.s_mapEff_in       = z[15]
IPT.s_mapNc_in        = z[16]
IPT.s_mapDhqT_in      = z[17]
LPT.s_mapWc_in        = z[18]
LPT.s_mapEff_in       = z[19]
…
FrontProp.s_Eff               = z[27]
…
LPT.NmechDes                  = z[35]
...
```

RearProp.Prop_in.Vind =z[44]
ScoopInlet.WcStd =z[45]
Burner.Fu_in.W =z[46]

FRES()

fresDP[1] = (Thrust_DP - Perf.Fn) / Perf.Fn
fresDP[2] = getResidueValue(5) --Mass flow rate balance in the nozzle
fresDP[3] = (IPC_Eff_DP - IPC.effPoly) / IPC.effPoly
fresDP[4] = 1- IPC.NcRdes
fresDP[5] = (IPC_PR_DP - IPC.PR) / IPC.PR
fresDP[6] = getResidueValue(3) --Mass flow rate balance in the HPC
fresDP[7] = (HPC_eff_DP - HPC.effPoly) / HPC.effPoly
fresDP[8] = 1- HPC.NcRdes
fresDP[9] = (HPC_PR_DP - HPC.PR) / HPC.PR
fresDP[10] = getResidueValue(1) -- Mass flow rate balance in the HPT
fresDP[11] = (HPT_eff_DP - HPT.eff) / HPT.eff
fresDP[12] = (HPT_NcRdesMap_DP - HPT.NcRdesMap) / HPT.NcRdesMap
fresDP[13] = getResidueValue(2) -- HP shaft power balance
fresDP[14] = getResidueValue(4) -- Mass flow rate balance in the IPT
fresDP[15] = (IPT_eff_DP - IPT.eff) / IPT.eff
fresDP[16] = (IPT_NcRdesMap_DP - IPT.NcRdesMap) / IPT.NcRdesMap
fresDP[17] = getResidueValue(7) -- IP shaft power balance
fresDP[18] = getResidueValue(6) -- Mass flow balance in the LPT
-- The LPT efficiency is calculated using the function described in section 2.2.3.1.1
fresDP[19] = (LPTEff(LPT.pwr/LPT.F_in.W, LPT.Me_in.Nmech, NbStages, V_A, r_{mean}) - LPT.eff) / LPT.eff
…
-- The low speed $\eta_{NET\ 1}$ is calculated using the function described in section 2.2.3.2.5
fresDP[27] = Prop_Tech_eff (BNbF, FrontProp.PowerLoading, K_{LP}) - FrontProp.ETAlowMn
…
fresDP[35] = 1- LPT.NcRdes
…
fresDP[44] = getResidueValue(8)
fresDP[45] = getResidueValue(9)
fresDP[45] = (Burner.F_out.Tt – TOC_TET) / TOC_TET

END FUNCTION

Appendix J – Profiles of the missions defining the payload-range diagram of the reference OR aircraft

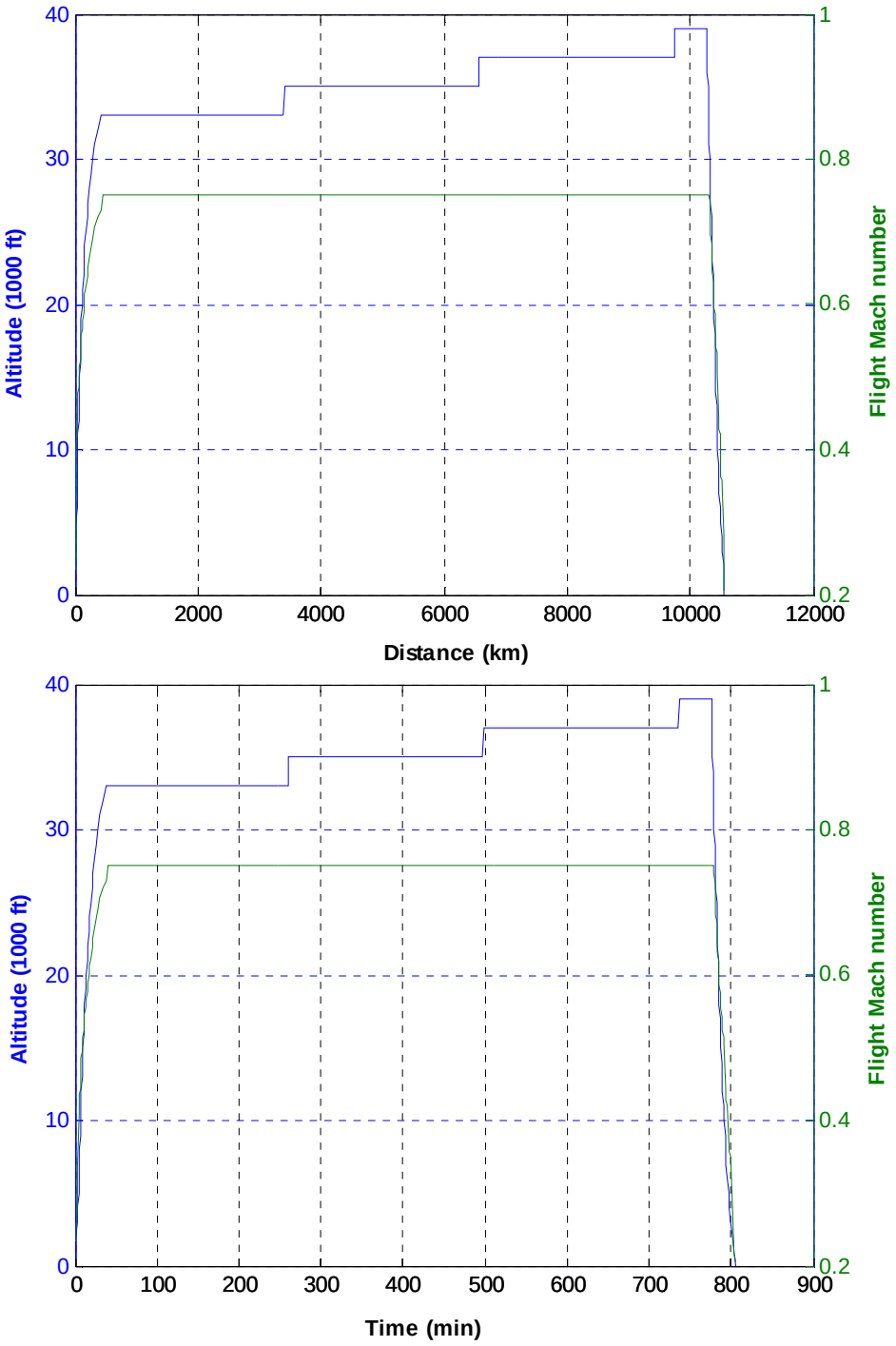

Figure J 1: Max payload and max fuel load mission profile

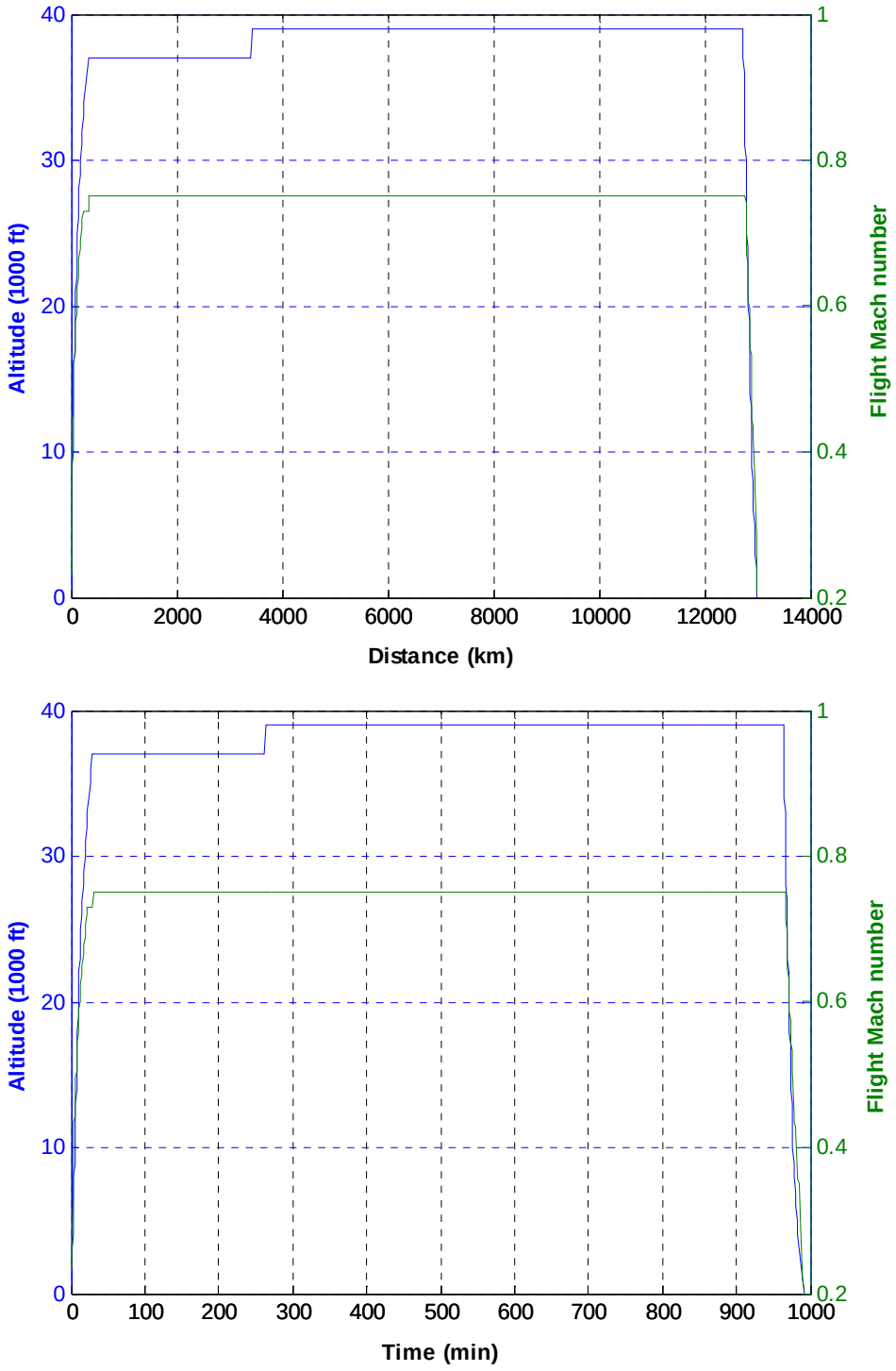

Figure J 2: No payload and max fuel load mission profile

Appendix K – Maps of the baseline GOR components

The maps of the baseline GOR engine are presented below. The black dots on the maps indicate the position of the DP.

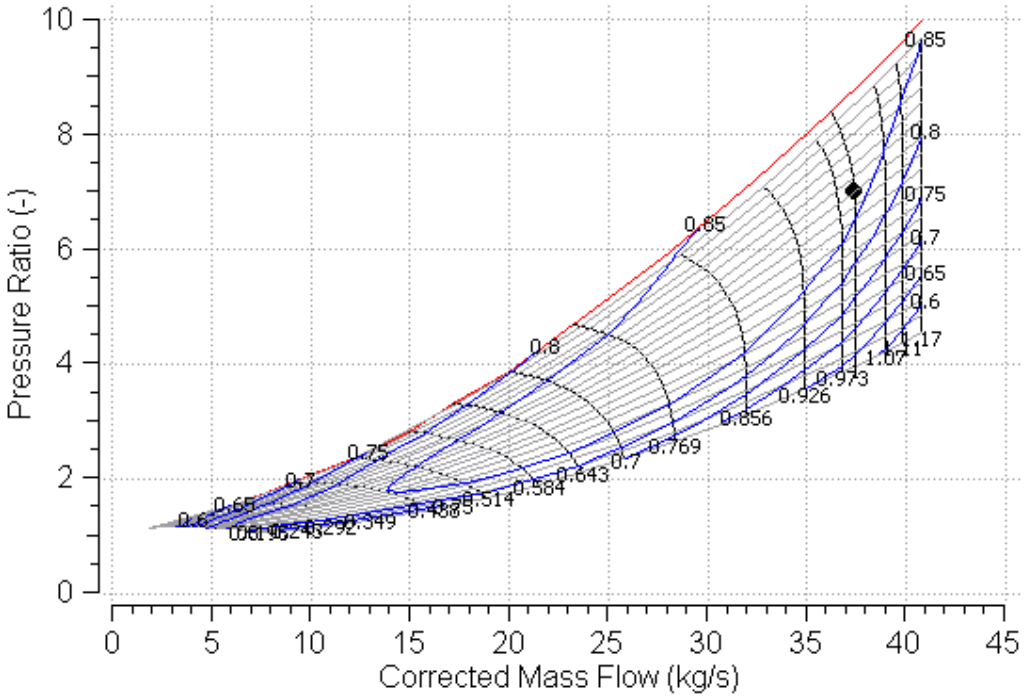

Figure K 1: IPC map

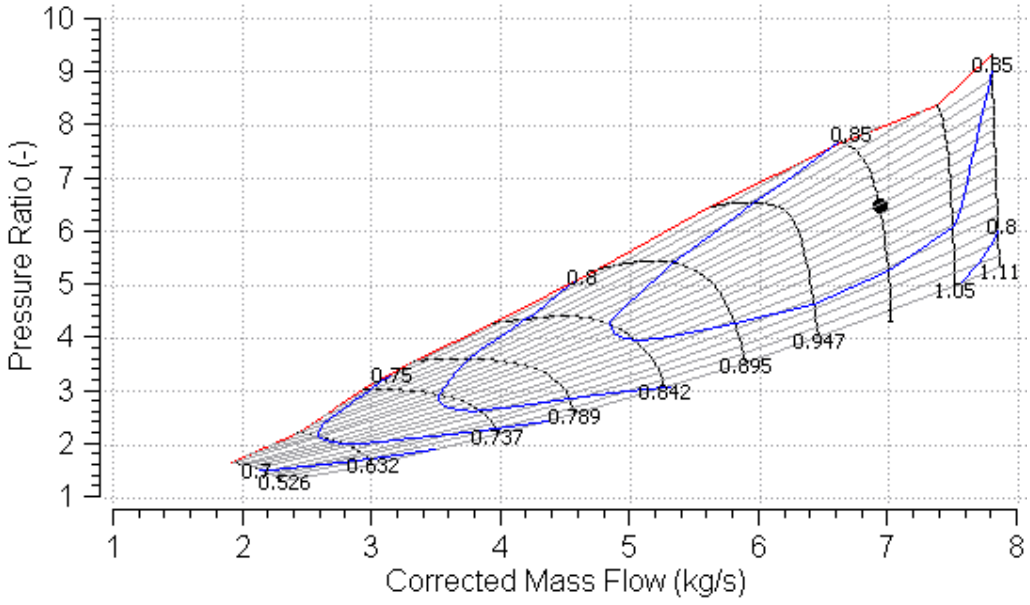

Figure K 2: HPC map

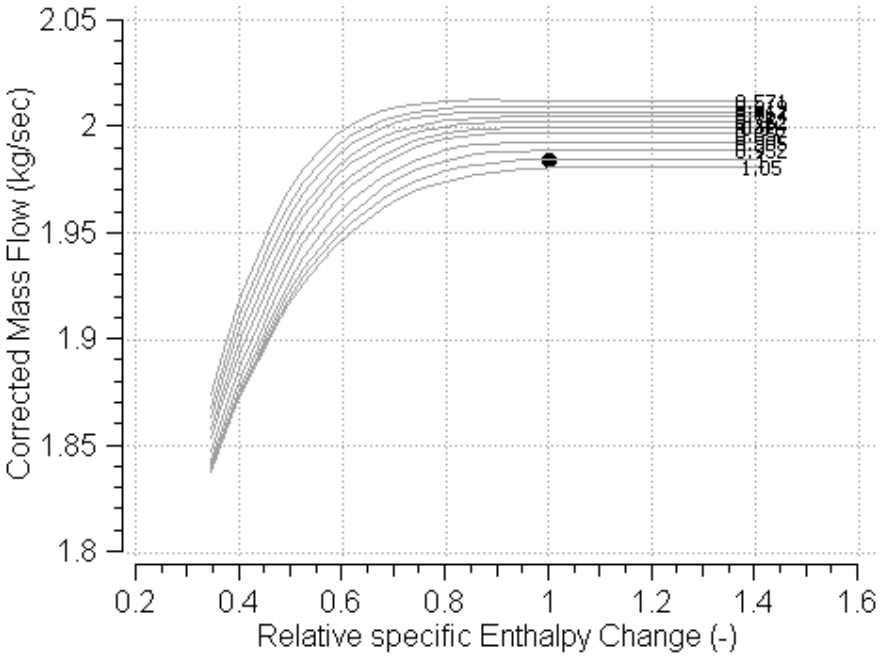

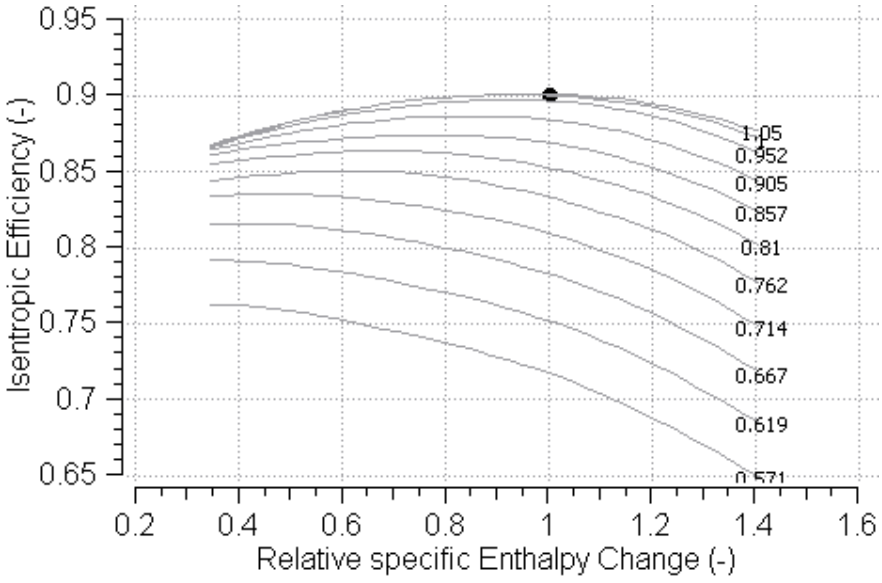

Figure K 3: HPT map

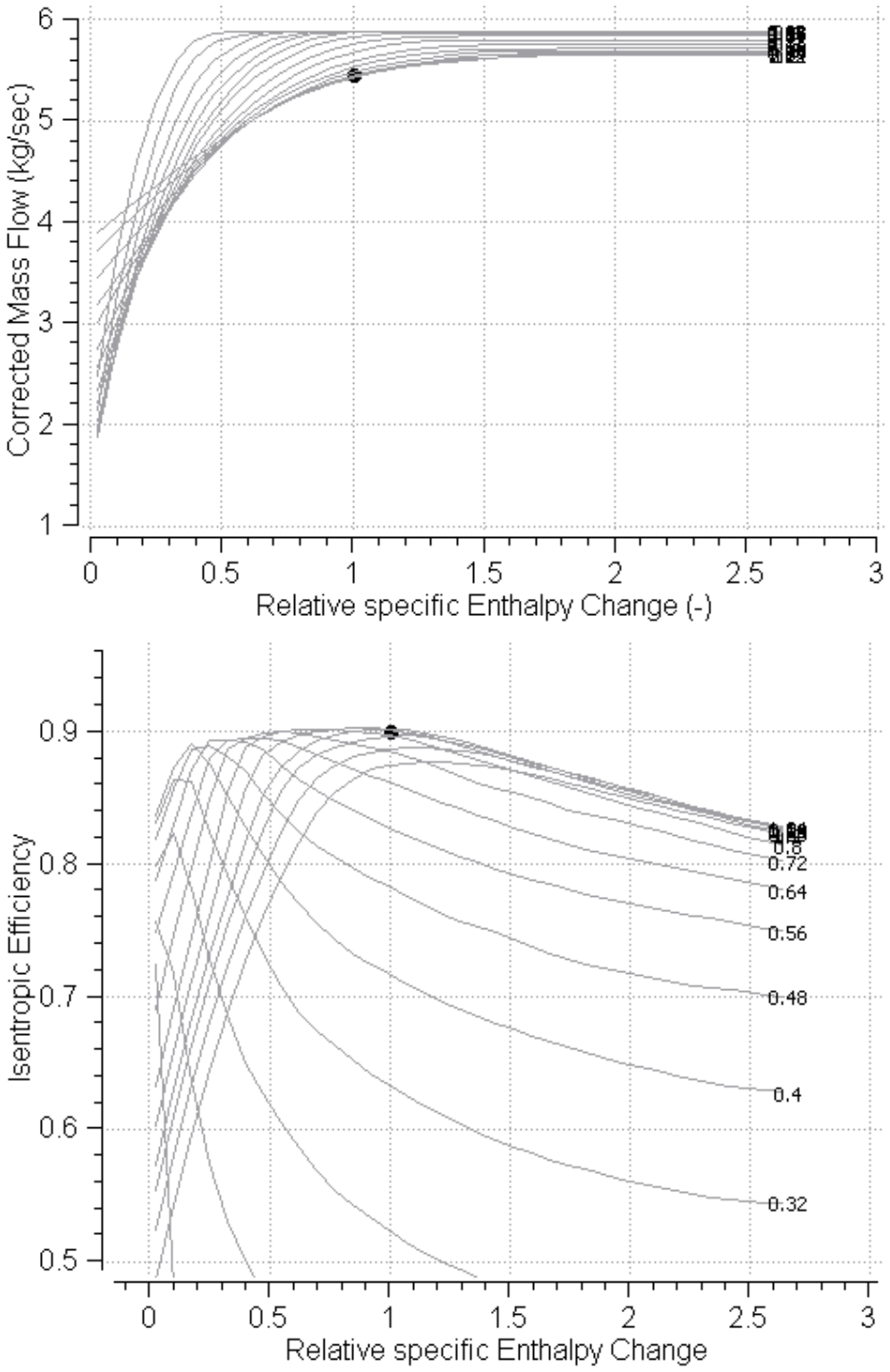

Figure K 4: IPT map

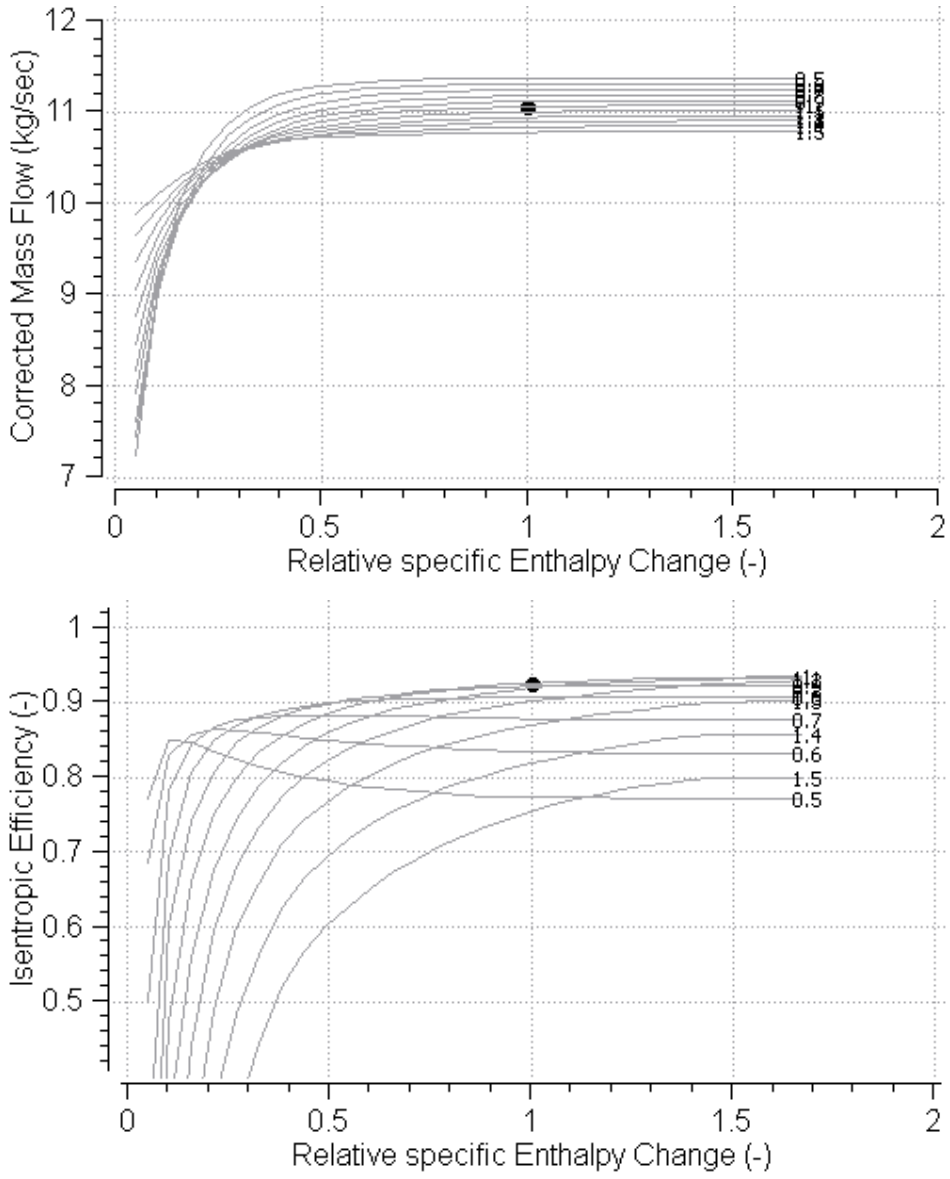

Figure K 5: LPT map

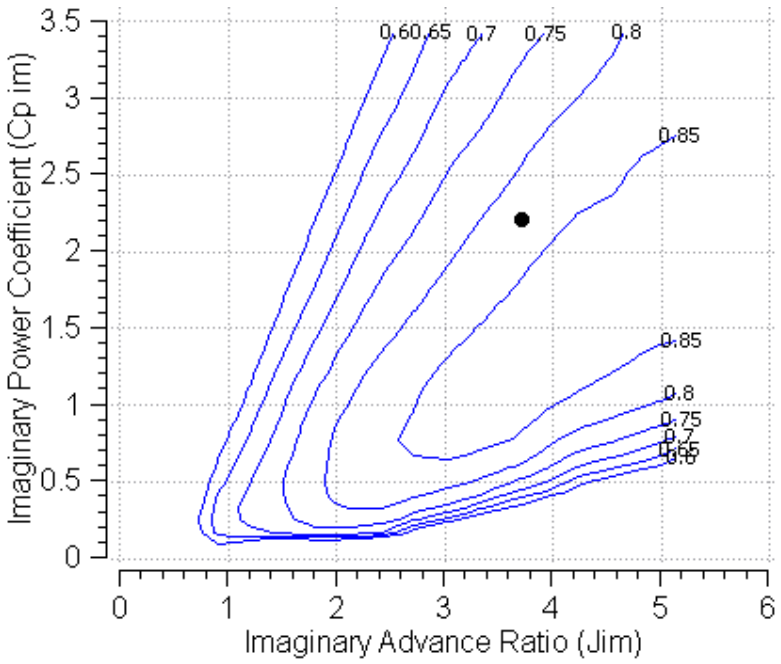

Figure K 6: Forward propeller map

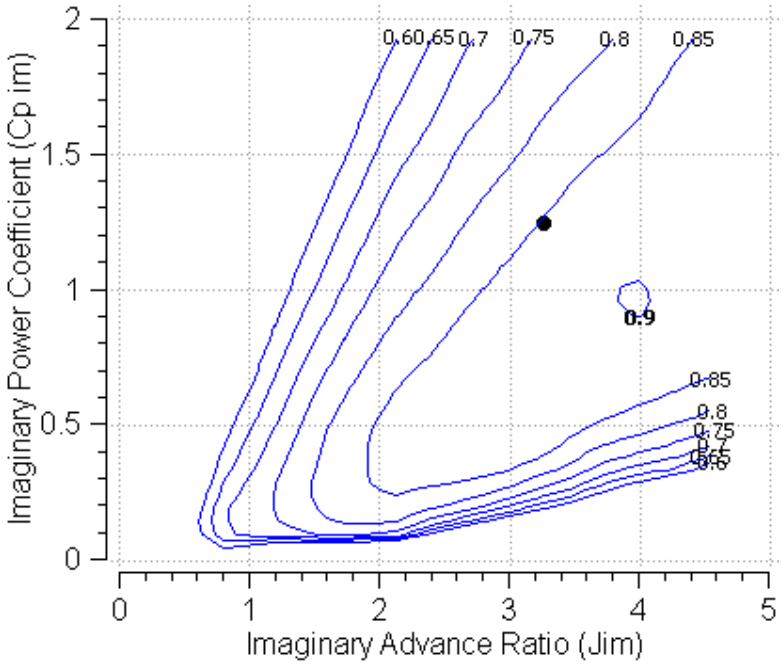

Figure K 7: Rear propeller map